October 1997 • NREL/CP-430-23722

Proceedings of the 1997 U.S. DOE Hydrogen Program Review

May 21-23, 1997
Herndon, Virginia

Sponsored by the
Office of Solar Thermal, Biomass
Power and Hydrogen Technologies
U.S. Department of Energy

National Renewable Energy Laboratory
1617 Cole Boulevard
Golden, Colorado 80401-3393
A national laboratory of the U.S. Department of Energy
Managed by Midwest Research Institute
for the U.S. Department of Energy
under contract No. DE-AC36-83CH10093

Prepared under Task No. HY711010

October 1997

NOTICE

Forward

The Department of Energy's Office of Utility Technologies Hydrogen Program supports a diverse portfolio of research and development (R&D), technology validation, and analysis and outreach. The R&D supported by the DOE Hydrogen Program focuses on near-term transitional strategies involving fossil fuels, and on the exploration of long-term, high-risk, renewable and sustainable concepts that have the potential to address future energy needs. While production of hydrogen has dominated the portfolio, storage is recognized as an important component of any system, including transportation, utility, and industrial applications. Efforts in the development of efficient end-use applications include hydrogen-fueled internal combustion engines, hydrogen burners, PEM fuel cells, and reversible fuel cells. In support of hydrogen systems, research is also conducted on safety and detection.

Technology validation efforts include the upcoming results of the FY96 competitive solicitation issued to begin the integration of hydrogen "components" into hydrogen systems. Focused on industry as the prime mover, respondents were asked to propose hydrogen systems that had the potential to be commercially successful in a relatively modest period of time. From the 22 respondents, nine were selected for awards in Phase I, which is focused on the development of business and research plans. A sampling of the successful proposals includes the evaluation of a system consisting of photovoltaics and electrolysis for the production of hydrogen with metal hydride storage, for near-term and niche market applications; the evaluation of the commercial and technical feasibility of supercritical water gasification of biomass and wastes; the evaluation of small industrial fuel cell vehicles with on-board hydrogen storage; the evaluation of high-value niche markets such as remote fuel cell power systems; and the evaluation of a home garage filling station or hydrogen vehicle refueling appliance. Because of the timing of these awards, the results will be presented at the 1998 Annual Peer Review.

Analysis and outreach are important components of the Hydrogen Program. Analysis provides programmatic guidance to individual projects and to the overall portfolio. Industry and public outreach are important to maintaining a strong stakeholder base, and to providing information on hydrogen energy systems.

The Program has incorporated an evaluation process that includes the input of outside reviewers, an evaluation of the project "fit" into programmatic goals and objectives, and other measures such as international recognition, generation of intellectual property, industry interest, and publication history. For the 1997 Annual Peer Review, six specialized review teams were established to provide expert commentary on progress for the 36 research and 5 analysis projects receiving funding in FY97. Indicative of the growing interest in hydrogen energy, researchers were given an opportunity to submit their technical papers to the peer-reviewed technical journal Energy & Fuels, for their special edition on hydrogen.

These Proceedings contain annual technical reports for 31 of the 41 projects reviewed at the 1997 Annual Peer Review, and serve as a reference on the status of hydrogen technologies support by the DOE Hydrogen Program. The special edition of Energy & Fuels will contain the remaining10 reports that were accepted for publication. The abstracts for these 10 reports are also included in these proceedings.

Catherine E. Gregoire Padró
Hydrogen Program Manager
National Renewable Energy Laboratory
Golden, Colorado

TABLE OF CONTENTS

Biological Systems

Electrochemical Systems

---

[*] This paper will appear in a special hydrogen edition of Energy & Fuels.

Thermal Systems

Storage and Separation Systems

---

* This paper will appear in a special hydrogen edition of Energy & Fuels.

* This paper will appear in a special hydrogen edition of Energy & Fuels.

Systems Analysis

[*] This paper will appear in a special hydrogen edition of Energy & Fuels.

HYDROGEN AND OXYGEN PRODUCTION IN MUTANT FUD26 OF *CHLAMYDOMONAS REINHARDTII*

E. Greenbaum, J. W. Lee, S. L. Blankinship, and C. V. Tevault
Oak Ridge National Laboratory
P. O. Box 2008
Oak Ridge, TN 37831-6194 USA

Abstract

Absolute measurements of photosynthetic reactions and associated parameters in *Chlamydomonas reinhardtii* mutant Fud26 have been performed and compared with predictions of the Z-scheme. Whereas the stoichiometric ratio of PS I to PS II is 0.081:1, the ratio of hydrogen to oxygen of individual single-turnover saturating flashes is approximately 1:1. This ratio is too large to be explained by a "leaky" Z-scheme model proposed by Boichenko [*Photosyn. Res.* **47**, 291-292 (1996)] in which 10-20 PS IIs operating in parallel send their reducing equivalents to a single PS I. In addition, comparative measurements of oxygen evolution coupled to carbon dioxide reduction in mutant Fud26 and wild-type *C. reinhardtii* 137c have been performed under light-limiting conditions. The rate of oxygen evolution in Fud26 was about 50% of the corresponding rate in wild-type. In order to account for these data with Boichenko's model, the antenna size of PS I in mutant Fud26 would have to be 4-5 times greater than the corresponding PS II antenna size. However, this is not the case. The PS I antenna is ≈150 Chl whereas that for PS II it is ≈320 Chl. The relative cross-sections for the hydrogen and oxygen photochemical reactions in mutant Fud26 are approximately equal. Comparative measurements of P700 from thylakoid membranes with intact algae indicated that P700 in mutant Fud26 is not degraded during thylakoid preparation. We have observed photosynthetic reactions in mutant Fud26 conflict with the Z-scheme. In nature these reactions may not occur at all or they may operate with varying amplitude simultaneously with the Z-scheme.

Introduction

It has recently been reported (Greenbaum *et al.*, 1995; Lee *et al.*, 1996) that mutants of the green alga *Chlamydomonas reinhardtii* that lack detectable levels of the Photosystem I (PS I) reaction center are capable of sustained simultaneous photoevolution of H_2 and O_2, CO_2 reduction and photoautrophic growth. The data indicated that under some circumstances PS II alone is sufficient

to generate reductant capable of driving hydrogen evolution and CO_2 fixation, not of course that the Z-scheme is universally wrong. Although the absence of PS I in mutants B4 and F8 for the data reported in the references was confirmed by physical, biochemical and genetic techniques, subsequent analyses in our own laboratories as well as those of colleagues to whom we have sent the mutants indicate that there is variability in the PS I content of the cultures depending on growth conditions. While some strains retain undetectable levels of P700, others contain variable (0-20%) amounts of wild-type P700. This property of mutants B4 and F8 has been communicated to the journals in which the results were initially published (Greenbaum *et al*, 1997). The fact that mutants B4 and F8 can synthesize fluctuating levels of PS I naturally makes one skeptical of the interpretation advanced in the above references that PS II can generate reductant that can drive hydrogen evolution and carbon dioxide fixation.

In his analysis of this work, Boichenko (1996) postulated a "leaky" model of the Z-scheme, illustrated schematically in Fig. 1. According to this model, under continuous high-intensity light PS I turns over with sufficient rapidity to accommodate reductant generated by multiple PS IIs thereby preserving a key requirement of the Z-scheme: Only PS I is capable of generating low-potential reductant that can be used for hydrogen evolution or carbon dioxide fixation. Based on comparative rates of photosynthesis with wild-type *Chlamydomonas reinhardtii* and known properties of PS I antenna size we felt that our earlier results were not consistent with this model even if PS I were present, but undetectable. Additional data confirming this point are now presented on the basis of direct measurement of absolute single-turnover saturating flash yields of hydrogen and oxygen production in mutant Fud26 as well as photosynthesis measurements under light-limiting conditions (O_2 evolution with CO_2 as electron acceptor).

Materials and Methods

Algae and Growth Conditions

Fud26, obtained from L. Mets, is an acetate-requiring mutant deficient in CP I that was isolated after 5-fluorodeoxyuridine mutagenesis and metronidazole selection, as first described by Bennoun *et al.* (1978). The mutation was shown by Girard-Bascou, (Girard-Bascou, 1987; Girard-Bascou *et al.*, 1987) to affect the psaB gene. This mutation is a 4 base pair deletion near the 3' end of the psaB gene. The resulting frame shift results in production of a truncated protein. For the experiments reported in this work, the mutant was grown on an acetate-containing minimal medium in 125 ml flasks on rotary shakers. Ceiling illumination from cool-white fluorescent lamps at 20 $\mu E/m^2/sec$ was used as the light source. Cultures of wild-type *C. reinhardtii* 137c were similarly grown for comparative measurements. The algae were subjected to two-hours dark respiration to deplete carbon reserves and minimize dark hydrogen production prior to light-driven hydrogen production measurements.

Hydrogen and Oxygen Measurement

The apparatus used for absolute measurement of single-turnover saturating hydrogen and oxygen flash yields is illustrated schematically in Fig. 2. The apparatus is comprised of a rapid flow system in which the electrolytic calibration cell, photoreaction chamber, connecting tubing, drying chamber

and sensor are connected in series. The sensor is an Ametek Model BT II high-temperature zirconium oxide fuel cell that can be used to measure either hydrogen or oxygen. The sensing element is a ZrO_2 ceramic membrane that operates as a reversible oxygen electrode at 735 C. The membrane, whose interior and exterior surfaces are coated with a thin film of platinum, is specifically permeable to O^{2-} ions. The reference side of the membrane is exposed to oxygen in room air. The sample side was connected to a UHP helium carrier flow and served the dual function of establishing anaerobiosis in the flow system and transporting photoproduced gas from either the calibration or photoreaction cell to the high temperature electrode. A combination concentric feed-through, delivery tube, vent, and O-ring seal at the base of the sensor transported the helium carrier (plus hydrogen or oxygen) to the interior of the closed end tubular ZrO_2 chamber and vented it to the atmosphere.

Calibration

Calibration of the apparatus was achieved with the in-line electrolysis cell indicated in Fig. 2. The calibration cell contained two electrodes, cathode and anode, only one of which was in the flow stream--depending on the polarity of the Keithley Model 220 Programmable Current Source that was connected to the electrodes. The other electrode was in a side arm separated from the flow stream by a fine frit disc that prevented gas produced by this electrode from entering the flow stream. The electrodes were ionically connected by a 1 mM KOH solution. This apparatus can be used for measurement of absolute bursts of hydrogen or oxygen from algae. Typically, calibration pulses of 25, 50, 75, and 100 $\mu A \times 1$ sec of hydrogen or oxygen were injected into the flow stream. *In situ* calibration curves were constructed for each experiment by integrating the area under each peak and converting it to an absolute amount hydrogen or oxygen using Faraday's Law of Electrochemical Equivalence. Deflections for hydrogen and oxygen are in opposite directions. When hydrogen enters the cell, it is burned with molecular oxygen at the inner electrode surface and decreases the oxygen partial pressure, causing an increase in cell voltage. Correspondingly, when oxygen enters the cell it increases the oxygen partial pressure causing a decrease in cell voltage. The cell has a Nernstian response that is proportional to the logarithm of the ratio of partial pressures of oxygen on either side of the ceramic membrane. The variation in response to each pulse based on repeated calibration injections was less than $\pm$ 10%. The response time of the apparatus to detect and resolve a single burst is about 10 seconds. The time depends on the flow rate of the helium carrier and the forward void volume of the flow system.

Light Sources, "Double Hitting" and Optical Paths

Single-turnover saturating flashes were achieved with a bank of eight concentric GenRad Model 1539 xenon stroboscopic flash lamps placed adjacent to the photoreaction chamber containing the algae as indicated in Fig. 2. The chamber was wrapped with several layers of yellow cellulose acetate film that attenuated most of the UV light. The lamps were triggered with a variable digital delay generator, Berkeley Nucleonics Model 7010. A group of four alternating lamps was connected to the prompt output of the 7010 whereas the second group of four was connected to the delayed output. The Model 1539 has three settings, high, medium, and low. It was determined experimentally that four lamps on high setting (see Fig. 5b) gave $\approx$95% saturation. The concentrations of chlorophyll used for the flash experiments were typically 10-15 μg chl/ml in a 20

ml volume. The rapid flow caused high turbulence in the algal suspension creating efficient optical paths for penetration of the reaction volume. The time profile of the flashes were measured with an EG&G Lite-Mike Model 560B which has a rise time of 5 ns and a fall time of 20 ns. Times profiles of the flashes were recorded with a Hewlett-Packard Model 54501A digitizing oscilloscope with a 100 MHz bandwidth. As explained in further detail in the Results and Discussion section, "double hitting" i.e., multiple turnovers of the hydrogen producing reactions within the flash envelope, cannot account for the measured absolute hydrogen yields and hydrogen to oxygen ratios. This was demonstrated by control experiments that deliberately broadened the flash envelope yet produced a null effect on hydrogen yield as the envelope was systematically broadened starting from the intrinsic 3 μsec full width at half maximum (FWHM) and incrementally introducing delays between the first and second groups of flash lamps.

Results and Discussion

Single-Turnover Hydrogen and Oxygen Flash Yields

Mutant Fud26 has a measured (Melis unpublished) ratio of PS I:PS II = 0.08:1. For pulsed light-driven H_2 or O_2 production in which the photochemistries of PS I and PS II are isolated, the leaky Z-scheme model of Fig. 1 predicts a single-turnover flash yield ratio of H_2:O_2=0.16:1 whereas the measured value, indicated in Fig. 3, is approximately 1. Eight such experiments with mutant Fud26 were performed of which Fig. 3 is representative. The ratio calculation is based on the Joliot (Joliot *et al.* 1969) measurement of oxygen oscillations of periodicity four and the (Kok *et al.*, 1970) model of oxygen evolution in which each PS II reaction center acts as an independent unit in the oxidation of water. According to this model oxygen evolution is a four-step process in which each S-state precursor is more oxidized than its predecessor by one oxidizing equivalent. Upon accumulation of four equivalents, state S_4 releases molecular oxygen on the timescale of 1 ms and resets the cycle. The damped oscillations and individual oxygen flash yields beyond flash number 10 in Fig. 3 are interpreted as the number of PS II reaction centers that are in state S_4 at the time of the flash. Therefore, O_2/flash = ¼ × PS II where PS II is the total amount of functional Photosystem II in the sample and O_2/flash is the total amount of oxygen produced per flash . It has been shown (Greenbaum, 1977) that the hydrogen analog of the classic Joliot oxygen flash experiment has a qualitatively different response pattern. As can be seen from the hydrogen data of Fig. 3, there are no hydrogen oscillations; the first flash is at the steady-state yield. Therefore, according to the Z-scheme, H_2/flash = ½ × PS I. It follows that H_2:O_2/flash = 2 × (PS I:PS II). This relationship is valid because the photochemistries of PS I and PS II for the experiments in Fig. 3 have been isolated and operate independently of each other. The hydrogen flash yields were done under anaerobic conditions with flashes spaced at 30 sec intervals; the intermediate S-states fully deactivate under these conditions. No oxygen is evolved per flash. The oxygen flash yields were done under the same anaerobic conditions in the presence of the oxidant and electron acceptor *p*-benzoquinone. As previously shown (Greenbaum and Mauzerall 1977) the presence of chemical oxidants enhances and activates the S-states. They also totally inhibit hydrogenase. Therefore, the experiments on the H_2:O_2 ratio taken in combination with the measurement of the PS I:PS II ratio provide a direct test of the model of Fig. 1. It can be seen in Fig. 3 that the measured ratio is H_2:O_2 ≈1. This value is not necessarily mechanistically significant and is lower than would be expected if all reductant generated by PS II through water oxidation were expressed as molecular hydrogen. However, the reducing conditions *required* for the H_2 measurement may result in lower quantum yields due to closed PS II traps.

In order to attribute these results to multiple turnovers of PS I within the flash profile, thereby preserving the model of Fig. 1, the hydrogen evolution reaction would have to turnover about 6 times within the flash envelope. Control experiments using double flash delayed techniques indicated that the measured ratio of H_2 to O_2 is not an artefact of multiple H_2 turnovers within the flash envelope. This was demonstrated by deliberately broadening the flash envelope and observing a null effect as the delay of the second flash spanned the envelope of the first. The technique is illustrated in Fig. 4. Fig. 4a illustrates the time profile of 8 stroboscopic flash lamps triggered simultaneously. The full width at half maximum for this group of lamps is 3 μsec. Figure 4b illustrates the variable delay, Δt, that can be introduced between the two groups of flashes. For example, in Fig. 4b, $\Delta t = 6$ μsec. The delay of the second flash with respect to the first can be varied at will. These experiments gave no indication of rapid multiple turnovers of hydrogen production occurring within the envelope of the flash lamp.

Although the samples of PS I-deficient mutants B4 and F8 used in previous work contained no detectable PS I, it is now known, as stated above, that these mutants may synthesize small amounts of PS I under some circumstances. However, as the data of Fig. 3 with mutant Fud26 clearly illustrate, the presence of detectable levels of PS I in this strain is not sufficient to account for the measured hydrogen flash yields if one assumes that only electrons from PS I can drive this reduction. Mutants B4 and F8 do not work well in this rapid flow apparatus, they tend to grow in clumps and are propelled out of the photoreaction chamber. These properties also make them unsuitable for studies with the bare platinum electrode technique.

Photosynthesis and Antenna Size Measurements

A similar conclusion may be drawn from the data of Fig. 5. In Fig. 5a comparative measurements of rates O_2 evolution coupled to CO_2 reduction for wild-type *Chlamydomonas reinhardtii* (grown under cool-white fluorescent lamps, PS I:PS II=0.7:1) and mutant Fud26 (PS I:PS II=0.08:1) are presented. It can be seen in Fig. 5a that under light-limiting conditions the rate of O_2 evolution in mutant Fud26 is approximately 50% that of 137c. In principle, the leaky version of the Z-scheme illustrated in Fig. 1 could account for this data if it is assumed that the antenna size of PS I in Fud26 is about 4.5 times that of its associated PS II. However, it is not. The PS I antenna is ≈150 Chls whereas that of PS II is ≈320 Chls. Put another way, the antenna size of PS I in mutant Fud26 is too small by a factor of 9 to explain the data with the model of Fig. 1.

In Fig. 5b, pulsed light saturation curves of O_2 and H_2 are presented. Following the logic of the Z-scheme, that only PS I that can photoevolve H_2 and correspondingly that only PS II can photoevolve O_2, the data of Fig. 5b provide a measurement of the *relative* antenna sizes of the photochemical hydrogen and oxygen reactions. Multiple experiments of this type indicated that the shapes of the pulsed light saturation curves can vary in overlap between ±15-20%. But the antenna size of H_2 photoproduction is certainly not 4.5 times that of O_2 photoproduction.

An *ad hoc* explanation for the Fud26 data is that P700 is really present at levels much greater than the PS I:PS II = 0.08: ratio suggests because of a hypothesized instability of P700 in Fud26 thylakoids that is absent in wild-type thylakoids. However, this hypothesis can be excluded because

P700 in whole cells of Fud26 had a relative value of 14.2% of P700 in intact wild-type *Chlamydomonas* (Owens *et al.* unpublished). In wild-type the measured ratio is PS I:PS II = 0.7. Therefore, normalizing the PS I content in Fud26 to the PS II content of wild-type we get the value PS I:PS II = 0.142 × 0.7 = 9.9%. This compares favorably with the 8.1% value that is obtained when PS I in Fud26 is normalized to its own PS II content. It can therefore be assumed that measurement of P700 in Fud26 thylakoids is not problematical.

The data indicate that an alternate photosynthetic pathway exits in which a small amount of PS I is necessary for CO_2 fixation, but not always in the role assigned to it by the Z-scheme. That is, some of the photoreductant generated by PS II may be used for H_2 production or CO_2 reduction without passing through PS I. As the data of Figs. 3 and 5 clearly illustrate, there is simply not enough PS I available to do the job. In addition to its Z-scheme role, PS I may provide ATP by cyclic electron flow (required for CO_2 fixation but not H_2 photoproduction) with a substantial fraction of the reducing equivalents generated directly by PS II in mutant Fud26. In the natural plant environment this mode of photosynthesis, "PS II photosynthesis," may not occur at all or it may operate with varying amplitude simultaneously with the Z-scheme.

Acknowledgments

The authors thank A. Melis for performing the measurements of photosystem content and antenna sizes in mutant Fud26. They also thank T. G. Owens, I. Vassieliev, and J. Golbeck for performing *in vivo* measurements of P700 and L. Mets for providing cultures of mutant Fud26. This work was supported by the Department of Energy Hydrogen Program. Oak Ridge National Laboratory is Managed by Lockheed Martin Energy Research Corp. for the U.S. Department of Energy under contract DE-AC05-96OR22464.

References

Bennoun, P., A. Masson, R. Piccioni, and N.-H. Chua. 1978. "Uniparental Mutants of *Chlaydomonas reinhardtii* Defective in Photosynthesis." *Photosyn. Res.*, 47:291-292.

Boichenko, V. A. 1996. "Can Photosystem I be a Photogenerator of Low Potential Reductant for CO_2 Fixation and H_2 Photoevolution?"

Girard-Bascou, J. 1987. "Mutations in Four Chloroplast Loci of *Chlamydomonas reinhardtii* Affecting the Photosystem I Reaction Centers." *Curr. Genet.*, 12:483-488.

Girard-Bascou, J., Y. Choquet, M. Schneider, M. Delosme, and M. Dron. 1987. "Characterization of a Chloroplast Mutation in the psaA2 Gene of *Chlamydomonas reinhardtii*." *Curr. Genet.*, 12:489-495.

Greenbaum, E., J. W. Lee, C. V. Tevault, S. L. Blankinship, and L. J. Mets. 1995. "CO_2 Fixation and Photoevolution of H_2 and O_2 in a Mutant of *Chlamydomonas* Lacking Photosystem I." *Nature*, 376:438-411.

Greenbaum, E., J. W. Lee, C. V. Tevault, S. L. Blankinship, L. J. Mets, and T. G. Owens. "Photosystem I Measurement in Mutants B4 and F8 of *C. reinhardtii*," submitted to *Nature* and *Science*, June 1997.

Greenbaum, E. 1977. "The Photosynthetic Unit of Hydrogen Evolution." *Science*, 196:878-879.

Greenbaum, E., and D. C. Mauzerall. 1977. "Oxygen Yield per flash of *Chlorella* Coupled to Chemical Oxidants under Anaerobic Conditions." *Photochem. Photobiol.*, 23:369-372.

Joliot, P., G. Barbieri, and R. Chaubaud. 1969. "Un Nouveau Modèle des Centres Photochimique du Systèm II." *Photochem. Photobiol.*, 10:309-329.

Kok, B., B. Forbush, and M. McGloin. 1970. "Cooperation of Charges in Photosynthetic O_2 Evolution-I. A Linear Four Step Mechanism." *Photochem. Photobiol.*, 11:457-475.

Lee, J. W., C. V. Tevault, T. G. Owens, and E. Greenbaum. 1996. "Oxygenic Photoautotrophic Growth Without Photosystem I." *Science*, 273:364-367.

Melis, A. Unpublished data. Samples of mutant Fud26 were pelleted, packed in dry ice and shipped by express courier from ORNL to UC Berkeley. Measurements were done within 48 hours of shipment.

Owens, T. G., I. R. Vassiliev, and J. H. Golbeck. Unpublished data.

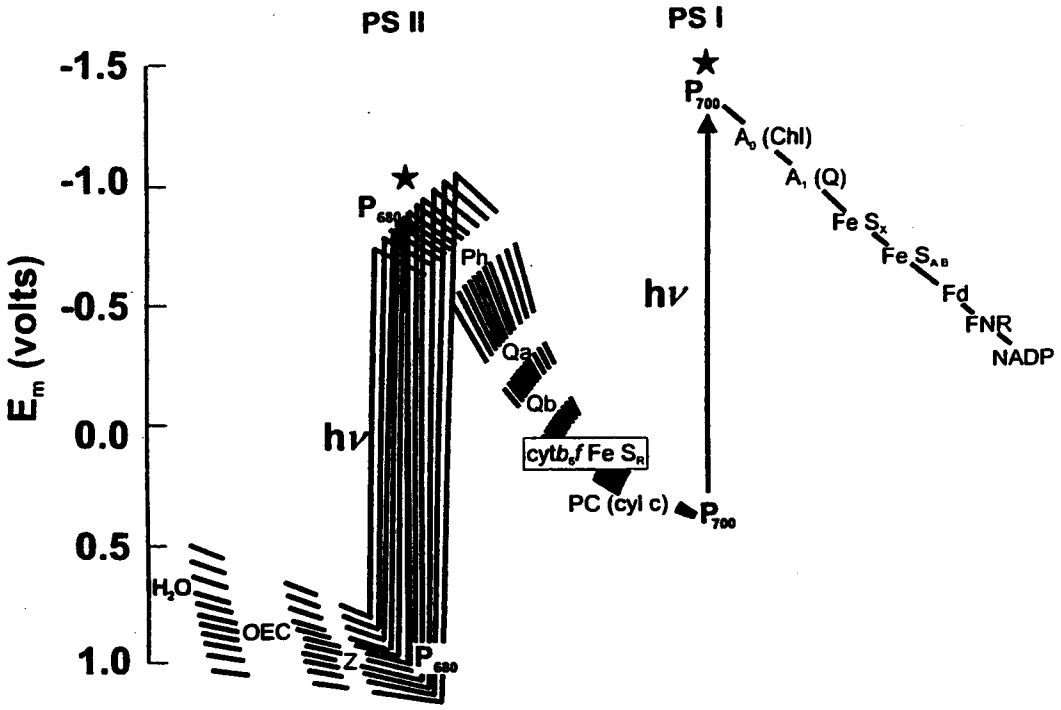

Fig. 1 Illustration of the "leaky" Z-scheme model of photosynthesis.

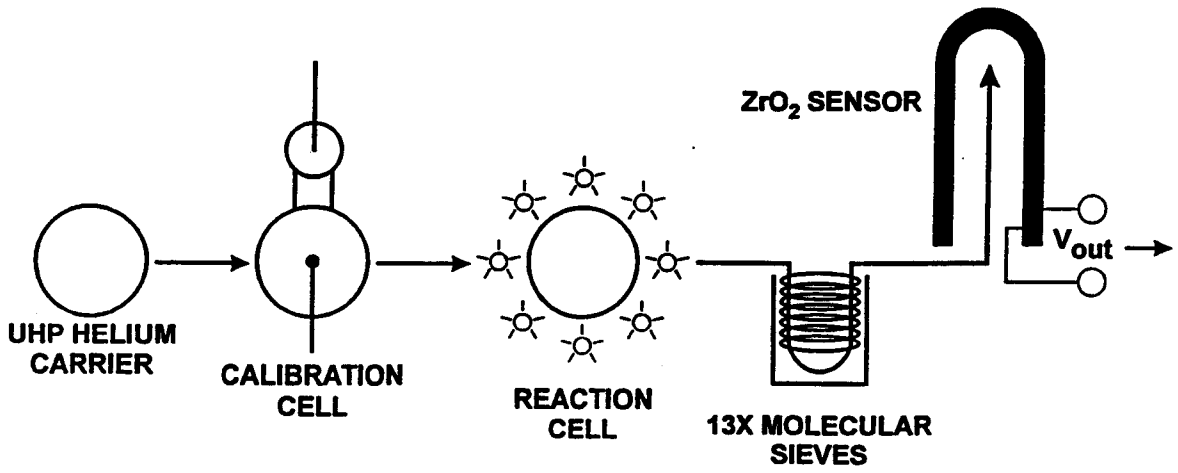

Fig. 2 Schematic illustration of the experimental apparatus used to measure absolute hydrogen and oxygen single-turnover saturating flash yields.

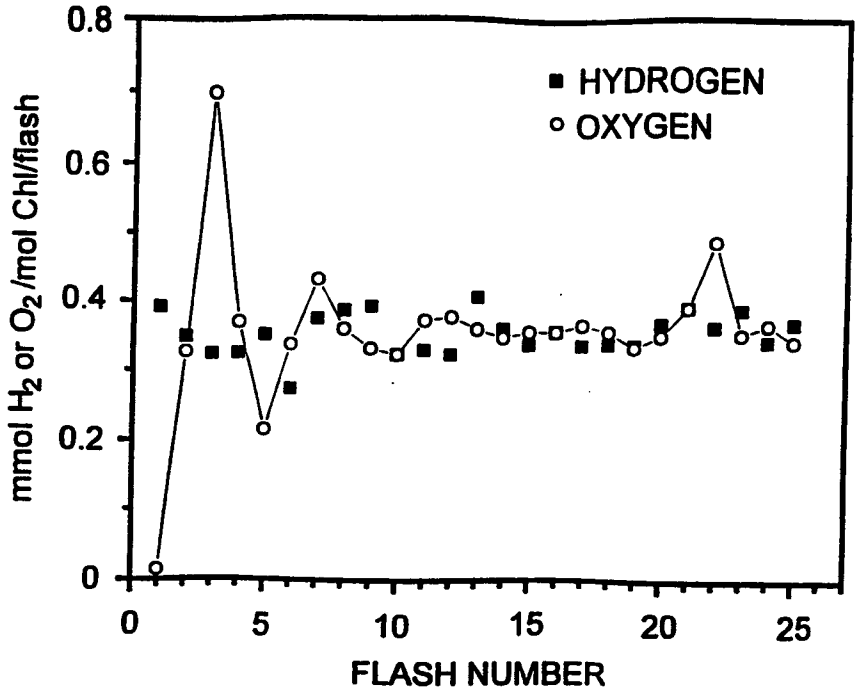

Fig. 3 Absolute flash yields of H_2 and O_2 from single-turnover saturating flashes of light in mutant Fud26. H_2 and O_2 yields were measured in separate experiments on the same algal samples under anaerobic conditions. For O_2 measurement, *p*-benzoquinone was added as the electron acceptor. The gas phase sensor was a ZrO_2 high temperature electrode in a rapid flow apparatus calibrated with an in line electrolysis cell. The light source was a bank of eight concentric Gen Rad 1539 xenon flash lamps triggered simultaneously by a Berkeley Nucleonics Corp. 7010 digital generator.

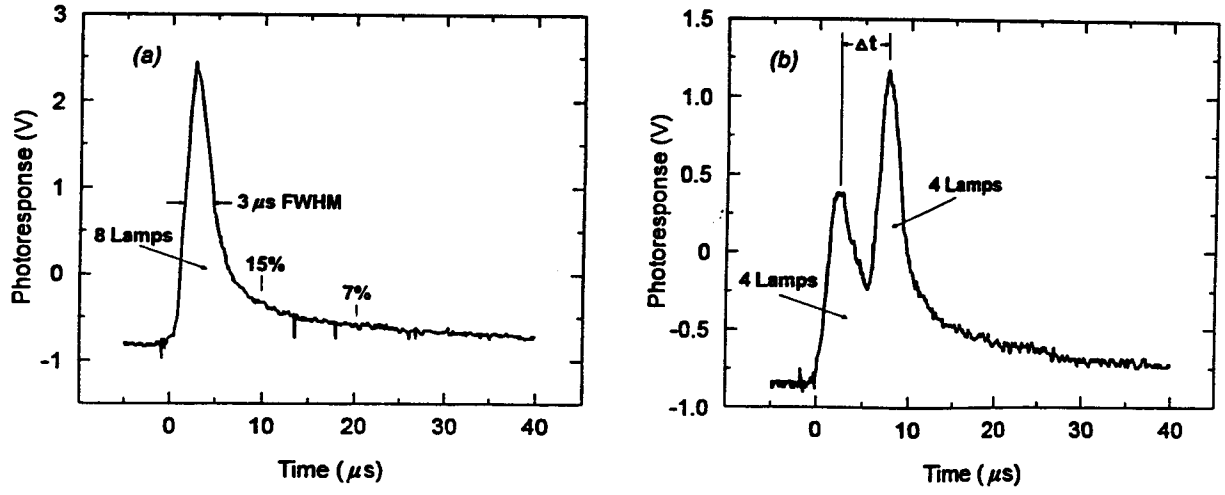

Fig. 4 Systematic study of the hypothesis of "double hitting" i.e. that multiple turnovers of the H_2 reaction occur within the finite envelope of the xenon flash lamp. No increase in H_2/flash was observed as the second flash was swept through the envelope of the first. These control experiments indicated that the flash yield ratios of H_2:O_2 were not an artefact of multiple H_2 turnovers within the flash envelope.

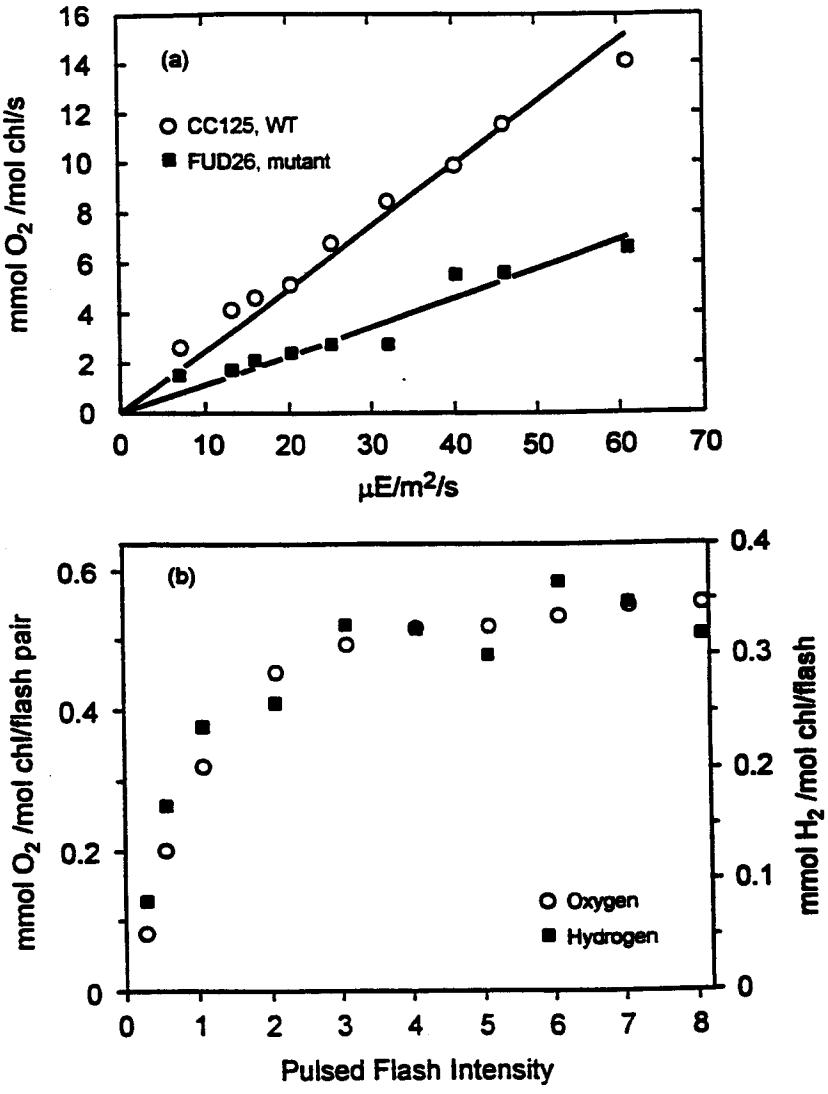

Fig. 5 (a) Comparative measurements of oxygen evolution coupled to CO_2 reduction in wild-type *Chlamydomonas reinhardtii* 137c and mutant Fud 26. (b) Measurement of the relative antenna sizes of PS I and PS II assuming, according to the Z-scheme, that it is only PS I that is capable of light-driven hydrogen production.

DEVELOPMENT OF AN EFFICIENT ALGAL H_2-PRODUCTION SYSTEM

Maria L. Ghirardi, Timothy Flynn, Sergei Markov and Michael Seibert
National Renewable Energy Laboratory, Golden, CO 80401

Abstract

Photosynthetic hydrogen evolution by green algae is catalyzed by a reversible hydrogenase enzyme that is extremely sensitive to inactivation by O_2, a by-product of photosynthetic water oxidation. Oxygen sensitivity has been one of the major barriers to the development of a commercial algal H_2-production system. The objective of our project is to generate O_2-tolerant, H_2-producing mutants from the green alga *Chlamydomonas reinhardtii* to be used in a photobiological water-splitting, H_2-producing system that is cost effective, renewable, scalable and non-polluting.

We have developed two approaches to obtain desired *C. reinhardtii* mutants, based either on the H_2-producing or H_2-uptake activity of the enzyme. The first approach depends on the ability of algal cells to produce H_2 in competition with a drug that, when reduced, releases toxic products. H_2-production selective pressure is applied in the presence of increasing O_2 stress to enrich for O_2-tolerant organisms. The second approach requires that algal cells grow, using H_2 as a source of electrons for CO_2 fixation. Addition of O_2 during the H_2-uptake selects for O_2-tolerant organisms.

Our previous work consisted of developing an assay for simultaneous measurement of H_2 and O_2 production, as well as establishing a reliable way of measuring O_2 tolerance by different algal strains based on estimating an O_2 I_{50} for H_2 evolution. In addition, we investigated the conditions required for application of H_2-production selective pressure. The efficacy of this selection was demonstrated by the isolation of a variant (D5) out of the parental cw15 (cell wall-less) population with an increased O_2 I_{50} for H_2 evolution. Finally, several laboratory-scale photobioreactors were built and tested using a mutant of *Anabaena variabilis* that lacks H_2-uptake activity, as a model system that would mimic an O_2-tolerant algal strain. We were able to demonstrate H_2 production efficiencies of 1-2% and continuous H_2-production capability for 8 months using the cyanobacterial mutant.

Current accomplishments include: (a) application of H_2-production selective pressure to a

mutagenized D5 population, with the resulting isolation of a new mutant (IM6) that exhibits a 470% increase in O_2 I_{50} for H_2 evolution compared to the cw15 parental population; (b) optimization of the H_2-uptake selective pressure approach and isolation of a mixed population of cells with a 50% higher O_2 I_{50} for H_2 evolution than the wild-type (WT) population; (c) development of a screen to rapidly identify H_2-producing mutants (survivors from the above selection pressures) on agar plates; and (d) operation of a photobioreactor containing the above-mentioned *A. variabilis* mutant in a continuous H_2-producing mode for over 18 months. Preliminary results on experiments that may lead to the cloning of the *C. reinhardtii* hydrogenase gene were also reported at the 1997 Hydrogen Program Review meeting and will not be discussed here.

Introduction

Photobiological hydrogen-production represents a potentially cost-effective system for renewable, non-polluting energy production. Green algae, for example, can photoproduce H_2 directly from water using the reversible hydrogenase enzyme. Hydrogenase-catalyzed hydrogen photoproduction, though potentially very efficient, has two major R&D challenges that currently limit commercial applications. The first is the low light saturation level of algal photosynthesis, and the second is the inherent O_2 sensitivity of the algal hydrogenase enzyme. NREL has focused on the second problem, while other laboratories have been addressing the first.

We have developed two types of selective pressures to isolate mutants from the green alga *Chlamydomonas reinhardtii* that produce H_2 in the presence of O_2. The two selective pressures are based on the reversible reactions catalyzed by the hydrogenase enzyme, i.e., H_2-production and H_2-uptake activities. H_2-production selective pressure depends on the competitive relationship between metronidazole and hydrogenase for electrons from photosynthetically-reduced ferredoxin (Fig. 1A). The procedure consists of a short (20-min) aerobic treatment of suspended algal cells with metronidazole in the light in the absence of CO_2. Under these conditions, wild-type (WT) cells will generate a reduced intermediate of metronidazole that produces toxic O_2 species that will kill the cell. However, if the cell has an alternative pathway for electron flow from ferredoxin (i.e., to an O_2-tolerant hydrogenase), it will survive. We have demonstrated that the number of survivors following a selective treatment depends on the metronidazole concentration, light intensity, state of activity of the hydrogenase (induced vs. non-induced), and the amount of added O_2 (Ghirardi et al., 1997). We also demonstrated the efficacy of the selective treatment by isolating a variant (which we call D5) of the cw15 (cell wall-less) parental population with a 330% higher O_2 I_{50} for H_2 evolution. However, the selection pressure is not very specific, and yields a large number of antenna and electron transport mutants with reduced rates of photosynthetic electron transport.

The second selective pressure that we are using is based on the H_2-uptake activity of the hydrogenase and was first examined by McBride et al. (1977) It involves incubating a suspension of algal cells under low light in the presence of H_2, CO_2, and DCMU (to block O_2 evolution). Under these conditions, algal cells must use H_2 as the sole source of reductant to fix CO_2 and grow (Fig. 1B). Addition of O_2 to the system selects for cells containing an O_2-tolerant hydrogenase since they should survive the pressure. The application of H_2-uptake (or photoreductive) pressure to *C. reinhardtii* cells yielded mutants that were able to evolve H_2 under higher O_2 concentrations. However, the mutants were also able to consume H_2 in the dark, in the presence of higher concentrations of O_2 (McBride et al., 1977) which may not be a desirable characteristic in a commercial photobioreactor. Despite this problem, the H_2-uptake selection has an important advantage over the H_2-production selective pressure. Namely, it should not select for any other types of mutants as is the case with the H_2-production pressure. For this reason, we have applied both types of selection approaches to populations of *C. reinhardtii*, and analyzed the characteristics of the survivors, in order to devise the best technique (or combination of techniques) to obtain competent, fully O_2-tolerant, H_2-producing mutants.

Results and Discussion

Basic Microbiology

We encountered several basic microbiological questions during our work this past year. These questions were related to the physiological H_2 evolution pathways in *C. reinhardtii*, to the ability of the cells to metabolize glucose, and to the sensitivity of the cell wall-less cw15 strain to mutagens. By providing answers to these questions, we were able to improve on the H_2-uptake selection approach, and to establish basic parameters for the subsequent mutagenesis work described below.

There are two possible pathways for hydrogen evolution in *C. reinhardtii*, depending on whether the cells are grown in the absence or presence of acetate. In the first case, all reductants for H_2 evolution originate from light-induced H_2O oxidation, and the reaction is totally sensitive to DCMU, an inhibitor of Photosystem II (PSII) activity. Exogenous acetate and perhaps other internally stored molecules may feed electrons to the photosynthetic electron transport chain at the level of plastoquinone, an intermediate between the two photosystems, PSI and PSII. In this instance, one should be able to detect light-induced H_2 evolution that is not inhibited by DCMU, but that is sensitive to the cytochrome b_6/f complex-inhibitor DBMIB (Maione & Gibbs, 1986). Table 1 shows that, indeed, 20% of the H_2 photoevolved by *C. reinhardtii* is insensitive to DCMU and must originate from the fermentation of storage material accumulated by the cells during growth, even when the cells are grown photoautotrophically. These results have a direct bearing on photoreductive selection, and they are the reason why we introduced a dark aerobic starvation step in our protocol, in order to ensure that the cells were depleted of all storage materials before imposition of the selective pressure (see below).

Table 1. Effect of electron transport inhibitors on algal hydrogen photoproduction.

Initial rate of H_2 evolution (μmoles · mg Chl^{-1} · h^{-1})	Inhibitor	% of control
41.21	none	100
43.51	none	100
37.65	none	100
6.53	50 μM DCMU	16
7.86	100 μM DCMU	19
8.20	400 μM DCMU	20
0	10 μM DBMIB	0
0	50 μM DBMIB	0

In order to anaerobically induce the reversible hydrogenase, we incubate algal cells for 4 hs in phosphate buffer and store them overnight at 4 °C, in the presence of an O_2-scavenging system that consists of glucose, catalase, and glucose oxidase (Ghirardi et al., 1997). *Chlamydomonas reinhardtii* is not thought to metabolize exogenously-added glucose (Harris, 1989). However, we needed to be sure that this information was reliable and that the algal cells were not fermenting glucose during the anaerobic induction period (thus storing reductants that could contribute to PSI-mediated H_2 evolution). Algal cells were grown three ways: photoautotrophically (minimal salt medium), or photoheterotrophically in the presence of either 15 mM sodium acetate or 5 mM added glucose. Table 2 shows the effect of the photosynthetic inhibitor DCMU on cell growth, estimated from turbidimetric assays. It is clear that treatment with DCMU inhibits all (or nearly all) photoautotrophic growth due to inhibition of H_2O oxidation (column 2). Addition of acetate to the growth medium (column 3) supported higher rates of growth, which were only partially inhibited by DCMU, indicating that acetate is taken up and metabolized by the organism. Substitution of glucose for acetate (coumn 4), on the other hand, resulted in lower rates of growth that were completely inhibited by DCMU. This confirms that exogenous glucose cannot support algal growth.

Table 2. Effect of DCMU and organic substrates on the growth of wild type *C. reinhardtii* cells in the light for four days. Growth was measured by the turbidimetric assay of the culture OD at 750 nm (initial OD = 0.05). Minimal salts, minimal salts plus 15 mM sodium acetate, or minimal salts plus 5 mM glucose were used in the growth media. Values in parentheses are % of no DCMU controls.

DCMU (μM)	Salts	Salts and Acetate	Salts and Glucose
0	1.33 (100)	2.5 (100)	1.33 (100)
1	0.11 (8.3)	0.99 (40)	0.10 (7.5)
3	0.04 (3.0)	0.90 (36)	-
10	0.03 (2.3)	0.80 (32)	0.03 (2.3)
30	0.03 (2.3)	0.75 (30)	0.03 (2.3)

The third item that we investigated was the sensitivity of algae to a mutagen. The application of selective pressures to isolate O_2-tolerant mutants of *C. reinhardtii* requires pre-treatment of algal cells with a mutagen in order to induce random mutations. We have chosen nitrosoguanidine as our mutagen due to its ability to induce single-point mutations in algae (McBride et al., 1977; Harris, 1989). Figure 2A is a titration of the killing ability of nitrosoguanidine during a 45-min incubation in the dark. From the plotted curves it is possible to calculate an LD_{50} for the WT and the D5 variant of cw15. These values are approximately 8 and 1 μg/ml. It is interesting to note that the lack of a cell wall in the D5 variant increases its sensitivity to nitrosoguanidine. Figure 2B is a semi-logarithmic plot of the effect of 1 μg/ml nitrosoguanidine as a function of time of incubation, using the D5 variant. The results show that an incubation of about 30-40 min will kill 50% of the D5 cells. We subsequently used a 30-min treatment with 1 μg/ml nitrosoguanidine to mutagenize cell wall-less

and WT algae before application of the selective pressures.

H_2-Production Selective Pressure

Our protocol for isolation of O_2-tolerant, H_2-producing mutants of *C. reinhardtii* calls for the application of the H_2-production selective pressure under increasing concentrations of O_2 in order to select for organisms with increasingly higher tolerance to O_2. Last year we successfully isolated the D5 variant of *C. reinhardtii* with higher O_2 I_{50} for H_2 evolution by application of the H_2-production pressure to a parental population of the cw15 strain exposed to 2.8% O_2. We have sebsequently mutagenized suspensions of D5 cells with nitrosoguanidine (30-min treatment in the dark with 1 μg/ml nitrosoguanidine, which should kill about 50% of the algal cells; see Fig. 2), incubated them in the light for 2 days to allow chromosome segregation and mutation expression, and treated the populations with 58 mM metronidazole (this time under 5% O_2) in the light for 20 min as described previously (Ghirardi et al., 1997). The suspended cells were then washed with buffer and plated on minimal agar. Survivors were isolated after 3 weeks of photoautotrophic growth, transferred to liquid medium, anaerobically induced, and tested for O_2 sensitivity of H_2 evolution. Figure 3 shows that one of the surviving mutants, IM6, had an O_2 I_{50} that was 40% higher than that of the parental D5 (Seibert et al., in press). Overall, we increased the O_2 tolerance of the initial cw15 population by almost 470% with two applications of the selective pressure, and confirmed the suitability of the selection procedure for isolating more tolerant mutants. However, we are currently limited by the amount of time that it takes to screen each survivor for tolerance to O_2 and by the non-specificity of the selective procedure. This issue will be addressed in more detail below.

H_2-Uptake Selective Pressure

H_2-uptake selective pressure of McBride et al. (1977) was optimized. The procedure involves a number of steps: (a) mutagenesis for 30 min as described above; (b) growth in the light for 2-4 days to allow chromosome segregation and expression of the mutations; (c) dark aerobic starvation to deplete internal storage reserves; and (d) application of the selective pressure in the presence of O_2 for 5-7 days to eliminate WT organisms.

After optimization, the selective pressure was applied to a population of mutagenized WT cells. Mutagenesis was done with 1 μg/ml nitrosoguanidine for 30 min, which yielded a 70% survival rate. The mutagenized population was then placed under photoreductive selection pressure at 10% O_2. The survivors from the selective pressure were not plated but pooled together and assayed for O_2 sensitivity of H_2 evolution. Figure 4 shows that the O_2 I_{50} of the mixed survivor population increased by about 50% over that of the parental WT strain, confirming the efficacy of the selective pressure. However, as was the case with the survivors from H_2-production selective pressure, the assay for O_2 sensitivity is very time-consuming and has been the limiting factor in the identification of better mutants.

Screening

As mentioned above, our progress has been limited by the lack of a fast screen for H_2-producing mutants. Dave Benson at NREL has developed a very sensitive chemochromic film as part of a H_2

sensor system for transportation vehicles (Benson et al., 1996) under the DOE Hydrogen Program. We worked in collaboration with Dave Benson's group to adapt this WO_3 film for detection of H_2-production by single algal colonies on agar plates. Preliminary results indicate that the film is sensitive to a few nanomoles of H_2. In order to use the film to detect H_2 evolution by algal colonies, we placed the chemochromic film on top of the plated algal colonies. The algal colonies were first covered by a piece of filter paper to avoid adsorption of the cells onto the film. The system was illuminated from the bottom for about 3 min with incandescent light to initiate H_2 evolution. Figure 5 presents our initial results. The first panel (A) shows an agar plate containing algal colonies covered with filter paper and the chemochromic film; a grid is superimposed onto the H_2-sensing film. Panel B shows the same system during an illumination period which causes the colonies to produce H_2. Panel C shows the chemochromic film (after removal from the algae-containing plate) marked with purple spots that correspond to areas sensitized by H_2 from the individual colonies. Finally, panel D shows the reversibility of the chromic response when the film is exposed to air for about 5 min, proving that H_2 in fact was detected. Future experiments will optimize the system for use in the presence of O_2 so that O_2-tolerant, H_2-producing mutants can be identifed rapidly.

Conclusions and Future Work

We have made substantial progress over the past year, particularly with respect to optimizing the photoreductive selective procedure and development of a rapid screen for mutants that produce H_2 at high rates. Although improved mutants were isolated this year, we expect to significantly accelerate the generation and selection of mutants during the next year and to combine the two selective pressures to yield more desirable mutants.

Finally, we are also initiating a collaboration with Professor Anastasios Melis at the University of California, Berkeley, to develop molecular biological tools for the isolation of O_2-tolerant mutants. The approach will involve cloning the hydrogenase gene in *C. reinhardtii* and, using site-directed mutagenesis, will attempt to improve the tolerance of the enzyme to O_2. This concept has been applied to the uptake hydrogenase of the nitrogen-fixing bacterium *Azotobacter vinelandii* by McTavish et al. (1995), who showed that substitution of a cysteine by a serine in the non-catalytic subunit of this enzyme decreased the O_2 sensitivity of the protein.

REFERENCES

Benson, D.K., C.E. Tracy, and C. Bechinger. 1996. "Design and Development of a Low-Cost Fiber-Optic Hydrogen Detector". In *Proceedings of the 1996 U.S. DOE Hydrogen Program Review*, vol. II, 605-624, NREL/CP-21908430.

Ghirardi, M.L., R.K. Togasaki, and M. Seibert. 1997. " Oxygen Sensitivity of Algal H_2-Production". *Appl. Biochem. Biotechnol.* **63-65**, 141-151.

McBride, A.C., S. Lien, R.K. Togasaki, and A. San Pietro. 1977. "Mutational Analysis of *Chlamydomonas reinhardi*: Application to Biological Solar Energy Conversion". In *Biological Solar Energy Conversion* (A. Mitsui, S. Miyachi, A. San Pietro, and S. Tamura, eds.), Academic Press, New York.

Harris, E.H. 1989. *The Chlamydomonas Sourcebook*, Academic Press, New York.

Maione, T.E., and M. Gibbs. 1986. " Association of the Chloroplastic Respiratory and Photosynthetic Electron Transport Chains of *Chlamydomonas reinhardii* with Photoreduction and the Oxyhydrogen Reaction". *Plant Physiol.* **80**, 364-368.

Seibert, M., Ghirardi, M.L., Maness, P.C., and Weaver, P. "Photobiological Production of Renewqable Fuels, Chemicals, and Materials". In *Proceedings of the AAA Biotec Conference* (Ferrere, Italy), in press.

McTavish, H., Sayavedra-Soto, L.A., and Arp, D.J. 1995. "Substitution of *Azotobacter vinelandii* Hydrogenase Small-Subunit Cysteines by Serines can Create Insensitivity to Inhibition by O_2 and Preferentially Damages H_2 Oxidation over H_2 Evolution". *J. Bacteriol.* **177**, 3960-3964.

FIGURE LEGENDS

FIGURE 1. Selective pressures used to isolate O_2-tolerant, H_2-producing mutants of *C. reinhardtii*. **A.** H_2-production selection is based on survival following a short treatment with metronidazole (MNZ) in the presence of controlled concentrations of O_2 (to inhibit wild-type hydrogenase) and in the absence of CO_2. **B.** H_2-uptake selection requires algal growth in the presence of DCMU (an inhibitor of O_2 evolution), H_2 as a source of reductant, and CO_2. Oxygen is added to inhibit wild-type hydrogenase activity.

FIGURE 2. Effect of nitrosoguanidine on the number of viable *C. reinhardtii* cells following treatment with the mutagen. **A.** Survivors (%) as a function of nitrosoguanidine concentration. Both WT (open circles) and the cell wall-less D5 variant (closed circles) were treated with different concentrations of the mutagen for 45 min in the dark. After washing, cell suspensions were plated and the number of surviving colonies was determined. **B.** Semilogarithmic plot of the number of survivors (cells/ml) following treatments with 1 μg/ml nitrosoguanidine as a function of incubation time.

FIGURE 3. Oxygen titration of the rates of H_2 evolution by cw15 (open circles), the D5 variant (closed circles) and the IM6 mutant (asterisks). The O_2 I_{50} for each organism is estimated by the concentration of added O_2 that lowers the rate of H_2 evolution to half of the value measured in the absence of added O_2 (V_0, Y-axis intercept).

FIGURE 4. Oxygen titration of the rates of H_2 evolution by survivors from the H_2-uptake selective pressure (PRS1). The dotted curve represents the data for the control, WT cells.

FIGURE 5. Screen for H_2-producing algal colonies. (A) Agar plate containing individual algal colonies, covered first with a piece of filter paper and then a chemochromic film (a grid was placed over the H_2-detecting film to allow for easy identification of the individual colonies). (B) The system was illuminated from the bottom to induce algal H_2 evolution. (C) The chemochromic film was removed from the plate containing the algal colonies and placed on a white background in order to allow for easy observation of the purple spots on the film, which correspond to areas exposed to H_2. Note differences in intensity between different areas on the grid. (D) The sensitized film was exposed to air for 5 min and the spots disappeared, indicating that H_2 was detected in (C).

FIGURE 1

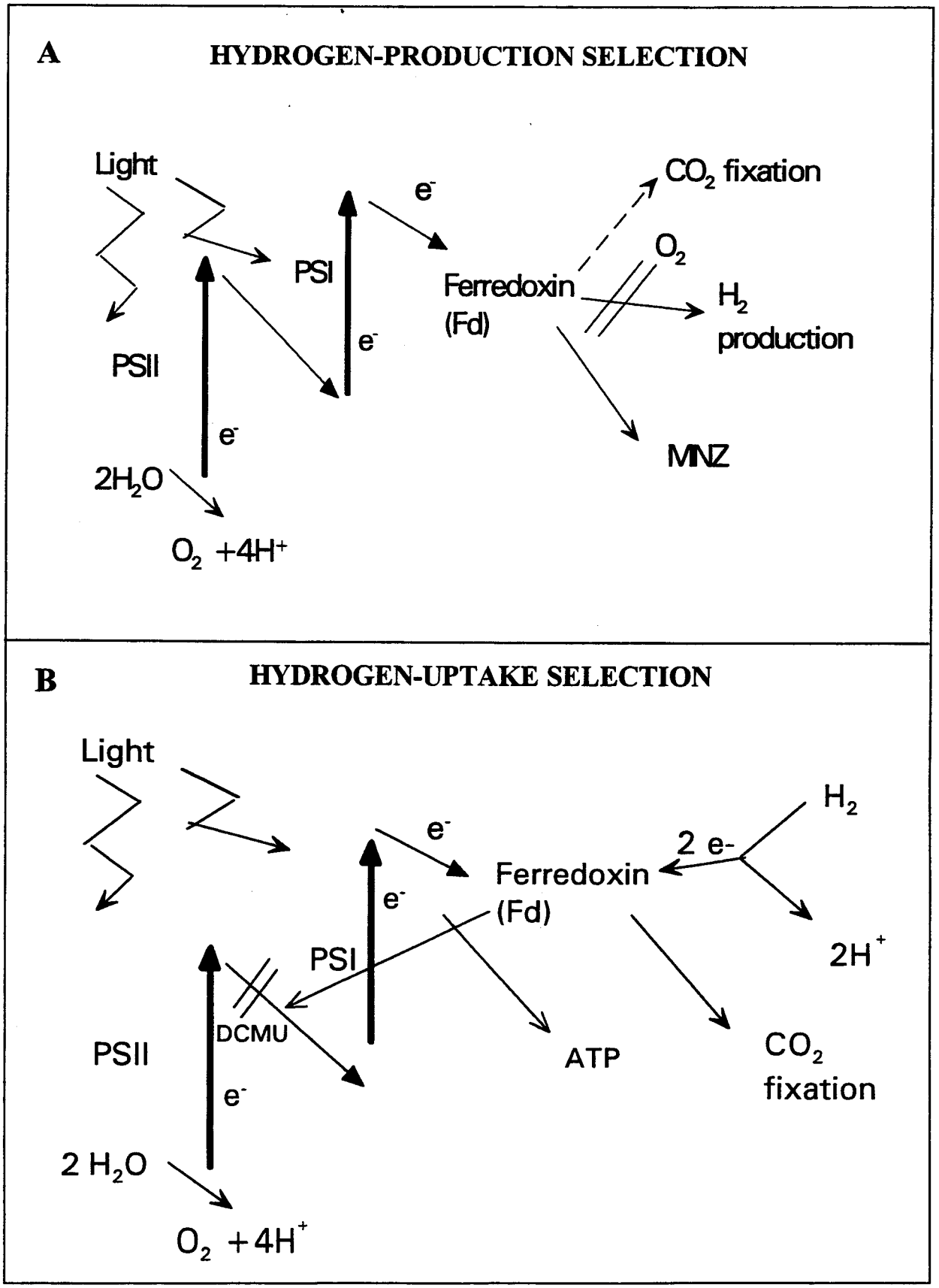
A
HYDROGEN-PRODUCTION SELECTION
Light
PSI
e-
CO2 fixation
O2
Ferredoxin
(Fd)
H2
production
PSII
e-
MNZ
2H2O
O2 +4H+
B
HYDROGEN-UPTAKE SELECTION
Light
H2
e-
2 e-
Ferredoxin
(Fd)
PSI
2H+
DCMU
PSII
ATP
CO2
fixation
2 H2O
O2 +4H+

FIGURE 2

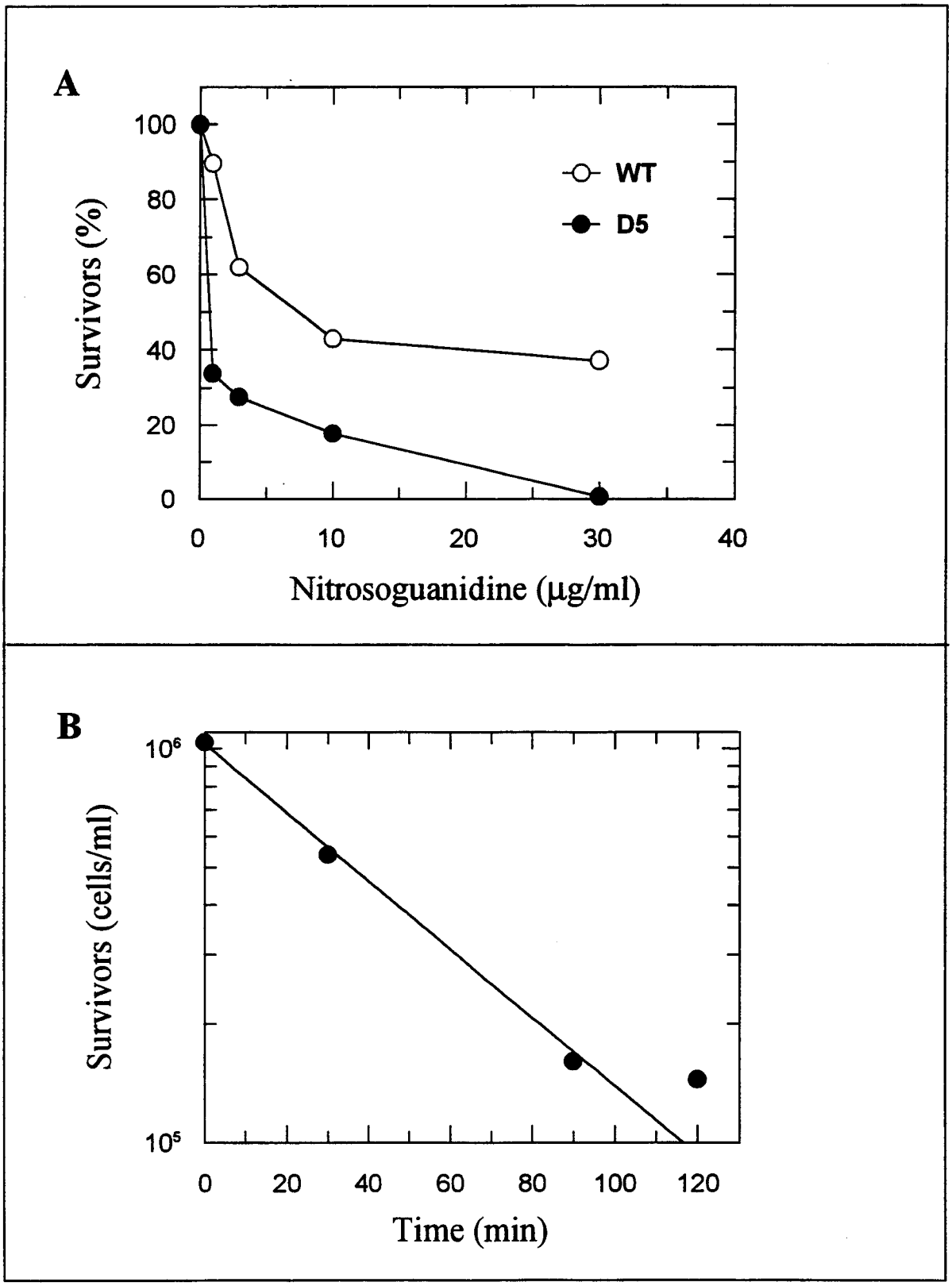
A
100
80
60
40
20
0
Survivors (%)
WT
D5
0
10
20
30
40
Nitrosoguanidine (µg/ml)
B
10^6
10^5
Survivors (cells/ml)
0
20
40
60
80
100
120
Time (min)

FIGURE 3

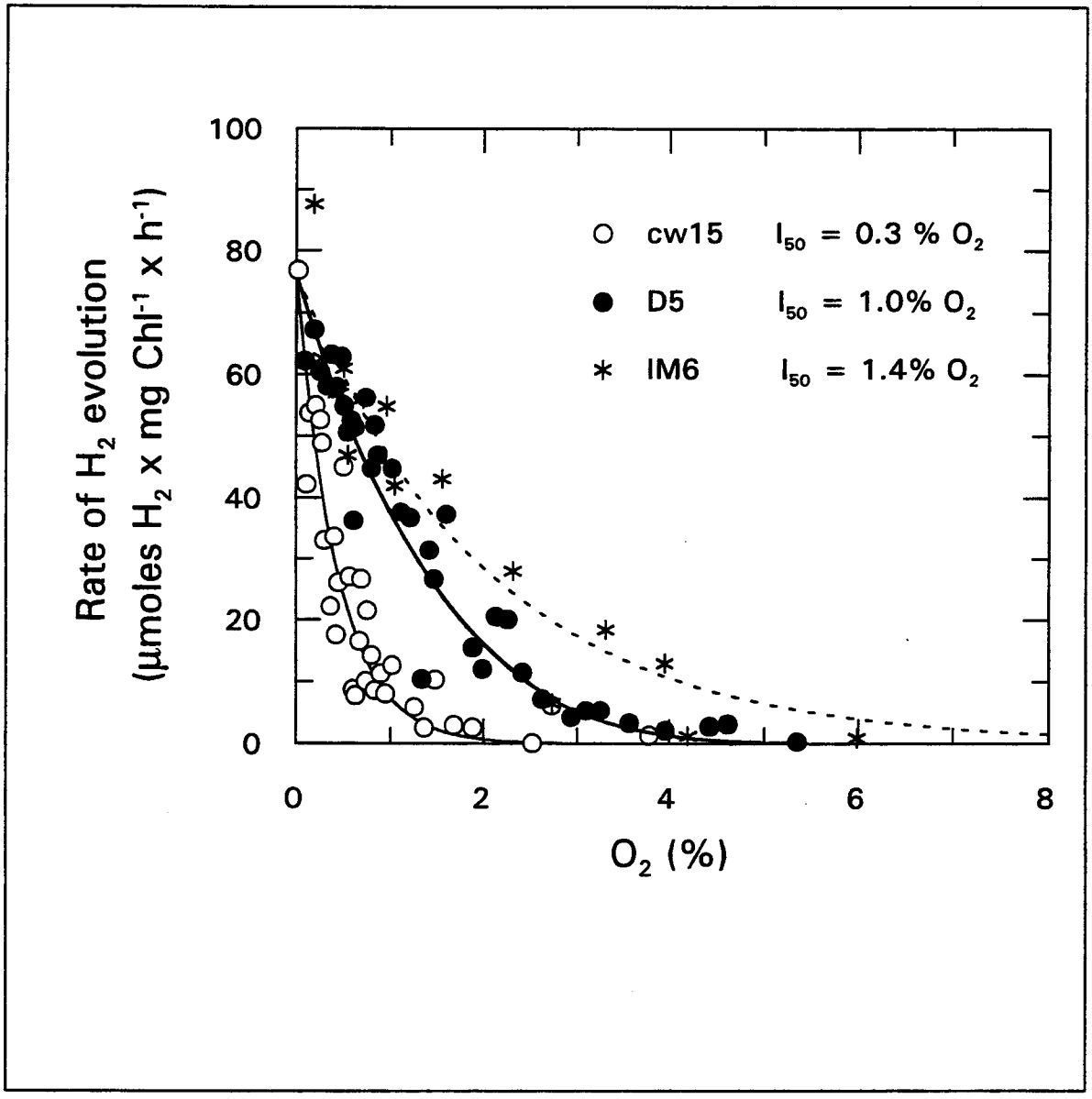
Rate of H_2 evolution
(µmoles H_2 x mg Chl^{-1} x h^{-1})
100
80
60
40
20
0
0
2
4
6
8
O_2 (%)
cw15 I_{50} = 0.3 % O_2
D5 I_{50} = 1.0% O_2
IM6 I_{50} = 1.4% O_2

FIGURE 4

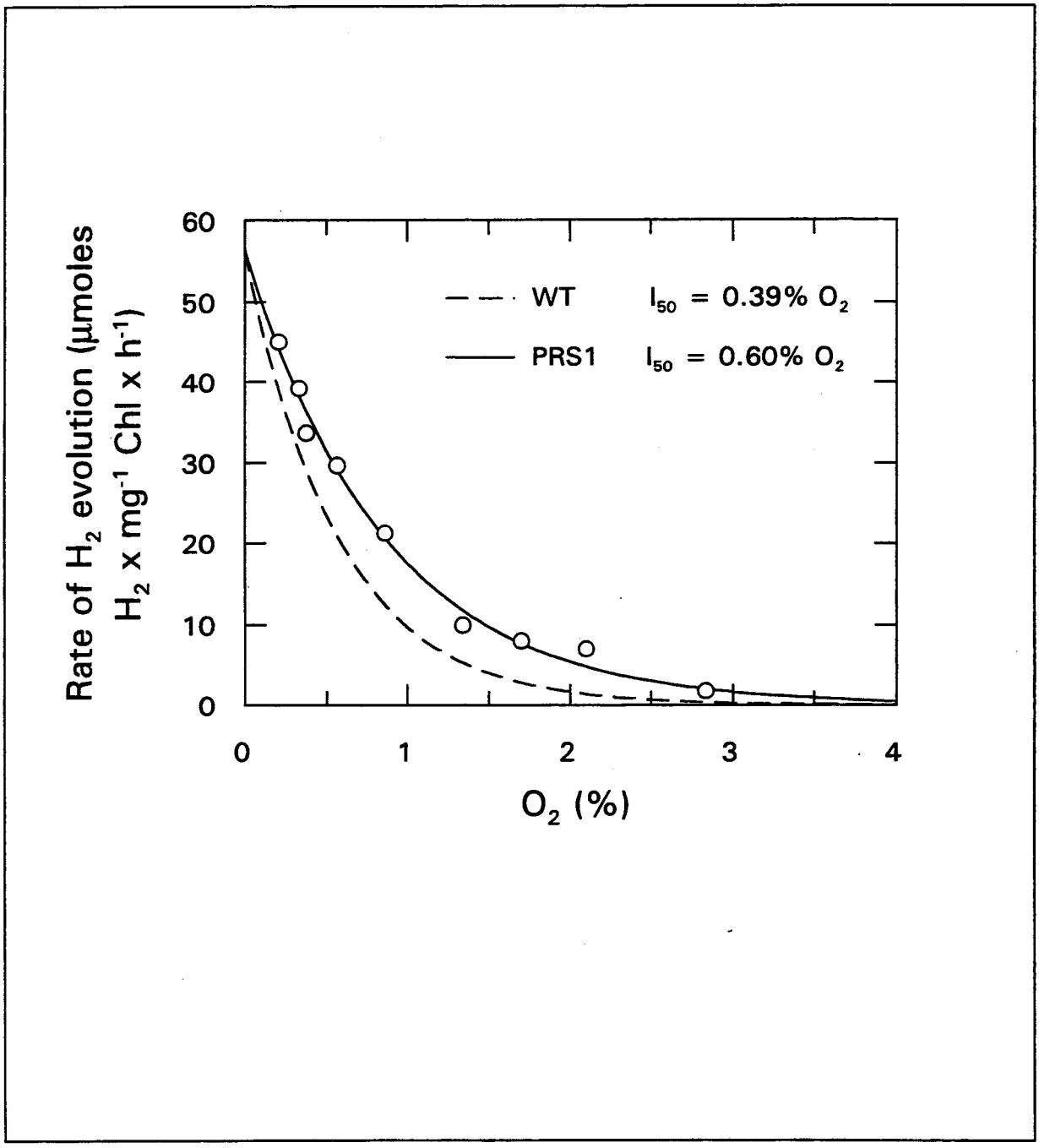
Rate of H_2 evolution (µmoles H_2 x mg^{-1} Chl x h^{-1})
60
50
40
30
20
10
0
0
1
2
3
4
O_2 (%)
WT I_{50} = 0.39% O_2
PRS1 I_{50} = 0.60% O_2

FIGURE 5

A

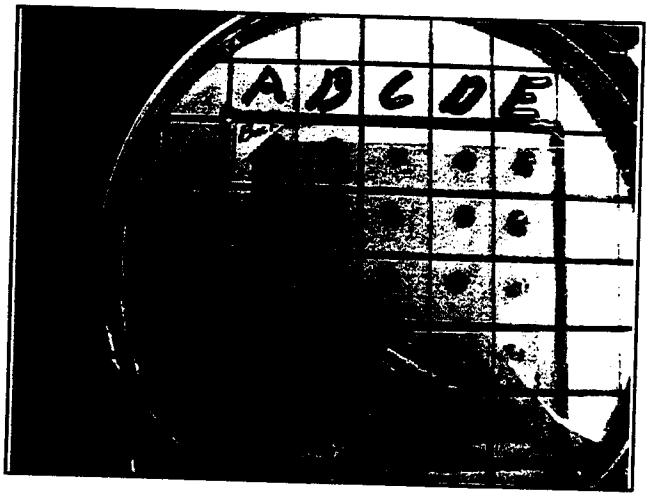

B

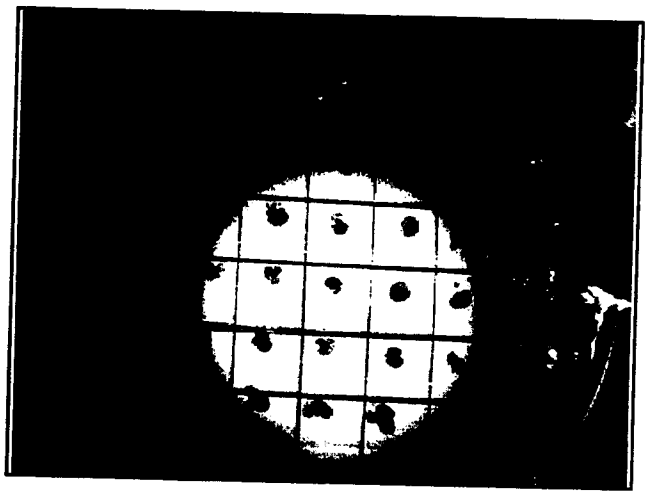

C

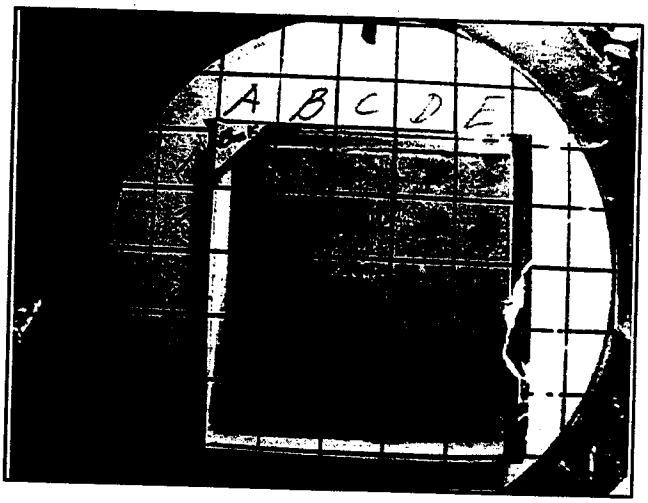

D

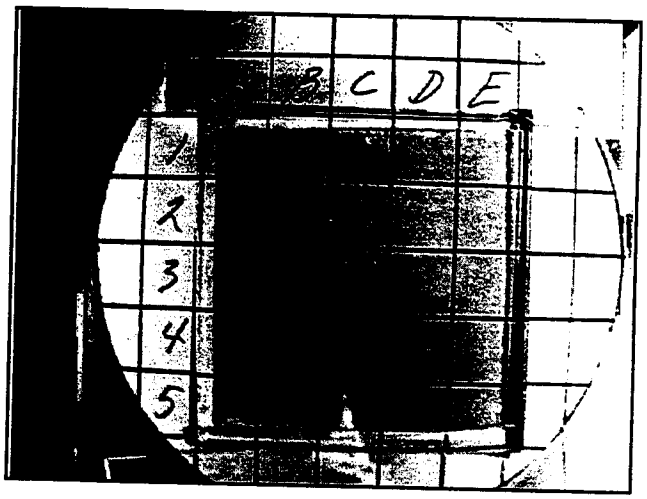

SUSTAINABLE BIOREACTOR SYSTEMS FOR PRODUCING HYDROGEN

Oskar R. Zaborsky, Ph.D.
Director, Marine Biotechnology Center
Williamson-Matsunaga FREE Scholar in Hydrogen Systems
University of Hawaii at Manoa
Hawaii Natural Energy Institute
Marine Biotechnology Center
2540 Dole Street, Holmes 246
Honolulu, HI 96822

Abstract

The goal of this project is to generate hydrogen from water using solar energy and marine microalgae under sustainable conditions. This project has two major objectives: (1) Design an appropriate sustainable bioreactor system that can employ the Mitsui-Miami strains and other tropical marine microbes for the efficient production of hydrogen; and (2) Maintain the International Marine Biotechnology Culture Collection, part of which is composed of the Mitsui-Miami collection, for benefit of the DOE Hydrogen Program.

Our approach is based on a two-stage process that uses a single organism for producing hydrogen gas. Stage 1 is the growth of the microbe; stage 2 is the generation of the hydrogen gas. The system is also amenable to a single-stage indirect system whereby hydrogen can be produced in the same bioreactor configuration. The integration of biology with reactor engineering will provide important insight into the workings of the outdoor system and provide critical feed-back to improvements that need to be made in particular strains through either physiological optimization or through genetic engineering.

The project involves collaboration with Mario R. Tredici, University of Florence, and John R. Benemann, University of California, Berkeley, and is part of the International Energy Agency's biohydrogen program.

Introduction

Over the past twenty years, advances have been made in the elucidation of the complex physiological, biochemical, and genetic processes underlying the hydrogen evolution capabilities

of microalgae and bacteria. In the area of engineering research and system integration, however, little progress has been made. In fact, no hydrogen-evolving process that showed promise has been demonstrated in the field for any length of time let alone commercialized. Additionally, even those processes that have shown promise in laboratory settings have not been evaluated for performance, at most being in continuous operation for only a few days. Importantly, the solar conversion efficiencies of these systems at best were below 3%.

Objective

The overall goal of Hawaii's biohydrogen program is to generate hydrogen from water using solar energy and marine microalgae under sustainable conditions. Specific bioprocess engineering objectives include the design, construction, testing and validation of a sustainable bioreactor system. Specific objectives relating to biology include examining and optimizing key physiological parameters of the cyanobacteria that are critical for sustained operations. Another objective is to utilize the Mitsui-Miami culture collection of hydrogen-producing microorganisms, now part of the International Marine Biotechnology Culture Collection, IMBCC.

The effort is a 3-year project. Several areas of research and tasks need to be pursued. These include: (1) sustainable bioreactor system design; (2) hydrogen-producing microbes for the bioprocess; (3) genetic characterization and strain improvement; and (4) maintenance of IMBCC. The realization of the envisioned process will require the joint development of both the hardware, namely reliable and inexpensive bioreactors, and system "software," namely the cyanobacterial strains that are able to grow and produce hydrogen effectively.

Approach

Our approach for a sustainable bioreactor system is based primarily on a two-stage process that uses but one single organisms for producing hydrogen gas. Stage 1 is the growth of the microbe; stage 2 is the generation of the hydrogen gas. The overall process entails several steps: (1) the growth of cyanobacteria in open bioreactors (ponds) to accumulate carbohydrates using solar energy; (2) the concentration of the algal biomass followed by the anaerobic adaptation in the dark to turn on the biochemical machinery that is able to produce hydrogen; (3) the generation of hydrogen from the stored carbohydrates in the adapted cyanobacteria with solar energy (the second light-dependent step); and (4) the recycling of the carbohydrate-depleted algae to the initial growth bioreactors (ponds).

Our proposed system is also amenable to a single-stage indirect process whereby hydrogen can be produced in the same bioreactor configuration.

Cyanobacteria, like other algae, induce a hydrogen-evolving system under dark anaerobic conditions, and subsequently can generate hydrogen in the light. Cyanobacteria can accumulate large quantities of carbohydrates when limited for nitrogen. The ability to grow cyanobacteria in large-scale (> 10 ha) has already been demonstrated (Cyanotech Corporation). This project will initially utilize the IMBCC as the primary source of cyanobacteria that should be suitable for the process. Strains will be screened for key characteristics such as carbohydrate accumulation (total, productivity), dark-anaerobic hydrogenase induction (rate, maximal), and light-driven hydrogen evolution (effects of light, extent of utilization of stored carbohydrates, inhibition by oxygen).

Stage 1 involves producing dense cultures of filamentous, non-heterocystous cyanobacteria and optimizing biomass through innovative tubular photobioreactors, work that is being done in collaboration with M. Tredici, University of Florence (Tredici and Materassi, 1992). Stage 2 entails manipulating the cells to induce the enzyme systems that enable light-driven hydrogen production. The approach for Year 1 is to focus on the outdoor photobioreactor and production of high-density mass culture of Arthrospira sp. (formerly Spirulina) and another species (Oscillatoria

sp.). Physiological studies will be initiated after establishing the basic operating parameters of the bioreactor.

Technical Goals

Technical goals include designing, constructing, and testing tubular photobioreactors that offer superior operational characteristics yet are inexpensive to construct and operate for hydrogen production. Technical goals include understanding and manipulating the physiological and genetic parameters of the microalgae to optimize the system (both bioreactors and biological components). The prime near-term technical goal is to test the tubular bioreactors with a few microalgae strains and to compare productivities.

Major Barriers to Meeting Technical Goals

Major barriers are: (1) understanding in sufficient detail the physiological aspects of the microalgae for sustained mass culturing; (2) developing proper protocols for adapting the selected microalgae for continuous hydrogen production; (3) regulatory constraints imposed on the use of the Mitsui-Miami cultures for outdoor experimentation by the State of Hawaii; and (4) integrating the biology with the engineering.

Past Results

This project, with its emphasis on photobioreactor systems and the two-stage biophotolysis process is a new project. A previous project, under the guidance of other personnel, focused on the transfer of the Mitsui-Miami culture collection and characterization of strains. Based on the directives of the 1996 DOE review panel, the culture collection work has been reduced to a minimum needed for maintaining and distributing strains (Zaborsky and Baker, 1996). A publication from previous DOE support to Hawaii personnel has appeared (Gubili and Borthakur, 1996).

Current Year Accomplishments and Status

This project was initiated in late February 1997 with the design and construction of the prototype photobioreactors at the Kewalo Basin site in Honolulu. The operational characteristics of the tubular photobioreactors in Hawaii are being tested with Arthrospira sp. (Spirulina) to develop protocols for high-density, high-productivity cultures under local conditions of light and temperature and to compare these with prior experience in Italy. The development and implementation of an automated monitoring system that records ambient light, culture temperature, dissolved oxygen concentration, and pH was achieved. Figures 1-3 present features of the tubular photobioreactor and preliminary data of its performance.

Figures 1-3

Further improvements in bioreactor design and operations are in progress. Investigations of relationships among daily incident light, culture dilution regime, and culture density and rate of biomass production have been initiated.

The project was initiated a few months ago and it is premature to conduct an economic evaluation or systems analysis. However, a preliminary analysis of the two-stage biophotolysis process has been carried out by Benemann (Benemann, 1995), concluding that if certain research goals can be met (e.g., overcoming light saturation to achieve high photosynthetic efficiency), the overall cost of hydrogen production would be below $15/MMBTU. A key issue is the cost of the photobioreactors, both capital and operating. This project will develop detailed information to permit a more detailed cost analysis. The need for stand-alone energy systems in Hawaii coupled

with favorable environmental conditions suggest that this is the most likely location for the development and application of such systems.

Plans for Future Work

Major actions for Year 1 include the following: (A) establish an outdoor bioreactor operation consisting of innovative sustainable photobioreactors for algal cultivation and hydrogen production. Specific subtasks include: (1) Complete the outdoor bioreactor, including hardware, sensors, data logging and feedback controls (pH, pO_2, temperature), and dilution system; (2) Maximize culture productivities and solar conversion efficiencies, and carry-out experiments with nitrogen limitation of cultures; and (3) establish the outdoor bioreactor subsystem suitable for hydrogen production (e.g., glass tubular reactor) and test for H_2 handling and containment. The biological aspects of the work (B) are to demonstrate in the laboratory the individual components of the two-stage bioprocess using filamentous marine cyanobacteria. Specific subtasks include: (1) Nitrogen limitation of cyanobacteria cultures, carbohydrate accumulation and productivity effects; (2) Hydrogenase induction of nitrogen-limited cultures and dark anaerobic hydrogen production and fermentation activities; and (3) Hydrogen evolution in the light by anaerobically adapted cultures. Additionally, IMBCC cultures will be maintained and distributed.

This project, being funded by DOE, is part of an International Energy Agency (IEA) project on biological hydrogen production. The project is also a part of a general U.S.-Japan understanding that fosters binational cooperative research in biological hydrogen production. DOE is providing funding for the transfer of the Mitsui-Miami collection, the establishment of a scientific base of the IMBCC collection, and for the dissemination of the Mitsui-Miami strains to other qualified researchers at national laboratories and industry. Funding from Japan is being used in two ways. Funding from the Research Institute of Innovative Technology for the Earth (RITE) is being used to evaluate photosynthetic bacteria in the Mitsui-Miami collection for active hydrogen production. Funding from Marine Biotechnology Institute, Co., Ltd. is used for database improvements.

Interest in the tubular photobioreactors and the culture collection is evident. During the past few months, discussions have been held with various firms.

Acknowledgment

This material is based on work supported by the Department of Energy, Hydrogen Program, under award No. DE-FC36-97GO10202, O.R. Zaborsky, principal investigator. Any opinions, findings and conclusions or recommendations expressed in this publication are those of the authors and do not necessarily reflect the views of the Department of Energy.

The author gratefully acknowledges the contribution of the following individuals who are part of the scientific project team: John R. Benemann, University of California, Berkeley, Department of Civil Engineering; Mario R. Tredici, University of Florence; James P. Szyper, Hawaii Institute of Marine Biology, and Brandon A. Yoza, Hawaii Natural Energy Institute. We especially thank Mitsufumi Matsumoto, a visiting student from the Tokyo University of Agriculture and Technology and being supported by Japan's Ministry of Education, for his contributions and Karynne Morgan, Hawaii Natural Energy Institute, for her administrative assistance. The principal investigator thanks Dulal Borthakur, Department of Plant Molecular Physiology, and Gerald Cysewski, Cyanotech Corporation, for *Arthrospira* sp. starter cultures.

References

Benemann, J. R., Photobiological Hydrogen Production, Report to the Pittsburgh Energy Technology Center (1995).

Cyanotech Corporation: Corporate Profile, Cyanotech Corporation, Kailua-Kona, Hawaii (1996).

Gubili, J. and Borthakur, D., The Use of PCR Cloning and Screening Strategy to Identify Lambda Clones Containing the hupB Gene of *Anabaena* sp. strain PCC7120, Journal of Microbiological Methods, 27, 175-182 (1996).

Tredici, M. R. and Materassi, R., From Open Ponds to Vertical Alveolar Panels: The Italian Experience in the Development of Reactors for the Mass Cultivation of Phototrophic Microorganisms, Journal of Applied Phycology, 4, 221-231 (1992).

Zaborsky, O.R. and Baker, K., International Marine Biotechnology Culture Collection (IMBCC), Proceedings of the 1996 U.S. DOE Hydrogen Program Review, Volume I, May 1-2, pp 397-404, National Renewable Energy Laboratory (1996).

Figure Legends

Figure 1. Tredici-design tubular photobioreactor at Kewalo Basin, Honolulu, Hawaii.

Figure 2. Close-up view of tubular photobioreactor showing sparging gas bubbles for effective internal gas exchange.

Figure 3. Time course of *Arthrospira* sp. biomass in the tubular photobioreactor during constant daily medium renewal.

Figure 1

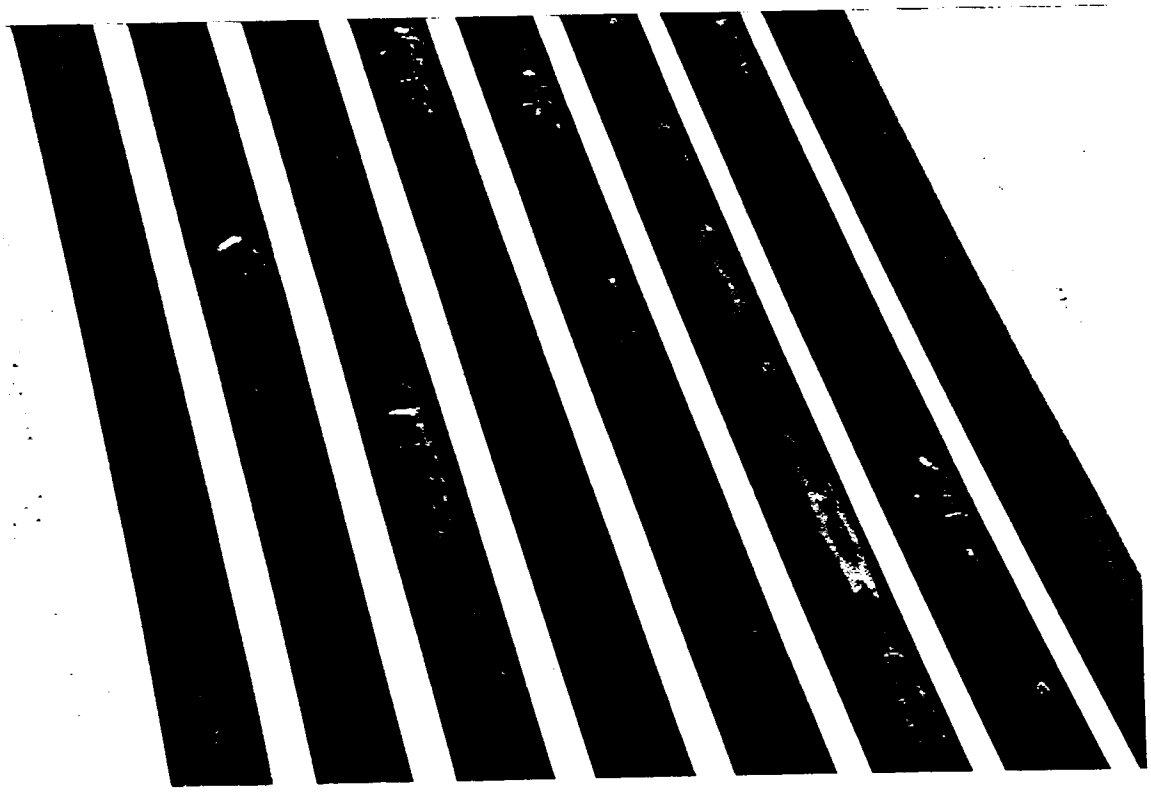

Figure 2

Figure 3

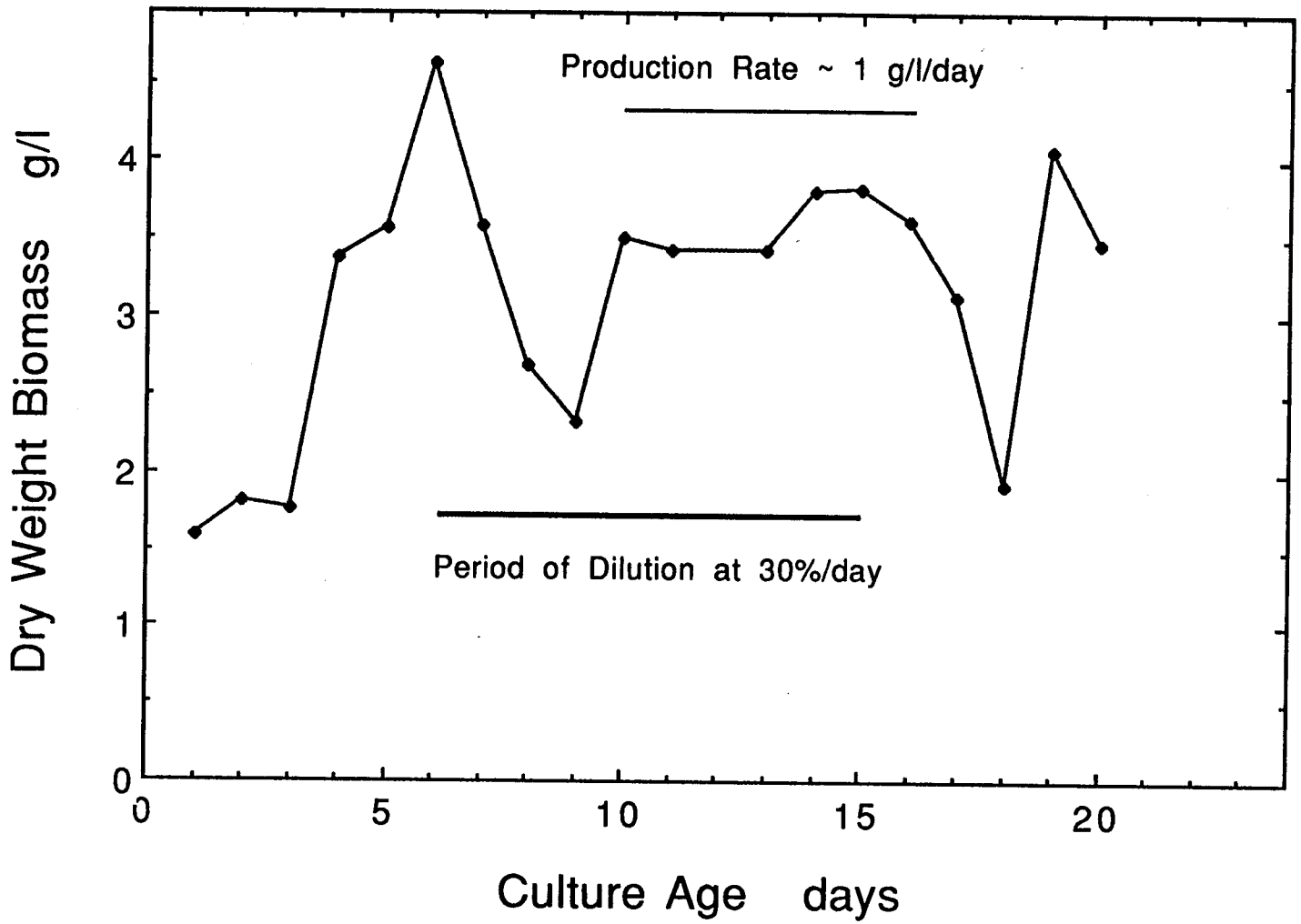
Production Rate ~ 1 g/l/day
Period of Dilution at 30%/day
Dry Weight Biomass g/l
Culture Age days
0
1
2
3
4
0
5
10
15
20

Biological H_2 from Syngas and from H_2O

P. Weaver, P.-C. Maness, S. Markov, and S. Martin
National Renewable Energy Laboratory
Golden, Colorado 80401

Summary

The two stand-alone objectives of the research are to economically produce neat H_2 in the near term from biomass (thermally gasified to syngas) and in the mid term from H_2O using cyanobacteria or algae with an oxygen-tolerant bacterial hydrogenase.

Photosynthetic bacteria have four different terminal enzymes that mediate their H_2 metabolisms—nitrogenase, uptake hydrogenase, fermentative hydrogenase, and carbon monoxide-linked hydrogenase. Each has been microbiologically and biochemically examined for their potential to specifically generate H_2 in large-scale processes. Based on measurements of maximal activities, stabilities, energy requirements, equilibria, and partial pressures of the H_2 producing reactions, the CO-linked hydrogenase is easily the most suited for practical applications. The enzyme mediates H_2 production from CO at rates up to 1.5 $mmol \cdot min^{-1} \cdot g$ cell dry $weight^{-1}$ at near ambient temperature and pressure. At biological temperatures, equilibrium for the CO shift into H_2 lies far towards H_2 production. Less than 0.1 ppm of CO remains after a 20% CO gas phase is acted upon by bacteria. The necessary contact time between CO and bacteria is approximately ten seconds. Similar biological activities are observed with thermally generated fuel gases. The product gas can be directly used in fuel cells. New bacterial isolates from nature and mutant strains are being selected to further improve the novel technology. Oxygen-resistant enzymes identified in some bacterial strains could lead to a more general, second generation technology mediating the solar production of neat H_2 from H_2O.

Presently, mass transfer of gaseous CO limits the bacterial production of H_2 from fuel gases. New bioreactor designs have significantly enhanced shift rates. Vapor-phase and bubble-train bioreactors employing immobilized or suspended bacteria are being scaled up. A User Facility has been established for the safe engineering scale up and validation of solar or dark technologies for the Hydrogen Program. The first system to be tested at the site will integrate fuel gas generators with biological shift reactors and a PEM fuel cell.

Introduction: An economic process for producing hydrogen, whether biologically or chemically based, would ideally be (1) H_2O derived, (2) solar driven, (3) highly efficient, (4) durable, (5) insensitive to hydrogen partial pressure, and (6) inexpensive to build and operate. A complete system fulfilling all of these goals is not currently available. Of the biological options, systems employing intact cells of photosynthetic bacteria are the most advanced. Unlike cyanobacteria or algae, however, photosynthetic bacteria do not oxidize water and therefore do not directly fulfill criterion (1). They do, however, evolve H_2 from biomass (previously photosynthetically generated from H_2O and CO_2). These bacteria employ several different enzymatic mechanisms that may have commercial potential for possible near term applications of H_2 production from biomass. One mechanism that incorporates thermal and biological processes appears particularly promising: thermally generated fuel gases derived from biomass can be sufficiently conditioned by bacterial catalysts in a one-step process that they may be directly injected into platinum-electrode, hydrogen fuel cells.

A complete system of sustained hydrogen production based on the direct photooxidation of water is more difficult to achieve. Oxygen production is inherent in the oxidation of water, and the hydrogen-evolving enzymes of cyanobacteria and algae are usually rapidly inactivated by oxygen. A number of newly isolated photosynthetic bacterial strains contain an O_2-resistant, evolving hydrogenase enzyme. This hydrogenase has been partially purified from two strains of bacteria, where it is found tightly bound to membrane fractions. The enzymes require an additional electron mediator for H_2 production. Genetic transfer and expression of the oxygen-resistant, bacterial hydrogenase enzyme and cofactor in a cyanobacterial or algal host could provide a method for the linkage of photoreduced ferredoxin to an evolving hydrogenase, even in the simultaneous presence of photoevolved oxygen. This type of genetic construct could grow naturally when CO_2 was present, but would concomitantly photoevolve H_2 and O_2 from water in the absence of CO_2. Creation of a recombinant microbe to fulfill all of the ideal criteria listed above is considered an early mid-term goal.

Approach: The two stand-alone objectives of the research are to economically produce H_2 in the near term from biomass (thermally gasified to syngas) using ambient temperature bacteria as catalysts and in the mid term from H_2O using cyanobacteria or algae with an oxygen-tolerant bacterial hydrogenase.

Past Results: Photosynthetic bacteria have four different terminal enzymes that mediate their H_2 metabolisms—nitrogenase, uptake hydrogenase, fermentative hydrogenase, and carbon monoxide-linked hydrogenase. Each has been microbiologically and biochemically examined for their potential to specifically generate H_2 in large-scale processes.

Of the intact cell metabolisms of phototrophs that evolve hydrogen, the nitrogenase-mediated reactions have been the most studied. Nearly all isolates of photosynthetic bacteria have a nitrogenase enzyme complex (Weaver et al. 1975), which, in the absence of ammonium ion or dinitrogen gas and in the presence of oxidizable organic materials, functions to reduce protons and evolve hydrogen. A large variety of soluble organic acids, alcohols, and sugars can be nearly totally photoconverted into H_2 and CO_2 by this metabolism. Rates of 131 μmol H_2 evolved/min·g cell dry weight have been obtained in saturating light. Hydrogen evolution is largely light dependent (Schultz et al. 1985) and strongly exergonic. The hydrolysis of about 4 ATP (largely synthesized in light) is

required to generate each H_2 and can drive the gas production to equilibrium pressures in excess of 100 atmospheres. Radiant energy conversion efficiencies (ignoring the chemical energy of the organic substrate) are about 5.3% for the most active strains of photosynthetic bacteria. The best outdoor, solar-driven efficiency is 3.4%. Cultures grown on glutamate as the nitrogen source produced H_2 at linear rates for 7-10 days before *nif*$^-$ strains began to dominate the cultures. Experiments with weekly feedings of N_2 maintained the *nif*$^+$ wild-type genotype dominant and active H_2 production could be observed for more than 30 days. Even with the assumption that the best strains and conditions could be maintained, the maximum solar conversion efficiencies that could be expected are probably less than 10%, however, due to the large energy expenditure of the bacteria in performing this H_2-evolving metabolism. Non-sterile, solar-driven cultures (200-300 liter scale) were susceptible to contamination by sulfate-reducing and methanogenic bacteria growing on the evolved H_2 plus CO_2. Limiting the available fixed nitrogen, including that present in sedimented photosynthetic bacteria, is necessary to limit H_2S and CH_4 evolution by the contaminants. Algal growth is similarly inhibited by this method and also by the strongly reducing conditions. An in-house cost analysis of the process has been performed (Herlevich and Karpuk). First year costs for H_2 production, clean-up, and compression are estimated at \$24.40 per 10^6 Btu at 5% solar energy conversion and \$15.70 per 10^6 Btu at 10% conversion efficiency.

Many strains of photosynthetic bacteria also produce hydrogen from organic substrates by way of a fermentative hydrogenase enzyme when grown in intermittent or low, continuous light (Schultz and Weaver 1982). High, continuous light represses synthesis of the enzyme. The enzyme does not require ATP. It can mediate hydrogen production at rates more than 3-fold those of nitrogenase, or about 440 μmol H_2/min·g cells. However, it equilibrates at low partial pressures of about 0.1 atmospheres of H_2. The active rates of hydrogen production can thus only be maintained by sparging with inert gas, by vacuuming, or by scavenging with a hydrogen-consuming process. Sparging or vacuuming are considered prohibitively expensive, although closed-loop, sparged systems connected to fuel cells may be effective. Methanogenic bacteria strongly contaminate non-sterile cultures. In fact, methanogenic bacteria naturally scavenge the H_2 to such low levels that they are extremely effective in maintaining the H_2 partial pressure considerably below the equilibrium pressure, which functions to "pull" the conversion of organic materials into H_2 and CO_2 and then into CH_4. This apparently natural process is the basis for an NREL patent on solar-enhanced anaerobic digestion (Weaver, 1990).

A unique type of hydrogen producing activity was found in a strain of photosynthetic bacteria by Uffen (1976) that functioned only in darkness to shift CO (and H_2O) into H_2 (and CO_2). We have isolated more than 400 strains of photosynthetic bacteria from local sites that perform this shift reaction in darkness, as does the Uffen strain, but will also quantitatively assimilate CO into new cell mass in light, unlike the Uffen strain, which makes them easy to grow. We have tested many of our strains for CO shift activity and growth with crude (water-scrubbed only) synthesis gas (primarily CO and H_2) generated from thermally gasified wood chips. In light, the novel photosynthetic bacteria assimilate the CO and H_2 components and a portion of the trace gases. In darkness, all of the isolates respond similarly by shifting the CO component of synthesis gas into additional H_2, thereby leaving a product gas highly enriched in H_2 (with CO_2 and trace pyrolysis gases). No inhibitory effects of synthesis gas on long-term photosynthetic growth were noted. At ambient temperature and pressure conditions and starting from 200,000 ppm of CO in the gas phase, less than 0.1 ppm of CO remained

at equilibrium. The product gas could be fed directly into a phosphoric acid fuel cell with generation of electrical power. No harmful effects to the fuel cell were noted.

Bacterial catalyzed rates as high as 1.5 mmol H_2 produced from CO per min per g cell dry weight were obtained from vigorously agitated cultures at low cell density. Less actively stirred cells at more normal cell densities (2-6 g cells per liter) exhibit H_2 production rates of 10-100 µmol per min per g cells, reflecting a limiting mass transfer of CO into solution. Gas pressures (10% CO) of more than 12 atmospheres strongly increased shift rates but were still limiting.

Bacterial cultures grown in light with 20% CO in the gas phase are probably not maximally induced for CO shift activity. The specific activity for CO shift activity increased by a factor of six when light-grown cultures were incubated in darkness in a Paar cell at seven atmospheres of 20% CO gas pressure. This indicates that increased availability of CO to the cells causes a further derepression of shift activity enzymes. Cultures can be adapted easily to two atmospheres of 100% CO, but do not adapt to seven atmospheres of 100% CO. Inert gas at similar pressures had no effect. The capability of running syngas shift reactors at a few atmospheres of pressure is being incorporated into new reactor designs.

A variety of bioreactor designs that show enhanced mass transport of CO (at near ambient pressure) were built and tested. Hollow-fiber reactors (0.5 m^2 surface area) with bacterial cells immobilized on the outer fiber surfaces evolved H_2 at rates of about 0.3-0.7 $mmol \cdot min^{-1} \cdot g\ cdw^{-1}$. One such reactor produced H_2 from CO (10% in N_2) continuously over a 15 month period with only occasional changes of medium. No detectable levels of CO remained in the effluent gas stream.

Current Results: Due to limiting mass transfer of CO during assay conditions, it has been difficult to compare bacterial shift activities between the more than 450 wild-type and mutant strains that we have isolated to-date. A new assay was developed that is independent of mass transfer. Bubbles of CO were added to suspensions of the bacterial strains in syringes and agitated vigorously. At time zero the bubble was expelled from the syringe and liquid samples of the bacterial suspension were injected at precise time intervals into an anaerobic solution of reduced hemoglobin. The hemoglobin rapidly quenches further shift activity by binding the remaining CO in solution to form carboxyhemoglobin, which has a distinctive spectral absorbance that can be readily quantitated from difference spectra. All of the bacterial strains exhibit a linear uptake of CO from solution until the dissolved CO approaches the K_s value (the CO concentration at which shift rates are one-half maximal). Different strains tested have K_s values of 3-8 μM. At normal cell densities in solution, CO concentrations drop to the K_s value in 3-5 seconds. CO concentrations drop to 0.2nM (the assay limit of resolution) in 6-8 seconds. This value of CO in solution is equivalent to about 200 ppm of CO in an equilibrated gas phase. Kinetic rates for the further shift of remaining CO below 200 ppm and the time necessary to generate a conditioned gas with less than 10 ppm residual CO are currently unknown; however, FTIR analysis after long-term contact with a bacterial suspension indicate the conditioned gas contains less than 0.1 ppm CO.

CO shift rates are strongly dependent upon ambient temperature. An increase from 30°C to 45°C causes a 2.5-fold increase in shift rate. To take further advantage of this response, twenty-four different hot springs sites with temperatures ranging from 45-70°C were sampled for biological shift

activity. About twelve of the enrichment cultures from these sites show such activity. As yet, none of the bacterial strains are in pure culture but preliminary indications are that shift rates are enhanced. The higher temperature tolerance may be of additional value in requiring less cooling of thermochemically generated fuel gases. The negative impacts that higher temperatures have on gas solubility and equilibrium conditions remain to be determined.

A mutant strain of photosynthetic bacteria was selected by growing a culture on CO in light in the presence of 5% O_2. Strain CBS-2 responds to the imposed culturing conditions by synthesizing 340% of the hydrogenase activity of its parent. The isolated hydrogenase from this strain exhibits a half-life of seventeen hours stirred in full air. This is especially striking when compared to a two minute half-life of some other hydrogenases under similar conditions. Attempts to couple this hydrogenase to photoreductants generated during oxygenic photosynthesis are being pursued. Of particular importance, the O_2-resistant hydrogenase exhibits no oxy-hydrogenase activity in the presence of H_2 and O_2.

Investigations into bioreactor designs that promote mass transfer of gaseous substrates have narrowed to primarily two types. For bacteria in suspension, a bubble-train design essentially acts as a compact version of a bubble tower. Bubbles of CO are injected into the base of a vertical, helically wound tubing bioreactor containing a continuously circulated bacterial suspension. The contact time of the bubbles with the aqueous suspension is dependent upon the aqueous pumping speed which controls the bubble rise time. Shift rates up to 0.7 mmol· min^{-1} .g cdw were obtained. The reactor is suitable for use in a pressurized mode that could lead to further enhancement of shift rates. However, safety concerns have precluded its operation in this mode to-date.

Vapor phase bioreactors have been constructed using immobilized bacteria on high-surface-area solid supports. Most promising is a low cost, low energy input bioreactor made by immobilizing bacteria on the 30 μm diameter fibers of a horizontal, inverted nylon carpet. The nylon fibers extend downward and partially contact an aqueous reservoir of medium which wicks water and minerals to the immobilized bacteria in contact with the gas phase. A CO-containing gas phase easily passes through the carpet nap between the carpet base and the reservoir and is rapidly shifted into H_2 by the bacteria. A 10% CO stream can be totally shifted within 30 cm of transit through the bioreactor. Specific activities are difficult to ascertain however, due to the unknown densities of bacterial cells.

The reservoir of vapor phase bioreactors confers another advantage. The optimum pH for the shift reaction is 8.5 to 9.0. Up to 90% of the CO_2 product of the shift reaction partitions into the reservoir as bicarbonate ion, leaving the effluent gas highly enriched in H_2. Relatively undiluted by CO_2, the energy content of the product gas is increased nearly 30%. Build up of carbonic acid in the reservoir soon inhibits bacterial activity as does titration with alkali which leads to inhibitory ionic strength. However, the CO_2 can be vented separately from the bioreactor by occasional pumping of the reservoir through an external loop and gas stripping the CO_2 to air before returning the aqueous phase to the bioreactor.

In order to safely scale-up the shift reactors and validate the incipient technology with real fuel gases over prolonged periods, the Outdoor Photobiology Test Area is being constructed. A 10' x 20' prefabricated building has been added to the OPTA site that will contain a small biomass gasifier as

well as a steam reformer to generate fuel gases on a continuous basis. Coupled with bioreactors, the completely automated system will provide a H_2 gas stream suitable for fuel cell injection at 1-14 liters per minute. Designed as a User Facility for the Hydrogen Program, the OPTA site can maintain temperature control for up to 3,000 liters of microbial culture year round. Three separate solar-driven or dark experiments can be controlled and monitored simultaneously. Although the site was vandalized earlier in the year, it will be ready for some applications by the end of summer, 1997.

Future Work: Further mutant selections should result in significantly increased specific activities in the CO shift reaction. Thermophiles will also be selected. Strains with a lower K_s for CO will be sought. Necessary cofactors for the O_2 - tolerant hydrogenase will be characterized. The Outdoor Photobiology Test Area will be re-established with both a propane steam reformer and a small downdraft biomass gasifier to generate fuel gases at the rate of 1-14 liters per minute. Scaled-up shift bioreactors will operate continuously on the fuel gases and long-term operation will be automated and monitored.

Economic Evaluation/Systems Analysis: Analyses are being performed on a separate task in the Hydrogen Program. The bacterial shift reaction is being examined as a possible low cost, single-step gas conditioning process for crude syngas. The projected cost of hydrogen is $17/GJ using a base case of purchased biomass at $46/ton and thermal gasification with biological shift (15% ROI). If biomass is purchased at $22/ton, the price of pure H_2 drops to $13.5/GJ, well within current market prices. A 10-fold increase in specific shift activity (from 1.5 $mmol \cdot min^{-1} \cdot g\ cdw^{-1}$) will decrease the cost by $4.70/GJ. If further gas purification is not needed to remove the remaining CO_2, the selling price is further reduced another $3.80/GJ. For many gas uses, such as in PEM or phosphoric acid fuel cells, it is only necessary that the gas stream be free of CO and H_2S, while not necessarily totally free of CO_2. In these applications the cost of further gas purification can be discounted.

Projected Goals: The equilibrium constant of the CO shift reaction at room temperature is sufficiently large to generate a bacterially conditioned syngas stream with sub-ppm concentrations of CO remaining. Assuming there is no appreciable sulfide present as well, the gas stream is clean enough (with or without CO_2 diminishment) to be directly injected into phosphoric acid or PEM fuel cells. This would effectively eliminate the costs (see Economics) for pressure-swing absorption (or similar gas clean-up process) to yield neat H_2 for fuel cell use. Our near-term goal will be for this type of fuel cell application.

A genetic construct containing an O_2-tolerant hydrogenase would create an inexpensive photobiological catalyst that would switch in the absence of CO_2 from a growth mode to a H_2-producing mode at nearly maximal solar conversion efficiency. The successful construction and testing of such an oxygenic phototroph is our mid-term goal to photobiologically produce H_2 from H_2O in a single-stage bioreactor.

Major Barriers: The long-term effects on bacteria of trace components in syngas have not been examined and may necessitate more frequent change-out of bacteria. Mass transfer of CO to the bacteria remains rate limiting and needs to be enhanced. Genetic enhancement can easily match any large increase in mass transfer rates. There are a few more unknowns in the photobiological process to produce H_2 from H_2O. The O_2-tolerant hydrogenase must be genetically transferred and expressed

in a biophotolytic host and shown to be active in linking to photoreductants. This has been demonstrated in mixed extracts, however.

References:

Herlevich, A., and M. Karpuk. 1982. SERI/TP-235-1548, 12 pp.

Schultz, J.E., and P.F. Weaver. 1982. *J. Bacteriol.*, 149:181-190.

Schultz, J.E., J.W. Gotto, P.F. Weaver, and D.C. Yoch. 1985. *J. Bacteriol.*, 162:1322-1324.

Uffen, R.L. 1976. *Proc. Nat. Acad. Sci.*, 73:3298-3302.

Weaver, P.F. U.S. Patent #4,919,813, issued April 24, 1990.

Weaver, P.F., J.D. Wall, and H. Gest. 1975. *Arch. Microbiol.*, 105:207-216.

A POLYMER ELECTROLYTE FUEL CELL STACK FOR STATIONARY POWER GENERATION FROM HYDROGEN FUEL

Christine Zawodzinski, Mahlon Wilson and Shimshon Gottesfeld

Materials Science and Technology Division
Los Alamos National laboratory
Los Alamos , NM 87545

Abstract

The fuel cell represents a key element in efforts to demonstrate and implement hydrogen fuel for electric power generation. The central objective of this project is to develop and demonstrate a 4 kW, hydrogen-fueled polymer electrolyte fuel cell (PEFC) stack, based on non-machined stainless steel hardware and on membrane/electrode assemblies (MEAs) of low catalyst loadings. This is to be accomplished by working jointly with a fuel cell stack manufacturer (H Power), based on a CRADA. Specific performance goals are 57% energy conversion efficiency hydrogen-to- electricity (DC) at a power density of 0.6 kW/liter. The cost goal is 600 $/kW, based on present materials costs. This stack should thus demonstrate the basic features of manufacturability, overall low cost and high energy conversion efficiency.

Central achievements in this project during the last 12 months have been:

(1) 2000 hours of continuous testing of a 100 cm^2 cell, based on 316 stainless steel screens/ sheets as gas flow fields/bipolar plates, was successfully completed. There was no significant rise in the high frequency resistance of the cell after 2000 hours of continuous operation.(2) Tests with similar stainless steel hardware repeated successfully at H Power under ambient pressure conditions. (3) A "cartridge" concept was introduced and implemented for effective stack fabrication. Individual cell components are adhered together between metal foil plates, resulting in bonded cartridges of, e.g., four cells each, and the stack is designed to be assembled by combining such units with removable cooling plates. This enables quick and easy stack assembly and makes it possible to remove and replace problem cells. (4) A short stack of four cells based on stainless steel hardware has exhibited performance close to that of a single cell. (5) Extensive corrosion testing has been implemented to evaluate realistically the viability of stainless steel based hardware for long-term stable stack operation.

Future work is to focus on implementation of non-machined metal hardware for fabrication and demonstration of a 4 kW stack operating on hydrogen and air. The 4 kW stack is scheduled to be demonstrated by April 1998. The location/ type of demonstration is to be coordinated with the Hydrogen Program office. Because an ambient pressure stack is to be demonstrated first , according to newly defined programmatic requirements, a novel mode of stack humidification developed by us recently will be implemented, based on liquid water supply to the cell through the anode backing. This will allow optimized ambient pressure operation of the stack. Some modifications of the stainless steel hardware will be required to accommodate ambient pressure operation.

Background

The high efficiency combined with very low environmental emissions and modular construction have fostered continued interest for the last thirty years in fuel cell technology for utility, customer-side-of-the-meter and transportation applications. Among the family of fuel cell technologies, polymer electrolyte (PEM) fuel cells have some uniquely attractive features, including a combination of high power density and high chemical-to-electric energy conversion efficiency, fast and easy start-up, high reliability and highly durable and benign materials of construction. Nevertheless, the application of PEM fuel cell technology for utility and /or stand alone applications was judged in the past to be too expensive for any terrestrial applications and, also, to be too sensitive to low levels of carbon monoxide in reformed carbonaceous (most likely natural gas) fuel feed streams. Both of these barriers for implementation of PEM fuel cells in utility and/or stand alone applications have been significantly lowered in the last few years but a remaining important barrier has been the need for a PEM fuel cell stack technology which is (a) of lower intrinsic cost, and (b) lends itself easily to large scale manufacturing.

To express the requirements from a viable stack technology in specific terms, the lowering of the cost means primarily lowering of intrinsic materials costs, including catalyst, membrane and stack hardware materials. The latter include primarily the flow field/bipolar plate. The "manufacturability" of the stack is improved as the complexity of the forming processes, particularly forming of the bipolar plate/flow field, is minimized. Typically, minimization of the complexity in such forming processes is achieved when machining is completely eliminated, replacing it by processes based , e.g., on stamping and punching for metal hardware, or on molding for carbon based composites. Although machining is understood to be unsatisfactory for large scale and low cost manufacturing, present day fuel cell stack technology is still based on machined graphite plates as the bipolar plate/flow field combination. To achieve the central target of our project, the demonstration of low cost PEM fuel cell stack technology of clear manufacturability advantages, we have focused on the following elements:

(a) Demonstrate at LANL the fabrication and quality of larger scale membrane/electrode assemblies (M&Es) based on low catalyst loadings. Such M&Es have been developed previously at LANL but demonstrated only in smaller cells of several cm^2 in area,

(b) Develop and demonstrate at LANL innovative stack technologies based on non-machined stainless steel components, that would best satisfy the combined requirements of low cost materials and manufacturability.

(c) Have such M&Es and cell hardware be tested, evaluated and, possibly, further scaled up at H Power, our CRADA partner.

These tasks are to culminate in a demonstration of a 4-5 kW prototype stack with the combined properties of low cost and manufacturability (now scheduled 4/98 in the context of a PUV) .

Progress This Year

(1) 2000 hours of continuous testing of a 100 cm^2 cell, based on 316 stainless steel screens/ foils successfully completed.

Figures 1 describes schematically the construction of "picture framed" membrane/electrode (M&E) with carbon paper backings, and Figure 2 describes schematically the assembly of a single cell with a pair of course and fine stainless steel screens on each side of the framed M&E. The combination of two screens has been required to achieve effective gas distribution, provided by the course screen, and appropriate screen/carbon paper contact, provided by the fine screen. Automated fabrication of catalyzed membranes of larger areas with ultra-low Pt loadings was previously developed by us as part of this project, employing a computer controlled X-Y recorder (reported in last year's Annual Technical Review Proceedings).

SS Screen and Foil Hardware:
Assembly of a Picture Frame MEA

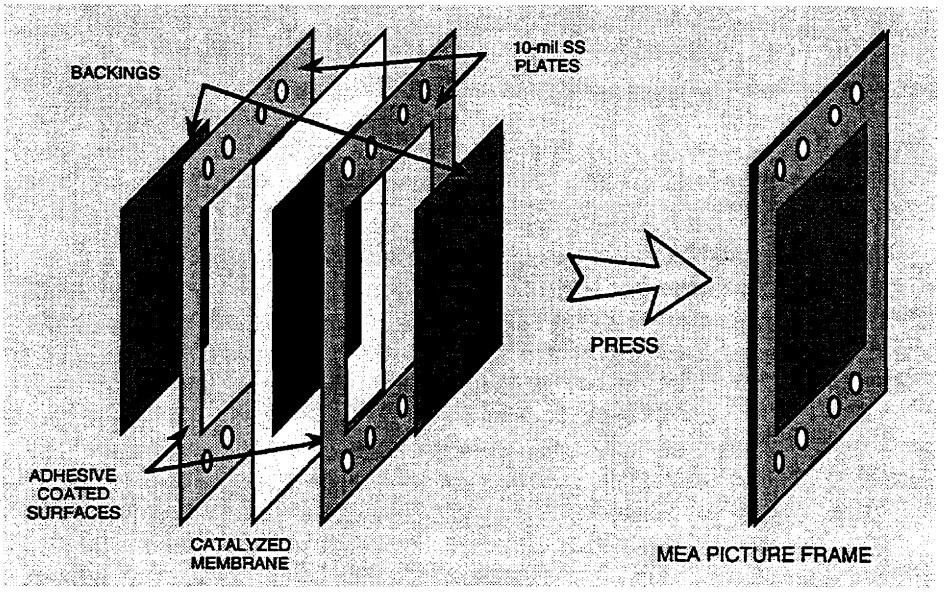

ELECTRONICS RESEARCH — Los Alamos Materials Science and Tech

FIGURE 1

As shown in Figure 2, the structure of the cell developed by us is very simple and based on inexpensive off-the-shelf 316 stainless steel screens and foils.

SS Screen and Foil Hardware: Unit Cell Components

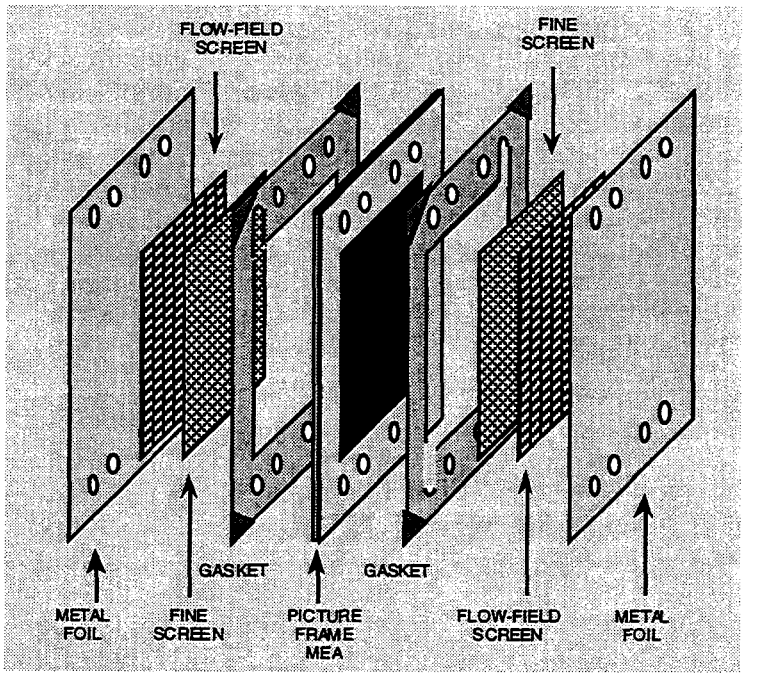

FIGURE 2

Continuous testing of such a cell for 2000 hours was completed during this year, addressing the most important concern regarding such simple, metal hardware-based cells, i.e., long term stability of the stainless steel hardware in terms of any development of resistive surface films and any leaching of metal ions that could "poison" the ionomeric membrane. The most effective probing of these two potential failure modes is based on measurements of the high frequency resistance of the cell during the life test. Failure of the stainless steel hardware, associated with either excessive growth of oxide films or leaching of metal ions which foul the membrane, will be reflected by an increase in the ohmic (high frequency) resistance of the cell. To measure separately losses associated with the metal hardware on each side of the cell, special probes were connected to the individual parts shown in figure 2. Figure 3 thus shows resistances associated with each side of the cell, as well total cell resistance, as function of time during the life test. Figure 3 shows that the resistance of the cell has not increased at all during 2000 hours of continuous testing. (Lowering of resistanc seen around 800 hours into the life test was caused by stronger "torquing" across the cell at that point in the test). Such lack of any increase in cell resistance serves as very good indication that, at least at single cell level, 316 stainless steel seems to exhibit high degree of material's stability on either anode or cathode side of the fuel cell constructed according to the scheme shown in Figure 2. We believe that this stability is enabled in large part by this type of cell structure, that does not involve any direct contact between metal and membrane electrolyte.

Life Test with 316 SS Hardware: Hardware Contribution to Cell Resistance

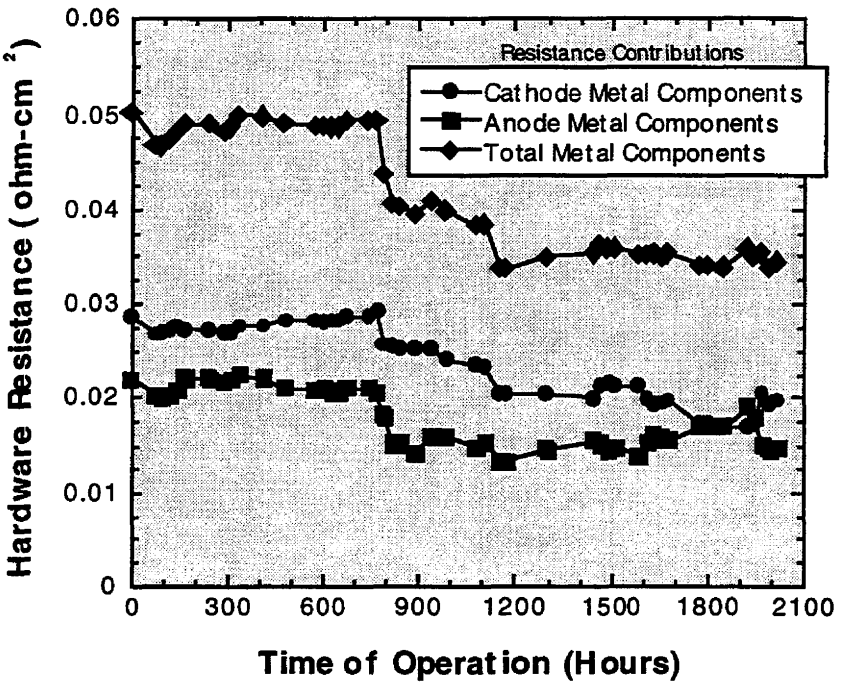

ELECTRONICS RESEARCH — Los Alamos Materials Science and Tech

FIGURE 3

Figure 4 shows the 100 cm^2 cell performance (polarization curves) as function of time over the 2000 hours life test. This is the same cell for which resistance measurements are shown in figure 3. Figure 4 shows good, stable performance up to 1650 hours for this hydrogen/air cell, particularly in the relevant voltage domain for stationary power generation (V> 0.7V), followed by some drop in performance indicated toward the end of 2000 hours test. Since the resistance has been found stable through the duration of the 2000 hours test (Figure 3), the drop in performance must be the result of lowering in performance of one of the electrodes. We traced the problem to excessive accumulation with time of liquid water in the cathode flow field. To repair this problem, a better design of the cathode fine screen is required, that would minimize excessive collection of liquid water next to the hydrophobic carbon paper backing leading to loss of backing hydrophobicity with time. Experiments with fine screens of flatter profiles have shown good promise in overcoming this excessive water accumulation problem in the cathode.

As final comment re. figure 4, we note that the good performance obtained for our 100 cm^2 cell which employs a non-machined, highly simple flow field based on a metal screen, is direct indication of the high efficiency of such flow fields in distributing reactant gases along electrode areas of substantial size. We reported last year on analysis of the flow pattern along a screen-based flow field with diagonally opposed inlet and outlet , concluding that, in spite of it's simplicity, it exhibits similar impedances to gas flow for all different paths between inlet and outlet, thus ensuring uniform gas distribution and uniform current density.

Life Test with 316 SS Hardware: Polarization Curves

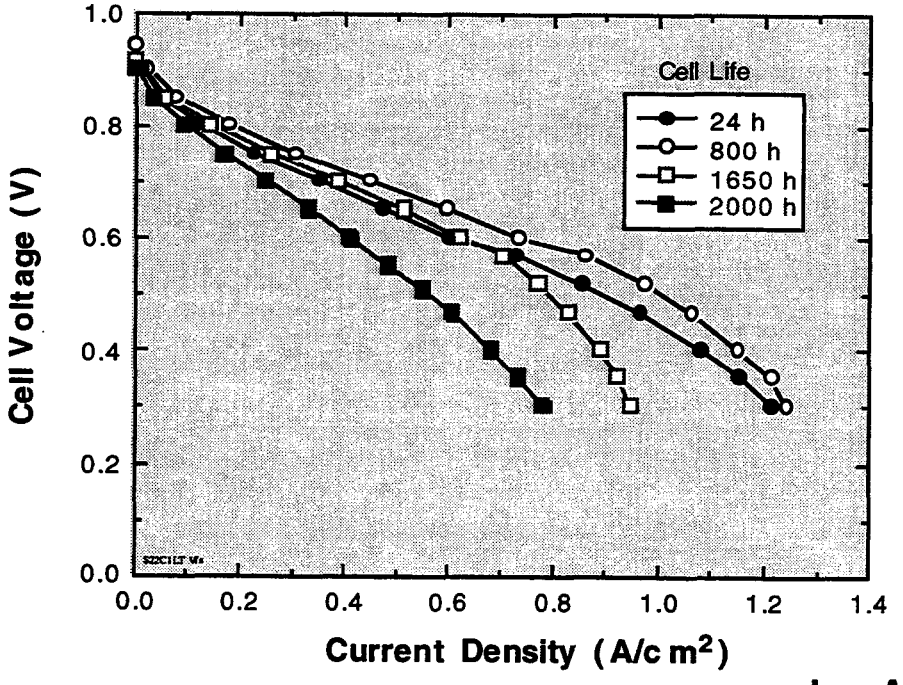

ELECTRONICS RESEARCH — Los Alamos Materials Science and Tech

FIGURE 4

Operation conditions for the cell: Nafion™ 112 membrane, 0.14 mgPt/cm^2, P_{H2}/P_{Air} = 3/3 atm, T_{cell} = 80°C.

(2) Successful Test of a Short Stack based on stainless steel hardware

Following the encouraging results of life testing of our single cell with 316 stainless steel hardware, we advanced to putting together a short stack and testing it. Figure 5 shows the overall stack structure adapted based on constructing cartridges of cells of the type shown in figure 2.

As shown in figure 6, the short stack test results have shown that the single cell performance could be repeated in a 4 cell stack within the relevant voltage domain , demonstrating viability of the stainless steel hardware and of the concept of cartridges of cells separated by cooling plates which employ similar stainless steel screens. The slight drop in performance at higher current density is again indicating the significance of effective water management in the cathode. As noted above, we do have strategies for further improvements in cathode water management. Also, this problem may have different solutions as we move to ambient pressure stack configurations.

SS Screen and Foil Hardware: Stack of Cartridges plus Cooling Plates

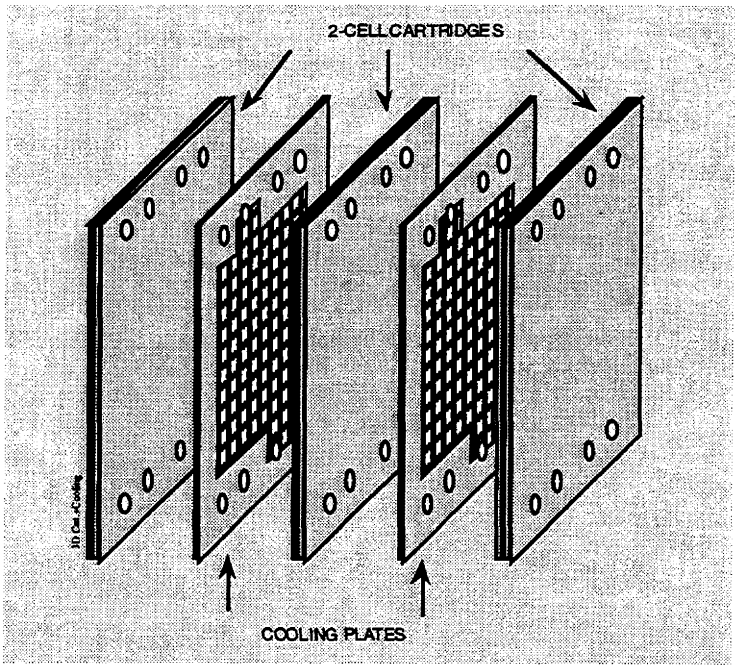

FIGURE 5

(3) In-Cell and External Corrosion Testing of 316 Stainless steel

The most rigorous way for addressing the issue of long-term immunity of stainless steel hardware in the PEM fuel cell, is based on testing of metal ion release within the operating cell/stack, or outside the cell under conditions which mimic those in an operating cell. External testing can also be attempted under conditions of "accelerated corrosion testing ", that hopefully mimic within short testing times the extent of very long term corrosion in an operating stack. For testing of metal ion release within the operating cell, water samples were collected from test station humidifier lines (electrode inlets) and from electrode outlet streams for the single cell (2000 hours test) and for the 4 cell stack, and were analyzed for chloride ion and the metals in 316 stainless steel. In general, the water from the operating cell contained < 0.5 ppm chloride and 20 ppb or less of Mn, Cr, Mo, and Mg. Nickel was present at about 0.2 ppm and iron at <0.04 ppm. Water collected from the anode and cathode outlets of a 4-cell stack had a lower Ni concentration (about 0.035 ppm) compared to inlet water, but showed somewhat elevated levels of Fe. The cathode outlet water also had a somewhat elevated Cr concentration. These results are summarized in Table 1. The decrease in Ni and Mn concentration in the water passing through the operating fuel cell may indicate slow uptake of metal ions from inlet water over time. This can be prevented by incorporating an in-line demineralizer to clean the water upstream the cell of any ionic contaminants. Overall, very low leaching levels were detected in the water exhausting single cells, and slightly higher in water exhausting a stack (Table 1).

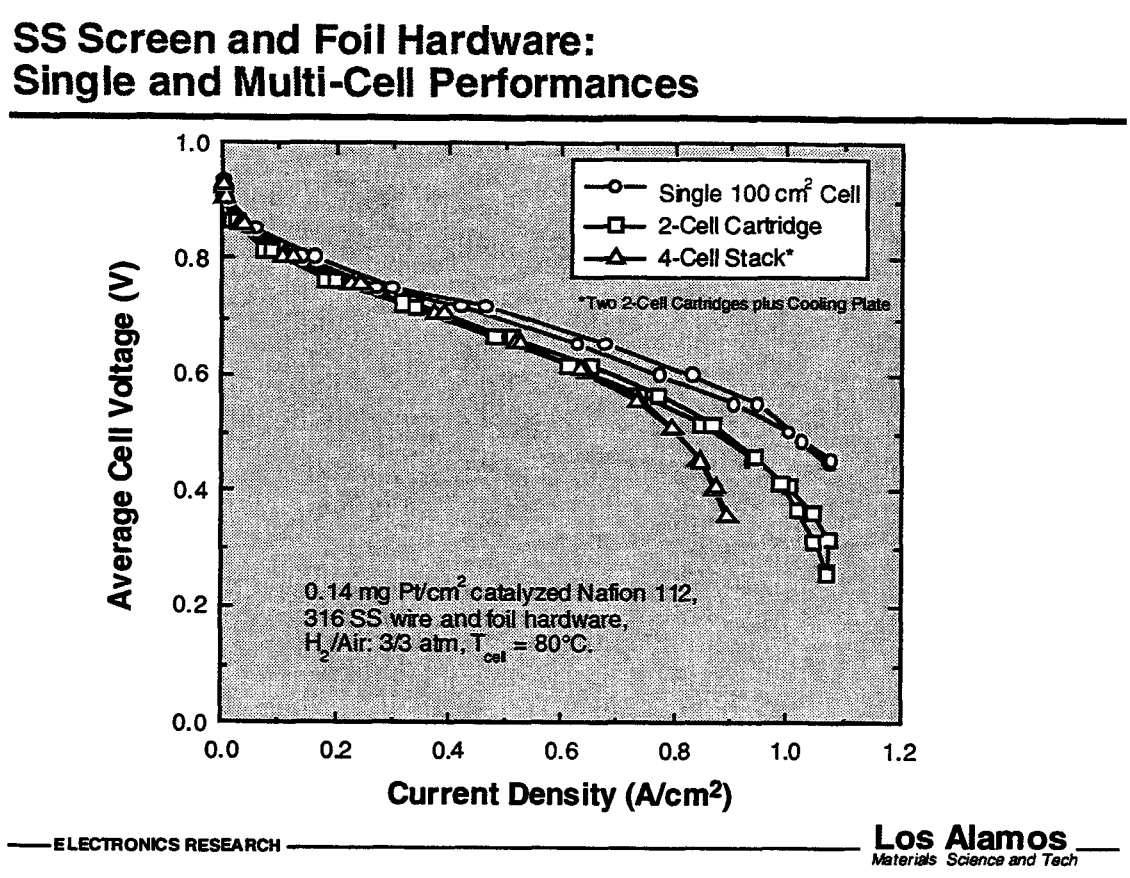

FIGURE 6

In attempted "accelerated corrosion tests", samples of 316 stainless steel (1 sq. in., 0.010" thick) were immersed for approximately 250 hours in 0.010 M H_2SO_4, with or without 10 ppm chloride added, and sparged with either air or hydrogen. Solution temperatures were initially maintained at 60°C, then increased to 80°C. At 250 hours, the solutions were analyzed for chloride ion and for metal ions. Chloride ion concentrations did not change between initial and final solutions, and in general, metal ion concentrations were elevated in the final solutions. Solutions exposed to hydrogen had higher levels of metal concentrations than those exposed to air. These findings are summarized in Table 2.

On visual inspection, samples exposed to air appeared as bright and shiny as before immersion, whereas the samples exposed to hydrogen had some surface discoloration. This discoloration was determined by EDS to be associated with slight variations in the properies of the thin passive film. It is not clear that these immersion test conditions are representative -- particularly the very low pH (=2) may be highly exaggerated vs. realistic expectations in an operating stack, causing the apparent marginal flaw in passivity of this alloy in contact with hydrogen.

Table I. Water Sample Analyses

Sample	Mn (ppm)	Ni (ppm)	Cr (ppm)	Mo (ppm)	Mg (ppm)	Fe (ppm)	Cl (ppm)
Cathode outlet H_2O from 2000 hr. cell	< 0.005	0.011 ± 0.005	< 0.005	< 0.005	0.029 ± 0.010	< 0.040	< 0.5
Cathode inlet H_2O from test station	0.017 ± 0.005	0.190 ± 0.030	< 0.005	< 0.005	0.014 ± 0.006	< 0.040	< 0.5
Cathode outlet H_2O from 4-cell stack	0.012 ± 0.005	0.035 ± 0.009	0.050 ± 0.020	0.007 ± 0.005	0.007 ± 0.005	0.740 ± 0.07	3 ±0.51
Anode inlet H_2O from test station	0.011 ± 0.005	0.220 ± 0.030	< 0.005	0.006 ± 0.005	0.012 ± 0.005	< 0.040	< 0.5
Anode outlet H_2O from 4-cell stack	0.009 ± 0.005	0.034 ± 0.005	0.007 ± 0.005	0.008 ± 0.005	0.023 ± 0.007	0.180 ± 0.04	< 0.5

Water samples were collected from operating cells and from humidifier lines. The samples were analyzed by ICP - MS (Mn, Ni, Cr, Mo, Mg), ICP - ES (Fe), and IC (Cl).

Table II. Aggressive Immersion Testing

Sample	Mn (ppm)	Ni (ppm)	Cr (ppm)	Mo (ppm)	Mg (ppm)	Fe (ppm)	Cl (ppm)	% wt. loss	Corr rate (µm / yr.)	Surface of 316 SS
A: initial	< 0.005	< 0.005	< 0.005	< 0.005	0.028 ± 0.007	< 0.04	4.0 ± 0.5	NA	NA	Shiny
A: final (air)	0.027 ± 0.005	0.100 ± 0.010	0.105 ± 0.006	0.020 ± 0.010	0.044 ± 0.006	0.790 ± 0.079	4.2 ±0.5	0.01	0.6	Same as initial
A: final (H_2)	0.900 ± 0.100	7.600 ± 0.300	10.300 ± 0.500	1.000 ±0.300	0.110 ± 0.010	41.0 ± 4.1	4.1 ± 0.5	0.4	17	Significant discoloration
B: initial	< 0.005	< 0.005	< 0.005	< 0.005	< 0.005	< 0.04	8.0 ± 0.8	NA	NA	Shiny
B: final (air)	0.025 ± 0.005	0.080 ± 0.010	0.098 ± 0.007	0.020 ± 0.010	0.034 ± 0.005	0.590 ± 0.059	8.4 ± 0.8	0.02	0.7	Same as initial
B: final (H_2)	1.600 ± 0.300	13.00 ± 1.000	18.000 ± 1.000	2.800 ± 0.500	19 ± 5	71.0 ± 7.1	8.4 ± 0.8	0.02	0.7	Some discoloration

Samples of 316 SS (1 sq. in., 0.010" thick) were immersed for approximately 250 hrs. in the solutions listed below while sparged with either air or hydrogen. Solution temperatures were initially maintained at 60°C, then increased to 80°C. Solution A: 0.010 M H_2SO_4, Solution B: 0.010 M H_2SO_4 + 10 ppm NaCl. The solution samples were analyzed by ICP-MS (Mn, Ni, Cr, Mo, Mg), ICP - ES (Fe), and IC (Cl).

In conclusion, while overall the level of metal ion leaching has been found low-to-very low in these tests, indications of higher levels of metal ion release from the stack vs. the single cell and of higher apparent vulnerability of samples in contact with hydrogen when the acidity becomes significant , call for further testing to clarify their exact significance. Having a stack based on stainless steel hardware corrosion-immune to the degree required for stable long-term operation, seems achievable from the results shown in figure 3 and from our initial corrosion tests. This target will, however, remain a significant challenge in the final design and fabrication of such ultra-simple, low cost stacks.

Future Plans

(1) Future work is to focus on implementation of metal hardware for fabrication and demonstration of a 4 kW stack operating on hydrogen and air. The 4 kW stack is scheduled to be demonstrated April 1998. The location/ type of demonstration is to be coordinated with the Hydrogen Program office. For the ambient pressure stack to be demonstrated on April '98, we will apply a novel mode of stack humidification developed by us recently, based on liquid water supply to the cell through the anode backing. This will allow effective operation of the stack at ambient pressure.

(2) Following completion of fabrication and demonstration of the 4 kW metal hardware stack, we plan to pursue a 10 kW ambient pressure, metal hardware stack, to be fabricated and demonstrated first in a small "neighborhood vehicle".

(3) We plan to continue comprehensive testing of stainless steel alloy passivity under fuel cell operation conditions, and optimize the design and the exact type of alloys chosen according to such tests.

References

1. Simon Cleghorn, Xiaoming Ren, Thomas Springer, Mahlon Wilson, Christine Zawodzinski, Thomas Zawodzinski and Shimshon Gottesfeld, "PEM Fuel Cells For Transportation And Stationary Power Generation Applications", *Hydrogen Energy Progress* XI, pp. 1637 - 1646, 1996 (Keynote Lecture at the 11th World Hydrogen Conference, Stuttgart, Germany, June 1996).

2. Christine Zawodzinski, Mahlon Wilson and Shimshon Gottesfeld, "Stainless steel Wire Mesh Flow Fields for PEFCs", Fuel Cell Seminar 1996 (Courtesy Associates Inc), pp. 659-662.

3. Christine Zawodzinski, Mahlon Wilson and Shimshon Gotetsfeld, "Low Cost PEM Fuel Cell Hardware Based on Metal Screen Flow Fields", Extended Abstract No. 793, The Electrochemical Society Meeting in San Antonio, October 1996.

Regenerative Fuel Cell Systems

Fred Mitlitsky,* Blake Myers, and Andrew H. Weisberg

Lawrence Livermore National Laboratory, 7000 East Avenue, L-045, Livermore, CA 94551
(510) 423-4852, FAX: (510) 423-9178, fm@llnl.gov

Revised Aug 12, 1997

Regenerative fuel cell (RFC) systems produce power and electrolytically regenerate their reactants using stacks of electrochemical cells. Energy storage systems with extremely high specific energy (>400 Wh/kg) have been designed that use lightweight pressure vessels to contain the gases generated by reversible (unitized) regenerative fuel cells (URFCs). Progress is reported on the development, integration, and operation of rechargeable energy storage systems with such high specific energy. A primary fuel cell test rig with a single cell (46 cm^2 active area) has been modified and operated reversibly as a URFC (for up to 2010 cycles on a single cell). This URFC uses bifunctional electrodes (oxidation and reduction electrodes reverse roles when switching from charge to discharge, as with a rechargeable battery) and cathode feed electrolysis (water is fed from the hydrogen side of the cell). Lightweight pressure vessels with performance factors (burst pressure * internal volume / tank weight) >50 km (2.0 million inches) have been designed, and a vessel with performance factor of 40 km (1.6 million inches) was fabricated. These vessels use lightweight bladder liners that act as inflatable mandrels for composite overwrap and provide the permeation barrier for gas storage. Bladders are fabricated using materials that are compatible with humidified, electrolyzed gases, and are designed to be compatible with elevated temperatures that occur during fast fills or epoxy curing cycles. RFC systems are considered that use hydrogen/oxygen, hydrogen/air, or hydrogen/halogen chemistries. Hydrogen/halogen URFCs are capable of higher round-trip efficiency than hydrogen/oxygen URFCs, but are significantly heavier. Therefore, hydrogen/halogen URFCs are advantageous for stationary applications, whereas hydrogen/oxygen URFCs are advantageous for mobile applications. Safety aspects of halogens may prohibit their use in densely populated areas and some commercial applications, so these niches can also benefit from hydrogen/oxygen URFCs.

This paper will appear in a special hydrogen edition of Energy & Fuels.

THE PALM DESERT RENEWABLE HYDROGEN TRANSPORTATION SYSTEM

Peter Lehman and Susan Ornelas
Schatz Energy Research Center
Humboldt State University
Arcata, CA 95521

Abstract

This paper describes the Schatz Energy Research Center (SERC) progress on the Palm Desert Renewable Hydrogen Transportation System Project for the period of July 1996 through June 1997. The project began in March 1996.

The goal of the Palm Desert Project is to develop a clean and sustainable transportation system for a community. The project demonstrates the practical utility of hydrogen as a transportation fuel and the proton exchange membrane (PEM) fuel cell as a vehicle power system. This system is being developed for the City of Palm Desert in Southern California, as the air quality in this area is very polluted, mostly from motor vehicles. The project includes designing and building 4 fuel cell powered vehicles, a solar hydrogen generating and refueling station, and a fuel cell vehicle diagnostic center.

Over this last year, SERC has built 3 fuel cell powered personal utility vehicles and delivered them to the City of Palm Desert. The hydrogen refueling station is being designed and it is anticipated that construction will begin in the fall of 1997. The vehicles are currently being refueled at a temporary refueling station. The diagnostic center is being designed and maintenance procedures as well as computer diagnostic programs for the fuel cell vehicles are being developed.

The vehicles are being driven daily by city employees. The cart drivers are pleased with the performance of the vehicles, and it is very exciting that fuel cell powered vehicle technology is on the street and performing well.

Rationale

The main objectives for this project are to develop a clean transportation system for the City of Palm Desert in Southern California and to further research on proton exchange membrane (PEM) fuel cell and hydrogen technologies, in order to promote a clean and sustainable energy future. Some of the background societal conditions which led up to this project are:

- Smoggy air lowers the quality of life of the over 75% of Americans who live in large cities. A 1996 study using Harvard and American Cancer Society research and linking deaths to air pollution showed that the Riverside-San Bernardino region topped the nation in the death rate per capita blamed on particulates. The study linked 17% of cardiopulmonary deaths in the greater Los Angeles area to pollution. This number exceeds the number of people who died from auto accidents.

- In the near future, zero emission vehicles (ZEVs) will be required in California, Massachusetts and New York. The research and development on fuel cell technology and its integration into user ready, street safe vehicles will aid in producing ZEVs to meet these mandates.

- In order for this technology to be integrated into our society, people must overcome their fear of hydrogen and learn its benefits. A complete hydrogen fuel cell powered transportation system operating in a community will go far to dispel these fears and educate citizens.

- Development of a clean, sustainable transportation system would eliminate criteria pollutants, decrease reliance on imported petroleum, and improve public health.

History of the Schatz Energy Research Center

Schatz Energy Research Center began the three year, $3.9M Palm Desert Renewable Hydrogen Transportation System Project in January of 1996. During the years of 1990 to 1995, SERC built, and continues to operate, an automatic solar hydrogen-fuel cell energy system which powers an air compressor at the Humboldt State University Telonicher Marine Laboratory. In addition, SERC developed a fully equipped fuel cell laboratory and production facility and built its first fuel cells, as well as a prototype fuel cell powered PUV. The prototype PUV was completed on schedule and debuted on November 5, 1995 at the Palm Desert Golf Cart Parade. The cart performs well and meets our initial goals.

Technical Goals

The outcome of this project will be a complete, operating model transportation system based on hydrogen and fuel cell powered vehicles. This is the first time that solar derived hydrogen will be produced and used in fuel cells to power motor vehicles. The project provides the opportunity to collect data to help understand how differences in system components can affect overall performance, thus gaining information directly relevant to the nation's future transportation system. Success will also result in new materials and manufacturing techniques for fuel cell power systems that will help commercialize the technology.

In order to achieve the overall goal, the following specific objectives will be met. They are:

- Design and construct 3 personal utility vehicles (PUVs) and 1 neighborhood electric vehicle (NEV) and deliver them to the City of Palm Desert. These fuel cell powered vehicles will be

driven around the City for normal day-to-day activities and their performance will be recorded and evaluated.

- Design and construct a solar hydrogen refueling station in the City. The facility will use photovoltaic electrolysis to produce the hydrogen which will be compressed and stored. Fuel dispensing to the vehicles will occur at a refueling island and be convenient and safe.

- Equip a fuel cell vehicle maintenance facility at the City's corporation yard. This facility will have diagnostic capability; personnel will be trained to maintain and service the vehicles.

Barriers to Technical Goals

Technical and societal barriers have surfaced during the course of the development of this technology. These include:

- Permitting - In order to comply with the Field Act , plans for the solar hydrogen generating and refueling station must be reviewed by the Office of the State Architect. A building permit will be required as well, meaning the station will have to meet building, electric, plumbing and fire codes.

- Insurance - SERC PUVs are covered under the Humboldt State University general policy , even though they use an unconventional power source. Currently the battery-powered NEV is insured with a conventional insurance agent. Car insurance will be difficult to obtain once the vehicle is retrofitted with a fuel cell, since no data exists for the insurance industry to calculate risk. This issue will dictate whether or not the NEV may be legally driven. Liability insurance issues have also delayed the approval process for the refueling station, although these are largely resolved now. Frequent visits to Palm Desert to meet with both City and College of the Desert officials and personnel have been successful in creating an amicable resolution to these issues.

- Availability of appropriate and certified system components - Many of the components SERC will be using for the NEV and solar hydrogen station will be integrated in such systems for the first time. Although some are off-the-shelf items, others will have to be custom-made and extensively tested. Certification is another issue; finding components certified for hydrogen use is sometimes difficult, costly, and/or time consuming.

Current Year Accomplishment/Status

During the past year SERC has designed and built a three fuel cell powered PUVs, all of which have been delivered to the City of Palm Desert. This process involved:

- designing, building, and testing a 5.0 kW proton exchange membrane (PEM) fuel cell as a power plant for the PUVs.
- designing, building and testing peripherals including the air delivery, fuel storage and delivery, refueling, water circulation, cooling, and electrical systems.
- devising and implementing a control algorithm for the fuel cell power plant in the PUVs.
- designing and building a test bench in which running conditions in the PUVs could be simulated and the fuel cell and its peripheral systems tested.
- installing an onboard computer and associated input/output electronics into the PUVs and debugging.
- assembling and road testing the PUVs.

Along with designing and building the PUVs, SERC has:

- designed and installed a temporary hydrogen refueling station at the College of the Desert (COD). The station is operated by COD personnel who have been trained by SERC and it will serve until the solar hydrogen refueling station is open.
- secured a site for the solar hydrogen refueling station on the COD campus. This has been a lengthy process which involved COD and City officials and their attorneys.
- begun the design of the solar hydrogen generating and refueling station and initiated the permitting process. This has included completion of a PV system simulation and sizing of the array, a hazards analysis, a site plan, a floor plan of the generation building, preliminary landscaping plan and architectural rough sketches.
- begun testing several types of electrode and membrane materials in order to increase the power density of the fuel cell. So far this year, SERC has seen a 50% improvement in fuel cell performance.
- acquired, instrumented and tested an NEV, begun the design of a fuel cell power system appropriate to the NEV, and initiated fuel cell testing necessary to determine the configuration of the NEV stack.
- coordinated activities with Sandia National Laboratory to develop an on-board metal hydride storage system for a PUV.

Design and Performance of the Personal Utility Vehicles (PUVs)

Initially, we determined what design criteria were important for the fuel cell vehicle. These criteria defined the technologies we would need to develop a successful design. Listed below in Table 1 are the PUV design criteria and the associated resultant technologies.

Table 1: PUV Design Criteria and Resultant Technologies

Design Criteria	Resultant Technology
Established cart with efficient motor and motor controller	EZ-GO Golf Cart
Sufficient power for quick acceleration	Parallel hybrid design with 20 amp-hr, Pb acid battery
Convenient and simple operation	On-board computer with straightforward operational algorithm and start-up sequence
Diagnostic capability	Numerous on-board transducers and lap-top readout capability
Safety	Inherently safe design and numerous safety interlocks
Sufficient voltage for PUV traction bus	64 cell stack
Sufficient power for hill climbing	300 sq cm active area
Low parasitic load	Low pressure operation, use of high efficiency blower, optimum 5-10% parasitic load
Sufficient cooling capacity	Water cooling with large heat exchange area
Efficient operation	0.71 volts/cell @ cruising, 57% stack efficiency

The original, battery powered E-Z-GO cart was instrumented and tested to determine the necessary operational criteria. Next, the subsystems were designed and tested. The subsystems include the cooling, gas storage and delivery, air delivery, and electrical systems. All the components were

assembled on a prototype bench which was fitted with a programmable load to mimic driving cycles. Numerous tests were performed to optimize the operational algorithm and wring out bugs. The vehicles were then gutted, structural changes made and a custom, fiberglass cover was crafted to cover the gas storage area. Then the fuel cell and subsystems, including the on-board computer and transducers were installed in the PUVs.

PUV 1 was completed and delivered to Palm Desert in September of 1996 and PUVs 2&3 were completed and delivered in May of 1997. They were all road tested and final adjustments made before being shipped. Some improvements in the design were made on PUVs 2&3, as compared to PUV 1. The improvements to PUVs 2 & 3 include an in-house designed excess flow device for improved safety, an internal data collection system within the control computer, improved graphite and lower platinum loading on the fuel cell, a refined dashboard user interface to facilitate ease of use, and attractive wooden flatbeds were added for improved user utility. Table 2 outlines the operating specifications for PUV 2 &3. Note that the PUVs have a gasoline use equivalency of approximately 120 miles per gallon, which is equivalent to 0.30 kWh of hydrogen per mile.

Table 1: Personal Utility Vehicle (PUV) 2 & 3 Specifications

Fuel cell type	Proton Exchange Membrane
Fuel cell power	4.8 kW (6.4 hp)
Number of cells	64
Hydrogen energy consumption	0.30 kWh/mile
Mileage (gasoline energy equivalent)	120 mpg
Fuel cell system weight	200 lbs
Traction bus voltage	36 volts (nominal)
Electric motor size	1.5 kW (9.0 hp)
Hybrid battery size	19 amp-hrs
Cruising speed	15 mph
Fuel cell net power at cruising speed	1.8 kW
Hydrogen tank volume	11.8 liters
Hydrogen gas storage pressure	2,000 psig
Range	15 miles
Refueling time	2 minutes

When the PUVs were being road tested before delivery, performance data were recorded. Figure 1 shows the operating characteristics of the fuel cell power system in PUV 2 in a 70 second interval, starting from standstill and accelerating. Figure 2 shows the same information, but highlights the first ten seconds of the test. The plots show the power out of the fuel cell, the power to or from the batteries, and the power to the traction bus, which in turn runs the motor controller. At idle, the power to the traction bus is zero and the fuel cell produces the power to charge the battery. During acceleration, the battery does most of the work for 1.5 seconds, at which time the power output of the fuel cell begins to steadily increase. Battery and fuel cell power output are equal at 3 seconds. By 6 seconds after startup, the fuel cell is providing all the power to run the motor, charge the battery and meet the parasitic load. Note on Figure 1 that the battery is back to full charge by 70 seconds.

Figure 3 shows the line of best fit for the parasitic load as a function of the fuel cell power. The parasitic load is the load from all the subsystems. Note that the best fit line falls at approximately 9% at the cruising power of 2.2 kW. This low parasitic load is one of the original design criteria and is important to optimize the net efficiency of the system.

Figure 4 shows the speed (mph) of PUV 2 as compared to the original E-Z-GO golf cart, over a period of one minute. Within just 5 seconds, the fuel cell adapted PUV begins achieving greater

speed than the original golf cart and by 20 seconds it is operating at 15 mph compared to the 12 mph at which the battery powered golf cart operates. Greater speed is attained in the PUV because the traction bus operates at a higher voltage. The fuel cell acts as a generator, keeping the batteries charged, which in turn allows the vehicle to operate at the higher voltage.

Conclusions

The first year and a half of this project have been very productive. Advancements have been made in PEM fuel cell technology and three fuel cell powered vehicles are operating on the road. They are being driven successfully, not by specialized technicians, but by regular people in their daily lives. The attention which we paid to vehicle performance, safety and ease of user interface have proven to be important criteria to the successful adaptation of this technology.

The whole demonstration transportation system in the City of Palm Desert, with the four hydrogen powered vehicles and the solar hydrogen refueling station will be an inspiration to other cities, especially cities suffering from automobile induced air pollution. This demonstration site and the advancement of the hydrogen fuel cell technology, will assist people in the future by both alleviating their fears about hydrogen, and illustrating to them the potential of hydrogen as a clean, renewable energy source.

Plans for Future Work

In the coming year SERC intends to:

- complete the design of a fuel cell powered NEV. This will include completing design comparisons for the NEV and a decision on the power system, documenting the electrical system, and determining which components will be needed and testing them.
- acquire components for and build, test, and deliver a fuel cell powered NEV.
- monitor, maintain and operate all vehicles and begin the process of technology transfer to an employee in Palm Desert.
- complete the design and permitting of the solar hydrogen generating and refueling facility. We have been in contact with the architect, and are in the process of drawing up plans for the station with it's necessary equipment in place, as well as, designing the landscaping for the grounds to meet COD specifications.
- acquire components for and build, test, and deliver the solar hydrogen generating and refueling facility.
- continue the design of a fuel cell service and diagnostic center.

Status of Economic Evaluation

This is a research and demonstration project. Economic evaluation of our prototype vehicles and solar hydrogen generating system is not applicable.

Publications/Awards/Events:

Articles about the project have appeared in:

Popular Science (September 1996, October 1996)

Motorland Magazine -a publication of the American Automobile Association (Nov/Dec 1996)

A video about the project has appeared on:

Understanding Cars, The Learning Channel, May, 1997

Peter Lehman and Charles Chamberlin made the following presentations in 1996 and early 1997:

Lehman, P. A., "Palm Desert Renewable Hydrogen Transportation System", DOE Hydrogen Technical Review Meeting, Washington, D.C., May 1997.

Lehman, P. A., "The Palm Desert Project," Meeting at the City of Palm Springs to discuss clean transportation in the Coachella Valley, April 1997.

Lehman, P.A., "Fuel Cell Powered Electric Vehicles", Monthly Meeting of the HSU Society of Sigma Xi, April 1997.

Lehman, P. A., "The Palm Desert Project," 8th Annual National Hydrogen Association Meeting, Alexandria, VA, March 1997.

Lehman, P.A., "Fuel Cell Powered Electric Vehicles," Monthly Meeting of the Northern California American Chemical Society, February 1997

Lehman, P.A., "Fuel Cell Basics," South Coast Air Quality Management District, February 1997

Lehman, P.A., "Recent Progress in the Palm Desert Project," World Car Conference, Riverside, CA, January 1997. Also session chairman for "Fuel Cells and Infrastructure I and II."

Lehman, P.A., "Design and Performance of SERC's Prototype Fuel Cell Powered Vehicle," Commercializing Fuel Cell Vehicles Conference, Chicago, September 1996.

Lehman, P.A. and Chamberlin, C.E., "Design and Performance of SERC's Prototype Fuel Cell Powered Vehicle," Fuel Cell Seminar, Orlando, November 1996.

Lehman, P.A., "The Palm Desert Project," DOE Annual Review Meeting, Miami Beach, May 1996.

Chamberlin, C.E. and Lehman, P.A., "Design and Performance of SERC's Prototype Fuel Cell Vehicle," 7th Annual National Hydrogen Association Meeting, Alexandria, VA, April, 1996.

Lehman, P.A., "Design and Performance of SERC's Fuel Cell Powered Vehicle," World Car Conference, Riverside, CA, January 1996.

SERC personnel also gave lectures, talks, and tours in our facilities on campus, to university students, emeritus faculty, business people, and community organizations. Two of our staff were well received at two seperate high schools career fairs where they spoke on our work at the Center and the engineering profession in general.

Acknowledgments

The authors gratefully acknowledge generous grant funding from Mr.L.W. Schatz of General Plastics Manufacturing Co., Tacoma, WA, USA, and the assistance of SERC's Co-director, Dr. C. Chamberlin, as well as the staff: G. Chapman, A. Cohen, S. Cohen, J. Glandt, R. Glover, R. Herick, A. Jacobson, A. LaVen, R. Mayberry, S. Ornelas, C. Parra, G. Pauletto, M. Rocheleau, L. Reid, R. Reid, R. Ward and J. Zoellick.

SERC has contacts in the following companies, which are partners in the project:

Teledyne /Brown Engineering - Energy Systems
W. L. Gore & Associates
DuPont
ASE Americas

Students Associated with the Program

There are six students (one graduate and five undergraduate) involved with this project. All are studying Environmental Resources Engineering at Humboldt State University.

Figure Titles

Figure 1: Power Use Vs. Time (70 sec)

Figure 2: Power Use Vs. Time (10 sec)

Figure 3: Parasitic Load Vs. Fuel Cell Power

Figure 4: Speed of the PUV and the Original Battery Golf Cart Vs. Time

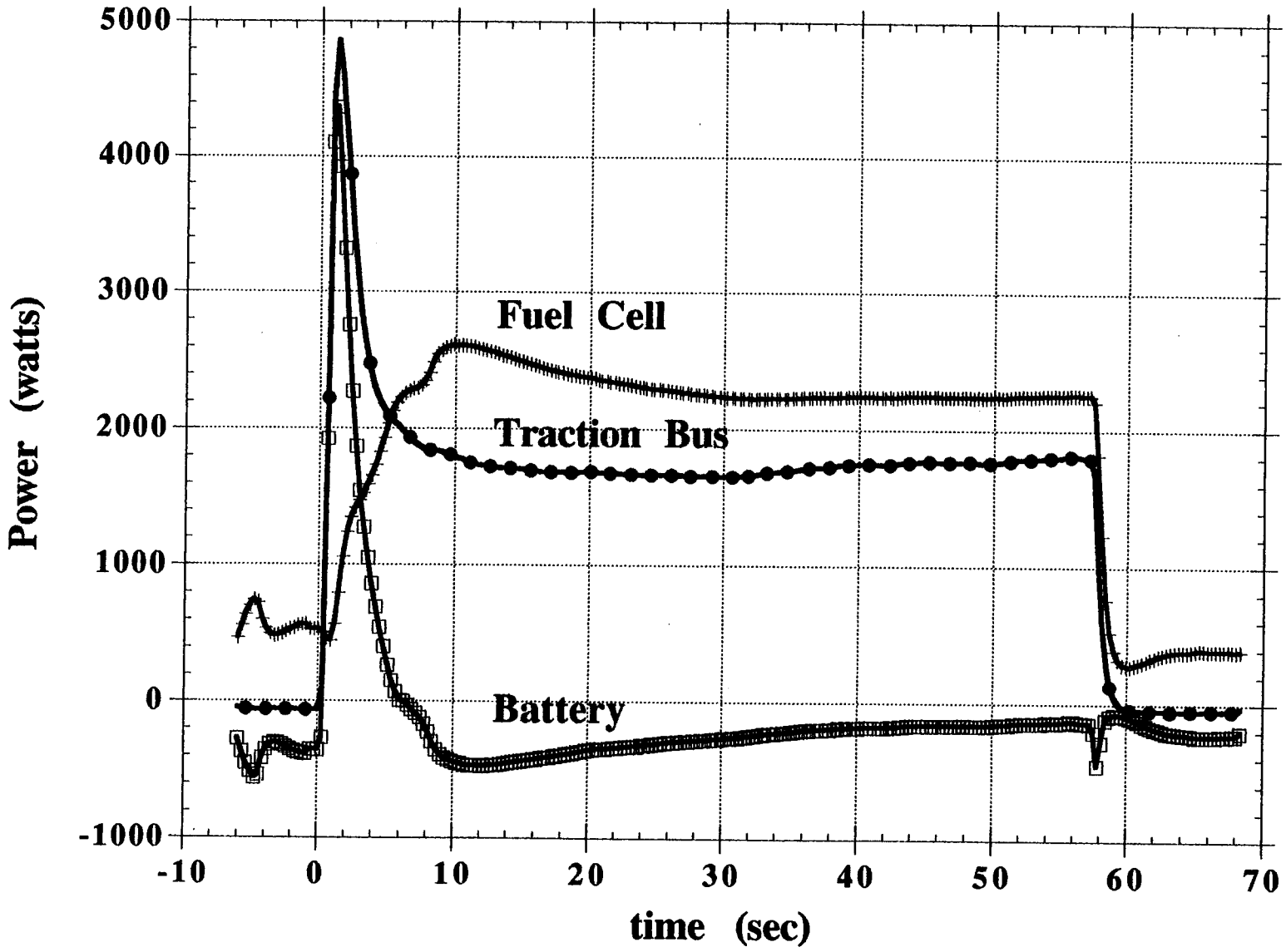
5000
4000
3000
2000
1000
0
-1000
Power (watts)
-10
0
10
20
30
40
50
60
70
time (sec)
Fuel Cell
Traction Bus
Battery

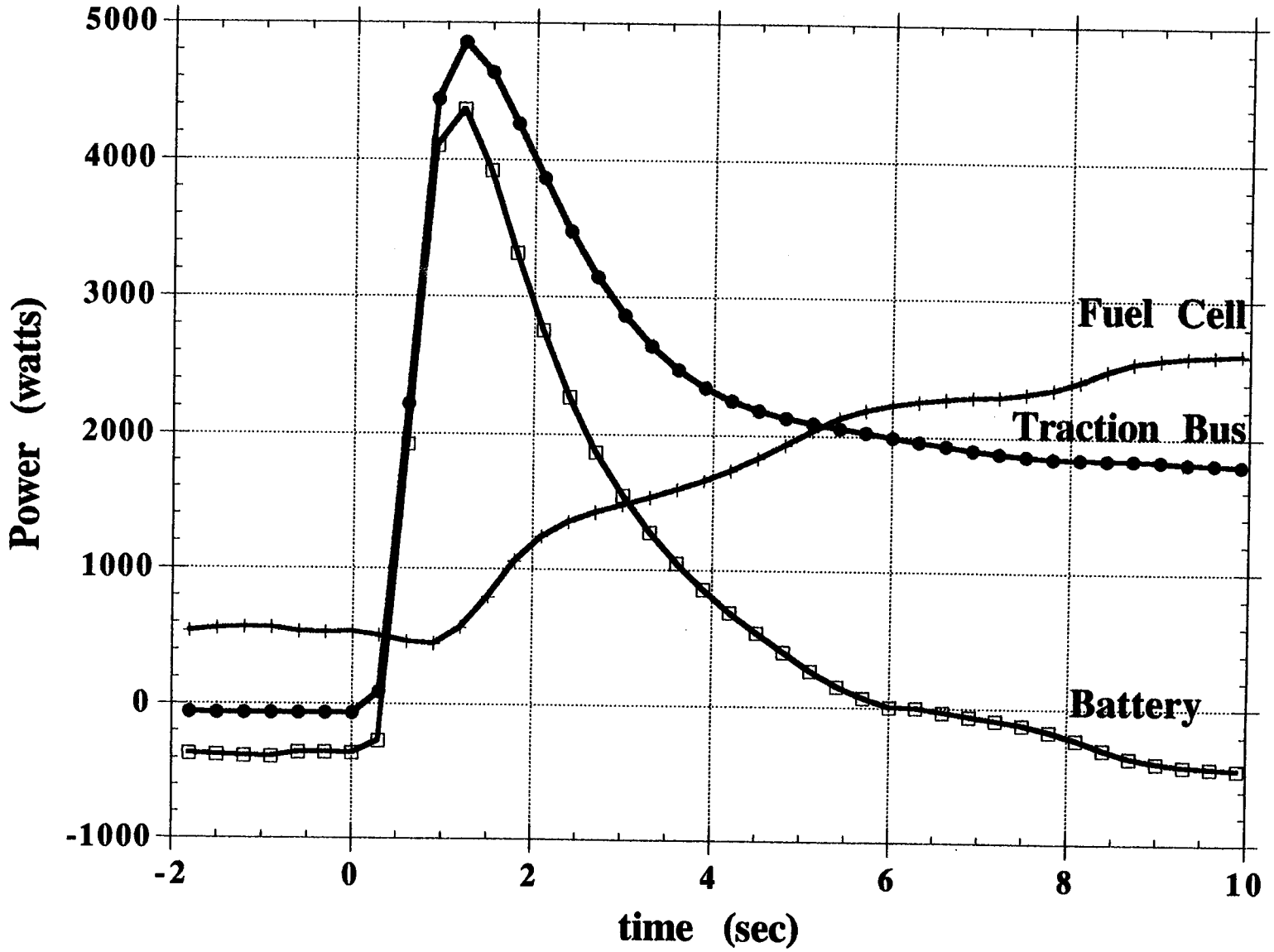
5000
4000
3000
2000
1000
0
-1000
Power (watts)
-2
0
2
4
6
8
10
time (sec)
Fuel Cell
Traction Bus
Battery

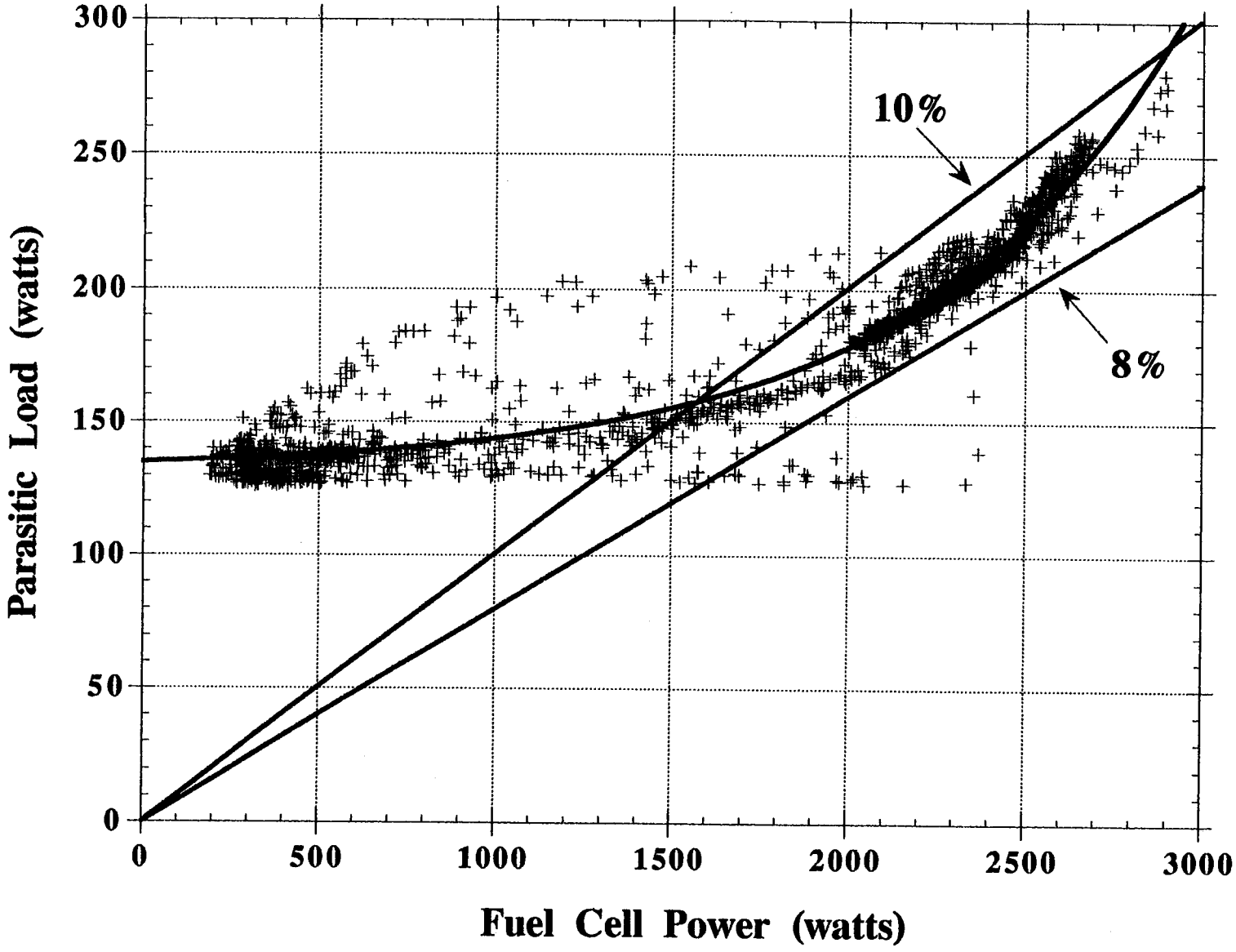
Parasitic Load (watts)
300
250
200
150
100
50
0
0
500
1000
1500
2000
2500
3000
Fuel Cell Power (watts)
10%
8%

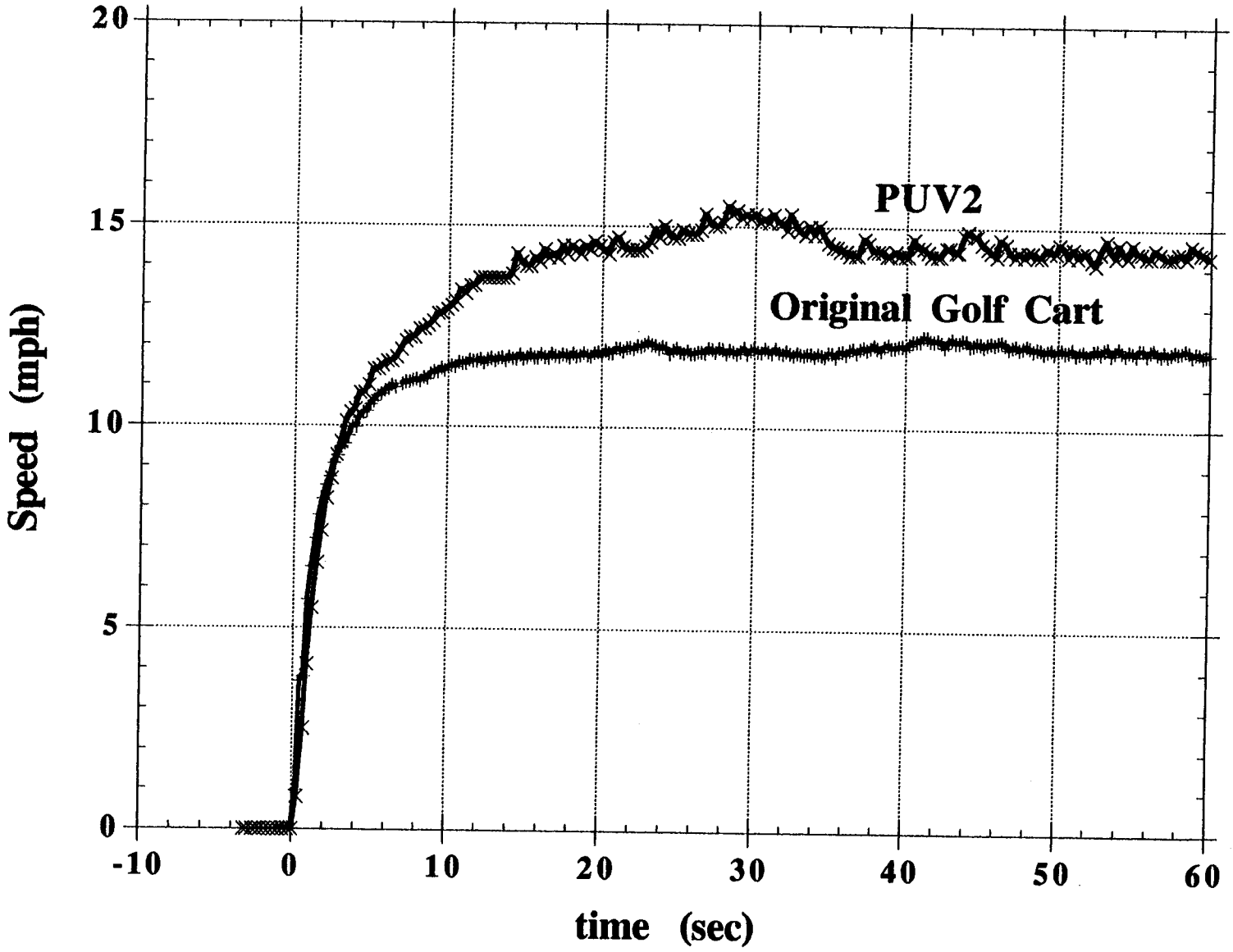
20
15
10
5
0
Speed (mph)
PUV2
Original Golf Cart
-10
0
10
20
30
40
50
60
time (sec)

200 KW HYDROGEN FUELED FUEL CELL POWER PLANT

Valerie Maston
International Fuel Cells
South Windsor, CT 06074

Abstract

IFC has designed a hydrogen fueled version of its standard PC25™ C fuel cell power plant. The standard PC25™ C is a 200 kW, natural gas fueled phosphoric acid fuel cell power plant that is commercially available. The program to accomplish the fuel change involved deleting the natural gas processing elements, designing a new fuel pretreatment subsystem, modifying the water and thermal management subsystem, developing a hydrogen burner to combust any unconsumed hydrogen, and modifying the control system. Additionally, the required modifications to the manufacturing and assembly procedures necessary to allow the hydrogen fueled power plant to be manufactured in conjunction with the on–going production of the standard PC25™ C power plants was identified. This work establishes for the DOE the design and manufacturing plan for the first commercially available 200 kW hydrogen fueled fuel cell power plant.

Introduction

IFC has designed an optimized 200 kW PAFC hydrogen fueled power plant for commercial production. The basis for this program is IFC's commercially available natural gas fueled PC25 ™ C power plant and an existing demonstration hydrogen power plant for a European customer. To meet the program goals, IFC developed a hydrogen fuel specification, designed an optimized power plant to operate on the specified fuel, identified an improved manufacturing process for the new power plant, and as cost share activity developed cell stack improvements.

Hydrogen Fuel Specification

A survey of available hydrogen fuels was conducted to provide a basis for the fuel specification. The available sources were found to be commercial pressurized hydrogen gas, commercial liquefied hydrogen, hydrogen gas from electrolysis, and hydrogen rich gas by–product from the Chlor–Alkali and Petroleum Industries. Table 1 is the summary of the hydrogen fuel sources and their compositions.

Table 1. Summary of Hydrogen Fuel Sources

	Air Products		Praxair	Renewables Solar/Wind	OxyTech	Oglethorpe Power	Ashland Petroleum
	Std–Purity Liquid	Ind–Grade Gas	Gas	Electrolysis Product	Chlor–Alkali (diaph. cell) By–Product	Customer Chlorate By–Product	Petroleum By–Product
Hydrogen, %	>99.999	>99.95	>99.99	>99.95	99.7–99.8	92.68	86.5
ppm							
Oxygen	<2	<5		<10	1500–2500	18500	
Argon				<10			
Nitrogen	<5	<400	<100	<10	40–200		5000
Methane	<4	<10		<10			39000
Ethane							40000
Propane							28000
Isobutane							8000
n–Butane							6000
Pentanes & heavier							9000
Carbon Dioxide				<10	0–800		
Carbon Monoxide			<3		trace		
CO + CO2	<1	<10					
NaOH					500–700		
NaCl					5–10		
Chlorine						0.3	
Chlorine Dioxide						0.3	
Ammonia						6	

Except for the hydrogen rich gas from the Petroleum Industry, all the other sources of hydrogen fuel were at least 98% hydrogen on a dry basis. The hydrogen rich gas by–product from the Chlor–Alkali Industry, which includes hydrogen from both chlorine and chlorate production, has unacceptably high levels of oxygen and depending on the type of cell used has high levels of chlorine, ammonia, salts, or mercury. The wide range of possible contaminants from the Chlor–Alkali gas made it impossible to establish one gas clean up system for all the Chlor–Alkali off–gases.

The Petroleum Industry hydrogen rich fuel is being addressed separately. This hydrogen rich gas by–product contains substantial amounts of heavy hydrocarbons. These hydrocarbons represent 50% of the heating value of the gas even though they only represent a mole fraction of 15%. Two methods of using such a hydrogen rich gas sources are being examined. The first is using activated carbon beds to remove the heavy hydrocarbons prior to the hydrogen power plant. The other method being evaluated is using this gas in a natural gas PC25™ C with a modified reformer matched to the petroleum by–product gas. The methods will be compared based on the estimated design and development costs of each system. A final recommendation on the approach to be used for the Petroleum Industry gas will be made once the evaluation of the two methods is completed.

Hydrogen Power Plant Specification

The hydrogen power plant design was based on the hydrogen fuels identified in Task 1. The results of this effort yielded an improvement of 2% in the electrical efficiency above the existing hydrogen power plant design. For this program, cell testing and stack modeling were done to establish flow conditions that would allow for the power plant to be over 44% electrically efficient. The stack cooling flows were changed which optimized steam production and reduced the number of components. A hydrogen burner was placed in the anode exhaust stream, which allowed for the removal of the acid scrubber and cupola from the demonstration design. The manufacturing procedures were reviewed and modifications were made to the design that optimize the build sequence and time to produce the power plant.

The following options currently available on the natural gas power plant were incorporated into this design. This power plant, unlike the existing hydrogen power plant, can be operated either grid connected or grid independent. There are two possible high grade heat options available for this power plant. The first one uses the hot water in the cooling loop to provide the customer with up to 300,000 BTU/hr of 250° F thermal energy. The second option, exclusive to the hydrogen power plant, includes the first option plus takes advantage of excess steam that can be produced by the stack. This second option allows for over 400,000 BTU/hr of high grade heat at 250° F to be removed from the power plant. This unit is a 60 Hz unit.

Cell Stack Improvements

IFC's cost share on this program was in the area of cell stack improvements. Two specific repeat parts, the separator plates and the coolers, were improved in this program. Several production trial lots were run to optimize production and improve the separator performance. The separator plate design that was selected had improved (reduced) permeability and a higher yield. This separator plate design has now been incorporated into the production bill of material. The development work on the coolers examined going to a molded cooler. Molding the cooler plates, will improve the manufacturing process. Also, methods of increasing the cooler heat transfer were examined. At the

completion of the cost share activity, the molded coolers had passed the initial testing and were being prepared to be tested in a full area substack. If the subsequent testing is successful, molded coolers will be incorporated into the production bill of material in 1998.

Conclusion

The hydrogen power plant design increased the electrical efficiency of the power plant to over 44% for this design as compared to 40% for natural gas and 42% for the existing hydrogen power plant. Delivery of high grade heat was determined to be feasible and two options were identified. The number of components was reduced and the manufacturing process was optimized. At the conclusion of this program there will be a hydrogen power plant design that can be produced at a commercial scale and this power plant will be compatible with renewable hydrogen fuel sources.

Acknowledgements

IFC would like to acknowledge the DOE for their funding of this program and the following individuals and companies for their contribution to our fuel survey:

T. F. Florkiewicz of OxyTech Systems, Inc.

Tom Halverson of Praxair, Inc.

Jim McElroy of Hamilton Standard

Venki Raman of Air Products and Chemicals, Inc.

Robert H. Wombles of Ashland Petroleum Company

EVALUATION OF A PROTOTYPE HYDROGEN SENSOR FOR USE IN SAFETY APPLICATIONS

Barbara Hoffheins
Tim McKnight
Robert Lauf
Rob Smith
April McMillan
Oak Ridge National Laboratory
P.O. Box 2008
Oak Ridge, Tennessee 37831-6004

Abstract

Through a Cooperative Research and Development Agreement (CRADA) Oak Ridge National Laboratory and DCH Technology, Inc. are partners in the development of a low cost hydrogen sensor for personnel and equipment safety applications in areas where hydrogen is produced, stored, or transported. The CRADA objective is to verify the performance, manufacturability, and reliability of a very low cost thick film sensor based on ORNL-patented technology. Our initial tasks under this program were to study existing sensor performance data, identify tests and evaluations to complete our characterization, and conduct post-exposure tests to determine what effects hydrogen exposure and elevated temperatures have on sensor materials. Additionally, fabrication methods were evaluated to understand any limitations of the sensor materials or fabrication techniques.

Introduction

Hydrogen sensors are needed in many industrial, military, and commercial environments for the protection of personnel and equipment. Examples include hydrogen furnaces, battery charging systems, submarines, aerospace vehicles, and nuclear reactors. Further, inexpensive and reliable sensors for leak detection, lower explosive limit detection, and concentration monitors would be enabling instrumentation for U.S. Department of Energy Hydrogen Program sponsored research to develop hydrogen based energy and fuel technologies. Some of the sensor requirements include reliability, low cost, small size, selectivity for hydrogen, resistance to poisoning, and operation in various combinations of atmospheres and temperatures. Of the commercially available hydrogen sensors, none can address all of the above requirements because of lack of selectivity, size, cost, or other operational constraints. Presently, some hydrogen leak problems are addressed by a general-purpose instrument, such as a gas chromatograph (GC), configured as a lower explosive level (LEL) sensor because it distinguishes hydrogen from other substances; however, the GC requires a large equipment package that occupies valuable space and maintenance costs can be expensive. Igniter systems in containment areas of nuclear reactors have similar shortcomings and their size and limited distribution make them ineffective for the detection of hydrogen "pockets" that can be widely scattered.

Researchers at Oak Ridge National Laboratory (ORNL) have designed a solid-state hydrogen sensor using thick film technology (Lauf et al. 1994, Hoffheins et al. 1995). The sensor mechanism is based upon the changes in electrical resistivity of palladium metal corresponding to the amount of absorbed hydrogen. When the surface of palladium or a palladium alloy is exposed to gaseous hydrogen, hydrogen molecules will dissociate and diffuse into the metal, ultimately reaching an equilibrium concentration that is a well-characterized function of the temperature and hydrogen partial pressure (Lewis 1967). The concentration of hydrogen in the palladium can be measured through several physical effects, e.g., volumetric expansion, resistivity, potentiometric effects and researchers elsewhere have documented various hydrogen sensing techniques based upon the palladium-hydrogen relationship (Michaels et al. 1964, Lundström 1981/82, Lundström 1981/82, Lechuga 1991, Shaver 1969, Godwin 1975, Butler 1984, Hughes 1992). The ORNL sensor is most similar to a primitive detector developed at Bendix Corp. in 1964 (Michaels 1964). An additional similarity between the ORNL and Bendix sensors is that they both achieve some temperature compensation by measuring the difference in resistance between "exposed" and "passivated" palladium resistors.

Sensor Design and Construction

Using photolithography methods, we originally designed and constructed a thin film sensor consisting of four palladium serpentine patterns or legs connected as a Wheatstone bridge. Three of the palladium legs were passivated with SiO_2, Mg_2O_5, or other insulating and hydrogen impermeable materials. This passivation layer provided temperature compensation for palladium so that resistance changes measured by the Wheatstone bridge reflected only the change due to hydrogen absorption.

Initial tests successfully demonstrated the thin-film sensor's response to hydrogen gas in argon and air under ambient temperature and pressure and, in a separate test, while immersed in dielectric oil at temperatures between 25 and 90°C (Hoffheins et al. 1993).

We concluded that adapting the design for thick-film fabrication would achieve several improvements. Effective passivations, difficult to achieve with thin films, can be made more impermeable using glass-based, thick-film compositions. Glass frit, an important component of most thick-film compositions, is formulated to provide maximum adhesion, chemical resistance, and stability over a wide range of operating conditions. Another possible advantage might be that thick film metallizations would have greater total surface area, increasing sensitivity and/or decreasing response time, although this might be accompanied by more complex surface chemistry. A thick-film sensor is also inherently simpler, more rugged, and much less expensive to manufacture in quantity. These ideas were incorporated in our thick film hydrogen sensor design patented in 1995 (Hoffheins 1995). The palladium resistor material used in fabricating sensor samples was developed and patented by DuPont Electronics (Felten 1994) as a result of a collaborative effort.

A thick-film sensor was designed and constructed, Figure 1. The sensor is an electronic circuit based principally upon three thick film components: 1) a conductor layer, which joins the palladium segments and provides connection points for power and signal circuitry, 2) the palladium resistor layer, composed of the four serpentine palladium segments, and 3) the passivation layer, which forms a hydrogen-impermeably barrier over two of the palladium segments. Each layer is separately printed and fired onto a ceramic substrate. With the development of the palladium composition, all of the sensor materials are off-the-shelf components. Tests were conducted to demonstrate responsiveness to concentrations of hydrogen from 0.5% to 4%. Under a project funded by the Electric Power Research Institute, we tested the sensor at elevated temperatures to 200°C, relative humidity to 100%, and at hydrogen concentrations up to 30% hydrogen in air.

Summary of Previous Results

Sensor testing was conducted at two separate facilities at ORNL, the Harsh Environment Test Bed (HETB) and the Metrology Research and Development Laboratory (MRDL). Preliminary testing has characterized performance characteristics such as sensitivity, time response, reliability and repeatability, and sensitivity to environmental conditions such as extreme temperatures and high humidity/steam exposure.

Response

Theoretically, the diffusion of hydrogen into a thin layer of palladium occurs on the order of milliseconds; in laboratory tests, however, the test setup can prevent direct observation of the actual response time of the sensor. Typical response times for the sensor range between 20-30 seconds and recovery times are of the same magnitude. These numbers include the time constant of the test bed, which ranged between 2 and 7 seconds, depending upon the facility used for the test. In addition, there is a modest trend of slightly faster response at higher temperatures, as one would expect from kinetic theory.

Linearity

The sensor features predictable linearity over a wide range of use (1%-30% hydrogen). Figure 2 illustrates the sensor response to gradually stepped concentrations of hydrogen to 17% in air and the corresponding linear fit. Figure 3 shows the sensor response for a range of hydrogen concentrations to 30% in a nitrogen atmosphere at 91°C. Questions remain regarding linearity of response at the low end (<1%), as well as upper limit of operation. As specifications are developed for DOE Hydrogen Program-related applications, we will be able to tailor our investigations for limits of detection appropriately.

Stability

The sensor output remains very consistent in low hydrogen atmospheres (<3%). We have observed a baseline shifting after cycling the sensor in higher concentrations. This may be related to some permanent alteration in the structure of the palladium metallization at the higher concentrations, which may be improved by further materials study.

Temperature Effects

As temperature increases, the amount of hydrogen dissolved in Pd at a given hydrogen partial pressure decreases. We have noted a corresponding decrease in sensor output for higher temperatures. Output curves for each temperature profile are linear and will therefore permit active temperature compensation to be incorporated into the mature device.

Humidity Effects

Experimental data indicate that, over a multi-month, power-on dwell time, moisture adsorbing to the sensor surface was detrimental to the sensor speed, slowing response by up to 10×. We have proposed covering the active palladium legs with Teflon or other hydrogen-permeable materials to exclude moisture and other possible contaminants. However, the positive effects of filtering coverings (such as sol gels) on response time must be investigated.

Post-Exposure Analysis

Several of the thick film sensors were analyzed microscopically to better understand high temperature and high concentration effects. Of primary concern is the long term durability of the palladium metallization. Most thick film compositions are developed to be stable or "passive" under all operating conditions. Here we require a material to be "active" repeatably and reliably. As stated earlier, palladium metallization undergoes a volumetric expansion as hydrogen is absorbed. At higher concentrations, this can be irreversible. We observed this effect in several of the sensors that were exposed to high hydrogen concentrations.

Palladium Conductor

One sensor was exposed to a range of hydrogen gas concentrations from 0.5% to 30% hydrogen, first with nitrogen as a matrix gas and then with air as the matrix. The test temperatures were

20°C, 100°C, and 200°C. At each temperature level, the sensor was exposed to the range of H_2 concentrations between 0.5% and 30%. This sensor failed after multiple exposures to the higher concentrations of hydrogen. The palladium layers actually peeled up and came off of the substrate, Figure 4. This was attributed to the volumetric expansion that palladium undergoes when the partial pressure of hydrogen is sufficiently high. It could be that repetitive swelling and shrinkage caused by cyclic exposures to hydrogen could cause degradation of the palladium traces and eventual sensor failure.

Figure 5 is a SEM photograph of the palladium metallization that has not been exposed to hydrogen. Note that the layer is porous, but relatively uniform with apparently good electrical continuity throughout and good adhesion to the substrate.

The palladium metallization in Figure 6 was cycled through hydrogen many times, including concentrations up to 30%. The sensor never failed and the metallization appears to have maintained its porosity. However, it has also developed cracks and eroded somewhat. The effect is more prevalent at the edges of the deposition.

Figure 7 depicts palladium metallization of a sensor that was cycled through several exposures to hydrogen (up to 30%) and finally failed. The surface appears rough and irregular, with fissures along the edges of the deposition and obvious voids where material has flaked off. Also, the deposition does not appear to be fully in contact with the substrate at the edges of the metallization. Sections of the metallization have broken away from the substrate.

Electrical Connections

Electrical connections to the sensor were made in a variety of ways, including with various solders and with conductive epoxies. Any of these connections would be adequate for a temperature range not exceeding 100°C; however, some of the testing did expose the sensors to temperatures of 200°C and most laboratory solder joints failed, as expected, during the initial temperature excursion or later during other high temperature tests.

Glass Passivation

Some sensors were fabricated with one layer of the passivating glass material. When these sensors were exposed to concentrations of hydrogen at 4% and above, hydrogen was able to penetrate the glass layer. We suspect that a single glass layer does not provide adequate impermeability to hydrogen. Also, we know that fabrication conditions must be controlled to prevent the formation of gas bubbles that break during firing, leaving small holes in the glass that allow hydrogen to migrate between the reference palladium legs and the atmosphere. Later tests with additional layers of glass (two or more) prevented the entry of hydrogen.

Evaluation of Cross Sensitivity

We recently exposed these sensors to carbon monoxide (CO), methane (CH_4), and propane (C_3H_8). Many gas sensors are not selective for hydrogen and have cross sensitivity to organics and other reducing gases. Because the underlying principle of this sensor is based upon a

selective absorption of *only* hydrogen, we do not expect it to be influenced by the presence of other gases. However, it is reasonable to expect that some of these gases would be commonly or occasionally present in the application areas envisioned for these sensors and we would want to prove conclusively that these gases have little or no effect on the sensor performance. Figures 8 and 9 demonstrate that separate exposures to CO, CH_4, and C_3H_8 provoked little or no sensor response. A future test will be to compare sensor responses to hydrogen alone to responses to mixes of these gases with H_2 to ensure these gases have no poisoning effect on response.

Discussion of Results

In general, current evaluation of the palladium based thick film sensor indicates several favorable results. Optimizing materials for reliable sensor operation appears to be the most critical issue at this point.

The sensor itself is rugged and mechanically stable, and is inherently well suited to a large range of environmental conditions. Normal temperature and humidity variations in buildings, out of doors, or in environmental enclosures containing heat-producing electronic equipment do not appear to be a barrier to operation or commercialization of the sensor.

Repeated cycling of the hydrogen sensor between lower and higher hydrogen concentrations (30%) and possibly at elevated temperatures adversely affects the structure of the metallization and compromises its adhesion to the sensor substrate, sometimes leading to catastrophic failure. Although many end use applications would not experience high levels of hydrogen, nevertheless, it will be important to also understand the effects of repeated cycling of lower concentrations over a period of time. We know that other palladium alloys can likely extend the operation of the sensor into higher hydrogen concentration levels and provide protection against structural degradation. Also, the palladium composition can be altered to ensure a more durable structure.

We are actively working with DuPont Electronics to develop a new sensor paste that has improved adhesion and long term performance. This process will be iterative. We will test for longevity with repeated cycling at high and low concentrations, and then make recommendations for additional improvements. These tests will also help to determine the ultimate lifetime of the sensor for particular environments.

Factors that influence the passivation effectiveness will continue to be evaluated. It is conceivable that other passivation materials will be more impermeable than the selected material or that multiple layers may be essential for reliable sensor operation. From the standpoint of fabrication, it would be more economical to only require one passivation layer.

The sensor performs reliably over a wide range of temperatures (ambient to 200°C); however, the existing electrical connection scheme (solder) usually fails around 200°C. This is typical for most solders. We are experimenting with conductive epoxies, but believe that wire-bonding attachments are probably the most promising long term approach.

Conclusions

In general, we determined that the sensor performs well under tested regimes of elevated temperature, humidity and has a linear response to concentration. Our tests indicate that the sensor output is repeatable and reliable for concentrations of hydrogen from 1% to 30% in air. At the same time, we observed that improvements to sensor materials and packaging could be made but should be tailored for the intended use. For example, the sensor metallization does fatigue after repeated cycling through high concentrations of hydrogen, nevertheless, many applications envisioned for the sensor would never experience frequent high concentration cycling of hydrogen. Also, we have experienced connector failure during exposure to high temperatures (200°C); however, some of the application areas may not require a more rugged (and potentially more expensive) package design.

The current method of using thick film techniques for sensor manufacture takes advantage of a mature and relatively inexpensive technique for quantities in the 100s of units. The relatively high processing temperatures (500 to 1000°C) renders a device able to survive wider thermal ranges than commercially available sensors. The sensor mechanism is selective for hydrogen, although more definitive studies of cross-sensitivity of the sensor are planned. The sensor fabrication is compatible with many sensor and detector packaging schemes, and promises an inexpensive and effective method for a wide variety of hydrogen sensing applications.

The reported results are very encouraging. We believe we are well on the path toward providing enabling technology for the hydrogen economy through the development of a reliable, affordable hydrogen sensor for safety, control, and distributed monitoring. The sensor performs well under a variety of environmental conditions. Sensor fabrication methods involve mature practices, inexpensive set-up, and the use of off-the-shelf products. The sensor design can be easily reconfigured and packaged for many types of applications, including those requiring portable and battery-operated devices.

Acknowledgements

Oak Ridge National Laboratory is managed by Lockheed Martin Energy Research Corp. for the U.S. Department of Energy under contract DE-AC05-84OR22464. The current project was funded by the U.S. Department of Energy, Energy Efficiency and Renewable Energy, Office of Utility Technologies.

References

Butler, A. 1984. "Optical Fiber Hydrogen Sensor." *Appl. Phys. Lett.*, 45: 1007-9.

Felten, J. J. 1994. "Palladium Thick Film Conductor." U.S. Patent No. 5,338,708.

Godwin, J., and R.V. Klint. 1975. "Hydrogen Detector System." U.S. Patent 3,927,555.

Hoffheins, B.S., and Haberman, D.P. May 23, 1997. DOE Technical Peer Review.

Hoffheins, B.S., and R.J. Lauf. 1995. "Thick Film Hydrogen Sensor." U.S. Patent No. 5,451,920.

Hoffheins, B.S., R.J. Lauf, and S.E. Nave. 1993. "Solid-state, Resistive Hydrogen Sensors for Safety Monitoring." *Instrumentation, Controls, and Automation in the Power Industry*, 36, *Proc. Third Int'l. Joint ISA and POWID/EPRI Controls & Instrumentation Symposium, Instrument Society of America*, 189-203, Research Triangle Park, NC.

Hughes, R. C., R.J. Buss, S.W. Reynolds, M.W. Jenkins, and J.L. Rodriquez. 1992. *Wide Range H_2 Sensor Using Catalytic Alloys*, SAND--92-2382C, Albuquerque, NM: Sandia National Laboratory.

Lauf, R.J., B.S. Hoffheins, and P.H. Fleming. 1994. "Thin-Film Hydrogen Sensor." U.S. Patent 5,367,283.

Lechuga, L.M., A. Calle, D. Golmayo, and F. Briones. 1991. "Hydrogen Sensor Based on a Pt/GaAs Schottky Diode." *Sens. Actuators B*, 4: 515-18.

Lewis, A. 1967. *The Palladium Hydrogen System.* New York: Academic Press.

Lundström, I. 1981/82. "Hydrogen-Sensitive MOS Structures. Part 1: Principles and Applications." *Sens. Actuators*, 2: 403-26.

Lundström, I. 1981/82. "Hydrogen-Sensitive MOS Structures. Part 2: Characterization." *Sens. Actuators*, 2: 105-38.

Michaels, A. 1964. *Design, Development, and Prototype Fabrication of an Area Hydrogen Detector*, NAS8-5282, Southfield, MI: Bendix Corp.

Shaver, J. 1969. "Bimetal Strip Hydrogen Gas Detectors." *Rev. Sci. Instr.*, 40: 901-5.

Figure Captions

Figure 1. The ORNL Thick-film Hydrogen Sensor (2.2x)

Figure 2. Linearity of Sensor Response Under Gradual Accumulation Conditions

Figure 3. Sensor Output for a Range of Hydrogen Concentrations
Stability

Figure 4. SEM Photo of Palladium Metallization at 140×

Figure 5. SEM Photo of Palladium Metallization that was not Exposed to Hydrogen (220×)

Figure 6. SEM Photo of Palladium Metallization (light areas) Cycled through Many Exposures to Hydrogen

Figure 7. SEM Photo of Palladium Metallization Cycled Numerous Times with Hydrogen and High Temperatures (220×)

Figure 8. Separate Exposures to Hydrogen (first) and Carbon Monoxide Indicate Little Sensitivity to Carbon Monoxide.

Figure 9. Separate Exposures to Hydrogen (left), Propane (center), and Methane (right), Indicate Little or no Sensitivity to Propane or Methane.

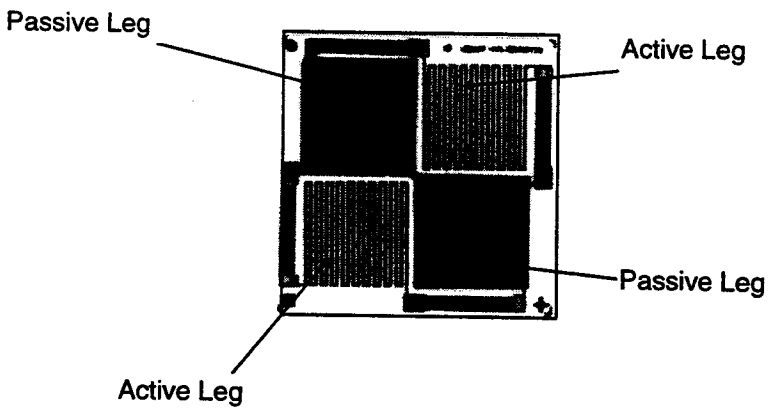

Figure 1.

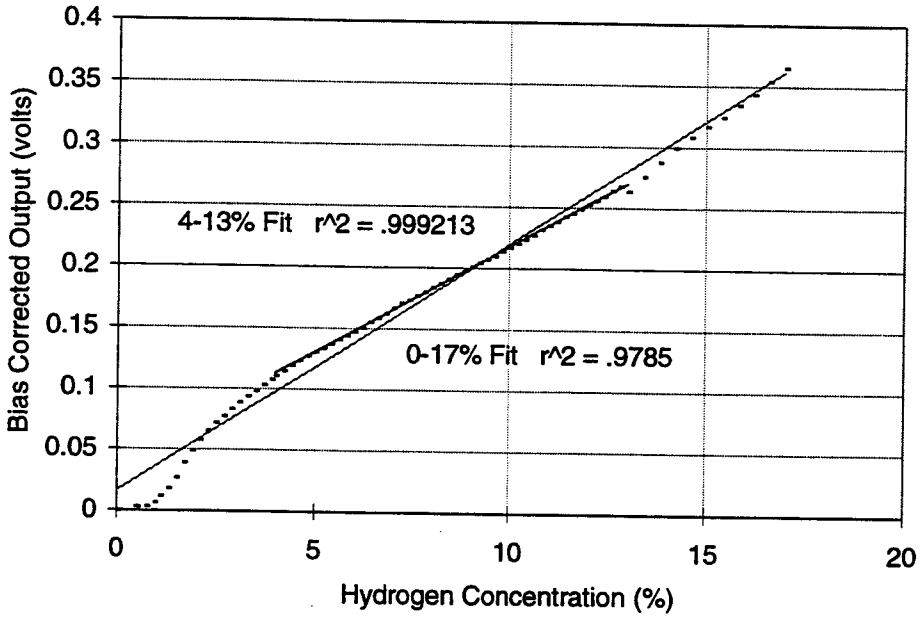

Figure 2.

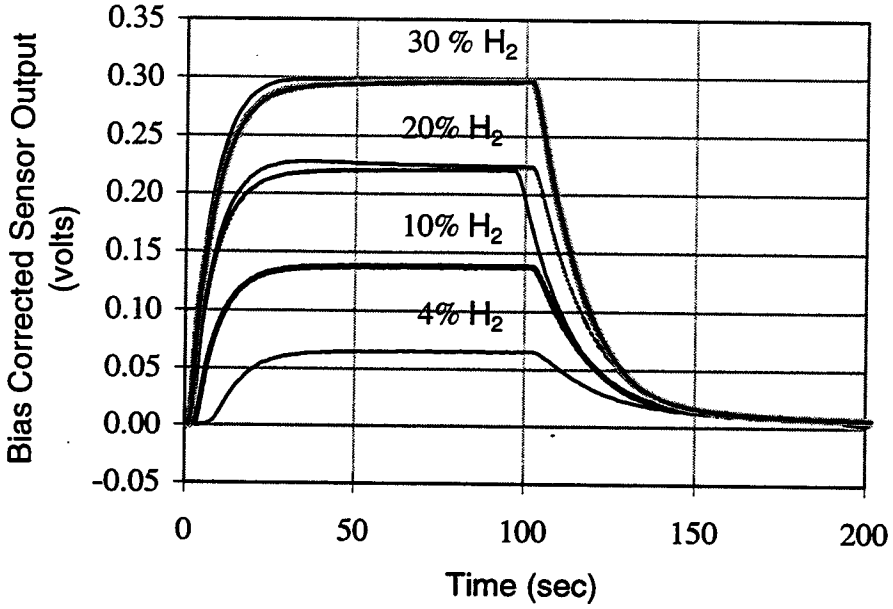

Figure 3.

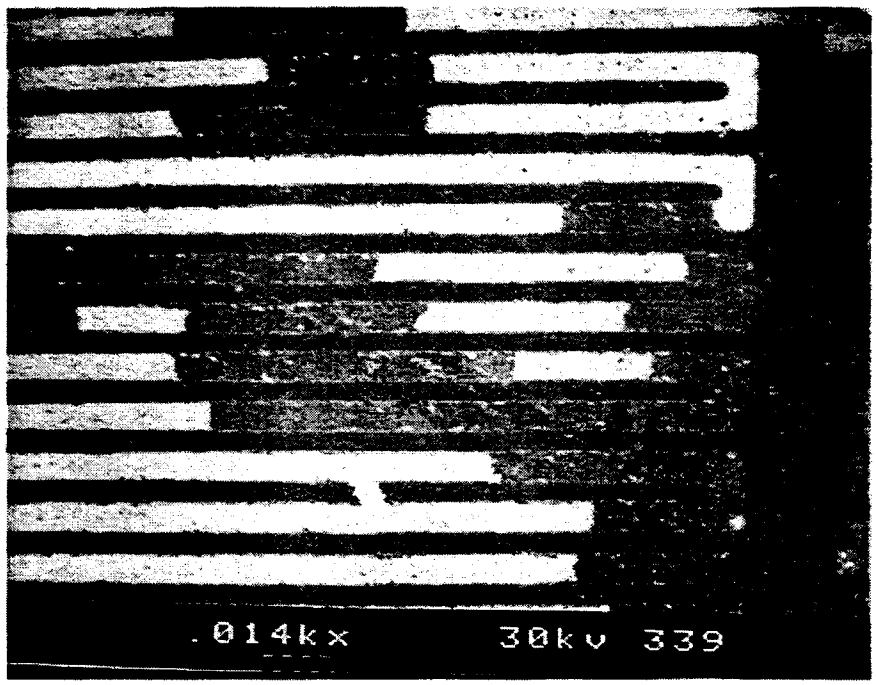

Figure 4.

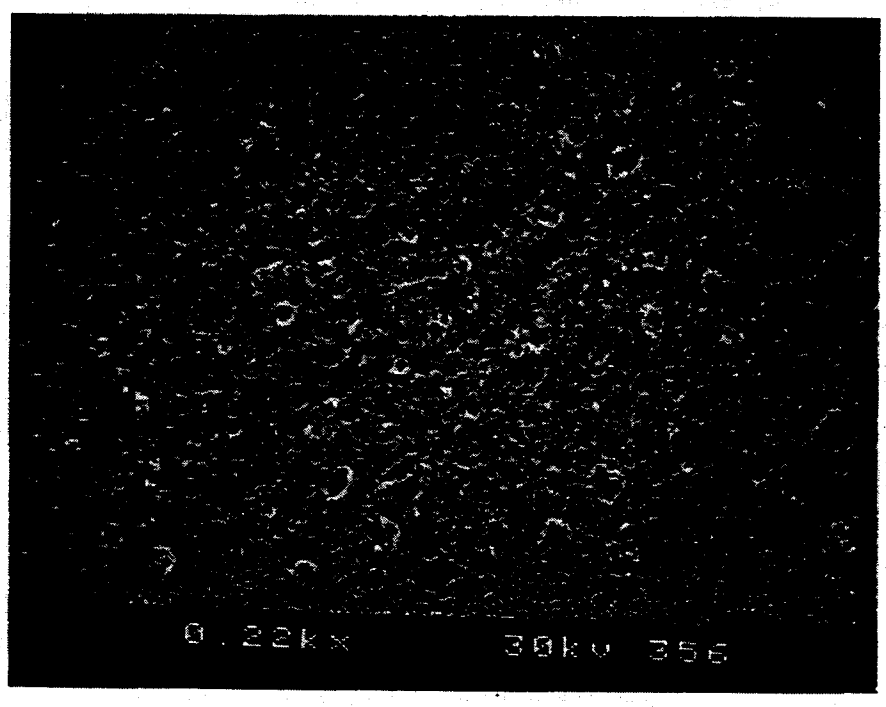

Figure 5.

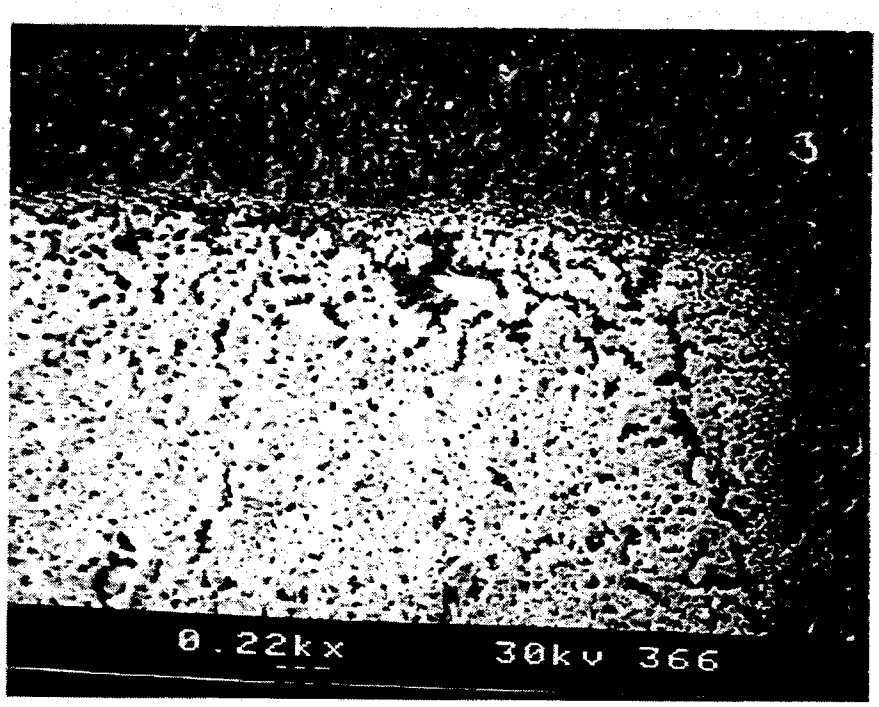

Figure 6.

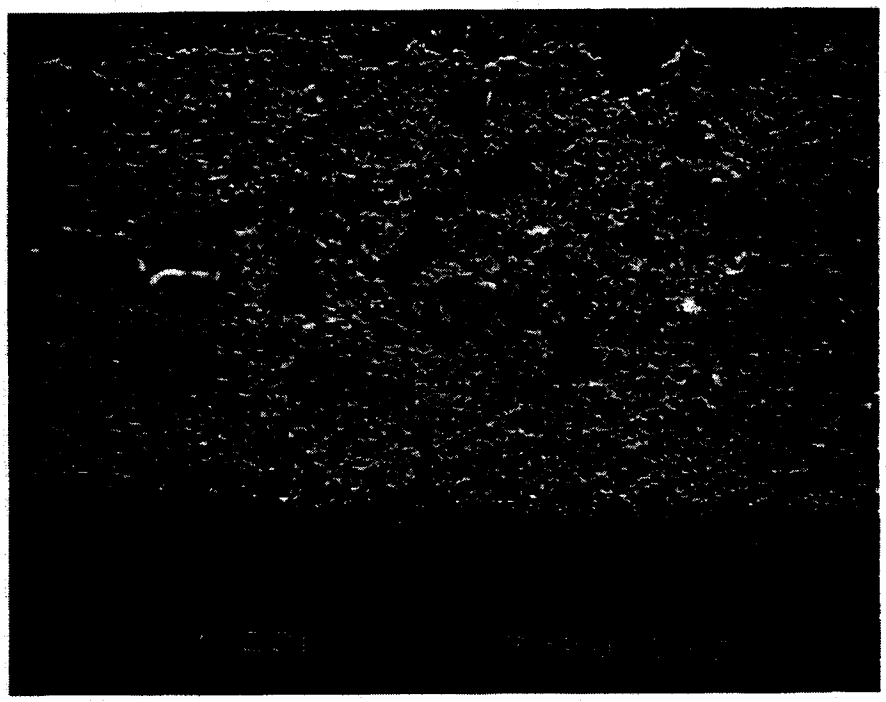

Figure 7.

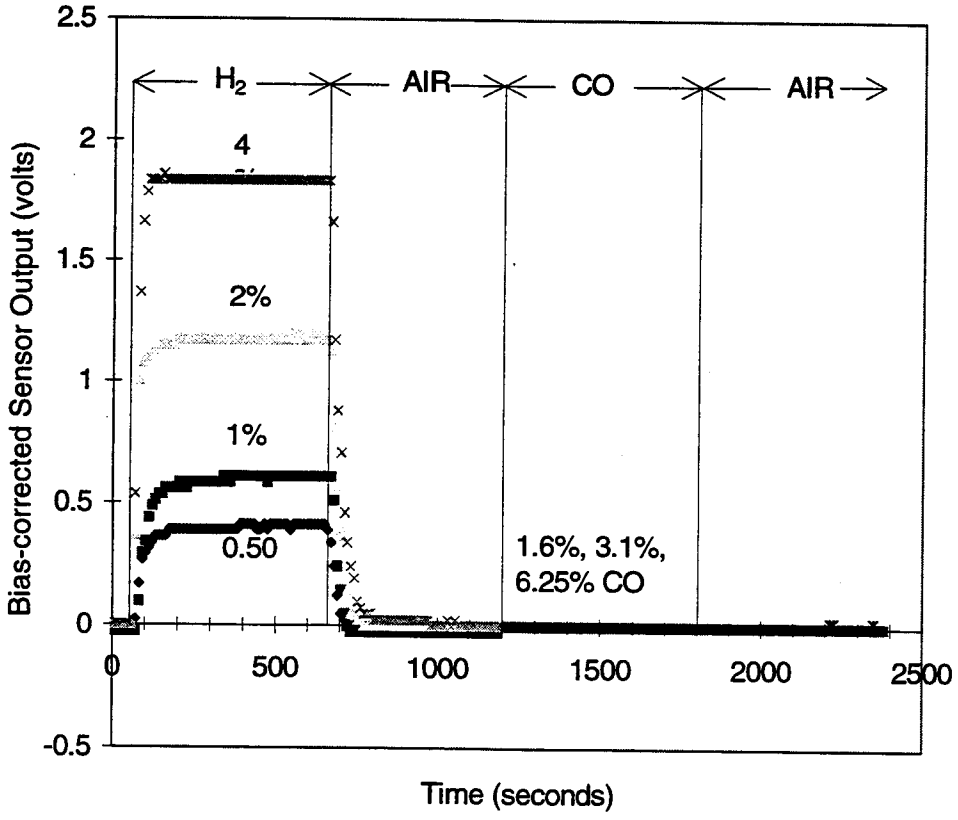

Figure 8.

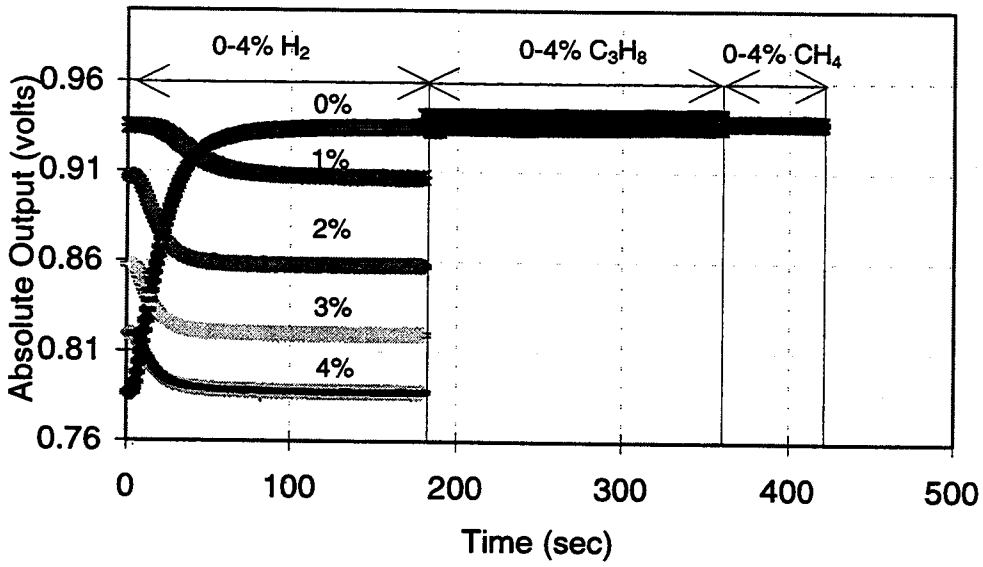
0-4% H_2
0-4% C_3H_8
0-4% CH_4
0%
1%
2%
3%
4%
Absolute Output (volts)
0.96
0.91
0.86
0.81
0.76
0
100
200
300
400
500
Time (sec)

Figure 9.

DESIGN AND DEVELOPMENT OF A LOW-COST FIBER-OPTIC HYDROGEN DETECTOR

David K. Benson, C. E. Tracy and Clemens Bechinger
National Renewable Energy Laboratory
Golden, Colorado 80401

Abstract

A cost-effective detector for hydrogen gas leaks will be needed in many hydrogen-fueled technologies of the future. In particular, the hydrogen-fueled automobile may require hydrogen leak sensors in several locations and their cost could be prohibitive if conventional sensor technology is used. This project is directed at the development of low-cost fiber-optic (FO) hydrogen gas detectors that could provide adequate sensitivity, response speeds and reliability in an automobile application. The FO sensor relies upon a reversible chemical reaction between gaseous hydrogen in air and a thin film of tungsten oxide. We have studied the kinetics of this hydrogen reaction with the sensor coating systematically. Different design concepts have been evaluated. The initial sensor design consisted of a thin tungsten oxide film coating on the flat end of a polymer or glass optical fiber. A very thin overcoating of palladium catalyzes the reaction between the hydrogen and the tungsten oxide and reflects a light beam back along the optical fiber to a light intensity monitor. When the hydrogen reacts with the coating, the tungsten oxide becomes optically absorptive and attenuates the reflected light. The sensitivity and response speed of this sensor were studied over a range of temperatures and found to be too slow for the intended application. A faster sensor design was invented that relies upon the resonant absorption of light at a beveled facet on the end of the optical fiber. The resonance occurs when the incident light strikes the metal coated facet at an angle just above the critical angle for total internal reflection. The evanescent wave stimulates resonant absorption of the light at certain wavelengths by free electrons in the metal to produce a so-called surface-plasmons (SP). An overcoat of thin tungsten oxide on top of the metal film is designed to provide an optical wave-guide for light at the surface plasmon resonance. The two layer coating produces a coupled resonance at the SP wavelength that is very sensitive to the optical constants of the tungsten oxide. When hydrogen reacts with the tungsten oxide the resonance frequency shifts and this shift is detected in the spectrum of the reflected light beam. The intensity of the total reflected light beam is used to produce an internal reference signal for comparison to the intensity of the narrow wavelength resonance. The ratio of these two signals cancels out the signal noise that is due to variation in the intensity of the light source and in the transmittance of the optical fiber. A patent application is in process and a small business partner has formed a CRADA with NREL to develop a commercial detector based upon this design.

The Concept

A cost-effective hydrogen gas detector is needed wherever a hydrogen leak can pose a safety hazard. Since hydrogen is not toxic, the purpose of the detector is to provide warning, activate safety shut-off valves, switch on ventilation fans, etc. before a hydrogen concentration approaches the lower deflagration limit, about 4% in air. A high sensitivity is probably not needed, so long as the sensors can be located where hydrogen accumulation will occur.

A fiber-optic (FO) hydrogen gas detector has some potential advantages over conventional detectors that use hydrogen-sensitive semiconductor or metal film resistors. The FO detector can be deployed over distances without electrical wiring. Since the hydrogen sensor signal is communicated optically, it is not susceptible to electromagnetic interference (EMI) and does not extend an electrical energy source to the site of the potential hydrogen leak where an electrical fault could cause ignition. The absence of EMI may be particularly important in hydrogen fuel-cell powered vehicles with large electric traction motors. In cost-sensitive applications such as hydrogen-fueled automobiles, the probable lower costs of a FO hydrogen detector may be important. The initial cost of optical fibers may be less than copper wires and the cost burden during recycling of the vehicle may be less with optical fibers than with copper wires. This last feature is of growing importance as the automobile industry becomes financially responsible for the vehicle from "cradle to grave". Removing copper wiring from a vehicle chassis before remelting the steel scrap is a significant cost, partially avoided if glass or polymer optical fiber is used instead of copper wiring. If the copper is not removed, the quality and value of the scrap steel is reduced.

The FO sensors we have studied consist of a thin film coating on the end of the fiber. This coating reacts reversibly with hydrogen gas in air and undergoes a change in its optical properties. A light beam from a central source reflects from the coating and returns to a centrally located light detector. Changes in the character of the reflected optical beam signal the presence of hydrogen gas at the sensor end of the optical fiber. An electrical signal from the light detector is processed and used to activate appropriate safety measures. A central light source may be used for several FO sensors, but each individual sensor will require two dedicated light detectors to monitor its hydrogen-response signal and its hydrogen-insensitive reference signal.

Approach

Three different designs for a FO sensor were explored and a new, improved design was invented. Initially, we evaluated the design of Ito (Ito 1984). This sensor consists of a thin film of amorphous tungsten oxide applied to the polished, flat end of the fiber plus a thin reflective overlay of palladium. When the coating is exposed to hydrogen gas, some of the hydrogen adsorbs and reacts with the palladium to form a solid solution of hydrogen in palladium (or a palladium hydride at higher concentrations), some of the atomic hydrogen diffuses through the palladium and reacts with the tungsten oxide. An insertion compound, nominally H_xWO_{3-y}, is formed with x varying, depending upon the concentration of the hydrogen in the air. For best sensitivity, the tungsten oxide should be substoichiometric, e.g., y>0 (Zhang 1996 and Bechinger 1997). The hydrogen insertion is accompanied by the introduction of reduced valence states, W^{+5} in the H_xWO_{3-y}. Optical excitation of electrons trapped near these point defects as so-called polarons cause a broad absorption band between about 400 and 1300 nm. Consequently, light in this wavelength range is attenuated when reflected from the coating if the sensor is exposed to hydrogen gas. When hydrogen gas is removed, the inserted hydrogen leaves the H_xWO_{3-y} spontaneously through the palladium film and is oxidized to water in the air. The intensity of the reflected light beam is the signal used to monitor the hydrogen sensor.

A potentially faster, simpler detector design was also examined briefly. This design makes use of the thin palladium film alone as the hydrogen sensor coating (Butler 1991). The reaction with the hydrogen changes the optical reflectance of the palladium film enough to make a suitably sensitive sensor. However, much of the change in reflectance is due to expansion of the palladium as it forms a hydride. This expansion distorts the film into an "orange peal" texture that is not very reproducible and eventually causes the film to flake off the optical fiber. Note that the thicknesses of the palladium films used in the Ito and other designs to be described below are small enough that these chemical expansion stresses do not cause disruption of the films.

Another configuration using a palladium film was also considered. This design is more sensitive and uses a thinner film that is less susceptible to flaking. In this design the palladium is placed on the face of a glass prism and the light beam is directed through the prism so as to reflect internally back into the prism and from the palladium film back to a detector (Sadowski 1994). At any wavelength there is a certain angle (somewhat larger than the critical angle for total internal reflection at the glass-air interface) at which the electric field of the incident light wave excites a resonance response in the free-electron cloud of the metal. The resonant-excited electrons form a so-called surface plasmon (SP) (Sambles 1991). At this resonance condition, the energy of the p-polarized portion of the light beam is transferred to the metal and dissipated as heat or re-radiated into the air. Whenever the electrical characteristics of the metal are changed, as for example by absorption of hydrogen, the conditions for this resonance change. The shift in the resonance condition can be detected quite sensitively in a number of ways. Unfortunately, this configuration is very sensitive to adsorbed gases and is not very selective. It detects any adsorbed gas including carbon dioxide and even helium about as well as hydrogen.

A generic problem with the FO sensors was also discovered. Whenever the optical fiber is bent or subjected to a significant temperature gradient, its light transmission decreases. Whenever the connectors connecting the optical fiber to the light source or to the sensor head are shocked, their light transmission may change. These spurious changes in light transmission could superimpose a severe noise background upon the hydrogen detector, particularly in a moving vehicle.

A new detector design was invented that also uses a SP resonance effect, but with a configuration that is less sensitive to adsorbed gases. In this new configuration, the resonance condition is affected by the bulk optical property changes in a tungsten oxide film overlying a thin metal film. The thin metal film is chosen to create the coupling condition between the light beam and the dielectric tungsten oxide film. The tungsten oxide film thickness is chosen so that a so-called "guided wave" is produced at the critical SP resonance wavelength of the light (Raether 1988). The guided wave propagates along the tungsten oxide film, reflecting many times from both surfaces before being dissipated. In its many traverses of the tungsten oxide film, it interacts with the full thickness of the film many times. Consequently, the resonance condition of this sensor design is dominated by the bulk properties of the thin tungsten oxide film and is most strongly affected by changes in it as, for example, when it reacts with hydrogen gas.

In our new sensor design, we use two reflected light detectors, one which detects the SP wavelengths and the other which detects all of the reflected light. This second reflected light detector serves as a reference beam which is not significantly affected by the presence of hydrogen, but is affected by any changes in the transmission of the optical fiber and connectors in exactly the same way as is the reflected light beam that carries the hydrogen signal. By taking the ratio of the two light detector signals, we cancel out the noisy, changing fiber transmission and preserve a signal that changes only in response to the presence of hydrogen.

An NREL patent on this design is pending and a small business CRADA partner is planning to develop commercial hydrogen detectors based on this design for various applications.

Experiments

Measurements of the sensitivity and speed of sensor coatings were made in an ultra-high vacuum system used to provide precise pressures of mixed gases. The gas pressure is measured with cold-cathode ion-gages and capacitance manometers that are calibrated against a built-in spinning-rotor gage. A differentially pumped residual gas analyzer with controllable pressure-drop orifice allows mass-spectrometric analysis of gases over a very wide range of pressures. Hydrogen is provided on demand from an electrolytic hydrogen generator. Other gases are supplied from compressed cylinders. Gases are mixed in a separate chamber before admission to the sample.

The sample chamber (Fig. 1) is a stainless-steel vacuum six-way cross with a small sapphire window through which light from a fiber-optic source is coupled. In all of the experiments , monochromatic light from a laser diode (850 nm) was passed through a polymer optical fiber and through the sapphire window into the vacuum chamber where it interacted with the sensor coating and then reflected back through the same window, along the same fiber to a beam splitter where it was directed to a photodiode light detector. The intensity of the reflected light (typically tens of microwatts) was detected by a photodiode and recorded on a PC through an RS232 connection. Sensor coatings were usually applied to microscope slide glass and monitored optically through the glass. Samples were placed with the glass substrate in contact with the sapphire window. The leg of the cross containing the sample was equipped with an external cooling coil and electrical heater with which the temperature of the sample could be controlled at any set temperature between about 0 and 100 C.

Experiments with the new SP resonance sensor coatings were initially conducted with an optical benchtop setup shown schematically in Fig.2. The coatings were applied to one face of a right angle glass prism. A helium-neon laser provided the light source and the resonance was scanned by rotating the prism or the incident light beam to sweep through the critical incidence angle at the internal surface of the coating.

Results

The kinetics of the sensor film reaction with hydrogen gas and its recovery rate in vacuum and in oxygen were studied systematically at three temperatures: 25, 52 and 82 C. Figure 3 shows a typical record of several cycles of reflected light signal during exposure of the sensor film to hydrogen, vacuum and oxygen. Results from a sensor film were reproducible and showed no degradation over a period of several months in the test apparatus. The structure of the sensor coatings reported in this section was: borosilicate glass; WO_3 (170 nm)/Pd (20 nm).

Figure 4 shows a typical response signal as a function of time after exposure to hydrogen. Figure 5 shows a similar recovery curve in vacuum and figure 6 shows recovery in oxygen (after a short period in vacuum while the hydrogen was removed, before admitting oxygen). All of these response and recovery curves were found to fit a double exponential time function. Figure 7 shows a typical response curve and its fit to a double exponential curve. One fast and one slow time constant could be extracted from the curves by fitting. The slow response time constant was found to exhibit a temperature dependence characteristic of a thermally activated process with an activation energy of 0.77 eV per atom (Fig. 8a). The fast time constant, while more difficult to extract accurately, also appears to show an activation energy of about 0.8 eV/atom too (curve b). In the figure, data are shown for response to hydrogen at three pressures, 7.6 torr, 15.2 torr and 30. 4 torr (30.4 torr corresponds to 4% of one atmosphere, the lower deflagration limit for hydrogen in air). Notice that the hydrogen detection time constants were independent of hydrogen pressure over this range. The recovery curves also exhibit two time constants, but one is so dominant that it is difficult to extract an accurate estimate of the second, faster time constant (Fig. 9).

The Ito sensor design produces a reliable signal only with a significant change in the optical absorption of the tungsten oxide. Our measurements of the kinetics of the hydrogen reaction clearly indicates that the kinetics of such a change would be characterized by the slower time constant and would be too slow for the Ito design to be used in a safety-critical hydrogen leak detector. Consequently, we have investigated the use of a much more sensitive design that can produce a signal from the earliest (and fastest) part of the hydrogen/WO_3 reaction.

The new sensor design is shown schematically in Figure 10. The sensor coating is applied to a faceted end of an optical fiber. Angled facets are at 45 degrees to the fiber axis so that a double reflection from these facets returns the light down the fiber. The coating consists of a thin reflective metal layer covered by a thin layer of amorphous tungsten oxide. The metal and its thickness are chosen to produce a surface plasmon (SP) resonance at a 45 degree incidence angle for a suitable wavelength of light. In order to get a sharp resonance, the metal must be highly conductive and silver or gold are preferred. The thickness of the tungsten oxide is selected to create a "waveguide" effect for this wavelength of light. This is a resonance condition itself in which the light is multiply reflected within the tungsten oxide film. In effect, this two-layer coating acts as a pair of coupled resonators at the SP resonance wavelength. No resonance occurs at the uncoated facet which completely reflects the light from the facing facet back down the fiber or completely reflects the light striking it from the light source onto the facing facet because of the total internal reflection condition at the glass/air interface.

The shift in the resonance wavelength is converted into an amplitude signal by using a narrow bandpass filter between the fiber and the photodiode light detector. The passband of the filter is selected to transmit the light from the portion of the spectrum containing the SP resonance in the absence of hydrogen. Because of the resonance absorption in the coating, the signal intensity is low. Whenever hydrogen is present, the wavelength of the SP resonance shifts and more light get through the filter causing an increase in the photodiode current. A second detector is unfiltered. It monitors the intensity of the entire reflected light spectrum and serves as a reference beam detector. If the transmittance of the optical fiber or its connectors change over time, both photodiode signals will be affected in the same way. A new signal, the ratio of the hydrogen-sensitive to the reference signals, is produced with an analog divide circuit so that the new signal cancels our changes in the fiber transmittance, but retains the hydrogen response.

Figure 11 shows the expected shift in SP guided-wave resonance for a typical sensor coating assuming that the real part of the optical dielectric constant of the tungsten oxide is increased by 1 % upon reaction with hydrogen. In this case the coating consists of 52 nm of gold plus 229.5 nm of tungsten oxide on a glass substrate. The angle of incidence is 45 degrees. The resonance shown here is the s-polarized portion of the beam which participates only because of the guided wave geometry. A p-polarized resonance also occurs at 660 nm. The calculation was made with the thin film optical modeling code from the Thin Film Center, Inc. (Macleod 1995).

Discussion

The double time constant may be due to two different kinds of sites for hydrogen in the H_xWO_3. This hypothesis has been used by one of us to explain the observed rate of bleaching in photochromically colored tungsten oxide (Bechinger 1994a). The faster time constant was associated with sites that are more readily accessible to diffusing hydrogen because they are on the pore surfaces in the nano-porous WO_3 thin film, whereas the slower time constant was associated with sites on the interior of the nano-crystals of the WO_3. We also found that the transport of the hydrogen through the WO_3 is not a thermally activated process, but is more characteristic of a phonon-assisted tunnelling process with a $T^{1/4}$ temperature dependence (Bechinger 1994b). This unusual process is likely to be due to hydrogen migration by OH-ion exchange between adjacent surface hydroxylated sites on the interior pore surfaces of the WO_3 film as first suggested by

Arnoldussen (Arnoldussen 1981).
The hydrogen pressure independence that we have observed in the hydrogen reaction with the sensor films is consistent with a set of reactions in which the hydrogen activity at the palladium/tungsten oxide interface is nearly constant. Such a condition may be explained by a hydrogen surface adsorbate saturated condition at the palladium/hydrogen interface and the formation of a palladium alpha-phase hydrogen solid-solution with (nearly) constant hydrogen activity.

At 25 C and hydrogen pressure above 15 torr, we have observed a small, anomolously fast response is superimposed upon the double exponential response. This may be an additional optical reflectance change in the palladium film itself as it undergoes a transformation from solid-solution (alpha-phase) to hydride (beta-) phase at these relatively high hydrogen concentrations (Fukai 1993).

A separate, detailed technical publication of these results will be prepared for publication later this year.

A small company, Amerisen, Inc. of Brookfield, Wisconsin has entered into a CRADA with NREL to develop a commercial fiber-optic hydrogen leak detector using the new design concepts .

Conclusions

Simple sensor designs have been studied over a range of temperatures to determine their sensitivity, speed and durability. While they are more than adequately sensitive for detecting hydrogen gas leaks in air, they were either too slow or unreliable. With a detection time constant of more than 30 seconds at room temperature and a recovery time constant of more than 30 minutes, the Ito sensor design (reflectance of a WO_3/Pd coating) would probably not qualify as a critical safety device. The lack of selectivity would make the Sadowski sensor design (simple SP resonance in Pd film) unsuitable for a safety-critical application because of false alarms. The susceptibility to degradation by hydrogen absorption/desorption would make the Butler sensor design (reflectance of a thin Pd film) unreliable. In addition, fluctuations in the FO transmittance due to optical fiber bending, temperature changes and connector movement was found to present a background signal noise problem with all of the FO detector designs. Such signal noise could be expected to be particularly serious in a moving vehicle.

A new sensor design was invented that has faster response and reduced susceptibility to background noise. The new sensor uses a surface-plasmon guided wave resonance in a thin coating of tungsten oxide on a thin silver or gold underlayer. The design has not yet been fully developed, but preliminary measurements show it to have greater response speed with a detection time constant of about 0.2 seconds and a recovery time constant of about 1 second at room temperature (Fig. 12). The new design also incorporates a reference beam signal that can be used to cancel out the variations in transmittance through the FO light path. A patent application has been filed for the new design.

Plans

The challenges to development of an acceptable hydrogen gas detector for automobile applications are severe. The detector must be adequately sensitive, but highly selective to hydrogen; and it must be robust, but cheap. Temperature changes at the sensor will cause changes in the SP resonance that must not be mistaken for a hydrogen signal. A method to compensate for such changes must be developed. A method to protect the thin hydrogen sensitive film from damaging effects of vapors including water vapor must be developed.

The new sensor design will be optimized and characterized in detail. Measurements will include sensitivity and speed over a range of temperatures and measurements of its susceptibility to interferences and/or degradation by other gases such as hydrocarbons, carbon oxides, water vapor, nitrogen oxides and sulfur

compounds.

We will work closely with our CRADA partner to develop a cost-effective, manufacturable hydrogen gas leak detector based on our new design.

We plan to publish the results from our measurements of the Ito sensor in a suitable technical journal and publish the preliminary results obtained with the newly invented sensor design once the patent application process is more advanced.

Acknowledgements

The authors gratefully acknowledge the assistance of our CRADA partners, Mr. Gregg Williams, president of MRT, Inc in Brookfield Wisconsin and Dr. David Haberman, president of DCH Technologies in Sherman Oaks, California and Mr. Matthew Keyser at NREL for developing computer controls and data acquisition programs for our measurements and Mr. James Dornbos at NREL for fabrication of much of our special optical and vacuum equipment. This work was funded by the U.S. Department of Energy's Hydrogen Program under contract No. DE-AC36-83CH10093.

References

Arnoldussen, T. C. 1981. "A Model for Electrochromic Tungsten Oxide Microstructure and Degradation," Electrochemical Science and Technology, Vol. 128, pp. 117-123.

Bechinger, C., D. Ebner, S. Herminghaus, and P. Leiderer. 1994a. "The dynamics of the photochromic effect in tungsten trioxide", Solid State Comm.,Vol. 89, No. 3, pp. 205-207.

Bechinger, C., S. Herminghaus, and P. Leiderer. 1994b. "Photoinduced doping of thin amorphous WO_3 films", Thin Solid Films, Vol. 239, pp. 156-160.

Bechinger, C., M. S. Burdis and J.-G. Zhang. 1997. "Comparison between Electrochromic and Photochromic Coloration Efficiency of Tungsten Oxide Films", Solid State Comm., Vol. 101, No. 10 pp. 753-756.

Butler, M. A. 1991. "Fiber Optic Sensor for Hydrogen Concentrations near the Explosive Limit", *J. Electrochem. Soc.*, 138:L46-47.

Fukai, Y. 1993. *The Metal-Hydrogen System*, Berlin, Springer-Verlag.

Ito, K. and T. Kubo. 1984. "Gas detection by hydrochromism." In *Proceedings of the 4th Sensor Symposium, 1984*, 153-156.

Macleod, A. 1995. *The Essential Macleod Thin-film Design Software User Manual,* Tucson, AZ, The Thin Film Center, Inc.

Raether, H. 1988. *Surface Plasmons,* Berlin, Springer-Verlag, p 21.

Sadowski, J. W. 1994. "Method for carrying out surface plasmon resonance measurement and sensor for use in method", U. S. Patent No. 5,322,798, June 21, 1994.

Sambles, J. R. , G. W. Bradbery and F. Yang. 1991. "Optical excitation of surface plasmons: an introduction.", *Contemporary Physics*, 32:173-183.

Zhang, Ji-Guang, D. K. Benson, C. E. Tracy, S. K. Deb, A. W. Czanderna and C. Bechinger. 1996. "Electrochromic Mechanism is a-WO_3 Films", Electrochemical Society Proceedings, Vol. 96-24, p 251- 259.

Figures

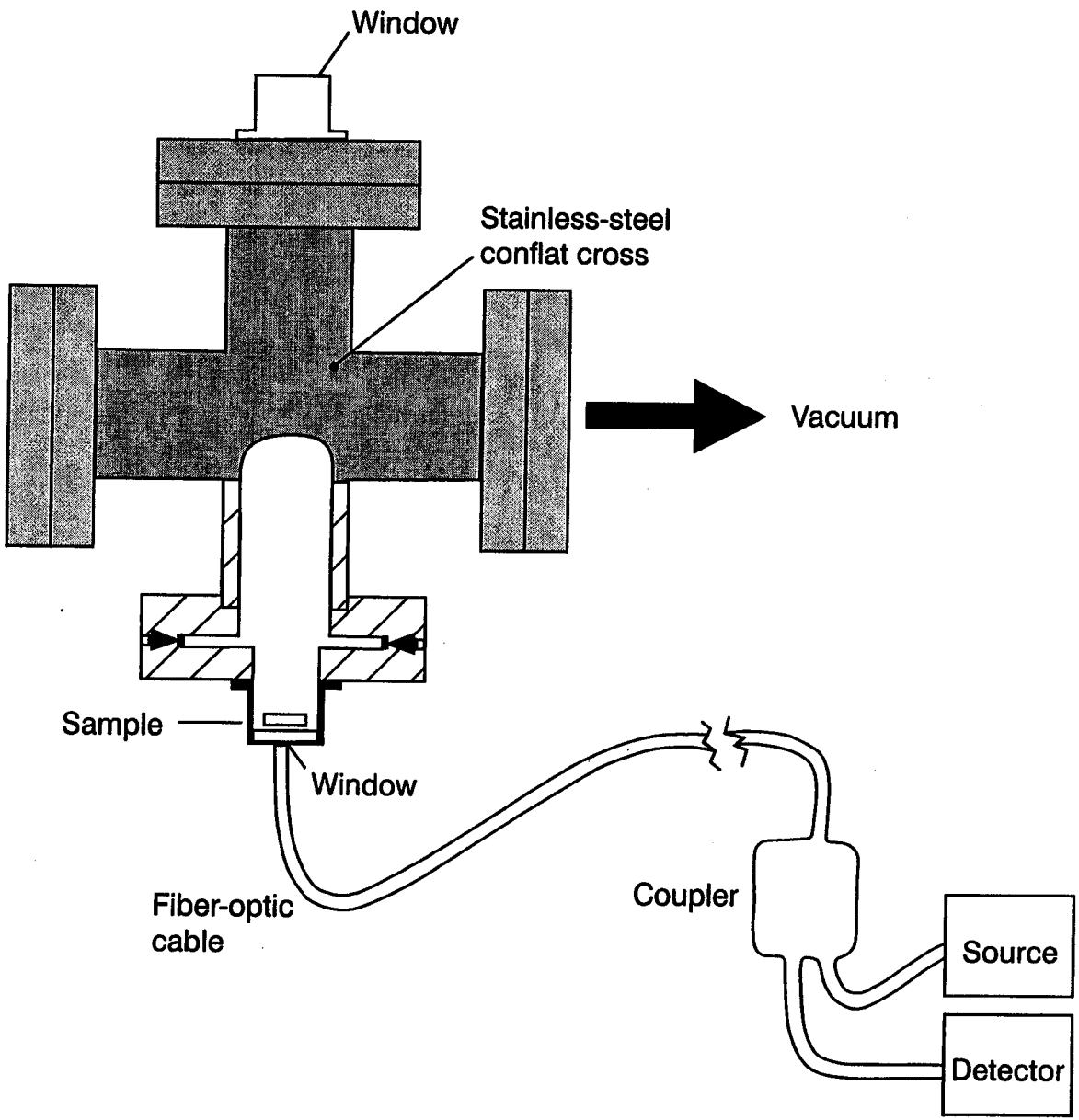
Window
Stainless-steel
conflat cross
Vacuum
Sample
Window
Fiber-optic
cable
Coupler
Source
Detector

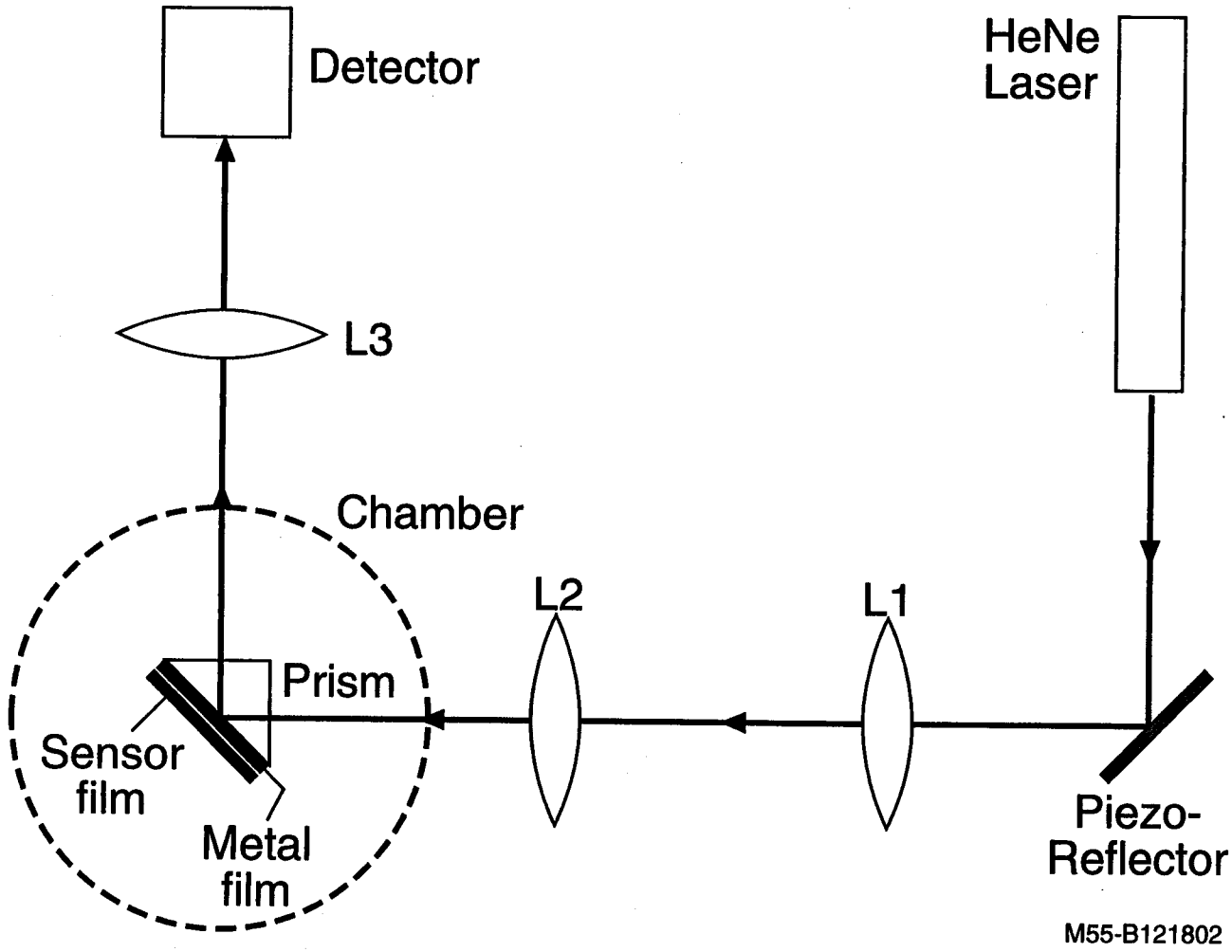
Detector
HeNe
Laser
L3
Chamber
L2
L1
Prism
Sensor
film
Metal
film
Piezo-
Reflector
M55-B121802

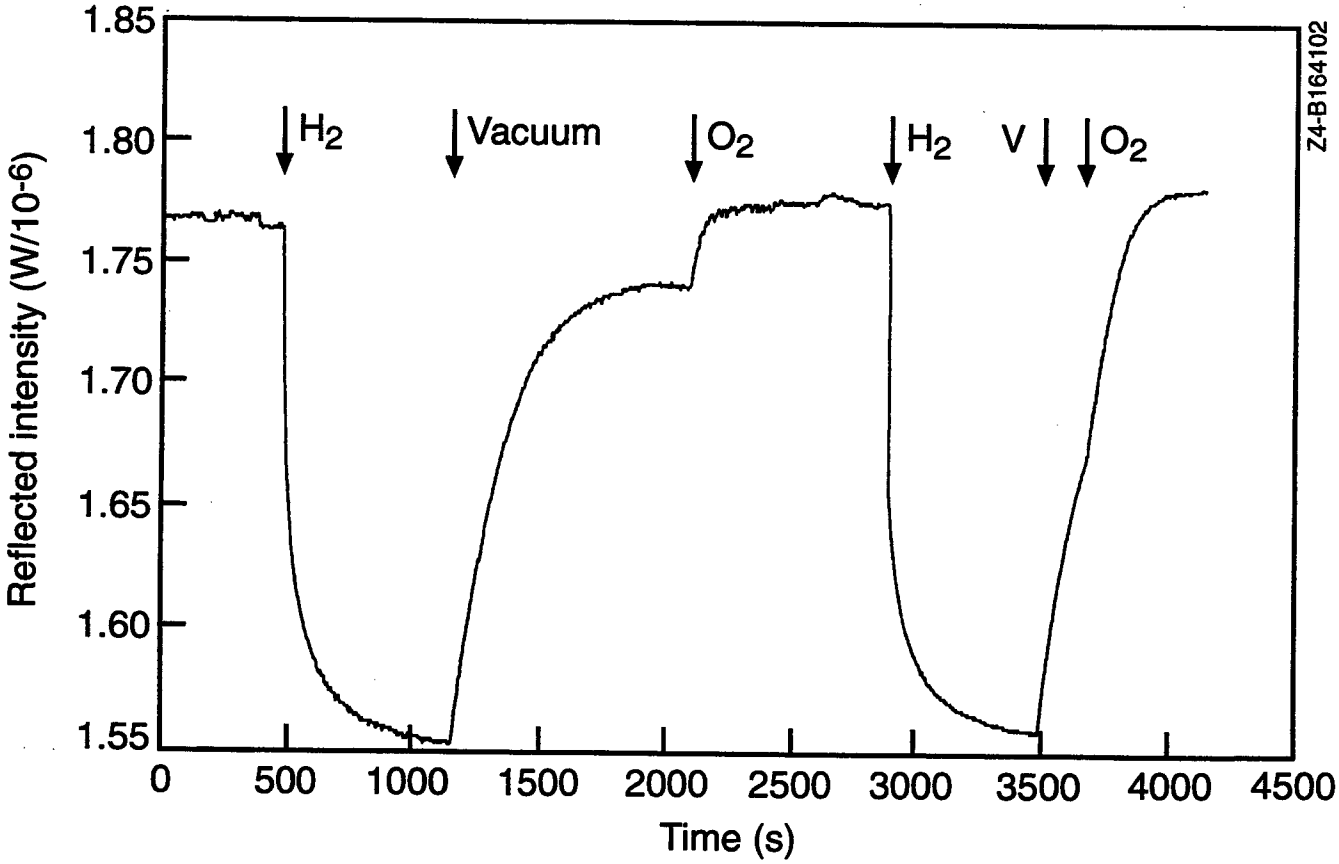
1.85
1.80
1.75
1.70
1.65
1.60
1.55
Reflected intensity (W/10-6)
H2
Vacuum
O2
H2
V
O2
0
500
1000
1500
2000
2500
3000
3500
4000
4500
Time (s)
Z4-B164102

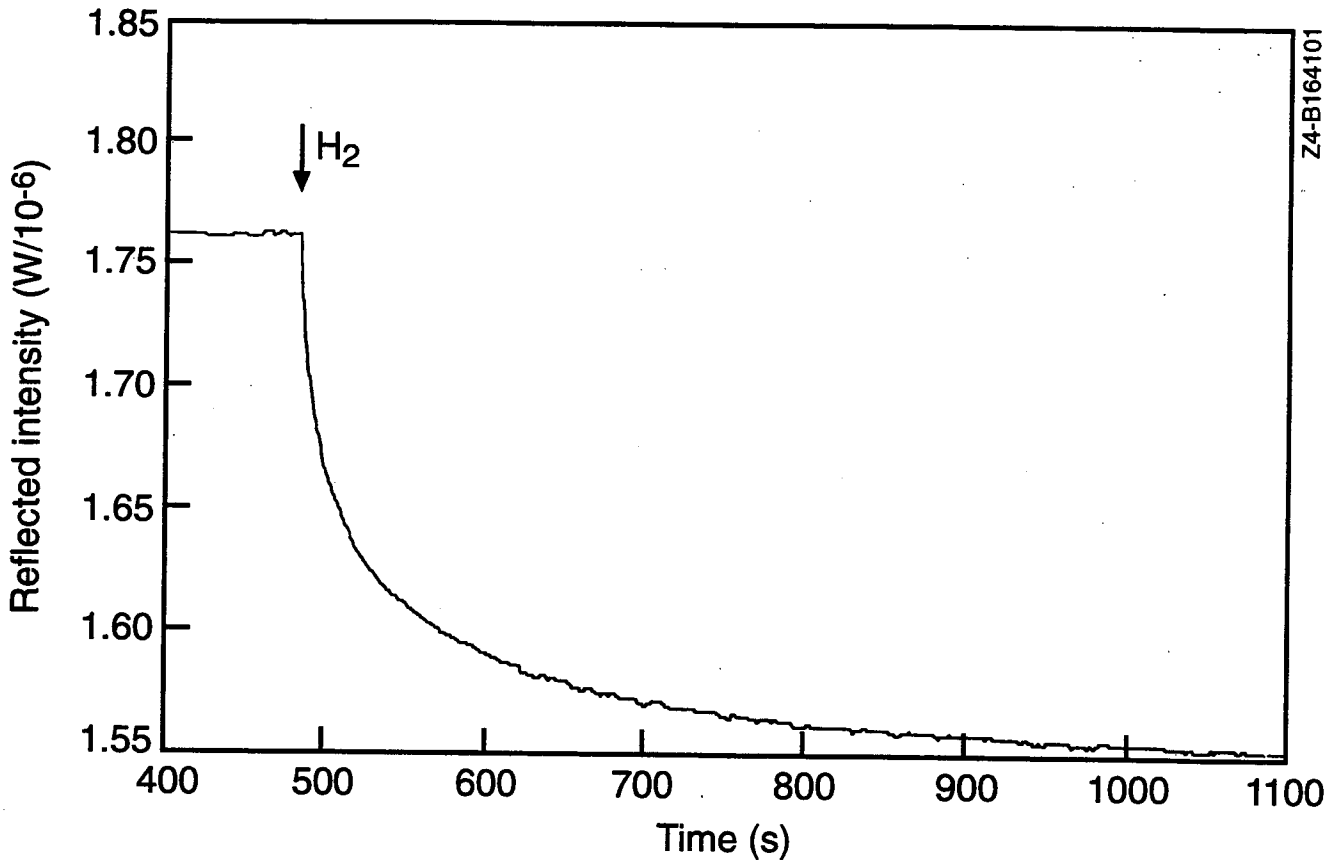
1.85
1.80
1.75
1.70
1.65
1.60
1.55
Reflected intensity (W/10-6)
H2
400
500
600
700
800
900
1000
1100
Time (s)
Z4-B164101

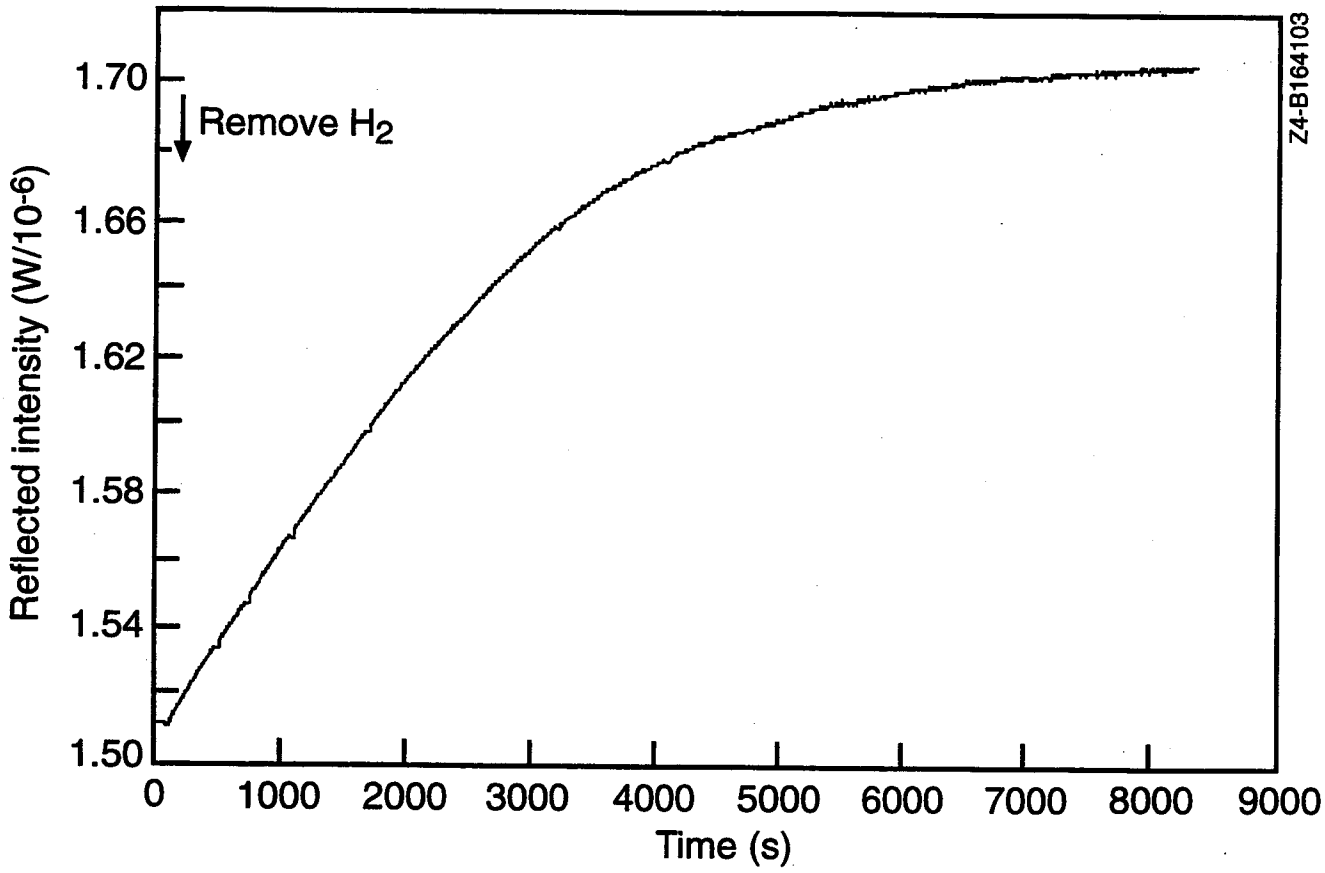
Remove H_2
Reflected intensity (W/10-6)
1.70
1.66
1.62
1.58
1.54
1.50
0
1000
2000
3000
4000
5000
6000
7000
8000
9000
Time (s)
Z4-B164103

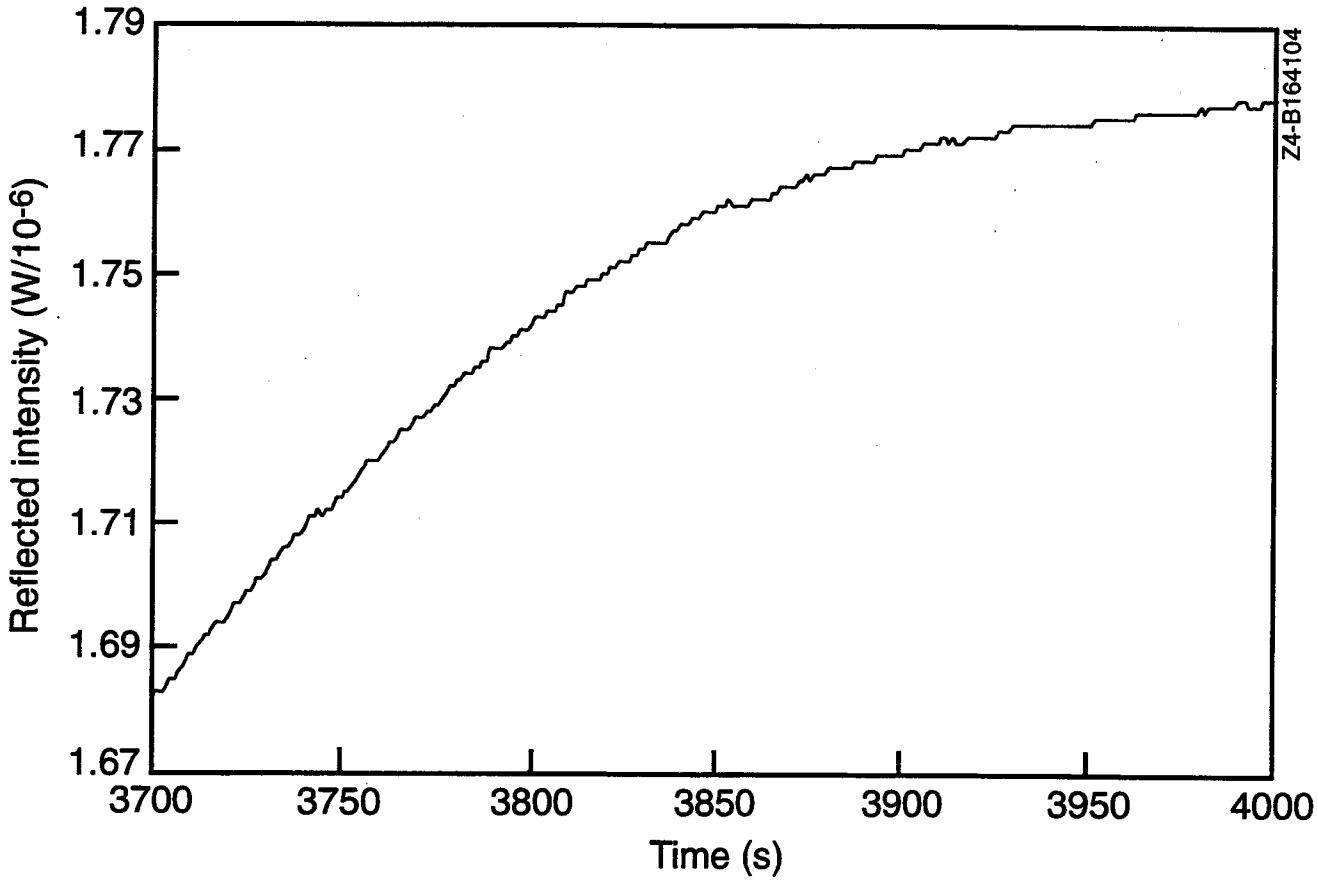
1.79
1.77
1.75
1.73
1.71
1.69
1.67
Reflected intensity (W/10-6)
3700
3750
3800
3850
3900
3950
4000
Time (s)
Z4-B164104

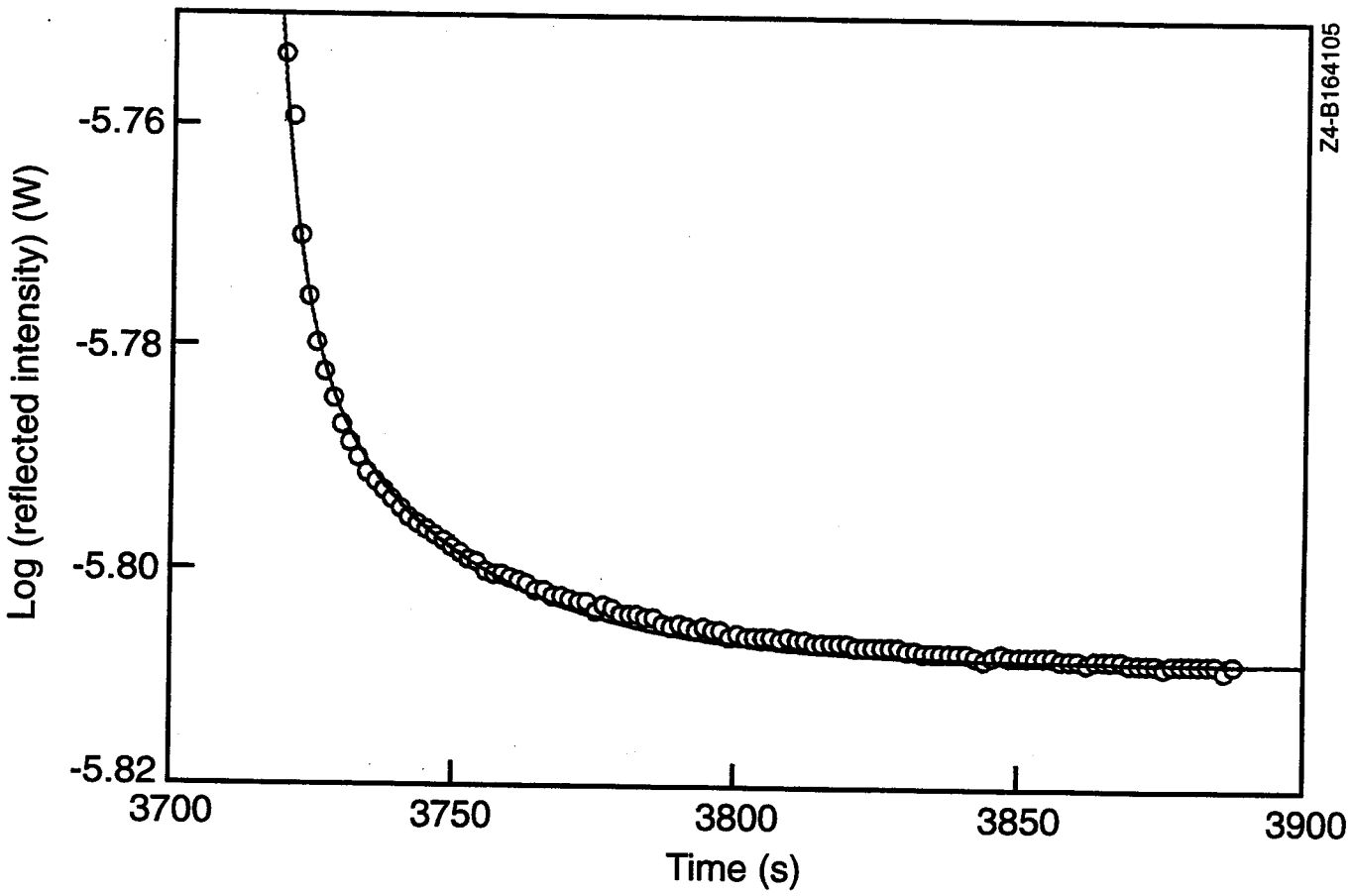
Log (reflected intensity) (W)
-5.76
-5.78
-5.80
-5.82
3700
3750
3800
3850
3900
Time (s)
Z4-B164105

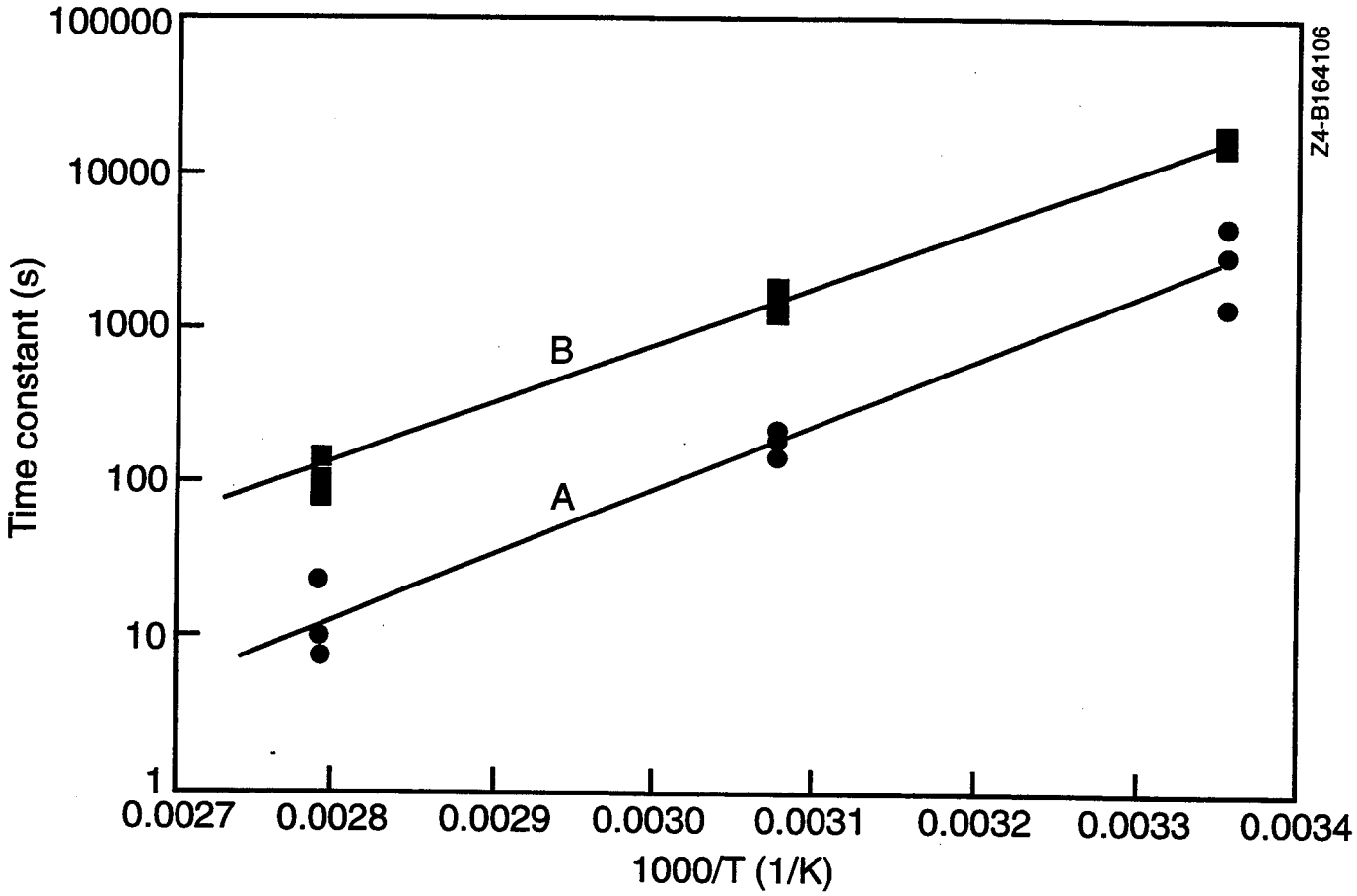
100000
10000
1000
100
10
1
Time constant (s)
B
A
0.0027
0.0028
0.0029
0.0030
0.0031
0.0032
0.0033
0.0034
1000/T (1/K)
Z4-B164106

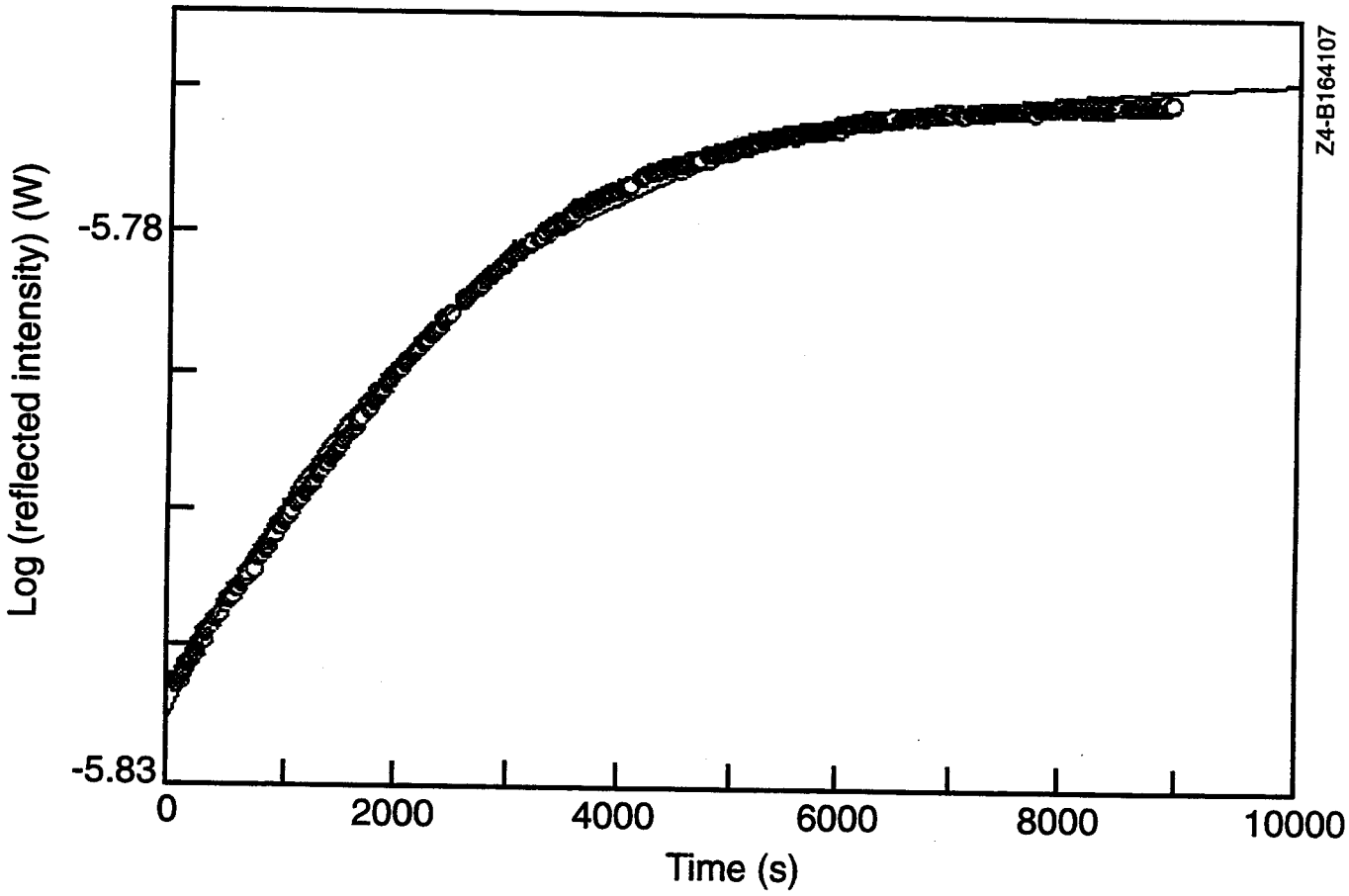
Log (reflected intensity) (W)
-5.78
-5.83
0
2000
4000
6000
8000
10000
Time (s)
Z4-B164107

Z1-B193301

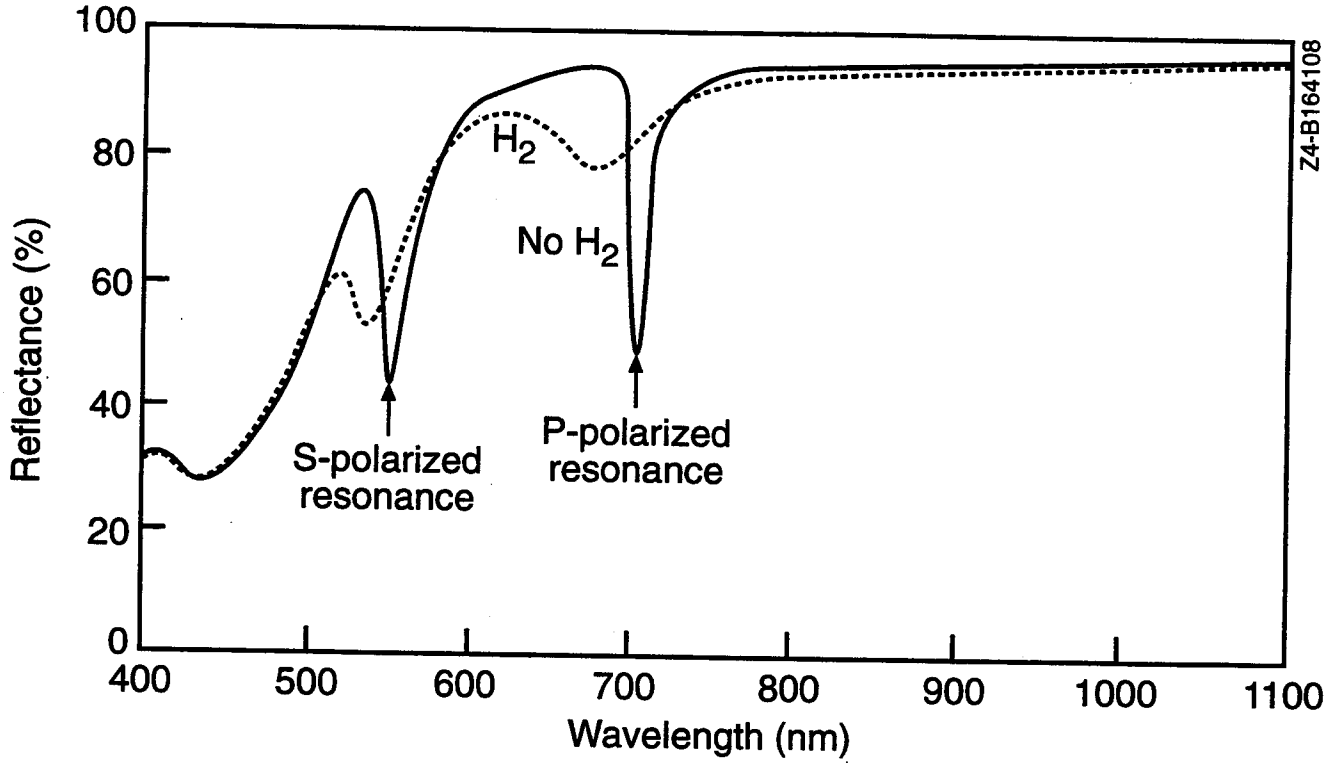
100
80
60
40
20
0
Reflectance (%)
400
500
600
700
800
900
1000
1100
Wavelength (nm)
H_2
No H_2
S-polarized resonance
P-polarized resonance
Z4-B164108

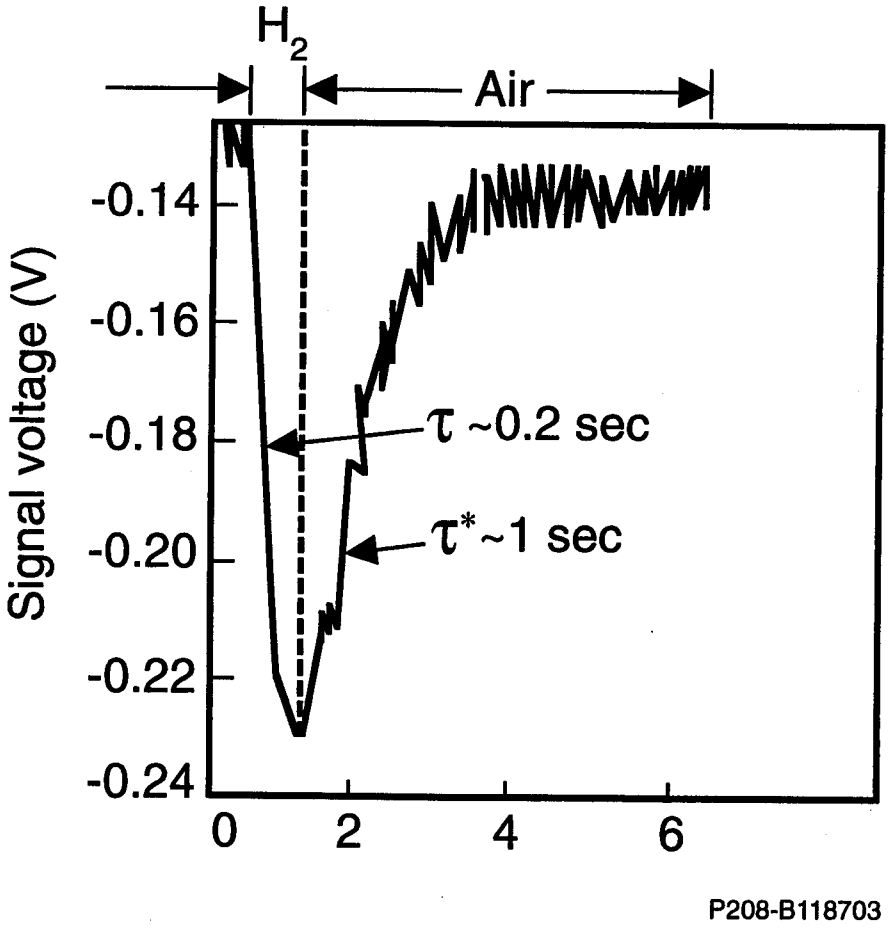
H2
Air
Signal voltage (V)
-0.14
-0.16
-0.18
-0.20
-0.22
-0.24
0
2
4
6
τ ~0.2 sec
τ* ~1 sec
P208-B118703

Characterization of Sulfonic Acid Containing Proton-Exchange Membranes. Thermal Stability, Thermohydrolytic Stability, Conductivity and Water Uptake

Robert W. Kopitzke and Clovis A. Linkous*

Florida Solar Energy Center, Cocoa, Florida 32922

calink@fsec.ucf.edu

Gordon L. Nelson

Florida Institute of Technology, Department of Chemistry, Melbourne, Florida 32901

The thermohydrolytic stability of five aromatic polymers, polytetrafluoroethylene, and sulfonic acid derivatives thereof, were determined using 24 hr exposures in saturated steam to generate thermogravimetric analysis curves. The steam-derived weight loss thermograms varied greatly from those obtained under dry, inert gas conditions. In an inert atmosphere, the aromatic polymers were more stable than their sulfonic acid derivatives, while in saturated steam, they were approximately the same. The relative stability of the ionomers were also different, with the perfluoroalkyl sulfonate (Nafion) being the least stable under inert conditions but most stable in saturated steam. The conductivity of the ionomers was measured at 20° C; Nafion was found to be an order of magnitude higher than the aromatic ionomers. This was attributable to the super-acidity of the fluorinated sulfonic acid group in contrast to the simple aromatic sulfonic acid group.

Introduction

A hydrogen-based energy economy would provide an excellent solution to our long term energy needs with minimal environmental impact. Using energy available from the sun, water can be electrochemically split in an electrolyzer to provide hydrogen as a fuel for both stationary and mobile applications. The hydrogen can then

be electrochemically recombined with oxygen from the air in a fuel cell to produce electrical energy and water, thus completing the cycle.

Considerable effort is being expended in making these electrochemical hydrogen energy transducers more cost effective. Various strategies purport to reduce the cost of fuel cells to $100/kW; this requires that cost reductions be made on all the components of the fuel cell.[1] One of these components is the electrolyte. Proton exchange membranes (PEM's) can act as solid electrolyte in both fuel cells and water electrolyzers. Currently, the most commonly employed PEM is the perfluoroalkyl ether sulfonic acid known as Nafion™. Current retail prices for the 117-grade material lie in the $750/m^2 range. Developing new, less expensive PEM's with the requisite conductivity, durability and hydrolytic stability is the focus of our research.

Previously, over 40 different polymers, all known to have exceptional thermal and chemical stability were examined for their stability under steam/O_2 and steam/H_2.[2] At 0.5 atm steam pressure, many of the polymers were stable at 200° C, and several showed good stability at 300° C. From this latter group, representatives of five polymer families were chosen for further work (1-5): poly(ether)etherketone (PEEK), polyethersulfone (PES), polybenzimidazole (PBI), polyphenylquinoxaline (PPQ), and polyimide (PI). The sulfonic acid derivatives of these polymers have been synthesized,[3] and a detailed electrochemical study of the sulfonated polyether(ether)ketone has also been done.[4] Because these membranes must function in a saturated water environment, knowledge of their thermohydrolytic stability is important. This work reports the thermogravimetric analysis (TGA) of the five aromatic polymers, their sulfonic acid derivatives, polytetrafluoroethylene, and Nafion as its ionomer derivative, under both inert and saturated steam conditions. Their water uptake and conductivity at 20° C is also reported.

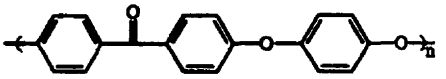

(1) Poly(ether)etherketone

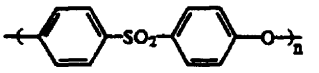

(2) Polyethersulfone

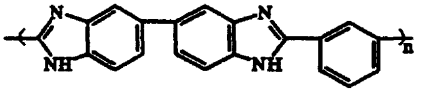

(3) Polybenzimidazole

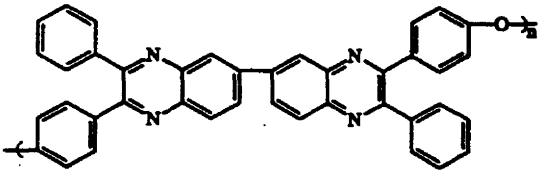

(4) Polyphenylquinoxaline

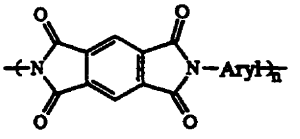

(5) Polyimide

Experimental Section

The sulfonic acid derivatives of the five base polymers were synthesized using a variety of literature methods. The sulfonated poly(ether)etherketone (S-PEEK) was made by dissolving PEEK powder in concentrated H_2SO_4.[5] Sulfonated polyethersulfone (S-PES) was made by adding sulfur trioxide to a solution of PES in CH_2Cl_2.[6] Sulfonated polybenzimidazole (S-PBI) was made by soaking thin films of PBI in 10% H_2SO_4 for two hours followed by a 90 second bake at 500° C.[7] Sulfonated polyphenylquinoxaline (S-PPQ) was made by a modification of this procedure, soaking in 50% H_2SO_4 and baking at 300° C. The sulfonated polyimide (S-PI) was prepared by copolymerization of oxydianiline (ODA) and the lithium salt of 2,5-diaminobenzene sulfonic acid in a 2:1 ratio with pyromellitic dianhydride (PMDA).[8]

The thermal stability of both the unsulfonated and the sulfonated polymers in an inert atmosphere (helium) was determined using a TA Instruments thermogravimetric analyzer using the "Hi-Res" TGA™ method and heating to 700° C.

This method consists of an initial 50° C/min ramp that quickly decelerates once weight loss commences. This is designed to give a constant rate of weight loss through the regions where weight change is occurring. The thermal stability in saturated steam (steam TGA) was done by exposing the polymers for twenty-four hours in a stainless steel PARR reactor equipped with a thermocouple, pressure gauge and gas inlet and outlet valves. Prior to the steam TGA, polymers were dried at 105° C, cooled in a dessicator, weighed and placed in the reactor (in tared, dried beakers) with enough water added to ensure a saturated atmosphere at the reaction temperature. The reactor was sealed, leak tested, placed in a PARR bomb heater and heated to the appropriate temperature. The temperature was ramped and maintained using a PARR controller. After twenty-four hours the bomb was cooled and the polymers were re-dried and weighed. The steam TGA was done every 25° C from 150-225° C.

The water uptake and conductivity of the sulfonated polymers were determined at room temperature (~ 20° C). Water uptake was determined on polymers that had been dried at 105° C, soaked in water overnight, then dabbed to remove surface moisture prior to weighing. The conductivity was determined by making resistance measurements using an a.c. bridge at 1000 Hz on membranes mounted in an electrochemical cell from Electrochem. Inc. The resistance of the membranes was recorded upon reaching a constant value. The ion density was determined by measuring the volume of a swollen membrane of known equivalence.

Results and Discussion

Thermogravimetric analysis. The thermogravimetric data from the saturated steam tests are given for both the unsulfonated and sulfonated polymers from 150-225 ° C (Figures 1 and 2). All of the polymers showed the expected decrease in weight with increasing steam temperature (and pressure). Because some measurable weight loss was detected even at the lower temperatures, it was difficult to pinpoint the onset

of polymer decomposition. Therefore, the temperature at 5% weight loss was selected as a figure of merit, as will be discussed below.

An important point is that steam-driven desulfonation is not the sole decomposition process occurring under these conditions. For example, at 200° C, PPQ and S-PPQ have weight losses of 14.6% and 10.1% while PES and S-PES have losses of 3.9% and 8.7%. Although in most cases the weight loss of the sulfonic acid derivative is greater than that of the base polymer, in all cases decomposition is occurring in the base polymers as well as in the sulfonated ones. That desulfonation is not the dominant process is perhaps surprising, since aromatic sulfonic acids are often desulfonated under high temperature, aqueous conditions.[9] On the other hand, several of these polymers, the polybenzimidazoles, the polyphenylquinoxalines and the polyimides are made by condensation reactions, so it is indeed possible that they could be hydrolyzed under these vigorous conditions.

One polymer that stood out because of its greater weight loss under saturated steam conditions was the sulfonated polyimide (S-PI). This polymer was synthesized from the lithium salt of 2,5-diaminobenzene sulfonic acid. The lithium salt was used because the free acid form of the diamine exists as a zwitterion, which inhibits polymerization. Attempts to convert the lithium salt of the final, cured polymer to the acid form by exchange in an HCl solution resulted in embrittlement of the polymer. This same effect was observed after steam exposure. The implication is that acid-catalyzed depolymerization was occurring in the polymer. This may be encouraged by the sulfonic acid moiety, since the depolymerization involves loss of an aromatic amine. The leaving group character of this amine would be enhanced by the electron-withdrawing nature of the sulfonic acid group.

As an estimate of stability, the 5% weight loss temperature was determined for both the helium and saturated steam TGA experiments (Figures 3 and 4). Under both sets of conditions the unsulfonated polymers had greater stability than their ionic derivatives; the only exception being for PTFE and Nafion in saturated steam. One significant difference between inert and steam conditions is the extent of variability in

temperatures at which 5% weight loss occurs. In helium this difference is in the range of 100-150° C in all but two cases; one of those cases, the polyimide pair, is likely due to the ionomer being tested in the lithium salt form instead of as the free acid; the reason for the exceptional stability of the S-PPQ is not known. In contrast, with the exception of the polyimide pair, the greatest difference between a pair of sulfonated and unsulfonated polymers in steam is 20° C. The range of stability for the sulfonated polymers is also much different in helium than in steam. In helium there is a range in excess of 200° C (305° C for Nafion and 522° C for S-PPQ) among the sulfonic acid polymers, but under saturated steam the temperature range is only 43° C. Under saturated steam, Nafion showed the highest stability among the sulfonated polymers, while under inert conditions it was lowest. Certainly ionomer stability in helium is not a good predictor of the its stability in saturated steam.

Water uptake and conductivity. The water uptake of the sulfonated polymers at room temperature (20° C) ranges from 5.5 moles H_2O per equivalent sulfonic acid (mol/eq) for S-PBI to 34 mol/eq for S-PEEK (Table 1). The value for Nafion of 11.5 is lower than the 20-21 reported for fully hydrated Nafion, but agrees with the value given for re-hydrated Nafion first dried at 105° C.[10] The water uptake of the S-PES membrane also compares well with reported literature values for PES polymers of similar sulfonic acid content.[6] S-PES polymers of much higher sulfonic acid content (lower equivalent weight) can be dissolved by boiling in water for extended periods of time. The low value of 5.5 mol/eq for S-PBI may be due to crosslinking of the polymer associated with the sulfonation method, as will be discussed further below. The value of 46% obtained for S-PEEK is higher than other uptake values measured in our lab; this may be partly due to differences in the density of the polymer films resulting from different film casting techniques. The high value suggests that the water molecules are associating with the entire polymer as opposed to just the sulfonic acid group or cluster, as is probably the case with the other polymers. The reason for this may be the more flexible nature of the polymer backbone. This is supported by the fact that heating in water gradually swells the

polymer to a gel-like state before dissolving it completely. In contrast, S-PPQ, which has a very high sulfonic acid content, does not swell significantly and does not dissolve in boiling water.

The protonic conductivity of these polymers (Table 2) covers four to five orders of magnitude. Several factors effect the conductivity of these membranes, which are related to the mechanism of the proton transport. In the presence of water the hydronium ion acts as charge carrier. The movement of charge can occur by the translational motion of water molecules or by transfer of protons and reorientation of water molecules.[11] Thus an increase in water content tends to increase the conductivity of a given polymer.[10] Another important factor is the hydrogen ion density as determined by the sulfonic acid. More sulfonic acid groups per unit volume translate into greater ion density and hence greater conductivity, although this factor must be coupled with the water content of the membrane. The sulfonic acid density is related to the mobile proton density through its acidity constant, K_A. The pK_A's of S-PEEK, S-PES and S-PPQ range from 2-3, which translates to between 5 and 10% dissociation of the sulfonic acid groups. Nafion, on the other hand, is a fluorosulfonic acid, whose acidity is estimated to be close to that of triflic acid, which is essentially 100% dissociated. This gives Nafion an effective order of magnitude increase in ionic density over the other polymers, which is reflected in its superior conductivity. Note that the ion density data in Table 2 assumes 100% dissociation of the sulfonic acid, so the actual values are lower for all the polymers except Nafion.

The gap in conductivity between the aromatic sulfonic acid ionomers and Nafion may be lessened in practice due to operation at elevated temperature. Typically, a PEM electrolytic cell is run at 80° C; this increase in temperature yields kinetic advantages for all of the polymers tested. However as the temperature increases, the gap between the acidity of Nafion and that of the other polymers decreases. In general, acidity in water increases by about one pK_A unit per 100° C temperature increase.[12] Given a similar change for the sulfonic acid polymers, a polymer with pK_A of 2 at room temperature would go from ~ 10 to 27 % dissociated

at 100° C, increasing the conductivity by a factor of about three. This prediction is born out by Arrhenius plots (log of conductivity vs. reciprocal temperature) of S-PEEK and Nafion in that the activation energy (slope) is greater for S-PEEK;[4] i.e., there is a greater increase in conductivity with temperature for the sulfonic acid bearing polymers than for the fluorosulfonic acid bearing one.

A second way to increase the acidity of the aromatic sulfonic acids would be to incorporate electron withdrawing groups onto the sulfonic acid-bearing rings of the polymer. Higher sulfonic acid contents could also be used on S-PEEK and S-PES to increase the ion density, but this approach would be limited because of increased susceptibility toward dissolution.

Conclusion

The polymers and ionomers tested showed superior thermal stability to Nafion in helium, but were slightly less stable in a saturated steam environment. At room temperature, Nafion conductivity was almost an order of magnitude better than the next highest polymer. This is due to Nafion's greater intrinsic acidity, resulting in a higher effective ion density. This difference could be lessened by increasing the temperature, which would lower the pK_A and increase the ion density of the unleveled aromatic sulfonic acid ionomers.

References

(1) Barbir, F.; Gómez. T. *Int J. Hydrogen Energy*, **1996**, *21*, 891-901.

(2) Linkous, C.A. *Int J. Hydrogen Energy*, **1993**, *18*, 641-646.

(3) Kopitzke, R.W.; Linkous, C.A.; Nelson, G.N. submitted to J. Polymer Sci.

(4) Linkous, C.A.; Kopitzke, R.W.; Anderson, H.R.; Nelson, G.N. "Investigation of sulfonated polyether(ether)ketone as a proton exchange membrane electrolyte," submitted to J. Electrochem. Soc.

(5) Bailly, C.; Williams, D.J.; Karasz, F.E.; MacKnight, W.J. *Polymer*, **1987**, *28*, 1009-1016.

(6) Nolte, R.; Ledjeff, K.; Bauer, M.; Mulhaupy, R. *J. Membr. Science* **1993**, *83*, 211-220.

(7) Kuder, J.E.; Chen, J.C. U.S. Patent No. 4,634,530, Celanese Corporation, **1987**.

(8) Bradshaw, J.; Tian, S.B.; Xu, G. *Solid State Ionics* **1994**, *73*, 147-151.

(9) Gilbert, E.E. *Sulfonation and Related Reactions* John Wiley & Sons, Inc., New York, 1965; pp 425-442.

(10) Zawodzinski, T.A., Jr.; Derouin, C.; Radzinski, S.; Sherman, R.J.; Smith, V.T.; Springer, T.E.; Gottesfeld, S. *J. Electrochem. Soc.* **1993**, *140*, 1041-1047.

(11) Kreuer, K. *J. Molecular Structure* **1988**, *177*, 265-276.

(12) Weast, R.C. Ed. *CRC Handbook of Chemistry and Physics*; CRC Press, Inc., Boca Raton, FL, 1983; p D-169.

Table 1. Water Uptake Data for Sulfonated Polymers at 20° C.

Polymer	Equivalent Weight	% Water Uptake	mol H_2O / SO_3H
S-PEEK	1332	46	34.3
S-PES	880	14	6.9
S-PPQ	285	51	8.0
S-PBI	447	22	5.5
S-PI	1134	14	9.0
Nafion	1100	19	11.5

Table 2: Conductivity Data For Sulfonated Polymers at 20° C

Sample	ρion (meq/cm^3)	Conductivity $(\Omega\text{-cm})^{-1}$
S-PEEK	0.65	2.9×10^{-3}
S-PES	1.30	1.8×10^{-4}
S-PPQ	2.75	9.8×10^{-3}
S-PBI	2.28	3.9×10^{-6}
S-PI	1.17	3.8×10^{-5}
Nafion	1.53	9.2×10^{-2}

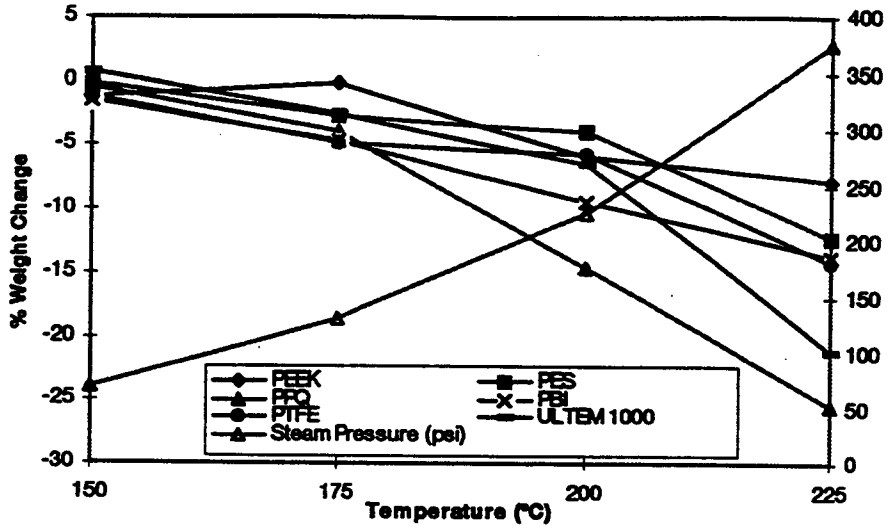

Figure 1. Weight Change Versus Temperature for Base Polymers in Saturated Steam

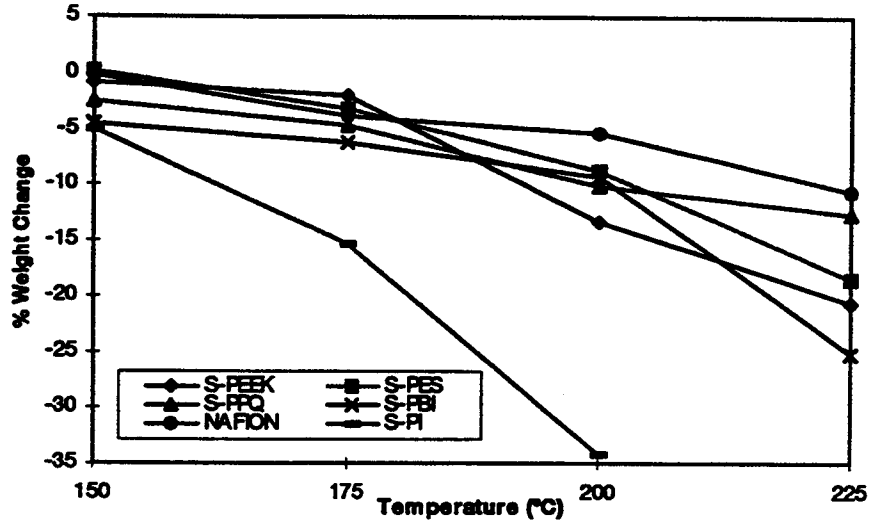

Figure 2. Weight Change Versus Temperature for Sulfonated Polymers in Saturated Steam

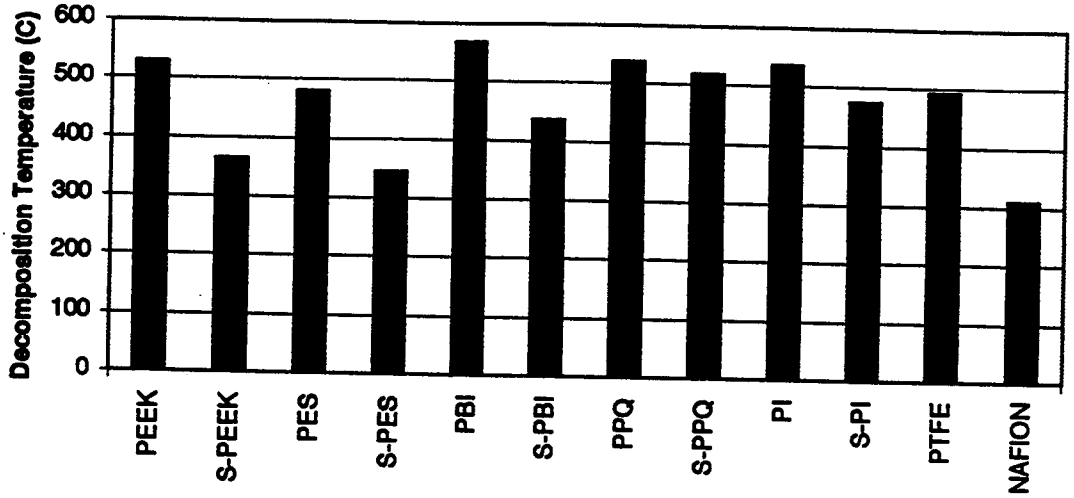

Figure 3. Temperature of 5% Weight Loss in Helium.

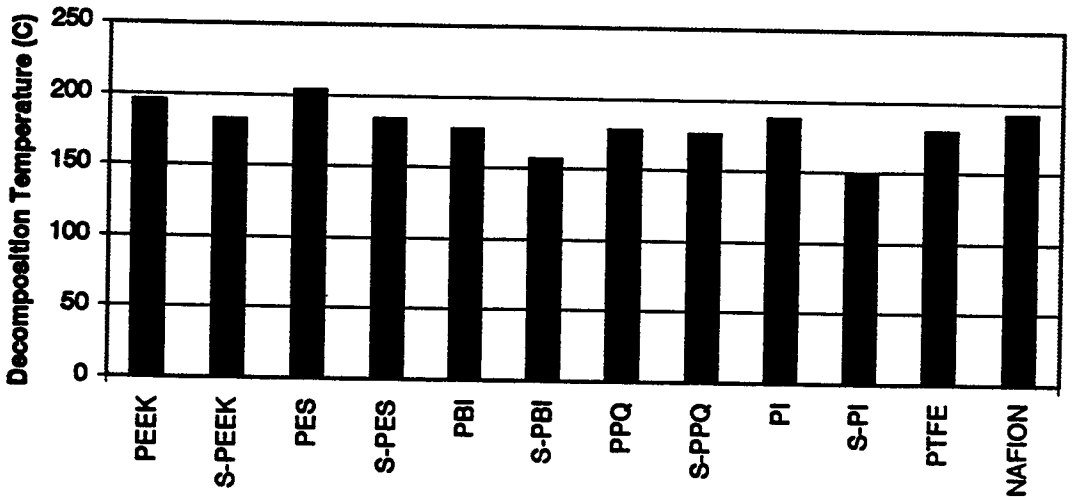

Figure 4. Temperature of 5% Weight Loss in Saturated Steam.

PHOTOELECTROCHEMICAL BASED DIRECT CONVERSION SYSTEMS FOR HYDROGEN PRODUCTION

Shyam Kocha, Xiaoping Gao, Art Frank, and John A. Turner
National Renewable Energy Laboratory
Golden, CO 80401-3393

Abstract

This work is focused on the use of photoelectrochemical devices for the direct production of hydrogen from sunlight and water. Two types of systems were studied, both involving multijunction devices. One set of cells consisted of a-Si triple junctions and the other a $GaInP_2$/GaAs tandem cell combination. Additional investigations were carried out on a-SiC double junctions. To catalyze the water decomposition process, the illuminated surface of the device was modified either by addition of platinum colloids or by coating with ruthenium dioxide.

Introduction

The thermodynamic potential for splitting water into hydrogen and oxygen at 25 °C is 1.23 volts. Adding overvoltage losses and some energy to drive the reaction at a reasonable rate we come to a voltage of about 1.6-1.8 volts for water decomposition. In fact, current commercial electrolyzers operate between 1.7 and 1.9 volts. Translating an energy of 1.9 eV into a corresponding wavelength of light, we come to 650 nm, which is in the lower energy red portion of the visible spectra. This means that almost the entire visible spectra has the energy capable of splitting water into hydrogen and oxygen. The key is to find the light harvesting system and a catalyst that can efficiently collect the energy and direct it towards the water splitting reaction. This paper will discuss our approach and current technical status in the area of photoelectrochemical water-splitting systems. This direct conversion system utilizes the process where an illuminated semiconductor immersed in aqueous solution, is used to decompose water directly. For any direct conversion process to be viable, the light harvesting system must generate enough voltage to decompose water, and the system must be stable in a water environment.

The goal of this research then is to develop a stable, cost effective, photoelectrochemical based system that will split water directly upon illumination, producing hydrogen and oxygen. Our focus for the light harvesting system involves the use of multijunction and tandem cell technology. Tandem cell technology connects photovoltaic layers (pn junctions) with different semiconductor bandgaps in series, one behind the other, in a single monolithic cascade device. This configuration offers a greater utilization of the solar spectrum, providing the highest theoretical conversion efficiency for any photoconversion system. The monolithic structure also minimizes the amount of active area needed for specific power applications. This work is directed at designing, testing, and optimizing multijunction cell technology for water splitting, and integrating it into a photoelectrolysis system. In summary, we hope to accomplish our objective by; (1) choice of semiconductor material and solid state structure; (2) surface modification to improve the energetics and stability and, (3) development of transparent and highly active catalysts.

Our efforts are directed at two promising semiconductor multijunction systems; III-V semiconducting materials (materials are made with various combinations of gallium, indium, arsenic and phosphorous), and amorphous silicon based systems. The III-V tandem cell structures are the semiconductors that solid state research groups are focusing on as the next generation of high efficiency solar cells. We are working with NREL's Photovoltaic and Basic Sciences Centers to provide us the state of the art III-V materials and structures.

A possible low cost direct conversion system for water splitting is one based on amorphous silicon (α-Si). Amorphorous silicon multijunction devices consist of multiple layers of a-Si cells. These multi-layer cells provide higher efficiency than single junction cells and reduce the amount of photodegradation that is common to all a-Si devices. The combination of lower system cost and higher efficiency, represent an important area of research for hydrogen production systems. Further, manufacturing capability for a-Si systems is high, with current production capability of these type of devices at over 20 megawatts per year in the US alone. Our approach here is to work with an industrial collaborator to develop optimized a-Si systems designed specifically for water splitting.

Discussion

Technical Approach and Results

Amorphous Silicon Systems

There are two main technological problems that must be solved before an α-Si based system could operate as a photoelectrolysis device: 1) its bandgap is insufficient to effect the decomposition of water and 2) α-Si is not stable in contact with aqueous electrolytes, it decomposes within a few minutes. The first issue is easily addressed because current state-of-the art α-Si triple junction devices can have voltages greater than 1.8 volts (even up to 2.3v), which is sufficient for water splitting. Stabilized efficiency for these systems can be greater than 10%.

There are two ways to approach the second issue with these devices, one approach taken by Rick Rocheleau at the University of Hawaii, is to use the back illumination system (the Solarex system where the cells are made on glass) and coat the cells with a thick layer of metal oxide catalysts. This is a more direct approach in that the semiconducting surface is never in direct contact with the electrolyte, however, it is more difficult to design a complete system with this configuration. The other approach is to use a front illumination system (the Energy Conversion Devices [ECD] system where the cells are deposited on stainless steel) and deposit a material on the semiconductor surface that is stable in aqueous solution in direct contact with the electrolyte. While this approach adds the requirement of a transparent protective coat and a transparent catalyst it also adds the possibility of an additional photojunction (a photoelectrochemical junction) that could add to the efficiency of the device. It also provides a system that is somewhat easier to engineer. Our work focuses on this second alternative.

Among the coating of interest are α-SiC, ITO, ZnO and SnO:F. Preliminary work at NREL has shown that α-SiC can provide a stable surface layer and is effective at protecting the underlying photovoltaic layers. ITO is also a strong possibility due its use as a transparent electrode. Zinc oxide is not a likely candidate because it has a rather narrow pH stability range. SnO:F is very stable, but it requires a fairly high substrate temperature for deposition. These higher temperatures can lead to major degradation in α-Si devices.

For this work we are partnering with Energy Conversion Devices to grow samples specifically for water splitting. For these samples, two areas of research were of interest to us: 1) a device structures that pushed electrons toward the semiconductor/electrolyte interface and 2) protective coatings for the surface that offered minimum light absorption, but stability at high and low pH. The reason we want electrons to be driven toward the semiconductor electrolyte interface is because we want hydrogen to be evolved from the illuminated surface. Of the two reactions involved in water splitting (hydrogen evolution and oxygen evolution), hydrogen evolution is the easiest, requiring the least amount a catalyst and it has the lowest overvoltage. We also expect that it will be easier to protect a surface under reducing conditions than under oxidizing conditions.

Additionally we are looking for devices that will operate at the maximum power point between 1.4 -1.6 volts. Water splitting in an electrolyzer requires around 1.8 volts (at 1 A/cm^2), but at solar intensities we work at lower current densities (2-15 ma/cm^2) and therefor we should be able to operate at lower voltages. We are therefore looking for device structures that operate at higher

currents and lower voltages than the standard voltages obtained from current triple junction devices.

Growing a-Si multijunctions specifically for this purpose, involves growing the a-Si layers in reverse order than what is usually done for the solid state device. Instead of growing the layers in the order n-i-p, they need to be grown in the order p-i-n. Since this is not the usual case, we expect the initial samples to be of lower quality that the standard PV devices. However, we expect that once the growth parameters have been optimized, the efficiency of these samples should be commensurate with the standard cells.

The first set of amorphous silicon tandem and triple cell samples from ECD were characterized with the expected results. None of the tandem cells developed sufficient voltage to split water and only a few of the triple cells generated enough voltage. Additionally, there was considerable variability in the efficiency and operating voltage of these triple cells. The efficiency varied from less that 0.5% to over 4.5%, with the best cell having an operating voltage of 1.4 volts, for maximum efficiency, an operating voltage of at least 1.5 is needed.

The second set of samples received from ECD were triple cells with an average voltage of ~1.9 volts, sufficient for water splitting. These samples do not have the a-SiC surface layer, that will be added as soon at ECD has the proper materials for growing the SiC. Unfortunately, due to funding problems, we were unable to complete that work during FY96.

Work on these cells is now continuing. We have used NREL's coating facility to grow varying thicknesses of ITO on the surface of the bare devices. Our approach is to look at varying thicknesses of ITO to look for maximum stability and transparency. Our first experiments in 10M KOH with a 500Å coating of ITO showed that the ITO dissolved after a few hours of operation. We expect these samples to be somewhat more stable in acid

III-V Tandem Cells

The production of hydrogen and oxygen gas was measured for the sample structure grown with a 0.1um layer of high doped p-$GaInP_2$ on top of the n-$GaInP_2$ surface emitter layer. The system was examined for the water splitting in 11 M KOH aqueous electrolyte solution. A photoelectrochemical cell was specially designed such that O_2 and H_2 could be collected separately in two thin tubes with a sensitivity of 10 μL. The volume was measured by the displacement of the water in the tubes. Possible air leakage for the system was checked before each experiment. Chemical identification was confirmed by gas chromatography (GC). The results were then compared with the total charge measured via an external coulometer. The light source was a 150W Xe lamp equipped with a water filter. The illumination intensity was about 13 sun incident at the window of the photoelectrochemical cell. The cell was sparged with argon gas for 15 minutes before measurements were taken. We expected that the total error of the volume measurement to be +/-10%, and the measurement error for the total charge to be very small, within 1%. The error of system was checked by splitting water using Pt as working and counter electrodes. The results, comparing the volumes calculated from total charge and GC data, show that the error is about 5%.

For photoelectrochemical measurements the electrodes were the Pt/Ru coated modified tandem cell with a RuOx coated Pt mesh counter electrode. The dark the i-v scans show that the current is small (in μA range). At an illumination intensity of ~ 13 suns, current starts at about +350 mV.

At zero bias (0 mV) the current density is around 20 - 30 mA/cm^2. Table 1 shows the experimental results and the expected volumes calculated from the total charge.

Table 1
11.7M KOH, 13 suns

	Day 1 (7.5h)		Day 2 (7.5h)	
	Measured (ml)	Calculated (ml)	Measured (ml)	Calculated (ml)
H_2	5.83	4.72	6.11	5.7
O_2	2.37	2.36	2.95	2.85
H_2/O_2 Ratio	2.46		2.07	
Charge (Q)	33.2		40	

The H_2 and O_2 calculated volumes are calculated from the measured charge Q(C) using Faraday's Law. The displacement volumes and the composition of the gases were confirmed by the GC. Note that the volume of oxygen measured from displacement is very close (within experimental error) to that calculated from the total charge, however the volume of hydrogen is about 23% higher for the first day experiment. On the second day the H_2/O_2 ratio is about 2 as expected. The results of gas chromatography and electrochemical experiments show the production of hydrogen and oxygen gases with a H_2:O_2 ratio of 2:1 and efficiency about 2-4 %.

A comment here concerning the measurement of that efficiency: For this calculation the light intensity was measured before the window of photoelectochemical cell, not on the semiconductor surface itself. Since there are adsorption and reflection losses from the solution and glass/solution/air interfaces along the light pathway to the electrode, the light incident on the semiconductor surface is much less than the light incident on the cell window. To provide an estimate of the true efficiency, a solid state tandem cell placed in the solution can be used and the photocurrent will be a direct measurement of the light intensity on the sample. For example, a tandem cell with a 20% efficiency, will give photocurrent at one sun condition of about 12 mA/cm2. In our cell, the solid state tandem cell gives a photocurrent of about 50 mA/cm^2 indicating an incident light intensity of about 4.2 suns, only one third of 13 suns measured at the window of the sample cell. This means that the efficiency should between 6 - 12%.

Table 2 details the results for another sample this time run for three days. The results are similar.

Table 2
11.7M KOH, 13 suns

	Day 1 (6h)		Day 2 (6h)		Day 3 (8.5h)	
	Measured (ml)	Calculated (ml)	Measured (ml)	Calculated (ml)	Measured (ml)	Calculated (ml)
H_2	1.8	1.4	2.2	2.05	4.2	3.74
O_2	0.6	0.7	1.	1.03	1.8	1.87
H_2/O_2 Ratio	3		2.2		2.3	
Charge (Q)	11		14.4		26.3	

The solutions in the photoelectrochemical cell were examined by ICP-AES. The results confirmed that $GaInP_2$/GaAs initially photodegrades as implied by the presence of Ga ions in the solution following photolysis. However the amount of Ga ion always much higher the that of In ion. Examination of the surface composition by XPS indicated that the film is composed mainly of indium-rich oxides. This confirms our expectation that indium oxide can provide a stabilizing interface for these samples. More XPS experiments are planned to determine the exact composition of the products on the surface.

Figure one shows the results of current voltage scans for three different KOH concentrations. This is from a sample that showed stoichiometeric water splitting over a period of 4 days. This data is from a 2 electrode current voltage scan for the illuminated cell (approximately 13 suns incident on the cell window). The intent of these experiments was to look for the optimum KOH concentration for PEC water splitting. We expected that at higher base concentrations, the kinetics of the oxygen evolution reaction would be faster, giving rise to higher currents.

There are two things to note in this data, the zero bias crossing point and the current plateau at high bias. The zero bias crossing point represents the maximum short circuit current for water splitting, and the operating point for the cell in photoelectrolysis mode. This comes from a combination of the voltage the cell is generating, and the voltage needed for water splitting at that current density. Of course, the current density will be a direct function of the light intensity. Ideally the current plateau should be reached just before or just at the zero bias line, indicating that the cell is generating exactly the energy needed to split water at that current density. Since the photovoltaic analog of this cell generates over 2.3 volts, we would expect that the plateau would be reached 500 mV before the zero bias point not 500 mV past it. The potential shift indicates that there a barrier to electron flow of some sort, for example some high resistance in the cell somewhere, or poor catalytic activity. Note, the water splitting efficiency of 5.7% (LHV) for a 5M KOH solution.

The plateau at higher bias represent the light limited current and the % represents the efficiency of water splitting if that current level crossed the zero bias line. The height of the plateau depends on the light intensity getting to the electrode and the activity of the catalyst. Since these scans are all at the same light intensity, the major factor for the height of these plateaus appears to be the amount and activity of the catalyst. These scans were done in the order of 1M, 5M, 11.7 M. Upon repeating the 1M scan (not shown) we find that the current plateau is very close to that of the 11.7 M. Observing the surface of the sample we noticed that there is a color change of the electrode surface which we interpret to be a decrease in the amount of catalysis on the surface. This give rise to open spots where the catalyst is not active and hydrogen evolution must occur at the bare electrode where there is a overvoltage loss of over 500 mV. It is not clear how or why the catalyst leaves, since it is insoluble in this electrolyte. This trend can also be seen in Tables I and II, note that the total charge per day increases from one day to the next, likely due to the same effect. Our initial explanation is that the gas evolution somehow takes the catalyst off, perhaps due to nonoptimum surface pretreatment, giving rise to a low sticking coefficient. Further experiments are planned to look at surface pretreatments to see if we can increase the lifetime of the catalytic coat.

Plans for Future Work:

In general, our future work will involve: the identification and growth of promising multi-junction systems including designing unique multi-junction systems focused specifically on water splitting; establishment of cooperative efforts to obtain samples or development of in-

house growth capabilities; and lifetime testing and efficiency measurements for working systems. The subject of the interaction of colloidal catalysts with the various tandem cell surfaces is also a very important area for future work. More specifically, we will focus on continued investigation of the III-V material system concentrating on tailoring the tandem cell structure specifically for an aqueous environment and the energetics of the water splitting reaction. We will be evaluating various surface treatments to enhance stability and energetics. The semiconductor corrision mechanisms will also be a point of study. We will also study nitridation as a surface treatment for increased surface stability. We will also continue working with our industrial collaborators to optimize the α-Si multi-junction systems for water splitting.

Major Barriers

In general, the major problems that must be addressed in order to produce a viable system are: stability of the semiconductor/electrolyte interface, and system energetics. Materials and catalysts must be found that protect the semiconductor surface, but allow electrons to pass through unimpeded. While we lack full understanding of the fundamental characteristics of the semiconductor/electrolyte interface, considerable progress has been made. For the a-Si multi-junction cells the design of the water-splitting cells must be optimized for maximum efficiency. For the III-V systems, to maximize their efficiency, materials and designs must be identified for lower voltage, higher current applications. Promising new systems currently under development may directly address this issue.

Figure Captions

Figure 1 Current-voltage scans for modified tandem cell, 13 suns illumination.

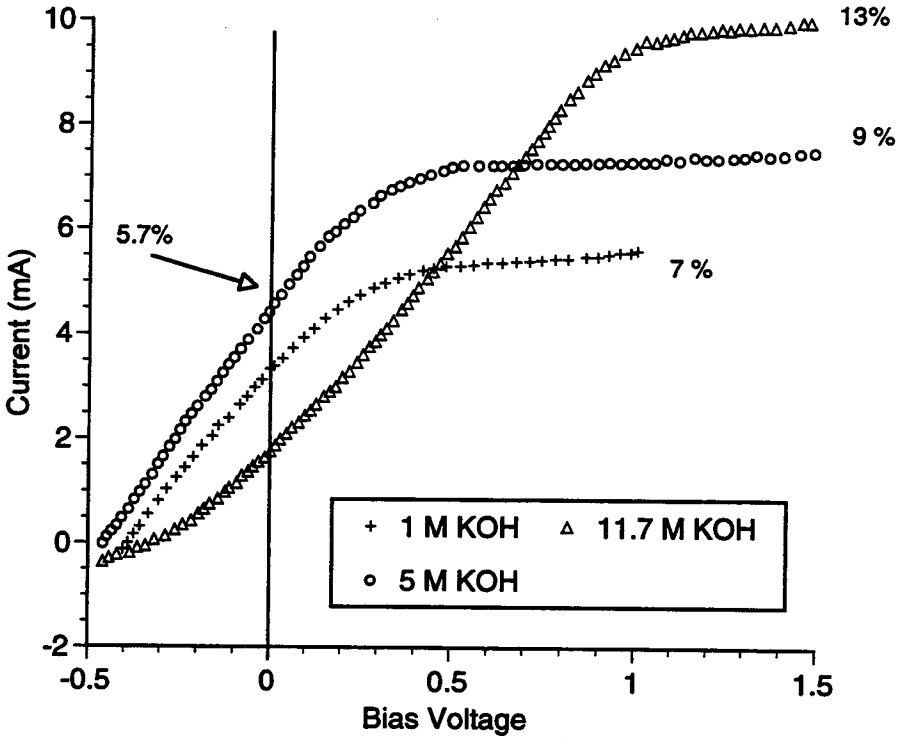
10
8
6
4
2
0
-2
Current (mA)
-0.5
0
0.5
1
1.5
Bias Voltage
5.7%
13%
9 %
7 %
1 M KOH
11.7 M KOH
5 M KOH

High Efficiency Photoelectrochemical Hydrogen Production using Multijunction Amorphous Silicon Photoelectrodes

Richard E. Rocheleau*, Eric L. Miller, Anupam Misra

Hawaii Natural Energy Institute

School of Ocean and Earth Science and Technology

University of Hawaii at Manoa

Honolulu, HI 96822, USA

ABSTRACT

Photoelectrochemical solar-to-hydrogen conversion efficiencies as high as 7.8% (based on the lower heating value of hydrogen) have been demonstrated in outdoor testing using photoelectrodes fabricated from triple junction amorphous silicon-solar cells. The tests were conducted in a specially designed Teflon sealed reactor in 1N KOH, with a photoactive area of 0.27 cm^2, and anode and cathode areas of 1 cm^2. The hydrogen production rates, inferred from direct measurement of the anodic/cathodic currents and confirmed by independent volumetric and gas chromatographic measurements of the evolved hydrogen, were in excellent agreement with the rates predicted based on the measured solid state JV behavior of the solar cell and the overpotentials of the thin-film catalysts. The thin film catalysts, CoMo hydrogen catalysts deposited by sputtering from a compound target and $NiFe_yO_x$ oxygen catalysts deposited from nickel-iron Permalloy target by reactive sputtering, have, in separate tests, shown no degradation after over 7200 hours of operation in 1N KOH electrolyte. During outdoor testing, the solar-to-hydrogen conversion efficiency decreased in the late

afternoon as the blue portion of the spectrum decreased, a result of the spectral sensitivity of the solar cell used to construct the photoelectrode. Detailed modeling of the multijunction amorphous silicon cells is being conducted to identify structures which are better load-matched to the catalyst performance and which could yield higher hydrogen production efficiencies. Future work to advance this technology includes development of improved thin-film catalysts and development of transparent protective coatings which will allow complete immersion of the active electrode into the electrolyte.

This paper will appear in a special hydrogen edition of Energy & Fuels.

Photolytic Decomposition of Water using a Dual Bed System

Darlene K. Slattery and Clovis A. Linkous*

Florida Solar Energy Center

1679 Clearlake Road

Cocoa, FL 32922-5703

Abstract

A dual bed system for photocatalytic water splitting is introduced and an I^-/IO_3^- couple suggested as a redox mediator. Initial studies using TiO_2 for oxygen production and InP for hydrogen evolution support the viability of the two bed system but led us to conclude that new semiconductors are needed.

The theoretical study of a number of organic dyes and pigments suggests that these compounds may have ionization potentials (IPs) that will make them suitable for the oxygen-evolving system as well as make a better spectral match with the solar spectrum. Justification for the chosen parameters is given and a list of nine possible organic semiconducting pigments is advanced.

Introduction

Dwindling petroleum reserves have been a major driving force in a number of research areas for more than 25 years. The energy crisis of the early 1970s emphasized the importance of developing alternative fuels to replace or supplement those derived from petroleum.

One such fuel, hydrogen, is easily obtained via the electrolysis of water. To split water, under normal conditions, a potential difference of 1.23 V must be established between the anode and cathode.

Research by Fujishima and Honda[1] showed that illumination of anodes made from n-type semiconductors greatly reduced the external voltage required to decompose water. The researchers constructed an electrochemical cell, using an n-type semiconductor as the anode and a platinum black counter electrode, Figure 1. The semiconductor electrode was irradiated, promoting an electron from the valence band to the conduction band and a current was established through the external circuit. The holes left in the valence band resulted in the oxidation of water at the semiconductor electrode and the electrons became available for the reduction of hydrogen at the Pt counter electrode. This decomposition was observed to occur at low current density without the application of any external voltage. The suggestion that solar energy could facilitate water splitting triggered research in numerous labs around the world.

The concept of photoelectrochemical conversion of solar energy has evolved over the years. The classic configuration for an electrochemical cell calls for two planar electrodes, positioned parallel to each other, but this is not the optimum arrangement for making use of solar energy. Such an arrangement requires the use of either an optically transparent counter electrode, which allows the light to pass through it and reach the semiconductor electrode, or as illustrated in Figure 1, the semiconductor must be deposited as a thin film on glass and irradiated from the backside. A better, simpler approach is to use the semiconductor as a powder, adding it directly to water, illuminating and allowing the H_2 and O_2 to bubble out. This eliminates the requirement for expensive single crystals while increasing the catalytic surface area and lowering the cost to assemble and use.[2] There are still a number of problems, however. The most obvious one is that the products are evolved together, with the product stream being 66% H_2 by volume, well within the limits of combustibility. Additionally, the wide band gap semiconductors necessary for splitting water in a single step do not make efficient use of the solar spectrum.

For a semiconductor to split water, it must have a conduction band that is negative of the voltage required to reduce water (negative of zero vs NHE), and a valence band that is positive of the potential required to oxidize water (1.23 V vs NHE). The semiconductors that have been identified for water decomposition are somewhat limited. Figure 2 illustrates the band edges of a number of those discussed in the literature. As can be seen, those capable of oxygen production are mostly metal oxides, while those favorable for hydrogen production are metal phosphides or sulfides. Only a very few are capable of simultaneous oxygen and hydrogen evolution.

As illustrated in Figure 2, the majority of these semiconductors have band gaps of around 3.0 eV. This band gap corresponds to an absorption of 400 nm light, which is at the UV edge of the visible spectrum. The amount of UV radiation that reaches the earth is but a small fraction of the total radiation. To increase efficiency, the semiconductor must be capable of absorbing in a region that contains a larger fraction of the impinging radiation. A material that absorbs between 450-600 nm, or has a band gap of 2.7-2.0, will be capable of making maximum use of the solar spectrum and still be able to split water.

A variety of approaches have been tried to increase the efficiency of the semiconductors that have a band gap wide enough for simultaneous water oxidation and reduction. One approach is to attach a sensitizer to the semiconductor.[3] When the sensitizer is excited by the visible light, it injects an electron into the conduction band of the semiconductor, where it is channeled to a catalytic site and reduces water to hydrogen. The oxidized sensitizer, in the presence of another catalyst, oxidizes water as the sensitizer returns to its reduced form.

Sensitizers that have been studied include phthalocyanines,[3,4] ruthenium (polypyridine) derivatives,[5,6] and porphyrins,[7,8] to mention a few. In some instances, to assist

in the charge separation and decrease the chances of recombination, surfactants are added to the system, stabilizing the intermediates.[9,10,11]

Water decomposition is complex because it is a four photon process for O_2 evolution and a two photon process for H_2 evolution. The various intermediate chemical steps represent a kinetic limitation that decreases quantum efficiency. One way that researchers have attempted to overcome this problem is by the use of a sacrificial electron donor or acceptor. For example, to better study the hydrogen producing reaction, the oxidized sensitizer is reduced in a nonreversible step by a reducing agent such as EDTA.[5] While this simplifies the reaction and allows separate optimization of the water-splitting half reactions, ultimately it is necessary to couple the two half reactions to complete the cycle.

An alternative to requiring one semiconductor to produce both oxygen and hydrogen is to use a dual bed photo system, as shown in the schematic in Figure 3. In such a system, one semiconductor is used to reduce water to hydrogen and another is used to oxidize water, evolving oxygen. It is then possible to make use of semiconductors with smaller band gaps that are more suited to the individual half reactions and that utilize more of the solar spectrum, thus, increasing efficiency. Additionally, the gases are evolved separately. The key to making such a system viable is a method for transferring electrons between the two beds. This can be accomplished by the use of a redox mediator, which is oxidized as the hydrogen is evolved and reduced as the oxygen is evolved. A well chosen compound will not only shuttle electrons between the two beds, but also will increase the amount of product formed by assisting in separating charges. The redox potential of the mediator couple must be more positive than the conduction band edge of the oxygen evolving semiconductor but more negative than the valence band edge of the hydrogen evolving semiconductor. This allows the excited electron from the conduction band of the oxidizing semiconductor to be given up to the mediator. Then in the reducing bed, the reduced mediator gives up its electron to the

valence band of the semiconductor. An energy band diagram for such a system is shown in Figure 4.

It is interesting to note the similarities between the system illustrated in Figure 4 and a scheme for photosynthesis. If instead of using a semiconductor in bed 1, chlorophyll is substituted, this becomes photosystem II where water is oxidized and an electron acceptor transfers the electrons to a series of transfer agents and, ultimately, photosystem I (bed 2). In photosystem I, light is absorbed by a different specialized chlorophyll and electrons are again promoted to an acceptor. In photosynthesis, this would ultimately result in $NADP^+$ being reduced to NADPH instead of the hydrogen formed in the dual bed system.

A dual bed system for the photocatalytic splitting of water is the topic of this paper.

Experimental

General. Reagents used were purchased from Fisher Scientific unless otherwise noted and all were used as received, with no further purification. Water splitting experiments were run batch-wise in a sealed 50 mL glass reaction vessel. The vessel was purged thoroughly to remove air and placed in front of a xenon lamp, with stirring, for six hours. A 1.0 mL sample of the gas over the sample was removed and injected into a gas chromatograph (GC) equipped with a thermal conductivity detector. The carrier gas for samples expected to contain H_2 was argon and for those containing O_2, the carrier was helium.

Oxygen Evolution. For O_2 evolving experiments, the preferred solution was 1.0 M NaOH containing 0.2 M KIO_3. To this solution was added 0.40 g of TiO_2 (DeGussa or Fisher) that had been loaded with 1.0 wt% Pt or Ir. Other experiments were run using WO_3 as the semiconductor but for these 1.0 M H_2SO_4 was substituted for the NaOH. The WO_3 was either purchased from Fisher or prepared as colloids.

Preparation of WO_3 Colloids. The colloidal WO_3 was prepared using a procedure suggested by Augustynski.[12] Dowex 50WX2 resin was prepared by stirring 25 g in distilled water overnight and then pouring the slurry into a column and draining off the excess water. The resin was then conditioned by passing 120 mL of 1 M H_2SO_4 through the column. The resin was next washed with distilled water until a neutral pH was obtained.

After preparing the column, 20 mL of 0.5 M Na_2WO_4 was slowly passed through the column, using water as the eluant. The product was collected once the pH of the liquid became acidic and was collected until it again became neutral.

Aliquots of the collected colloids were either used as is or were isolated from the solution by centrifuging if they were to be catalyst loaded.

Hydrogen Evolution. The H_2 evolving experiments also were run in 1.0 M NaOH but the redox mediator was KI and the semiconductor was InP (Strem or Cerac) loaded with Pt.

In experiments to study H_2 evolution in the presence of both I^- and IO_3^-, the initial concentrations were 0.8 M and 0.2 M, respectively. The sample was illuminated for six hours and the gases analyzed by GC. The InP was isolated from the solution, washed with distilled water and placed back into the standard hydrogen evolving solution that was initially free of IO_3^- and rerun.

Catalyst Loading. Catalyst loading, in all cases, was accomplished using a borohydride reduction. The TiO_2 or InP was placed in a 1.0 M solution of NaOH and either $IrCl_3$ (Aesar) or H_2PtCl_6 (Strem) was added to load at 1.0 wt%. An excess of sodium borohydride was added to an addition funnel containing 1.0 M NaOH and this solution was slowly added to the semiconductor suspension, with stirring, under an inert atmosphere. After the reduction was complete, the catalyst-loaded semiconductor was isolated via vacuum

filtration. For the catalyst loading of WO_3, it was necessary to substitute distilled water for the NaOH solutions.

Results and Discussion

Inorganic Oxide Photocatalysts. Florida Solar Energy Center has studied a dual bed system for several years.[13] Titanium dioxide was chosen for the oxidative bed, while indium phosphide was selected for the reductive bed. Both half reactions were catalyzed with platinum, and in the case of the TiO_2, iridium was also used. The Ir was found to nearly double the amount of oxygen formed, as shown in Table 1.

As part of an International Energy Agency, IEA, collaboration, we also investigated the use of WO_3 as a replacement for TiO_2. Because WO_3 is soluble in base, these experiments were run in H_2SO_4. It was confirmed that, in an acidic system, the WO_3 evolved more oxygen than did the TiO_2. However, this was still 25% less than produced by the TiO_2 in a basic solution.

As mentioned previously, the band gap of the transition metal oxides require the input of high energy radiation, decreasing efficiency. An additional problem with inorganic semiconductors is that photocorrosion occurs over a period of time, with InP being especially vulnerable. There are many literature references to the problem but little has been done to quantify it. Our experiments indicated that a loss of greater than 60% occurred over an eight hour day, when InP was run in 2.0 M HCl. Changing the solvent to 1.0 M NaOH alleviated this problem and had the added benefit of being compatible with the redox mediators that we were testing and, in the case of O_2 evolution, increasing the product yield.

A number of redox couples were studied, the most favorable being the I^-/IO_3^- couple. By using a basic solution with this mediator, the formation of I_3^- was avoided and so did not interfere with light absorption. A major advantage to the use of a redox mediator was

evidenced in the amount of gas evolved with and without the mediator present. When the redox mediator was omitted, the O_2 or H_2 above the sample was below our detection limits.

During tests to determine mediator concentration limits that still would allow the desired reaction, some unexpected results were obtained. In the presence of even small concentrations of IO_3^-, the InP was converted to a light gray material that was no longer hydrogen evolving. Because the solution circulating between the reaction beds would have both the reduced and oxidized forms of the mediator, the semiconductor, the mediator, or both require replacement.

Organic Photocatalysts. In addition to the sensitizers mentioned previously, researchers have also looked at organic dyes such as xanthenes,[14,15] rhodamines[16] and acridines[17] to increase the spectral response of the broad band semiconductors. One might wonder, however, why the presence of the inorganic semiconductor is necessary since dye aggregates are known, in many cases, to have the properties of organic semiconductors.[18,19] The ability of an excited organic dye to undergo electron transfer is a very well known phenomenon. In fact, the fields of silver halide photography and electrophotography are based on dye sensitization. In such cases, the dye may act as an electron acceptor or an electron donor, just as semiconductors do.

The dyes that are used in the photographic industry have highest occupied, HOMO, and lowest unoccupied, LUMO, molecular orbitals that have been matched to the energy levels of silver halide. In Figure 5, the HOMO of the sensitizing dye pinacyanol, is seen to be higher in energy than the valence band of the silver halide, and the LUMO lies above the conduction band. Although the energy of this dye, as well as the others shown, is appropriate for use in a hydrogen producing system, it is not negative enough to be of value in an oxygen producing system. To expect a dye to be useful for oxygen evolution, the HOMO, as will be

discussed below, would need to have an energy of about -7.5 eV and a transition energy of 2.0 eV.

An advantage of the organic materials is that the λ_{max} may be shifted by adding substituents onto the chromophores. Depending upon whether the substituent is an electron donor or acceptor, the λ_{max} may be shifted either bathochromically or hypsochromically. Additionally, replacing a single carbon atom with a heteroatom can have pronounced effects. Once a dye is identified that has the required HOMO, modifying substituents should allow optimal use of the solar spectrum.

Little data is available in the open literature regarding the absolute energy of the HOMOs, or equivalently the ionization potentials, of organic dyes. To determine the viability of using such compounds, the energy levels of a number of dyes were studied using Quantum CAChe® (Computer-Aided Chemistry) molecular modeling software. To establish the desired range for the gas phase ionization potentials, the following calculation was considered:

$$\Delta G^{\circ}_{H_2O} + E_{NHE} + e\eta_{H_2O/O_2} - e\Delta pH + IP_{corr} = IP$$

where:

$\Delta G^{\circ}_{H_2O}$ = energy required to decompose water (vs NHE) = 1.23 eV

E_{NHE} = conversion of H_2 electrode potential to absolute energy scale = 4.5eV

η_{H_2O/O_2} = anticipated required built-in oxidation overpotential for water splitting = 0.5 V

ΔpH = pH correction factor, varies according to whether solution is acidic or basic = 0- 0.84 V

IP_{corr} = Correction factor for gas vs surface IP = 1.3 eV

e = fundamental electronic charge

One must also allow for the discrepancy between theory and experiment so we arbitrarily set a target of 7.5 ± 0.7 eV.

Initial calculations with CAChe® resulted in ionization potentials that were obviously in error based upon known values from the literature. A series of compounds having structures similar to those of interest and which had known IPs were run in order to construct a calibration curve. Calculations were done using MOPAC's AM1 and PM3 methods and ZINDO's INDO/1 as well as Extended Huckel. The best correlation was obtained with the PM3 method. It was found that the values calculated were between 0.77 and 1.21 eV larger than the experimental values, see Table 2. Using this data, a linear regression gave the equation

$$IP_{calc} = 0.9261(IP_{exp}) + 1.4761$$

which was then used to obtain IPs for a large number of organic pigments. From these, nine were chosen for further study, as shown in Table 3.

Additional criteria that were considered in this selection was λ_{max}, insolubility, and lightfastness. These pigments will now be loaded with Pt or Ir catalyst and tested for their oxygen evolving ability.

Conclusions

Use of a dual bed photosystem for water splitting will better utilize the solar spectrum by employing semiconductors of narrower band gap. Each semiconductor can be matched to the half reaction of interest rather than requiring one to have a band gap large enough to encompass the energy requirements of both reactions.

The use of a redox mediator such as IO_3^-/I^- to couple the H_2 and O_2 evolving reactions was shown to be viable. The presence of the mediator increased the production of oxygen from virtually zero to 2.25 mL over six hours for Ir loaded TiO_2.

Calculations using CAChe® indicated that a number of organic pigments may have ionization potentials appropriate for use in an oxygen evolving system. Nine such compounds have been selected and are now undergoing testing.

Acknowledgments

This work is supported by the U.S. Department of Energy. The authors wish to thank Professors Harold S. Freeman, North Carolina State University, and Jan Augustynski, University of Geneva, Switzerland for their kind assistance.

References

(1) Fujishima, A.; Honda, K. *Nature* **1972**, *238*, 37-38.

(2) Pelizzetti, E.; Visca, M. In *Energy Resources through Photochemistry and Catalysis*, Gratzel, M., Ed.; Academic: New York, 1983; Chapter 8.

(3) Giraudeau, A.: Fan, F.R.; Bard, A.J. *J. Am. Chem. Soc.* **1980**, *102*(16), 5137-5142.

(4) Lever, A.B.P.; Licoccia, S.; Ramaswamy, B.S.; Bandil, S.A.; Stynes, D.V. *Inorg. Chem. Acta*, **1981**, *51*, 169-176.

(5) Gratzel, M. *Acc. Chem. Res.* **1981**, *14*, 376-384.

(6) Juris, A.; balzani, V. *Helv. Chim. Acta.*, **1981**, *64*, 2175-2182.

(7) Kalanasundaram, K.; Vlachopoulos, N.; Krishnan, V.; Monnier, A.; Gratzel, M. *J. Phys. Chem.* **1987**, *91*, 2342-2344.

(8) Darwent, J.R.; Douglas, P.; Harriman, A.; Porter, G.; Richoux, M.C. *Coord. Chem. Rev.*, **1982**, *44*, 83-126.

(9) Sprintschnik, G.; Sprintschnik, H.W.; Kirsch, P.P., Whitten, D.G. *J. Am. Chem. Soc.* **1976**, *98*(8), 2337-2338.

(10) Borgarello, E.; Kiwi, Pelizzetti, E.; Visca, M.; Gratzel, M., *Nature,* **1981,** 158-160.

(11) Infelta, P.P.; Gratzel, M.; Fendler, J.H. *J. Am. Chem. Soc.,* **1980,** *102*(5), 1479-1483.

(12) Augustynski, J., University of Geneva, Switzerland, personal communication, 1997.

(13) Linkous, C.A.; McKaige, G.T.; Slattery, D.K.; Ouellette, A.J.A.; Austin, B.C.N., "Solar Photocatalytic Hydrogen Production from Water using a Dual Bed Photosystem"; FSEC-CR-857-95, Florida Solar Energy Center, 1995.

(14) Mau, A.W.H.; Johansen, O.; Sasse, W.H.F. *Photochem. Photobiol.* **1985,** *41*(5), 503-509.

(15) Matsumura, M.; Mitsuda, K.; Yoshizawa, N.; Tsubomura, H. *Bull. Chem. Soc. Jpn.* **1981,** *54*, 692-695.

(16) Matsumura, M.; Matsudaira, S.; Tsubomura, H., Takata, M.; Yanagida, H. *Ind. Eng. Chem. Prod. Res. Dev.* **1980,** *19*, 415-421.

(17) Kalyanasundaram, K.; Gratzel, M. *J.C.S. Chem. Comm.* **1979,** 1137-1138.

(18) Sviridov, D.V.; Kulak, A.I. *New J. Chem.* **1991,** *15*(7), 539-544.

(19) Meier, H. In *Physical and Chemical Applications of Dyestuffs;* Top. Curr. Chem. 61; . Springer-Verlag: Berlin; 1976; pp 85-131.

Table 1. Oxygen Evolution Results

Semiconductor	Catalyst	mL O_2 for 1N H_2SO_4/IO_3^-	mL O_2 for 1N $NaOH/IO_3^-$
TiO_2	none	0.12	0.60
TiO_2	Pt	0.36	1.3
TiO_2	Ir	1.1	2.2
WO_3	none	0.06	N/A
WO_3	Pt	0.44	N/A
WO_3	Ir	1.72	N/A

Table 2. Ionization Potential Data using PM3

COMPOUND	EXPERIMENTAL IP	CALCULATED IP	ΔP
Pentacene	6.61	7.62	1.01
Violanthrene	6.40	7.61	1.21
Perylene	6.90	7.99	1.09
Naphthacene	6.95	7.87	0.92
Coronene	7.29	8.28	0.99
Pyrene	7.41	8.23	0.82
Anthracene	7.55	8.24	0.69
Phenanthrene	7.86	8.74	0.88
Naphthalene	8.26	9.24	0.98
Isoquinoline	8.53	9.18	0.65
Quinoline	8.62	9.24	0.62
Benzophenone	9.05	9.93	0.88
Pyridine	9.25	10.02	0.77
Phthalic Anhydride	10.0	10.82	0.82
Benzoquinone	10.04	10.93	0.89

Table 3. Proposed Pigments for Oxygen Evolution

Structure	Ionization Potential
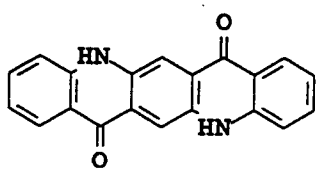	6.67
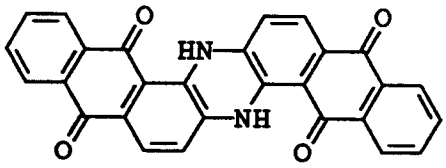	6.24
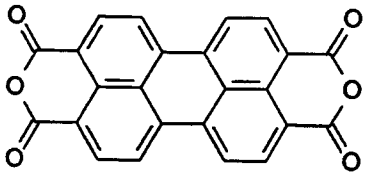	8.45
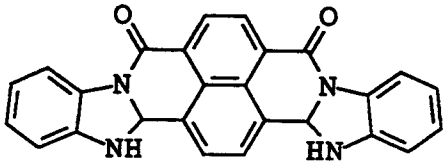	7.78
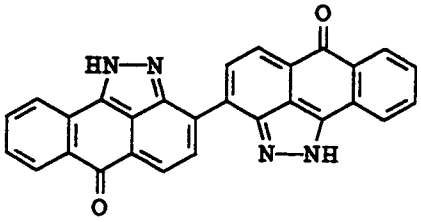	7.31
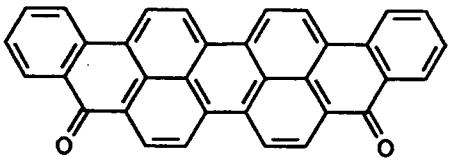	7.26

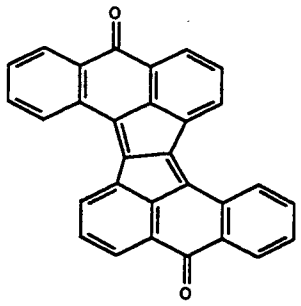

7.91

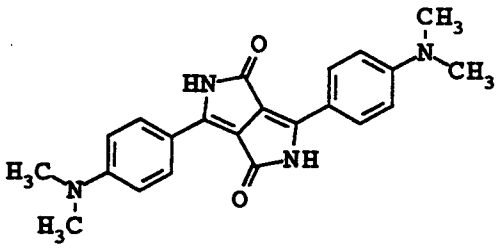

6.99

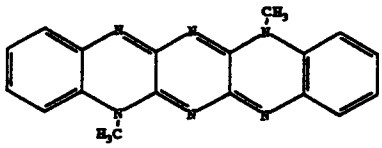

6.84

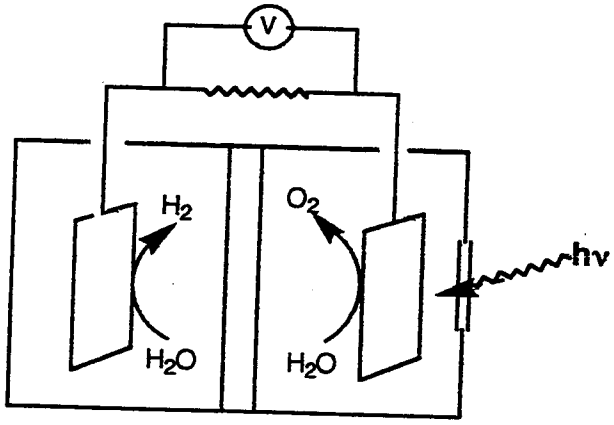

Figure 1. Electrochemical Cell with Light Illuminating a Semiconductor Electrode

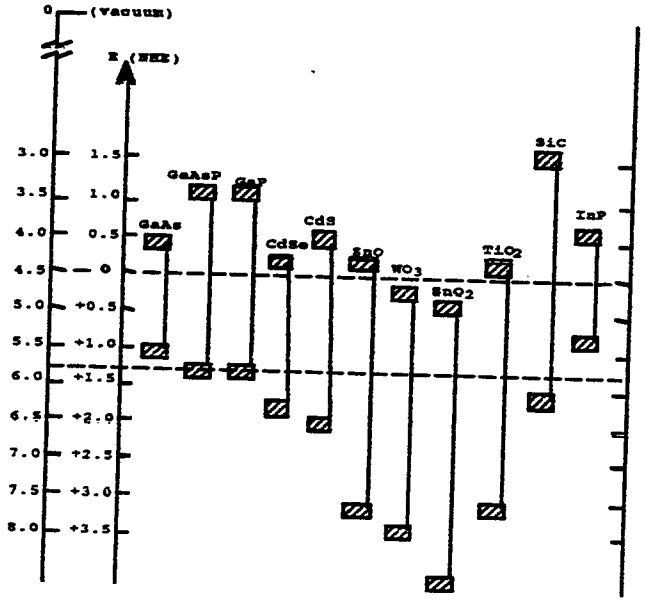

Figure 2. Band Edges of Various Semiconductors

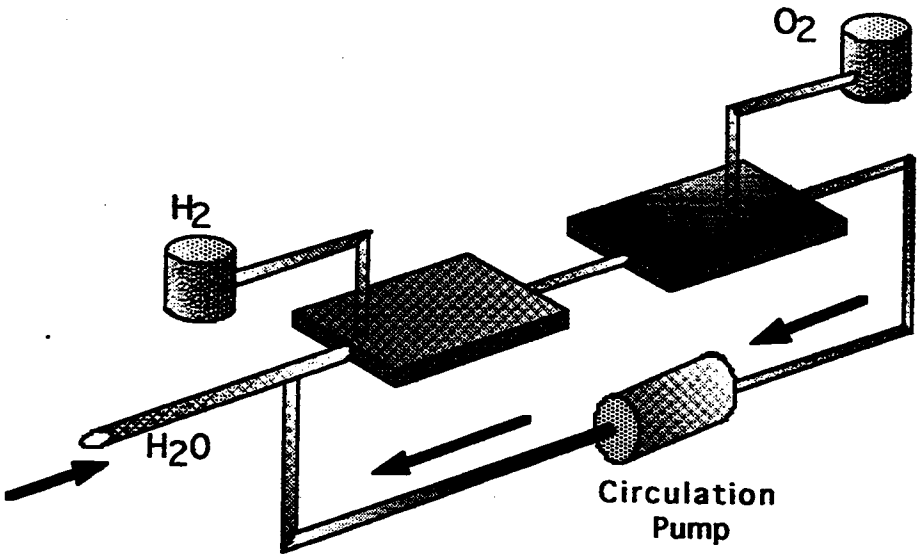

Figure 3. Schematic of the Dual Photoparticle Bed Concept for Water Splitting

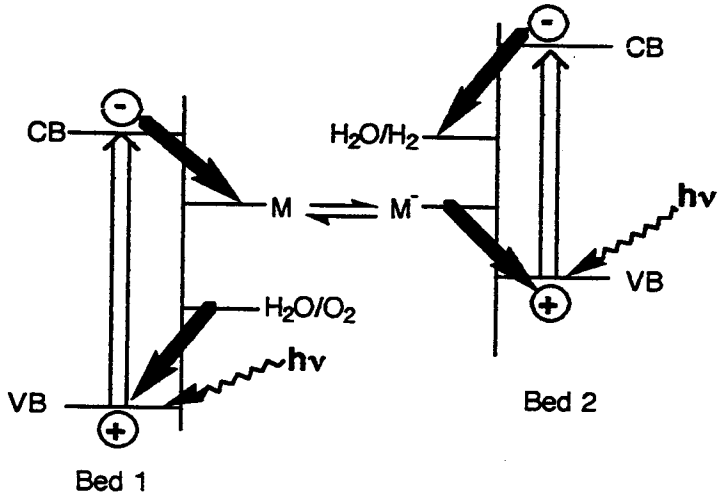

Figure 4. Energy Band Diagram for Dual Bed System

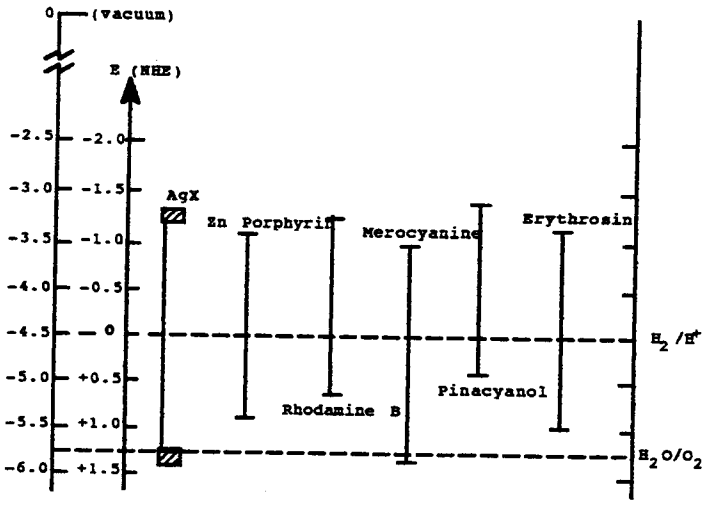

Figure 5. HOMO/LUMO Energies of Select Dyes

Total, Catalytic, Supercritical Steam Reforming of Biomass

Michael Jerry Antal, Jr. and Xiaodong Xu
Hawaii Natural Energy Institute and the Department of Mechanical Engineering
University of Hawaii at Manoa, Honolulu, HI 96822

Abstract

Wood sawdust, dry sewage sludge, or other particulate biomass can be mixed with a corn starch gel to form a viscous paste. This paste can be delivered to a supercritical flow reactor by means of a cement pump. Currently the paste mixture contains as little ass 5 wt % starch with as much as 5 wt % wood sawdust in water. Ongoing work indicates that the requirement for starch can be reduced to 3 wt %, and the particulate biomass content can be increased above 10 wt %. When rapidly heated in a flow reactor at pressures above the critical pressure of water (22 MPa), the paste vaporizes without the formation of char. A packed bed of carbon catalyst in the reactor operating at 650 °C causes the tarry vapors to react with water, producing hydrogen, carbon dioxide, and some methane with a trace of carbon monoxide. Thus we describe a practical method for the total, supercritical steam reforming of biomass to produce hydrogen at high pressure. The steam reforming process produces effectively no tar or char. Its only products are a hydrogen rich gas, and a clean water, which can be recycled.

Introduction

Current enthusiasm for the use of hydrogen as an alternative transportation fuel is founded on the expectation that hydrogen can be produced from renewable resources at a competitive price. One method of achieving this goal is the steam reforming of biomass (Antal, 1975; 1978a):

$$C_6H_{10}O_5 + 7\ H_2O \rightarrow 6\ CO_2 + 12\ H_2.$$

In this idealized, stoichiometric equation, cellulose (represented as $C_6H_{10}O_5$) reacts with water to produce hydrogen and carbon dioxide, mimicking the commercial manufacture of hydrogen from methane by catalytic steam reforming chemistry. More realistically, a practical technology must convert the cellulose, hemicellulose, lignin, and extractive components of the biomass feedstock to a gas rich in hydrogen and carbon dioxide, but also including some methane and carbon monoxide. Unfortunately, biomass does not react directly with low pressure steam to produce the desired products. Instead, significant amounts of tar and char are formed, and the gas contains higher hydrocarbons in addition to the desired light gases (Antal, 1978b, 1983, 1984, 1985a,b). The recent work of Corella and his colleagues (Herguido et al., 1992) nicely illustrates the situation. In a fluid bed operating at atmospheric pressure Corella's group observed yields of char from the steam gasification of wood sawdust in the range of 20 to 10 wt %, and yields of tar decreasing to 4 wt % as the temperature of the bed increased from 650 to 775 °C. But at the highest temperature, only 80% of the carbon in the feedstock is converted to gas. By employing a secondary, fluidized bed of calcined dolomite operating at 800 to 875 °C, Corella and his co-workers (Delgado et al., 1997) were able to convert almost all the tar to gas. Nevertheless, the char byproduct is not converted and represents an effective loss of gas. Thus the total steam reforming of biomass, as envisioned by equation (1) above, remains an elusive goal. The objective of the research described in this paper is to identify conditions which evoke the desired total steam reforming chemistry.

Apparatus and Experimental Procedures

The flow reactor used in this work (see Figure 1) is fabricated from Hastelloy C276 tubing with 9.53 mm OD x 6.22 mm ID x 1.016 m length. The reactant flow is quickly heated by an annulus heater (located along the reactor's centerline) and an entrance heater outside the reactor to temperatures above 800 °C. The annulus heater (3.18 mm OD x 15.2 cm heated length) delivers all its heat directly to the feed. The entrance heater is made from a split copper tube that is held in good thermal contact with the reactor, and an electrical heater which is coiled around the outer surface of the copper tube. Downstream of the entrance heater, the reactor's temperature is maintained in an isothermal condition by the furnace. The chief purpose of the furnace is to prevent heat loss: most of the heat required to lift the reactant flow to reaction temperature is provided by the entrance heater and the annulus heater. Carbon catalyst is usually packed in about 60% of the heated zone of the reactor, as well as the downstream cold section of the reactor. The reactor's temperature profile is monitored by 12 fixed, type K thermocouples held in good thermal contact with the reactor along its outer wall. Also, the reactant temperature is measured by a fixed, internal, annulus thermocouple which is located 5.08 cm upstream of the furnace. Pressure in the reactor is measured by an Omega PX302 pressure transducer. A Grove Mity-Mite model 91 back-pressure regulator reduces the pressure of the cold, two phase, product effluent from 28 to 0.1 MPa. After leaving the back-pressure regulator, the reaction products pass through a gas-liquid separator. The liquid product is collected over a measured time period to calculate the liquid outlet flow rate. The gas flow rate is measured using a wet test meter.

Three different types of feedstocks are used in this work: corn starch paste, poplar wood sawdust mixed in the corn starch paste, and a dry, particulate sewage sludge mixed in the corn starch

paste. Both the poplar sawdust and the sewage sludge (Water Technology International Corp.) are ground with a Wiley mill (Thomas Scientific) to 40 mesh before they are mixed with the paste. Table 1 gives elemental analyses of the feedstocks.

The feeder consists of a cylinder, a movable piston, and two end-caps (High Pressure Equipment). The cylinder is first filled with the feedstock, then the piston is placed on top of the feed, and the two end-caps are installed. Both the feeder and the reactor are pressurized separately to 28 MPa at the beginning of a run. During the time that the system is being brought up to temperature, water is pumped into the reactor by a Waters 510 HPLC pump. When the main body of the reactor reaches the desired temperature (usually 600-650 °C), the feeder is connected to the reactor. Thereafter, water flow to the reactor is terminated, and water flow to the feeder is initiated, displacing the paste feedstock into the reactor. Because the thermophysical properties of the paste are different than those of water, the temperature of the feed rises very rapidly in the entrance region of the reactor. To avoid excessively high temperatures, usually it is necessary to reduce the heat input to the feed from the annulus heater and the entrance heater.

Gas samples as taken by gas-tight syringes from the gas sample outlet of the separator. Analysis of the gas is conducted using a Hewlett-Packard model 5890 gas chromatograph equipped with flame ionization and thermal conductivity detectors. A 80/100 mesh carbosphere molecular sieve packed column is used, operating at 35 °C for 4.2 min, followed by a 15 °C/min ramp to 227 °C, another ramp of 70 °C/min to 350 °C, and a 5 min hold at 350 °C. The carrier gas is a mixture of 8% hydrogen in helium (AIRCO). A standard gas mixture obtained from AIRCO is used for day-to-day calibration. The TOC in the liquid effluent is determined by a Shimadzu model TOC-5000 total organic carbon analyzer.

Results

Activity 1: develop pumpable biomass pastes that are easily gasified.

To the best of our current knowledge, no pumps are available which can deliver wet wood sawdust (or water hyacinth, or banana tree stem particles, for example) to a reactor operating at 300 atm. Some commercially available pumps claim to be able to deliver sewage sludge to a high pressure environment (see below), but these pumps are much too large to be used with our existing equipment, and they are expensive. To make progress towards the goal of steam reforming biomass (and not model compounds, as in our earlier work), we needed to develop a new method for feeding biomass to our reactors.

After considerable thought and many discussions with colleagues, we decided to mimic the approach of the coal community to feeding pressurized, fluidized bed (PFB) combustors. As is well known, the feed to these combustors is a mixture of crushed coal, dolomite, water, and surfactant, which forms a viscous paste that is delivered to the PFB by large cement (piston in cylinder) pumps. We remark that the two PFB combustors at Vartaverket, Stockholm operate at 12 atm, and burn 60 mt/hr of coal. Following this approach, we searched for a method to make a pumpable paste from biomass. After some experimentation, we learned that a small amount of corn starch (<5 wt %),

mixed with water and heated, forms a thick paste to which 5 wt % (or more) dry sawdust can be added to make a pumpable mixture with properties similar to a coal paste. Although the analogy is not perfect, the corn starch can be viewed to play the role of the surfactant in the coal paste mixture. Actually, the corn starch hydrogen bonds with the water to make a loosely bound, macromolecular gel of starch and water. Thus the starch immobilizes the water and becomes a kind of lubricant matrix in which the fibrous sawdust particles freely move. This explains why biomass-starch pastes flow like a dream.

Of course, the first question asked about this approach is its cost. The following "back-of-the-envelope" calculation offers some insight into the economics of this approach. Non-edible "pearl" corn starch is available in bulk at $0.12 per lb from CPC International. This starch is usually used to make glues. The cost of sewage sludge disposal can be $100 per ton ($0.05 per lb). Thus a mixture of 5 lb corn starch with 10 lb sewage sludge in 85 lb of water has a value of ($0.60 - $0.50)/(15 lb) = $0.007 per pound of organic feed, which is a low cost feedstock by any standard. We remark that this mixture flows easily, but we have not yet examined our ability to gasify it. Also, we emphasize that we have not yet optimized our paste recipe. We have already identified a recipe which yields an attractive gel from only 3 wt % corn starch in water. Obviously, a reduction in the amount of corn starch required will have a big, favorable impact on the economics.

Corn starch pastes have advantages beyond those listed above. Like glycerol (a byproduct of biodiesel production), corn starch gels are easily gasified in supercritical water. Moreover, the thermochemistry of corn starch is similar to that of cellulose, so the paste behaves as though it contained only raw biomass. Of course, corn starch is free of sulfur and other heteroatoms. Finally, we remark that if it makes sense to ferment corn to make ethanol, why doesn't it make sense to gasify corn starch to make hydrogen?

In conclusion, we emphasize that our chief goal is to clarify the chemistry of hydrogen production by biomass gasification in supercritical water. Corn starch pastes enable us to feed biomass into our reactors and thereby realize our goal. Currently, we know of no other way to feed biomass into our reactors. In the future, if we discover a pump that can deliver wet wood sawdust (or other biomass) to our reactors, or if pump manufacturers develop such a pump, nothing will have been lost by our current emphasis of these pastes. They are simply a stratagem which enables us to study the chemistry that would prevail irrespective of the method by which biomass is fed to the reactor.

Activity 2: Gasification of realistic feedstocks.

Corn starch paste gasification.

Concentrated corn starch paste (10.4 wt %) was totally steam reformed over a carbon catalyst for more than 6 hours at flow rates of 1, 2, and 4 g/min. The liquid effluents at all flow rates were clear with a neutral pH and without smell. The TOC yields were negligible (< 0.6%). In agreement with these measurements, effectively all of the carbon in the feedstock was converted to gas. The gas composition from these runs is displayed in Table 2. Hydrogen, carbon dioxide, and methane were the main gas products, with trace amounts of carbon monoxide and ethane. The role of the steam reforming reaction was strongly evident: both the H efficiency and the O efficiency reached values as high as 1.6. Any value above 1.0 indicates that water is being consumed during gasification. The hydrogen mole fraction of the gas product increased as the flow rate in-

creased. No loss of catalyst activity or gasification performance was observed during the six hour period. In fact, the performance of the reactor improved significantly during the run.

Wood sawdust/corn starch paste gasification.

Mixtures of 5 wt % poplar wood sawdust in a 6 wt % corn starch paste were totally gasified at a flow rate of 2.0 g/min over a carbon catalyst. In each of the three runs, the organics were totally steam reformed to a gas composed of hydrogen, carbon dioxide, methane, and a trace of carbon monoxide. Significant amounts of water were consumed by the steam reforming chemistry. The water effluent during all three runs was clear with a neutral pH and a barely detectable odor. TOC analysis of the liquid effluent by a water quality lab indicated that about 0.2% of the organic carbon contained in the paste feed remained in the water effluent. Analysis of the activated carbon catalyst showed that its BET surface area had increased from 986 m^2/g to 1239 m^2/g. Results from the three runs are given in Tables 3-5.

Sewage sludge/corn starch paste gasification.

A mixture of 2.1 wt % (dry basis) sewage sludge (from Water Technology International Corporation, Canada) with 5.1 wt % corn starch was gasified at a flow rate of 2 g/min. The gas generation rate increased slightly from 164.3 to 189.2 mL/min during the first 2 hours of the experiment. After 2 hours of operation, the pressure in the feeder increased from 4000 to 5000 psi. To remove the restriction which was forming in the entrance region of the reactor, the feed was changed to a 1.2 M H_2O_2 in water solution, which was delivered to the reactor at 2 g/min. In less than 2 min the pressure throughout the system fell to 4000 psi. To fully clean the walls of the reactor, H_2O_2 was fed for a total of 40 min before the flow of sewage sludge paste was resumed. But during the third hour flow and pressure oscillations occurred, and the average gas generation rate was slightly lower (156.7 mL/min) than before. Throughout the experiment, the liquid effluent was clear, with a slight smell of ammonia and a pH of 7-8. The gas product contained hydrogen, carbon dioxide and methane, with a trace of carbon monoxide (see Table 6). Its composition was steady and good carbon (94-97%) and mass (96-99%) balances were obtained during the first 2 hours of operation. During the third hour, variations in the gas flow prevented a reliable determination of the carbon and mass balances. Results in Table 6 may be compared with those displayed in Tables 3-5 for the total supercritical steam reforming of wood sawdust. Apart from the feeding problems encountered with the sewage sludge, the results are similar.

Plugging

The narrow entrance region to the reactor usually plugs after 4 to 6 hours of operation. We were able to easily clear this plug by pumping a small amount of hydrogen peroxide into the reactor. The plug oxidizes immediately. A curious byproduct of the hydrogen peroxide treatment is a significant improvement in the yield of hydrogen, accompanied by a drop in methane formation. Evidently the oxidation activates the walls of the high nickel alloy towards steam reforming. We plan to study this phenomena in greater detail in the near future.

Activity 3: Identify a suitable, high pressure pump.

We are in the midst of a wide-ranging search for commercially available pumps that could meet our needs. Dr. Akira Suzuki with Organo Corporation, Japan advised us that pumps manufactured by Feluwa/Schlesiger & Co., and Niigata Worthington Co. should be able to deliver sewage sludge to a supercritical flow reactor. Mr. Dieter Uber of Dartmouth College has joined us for six weeks, and is currently evaluating these pumps, as well as searching for others.

Activity 4: Assist Air Products Corp. and NREL with an economic evaluation.

We have created a mailing list and are thereby providing our monthly reports to Air Products Corp., General Atomics, NREL, and others.

Conclusions

1. A semi-solid gel can be made from 5 wt % (or less) corn starch in water. Wood sawdust and other particulate biomass can be mixed into this gel and suspended therein, forming a thick paste. This paste is easily delivered to a supercritical flow reactor by a cement pump. Work is ongoing to minimize the amount of starch required, and to maximize the amount of biomass that can be mixed into the paste.
2. Above the critical pressure of water, wood sawdust can be steam reformed over a carbon catalyst to a gas composed entirely of hydrogen, carbon dioxide, methane, and a trace of carbon monoxide. There are effectively no tar or char byproducts. The liquid water effluent from the reactor has a low TOC value, a neutral pH, and no color. This water can be recycled to the reactor.
3. Early results indicate that sewage sludge behaves similarly to wood sawdust, but is more prone to deposit small amounts of carbon in the entry region of the reactor, which can eventually block the flow of feedstock to the reactor.
4. Trace amounts of carbon deposited in the entrance region of the reactor are easily and quickly removed by the delivery of water with some dissolved oxygen (or hydrogen peroxide) to the reactor. Some evidence suggests that this cleaning procedure may improve the performance of the gasifier.

Acknowledgments

This work was supported by NREL/DOE under cooperative agreement DE-FG36-94AL85804, and the Coral Industries Endowment of the University of Hawaii at Manoa. We thank Neil Rosmeissl (DOE), Dr. Ralph Overend (NREL), Dr. Patrick Takahashi and Dr. Richard Rocheleau (UH) for their interest in this work. We also thank Jose Arteiro (UH) for assistance with the experiments, Professor Angela Garcia (University of Alicante, Spain), and Professor Galen J. Suppes (University of Kansas) for useful advice.

References

Antal, M.J. In Hydrogen Energy, Part A; Veziroglu, T.N., Ed.; Plenum: New York, 1975.

Antal, M.J. In Toward a Solar Civilization; Williams, R.H., Ed.; MIT Press: Cambridge, MA, 1978a.

Antal, M.J. In Energy from Biomass and Wastes; Klass, D.L., Ed.; I.G.T.: Chicago, 1978b.

Antal, M.J. Effects of Reactor Severity on the Gas-Phase Pyrolysis of Cellulose- and Kraft Lignin-Derived Volatile Matter. *Ind. Eng. Chem. Prod. Res. Dev.* **1983**, 22, 366-375.

Antal, M.J. In Advances in Solar Energy; Boer, K.W., Duffie, J.A. Eds.; Plenum Press: New York, 1984.

Antal, M.J. In Fundamentals of Thermochemical Biomass Conversion; Overend, R.P., Milne, T.A., Mudge, L.K., Ed.; Elsevier: London, 1985a.

Antal, M.J. In Advances in Solar Energy; Boer, K.W., Duffie, J.A. Eds.; Plenum Press: New York, 1985b.

Delgado, J.; Aznar, M.P.; Corella, J. Biomass Gasification with Steam in Fluidized Bed: Effectiveness of CaO, MgO, and CaO-MgO for Hot Raw Gas Cleaning. *Ind. Eng. Chem. Res.* **1997**, 36, 1535-1543.

Herguido, J.; Corella, J.; Gonzalez-Saiz, J. Steam Gasification of Lignocellulosic Residues in a Fluidized Bed at a Small Pilot Scale. Effect of the Type of Feedstock. *Ind. Eng. Chem. Res.* **1992**, 31, 1274-1282.

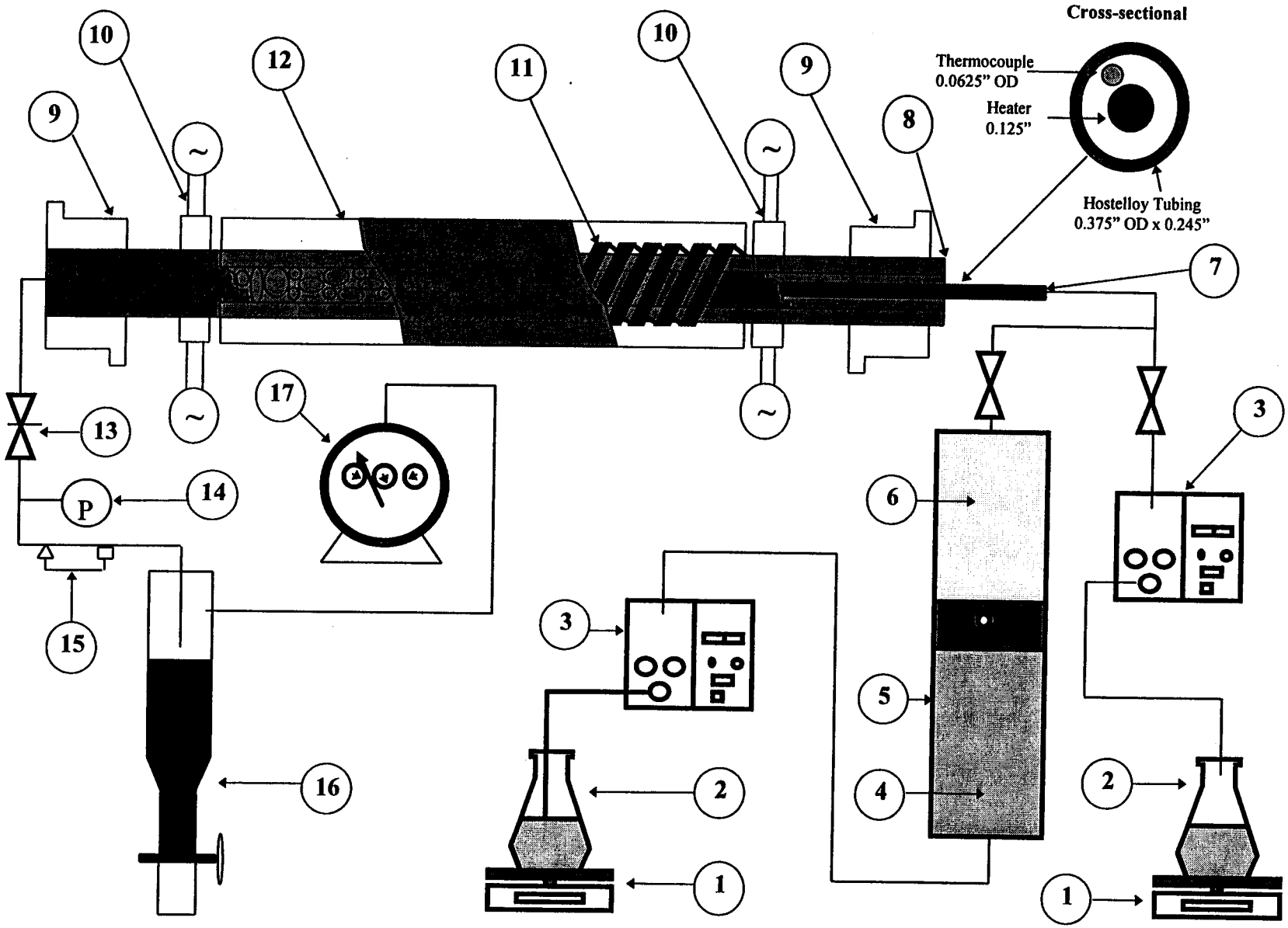

Figure 1: Supercritical flow reactor schematic: (1) balance; (2) flask; (3) HPLC pump; (4) water; (5) feeder; (6) biomass paste; (7) annulus heater; (8) Hastelloy C-276 tube; (9) cooling jacket; (10) heater; (11) furnace; (12) furnace shell; (13) valve; (14) pressure transducer; (15) back-pressure regulator; (16) liquid-gas separator; (17) wet test meter.

Table 1. Feedstocks Analysis

	Corn Starch[1]	Poplar Wood Sawdust[2]	Sewage Sludge[3]
Elemental Analysis - wt% (Dry Basis)			
C	41.1	49.4	39.8
H	6.5	6.0	6.5
O	52.4	45.1	26.8
N	N/A	0.06	5.92
S	N/A	N/A	0.64
Ash - wt%	N/A	0.16	N/A
Moisture Content - wt%	12.82	8.45	6.0

1. The data of C, H, and O were obtained from Merck Index (5th edition, 1983), the moisture content was measured.
2. The elemental analysis was conducted by Huffman Laboratories, Inc.
3. The elemental analysis data was provided by Water Technology International Corp.

Table 2. Gas Composition from Corn Starch (10.4 wt% Dry Basis) Gasification in Supercritical Water at 650°C, 28 MPa with Coconut Shell Activated Carbon Catalyst (Exp. Date: 2/20/97)

Flow Rate (g/min)	1.0			2.0			4.0			
Time on Stream (hr)	1.33	1.62	2.18	3.52	4.02	4.57	5.12	5.47	5.70	6.03
Product	Mole Fraction									
H_2	0.42	0.38	0.38	0.40	0.40	0.35	0.45	0.45	0.45	0.44
CO	0.015	0.013	0.011	0.012	0.012	0.011	0.019	0.016	0.016	0.015
CO_2	0.43	0.45	0.39	0.42	0.43	0.39	0.33	0.34	0.35	0.36
CH_4	0.19	0.21	0.22	0.19	0.19	0.18	0.13	0.13	0.14	0.14
C_2H_6	0.002	0.003	0.004	0.015	0.014	0.012	0.001	0.0	0.0	0.0
C Efficiency	1.0	1.0	0.97	1.02	1.04	1.01	1.0	1.03	1.05	1.10
H Efficiency	1.30	1.23	1.33	1.32	1.33	1.28	1.53	1.56	1.56	1.61
O Efficiency	1.41	1.40	1.25	1.40	1.45	1.38	1.48	1.53	1.54	1.62
H Balance	1.04	1.03	1.04	1.03	1.03	1.03	1.03	1.03	1.03	1.03
O Balance	1.04	1.04	1.03	1.03	1.04	1.04	1.02	1.03	1.03	1.03
Global Mass Balance	1.01	1.01	1.01	1.01	1.01	1.01	0.99	1.0	1.0	1.0
TOC Yield	0.5%	0.5%	0.5%	0.3%	0.3%	0.3%	0.4%	0.4%	0.4%	0.4%

Note:

$$\text{C (H, O) efficiency} = \frac{\text{g of C (H, O) in the gas}}{\text{g of C (H, O) from corn starch in the feed}}$$

$$\text{H (O) balance} = \frac{\text{g of H (O) in the gas + g of H (O) in the liquid effluent}}{\text{g of H (O) from (corn starch + water) in the feed}}$$

$$\text{Global mass balance} = \frac{\text{g of the gas + g of the liquid effluent}}{\text{g of the feed}}$$

$$\text{TOC yield} = \frac{\text{g of TOC in the liquid effluent}}{\text{g of the feed}}$$

Table 3. Gas Composition from Poplar Wood Sawdust (5.0 wt% Dry Basis) / Corn Starch (5.5 wt% Dry Basis) Gasification in Supercritical Water at 650°C, 28 MPa with Coconut Shell Activated Carbon Catalyst (Exp. Date: 3/25/97)

Flow Rate (g/min)	2.0					2.5
Time on Stream (hr)	1.0	1.42	1.83	2.27	2.70	3.32
Product	Mole Fraction					
H_2	0.36	0.34	0.35	0.33	0.33	0.35
CO	0.027	0.027	0.027	0.026	0.027	0.029
CO_2	0.45	0.45	0.46	0.45	0.45	0.44
CH_4	0.22	0.22	0.24	0.23	0.23	0.24
C_2H_6	0.002	0.002	0.002	0.002	0.002	0.002
C Efficiency	0.96	1.0	1.0	0.98	0.95	0.91
H Efficiency	1.31	1.35	1.37	1.30	1.27	1.28
O Efficiency	1.58	1.63	1.60	1.58	1.52	1.43
H Balance	1.04	1.04	1.04	1.04	1.04	N/A
O Balance	1.05	1.05	1.05	1.05	1.05	N/A
Global Mass Balance	1.02	1.03	1.03	1.02	1.02	N/A
TOC Yield	0.2%	0.2%	0.2%	0.3%	0.3%	N/A

Note:

$$\text{C (H, O) efficiency} = \frac{\text{g of C (H, O) in the gas}}{\text{g of C (H, O) from (poplar sawdust + corn starch) in the feed}}$$

$$\text{H (O) balance} = \frac{\text{g of H (O) in the gas + g of H (O) in the liquid effluent}}{\text{g of H (O) from (poplar sawdust + corn starch + water) in the feed}}$$

$$\text{Global mass balance} = \frac{\text{g of the gas + g of the liquid effluent}}{\text{g of the feed}}$$

$$\text{TOC yield} = \frac{\text{g of TOC in the liquid effluent}}{\text{g of the feed}}$$

Table 4. Gas Composition from Poplar Wood Sawdust (5.0 wt% Dry Basis) / Corn starch (5.55 wt% Dry Basis) Gasification in Supercritical Water at 650°C, 28 MPa with Coconut Shell Activated Carbon Catalyst (exp. date: 4/23/97)

Flow Rate (g/min)	2.0							
Time on Stream (hr)	0.45	0.95	1.5	2.0	2.5	3.0	3.55	3.95
Product	Mole Fraction							
H_2	0.55	0.49	0.51	0.49	0.50	0.49	0.48	0.49
CO	0.04	0.04	0.04	0.04	0.04	0.04	0.04	0.04
CO_2	0.33	0.40	0.42	0.40	0.42	0.40	0.40	0.38
CH_4	0.09	0.10	0.09	0.09	0.10	0.10	0.10	0.09
C_2H_6	0.001	0.001	0.001	0.0	0.0	0.0	0.0	0.0
C Efficiency	1.06	1.27	1.20	1.19	1.24	1.17	1.11	1.08
H Efficiency	1.99	1.97	1.80	1.78	1.88	1.79	1.68	1.71
O Efficiency	1.97	2.41	2.36	2.32	2.39	2.22	2.14	2.10
H Balance	1.05	1.04	1.03	1.0	1.01	0.97	0.96	0.96
O Balance	1.04	1.07	1.06	1.04	1.04	0.99	0.99	0.98
Global Mass Balance	1.02	1.05	1.04	1.02	1.02	0.97	0.96	0.96
TOC Yield	0.3%	0.3%	0.3%	0.2%	0.2%	0.2%	0.2%	0.2%

Note:

$$\text{C (H, O) efficiency} = \frac{\text{g of C (H, O) in the gas}}{\text{g of C (H, O) from (poplar sawdust + corn starch) in the feed}}$$

$$\text{H (O) balance} = \frac{\text{g of H (O) in the gas + g of H (O) in the liquid effluent}}{\text{g of H (O) from (poplar sawdust + corn starch + water) in the feed}}$$

$$\text{Global mass balance} = \frac{\text{g of the gas + g of the liquid effluent}}{\text{g of the feed}}$$

$$\text{TOC yield} = \frac{\text{g of TOC in the liquid effluent}}{\text{g of the feed}}$$

Table 5. Gas Composition from Poplar Wood Sawdust (5.05 wt% Dry Basis) / Corn starch (6.09 wt% Dry Basis) Gasification in Supercritical Water at 650 °C, 28 MPa with Coconut Shell Activated Carbon Catalyst (exp. date: 5/1/97)

Flow Rate (g/min)	2.0			
Time on Stream (hr)	0.55	1.28	1.95	3.03
Product	Mole Fraction			
H_2	0.45	0.42	0.42	0.42
CO	0.031	0.027	0.026	0.027
CO_2	0.35	0.39	0.37	0.38
CH_4	0.12	0.13	0.16	0.15
C_2H_6	0.002	0.001	0.002	0.001
C Efficiency	0.94	0.97	0.97	0.92
H Efficiency	1.54	1.44	1.53	1.41
O Efficiency	1.66	1.73	1.63	1.59
H Balance	1.01	1.0	1.01	1.0
O Balance	1.02	1.02	1.02	1.01
Global Mass Balance	0.99	0.99	0.99	0.98
TOC Yield	N/A	N/A	N/A	N/A

Note:

$$\text{C (H, O) Efficiency} = \frac{\text{g of C (H, O) in the gas}}{\text{g of C (H, O) from (poplar sawdust + corn starch) in the feed}}$$

$$\text{H (O) balance} = \frac{\text{g of H (O) in the gas + g of H (O) in the liquid effluent}}{\text{g of H (O) from (poplar sawdust + corn starch + water) in the feed}}$$

$$\text{Global mass balance} = \frac{\text{g of the gas + g of the liquid effluent}}{\text{g of the feed}}$$

$$\text{TOC yield} = \frac{\text{g of TOC in the liquid effluent}}{\text{g of the feed}}$$

Table 6. Gas Composition from sewage sludge (2.1 wt% Dry Basis) / Corn starch (5.1 wt% Dry Basis) Gasification in Supercritical Water at 650 °C, 28 MPa with Coconut Shell Activated Carbon Catalyst (exp. date: 5/15/97)

Flow Rate (g/min)	2.0		
Time on Stream (hr)	1.23	1.77	1.88
Product	Mole Fraction		
H_2	0.43	0.46	0.46
CO	0.005	0.005	0.006
CO_2	0.43	0.41	0.40
CH_4	0.17	0.19	0.19
C Efficiency	0.97	0.96	0.94
H Efficiency	1.29	1.39	1.37
O Efficiency	1.66	1.58	1.53
H Balance	1.01	1.02	1.02
O Balance	1.02	1.02	1.02
Global Mass Balance	0.99	0.99	0.98
TOC Yield	N/A	N/A	N/A

Note:

$$\text{C (H, O) efficiency} = \frac{\text{g of C (H, O) in the gas}}{\text{g of C (H, O) from (sewage sludge + corn starch) in the feed}}$$

$$\text{H (O) balance} = \frac{\text{g of H (O) in the gas + g of H (O) in the liquid effluent}}{\text{g of H (O) from (sewage sludge + corn starch + water) in the feed}}$$

$$\text{Global mass balance} = \frac{\text{g of the gas + g of the liquid effluent}}{\text{g of the feed}}$$

$$\text{TOC yield} = \frac{\text{g of TOC in the liquid effluent}}{\text{g of the feed}}$$

Plasma Reforming of Methane

L. Bromberg*, D.R. Cohn, A. Rabinovich
MIT Plasma Science and Fusion Center

C. O'Brien and S. Hochgreb
MIT Department of Mechanical Engineering

June 25, 1997

ABSTRACT

Thermal plasma technology can be used in the production of hydrogen and hydrogen-rich gases from a variety of fuels. This paper describes experiments and calculations of high temperature conversion of methane using homogeneous and heterogeneous processes. The thermal plasma is a highly energetic state of matter that is characterized by extremely high temperatures (several thousand degrees Celsius) and large amounts of ionization. The high temperatures accelerate the reactions involved in the reforming process.. Plasma reformers can be operated with a broad range of fuels; are very compact and are very light (due to high power density); have fast response time (fraction of a second); can be manufactured with minimal cost (they use simple metallic or carbon electrodes and simple power supplies); and have high conversion efficiencies. Hydrogen-rich gas (50-75% H_2; 25-50% CO) can be efficiently made in compact plasma reformers. Experiments have been carried out in a small device (2-3 kW) and without the use of efficient heat regeneration. For partial oxidation it was determined that the specific energy consumption in the plasma reforming processes is 40 MJ/kg H_2 (without the energy consumption reduction that can

be obtained from heat regeneration from an efficient heat exchanger). Larger plasmatron, better reactor thermal insulation, efficient heat regeneration and improved plasma catalysis could also play a major role in specific energy consumption reduction.. With an appropriate heat exchanger to provide a high degree of heat regeneration, the projected specific energy consumption is expected to be ~15-20 MJ/kg H_2. In addition, a system has been demonstrated for hydrogen production with low CO content (~2%) with power densities of ~10 kW (H_2 HHV)/liter of reactor, or ~4 liter/hr H_2 per liter of reactor. Power density should increase further with power and improved design.

Address for correspondence: L. Bromberg
MIT Plasma Science and Fusion Center
77 Massachusetts Ave
Cambridge, MA 02139
BROM@PFC.MIT.EDU
617-253-6919; FAX: 617-253-0700
Work performed under US DoE Contract DE-FG04-95AL88002

This paper will appear in a special hydrogen edition of Energy & Fuels.

HYDROGEN PRODUCTION FROM WASTES†

P.H. WALLMAN* and C.B. THORSNESS

Lawrence Livermore National Laboratory L-369
Livermore, California 94550
*Fax 1-510-423-4289
Email: hwallman@llnl.gov

J.D. WINTER

Montebello Technology Center, Texaco Inc.
South El Monte, California 91733

Abstract--A process for the conversion of municipal solid waste, automobile shredder residue and other plastic/rubber wastes to hydrogen is described both from a technical and an economic point of view. Pilot-plant and modeling results are tools in the analysis. The conversion is carried out in two major process steps. The first step or "pre-treatment" step is based on pyrolysis and results in an intermediate product, containing approximately 90% of the primary feed, in a suitable physical form for the second step. This second step is Texaco's high-temperature, high-pressure gasifier which is based on partial oxidation and converts the organic components to synthesis gas (CO and H_2).Total thermal conversion efficiency for waste to hydrogen is found to be a strong function of feedstock quality. For typical MSW feedstocks, an efficiency of 40-50% is predicted for an integrated process. Fossil-fuel feedstocks such as waste plastics and scrap tires result in efficiencies of the order 60-70%. The cost of produced hydrogen is approximately $15/GJ for typical MSW with a tipping fee of $50/ton, but drops to $6/ton for high-plastics waste that carry a tipping fee of $100/ton.

INTRODUCTION

Development of the technology necessary for conversion of waste feedstocks to hydrogen has the potential to address a number of economic, environmental, societal and resource issues. A path for the conversion of waste to hydrogen has the potential to be economically advantageous because management and disposal of waste is expensive, and the fees otherwise required for disposal become a credit against the cost of the produced hydrogen. Conversion of waste to hydrogen has the environmental advantage of decreasing the number of future landfills needed with a concomitant decrease in the associated water pollution issues.

†This work was performed under the auspices of the U. S. Department of Energy by Lawrence Livermore National Laboratory under contract No. W-7405-Eng-48.

Municipal Solid Waste (MSW) is a large, growing, and little-used energy resource. Approximately 210 million tons of MSW are produced annually in the United States, and the vast majority of this (70%)[1] eventually winds up in landfills. The main component of MSW is cellulose making MSW a predominantly renewable energy source. However, the plastic component of MSW, currently at 9.5 wt% as a national average, has seen its share increase over time. The plastic component of MSW is very important for two reasons: (1) its higher heating value is roughly double (40 MJ/kg) that of cellulose (20 MJ/kg) making it a high-energy material in the MSW context, and (2) plastics do not compost in contrast to the cellulose component of MSW (Composting is a treatment that can reduce the volume of MSW before landfill disposal).

Other waste feedstocks of considerable importance are automobile shredder residue (ASR) and scrap tires. The former is the residue after recyclable materials have been removed from scrapped automobiles and amounts to 3 million tons annually in the United States[2] most of which ends up in landfills. ASR is roughly half plastics and half inorganics giving it a heating value of approximately 20 MJ/kg. ASR amounts are predicted to increase with time because of automobile manufacturers increasing use of plastic components. Scrap tires amount to approximately 3.5 million tons annually in the United States[3] with a higher heating value of about 30 MJ/kg.

Our objective in this study has been to investigate a realistic process for conversion of these waste materials to hydrogen and environmentally acceptable by-products. Such a process is presented in this paper. Its conversion efficiency (higher heating value of hydrogen product/higher heating value of feedstock) is of the order 50% but dependent on feedstock heating value; higher-heating value feedstocks lead in general to higher efficiencies. Since MSW, ASR and scrap tires form a total U.S. energy resource of about 100 GW_t (t for thermal energy) a potential source of 50 GW_t of hydrogen exists in materials that carry negative value (so-called "tipping fees"). This amount of hydrogen would, for example, be sufficient to fuel 100 million fuel-cell vehicles with an assumed equivalent fuel efficiency of 80 miles/gallon and an assumed daily use of 25 miles.

PROCESS

The conversion process is based on Texaco's proven gasifier technology including associated gas cleanup and hydrogen separation processes. The primary technical challenge is the pre-treatment of the waste feedstock into a form suitable to use as feed to a Texaco gasifier. The Texaco gasifier has several advantages: 1) Oxygen is used as the oxidant, resulting in no dilution and no formation of NO_x; 2) hazardous metals contained in the feedstock are sequestered by the non-leachable slag; 3) the high temperature of the gasifier also insures the complete destruction of hazardous organics; 4) the process is commercially proven technology for hydrogen production.

Fig. 1 shows schematically the process on a relatively small (but still commercial) scale of 100 ton/day of waste feedstock. The pyrolyzer/sand heater are the central processing units of the pre-treatment section which has been the focus of the process development work. The balance of the process starting with the high-temperature gasifier is commercially available technology. As shown in Fig.1, the main characteristic of the pre-treatment is the separation between pyrolysis and combustion by recycling hot sand to the pyrolyzer for direct contact with waste feedstock. This results in pyrolysis of the feedstock without diluting the product gas with combustion products, and without volatilizing hazardous ash components. Combustion is required in the process to meet heating demand and is carried out in a separate vessel, and is thus decoupled from the actual conversion of the feedstock.

A modest amount of the waste fuel feed (~10%) is used for satisfying the pyrolyzer heating demand resulting in a modest amount of flue gas. This flue gas is one of the by-products of the process together with non-leachable slag, sulfur, ammonia and undiluted CO_2. Most of the CO_2 by-product (~90% of feed carbon) is in a pure state allowing easy transport from the plant for use or disposal. Except for NH_3, the amount of ash, S, and HCl are stoichiometrically equal to the feedstock contents of the corresponding constituents. In the case of NH_3, most of the feed nitrogen is converted to N_2 with a relatively minor portion going to NH_3.

The distribution of metal-containing inorganic contaminants of the feedstock between the slag and the gas scrubber liquid has not yet been determined in pilot-plant studies. Oxides of non-volatile metals such as Fe, Cu, Ni, and Cr are expected to be heavily concentrated in the slag. Volatile metals such as Pb, Hg and Zn on the other hand, are expected to be captured in the gas scrubbing step and be transferred to the scrubber solution. The metals are subsequently precipitated out from the scrubber solution as part of the water treatment section which is a necessary process step.

The specifics of the developed waste pre-treatment process are shown in Fig.2. Feed enters the pyrolysis side of the process together with hot recycle sand. Gas and solid products leave the pyrolyzer separately. The solid product containing the cooled-down sand is fed to a classification step where large feed-derived char and ash are separated from the fine-grain sand. Some fine-grain char remains with the sand that continues to the combustor section. The combustor section is a lift-pipe furnace that contacts the char-containing sand with air, or possibly a mixture of steam and oxygen because the gasification section uses oxygen (Use of oxygen results in a much smaller flue gas volume). An additional fuel for the lift-pipe combustor is the non-condensible gas from the pyrolysis section. Feed-derived ash is separated from sand before the sand is recycled to the pyrolyzer as heat transfer medium. The flue gas is sent to a scrubbing unit whose scrubber solution side is connected to the main scrubber circuit operating in the gasifier section of the plant.

Typical operating temperatures for the pyrolyzer and combustor outlet are 500°C and 850°C with a sand recycle rate about double the rate of waste feed. The combustor outlet temperature is determined by the fuel rate to the combustor which is a combination of fuel gas from the pyrolyzer and pyrolysis residue or "char" contained in the sand. Pyrolyzer temperature is set by the sand recycle rate and kept around 500°C for the purpose of minimizing fuel gas yield (This gas has a heating value of only 15 MJ/kg because of high CO_2 content). Fig.3 shows the relationship between pyrolyzer temperature, combustor temperature and recycle ratio.

The 1 ton/day pre-treatment pilot plant in operation at the Lawrence Livermore National Laboratory uses a simple moving bed pyrolyzer of 20 cm diameter. Consequently, the pilot-plant feed particle size is limited to a maximum of about 2 cm. Scaleup of the process will require a significant increase in the maximum particle size. This will be accomplished by using a rotating drum pyrolyzer on a commercial scale. The rotating drum provides mechanical mixing between feed material and recycle sand as well as size reduction of the feedstock because of the grinding action of the solids flow. This type of pyrolyzer will be used on the next pilot scale which is approximately 10 tons/day.

Typical yields from the 1 ton/day pilot plant operation are shown in Table 1. The char yields given in this table have been corrected because the heat loss in this small plant are atypically large (Char amounting to 9 wt% of feed was in fact burned but one third of this was expended to satisfy heat losses that are not present in larger plants). From a process point of view, the gas product which in terms of Btu content can satisfy the heat

requirement is the preferable combustor fuel. The 1 ton/day pilot plant does not have this process option but the next scale will include this significant process improvement.

The 1 ton/day pilot plant facility includes an off-line grinding facility which corresponds to a wet ball mill facility for a full-scale plant. In the grinding step the char and liquid components are combined to form a slurry for feed to the high-temperature gasifier. The wood-derived char and liquid products produced a slurry of 17 MJ/kg heating value and an acceptable particle size distribution with a relatively modest expenditure of energy (of the order 10 kWh_e/ton dry material).

Since only a small percentage of the primary feedstock is consumed in the pre-treatment process the resulting slurry will have the same heating value as the feedstock.The product yields of liquid, solid and gas from pyrolyzed plastics are quite similar to those of cellulose[4]. However, the liquid product composition is very different for the two feed types: Cellulose produces a liquid that contains about 50% water whereas plastics produce a liquid of organic compounds. Hence, plastic components in the feedstock will greatly increase the heating value of the slurry.

GASIFICATION PROCESS MODEL

Using the ASPEN PLUS simulator, a process model encompassing both pre-treatment and gasification has been developed. This model provides a means of evaluating the overall process with respect to major inputs and outputs and changes in operating strategies.

The gasifier model is based on chemical equilibrium calculations. Instead of attempting to model every reaction that actually occurs during gasification (which could be 50 or more), requiring detailed information on the kinetics of the reactions, reactor geometry and other parameters, the gasification process is modeled as a set of five reactions which approach equilibrium at the reactor temperature; thus, the gasifier output depends chiefly on those variables which affect chemical equilibrium: material inputs, temperature, and pressure. This is an approach that has been used in other models with acceptable results[5].

The gasifier model has been implemented in ASPEN Plus using two separate unit operation modules, though the physical gasifier is a single unit which also contains a quench reservoir at its bottom (not discussed here, and modeled as a separate section of the process). The first of the two ASPEN modules transforms the "non-conventional" MSW (lacking consistent chemical structure) into a stream of conventional components which can be manipulated by ASPEN Plus in traditional chemical process calculations in order to simulate the reactions within the gasifier. The second module accomplishes this latter task by modeling the gasification process as five chemical reactions which approach equilibrium at the gasifier temperature.

The following are the considered reactions:

1) $2\,H_2 + O_2 \leftrightarrow 2\,H_2O$

2) $CO + H_2O \leftrightarrow H_2 + CO_2$ (Water -gas shift reaction)

3) $CH_4 + H_2O \leftrightarrow 3\,H_2 + CO$ (Steam reforming reaction)

4) $COS + H_2 \leftrightarrow 4\,H_2S + CO$

5) $Cl_2 + H_2 <---> 2\,HCl$

It is assumed that the small amount of nitrogen leaves the reactor as N_2, although in reality some NH_3 is formed.

Table 2 shows the results of a comparison between model and experiment using Illinos#6 coal as feed. The result is that the Texaco gasifier is modeled with acceptable accuracy using a single fitted temperature approach to chemical equilibrium for the water-gas shift reaction. This fitted temperature is 1179°C, or an approach of -137°C, for the case in Table 2.

Using the gasifier model with MSW feed some important differences relative to coal are observed. Since the MSW-based slurry even with pre-treatment contains more water than a coal slurry, more heat is needed to bring the slurry up to gasifier temperature. Hence more fuel must undergo oxidation to CO_2 in order to produce the necessary heat, and the products have a CO/CO_2 ratio lower than that of the coal case. The end result is an overall efficiency, defined as energy content of the hydrogen product over the energy content of the feed that is poorer for MSW than for coal.

Fig.4 shows two performance metrics for the process (efficiency and oxygen consumption) as a function of feedstock energy content. The curves were calculated using the full ASPEN Plus model and a series of MSW and plastic mixtures. MSW by itself is characterized by the a feed of 12MJ/kg higher heating value. Typical raw MSW contains 25% water and 18% "ash" but the shredding and metals removal step is assumed to remove half of the ash. The remainder, at 25% moisture and 9% ash content, is assumed to be the feed to the pyrolyzer pre-treater. Fig.4 shows that the overall process efficiency is no more than 44% for the MSW feed. With a plastic enriched feed stream, the efficiency rises significantly. Hence, waste plastics (or scrap tires) are desirable feedstocks for the hydrogen production process. This result shows quantitatively how difficult it is for renewable feedstocks to displace fossil feedstocks. The underlying cause is the high content of both water and fuel-bound oxygen that must be heated to gasification temperature leading to high CO_2 yields from the gasifier. The gasifier oxygen consumption is also plotted in Fig.4 showing explicitly the high consumption of O_2 for the lean feedstocks.

Fig.4 also includes efficiency calculations for the hypothetical case of a gasifier without pre-treatment (hypothetical because the physical form of the feedstocks prevents their introduction to the injector nozzles of the high-pressure gasifier). It is important to note that the efficiency penalty for the pre-treatment section can be as low as 5-6 percentage points. However, this assumes highly efficient air pre-heating against the hot flue gases. In reality a large-surface air pre-heater may be uneconomical and a somewhat higher efficiency penalty may be optimal (such as the 10% penalty quoted in the process section).

PROCESS ECONOMICS

The economic evaluation of the process from a commercial perspective is one of the main objectives of this research. It will continue as the pre-treatment process is scaled up and integrated with gasification on the next scale. At present, a preliminary cost analysis has been performed with results that provide an economic comparison between the process and competing alternative processes.

Estimated costs of the pre-treatment section that processes raw MSW into a pumpable slurry, depending of assumptions, currently range from $35-50 per ton of MSW processed. About half the cost is related to capital equipment with a total cost of $100M for a large commercial scale (2500 ton/day). The assumed pyrolyzer is a directly-heated rotary drum. The final cost of the slurry is a function of the processing costs and the tipping fee obtained for disposal of the MSW. The average tipping fee for MSW in the United States is $57 but it has a broad range from $10/ton to $195/ton in some metropolitan areas[6].

To translate the cost of the slurry into a final hydrogen cost, a simple cost formula was developed based primarily on the work of Larson and Katofsky[7]. They estimate costs for production of hydrogen by gasification of biomass and present results in simple formulas which include a linear dependence on feedstock costs. Their approach is extended here in several ways. First, a factor explicitly accounting for the cost of oxygen in the gasification process is included. The motivation for this is the fact that gasification of MSW-derived slurry is below the optimal slurry heating value for the gasification process and hence requires more oxygen. Non-optimal slurry properties also lead to greater gas throughputs per unit of hydrogen production. Throughput effects are approximated by scaling the fixed part of the cost with a measure of gasification efficiency. In addition, the amount of hydrogen produced per unit of feed to the gasifier is made a function of the quality of the feed, as measured by its heating value. Finally, the cost of the feedstock is broken down into two components, the cost of MSW-derived slurry and the cost of a cofeed. The resulting formula for the hydrogen cost is obtained as

$$(1) \qquad P = 7.63\left(\frac{2.31}{\gamma}\right)^{0.6} + \frac{4}{\gamma} + \alpha[\eta S + (1-\eta)F]$$

where P is the hydrogen cost ($/GJ-$H_2$), S is the cost of the MSW slurry after pre-treatment ($/ton), F is the cost of cofeed ($/ton), and η is the fraction MSW slurry in the combined feed. α is the feed consumption parameter (ton/GJ-H_2) and γ is the oxygen utilization efficiency (mol-H_2/mol-O_2). The last two parameters are functions of the efficiency of the gasification process which in turn is a function of the overall effective heating value of the gasifier feed.

Using the efficiency and oxygen demand relationships of Fig. 4, Fig. 5 is obtained from relationship (1) with an assumed tipping fee of $50/ton. For MSW alone, at 12 MJ/kg, the cost of hydrogen is estimated to be $15 per GJ of H_2 (based on a heating value of 142 MJ/kg of H_2). This result means that hydrogen production costs from MSW via the proposed process are similar to those for coal derived hydrogen[8]. For slurries with higher heating values, obtained either by adding a cofeed such as waste motor oil, or using a plastics-enriched MSW, lower costs are possible. With plastics amounting to half of the plant's feedstock and a tipping fee of $100/(ton of combined feedstock) the H_2 production cost drops to $6/GJ of H_2 which is competitive with the cost of hydrogen produced from natural gas also estimated at $6/GJ.

CONCLUSIONS

Conversion of municipal solid waste and other waste feedstocks to hydrogen is carried out in two major process steps. The first step or "pre-treatment" step is based on pyrolysis and results in a combined liquid/solid product containing approximately 90% of the raw feed but in the form of a pumpable slurry. The second or high-temperature, high-pressure

gasifier step is based on partial oxidation and converts the organic components of the slurry to synthesis gas (CO and H_2). This processing step is a commercial process and so are the subsequent steps of the process. The final product is hydrogen that is separated from a mixture of H_2 and CO_2 (The CO_2 is a pure by-product). Total conversion efficiency (heating value of hydrogen product/heating value of feedstock) is a strong function of feedstock quality; the higher the feedstock heating value the higher the efficiency. For typical MSW feedstock an efficiency of 44% is predicted for an integrated process. Fossil-fuel feedstocks such as waste plastics and scrap tires result in efficiencies of the order 60-70%. Confirmation of these efficiency results for an integrated commercial-scale process with the different feedstocks is a major objective in future scaleup work.

The cost of produced hydrogen is also a strong function of feedstock quality. Among waste feedstocks MSW proved to be the most difficult both from a technical and economic point of view. At a tipping fee (negative cost) of $50/ton which is close to the U.S. average, the cost of MSW-derived hydrogen proved similar to coal-based hydrogen costs, or approximately 15/GJ. In today's energy markets hydrogen from natural gas is about a factor of two-and-half less expensive. To compete with natural gas-derived hydrogen at $6/GJ, the developed process must be fed with a waste stream of a minimum heating value around 25 MJ/kg which implies a large fossil-fuel component such as waste motor oil, waste plastic or scrap tires. In addition, this high-energy content feedstock must also carry a tipping fee of the order $100/ton for the product hydrogen cost to be $6/GJ.

REFERENCES

1. AIChE *Garbage- The Story of Waste Management and Recycling,* American Institute of Chemical engineers, 345 East 47th Street, New York, N.Y. 10017 (1994)

2. National Research Council of Canada *Automobile Shredder Residue- An Assessment of Thermal Recycling as a Recovery Option,* National Research Council of Canada (Ottawa), Canada K1A0R6 (1997).

3. EPA *Characterization of Municipal Solid Waste in the U.S.-1995 Update,* Office of Solid Waste and Emergency Response, Washington D.C. (1996).

4. A.K. Burnham and R.L. Braun *Kinetics of Polymer Decomposition,* Lawrence Livermore National Laboratory Report UCID-21293, Livermore, California (1987).

5. A.P. Watkinson, J.P. Lucas and C.J. Lim "A prediction of performance of commercial coal gasifiers" ***Fuel 70,*** 519 (1991).

6. Frost & Sullivan *U.S. Waste-to-Energy Markets,* Frost & Sullivan Consulting Office, 2525 Charleston Road, Mountain View, California 94043 (1996).

7. E.D. Larson and R. E. Katofsky *Production of Methanol and Hydrogen from Biomass,* The Center for Energy and Environmental Studies, Princeton University, Report. No. 271 (1992).

8. M. Steinberg and H.C. Cheng "Modern and Prospective Technologies for Hydrogen Production from Fossil Fuels" *Int.J. Hydrogen Energy 14,* 797 (1989).

Table 1. 1 Ton/day plant product yield distribution based on wood feedstock

Product	wt% of feed
Liquids	48
Char produced	17
Char burned	6
Gas	29

Table 2. Gasification model result compared with experimental results obtained by gasifying Illinois#6 coal in Texaco gasifier

Operating Conditions	
Gasifier temperature	1316°C
Gasifier pressure	4.08 MPa
Coal slurry feed	62.5 ton/h
Slurry water content	33 wt%
Oxygen feed rate	35.8 ton/h

Model matching conditions	
Water-gas shift reaction approach	-137°C
Heat losses, % of feed HHV	3.3 %

Component	Synthesis gas composition by model	Experimental synthesis gas composition
H_2	29.79	29.8
CO	41.73	41.0
CO_2	9.46	10.2
N_2	0.95	0.8
H_2S	1.03	1.1
COS	0.05	0.0
H_2O	16.95	17.1

FIGURE CAPTIONS

Fig.1 Process for conversion of waste to hydrogen on a small commercial scale (100 ton/day).

Fig.2 Pre-treatment step on a pilot-plant scale (1 ton/day)

Fig.3 Locus for 500°C pyrolyzer temperature. Sand temperature is equal to combustor outlet temperature.

Fig.4 Process efficiency and gasifier oxygen demand as functions of feedstock heating value.

Fig.5 Hydrogen cost as a function of feedstock heating value on large commercial scale. Assumed tipping fee (negative feedstock cost) $50/ton and cost of capital 15%.

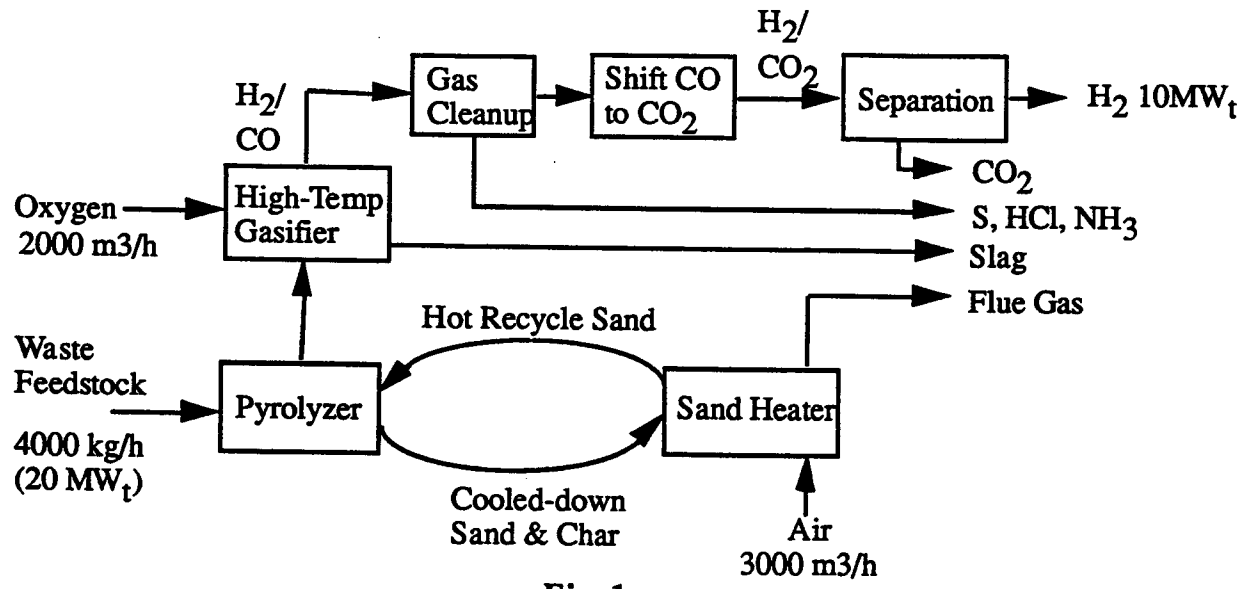
H_2/ CO
Gas Cleanup
Shift CO to CO_2
H_2/ CO_2
Separation
H_2 10MW_t
CO_2
Oxygen 2000 m3/h
High-Temp Gasifier
S, HCl, NH_3
Slag
Flue Gas
Hot Recycle Sand
Waste Feedstock
Pyrolyzer
Sand Heater
4000 kg/h (20 MW_t)
Cooled-down Sand & Char
Air 3000 m3/h

Fig.1

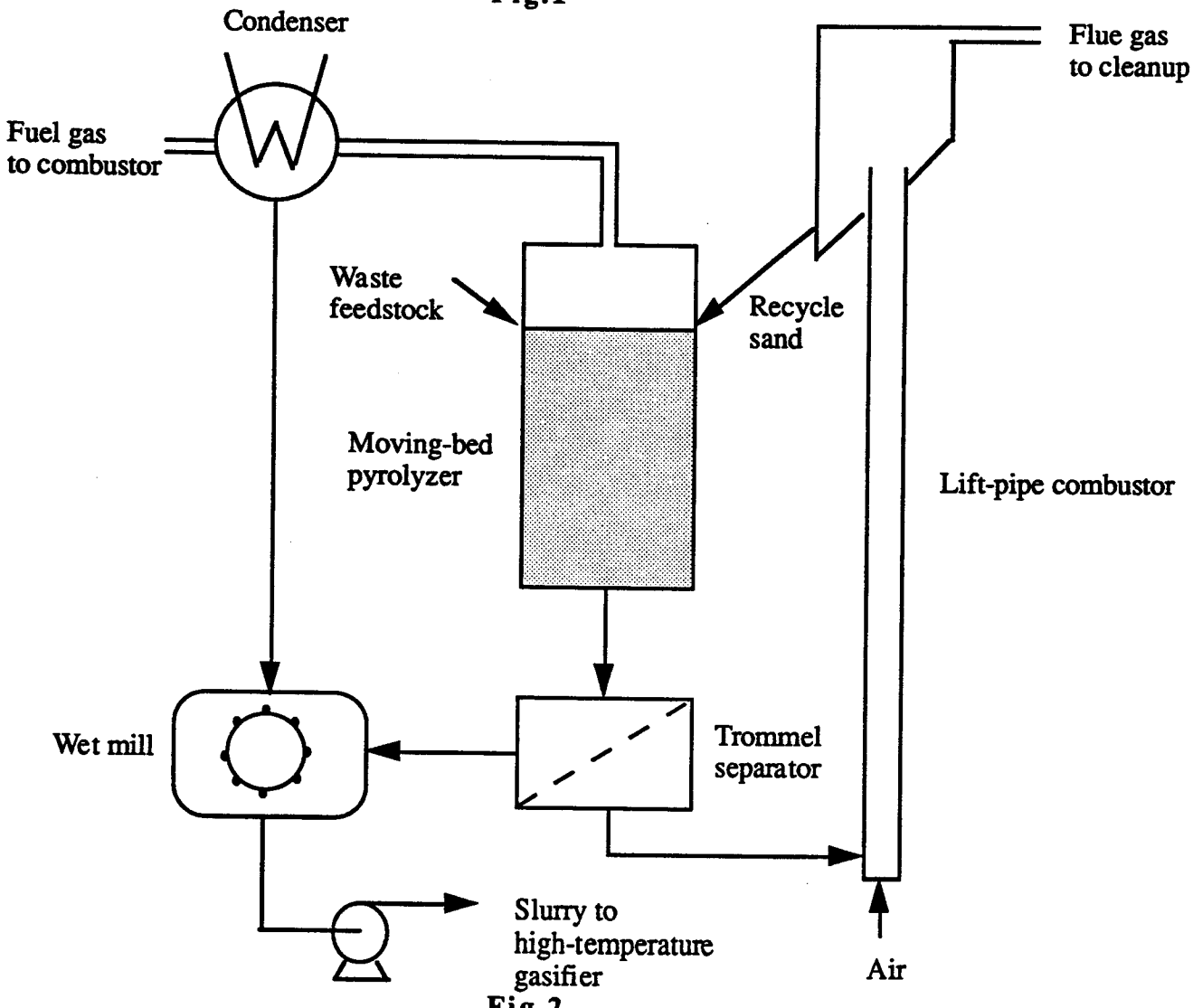
Condenser
Flue gas to cleanup
Fuel gas to combustor
Waste feedstock
Recycle sand
Moving-bed pyrolyzer
Lift-pipe combustor
Wet mill
Trommel separator
Slurry to high-temperature gasifier
Air

Fig.2

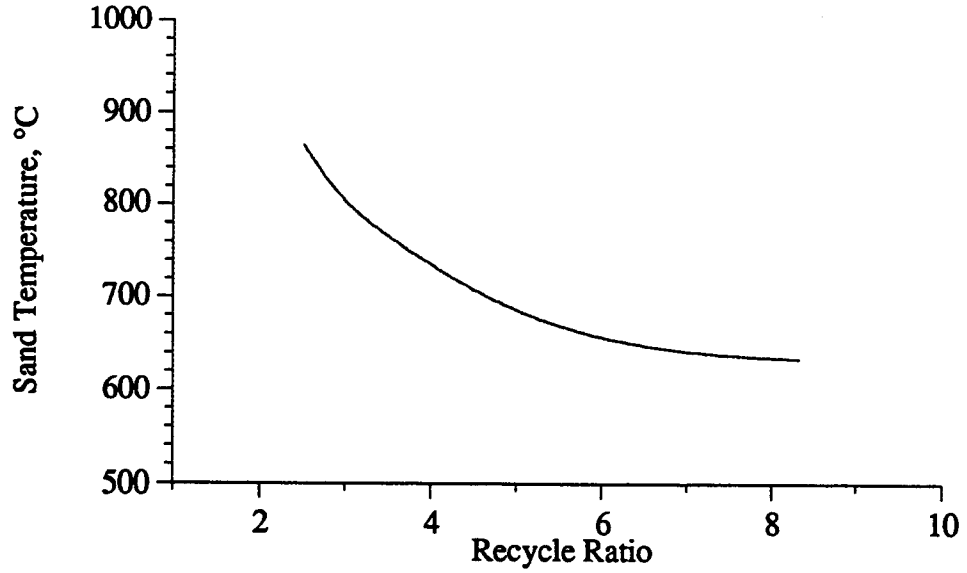
Sand Temperature, °C
1000
900
800
700
600
500
2
4
6
8
10
Recycle Ratio

Fig.3.

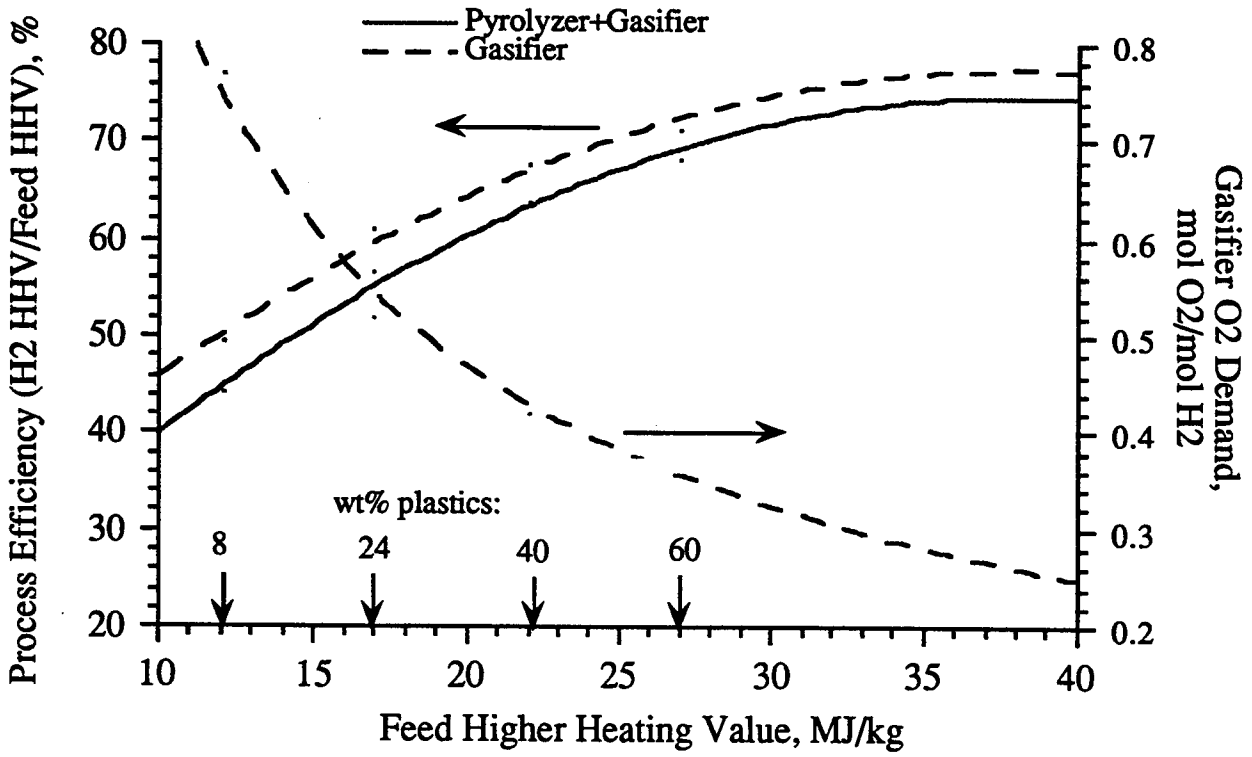
Pyrolyzer+Gasifier
Gasifier
Process Efficiency (H2 HHV/Feed HHV), %
Gasifier O2 Demand, mol O2/mol H2
80
70
60
50
40
30
20
0.8
0.7
0.6
0.5
0.4
0.3
0.2
wt% plastics:
8
24
40
60
10
15
20
25
30
35
40
Feed Higher Heating Value, MJ/kg

Fig.4.

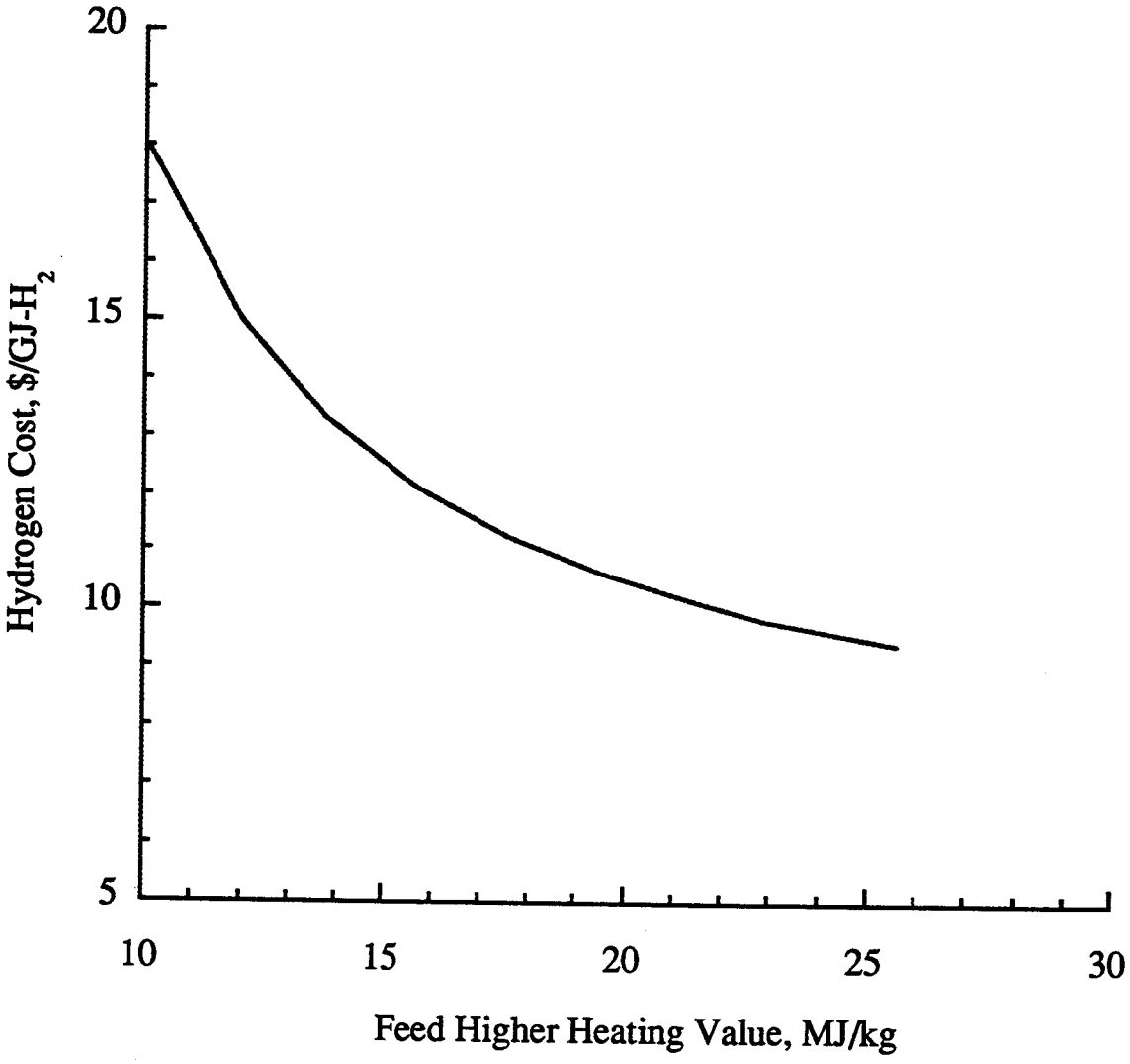
20
15
10
5
Hydrogen Cost, $/GJ-H2
10
15
20
25
30
Feed Higher Heating Value, MJ/kg

Fig.5.

Production of Hydrogen from Biomass by Catalytic Steam Reforming of Fast Pyrolysis Oils

Dingneng Wang, Stefan Czernik, and Esteban Chornet*

Center for Renewable Chemical Technologies and Materials

National Renewable Energy Laboratory (NREL), Golden, Colorado, USA 80401

Abstract

Hydrogen is of great interest as the cleanest fuel for power generation using fuel cells and for transportation. Biomass can be thermochemically converted to hydrogen can be carried out via two distinct strategies: (1) gasification followed by shift conversion, and (2) fast pyrolysis of biomass followed by catalytic steam reforming and shift conversion of specific fractions.

This paper presents the latter route. The process begins with fast pyrolysis of biomass to produce bio-oil, which (as a whole or its selected fractions) can be converted to hydrogen via catalytic steam reforming followed by a shift conversion step. Such a process has been demonstrated at the bench scale using model compounds and the aqueous fraction of poplar oil with commercial nickel-based steam-reforming catalysts. Hydrogen yields as high as 85% of the stoichiometric value have been obtained. Initial catalyst activity can be maintained through periodic regeneration via steam or carbon dioxide (CO_2) gasification of the carbonaceous deposits.

---

*Author to whom all correspondence should be addressed: Professor Esteban Chornet, National Renewable Energy Laboratory, 1617 Cole Boulevard, Golden, CO 80401. Phone: (303) 384-6124, Fax: (303) 384-6103, e-mail: chornete@tcplink.nrel.gov.

This paper will appear in a special hydrogen edition of Energy & Fuels.

Numerical Simulation of Vortex Pyrolysis Reactors for Condensable Tar Production from Biomass

R.S. MILLER and J. BELLAN†

Jet Propulsion Laboratory, California Institute of Technology, Pasadena, CA 91109-8099

† *Author for correspondence; Josette.Bellan@jpl.nasa.gov*

A numerical study is performed in order to evaluate the performance and optimal operating conditions of vortex pyrolysis reactors used for condensable tar production from biomass. A detailed mathematical model of porous biomass particle pyrolysis is coupled with a compressible Reynolds stress transport model for the turbulent reactor swirling flow. An initial evaluation of particle dimensionality effects is made through comparisons of single- (1D) and multi-dimensional particle simulations and reveals that the 1D particle model results in conservative estimates for total pyrolysis conversion times and tar collection. The observed deviations are due predominantly to geometry effects while directional effects from thermal conductivity and permeability variations are relatively small. Rapid ablative particle heating rates are attributed to a mechanical fragmentation of the biomass particles that is modeled using a critical porosity for matrix breakup. Optimal thermal conditions for tar production are observed for $900K$. Effects of biomass identity, particle size distribution, and reactor geometry and scale are discussed.

This paper will appear in a special hydrogen edition of Energy & Fuels.

SORPTION ENHANCED REACTION PROCESS (SERP) FOR THE PRODUCTION OF HYDROGEN

J. Hufton, S. Mayorga, T. Gaffney, S. Nataraj, S. Sircar
Air Products and Chemicals, Inc.
Allentown, PA 18195

Abstract

The Sorption Enhanced Reaction Process (SERP) is a novel process that is being developed for the production of lower cost hydrogen by steam-methane reforming (SMR). Phase I of the APCI/DOE SER project has been completed. An effective CO_2 adsorbent, E-4, has been developed which exceeds the goals stated at the beginning of the APCI/DOE program. In addition, the adsorbent is compatible with the SER catalyst and the active ingredient is not leachable in a steam environment. Production of this material has been scaled up to the kg range. A second family of high temperature CO_2 adsorbents has been identified. A representative of this class, H-2, exhibits a much higher CO_2 adsorption capacity than material E-4 at 350-400°C and in the presence of steam.

The H_2-SERP concept has been demonstrated in laboratory-scale equipment. Best performance thus far was obtained for a 1:3 adsorbent (E-4) / catalyst system operated at 450°C, 55 psig, and with a feed consisting of 11% CH_4 / 89% H_2O. For a 95% H_2 product, the methane conversion for the H_2-SERP system was 68%. The thermodynamic limit for the conversion and H_2 purity of a conventional catalyst-only system operated at these conditions is only 34% and 57%, respectively.

Economic analysis of a preliminary H_2-SERP design suggests that it can produce H_2 at a significantly lower cost than conventional reforming at a production rate of 2.5 MM SCFD.

Introduction

Energy needs in the long-range future will have to be obtained from renewable sources, for example sunlight. Hydrogen has been proposed to be an ideal energy carrier in this case since it is nonpolluting, does not contribute to global warming, and is regenerable from water with energy input. Before this type of energy economy dominates, though, there will be a transition period during which fossil fuel-based energy sources will be phased out. It is during this time that H_2 production from petroleum-based feedstock will be needed in order to spur development of the required H_2 supply infrastructures and energy conversion devices (e.g., electrolysis and photovoltaic units, fuel cells, etc...). Steam methane reforming, currently the most efficient, economical, and widely used industrial method for producing hydrogen (Yürüm, 1995), will likely be used to supply a large fraction of this hydrogen. The goal of this work is to develop an even more efficient process for reforming steam and methane to hydrogen product than the conventional SMR process.

Novel Sorption Enhanced Reaction Process

The concepts based on Le Chatelier's principle are very well known [Gluud et al., 1931], namely that (a) the conversion of reactants to products, and (b) the rate of forward reaction in an equilibrium-limited reaction can be increased by selectively removing some of the reaction products from the reaction zone. Numerous applications of this concept using fixed bed, continuous countercurrent moving bed, and simulated countercurrent moving bed chromatographic reactors have been published. The detailed review of the literature is given elsewhere [Carvill et al., 1996].

In the proposed sorption enhanced reaction process for H_2 production (H_2-SERP) the conventional steam methane reformation reaction is carried out:

$$CH_4 + 2\,H_2O \Leftrightarrow CO_2 + 4\,H_2$$

The reactants, steam and methane, are fed at 300-500°C and 50-250 psig into a reactor containing an admixture of reforming catalyst and an adsorbent for removing carbon dioxide. A reactor effluent consisting of essentially pure hydrogen (98+%) is produced during this step. Once the adsorbent is saturated with CO_2, it is regenerated in situ by using the principles of pressure swing adsorption. Several patent applications for the process and process integrations have been filed with the United States Patent Office by Air Products and Chemicals, Inc. [Sircar et al. 1995, Anand et al., 1995, Hufton et al., 1996, Nataraj et al., 1996].

The key benefits of producing H_2 by the present concept are: (i) reformation at a significantly lower temperature (300-500°C) than conventional SMR (800-1000°C), while achieving the same conversion of methane to hydrogen, (ii) significantly lower capital cost, (iii) production of product hydrogen at reactor pressure (200-400 psig) and at 98+% purity directly from the reactor, (iv) significant reduction or even elimination of downstream hydrogen purification steps, (v) reduction/elimination of CO as a by-product, (vi) minimization of side reactions, e.g., coking, and (vii) potential reduction of the excess steam used in conventional SMR.

A comparison of the conventional SMR process and the proposed H_2-SER process is shown in Table 1.

Table 1. H_2-SERP vs Conventional SMR for H_2 Production

	Conventional	SER Goals
Operating Temperature	800-1000°C	300-500°C
CH_4 to H_2 Conversion	80-85%	90+%
Reaction Product Composition	73.7% H_2 +9.4% CO_2+ 12.0% CO+4.8% CH_4 (Dry Basis)	98+% H_2
Product Pressure	200-400 psig	200-400 psig

The steps for the direct production of essentially pure H_2 by the cyclic H_2-SERP are shown in Figure 1 and are described below:

1. sorption-reaction step: The reactor is initially presaturated with a portion of the product H_2 at the desired reaction temperature and pressure. Steam and methane at a prescribed ratio (e.g., 2:1) are fed to the reactor and an essentially pure H_2 product (>98% purity) is collected as the reactor effluent. The reaction step is continued up to the point when the H_2 purity in the product decreases to a preset level. The feed is then diverted to a second identical reactor.

2. depressurization step: The reactor is countercurrently depressurized. The effluent gas can be recycled as feed to another reactor or used as fuel.

3. purge step: The reactor is countercurrently purged with a weakly adsorbing gas such as methane to desorb the CO_2. The desorption pressure may range between 0.2 and 1.1 atmospheres. The desorbed gas consists of CH_4, CO_2, H_2 and H_2O and is either separated for recycle of the CH_4 purge gas or used as fuel.

4. product purge step: The weakly adsorbing purge gas (CH_4) is countercurrently displaced from the reactor with product H_2. The displaced CH_4 is recycled as purge gas or used as fuel.

5. product pressurization: The reactor is countercurrently pressurized to the reaction pressure with pure H_2. At this point, the regeneration of the reactor is complete and it is ready to undergo a new cycle.

APCI/DOE Program Goals and Milestones

The key program goals and milestones for the cooperative APCI/DOE SER Project are listed in Table 2 along with the focus of the experimental program for 1995-1999:

Table 2. Program Goals and Milestones

Program Goals	Milestones
Sorbent Development	1995-1997
SER Process Demonstration	1996-1997
Economic Evaluation	1996-1999
Process Development Unit Design	1997-1998
Process Development Unit Construction / Operation	1998-1999

The key goals for the first phase of the program are to:

(i) Develop a CO_2 sorbent which is stable in the presence of high partial pressures of steam and maintains the desired CO_2 adsorption capacity under cyclic pressure swing conditions at 300-500°C.

(ii) Demonstrate the H_2-SERP concept in laboratory-scale process equipment.

(iii) Estimate first-pass economics to demonstrate the commercial attractiveness of H_2-SERP.

Phase I was recently completed and the results of this work are summarized in this document.

Experimental

The development of CO_2 sorbents for H_2-SERP has involved the synthesis, characterization and performance evaluation of a number of different families of sorbents. Three major experimental units have been constructed in-house for the exclusive purpose of these measurements. A TGA unit was used to determine the CO_2 working capacity under dry conditions and in the presence of low partial pressures of steam. The mass of the solid adsorbent is monitored as it is repetitively exposed to CO_2 (or a CO_2 / H_2O mixture) followed by N2. In addition to its extensive use as a quick screening tool, this unit was recently modified to permit accurate measurement of dry CO_2 adsorption isotherms at 300-500°C and under very low CO_2 partial pressures. Measurements of the CO_2 adsorption capacity expected in the H2-SERP system were made with the Binary Desorption Unit (BDU). In addition to CO_2, up to 10 atm of steam can be tolerated with this unit at 300-500°C, and both the CO_2 and H_2O adsorption capacities can be evaluated. A schematic of the BDU was previously provided by Anand et al. (1996). The stability of the adsorbent under

static hydrothermal conditions was evaluated with the Hydrothermal Stability Testing Unit (HSTU).

A 1" laboratory hydraulic Bonnot Extruder was also installed for the extrusion and pelletization of sorbents. Pelletized adsorbents are required for SER process testing and analysis in the BDU and HSTU.

An existing experimental apparatus constructed, with Air Product funds, for the investigation of another SER application was modified for performing steam methane reforming experiments. Steam generation and handling systems were added, the analysis systems were modified, and the additional safety issues were addressed. A ventilated reactor charging unit was also constructed for safely loading and unloading carcinogenic catalyst from the reactor. A simplified schematic of the process test unit was presented by Anand et al. (1996). The unit is capable of running in only a single-step mode rather than the fully cyclic mode of an industrial unit. The reactor dimensions are 3.8 cm ID and 177.8 cm long and it is housed in an electrical furnace. Steam is generated by vaporizing liquid water which is then mixed with methane and fed to the reactor. It is also possible to purge the reactor countercurrent to the feed direction with inert gas. The reactor pressure and temperature, and the effluent gas flow rate and composition are monitored as a function of time during an experiment. Analysis of these parameters permit characterization of the performance of the process.

Results and Discussion

High Temperature Sorbents for CO_2

The following criteria were developed for an acceptable CO_2 sorbent for performing steam-methane reforming by the SER concept:

(a) CO_2 working capacity > 0.3 mmole/g at 300-500°C in the presence of steam at high partial pressure (P_{H2O}) and at low partial pressures of CO_2 (P_{CO2}, 0.1 to 1 atm ; $(P_{H2O})/(P_{CO2}) > 20$);
(b) Fast ad(de)sorption kinetics for CO_2 at reaction and regeneration conditions;
(c) Stable CO_2 sorption capacity after repeated sorption/desorption cycles;
(d) Adequate mechanical strength after cyclic exposure to high pressure steam;
(e) Readily scaleable method for producing CO_2 sorbent in larger quantities;
(f) Environmentally benign sorbent and support.

During the first year of the APCI/DOE program, several families of CO_2 sorbents (both supported and unsupported) were prepared and evaluated. Details of this work can be found in Anand et al. (1996). The preferred adsorbent, referred to as E-4, was demonstrated to possess adequate CO_2 working capacity in dry CO_2. It also appeared to be hydrothermally stable since no loss of adsorption capacity for dry CO_2 was detected after extensive steaming (30 days) of the adsorbent. An adsorption isotherm was measured for <1.6 atm CO_2 in 10 atm H_2O which clearly indicated that the presence of excess water would not disrupt the CO_2 adsorption. Information regarding the kinetics of adsorption/desorption of CO_2 from E-4 were obtained from column

breakthrough measurements. The adsorption/desorption rates were found to be relatively fast. The highlights of the second year of materials development are outlined below.

An exhaustive study of the cyclic CO_2 working capacity of E-4 in the presence of 0.3 atm CO_2, 10 atm steam at 400°C was carried out with the BDU. The CO_2 capacity initially decreased and then stabilized at 0.45 mmole/g (Figure 2). This final capacity is above the initial target of 0.30 mmole/g.

Two issues regarding stability of the E-4 / catalyst system were investigated. The first study was to determine if the active ingredient of the adsorbent was mobile under reaction conditions. Thermodynamic calculations suggested that it was not. A column packed with adsorbent was steamed at 400°C for 72 hours and the solid-phase composition of active ingredient was measured along the length of the column. There was no change in the distribution of active ingredient, thus confirming the thermodynamic results. A second experiment was conducted to determine if the catalyst and adsorbent were compatible, i.e., would one poison the other. A mixture of the two solids was packed into a column and subjected to simulated reaction gas (1 atm CO_2, 10 atm H_2O, 400C) for 72 hours. The activity of the catalyst and the CO_2 adsorption capacity of the adsorbent did not change after this treatment. The materials appeared to be completely compatible.

The production of the E-4 material was scaled up to the kg range, and a total of five kilograms of adsorbent were prepared for process testing.

Further study of the degradation of the CO_2 adsorption capacity of E-4 upon exposure to steam/ CO_2 (Figure 2) led to the identification of an entirely new family of high temperature CO_2 adsorbents. These were based on mixed metal containing precursor salts and are referred to as materials H1-H5. Adsorbent H-2 and H-3 showed particularly interesting adsorptive properties. Adsorbent H-3 had an initial reversible dry CO_2 adsorption capacity of > 12 mmole/g at 375°C, which was a factor of ten greater than that of E-4. This adsorbent (H-3), however, was unable to maintain its high capacity in the presence of moisture. Adsorbent H-2 was evaluated to have reversible CO_2 capacities as high as 3 mmole/g. The working capacity of an extruded sample of H-2 leveled-off around 2.5 mmoles/g after 20 adsorption/desorption cycles (dry). Further testing demonstrated that this material was capable of adsorbing CO_2 even in the presence of 10 atm of steam, and that the adsorbent was stable in this environment. The material yielded a CO_2 working capacity of 1.1 mmole/g after 12 cycles of BDU runs with 0.3 atm CO_2 and 10 atm steam at 375°C. These results are presented in Figure 2 along with the data for material E-4. The CO_2 adsorption capacity for H-2 was found to be strongly temperature dependent; it decreased by 66% when the temperature was increased from 375 to 450°C. Current efforts with this material are focused on the measurement of the CO_2 isotherm shape, particularly in the range of low CO_2 partial pressures (with the modified TGA unit). This new adsorbent has the potential to significantly improve the CO_2 capacity of the SER reactors, which would decrease their size and cost.

Two materials-oriented patent applications were filed this year. The first (Nataraj et al., 1996) described material E-4 and how it fits within the H_2-SERP concept. The second (Mayorga et al., 1996) encompassed modified aluminas as SER adsorbents (B1-B7 and C1-C5). An invention disclosure has been submitted for the H-family adsorbents.

H_2-SER Process Experiments

The goal of this work was to experimentally demonstrate the concept of H_2-SERP, i.e., observe enhanced conversion of methane during an SER reaction step. A reactor was packed with a 1:1 mixture of adsorbent E-4 and commercial pre-reformer catalyst and reduced in H_2 at 450°C. The reactor was then cooled to 350°C, filled with pure H_2 to 55 psig and fed a gas containing 20% methane / 80% steam. The mole fraction of hydrogen in the effluent gas was initially high as H_2 from the void space of the reactor was removed. It then dropped and varied from 55 to 80%. The only other species in the effluent gas was methane; carbon oxides were not detected during this particular experiment. Integration of the effluent compositions and flow rate led to the evaluation of the CH_4 conversion and the average mole fraction of H_2 in the product. The former is actually a combination of the conversion and the recovery and is evaluated as the net amount of product hydrogen (total hydrogen out of the reactor minus the amount needed to initially pressurize the reactor) divided by the total amount of methane fed to the reactor. The average hydrogen mole fraction in the product was determined by assuming that all of the gas exiting the reactor was collected and mixed. The SERP unit yielded a CH_4 conversion of 30% and an average H_2 product purity of 70%. These values are both higher than would be expected from a catalyst-only reactor operating at equilibrium (8.2% CH_4 conversion, 24.7% H_2 purity). Thus, this experiment clearly demonstrates that the inclusion of a CO_2 adsorbent in the reactor substantially improves the conversion of reactants and product purity of the effluent gas. The SERP concept was demonstrated.

Further experiments were conducted to assess the effect of temperature, adsorbent / catalyst ratio, and steam / methane ratio of the feed gas on system performance. Increasing the temperature to 450°C improved the CH_4 conversion and H_2 product purity. The general effect of this change is to increase the CO_2 mole fraction in the gas that is passed to the adsorbent. Increasing the steam/methane ratio results in a similar effect, so it is not surprising that the same experimental observations were made. Thus, higher temperatures and higher steam/methane ratios were found to be desirable. Decreasing the adsorbent / catalyst ratio, i.e., going to a catalyst-rich system, did not appreciably change the effluent gas composition history. Thus, there was no effect on H_2 product purity. The overall productivity of the reactor fell, though, since the total amount of CO_2 adsorbent in the reactor was reduced.

Figure 3 illustrates the gas phase composition of the reactor effluent stream during the most attractive experiment conducted to date. The run was carried out with a reactor packed with a 1:3 mixture of adsorbent (E-4) / catalyst at 450°C, 55 psig, and with a feed consisting of 11% methane and 89% steam. The initial shaded area represents the amount of H_2 that was initially used to pressurize the reactor. Production of high purity hydrogen continues after this initial amount has exited the reactor. The effluent gas consists predominantly of H_2 and CH_4. Carbon dioxide was not detected by the GC/MS until the later part of the experiment. If the reaction step is terminated when the average H_2 product purity is 95%, then the methane conversion is found

to be 68%. Again, this is substantially higher than the equilibrium conversion of 34% and product purity of 57% expected for a catalyst-only system (thermodynamic calculations). The SERP reactor product purity is approaching the range where further separation may be unnecessary for some applications, which would impart a very large economic advantage over conventional processes.

Anand et al. (1996) described and illustrated a novel reactor concept for carrying out H_2-SERP based on a shell and tube reactor system and a condensing heat transfer fluid. This configuration will maintain the reactor at an essentially constant temperature while simultaneously providing heat to the endothermic reaction zone as it travels down the length of the column. A vendor of the heat transfer fluid has been consulted with this application and is eager to help in development of the system. The upper temperature limit for application of these fluids is around 400°C, and operation at higher temperatures will require some form of fluid reclamation. Thus, the most attractive SERP operation at 450 °C will be at the edge of heat transfer fluid technology.

A patent application (Nataraj et al., 1996) was filed which thoroughly describes the H_2-SERP concept and the function of the novel shell and tube reactor.

Preliminary Design and Economic Analysis

A preliminary process flow diagram was prepared for the H_2-SER process using the condensing vapor reactor. Heat and mass balances and equipment sizes were evaluated based on reasonable engineering assumptions. An economic analysis of the design was performed by the APCI H_2 business area which showed that the H_2-SER process can lower H_2 production costs by roughly 20 to 30% compared with conventional SMR (2.5 MM SCFD H_2 product).

An existing adsorption process simulator has been modified to include reaction terms so that it may be used to model the performance of the SER process.

Future Work

Future work regarding development of the CO_2 adsorbent will be focused on improving the shape of the CO_2 isotherm in the presence of steam. Ideally, the isotherm would be linear while maintaining a high CO_2 capacity at a CO_2 partial pressure of ~0.5 atm. An adsorbent characterized by this type of isotherm would require a minimum amount of purge gas during the regeneration steps of the process, and would therefore reduce process operating costs. Material E-4 exhibits a relatively steep increase at low CO_2 partial pressures. The isotherm shape of material H-2 has not yet been defined and will be the topic of short-term experiments. The modified TGA unit will make these analysis possible and expedient.

Efforts will also be directed towards the scale up of adsorbent production processes to the 30-50 kg range in preparation for supplying future process testing efforts.

The short term objective of process experiments will be to continue to explore the effects of various experimental parameters on process performance. An important variable of interest is the reaction pressure. Operation at higher pressure than 55 psig is desirable in order to minimize compression costs. Straightforward experimental modifications will be carried out to increase the maximum reaction pressure of the experimental system to 250 psig.

Process experiments conducted to date have been concerned with quantification of the reaction step only. The adsorbent is obviously regenerable since repetitive experiments with the same reactor packing yield similar enhancements in CH_4 conversion. It is not clear, though, how much purge gas is needed to effectively remove enough of the adsorbed CO_2 from the reactor. Insight into this question will be obtained by adding a more sensitive CO_2 detector to the reactor effluent and carefully quantifying the desorption steps.

The above question cannot be fully answered even with the additional desorption experiments since it is not clear what the effect of residual adsorbed CO_2 has on the reaction step output. This question can only be answered definitively by conducting fully cyclic experiments with two or more beds at cyclic steady state. We plan on constructing such a system, in fact, it is currently in the design stage. The unit will be fully automated and will include all of the necessary hardware to repetitively perform the entire H_2-SERP process. The unit will contain two reactors of industrially relevant size (1-2 in ID and 10-20 ft long). The proposed heat transfer system will be utilized so unanswered questions regarding the heat transfer fluid can be resolved. The unit will also allow for the investigation of specific reaction step feed rates (or G-rates, lbmole/hr-ft^2) which are of industrial magnitude and are roughly forty times greater than those used in the current experimental system.

Finally, as new information regarding the process or CO_2 adsorbent is developed (e.g., effect of higher G-rates, purge requirements, improved adsorbent CO_2 capacities, etc.), the preliminary H_2-SERP design will be revised and economic assessments will be refined. Parameters for the process simulator will be obtained from comparisons with lab-scale reactor data. The simulator will then be used to help design the industrial units.

Summary

An effective CO_2 adsorbent, E-4, has been developed which exceeds the goals stated at the beginning of the APCI/DOE program. In addition, the adsorbent is compatible with the SER catalyst and the active ingredient is not leachable in a steam environment. Production of this material has been scaled up to the kg range. A second family of high temperature CO_2 adsorbents has been identified. A representative of this class, H-2, exhibits a much higher CO_2 adsorption capacity than material E-4 at 350-400°C under dry gas and under steam conditions. This material has the potential to reduce the size of the SERP reactors. Future experiments are planned to investigate the shape of the adsorption isotherm for this material and to attempt to optimize this shape, if possible.

The H_2-SERP concept has been demonstrated. It is clear that including a CO_2 adsorbent along with the SMR catalyst enhances the methane conversion to products and improves the hydrogen purity of the effluent gas. The best performance thus far has been obtained for a 1:3 adsorbent (E-4) / catalyst system operated at 450 °C, 55 psig, and with a feed consisting of 11% CH_4 / 89% H_2O. For a 95% H_2 product, the methane conversion for the SERP system is 68%. The conversion and H_2 purity of a conventional catalyst-only system operated at these conditions is only 34% and 57%, respectively. Increasing the reactor temperature and steam / methane ratio improves the performance of the system. Future experiments are designed to extend the reaction step pressure range to 250 psig and to take efforts to quantify the desorption step. A second cyclic experimental unit based on two-bed operation is under design and will be used to answer questions which cannot be resolved with the current unit.

A process simulator has been developed and will be applied to the H_2-SERP system. Economic analysis of a preliminary H_2-SERP design suggests that it can produce H_2 at a significantly lower cost than conventional reforming at a production rate of 2.5 MM SCFD.

Acknowledgments

The authors would like to thank Joe Zenon and Jeff Brzozowski for performing most of the experiments and analysis described in this report. Thanks also to Robert Moore for carrying out the economic analysis and Grant Fox for developing the SER process simulator.

References

Anand, M., J. Hufton, S. Mayorga, S. Nataraj, S. Sircar, T. Gaffney, "Sorption Enhanced Reaction Process (SERP) for Production of Hydrogen", *Proceedings of the 1996 U.S. DOE Hydrogen Program Review*, **1**, 537 (1996).

Anand, M., Sircar, S., and Carvill, B.T., "Processes for Operating Equilibrium Controlled Reactions," U.S. Patent Pending (1995).

Carvill, B.T., Hufton, J.R., Anand, M., and Sircar, S., "Sorption Enhanced Reaction Process," *AICHE J.*, **42**, 2765 (1996)

Gluud, W., Keller, K., Schonfelder, R. and Klempt, W., "Production of Hydrogen," U.S. Patent 1,816,523 (1931).

Nataraj, S.N., Carvill, B.T., Hufton, J.R., Mayorga, S.M., Gaffney, T.R., and Brzozowski, J.R., "Process for Operating Equilibrium Controlled Reactions," U.S. Patent Pending (1996).

Hufton, J.R., Sircar, S., Baade, W.F., Abrardo, J.M., and Anand, M., "Integrated Steam Methane Reforming Process for Producing Carbon Monoxide," U.S. Patent Pending (1996).

Hufton, J.R., Sircar, S., Baade, W.F., Abrardo, J.M., and Anand, M., "Integrated Steam Methane Reforming Process for Producing Carbon Monoxide and Hydrogen," U.S. Patent Pending (1996).

Mayorga, S. G., Golden, T. C., Gaffney, T. R, Brzozowski, J. R., and Taylor, F. W., " Carbon Dioxide Pressure Swing Adsorption Process Using Modified Alumina Adsorbents," U. S. Patent Pending (1996).

Sircar, S., Anand, M., Carvill, B.T., Hufton, J.R., Mayorga, S.G., and Miller, R.N., "Sorption Enhanced Reaction Process for Production of Hydrogen," *Proceedings of the1995 U.S. DOE Hydrogen Program Review*, **1**, 815 (1995).

Yürüm, Y., "Hydrogen Production Methods", **Hydrogen Energy System**, Kluwer Academic Publishers, Netherlands, pp. 15-30 (1995).

List of Figures

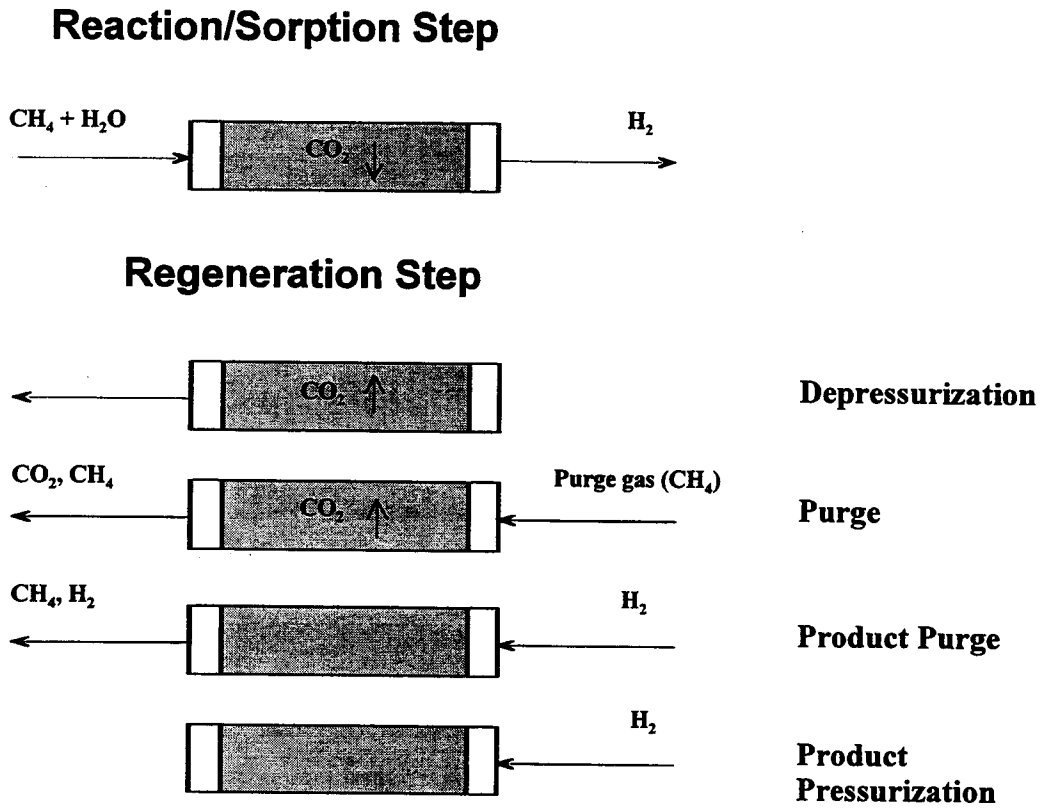

Figure 1
Hufton et al.

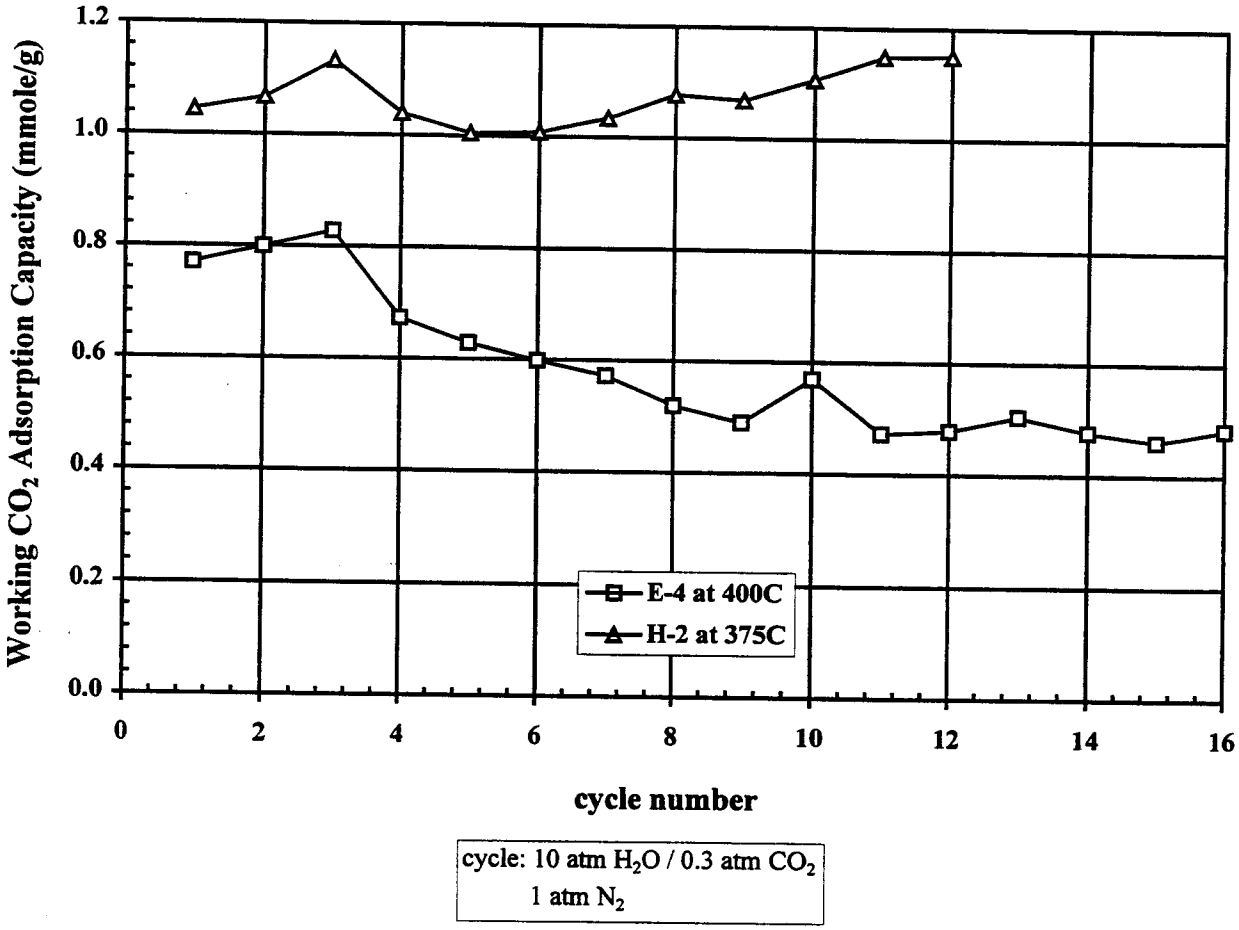

Figure 2
Hufton et al.

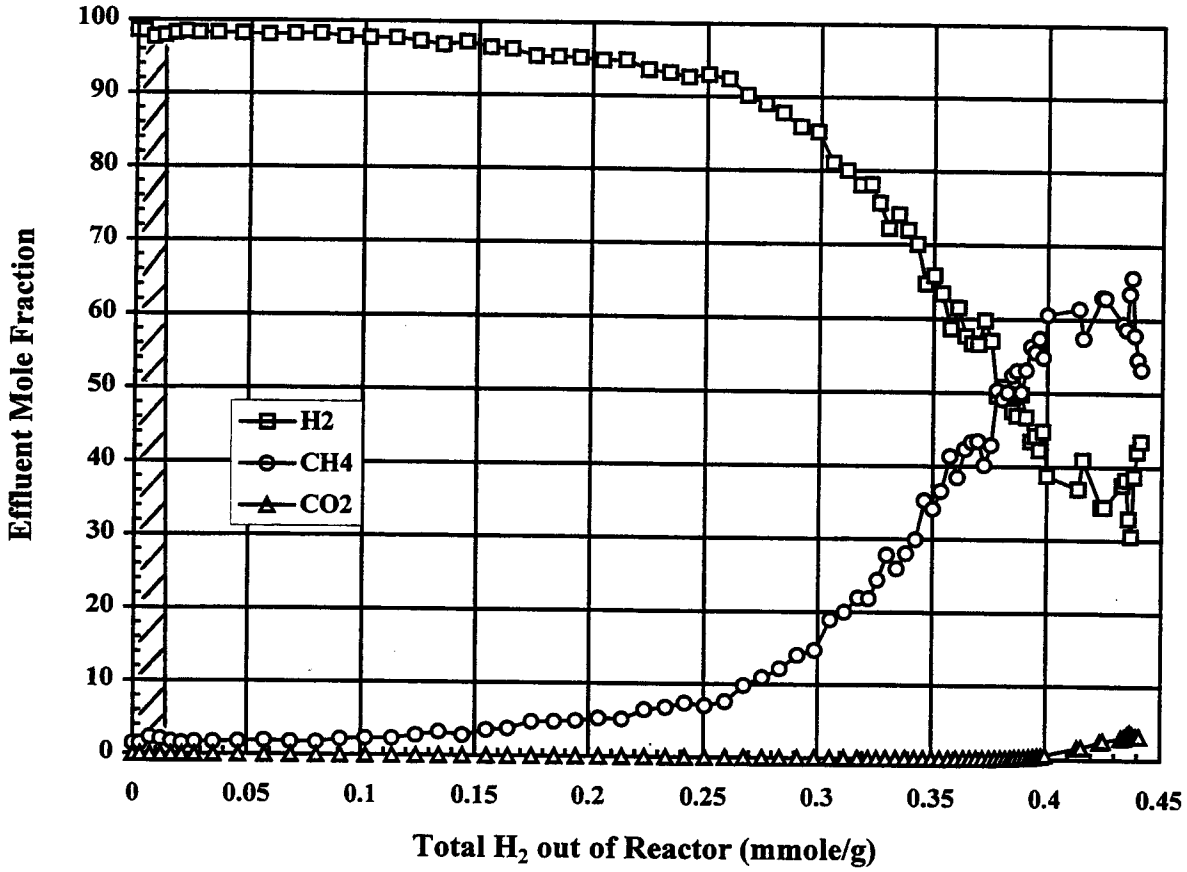

Figure 3
Hufton et al.

CO_2-Free Production of Hydrogen by Catalytic Pyrolysis of Hydrocarbon Fuel

Nazim Z. Muradov,

Florida Solar Energy Center, 1679 Clearlake Road, Cocoa, Florida 32922, U.S.A.

Abstract

All conventional options of hydrogen production from hydrocarbon fuel (primarily natural gas, NG), e.g. steam reforming (SR), partial oxidation and autothermal reforming, involve CO_2 production at some point in the technological chain of the process. Therefore, the main problem remains: how to produce hydrogen from hydrocarbon fuels without CO_2 emission. The capture of CO_2 from the SR process streams and its sequestration (underground or ocean disposal) is actively discussed in the literature. However this method is energy intensive, poses uncertain ecological consequences, and still does not completely eliminate CO_2 emission. Another approach is to decompose hydrocarbon fuels into hydrogen and carbon. The thermal decomposition of NG is a technologically simple one-step process without energy and material intensive gas separation stages and shows the potential to be a CO_2-free hydrogen production process. The experimental results on the thermocatalytic decomposition of gaseous (methane and propane) and liquid (hexane, gasoline and diesel fuel) hydrocarbons over metal-oxide and carbon-based catalysts are presented. Although transition metal catalysts produce gas with high initial hydrogen concentration, their activity rapidly drops due to the surface deposition of carbon. Carbon-based catalysts offer certain advantages over metal catalysts since there is no need for the carbon separation from the catalyst.

The pyrolysis of light liquid hydrocarbons, including gasoline, over activated carbon yields hydrogen-rich gas (40-50%v. H_2). The decomposition of methane in binary mixtures with saturated and unsaturated hydrocarbons was also studied. It was found that the addition of small amounts of unsaturated hydrocarbons (e.g. acetylene) to methane noticeably increases the steady state concentration of hydrogen in the effluent gas. The studied process can be the basis for the development of compact catalytic units for on-site production of hydrogen/methane blends from NG and liquid hydrocarbon fuels on gas refueling stations. The concept can also be used for a CO_2-free production of hydrogen for fuel cell applications.

This paper will appear in a special hydrogen edition of Energy & Fuels.

ASSESSMENT OF INFRASTRUCTURE REQUIREMENTS FOR HYDROGEN VEHICLE REFUELING STATIONS USING GLASS MICROSPHERES FOR HYDROGEN STORAGE

Joan M. Ogden
Center for Energy and Environmental Studies
Princeton University
Princeton, NJ 08544

Henrik Wallman and Jill Watz
Lawrence Livermore National Laboratories
University of California
Livermore, CA 94551

Abstract

Glass microspheres offer a potentially attractive way of storing hydrogen at high pressure. For several years researchers at Lawrence Livermore National Laboratory have studied the properties of microspheres for hydrogen storage. Starting in April 1997, researchers at Princeton University's Center for Energy and Environmental Studies began work on an assessment of the infrastructure requirements for hydrogen vehicle refueling stations using glass microspheres, in collaboration with researchers at LLNL. This builds on earlier work by Princeton on refueling infrastructure for hydrogen vehicles. Tasks to be performed under this study include the following:

1) Carry out conceptual designs of hydrogen refueling stations using glass microsphere storage. Model compression and heat energy requirements for glass microsphere charging and discharging cycle for demands appropriate for a hydrogen vehicle refueling station. Size refueling station equipment including discharge vessel, hydrogen compressors, storage capacity, dispensers, etc. Discuss design issues for refueling station designs using glass microspheres. Compare to other hydrogen refueling station options.

2) Estimate the economics of delivering hydrogen transportation fuel to vehicles for refueling station designs with glass microsphere storage. Compare to other hydrogen refueling station options.

In this paper, we report on our progress to date on these tasks, and outline future work.

Introduction

Glass microspheres offer a potentially attractive way of storing hydrogen at high pressure. For several years researchers at Lawrence Livermore National Laboratory have studied the properties of microspheres for hydrogen storage (Souers et.al 1978, Woerner et.al. 1979 Rambach 1994, Rambach et.al. 1995, 1996). Starting in April 1997, researchers at Princeton University's Center for Energy and Environmental Studies began work on an assessment of the infrastructure requirements for hydrogen vehicle refueling stations using glass microspheres, in collaboration with researchers at LLNL. This builds on earlier work by Princeton on refueling infrastructure for hydrogen vehicles (Ogden et.al 1995, Ogden 1997, Ogden et.al. 1997).

Tasks to be performed under this study include the following:

1) Carry out conceptual designs of hydrogen refueling stations using glass microsphere storage.

* Model compression and heat energy requirements for glass microsphere charging and discharging cycle for demands appropriate for a hydrogen vehicle refueling station. Size equipment needed for microsphere charging system (hydrogen compressors, pressure vessels, heat exchangers, etc.). Compare glass microspheres to other hydrogen storage technologies.

* Consider alternative options for microsphere charging including:

  Microspheres are charged at a remote location, delivered to the refueling station by truck and discharged to provide hydrogen for vehicles

  Microspheres are charged and discharged at the station from an onsite hydrogen production system or from a gas pipeline

* Size refueling station equipment including discharge vessel, hydrogen compressors, storage capacity, dispensers, etc.

* Discuss design issues for refueling station designs using glass microspheres. Compare to other hydrogen refueling station options.

2) Estimate the economics of delivering hydrogen transportation fuel to vehicles for refueling station designs with glass microsphere storage. Consider both the capital cost of refueling stations and the delivered cost of hydrogen transportation fuel. Compare to other hydrogen refueling station options.

In this paper, we report on our progress to date on these tasks, and outline future work.

General Considerations: Conceptual Design of Hydrogen Refueling Stations Using Glass Microsphere Storage

Here we present some general considerations for the design hydrogen vehicle refueling stations.

Hydrogen demand for vehicle refueling stations

To size the equipment needed for a refueling station, we must know the hydrogen demand. The daily hydrogen demand for a refueling station can be estimated if the vehicle characteristics and average driving patterns are known.

Assumed characteristics for hydrogen fuel cell vehicles are summarized in Table 1. In Table 2, we estimate the number of vehicle fueled per day and the total fleet supported for a hydrogen refueling station dispensing 1 million scf H2/day.

Most public gasoline refueling stations serve 80 to 1000 cars per day. A typical size for a transit bus garage is 60 to 200 buses.

Based on these numbers, we assume that the size range of interest for centralized refueling applications is about 0.1 to 2.0 million scf of H2 per day. This would support a total fleet of 14 to 280 fuel cell buses or 960 to 19,200 fuel cell passenger cars.

The hourly demand profile is also an important factor in sizing equipment. (For example, the station must be able to match peak fuel demands through storage capacity.) This will be discussed further in future work.

Description of hydrogen refueling stations with microsphere storage

In all cases, we assume that the hydrogen vehicles store hydrogen onboard as compressed gas at 5000 psi. Microspheres are used as an intermediate storage medium for hydrogen. That is, hydrogen is stored in microspheres (either at a remote centralized recharging facility or at the refueling station), and subsequently the microspheres are discharged at the station to provide hydrogen for vehicles.

Two types of refueling stations are considered:

* Microspheres are charged at a remote location, delivered to the refueling station by truck and discharged to provide hydrogen for vehicles (Figure 1).

* Microspheres are charged and discharged at the station from an onsite hydrogen production system or from a gas pipeline (Figure 2).

Comparison of Hydrogen Refueling Stations with Microsphere Intermediate Storage vs. Compressed Gas Hydrogen Intermediate Storage

A typical design for a gaseous hydrogen refueling station with compressed gas intermediate storage is shown in Figure 3. Here gaseous hydrogen is provided from an onsite production system, or via pipeline. The hydrogen is compressed into intermediate storage

in gas pressure cylinders at 5000 psi. As vehicles are refueled, hydrogen is drawn out of the cylinders in turn. If necessary, the pressure from intermediate storage can be "boosted" back to the desired vehicle onboard storage pressure.

One possibility for using microspheres in refueling stations is replacing compressed gas intermediate storage pressure vessels with microsphere-containing pressure vessels, as shown in Figure 2. The microspheres would stay in the pressure vessels during charging and discharging (except possibly during heating in an external heat exchanger). To store hydrogen, microspheres are heated to 250-350°C and then charged with pre-heated, pressurized hydrogen at pressures on the order of 5000-10,000 psi. To withdraw hydrogen for refueling vehicles, microspheres would be heated and hydrogen discharged. The hydrogen might then be compressed and possibly fed to a small buffer storage in pressure cylinders (to meet varying demand for fuel) before being dispensed to the vehicle.

Comparing Figures 2 and 3, we see that using microsphere-filled pressure vessels as intermediate storage would entail higher capital and energy costs than using ordinary compressed gas storage, because of the need to heat the microspheres and the hydrogen prior to charging. Moreover, there would be a time delay both on microsphere charging and on discharging, which could lead to a longer refueling time than with compressed gas intermediate storage.

We conclude there is no advantage in charging microspheres in pressure vessels for intermediate hydrogen storage at the refueling station, as compared to intermediate hydrogen storage in ordinary compressed gas vessels. We will now concentrate on systems where microspheres are charged remotely, and trucked to the station for discharge (as in Figure 1). Here microspheres must be compared to other options for hydrogen delivery, e.g. trucked in liquid hydrogen and truck delivered compressed gas tube trailers.

Estimate Of The Charging Time And Maximum Mass Fraction Of Hydrogen That Can Be Stored In A Microsphere Bed, As A Function Of $\Delta r/D$ And Charging Temperature.

In this section, we estimate the charging time and maximum mass fraction of hydrogen stored in the microsphere bed as a function of charging temperature, pressure and microsphere geometry. These calculations are necessary background for later estimates of energy requirements during charging and discharging, and for sizing refueling station equipment.

Estimate of the Charging and Discharging Times for Glass Microspheres

Equations for determining microsphere permeation time constant

Assume that we have a vessel with microspheres being charged from a compressor as shown in Figure 4. The temperature of the microspheres is taken to be Tcharge. The compressor can be designed to provide a constant flow rate of hydrogen at charging pressure and at temperature Tcharge. (It might also be possible to raise the compressor output pressure over time.) Pressure builds up in the interstices of the microsphere bed, and hydrogen permeates through the microsphere shells. The permeation rate is very

sensitive to temperature. In general, the pressure in the interstices (= Po the "outside pressure") and the pressure Pi inside the microspheres will be functions of time

The charging time for a glass microsphere with an outside pressure of $P_o(t)$ and inside pressure of $P_i(t)$ can be found by solving the following equations:

Mass flow across the shell due to permeation is given by:

$$dm_i(t)/dt = 4 \pi r_o^2 K(T) [P_o(t) - P_i(t)]/\Delta r \qquad [1]$$

where:

$m_i(t)$ = hydrogen mass inside one microsphere
r_o = outside radius of microsphere
ri = inside radius of microsphere
K(T) = permeability of microsphere shell to hydrogen at temperature T in units of kg/(s Pa m)
$P_i(t)$ = pressure of hydrogen inside the microsphere
$P_o(t)$ = pressure of hydrogen outside the microsphere
Δr = thickness of microsphere shell

Pressure inside the shell is (from the ideal gas law):

$$P_i(t) = m_i(t) R T/V_i \qquad [2]$$

where:

R = gas constant for hydrogen
T = charging temperature
V_i = volume inside the shell = $4/3 \pi r_i^3$
r_i = inside radius of microsphere = $r_o - \Delta r$

Combining Eqs. 1 and 2, we can solve for $P_i(t)$

$$dP_i(t)/dt = R T K(T) 4 \pi r_o^2/ [(4/3 \pi r_i^3) \Delta r] \times [P_o(t) - P_i(t)] \qquad [3]$$

In the limit $\Delta r << r_o$,

$$dP_i(t)/dt = 3 R T K(T) \times [P_o(t) - P_i(t)] /(r_i \Delta r) \qquad [4]$$

The permeation time constant τ is defined as

$$\tau = r_i \Delta r / [3 R T K(T)] \qquad [5]$$

and Eq. [4] can be rewritten as

$$dP_i(t)/dt = [P_o(t) - P_i(t)] / \tau \qquad [6]$$

Estimate of the permeability K and the permeability time constant τ

Following Rambach (1995, 1996), the permeability of glass to hydrogen is a strongly temperature dependent function given by:

$$K'(T) = Ko\ T \exp(-Q/T) \qquad [7]$$

where:

T = temperature of glass in ^{o}K

K'(T) = permeability of glass to hydrogen at temperature T in units of mol/(m s Pa) = $mol/m^3 \times m^2/(s \times Pa)$

$$Ko = [3.4 + 8 \times 10^{-4} M^3] \times 10^{-17} \qquad [8]$$

M = percentage of network modifers in glass
= 15 for microsphere glass

$$Q = 3600 + 165\ M \qquad [9]$$

Ko = permeability constant in units of mol/(m s Pa ^{o}K)

The permeability K'(T) is plotted in Figure 5 as a function of temperature T. For comparison with earlier work , we also plot K in units of mol/s/m/bar, finding good agreement with these results (Rambach 1995, 1996).

Converting permeability from units of mol/(s m Pa) to kg/(s m Pa), for use in Eqn. 5, we find

$$K(T) = K'(T) \times (kg\ H2/mol) = K'(T) \times 2.016 \times 10^{-3}$$

The permeation time constant τ is shown in Figure 6 as a function of temperature. The glass is essentially impermeable at ambient temperatures (the permeation time constant is tens of thousands of hours). As the temperature increases to 250-350^{o}C, the time constant becomes on the order of 0.1- 1 hour.

Solution for the charging time under various assumptions:

The total charging time is related to the permeation time, but also depends on how the filling is accomplished. Certain limits on the pressure must be observed during charging and discharging to avoid crushing or bursting the microspheres. In addition to limit the cost of compressors and charging vessel materials, pressures of 10,000 psi or less are desirable.

Crushing Limits During Charging

To avoid crushing the microspheres during charging, there is a maximum pressure differential across the shell $dP_{shellmax}$ which must not be exceeded.

$$Po(t) - Pi(t) < dP_{shellmax} \quad [10]$$

$dP_{shellmax}$ is assumed to be is related to the theoretical buckling pressure by:

$$dP_{shellmax} = f_{crush} \times P_{buckle} \quad [11]$$

where:

$dP_{shellmax}$ = maximum pressure difference allowed across the shell

P_{buckle}
= buckling pressure of microsphere under external pressure

$$= 8\ E\ (\Delta r/D)^2\ /\ [3(1-\nu^2)]^{0.5} \quad [12]$$

E = Young's modulus for the glass = 9×10^6 psi
(Rambach 1996)

ν = Poisson's ratio for the glass = 0.22
(Rambach 1996)

f_{crush} = fraction of theoretical buckling pressure allowed across shell . This factor is typically set to 10-20%, to account for imperfections in the shell structure.

D = outer diameter of microsphere = 25-200 microns

Δr = microsphere shell thickness (cm) = 0.5-20 microns

Step filling:

To avoid crushing, the pressure difference across the microspheres must be maintained at less that dPshellmax. One way to do this is to introduce pressure increases in steps. Although Po and Pi increase with time, the pressure difference never exceeds dPshellmax. During each step Po(t) is held constant for a time tstep, until enough hydrogen has permeated across the shell to approximately equalize the external and internal pressure. Then the pressure is stepped up again.

If $P_O(t)$ is held constant = $P_i(t_o) + dP_{shellmax}$ from t = to -> to + tstep, the pressure inside the shell is

$$P_i(t) = P_i(t_o) + dP_{shellmax} \times [1 - \exp(-t/\tau)] \quad [13[$$

where τ is given by Eq. 5.

$$\tau = r_i\ \Delta r/[3\ R\ T\ K(T)] \quad [14]$$

During each step about 3 permeation time constants are required for the internal pressure to reach 95% of the external pressure. The time to achieve a fill to a final pressure of Pcharge is approximately.

t_{charge} = time per step x number of steps needed = [15]

$3\,\tau$ x [Pcharge - $P_i(0)$]/dPshellmax

Ramp filling

If instead, we assume that the pressure difference across the microspheres is kept constant (at the maximum pressure difference allowed to avoid buckling),

$[P_o(t) - P_i(t)]$ = dPshellmax,

we find

$P_i(t) = P_i(0) +$ dPshellmax t/τ [16]

The time for charging is then

tcharge = τ x [Pcharge - $P_i(0)$]/dPshellmax [17]

In is important to note that Equation 17 represents a minimum charging time that can be achieved. It assumes that the permeation rate is well known, so that the compressor mass flow rate can be set to assure a constant pressure difference across the shell. Aside from the buckling pressure, the other factor affecting the charging time is the maximum charging pressure Pcharge which can be used. This is discussed below.

Limits on the Microsphere Charging and Discharging Pressures

The buckling limit determines the pressure difference allowed across the microsphere shell during charging. This was shown above to have an impact on the charging time. To avoid buckling while charging thin-shelled microspheres, a relatively large number of permeation time constants may be required to reach high pressure.

The mechanical properties of the microspheres and of the charging vessel also limit the absolute pressures which can be used on charging and discharging microspheres. This in turn, determines the maximum mass fraction of hydrogen which can be stored, and also impacts the charge and discharge times.

Burst Pressure of the Microspheres

The burst pressure of the microspheres (divided by some appropriate safety factor fs) must not be exceeded at any point during charging and discharging. The pressure difference between the inside pressure and outside pressure must be less than Pburst/fs at all times.

The burst pressure is given by:

P_{burst} = burst pressure of microsphere = $4\,\sigma_{max}\,\Delta r/D$ [18]

f_s = safety factor = 1.5

and:

$D = 2\,r_o$ = outer diameter of microsphere = 25-200 microns
r_o = outer radius of microsphere = 12.5-100 microns
Δr = microsphere shell thickness (cm) = 0.5-20 microns
r_i = inner radius of microsphere 12-80 microns
σ_{max} = hoop stress at failure = 150,000 psi
(engineered microspheres)
= 50,000 psi (commercial microspheres)

The highest likelihood of bursting is probably experienced during microsphere discharge. During discharging the charged microspheres are heated, and pressure builds up inside the spheres, from ambient storage pressure to some maximum. Since the permeation rate is a very sensitive function of temperature, the pressure inside the charged microspheres is not significantly decreased via permeation until discharge temperature is reached. In the case that the microspheres are heated relatively quickly to discharge temperature (e.g. the microsphere heating time is faster than the permeation time constant), the maximum pressure experienced during heating can be approximated by:

$$P_{inmax}(T_{discharge}) = P_{in}(T_{amb}) \times T_{discharge} \times Z(P_{inmax},T_{discharge})/(T_{amb} \times Z[P_{in}(T_{amb}), T_{amb}] \quad [19]$$

where:

Tdischarge = discharge temperature in degrees K

Tamb = ambient storage temp (^oK)

Pinmax(Tdischarge) = maximum pressure inside microsphere during discharge

Pin(Tamb) = pressure stored inside charged microsphere at ambient temperature Tamb

Z(Pinmax, Tdischarge) = compressibility of hydrogen at Pinmax, Tdischarge

Z[Pin(Tamb),Tamb]= compressibility of hydrogen at Pin(Tamb),Tamb

The pressure stored in the microspheres is related to the charging pressure and temperature as well by:

$$P_{in}(T_{amb}) = P_{charge} \times T_{amb}/T_{charge} \times Z[T_{amb}, P_{in}(T_{amb}]/Z(P_{charge}, T_{charge}) \quad [20]$$

Combining Eq.s 19 and 20 we find that the maximum pressure experienced by the microspheres during discharge can be related to the charging pressure and temperature as:

$$P_{inmax}(T_{discharge}) = P_{charge} \times T_{discharge}/T_{charge} \times Z(P_{inmax},T_{discharge})/Z(P_{charge}, T_{charge}) \quad [21]$$

If Tcharge = Tdischarge, Pinmax(Tdischarge) = Pcharge

If Tcharge = Tdischarge, the maximum internal pressure experienced by the microspheres during discharging is about equal to the charging pressure. So the burst pressure limit on the internal pressure during discharging translates into a limit on the charging pressure.

Pinmax(Tdischarge) = Pcharge, if Tcharge = Tdischarge

Pinmax(Tdischarge) < Pburst/fs, (to avoid bursting on discharge)

=> Pcharge < Pburst/fs [22]

Limits on the pressure allowed in the charging vessel

In addition, there is a maximum practical charging pressure Pmax in the charging vessel, which must not be exceeded. This is determined by materials limits on the charging vessel to perhaps 10,000 psi.

Pcharge < 10,000 psi [23]

Combined Limits on the Charging Pressure

In Figure 7 we plot the maximum allowed charging pressure as a function of microsphere aspect ratio $\Delta r/D$. We see that for thin microspheres, the charging pressure is limited by the burst pressure on discharge. At higher aspect ratios, the pressure vessel materials limit of 10,000 psi, sets a maximum on the charging pressure.

Charging Time as a Function of Charging Temperature and Microsphere Aspect Ratio

Limits on the charging pressure determine the charging time required to charge or discharge microspheres. The charging time is shown in Figure 8 as a function of microsphere aspect ratio and charging temperature, for ramp filling. [For step filling, the charge time would be about three times longer (Figure 9).] The charging time is strongly temperature dependent. Somewhat surprisingly, the thicker the shell (the larger $\Delta r/D$), the shorter the total charge time. This is true because the buckling limit dPshellmax is higher for thicker shells, so a larger pressure difference can be tolerated across the shell. Although the permeation time constant increases with $\Delta r\, r_i$, fewer time constants are needed to reach Pcharge, and the total charging time is reduced.

Estimate of the Maximum Mass Fraction of Hydrogen That Can Be Stored in the Bed

The limits on the charging pressure determine the maximum mass fraction of hydrogen which can be stored.

We assume an equation of state for hydrogen given by:

$$P = \rho H2\ Z\ R\ T \qquad [24]$$

where:

P = pressure

ρH2 = mass density of hydrogen at P,T
Z = compressibility at P,T
R = gas constant for H2
T = temperature

A useful equation for the hydrogen density is

$$\rho H2\ (P,T) = \rho H2_{ref} \times P/[T\ Z(P,T)\ ]/\ [P_{ref}/(T_{ref}\ Z_{ref})] \qquad [25]$$

For

Tref = 20°C
Pref = 1 atm

$\rho H2_{ref}$= 0.0841 kg/m^3
Zref = 1

The compressibility for hydrogen can be estimated as a function of temperature and pressure. We have used values from Black and Hartley, p. 726, to roughly estimate Z at several temperatures:

We find very approximately, for P/Pcrit>5,

$$Z(P, T=20\ C) = 1 + (P/Pcrit - 5) \times 0.0143 \qquad [26]$$

$$Z(P, T=150\ C) = 1 + (P/Pcrit - 5) \times 0.0101$$

$$Z(P, T=250\ C) = 1 + (P/Pcrit - 5) \times 0.0079$$

$$Z(P, T=350\ C) = 1 + (P/Pcrit - 5) \times 0.0062$$

Where

Pcrit = critical pressure for H2 = 191.1 psi
(Black + Hartley, p.741)

A more general expression for Z(P, T) can be derived from the data shown in Black and Hartley

This is given by:

$$Z\ (P,T) = 1 + (P/Pcrit - 5) \times [2.754 \times (T/Tcrit)^{-0.279} - 1]/35 \qquad [27]$$

where: Tcrit = 33.3°K

The compressibility of hydrogen is plotted in Fig 10 as a function of P and T.

The mass fraction of hydrogen which can be stored in the microsphere bed is given by:

$$f_{H2max} = \frac{4\pi/3\, r_i^3 \times \rho H2(P_{charge},T_{charge})}{[4\pi/3\, r_i^3 \times \rho H2(P_{charge},T_{charge}) + 4\pi/3\,(r_o^3 - r_i^3) \times \rho_{glass}]}$$

$$= \frac{\rho H2(P_{charge},T_{charge})}{\{\rho H2(P_{charge},T_{charge}) + [(r_o/r_i)^3 - 1] \times \rho_{glass}\}} \qquad [28]$$

where:

ρ_{glass} = density of glass in microsphere = 2500 kg/m^3

The maximum mass fraction of hydrogen which can be stored, using the limiting charging pressure in Figure 7, is shown in Figure 11. We see that for small aspect ratios, the maximum mass fraction is determined by the burst pressure on discharge, and for higher aspect ratios by the charging vessel pressure limit of 10,000 psi. The maximum mass fraction is limited to perhaps 6%. Thinner shells are favored to increase the mass fraction stored.

A Proposed Charging Cycle

A proposed charging and discharging cycle was developed.

We assume that the maximum charging pressure allowed is given by Eq.s 22 and 23. For thin shells, the limit is determined by the burst pressure on discharge, and for thicker shells by the maximum pressure the charging vessel can withstand (=10,000 psi) at charging temperatures of 250-350°C.

The following steps are followed while charging the microspheres with hydrogen:

1) The microspheres are heated to charging temperature (250-350°C)

2) Hydrogen is compressed from 150 psi (the assumed pressure from the hydrogen production system) to the limiting charging pressure allowed (See Figure 7).

3) Hydrogen is heated to charging temperature. This may be done as part of compression or separately.

4) The hydrogen is introduced into the charging vessel. The rate at which the hydrogen flows into the charging vessel is set so that the maximum allowed differential pressure across the shell (dPshellmax = some fraction of the buckling pressure) is not exceeded. (Generally, the pressure difference should be less than about 10-20% of the buckling pressure according to Woerner et. al.). The pressure difference across the shell is kept less than dPshellmax as the pressure inside the sheels and in the interstices increases with time. At the end of charging, the hydrogen in the spheres and in the interstices is at Pcharge.

5) The microsphere vessel is closed and cooled to ambient temperature Tamb = 20°C. The final pressure inside the microspheres is about Pin(Tamb) = Pcharge x Tamb x Zamb/ (Tcharge x Zcharge). For charging temperatures of about 300°C, this is roughly half the charging pressure.

6) The pressurized hydrogen remaining in the interstices of the bed is purged from the charging vessel, and used to charge up the next microsphere bed.

7) The cooled, fully charged microspheres are trucked to a remote site for discharging.

During discharge the microspheres are heated to discharge temperature (250-350°C). As the hydrogen is released from the spheres, it is introduced into intermediate storage pressure cylinders, prior to use for refueling. The pressure of the hydrogen released depends on the flow rate out of the spheres. It will decrease with time, as the microspheres are discharged. In any case, the maximum pressure which can be recovered is significantly less than the charging pressure.

Energy Required For Microsphere Charging And Discharging

Before working out conceptual designs of hydrogen refueling stations using microsphere storage, we estimate the energy requirements for microsphere charging and discharging. The energy requirements are for heating (both the glass in the microspheres themselves, and the hydrogen), and for hydrogen compression.

Energy Required to Heat Glass

Assuming we know the mass fraction fH2 of hydrogen stored in the bed, the energy stored in the bed is

EH2 (kJ/kg bed) = fH2 (kg H2 stored/kg bed) * HHV H2 (kJ/kg) [29]

where:

EH2 = hydrogen energy stored per unit of total bed mass including spheres and hydrogen (kJ/kg bed)
fH2 = mass fraction of hydrogen in the bed (kg H2/kg bed)
HHV H2 = higher heating value of hydrogen = 142,400 kJ/kg

The mass fraction of glass in the bed is simply 1-fH2. So the energy required to heat the glass from Tamb to Tcharge is:

Qheatglass = (1-fH2) x cglass x (Tcharge - Tamb) [30]

where:

Qheatglass = energy required per kg of bed mass to heat glass (kJ/kg bed mass)
(1-fH2) = glass mass fraction of bed mass
cglass = specific heat of glass = 0.84 kJ/kg/°K
Tcharge = microsphere charging temperature (°K)
Tamb = ambient temp = initial temp of microspheres(°K)

The ratio of the energy required to heat the glass to the hydrogen stored is given by

Rheatglass =
Qheatglass/EH2 = (1-fH2) x cglass x (Tcharge - Tamb)/(fH2* HHV H2)
[31]

Based on the maximum hydrogen mass fractions calculated above as a function of aspect ratio and charging temperature, we can estimate the ratio Rheatglass as a function of charging temperature and microsphere aspect ratio. This turns out to be 2.5-5% of the higher heating value of hydrogen stored for typical values. As the aspect ratio increases, so does the amount of glass and the heating requirement.

Energy to Compress Hydrogen to Charging Pressure

The compressor power for isentropic compression is calculated via:

P_{cm}=

$$Q_h \times (P_b/T_b) \times (T_1/n_c) \times Z \times [N\gamma/(\gamma-1)] \times [(P_{out}/P_{in})^{[(\gamma-1)/N\gamma]} - 1]/1000 \quad [32]$$

where:

P_{cm} = compressor power requirement (kW)
Q_h = gas flow rate in Nm^3/s
P_b = reference pressure = 101,300 Newtons/m^2 (atmospheric pressure)
T_b = reference temperature = 298°K
T_1 = initial gas temperature = 298°K
P_{in}=inlet pressure to compressor
P_{out}=outlet pressure from compressor
N = number of compressor stages
n_c = compressor efficiency = 55% for small hydrogen compressors (100 kW - 1 MW) and 70% for large (pipeline scale) natural gas and hydrogen compressors.
Z = compressibility = (see eqn. 26 for Z(P,T))
γ = ratio of specific heats
(for hydrogen = 1.41)

For hydrogen the compressor power needed is given by:

$$P_{cm}H2 = Q_{scfsH2} \times 9.84/n_c \times Z \times N \times [(P_{out}/P_{in})^{0.291/N} - 1] \quad [33]$$

where:

Q_{scfsH2} = hydrogen flow rate in scf/s

The energy required for compression is given by (in kJ electric energy/scf H2 compressed):

$$Ecompress = P_{cm}H2/Q_{scfsH2} = 9.84/n_c \times Z \times N \times [(P_{out}/P_{in})^{0.291/N} - 1] \quad [34]$$

Not all the hydrogen that is compressed permeates into the microspheres -- some is left in the interstices. So we compare the compression energy requirements to the energy of the hydrogen that is actually stored in the microspheres. Comparing the total volume of hydrogen compressed to that which is actually stored, we see that the fraction of the bed volume taken up by the inside of the microspheres is

$$fp \times (ri/ro)^3$$

Where

fp = packing fraction = 0.63 for uniform sized spheres. (This might be made higher for bimodal distrbutions of sphere sizes.)

The fraction taken up by the interstices is

$$(1-fp)$$

The rest of the space is taken up by the glass shells.

The ratio of the energy required to compress the hydrogen to the total hydrogen energy stored in the bed is given by

$$Rcompress = Ecompress\ [1-fp + fp \times (ri/ro)^3]/[fp \times (ri/ro)^3 \times HHV\ H2] \quad [35]$$

For the range of values considered, compression requires electrical energy equal to about 6-8% of the higher heating value of hydrogen stored.

At least some of the compression energy spent on hydrogen left in the interstices can be recovered, however. The hydrogen left in the interstices is assumed to be purged at high pressure after charging and cooling, and is used to partially charge a second microsphere bed. Extracting this hydrogen at pressure saves on compression costs for the second bed.

The amount of compression energy which might be saved can be approximated by estimating the volume of hydrogen gas available in the interstices and its pressure, as compared to the volume and pressure needed to charge the next bed.

$$\text{Volume in interstices/Total Charging Volume Needed} = (1-fp)/[1-fp + fp \times (ri/ro)^3]$$

Assuming that

fp = 0.63
ro=25 cm
ri = 24 cm

We find that the Volume in interstices/Total Charging Volume Needed = 0.40

$$\text{Pressure of cooled gas in the interstices} = P_{interstices}(T_{amb}) = P_{charge} \times T_{amb}/T_{charge} \times Z[T_{amb}, P_{insterstices}]/Z(P_{charge}, T_{charge})$$

As an example, we assume:

$$T_{amb} = 20^oC$$

Tcharge = 350°C
Pcharge = min(Pburst/fs, 10000 psi) = 8000 psi, if Δr/D = 0.02
Z is given by Eq. 26

For these assumptions, we find (reading Z from Fig 10)

Pinterstices(20°C) = 8000 psi x (293°K/623°K) x 1.5/1.2 = 4700 psi

For this case, about 40% of the hydrogen gas volume needed to recharge a second bed has already been raised to 4700 psi. To compress 4700 psi hydrogen to 8000 psi requires only 13.6% as much energy per scf as raising 200 psi hydrogen to 8000 psi. So the overall hydrogen compression requirement is reduced by about 35%.

For the assumed values in this example, hydrogen compression from 200 to 8000 psi requires electrical energy equivalent to about 7% of the HHV of the hydrogen stored. If pressurized hydrogen is recovered from the interstices of a cooled bed for use in a second bed, about 35% of this energy can be saved, so this number is reduced to about 4.6% for the second bed. In theory, if a sequence of beds are being charged, so that some cooled hydrogen is always available for recovery, the compression requirement could approach 4.6%.

The recovered hydrogen must still be heated to charging temperature, which adds to energy requirements.

Energy to Heat Hydrogen to Charging Temperature

Hydrogen is assumed to be heated prior to introduction into the charging vessel. The hydrogen inside the microspheres plus that in the interstices must be heated. The energy to heat hydrogen from ambient to charging temperature can be estimated as follows:

EheatH2 =

$$cH2 \times (Tcharge - Tamb) \times \rho_{H2}(Pcharge, Tcharge) \times [1 - fp + fp \times (ri/ro)^3] \quad [36]$$

where:

EheatH2 = the energy required per unit of bed volume to heat hydrogen from Tamb to Tcharge (kJ/m3 bed volume)
cH2 = specific heat of hydrogen = 14.6 kJ/kg °K
Tcharge = charging temperature
Tamb = initial temp of hydrogen
$[1-fp + fp \times (ri/ro)^3]$ = fraction of bed volume taken up by interstices plus the inside of the spheres

The energy stored in hydrogen per unit of bed volume is

$$EH2stor = [fp \times (ri/ro)^3 \times HHV\ H2] \times \rho_{H2}(Pcharge, Tcharge)$$

The ratio of the heating energy required to the hydrogen energy stored is

RheatH2
= EheatH2/EH2stor =

$$cH2 \times (Tcharge-Tamb) \times [1-fp + fp \times (ri/ro)^3]/[fp \times (ri/ro)^3 \times HHV\ H2] \quad [37]$$

For the range of values considered, hydrogen heating requires energy equivalent to about 5% of the HHV of hydrogen stored.

However, this may be an overestimate of the heat energy required, as some heating will occur during compression. If we assume isentropic compression the ratio of the inlet and outlet gas temperatures from the compressor is given by:

$$(T2/T1) = (P2/P1)^{(k-1)/k} \quad [38]$$

where:

T2 = outlet temperature (^oK)
T1 = inlet temperature (^oK)
P2 = outlet pressure
P1 = inlet pressure
k = ratio of specific heats = 1.41 for hydrogen

Assuming that T1=20^{o}C and P1 = 200 psi,

we find that for P2 = 10,000 psi, the outlet temperature is 642^{o}C.
If P2 = 5000 psi, T2 = 475 ^{o}C. The hydrogen exiting the compressor will be hot enough as a result of compression, so that no extra heating is needed.

Depending on the compressor design, we may decide to cool the gas between stages. In this case, we can assume isothermal compression until the last stage or two. If we assume that the first two stages in a four stage compressor are intercooled and allow isentropic compression for the last two stages, the outlet temperature of the hydrogen gas should be about 370^{o}C. If all but the last stage is intercooled, the exit temperature is about 165^{o}C.

In the case described in the previous section where some of the hydrogen for recharging a second bed is recovered from the interstices of a cooled bed, the temperature rise in compression is modest, perhaps 65-80^{o}C. So the hydrogen gas heating requirement for the recovered hydrogen from the interstices is reduced by only 20-25%. In this case, if we claim a reduction of compression energy from 7% to 4.6% (by recovering hydrogen from the interstices), it would be fair to claim an overall reduction in the hydrogen heating requirement of about 70% (by allowing heating during compression). Hydrogen heating requires energy equivalent to 5% of the HHV of hydrogen stored. If this is reduced by 70%, the requirement would be only 1.5%. So in an optimal case, with credits for both 1) compression energy recovered from hydrogen in the interstices and 2) heating during compression, we might reduce the overall energy requirements by about 6%.

Energy to Heat Glass During Discharge

This will have the same form as the energy requirement for heating glass for charging.

$$Rheatglass = (1-fH2) \times cglass \times (Tdischarge - Tamb)/(fH2^* HHV\ H2) \quad [39]$$

This is about 2.5-5% of the higher heating value of hydrogen stored

Energy to Heat Stored Hydrogen During Discharge

During discharge, we need only heat the hydrogen actually stored in the microspheres. The ratio of the heating energy required to the hydrogen energy stored is

$$RheatH2 = cH2 \times (Tcharge-Tamb)/ HHV\ H2 \qquad [40]$$

The heating requirement on discharge is about 2.8-3.3% of the higher heating value of hydrogen stored for discharge temperatures of 300-350°C.

Energy Requirements For The Proposed Charging And Discharging Cycle

Using the equations above, the energy requirements for microsphere charging and discharging can be estimated. These are shown in Figures 12 and 13 as a function of microsphere aspect ratio ($\Delta r/D$) and charging/discharging temperature. We see that microsphere charging and discharging takes energy equal to perhaps 18-28% of the higher heating value of the stored hydrogen energy to accomplish. The total charge/discharge cycle energy requirements are still considerably less than those for liquid hydrogen (which are roughly 33-40%). However, these figures are conservative in that they assume no credit for hydrogen heating during compression or for avoiding compression by recovering hydrogen from the interstices of charged cooled beds at pressure.

The total charging energy requirement might be reduced about 3-4 percentage points by allowing heating during compression (so that the hydrogen need not be heated separately during charging). Another way of reducing charging energy requirements is by recovering the hydrogen from the interstices of a charged, cooled bed at pressure, as partial input to a second bed to be charged. (The energy saving here might be 2-3 percentage points or so.) As discussed above, the total charging energy reduction might be about 6% of the HHV of hydrogen. The energy required for discharge is determined by the heat capacities of hydrogen and glass. If energy reductions are taken for recovering hydrogen from the interstices, and for heating hydrogen during compression, the overall energy requirements for charging and discharing are reduced (see Figure 14) to perhaps 13-20% of the HHV of hydrogen.

From the standpoint of energy requirements, lower aspect ratio microspheres are favored, as they have lower glass heating requirements. They will also have a higher mass fraction of hydrogen stored.

From Figures 9 and 13, we see that there is a trade-off between higher energy requirements at higher charging/discharging temperatures, vs. faster charge and discharge times.

Optimizing these factors with the rest of the station requirements is a topic for future work.

Conclusions to Date

* Preliminary estimates of the requirements for refueling stations with glass microspheres were made. Refueling stations where microspheres are charged remotely and trucked in for discharge were identified as a prefered design.

* Estimates were made of the microsphere charging time as a function of charging temperature and microsphere aspect ratio ($\Delta r/D$). The charging time depends on the permeation time constant (which is in turn strongly temperature dependent). For typical values the permeation time constant is on the order of 0.1-1.0 hours for charging temperatures of 250-350°C.

* The charging time also depends on how the filling is accomplished. Certain limits on the pressure must be observed during charging and discharging to avoid crushing or bursting the microspheres. In addition to limit the cost of compressors and charging vessel materials, pressures of 10,000 psi or less are desirable.

* To avoid crushing the microspheres, the maximume allowed pressure difference across the microsphere shell dPshellmax must be kept less than some fraction (taken here to be 10-20%) of the theoretical buckling pressure. This determines the charging time:

$t_{charge} = \tau \times (P_{charge} - P_{init})/dP_{shellmax}$ (for ramp filling, the best case)

where τ is the permeation time constant.

* To avoid bursting the microspheres on discharge, the charging pressure must be kept below the theoretical burst pressure Pburst divided by some safety factor.

$P_{charge} < P_{burst}/fs$

In addition, there are charging vessel material and compressor constraints, which limit the charging pressure to less than 10,000 psi. In general the maximum charging pressure allowed is:

$P_{charge} = \min (10000 \text{ psi}, P_{burst}/fs)$

* The maximum mass fraction of hydrogen that can be stored was estimated as a function of microsphere aspect ratio and charging temperature. The maximum storage was possible for small aspect ratios (0.01-0.02). A maximum of about 6% hydrogen by weight could be stored (limited by avoiding bursting the microspheres on discharge).

* A charging and discharging cycle was proposed. The energy required for charging and discharging was found to be 13-20% of the higher heating value of hydrogen, if heating is allowed during hydrogen compression, and if pressurized hydrogen is recovered from the interstices of charged, cooled beds for use in charging a second bed. (If

no credits were taken, these numbers were about 6 percentage points higher.) Lower aspect ratios were favored for low energy requirements.

* There is a tradeoff between higher energy requirements at higher charging temperatures vs. faster charging times.

Future Work: Conceptual Design of a Hydrogen Refueling Station with Glass Microsphere Storage

A refueling station using glass microspheres is sketched in Figure 1. In future work we will size the equipment needed. This includes the following:

1) Vessels for storing enough charged microspheres for one day's hydrogen demand (assuming that microspheres are truck-delivered once a day).

2) Vessels for holding discharged microspheres for truck pick-up and return to a central recharging site.

3) A discharge chamber, where microspheres are heated to discharge temperature, and hydrogen is taken off at pressure. The total discharge time is on the order of one or more hours. The microsphere bed can be thought of as a hydrogen source which produces hydrogen at a constant rate over a period of hours. To match a variable demand such as vehicle refueling, some buffer storage is needed.

4) Heat exchanger for cooling the hydrogen from discharge temperature to ambient.

5) A compressor where the hydrogen is compressed from it's discharge pressure to an intermediate storage pressure of 5000 psi.

6) A set of buffer gas cylinders for intermediate storage of hydrogen at 5000 psi. This helps meet variable demand for fuel during the day. The buffer would hold enough hydrogen to meet spikes in demand.

7) A booster compressor to boost the hydrogen withdrawn from buffer storage to dispensing pressure.

8) A dispenser to vehicles.

Economic comparisons can then be carried out. We will estimate the economics of delivering hydrogen transportation fuel to vehicles for refueling station designs with glass microsphere storage, considering both the capital cost of refueling stations and the delivered cost of hydrogen transportation fuel. Finally we will compare refueling stations with microspheres to other hydrogen refueling station options.

For refueling station applications, it may be especially interesting to compare microspheres to liquid hydrogen. In each case, gaseous hydrogen produced centrally at large scale and low cost, and then put into a stored form (e.g. liquid hydrogen or microspheres) that is more readily transported. The stored hydrogen (liquid hydrogen or microspheres) is trucked to a refueling station. Gaseous hydrogen at 5000 psi is made available by processing the transported liquid hydrogen or microspheres at the refueling station.

Acknowledgements

This work was performed under the auspices of the U. S. Department of Energy by Lawrence Livermore National Laboratory under contract No. W-7405-Eng-48.

References

Black, W.Z. and J.G. Hartley 1985. Thermodynamics, Harper and Row, New York.

Ogden, J.M., E. Dennis, M. Steinbugler and J. Strohbehn Jan. 18, 1995. "Hydrogen Energy Systems Studies," final report to USDOE for Contract No. XR-11265-2.

Ogden, J.M. January 19-22, 1997. "Infrastructure for Hydrogen Fuel Cell Vehicles: A Southern California Case Study," Proceedings of the '97 World Car Conference, Riverside, CA.

Ogden, J.M., M. Steinbugler and T. Kreutz, March 11-13, 1997. "Hydrogen as a Fuel for Fuel Cell Vehicles: A Technical and Economic Comparison," Proceedings of the 8th National Hydrogen Association Meeting.

Rambach, Glenn D. and Charles Hendricks, May 1-2, 1996. "Hydrogen Transport and Storage in Engineered Glass Microspheres," Proceedings of 1996 USDOE Hydrogen Program Review Meeting, Miami, FL, NREL/CP-430-21968, pp. 765-772.

Rambach, Glenn D. April 18-21, 1995 "Hydrogen Transport and Storage in Engineered Glass Microspheres," Proceedings of 1995 USDOE Hydrogen Program Review Meeting, Miami, FL, NREL/CP-430-20036, pp. 509-520.

Rambach, Glenn D., March 7-9 1995. "Hydrogen Transport and Storage in Engineered Glass Microspheres," Proceedings of the Sixth Annual U.S. Hydrogen Meeting, National Hydrogen Association, 1800 M Street NW, Washington, DC 20036, pp. 163-172.

Rambach, Glenn D. and Charles Hendricks, April 1994. "Hydrogen Transport and Storage in Engineered Glass Microspheres," Proceedings of 1994 USDOE Hydrogen Program Review Meeting, Coral Gables, FL.

Souers, P.C., I. Moen, R.O. Lindahl, and R.T. Tsugawa, 1978. "Permeation Eccentricities of He, Ne, and D-T in Soda-Lime Glass Microbubbles," Journal of American Ceramic Society, vol. 61, No.1-2, pp. 42-46.

Woerner, R.L., B.W. Weinstein, I Moen, and J. Rittmann, 1979. "Working Strengths and D-T Fill Procedures for Glass Microsphere Laser Fusion Targets," Technical Report UCRL-82728, Lawrence Livermore National Laboratory.

TABLE 1. ASSUMED CHARACTERISTICS OF FUEL CELL VEHICLES

	PEM FC Bus	PEM FC Car
Fuel economy	52 scf H2/mile = 6.9 mpg Diesel equivalent [a]	106 mpg gasoline equiv. on the combined FUDS/FHDS drving cycle[b]
Miles/yr	50,000[c]	11,140[d]
Fuel Storage	H2 gas @3600 psi	H2 gas @5000 psi, assuming 7.5% hydrogen storage by weight and 50 kg total
Hydrogen stored onboard (scf)	13,000[a]	1475
Range (mi)	250[a]	425[b]
Energy use per year (GJ/yr)[e]	976	13.7
Hydrogen use per day (scf/day)	7120	104
Hydrogen use per year (million scf/yr)[f]	2.60	0.038

a. Based on the efficiency of the Ballard Phase II PEMFC bus (Larson, Worrell and Chen 1996). The mile per gallon gasoline equivalent efficiency for a fuel cell vehicle is estimated assuming that 1 gallon of gasoline contains 0.1308 GJ (HHV) and that 1 scf of hydrogen contains 362 kJ (HHV).

b. For a mid-size automobile, with PNGV type characteristics ("glider weight"=800 kg, aerodynamic drag coeff = 0.20, rolling resistance=0.007), and a PEM fuel cell. (See Ogden, Steinbugler and Kreutz 1997).

c. Typical annual mileage for a bus in the LA Basin (E. Chaiboonma, LA Metropolitan Transit Authority, private communications 1995, 1996).

d. Typical annual mileage for a passenger car in the LA Basin. (R. George, SCAQMD, private communications 1995, 1996).

e. Energy use was estimated assuming that the HHV of gasoline is 0.1308 GJ/gallon.

f. Hydrogen use was estimated based on the HHV of hydrogen, 362 GJ = 1 million scf

TABLE 2. FUEL CELL VEHICLES AND HYDROGEN USE

Hydrogen Use	FCVs refueled/day	Total Fleet Fueled
1 million scf H2/day	700 FCV cars/day	Total fleet of 9615 FCV cars
	80 FC Buses/day	Total fleet of 140 FCV Buses

The hydrogen use per for an average fuel cell vehicle is calculated as follows.

Hydrogen use per day per FCV (scf H2/day) =
Annual mileage (mi)/365 days/yr /Equiv. Fuel Economy (mi/gallon gasoline equiv. energy)
x Gasoline HHV (GJ/gallon)/ H2 HHV (GJ/scf)

If a station dispenses 1 million scf/day, it could supply a fleet of FCVs given by:

FCVs in fleet = 1 million scf/day/Hydrogen use per day per FCV (scf H2/day)

The hydrogen demand per day from a refueling station would be given by:

H2 dispensed per day (scf/day) = # vehicles in fleet supported x
H2 demand per vehicle per day (scf/vehicle/day)

The number of vehicles served daily in the refueling station can then be calculated. We assume that the vehicles refuel when the tank is close to empty. If the range of the vehicle is known, we can estimate how many times it must refuel per year, and how many vehicles are refueled on average per day.

Refuelings/year/vehicle = Annual mileage (mi)/Range (mi)
Cars refueled per day
= # Refuelings per year/365 days/year x Total fleet of vehicles served
= Annual mileage (mi)/Range (mi) /365 days/year x Total fleet of vehicles served

Annual mileage, range and fuel economy for PEMFC passenger cars and buses are taken from Table 1.

Figures

Figure 1. Microsphere Hydrogen Storage for Use in Refueling Stations: Remote Microsphere Recharging

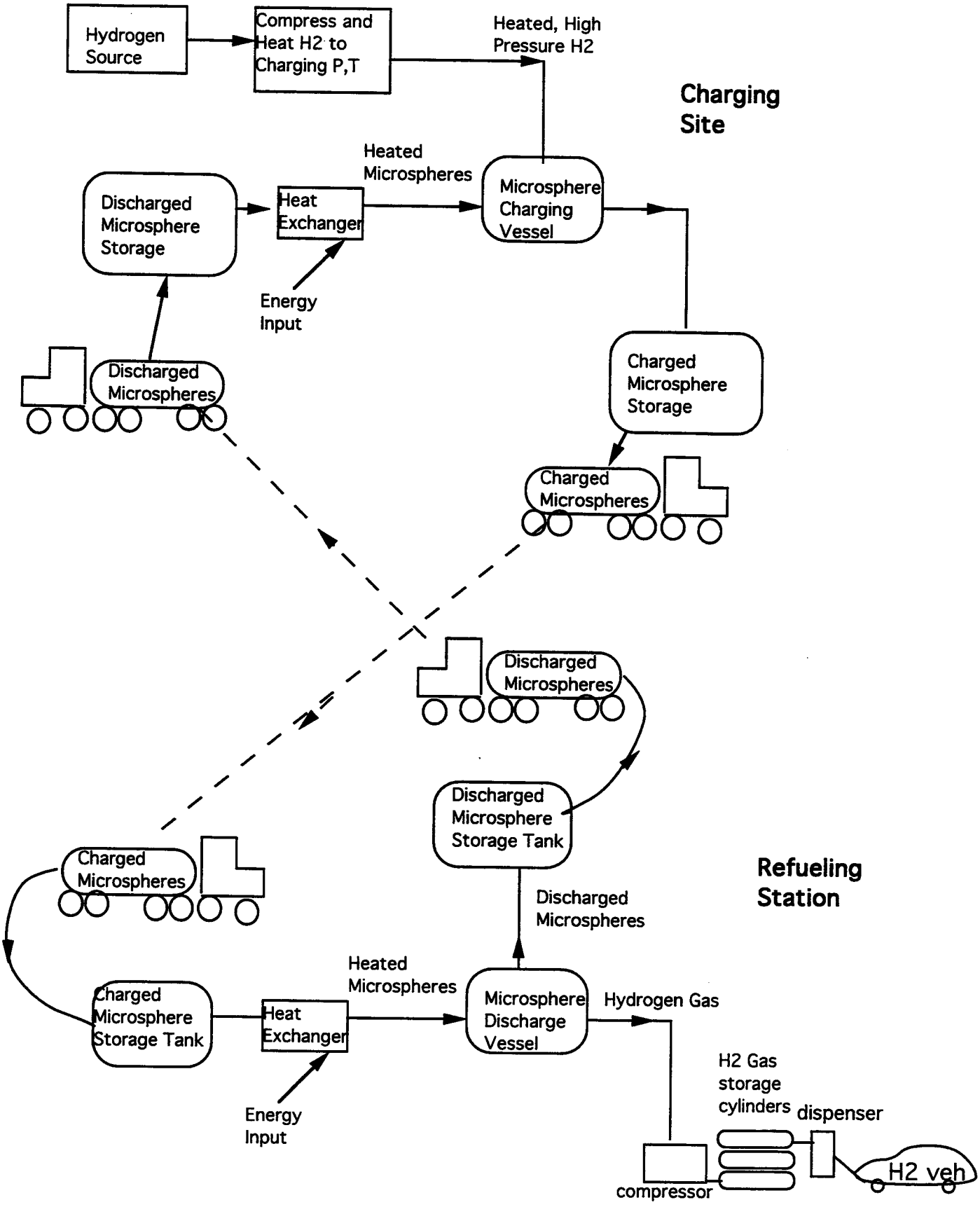

Figure 2. Microsphere Hydrogen Storage for Use in Refueling Stations: Microsphere Charging at Station

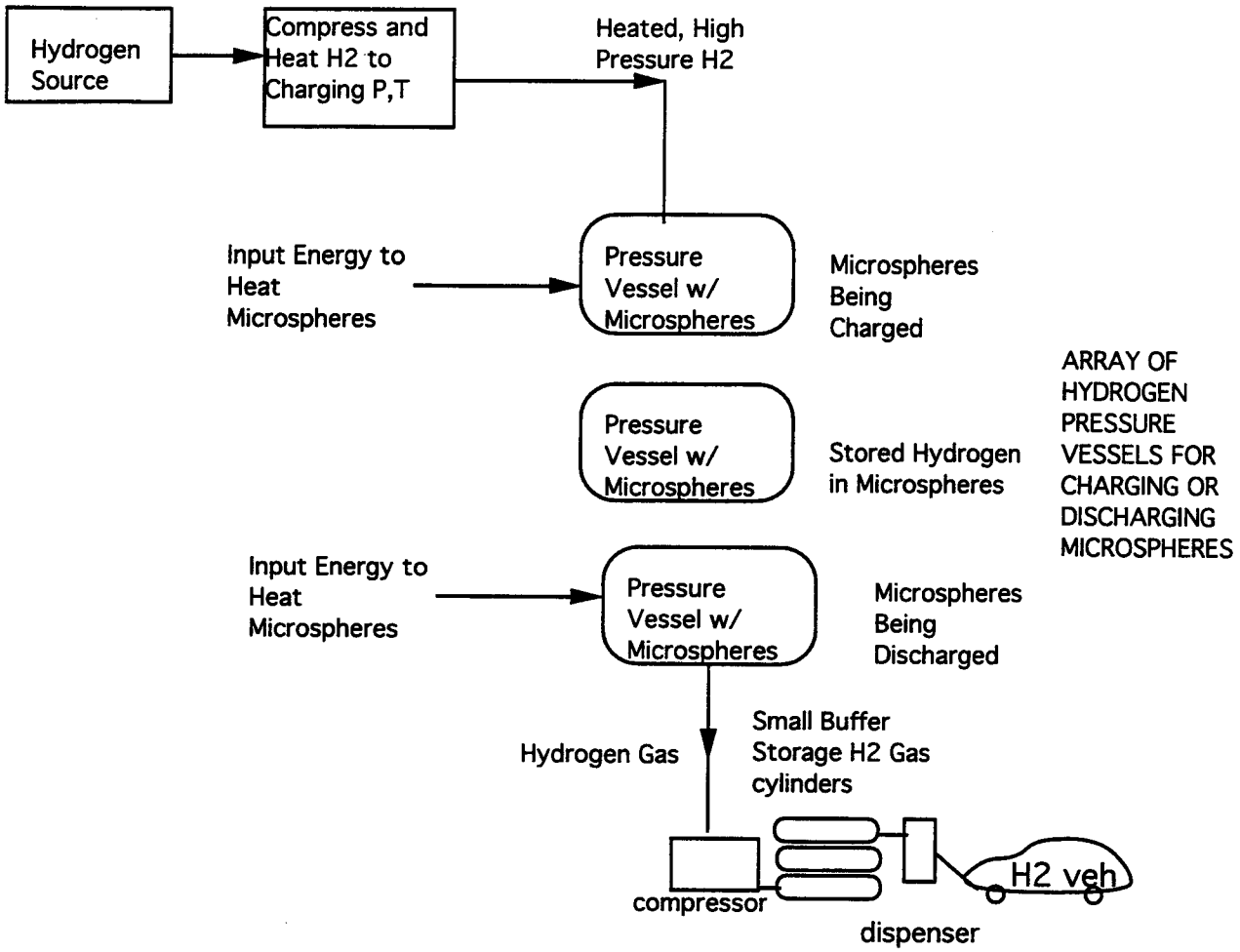

Figure 3. Hydrogen Refueling Station with Compressed Gas Storage

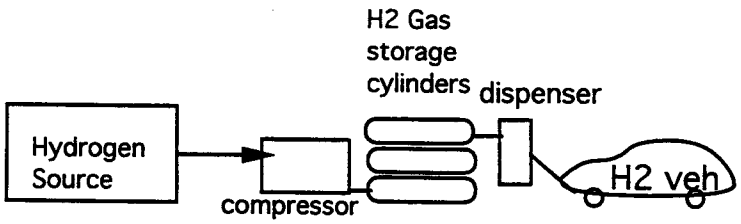

Figure 4. Glass Microsphere Charging System

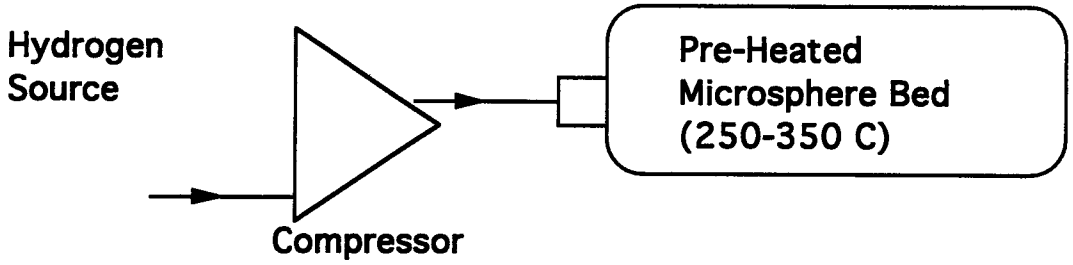

Individual Microsphere During Charging

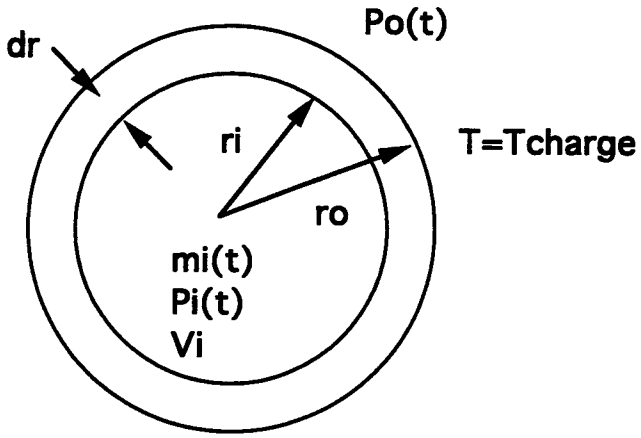

Fig. 5. Permeability K(T) as a function of Glass Temperature

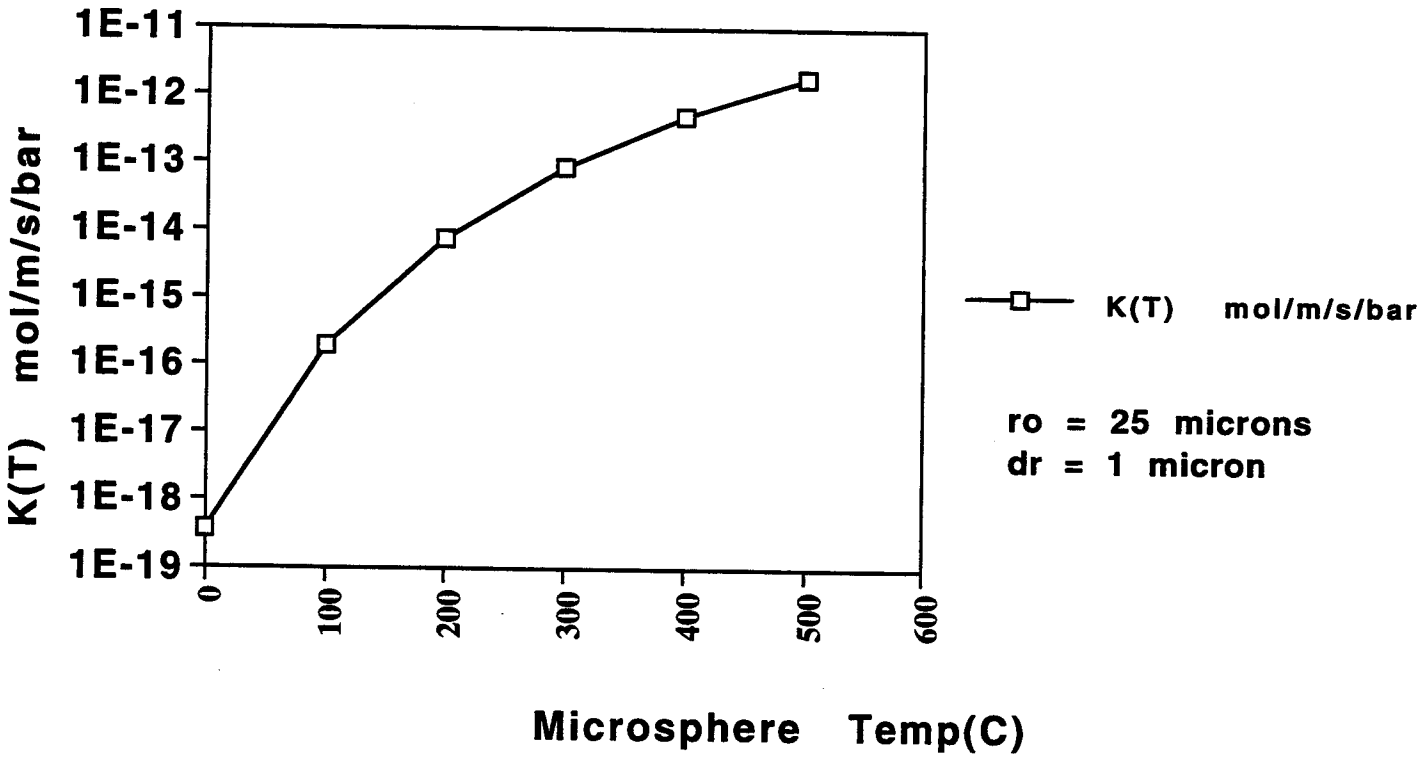

Fig. 6. Permeation Time Constant (hr) for Glass Microspheres With H2 vs. Glass Temperature

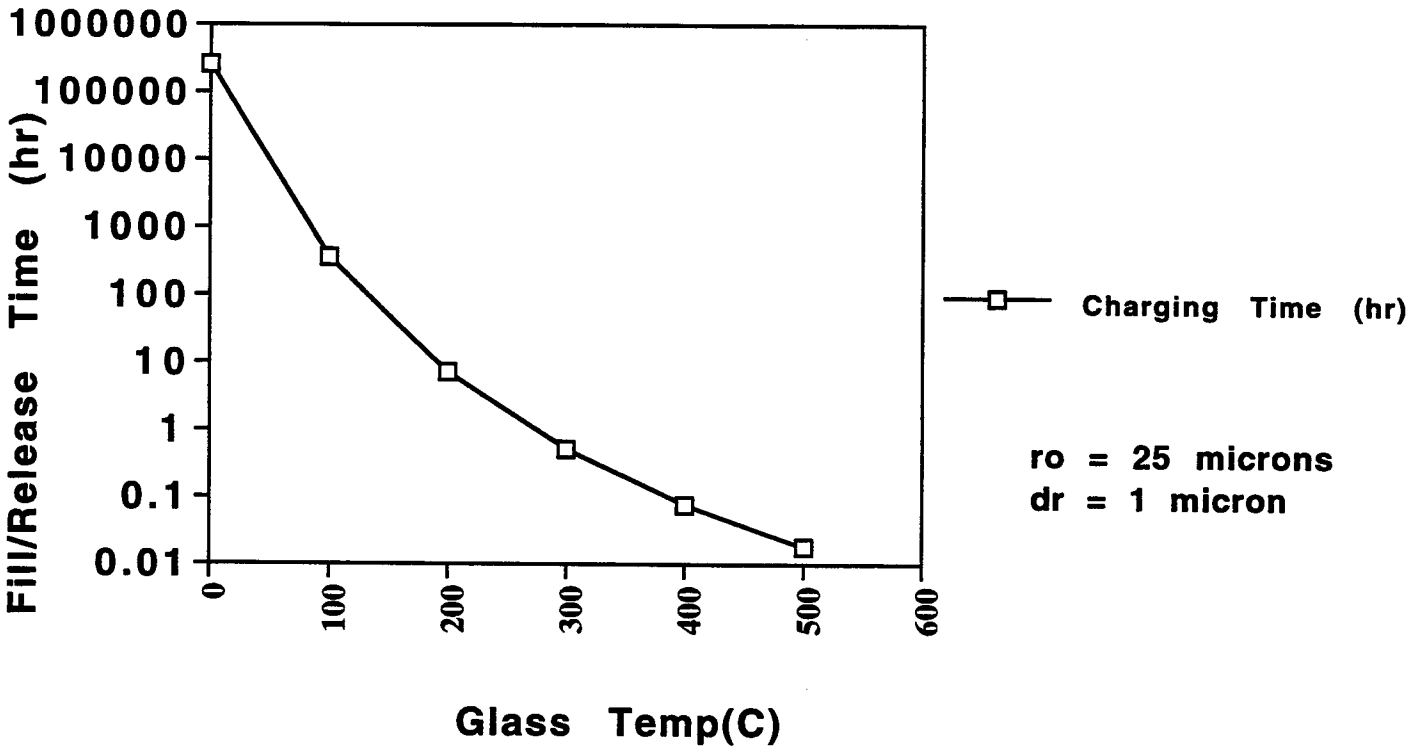

Fig. 7. Maximum Allowed Charging Pressure

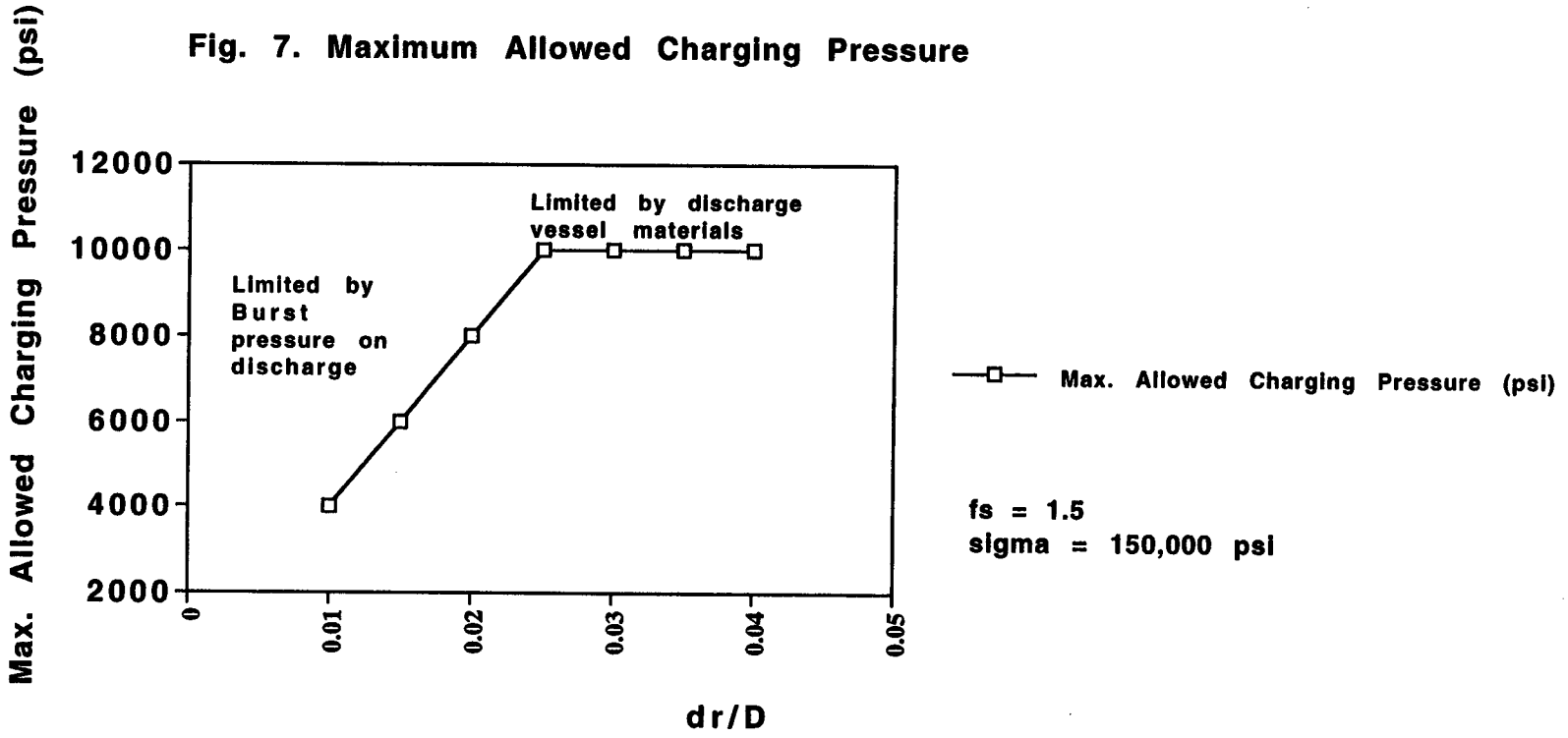

Fig. 8. Charging Time to Fill Microspheres as a Function of Sphere thickness/diameter and Charging Temperature: Ramp Filling

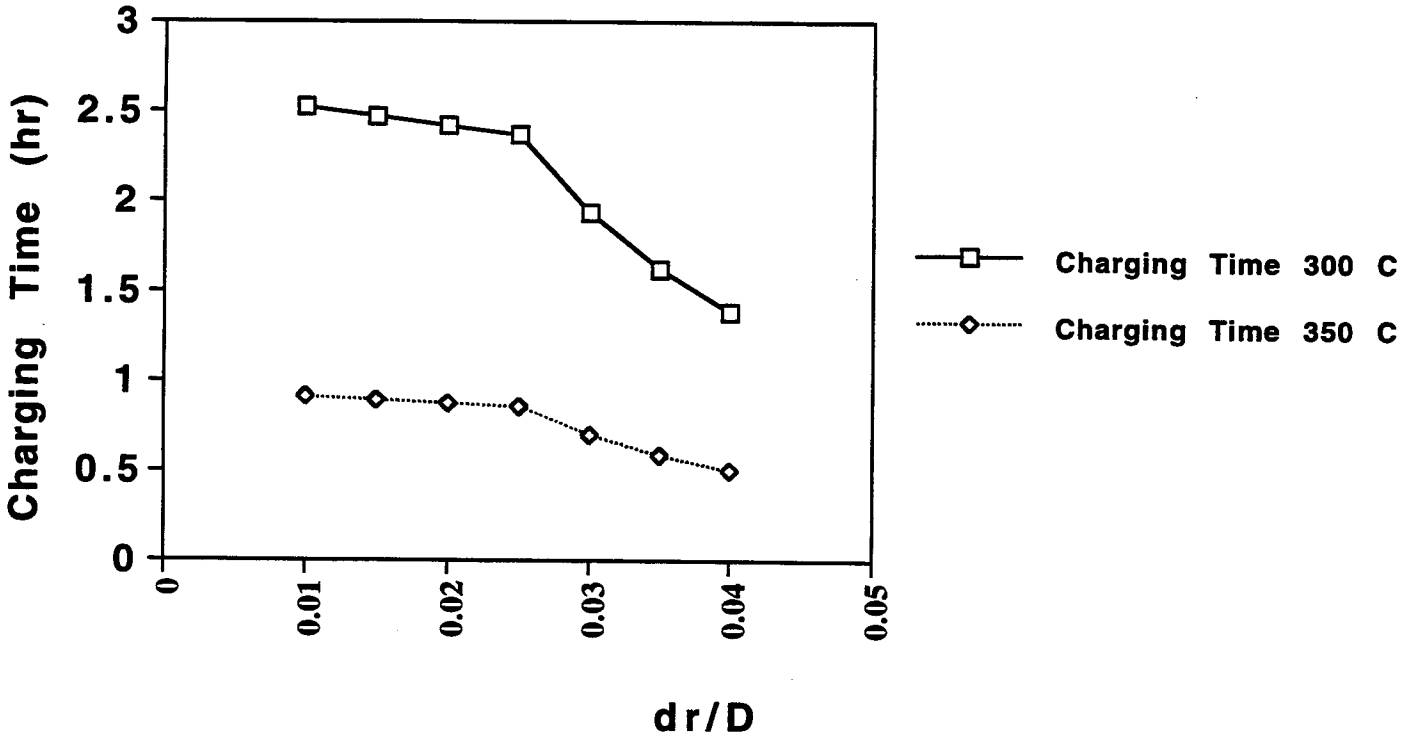

Figure 9. Charging Time to Fill Microspheres as a Function of Sphere thickness/diameter and Charging Temperature: Step Filling

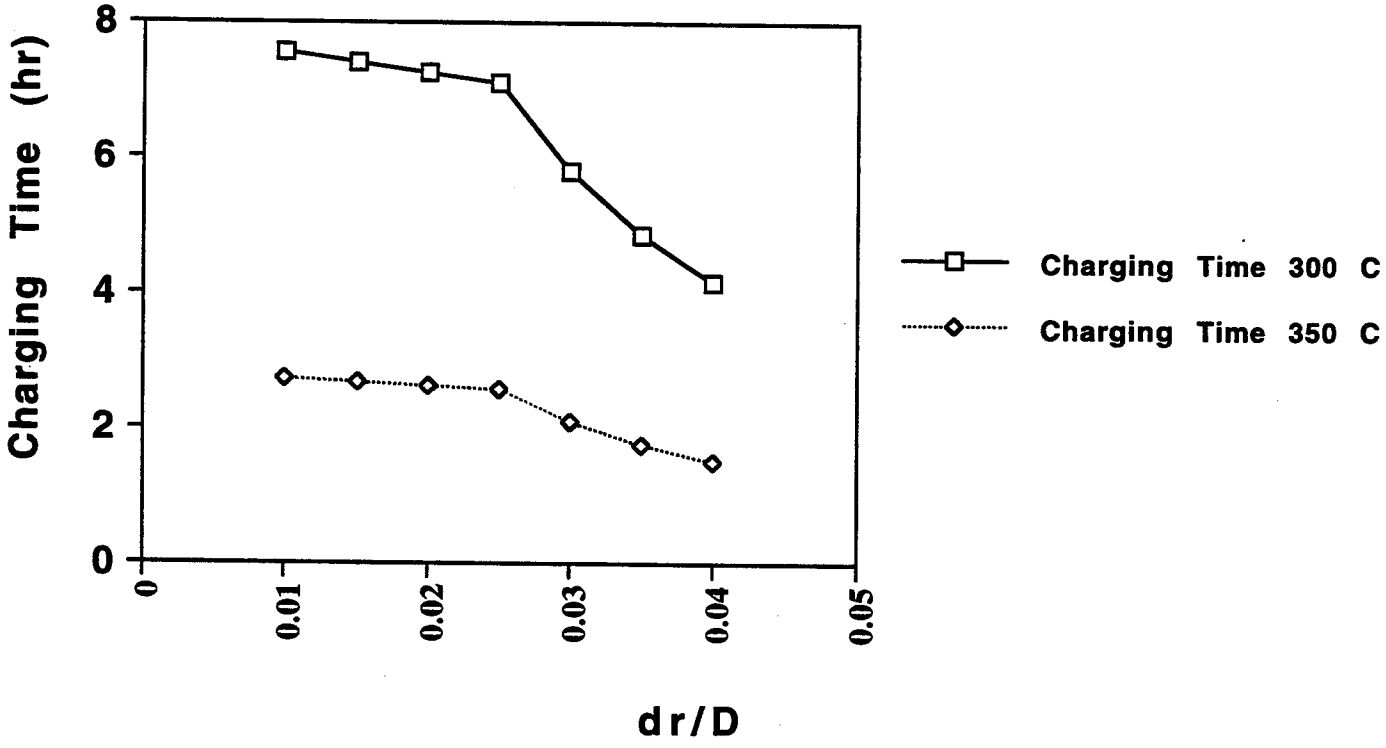

Fig. 10. Compressibility of Hydrogen as a Function of Temperature and Pressure (Black & Hartley)

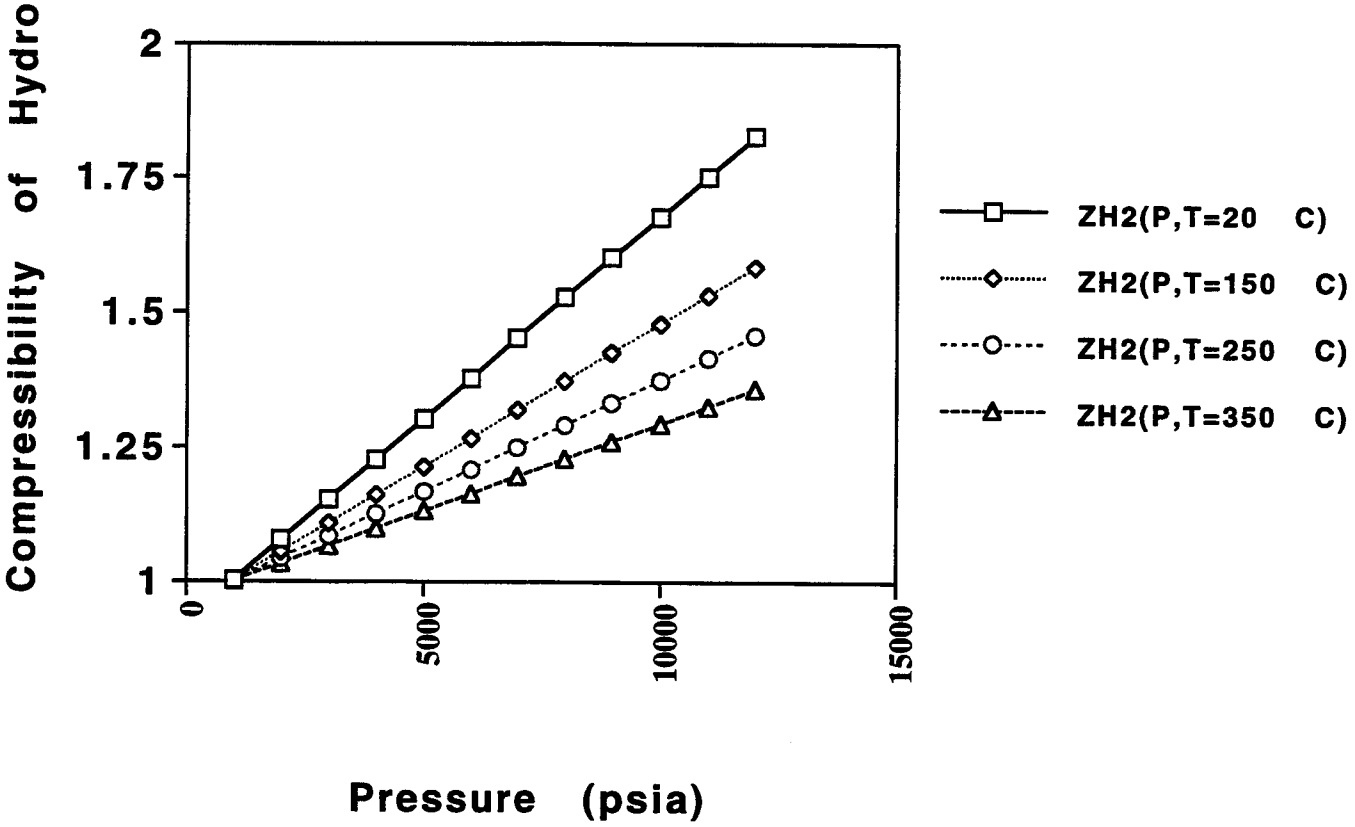

Fig. 11. Maximum Mass Fraction of Hydrogen That Can Be Stored at Maximum Charging Pressure as a Function of Sphere thickness/diameter and Charging Temperature

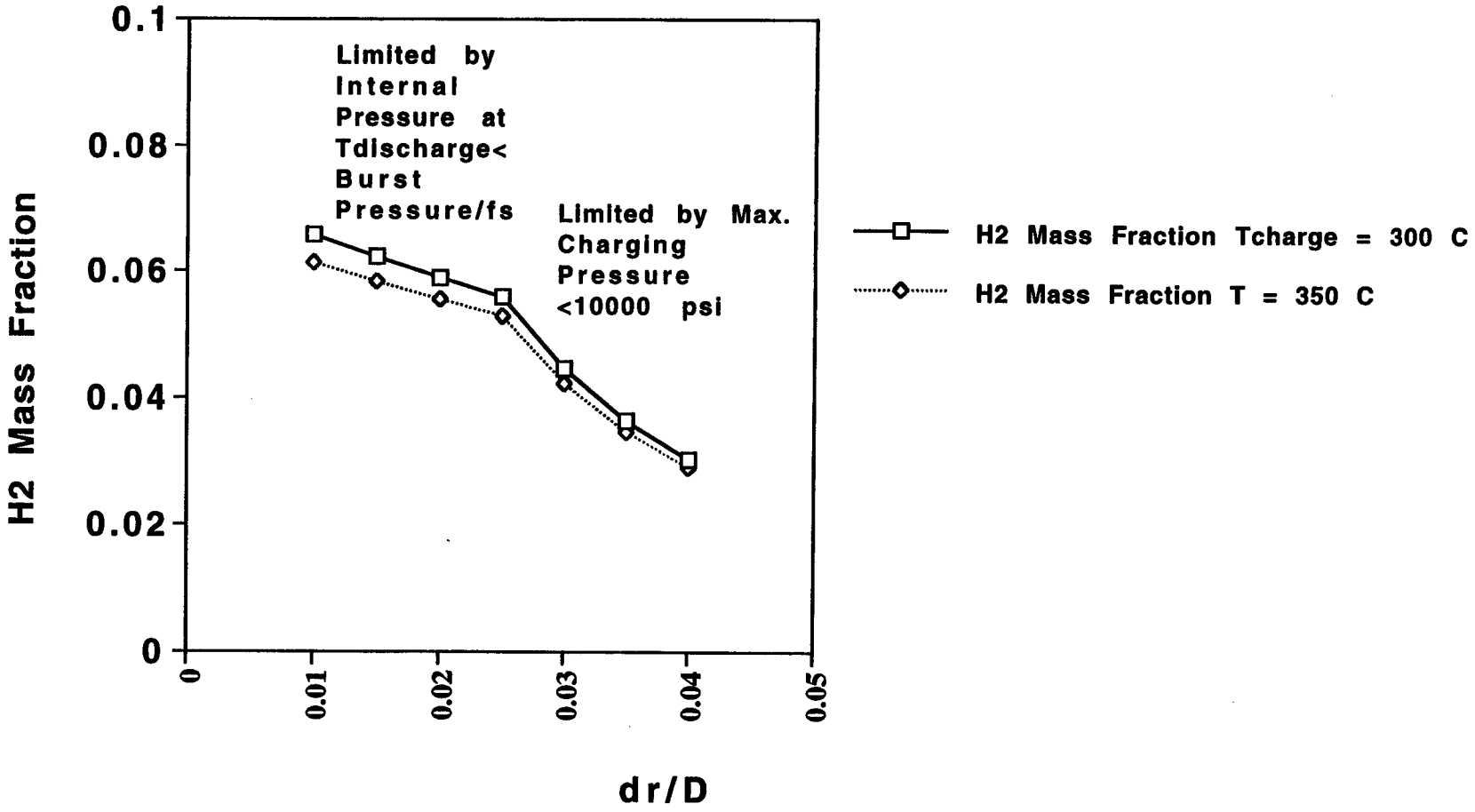

Fig.12 Energy Requirements for Microsphere Charging and Discharging as a Fraction of HHV of H2 Stored

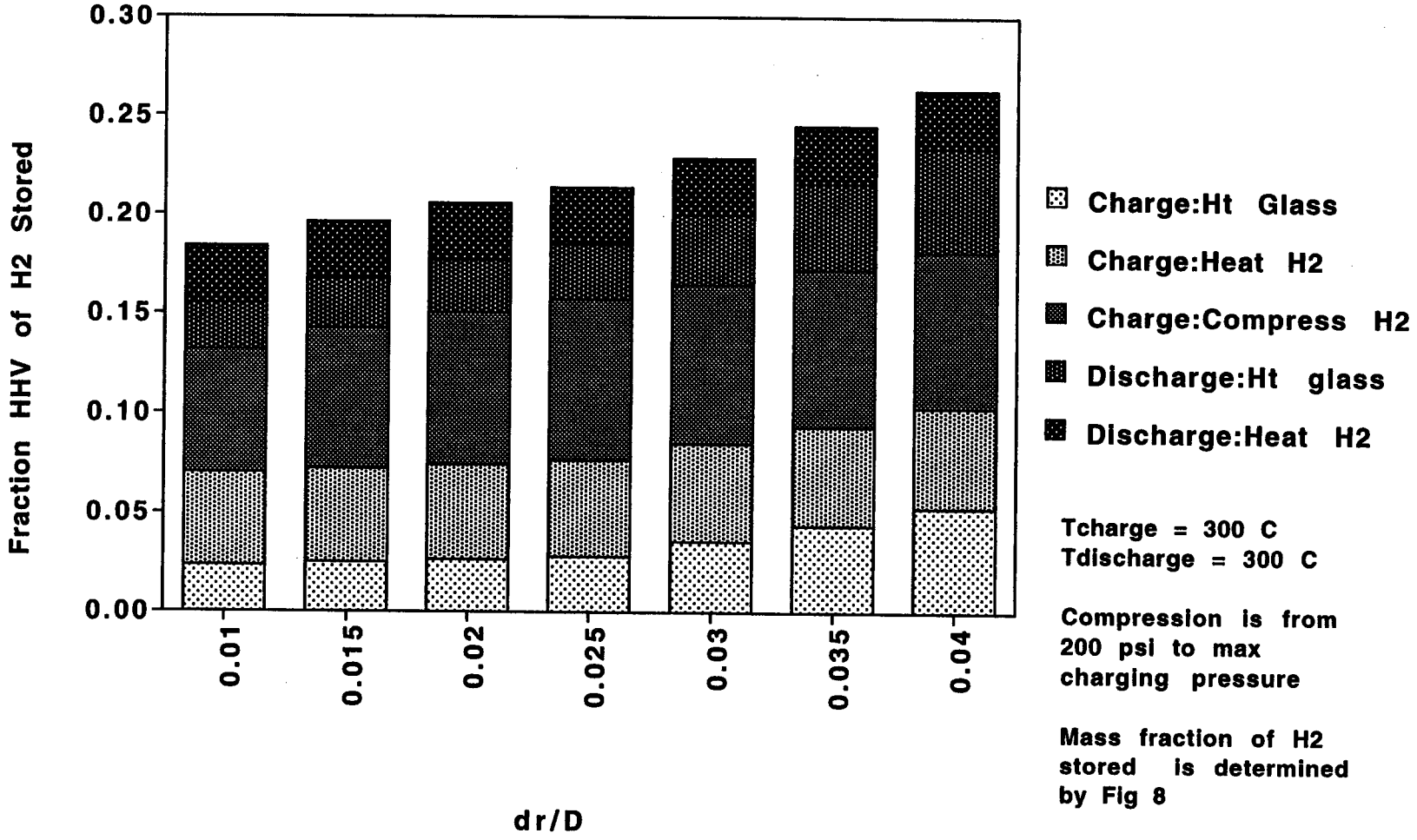

Fig. 13. Total Energy Requirements for Charging and Discharging Microspheres as a Function of dr/D and Charge/Discharge Temperature

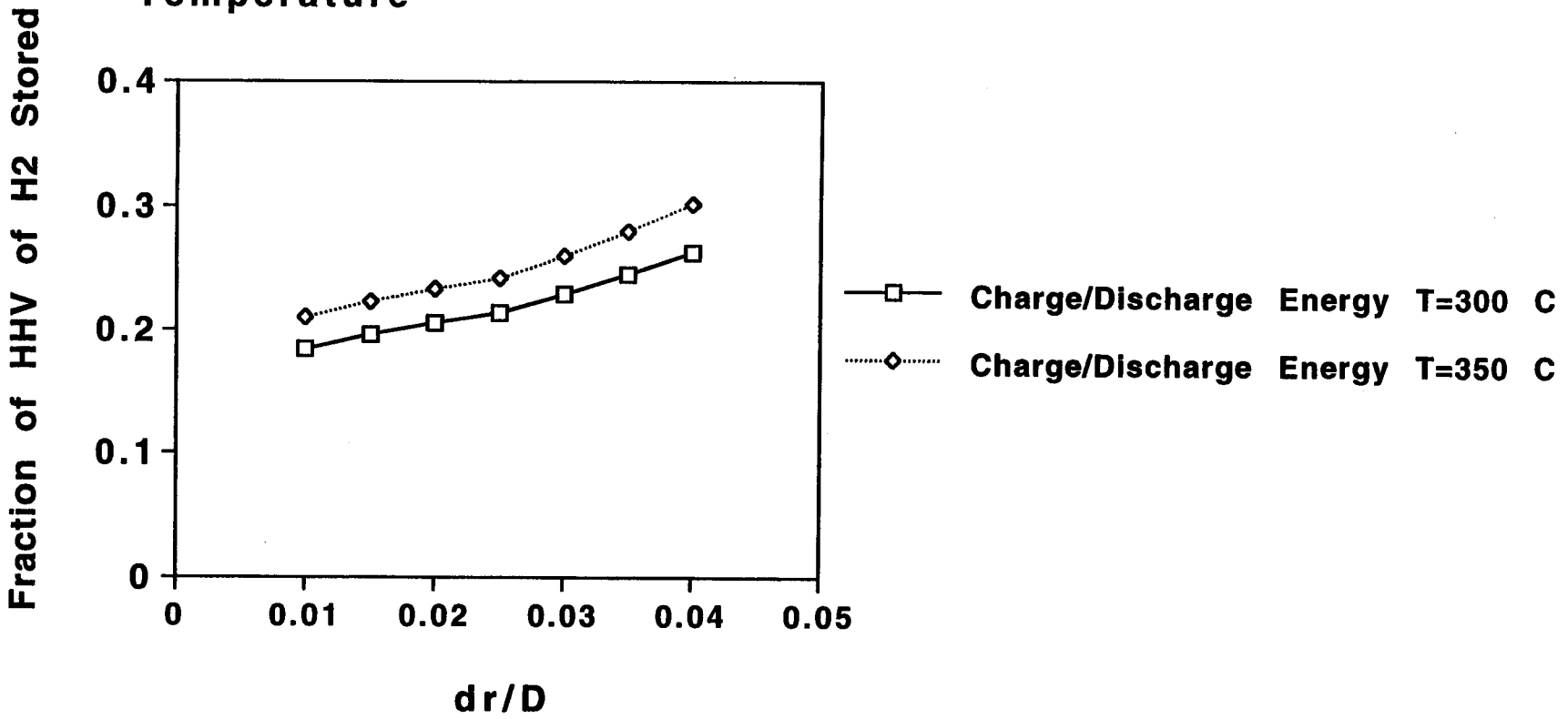

Fig.14. Energy Requirements for Microsphere Charging and Discharging as a Fraction of HHV of H2 Stored: With Credit for Hydrogen Heating During Compression and Recovery of Pressurized H2 from Interstices

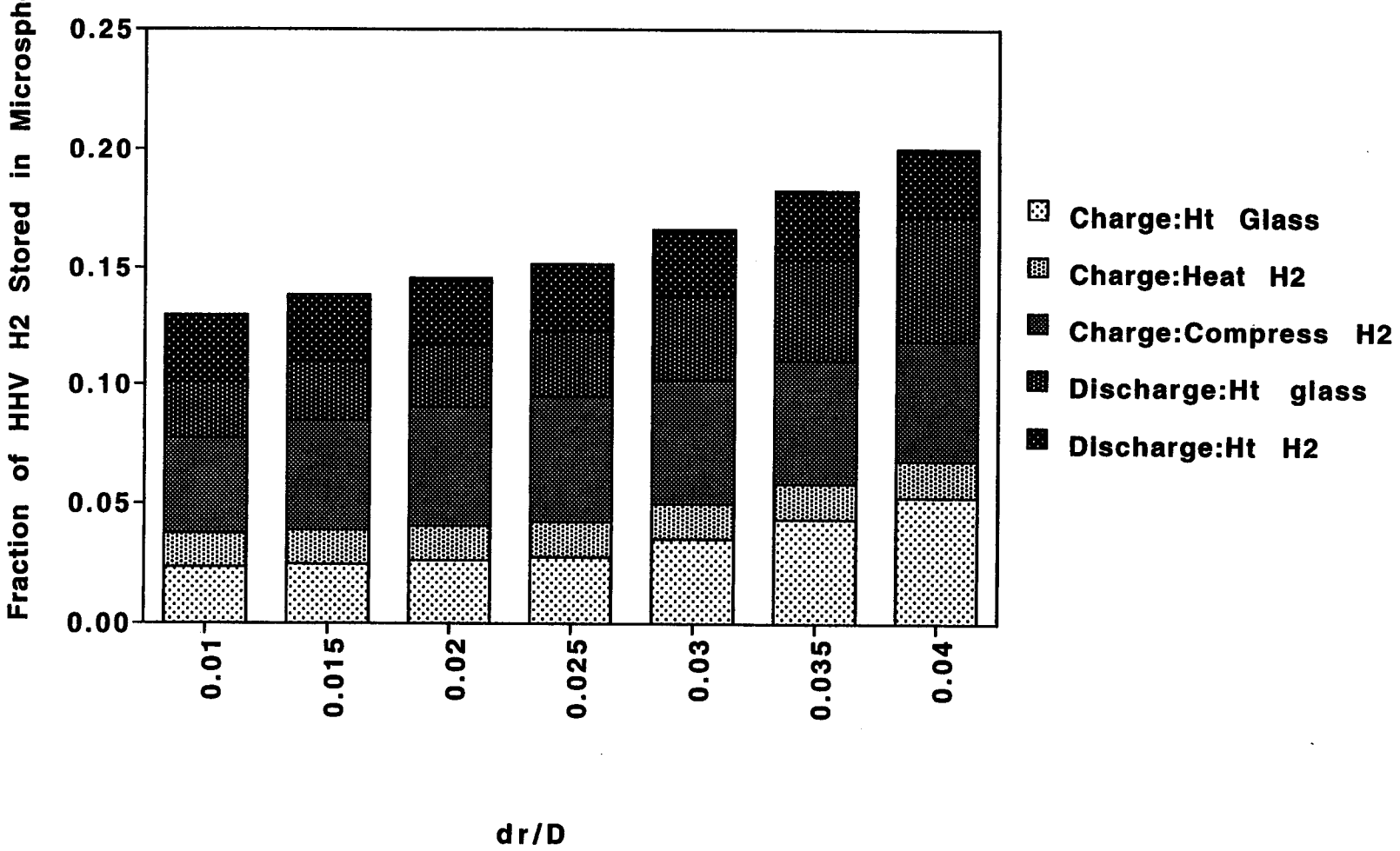

CARBON NANOTUBE MATERIALS FOR HYDROGEN STORAGE

A.C. Dillon, P.A. Parilla, K.M. Jones, J.D. Webb, M.D. Landry, and M.J. Heben
National Renewable Energy Laboratory
Golden, CO 80401-3393

Abstract

Although hydrogen provides more energy than either gasoline or natural gas on a weight basis, its drawbacks for vehicular use become apparent when the weight, volume, and round-trip energy costs of a hydrogen fuel storage system are considered. New approaches enabling more compact, lightweight, and energy efficient hydrogen storage are required in order for the wide-spread use of hydrogen powered vehicles to become a reality. Although several hydrogen storage options exist, no approach satisfies all of the efficiency, size, weight, cost and safety requirements for transportation use. We have shown in previous work that carbon single-wall nanotubes (SWNTs) are essentially elongated pores of molecular dimensions and are capable of stabilizing hydrogen at relatively high temperatures and low pressures by adsorption. This behavior is unique to these materials and indicates that SWNTs are the ideal building block for constructing safe, efficient, and high energy density adsorbents for hydrogen storage applications. In past work we developed methods for preparing and opening SWNTs, and discovered the unique adsorption properties of these new materials. During this year we have made additional significant progress in manipulating and understanding the behavior of SWNTs so that high performance adsorbents may be fabricated in a cost effective manner. Specifically, we have verified that hydrogen is stabilized by physical rather than chemical interactions, measured the strength of interaction to be ~ 5 times higher than for adsorption on planar graphite, performed infrared absorption spectroscopy to determine the chemical nature of the surface terminations before, during, and after oxidation, and developed laser-based methods for the high-yield synthesis of these important new materials.

Statement of the Problem / Relevance of the Work

Background

With the 1990 Clean Air Act and the 1992 Energy Policy Act, the United States recognized the need for a long term transition strategy to cleaner transportation fuels (Cannon 1995). This realization comes while the U.S. continues to increase petroleum imports beyond 50% of total oil consumption, with nearly 50% of the total oil consumed being used in the transportation sector (N.E.S. 1991/1992). Because of the potential for tremendous adverse environmental, economic, and national security impacts, fossil fuels must be replaced with pollution-free fuels derived from renewable resources. Hydrogen is an ideal candidate as it is available from domestic renewable resources, and usable without pollution. It could therefore provide the long-term solution to the problems created by the Nation's dependence on fossil fuel.

Interest in hydrogen as a fuel has grown dramatically since 1990, and many advances in hydrogen production and utilization technologies have been made. However, hydrogen storage technology must be significantly advanced in performance and cost effectiveness if the U.S. is to establish a hydrogen based transportation system. As described in the U.S. DOE Hydrogen Program Plan for FY 1993 - FY 1997, compact and lightweight hydrogen storage systems for transportation do not presently exist.

Hydrogen provides more energy than either gasoline or natural gas on a weight basis. It is only when the weight, volume, and round-trip energy costs of the entire fuel storage system and charging/discharging cycle is considered that hydrogen's drawbacks become apparent. New approaches enabling more compact, lightweight, and energy efficient hydrogen storage are required in order for the wide-spread use of hydrogen powered vehicles to become a reality.

Research and development geared towards implementation of a national hydrogen energy economy has many indirect economic benefits. With almost 600 million vehicles in the world in 1992 - double the number in 1973 - the conflict between energy requirements, power generation, and environmental concerns is felt on a world-wide basis (Flavin and Lessen 1994). Thus, in addition to providing domestic energy alternatives, investment in hydrogen energy research will result in opportunities for U.S. technologies in over-seas markets.

Currently Available Hydrogen Storage Technologies

Hydrogen can be made available on-board vehicles in containers of compressed or liquefied H_2, in metal hydrides, or by gas-on-solid adsorption. Hydrogen can also be generated on-board by reaction or decomposition of a hydrogen containing molecular species (Dillon et al. 1995). Although each method possesses desirable characteristics, no approach satisfies all of the efficiency, size, weight, cost and safety requirements for transportation or utility use. The D.O.E. energy density goals for vehicular hydrogen storage call for systems with 6.5 wt % H_2 and 62 kg H_2/m^3 to provide a 350 mile range in a fuel cell powered vehicle. This requirement amounts to the storage of ~2.9 kg of H_2 in the weight and volume occupied by a conventional gasoline tank. These storage density goals will only be met with significant advances in the capabilities of hydrogen storage technologies.

Gas-on-solid adsorption is an inherently safe and potentially high energy density hydrogen storage method which should be more energy efficient than either chemical or metal hydrides, and compressed gas storage. Consequently, the hydrogen storage properties of high-surface-area "activated" carbons have been extensively studied (Schwarz 1; Carpetis and Peschka 1980;

Schwarz 1993). However, activated carbons are ineffective in hydrogen storage systems because only a small fraction of the pores in the typically wide pore-size distribution are small enough to interact strongly with gas phase hydrogen molecules.

Technical Approach and Summary of Past Work

The gas adsorption performance of a porous solid is maximized when all pores are not larger than a few molecular diameters (Gregg and Sing 1982). Under these conditions the potential fields from the walls of the so-called micropores overlap to produce a stronger interaction than would be possible for adsorption on a semi-infinite plane. At sufficiently low temperatures, where the escaping tendency of the gas is much less than the adsorption potential, the entire micropore may be filled with a condensed adsorbate phase. For the case of hydrogen, with a van der Waals diameter of 2.89 Å (Breck 1974) pores would be required to be smaller than ~40 Å to access this nanocapillary filling regime. Sufficiently small pores would exhibit an adsorption potential strong enough to localize H_2 at relatively high temperatures. Ideally, the entire porous volume of an adsorbent would be of the microporous variety, and the volume and mass of the adsorbent skeleton would be the minimum necessary to develop the adsorption potential and provide sufficient thermal conductivity for management of heat fluxes associated with adsorption and desorption.

We have been working on the idea that aligned and self-assembled single wall carbon nanotubes could serve as ideal hydrogen adsorbents since 1993. The concept was motivated by theoretical calculations which suggested (Pederson and Broughton 1992) that adsorption forces for polarizable molecules within SWNTs would be stronger than for adsorption on ordinary graphite. Thus, high H_2 storage capacities could be achieved at relatively high temperatures and low pressures as compared to adsorption on activated carbons.

In the Proceedings of the 1994 Hydrogen Program Review, we presented microbalance data which demonstrated gravimetric hydrogen storage densities of up to 8.4 wt% at 82 K and 570 torr on samples containing carbon nanotubes. This substantial uptake at low hydrogen pressures demonstrated the strong interaction between hydrogen and these materials, consistent with higher heats of adsorption than can be found with activated carbons.

In the 1995 Hydrogen Program Review Proceedings, we presented the results of our temperature programmed desorption (TPD) studies which showed significant H_2 adsorption near room temperatures. The adsorption energies on nanotube materials were estimated to be a factor of 2-3 times higher than the maximum that has been observed for hydrogen adsorption on conventional activated carbons. To our knowledge, these are the first results which demonstrate the existence of stable adsorbed hydrogen *on any type of carbon at temperatures in excess of 285 K*. We also presented an analysis of nanotube production yields versus rod translation rate in our arc-discharge SWNT generator.

In 1996 we performed a detailed comparative investigation of the hydrogen adsorption properties of SWNT materials, activated carbon, and exfoliated graphite. We also determined that the cobalt nanoparticles present in the arc-generated soots do not play a role in the observed hydrogen uptake. We determined the amount of hydrogen which is stable at near room temperatures on a SWNT basis is ~ 10 wt%, and found that an initial heating in vacuum is essential for producing high temperature hydrogen adsorption. Further experiments suggested that SWNTs are selectively opened by oxidation during this heating, and that H_2O is more selective in oxidation than O_2 due to hydrogen termination of dangling bonds at the edges of opened nanotubes. Purposeful oxidation in H_2O resulted in hydrogen storage capacities which were improved by more than a factor of three. We also correlated the measured nanotube densities produced by specific synthesis rod translation rates during arc-discharge with hydrogen storage capacities determined by TPD. Finally, we utilized NREL's High Flux Solar Furnace to form nanotubes by a new and potentially

less expensive route for the first time.

During the past year we have confirmed that H_2 is stabilized by purely physical - rather than chemical - binding. The desorption of hydrogen was found to fit 1st order desorption kinetics as expected for physisorbed H_2. We also determined that the activation energy for desorption of hydrogen is 19.6 kJ/mol. This value is approximately five times higher than the value expected for desorption of physisorbed H_2 from planar graphite and demonstrates that SWNT soots can provide very stable environments for H_2 binding. We have also performed studies to determine why heating in vacuum is necessary for enabling high temperature hydrogen adsorption. To complement the temperature programmed reaction mass spectroscopy data presented last year we performed diffuse reflectance Fourier transform infrared (DRFTIR) spectroscopy to determine the concentrations and identities of chemisorbed species bound to the carbon surface as a function of temperature. These measurements enabled a more detailed view of the "self-oxidation" mechanism which allows high-temperature adsorption of hydrogen to occur in SWNT materials. In the past year we have also begun synthesizing SWNT materials in much higher yield than is currently possible with arc-discharge by using a laser vaporization process. Future experiments will investigate H_2 adsorption on gram quantities of SWNTs now that larger quantities are available with the new synthetic procedures.

Experimental

Synthesis

The arc-generated carbon nanotube soots were produced by co-evaporating cobalt /carbon mixtures in a spark-gap evaporator as described elsewhere (Dillon et al. 1996). Briefly, two graphite electrodes of differing diameters (6 and 13 mm) were mounted on the base plate of the evaporator by electrically isolated positioners. The 6 mm graphite rod was doped with cobalt by drilling-out and refilling a 2.9 mm hole with a cobalt/carbon mixture. The cobalt density averaged across the diameter of the rod was ~3 at %. Prior to all synthesis runs, the evaporator was evacuated to ~10^{-6} torr and back-filled with helium to ~ 500 torr.

Laser-generated carbon nanotube materials were produced with metal-graphite composite targets in a laser-vaporization apparatus (Guo et al. 1995), and supplied to us by the Smalley Group at Rice University. A computer controlled scanning laser beam (300 mJ /pulse at .532 μ) was focused to a 6-7 mm diameter spot on the target surface. The target was mounted in a 1" quartz tube which was evacuated to 10 mtorr and then filled with 500 torr of argon flowing at 50 sccm. The quartz tube surrounding the sample was contained in a high temperature furnace at 1200 C. During laser vaporization the soot was deposited onto a water cooled copper collector positioned downstream of the furnace. The targets were uniformly mixed metal/graphite composite rods made by a three step process (Guo et al. 1995). Other laser-generated SWNT samples were produced in our laboratory using different laser-vaporization procedures. These materials have not yet been studied for their hydrogen adsorption properties, and the details of their synthesis will be described later in this report.

Temperature Programmed Desorption

The ultra-high-vacuum (UHV) chamber employed for the temperature programmed desorption (TPD) studies has been previously described (Dillon et al. 1996). The sample is mounted at the bottom of a liquid nitrogen cooled cryostat, and a mass spectrometer provides for line-of-site detection of desorbing species. An ion gauge and capacitance manometer are employed to monitor pressure. Gas exposure is controlled with a variable conductance leak valve. Isolation gate valves separate the sample compartment during high-pressure gas exposures. However, a leak valve may be used to transfer species to the mass spectrometer.

Diffuse Reflectance Fourier Transform Infrared Spectroscopy

The experimental set-up for the diffuse reflectance Fourier transform infrared (DRFTIR) spectroscopy studies is displayed in Figure 1. Powders of the carbon nanotube soots were dispersed in Spectra Tech diamond powder at a concentration of 4 wt%. The sample was then loaded into a vacuum chamber designed for *in-situ* DRFTIR studies. The chamber was evacuated to < 1 mtorr and spectra were obtained with a Nicolet 800 spectrometer and a mercury cadmium telluride (MCT) detector.

The nanotube samples were heated between 400 - 900 K at 40 K increments. The sample was held at each temperature for 1 min. and then cooled to 300 K where DRFTIR spectra were subsequently recorded. A total of 500 scans were added achieving a resolution of 3-4 cm^{-1}. All spectra were referenced to an initial 1000 scan DRFTIR spectrum of the carbon/diamond powder at 300 K.

Results and Discussion

As described in last year's Hydrogen Program Review, a high-temperature TPD peak representing a population of structurally unique sites is found at 288 K after SWNT soots are heated in vacuum to 970 K at 1 K/s. The adsorbed H_2 is stable at 223 K while in contact with vacuum and does not redistribute to other sites during evacuation or cooling. Figure 2 shows the TPD spectra when the high-temperature sites were selectively populated by evacuating the chamber with a sample temperature of 223 K after a 10 min. H_2 exposure at 273 K. Variation of the hydrogen pressure between 25 and 300 torr produced coverages between ~0.3 and saturation (Dillon et al. 1997). The shift in peak temperature from 299 to 285 K with decreasing coverage is explained by first-order desorption of physisorbed H_2 with either coverage dependent desorption energies (Madix 1979) or equilibrium readsorption (Ibok and Ollis 1980). Shifts of 100 K or more are expected for the second-order desorption kinetics which would characterize the desorption of chemisorbed H_2 (Madix 1979). First-order desorption is described by $\ln(T_m^2/\beta) = E_d/RT_m$ where T_m is the temperature at the peak maximum, E_d is the desorption activation energy, β is the heating rate, and R is the universal gas constant (Madix 1979). T_m was measured for β between 0.3 and 30 K/s after only the high-temperature sites were populated at 300 torr. A plot of $\ln(T_m^2/\beta)$ vs. $1/T_m$ yields a straight line (Fig. 3), confirming that H_2 is physisorbed in the high-temperature sites. The desorption activation energy, which is equivalent to the heat of adsorption in the case of physisorption (Madix 1979), is 19.6 kJ/mol.

Self-Oxidation Upon Heating in Vacuum

As reported last year, the high-temperature hydrogen adsorption site cannot be populated unless the sample is heated in vacuum to 970 K at 1 K/s with the accompanying evolution of CO, H_2O and CO_2. Figure 4 displays the desorption species detected for the arc-generated material. Water and CO_2 signals are observed to increase significantly above 400 K with peak temperatures of 560 K and 600 K, respectively. At temperatures > 640 K the H_2O and CO_2 pressures decrease and CO evolution becomes dominant. The desorption spectrum produced during outgassing of laser-generated materials is very similar in shape to the spectrum observed from the arc-generated material, but the integrated TPD intensities are about one order of magnitude less. The outgassing signals are more intense from the arc-generated materials, and are likely produced by the breakdown of surface groups attached to amorphous carbon components which are present in both types of materials but more prevalent in arc-discharge soots. The degassed material is highly reactive as the surface species can be regenerated by exposing the sample to atmosphere at room temperature.

DRFTIR studies were employed to elucidate the surface decomposition mechanisms which occur

during outgassing. Figure 5 displays spectra of the arc-generated soot after heating to various temperatures in vacuum. All spectra are referenced to an initial spectrum of the carbon soot/diamond powder at 300 K. Significant losses in absorbances with increasing temperature at 3496, 1710 and 1040 cm^{-1} can be assigned to O-H, C=O and C-O stretching vibrations, respectively. The very broad feature of the O-H stretching vibration centered at 3496 cm^{-1} indicates a large population of hydrogen bonded surface hydroxyl groups. Similar spectral features are observed in DRFTIR studies of activated carbons (Meldrum and Rochester 1990).

The changes in the DRFTIR spectra in the region between 1330 - 1520 cm^{-1} in Fig. 5 are associated with C-C vibrations. The decrease in the vibrational feature at 1330 cm^{-1} with increasing temperature is consistent with a reduction in the C-C stretch observed for sp^3 bonded C species in amorphous carbon films (Sunil et al. 1991). An increase in infrared absorbance is also observed at 1520 cm^{-1}, and may be attributed to the skeletal-ring breathing modes of aromatic compounds which occur near 1500 cm^{-1} (Belamy 1975). The DRFTIR spectra therefore suggest that amorphous carbon fractions of the nanotube soots are annealed to form cyclic aromatic structures during degassing.

The normalized integrated absorbances of the O-H, C=O and C-O stretching vibrations are shown as a function of temperature in Fig. 6. The O-H stretching vibration is observed to decrease dramatically between 300-860 K. The C=O and C-O stretching vibrations also decrease and track each other across the same temperature range suggesting that they are associated with the breakdown of a single species such as a lactone. The infrared spectra coupled with the H_2O and CO_2 desorption signals in the TPD spectra of Fig. 4 therefore suggest the following decomposition mechanisms for surface species:

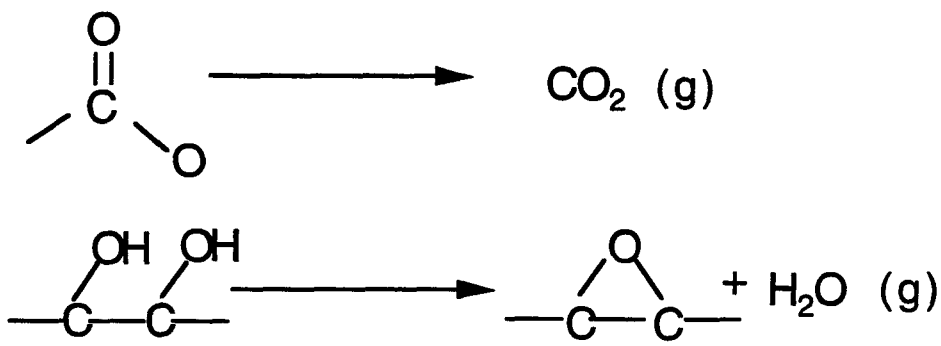

The CO_2 and H_2O evolution in Fig. 4 is reduced at temperatures >700 K while the CO signal is increased. In addition, the O-H, C=O and C-O stretching vibrations continue to decrease in Fig. 6 for temperatures > 700 K. Together, these experimental results indicate that above 700K desorbing CO_2 and H_2O oxidize various carbon species producing CO as a reaction product.

Controlled Oxidation of Arc- and Laser-generated Materials

Controlled oxidation experiments were performed for both arc- and laser-generated materials in order to optimize methods for opening and purifying single-wall carbon nanotubes. Following an initial outgassing procedure a sample of arc-generated material was heated between 325-975 K at 1 K/s in 1 torr H_2O. Above 600 K, increases in the partial pressures of CO and H_2 were detected by the mass spectrometer with a concurrent decrease in the H_2O pressure, demonstrating oxidation of the carbon surfaces as $C_s + H_2O$ ----> $CO + H_2$. Subsequent hydrogen TPD studies revealed an increase in hydrogen adsorption at near ambient temperatures indicating that more nanotube interiors could be accessed after the oxidation process (Dillon et al. 1997). The hydrogen adsorption at lower temperature (< 200 K) was decreased, however, indicating that adsorption

sites associated with nanoporous environments in amorphous carbon or graphitic components had been consumed (Dillon et al. 1996). Thus, controlled oxidation with 1 torr of H_2O results in oxidation of amorphous carbon and graphitic edges, and the apparent opening and partial purification of SWNTs. Unfortunately, it was not possible to obtain highly pure quantities of SWNTs as prolonged oxidation in H_2O ultimately resulted in the loss of the very small fraction of SWNTs prior to consumption of all other carbon fractions (Dillon et al. 1996).

The oxidation of arc-generated carbon nanotube material by heating between 325-975 K at 1 K/s in 1 Torr O_2 was also explored. An increase in the partial pressure of CO_2 corresponding to a decrease in the O_2 pressure was detected above 600 K again indicating the oxidation of the carbon substrate. However, in sharp contrast to the hydrogen adsorption studies after oxidation in water, no hydrogen adsorption at ambient temperatures was observed. Subsequent TEM investigations revealed that the SWNTs had been completely consumed during the oxidation process (Dillon et al. 1996).

For comparison, controlled oxidation of laser-generated soots containing very high densities of SWNTs was also explored. The materials were outgassed in vacuum and oxidized in 1 torr H_2O between 325-975 K at 1 K/s. Here, the procedure did not allow hydrogen to be adsorbed at near ambient temperatures as would be expected if arc-generated materials had been used. In a more aggressive oxidation experiment, the laser-generated material was heated in 8% water vapor / 92% argon with a total pressure of 1200 psi and a temperature of 800 K. Again no hydrogen adsorption at ambient temperatures was observed after this high pressure water oxidation. As discussed in detail in the next section, there are several explanations for this behavior.

The effect of controlled oxidation with O_2 on the laser-generated material was also strikingly different than that behavior observed for arc-generated material. After the laser-generated carbon soot was oxidized in 1 torr O_2 for 10 min. at ~ 1050 K approximately 1/3 of the initial material remained. Figure 7 displays TEM images of a) the initial laser vaporization material and b) the material remaining after oxidation. In Fig. 7a, large bundles of 13.8 Å diameter SWNTs are clearly observed spanning the entire image. In addition, metal nanoclusters and amorphous soot are also observed interlacing the SWNTs. Figure 7b shows that oxidation in O_2 results in the consumption of the amorphous carbon components leaving purified SWNTs, oxidized metal particles, and some unreacted carbon. As noted above, this same oxidation would completely destroy the SWNT fraction in materials produced by arc-discharge.

Differing Mechanisms for Oxidation

The arc-generated SWNTs are evidently opened by oxidation in 1 torr of H_2O between 325-975 K but are consumed by oxidation in O_2 under identical conditions. The temperature programmed reaction products from the arc-generated material indicate that water is oxidizing surface carbon to produce CO and H_2 while oxidation in O_2 results in the production of CO_2. In the outgassing process, water is generated by desorption from the material and some portion of this water reacts with surface carbon to produce CO. In this case, the hydrogen evolution (not shown in Fig. 4) during the dynamic desorption/reaction of water cannot be directly correlated with evolving CO according to the reaction $C_s + H_2O \rightarrow CO + H_2$. The TPD spectra are complicated by the fact that CO is also being generated while CO_2 oxidizes surface carbon.

It is possible that oxidation of the SWNT caps in water may occur with hydrogen termination of the carbon dangling bonds thereby passivating the tubes against complete oxidative consumption. The amorphous components of the soots likely undergo oxidation in water producing CO and H_2 as indicated by the TPD data. Because the nanotube caps make up such a small fraction of the material, the temperature programmed reaction products observed during oxidation can not be used to establish their oxidation mechanism.

In order to elucidate the oxidation mechanism of the nanotube caps, the arc-generated material was heated at 1 K/s in D_2O between 325-975 K. The reaction with D_2O provided a means of cleanly determining the addition of D without interference from desorbing H_2 associated with H introduced by reaction with water while the samples were exposed to lab air. The temperature programmed desorption spectrum obtained following this oxidation in D_2O is displayed in Fig. 8. At temperatures above 800 K an increase in the background pressure of deuterium is observed, consistent with the release of chemisorbed D_2. The TPD results show that some hydrogen (deuterium) addition occurs during the oxidation of carbon nanotube soots with water. The high desorption temperature in Fig. 8 is consistent with the formation of a very stable C-H (D) bond.

Figure 9 displays DRFTIR difference spectra of the laser-generated material at various temperatures while heating in vacuum. As with the arc-generated materials a broad decrease in infrared absorption is observed at 3508 cm^{-1} indicating the decomposition reaction 2COH --> COC + H_2O. However, unlike the spectra in Fig. 5, an increase in infrared absorbance centered at 3216 cm^{-1} is observed in Fig. 9 for the laser-generated material. The infrared feature at 3216 cm^{-1} may be attributed to the C-H stretching vibration of H attached to an aromatic carbon system. This increase in aromatic hydrogen can be attributed to hydrogen termination of graphitic carbon dangling bonds present at either the edges of graphitic platelets or the open ends of carbon nanotubes. The increase in infrared absorbance of the C-H stretching vibration was not observed for the arc-generated material presumably due to the small quantity of SWNTs. It will be quite interesting to repeat these experiments on laser-generated materials purified by oxidation processes (Fig. 7b). Collectively these DRFTIR results and the deuterium TPD signal of Fig. 8 are consistent with the idea that water is a more selective oxidant for the removal of SWNT caps due to hydrogen termination of the carbon dangling bonds.

Hydrogen adsorption studied on laser-generated materials were unable to detect adsorbed H_2 at near ambient temperatures as is found with arc-generated materials (Dillon et al. 1997). Several possibilities could account for this discrepancy. It is possible that the slightly larger diameter laser-generated tubes (13.8 Å compared with 12 Å) do not stabilize physisorbed H_2 against desorption at the experimental base pressure of the chamber ($< 5 \times 10^{-8}$ torr). It is also quite possible that the laser-generated tube caps were not actually removed by oxidation. The (10,10) tube which predominates in the laser-generated material is thought to be capped by one half of a C_{240} fullerene. This cap would be much more stable than any cap which could form on the (9,9) tubes which are typically produced by arc-discharge. The stability against oxidation of the (10,10) tube cap relative to the (9,9) tube cap rationalizes the fact that laser-generated SWNTs are purified under conditions which fully combust arc-discharge tubes. Furthermore, the higher-yield laser-generation process results in the formation of tubes which are considerably longer than those synthesized by arc-generation. The relatively low density of caps and ends and the increased number of tubes per bundle may affect the kinetics for oxidation of the tube ends. Finally, the longer tubes also stand a greater chance of being kinked so that the total length is unavailable for hydrogen adsorption, and filling the tubes deeply along their lengths may well be diffusion limited. Future investigations will explore hydrogen adsorption on purified laser-generated SWNTs with higher pressures of H_2, methods for cutting SWNTs into shorter lengths, and the effect of nanotube length and diameter on H_2 uptake.

Hydrogen Reduction of Laser-Generated SWNTs

The direct reduction of laser-generated SWNTs with hydrogen was also explored. A sample of laser-generated soot was heated in 2 torr H_2 for 10 min. at 775 K. Subsequent hydrogen desorption was not observed in temperature programmed desorption spectra between 300-900 K. The sample was then heated at 773 K for 10 min. in a high pressure furnace with H_2 at 650 psi. Figure 10 reveals the H_2 TPD spectrum of the high pressure treated sample. A hydrogen

desorption signal centered at 716 K indicating the addition of hydrogen to the carbon surfaces is clearly observed. The integrated area under the H_2 TPD signal corresponds to an amount of hydrogen equivalent to ~ 0.1 wt% of the material. Qualitatively, the amount of chemisorbed H_2 is too great to be explained only by hydrogenation of nanotube ends. In contrast to the D_2 desorption data presented in Fig. 8, the majority of the H_2 evolves a full 200 K earlier, indicating a weaker bond to the surface. This observation is consistent with the idea that the hydrogenation occurs by addition to the π-stabilized network of the nanotube walls rather than by terminating dangling bonds. These species are expected to be less stable than those terminating the tube ends and consequently have a lower desorption temperature. Failure to detect the reaction at lower pressures of H_2 may be attributed to diffusion limitations between the densely packed SWNTs, or a lack of driving force for hydrogenation. Nanotube hydrogenation will be studied in more detail in the upcoming year to determine if chemical binding of hydrogen to SWNT surfaces could be used for hydrogen storage in certain applications.

Synthesis of SWNTs by Laser-Vaporization

We have recently begun to employ laser-vaporization as a technique for SWNT synthesis. The technique has recently been shown to be capable of producing SWNTs in yields approaching 90% (Thess et al. 1996). Figure 11 is a schematic of the experimental apparatus we have constructed for laser-based production of SWNTs. Briefly, 1.06 micron photons are produced by a Nd:Yag laser and directed by a scanning mirror onto the surface of a carbon target which is doped with transition metal catalysts. The energy of the laser beam is effective at heating the surface of the carbon target to temperatures above the vaporization point of carbon and SWNTs are formed during the subsequent condensation of the carbon vapor. In initial experiments we have produced SWNTs at > 60 % yield. Figure 12 compares TEM images of typical materials produced by arc-discharge and laser-vaporization, and the improved SWNT purity is readily observed. The synthesis can be performed with the laser operating in either pulsed or continuous mode, and external heating of the reactor vessel is not required. The experimental set-up allows variation in the laser energy density, raster sweep rate, and pulse period. Future work will be directed at optimizing the purity and rate for SWNT production.

Conclusions

Temperature programmed desorption spectroscopy techniques were used to demonstrate that hydrogen is physically- rather than chemically- bound to SWNT materials produced by arc-discharge. The heat of adsorption for hydrogen was measure to be 19.6 kJ/mol which is ~ 5 times higher than is found for planar graphite.

Diffuse reflectance Fourier transform infrared (DRFTIR) spectroscopy was employed to elucidate the oxidation mechanisms of both arc- and laser-generated carbon single-wall nanotube materials. The oxidation behavior of these two materials was found to be surprisingly different. Both arc- and laser-generated SWNT materials undergo "self-oxidation" while heating in vacuum due to the decomposition of the surface hydroxyl and carbonyl species and a corresponding desorption of oxidizers such as H_2O and CO_2. For the arc-generated materials this oxidation apparently results in the removal of the nanotube caps and the SWNTs may then adsorb molecular hydrogen at near ambient pressures. For the laser-generated materials hydrogen adsorption at near ambient temperatures is not observed following heating in vacuum. Further work is required to determine if the more stable caps are removed by the currently utilized oxidation processes, or if the larger diameter SWNTs require over-pressure of hydrogen in order to stabilize physisorbed H_2. Alternatively, entrance of hydrogen may be hindered by poor diffusion kinetics due to a bend or kink in the long SWNTs. If so, it will be important to develop methods to cut and shorten the tubes produced by laser vaporization.

The reduction of laser-generated soots has also been studied. Hydrogenation of the carbon material occurs after 10 min. at 775 K in 650 psi H_2. Approximately 0.1 wt% of hydrogen is added to the material by this route, and the addition occurs mostly on the planar surfaces of the carbon nanotubes. The reaction is undetected after exposure at a lower H_2 pressure of 2 torr for the same time and temperature perhaps due to insufficient thermodynamic driving-force or diffusion limitations.

We have also developed laser-vaporization methods for the high yield synthesis of SWNT materials, and developed strategies for purifying the resultant tubes. These capabilities will allow us to investigate the hydrogen storage properties of gram quantities of SWNTs at pressures greater than one atmosphere.

References

Belamy, L. J. (1975). The Infrared Spectra of Complex Molecules. London, Chapman and Hall Ltd.

Breck, D. W. (1974). Zeolite Molecular Sieves: Structure, Chemistry and Use. New York, Wiley.

Cannon, J. S. (1995). Harnessing Hydrogen. New York, INFORM, Inc.

Carpetis, C. and W. Peschka (1980). "A Study of Hydrogen Storage by Use of Cryoadsorbents." *Int. J. Hydrogen Energy* **5**: 539-554.

Dillon, A. C., T. A. Bekkedahl, A. F. Cahill, K. M. Jones and M. J. Heben (1995). Carbon Nanotube Materials for Hydrogen Storage. Proceedings of the U.S. DOE Hydrogen Program Review, Coral Gables, FL,

Dillon, A. C., T. A. Bekkedahl, K. M. Jones and M. J. Heben (1996). The Oxidative Opening and Filling by Hydrogen of Single Wall Carbon Nanotubes. Recent Advances in the Physics and Chemistry of Fullerenes and Related Materials, Los Angeles, CA, Electrochemical Society Inc.

Dillon, A. C., K. M. Jones, T. A. Bekkedahl, C. H. Kiang, D. S. Bethune and M. J. Heben (1997). "Storage of Hydrogen in Single-Wall Carbon Nanotubes." *Nature* **386**: 377-379.

Flavin, C. and N. Lessen (1994). Power Surge. New York, W.W. Norton & Co.

Gregg, S. J. and K. S. W. Sing (1982). Adsorption, Surface Area and Porosity. London, Academic Press.

Guo, T., P. Nikolaev, A. Thess, D. T. Colbert and R. E. Smalley (1995). "Catalytic growth of single-walled nanotubes by laser vaporization." *Chemical Physics Letters* **243**: 49-54.

Ibok, E. E. and D. F. Ollis (1980). "Temperature Programmed Desorption from Porous Catalysts: Shape Index Analysis." *Journal of Catalysis* **66**: 391.

Madix, R. J. (1979). The application of flash desorption spectroscopy to chemical reactions on surfaces: temperature programmed reaction spectroscopy. Chemistry and Physics of Solid Surfaces. Boca Raton, CRC Press. 63-72.

Meldrum, B. J. and C. H. Rochester (1990). "*In situ* Infrared Study of the Surface Oxidation of Activated Carbon in Oxygen and Carbon Dioxide." *Journal of the Chemical Society, Faraday Transactions* **86**: 861.

N.E.S. (1991/1992). "National Energy Strategy." :

Pederson, M. R. and J. Q. Broughton (1992). "Nanocapillarity in Fullerene Tubules." *Physical Review Letters* **69**: 2689.

Schwarz, J. A. (1). Modification Assisted Cold Storage (MACS). contract report to Brookhaven National Laboratories, contract # 186193-S.,

Schwarz, J. A. (1993). Activated Carbon Based Storage System. Proceedings of the 1993 DOE/NREL Hydrogen Program Review, Cocoa Beach, FL.,

Sunil, D., V. D. Vankar and K. L. Chopra (1991). "Infrared and Ellipsometric Studies of Amorphous Hydrogenated Carbon Films." *Journal of Applied Physics* **69**: 3719.

Thess, A., R. Lee, P. Nikolaev, H.Dai, P. Patit, J. Robert, C. Xu, Y. H. Lee, et al. (1996). "Crystalline Ropes of Metallic Carbon Nanotubes." *Science* **273**: 483.

Acknowledgments

We would like to acknowledge the Department of Energy Hydrogen Program for funding, and thank R. Smalley and his research group at Rice University for providing the laser-generated SWNT materials.

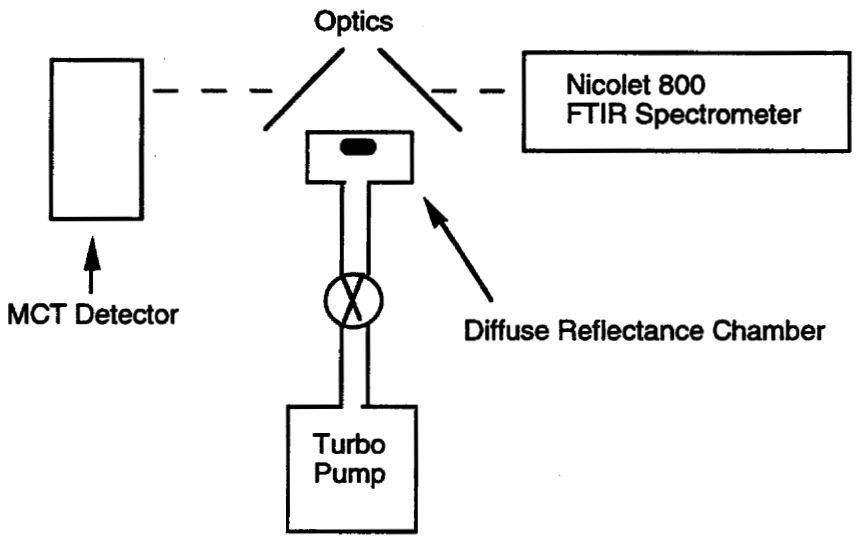

Figure 1: Experimental apparatus for diffuse reflectance infrared spectroscopy.

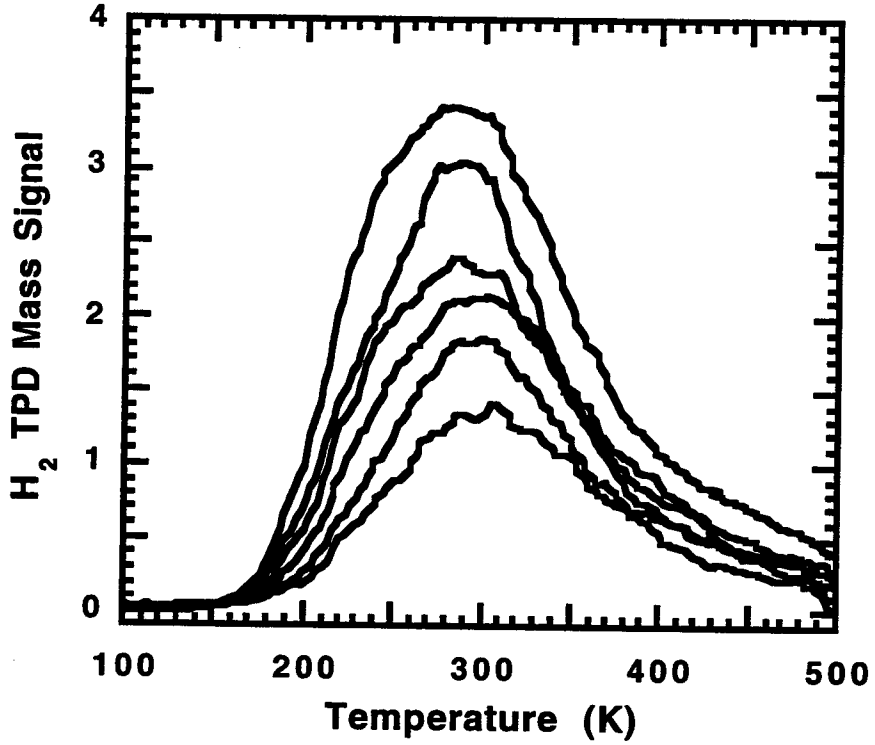

Figure 2: Temperature programmed desorption spectra from arc-discharge materials for hydrogen coverages between 0.3 and saturation.

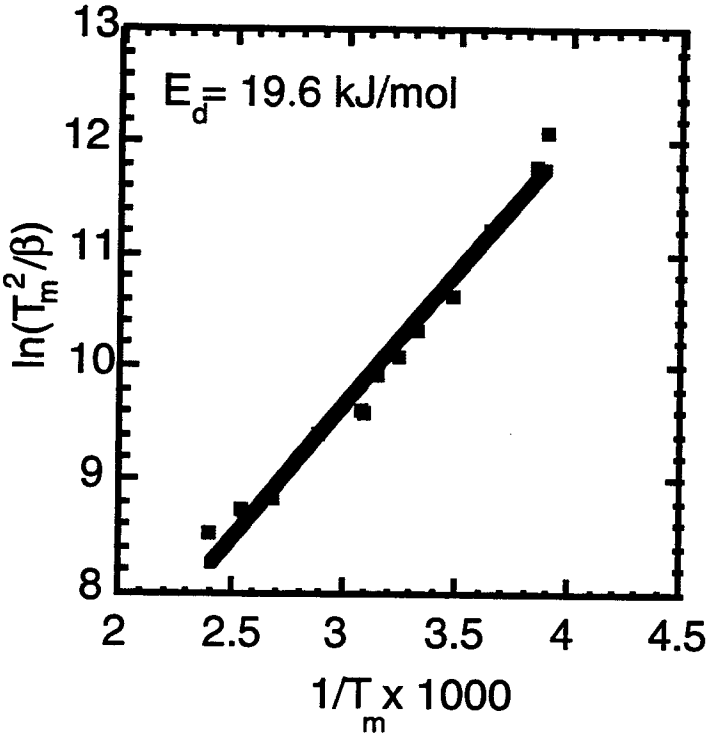

Figure 3: Plot of $\ln(T_m^2/\beta)$ vs. $1/T_m$ for arc-discharge material with ß ranging from 0.3 to 30 K/s. Straight line behavior shows 1st order desorption for H_2.

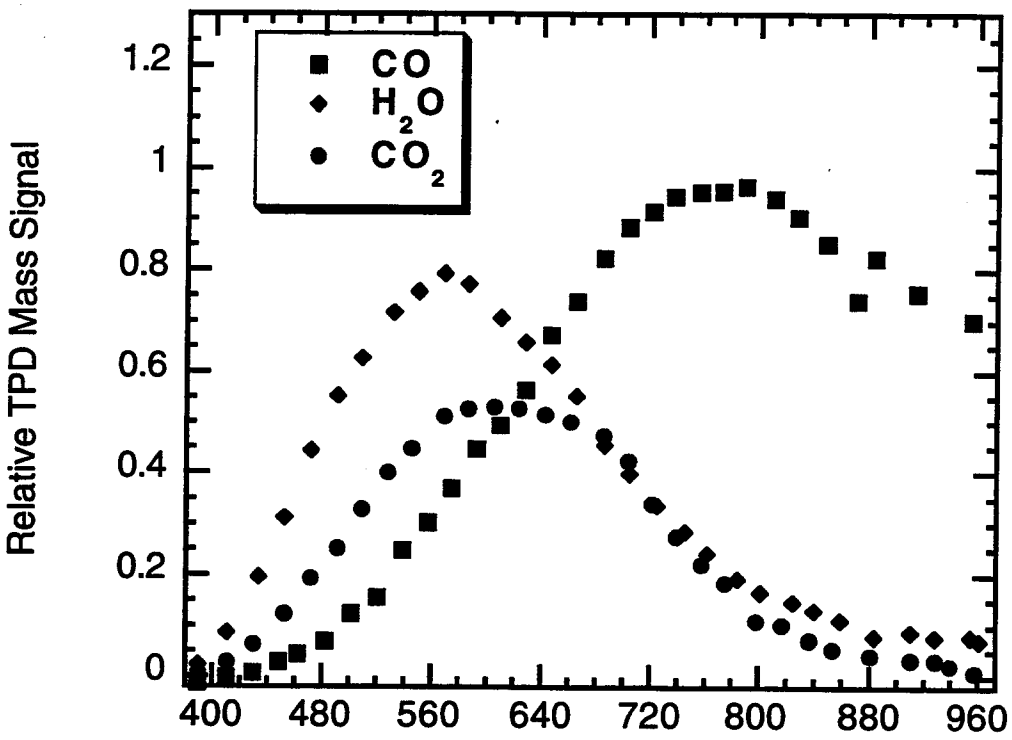

Figure 4: TPD spectra of desorbing H_2O, CO_2 and CO during outgassing of arc-generated SWNT material in vacuum.

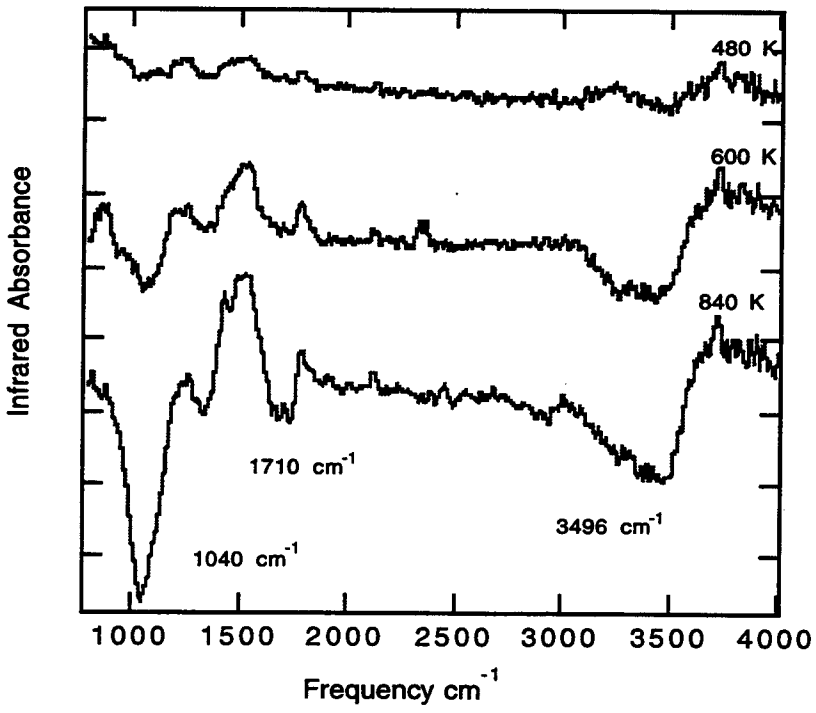

Figure 5: DRFTIR difference spectra of arc-generated SWNT material as a function of heating in vacuum.

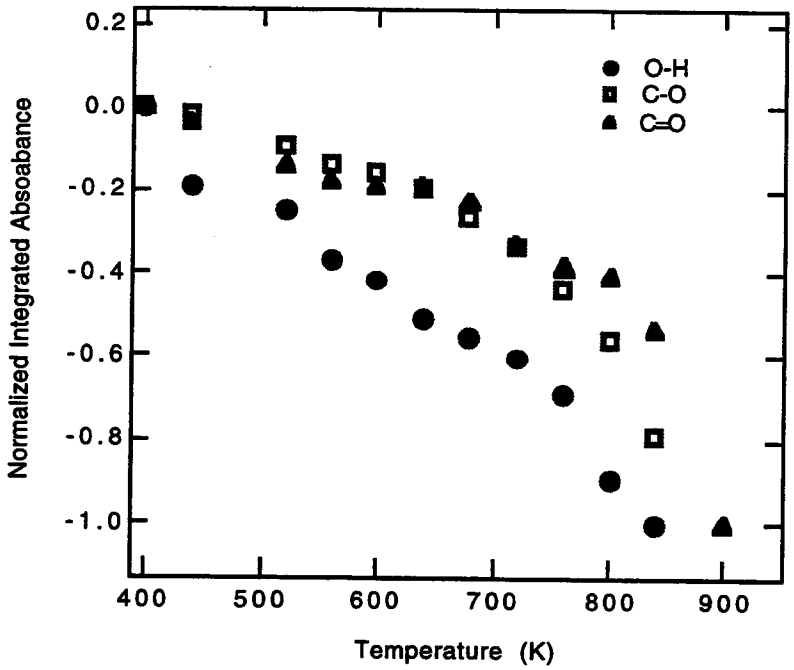

Figure 6: Normalized integrated absorbances of O-H, C-O and C=O stretching vibrations as a function of temperature for outgassing arc-generated material.

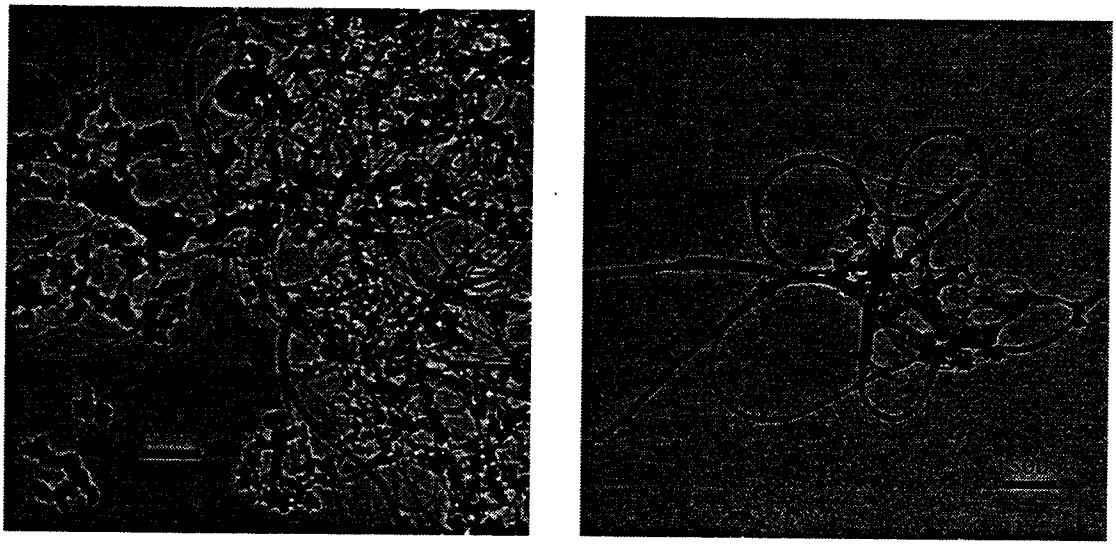

a) b)

Figure 7: TEM images of a) as prepared laser-generated SWNT material and b) laser-generated soot oxidized for 10 min. in 1 torr O_2 at ~1050 K.

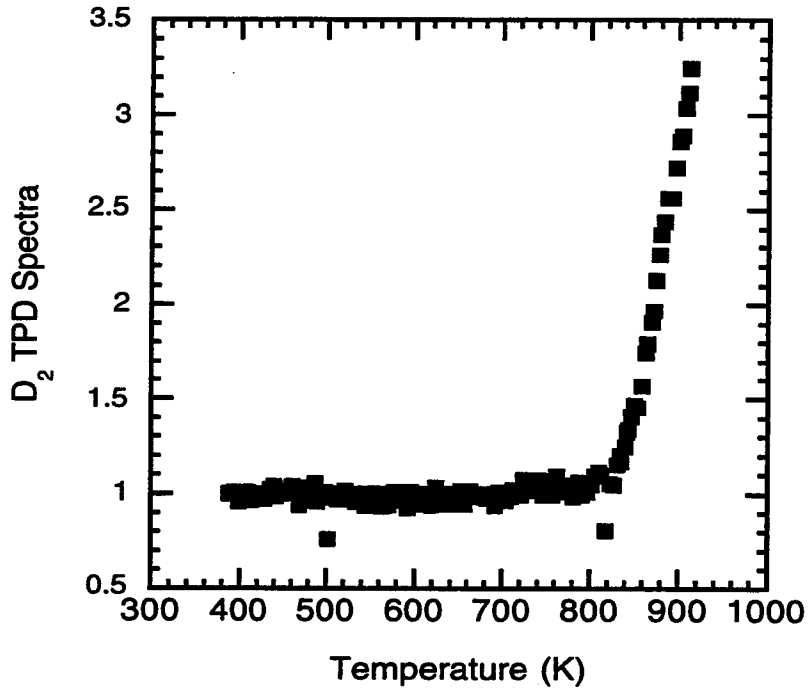

Figure 8: Deuterium TPD spectrum following oxidation of arc-generated SWNT material in D_2O.

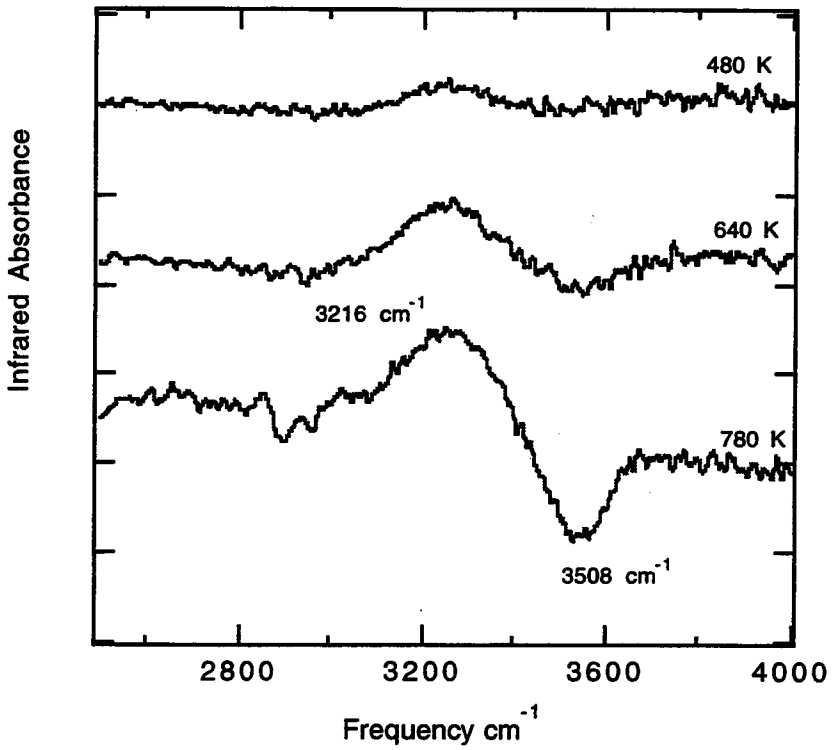

Figure 9: DRFTIR difference spectra of laser-generated SWNT material vs heating in vacuum.

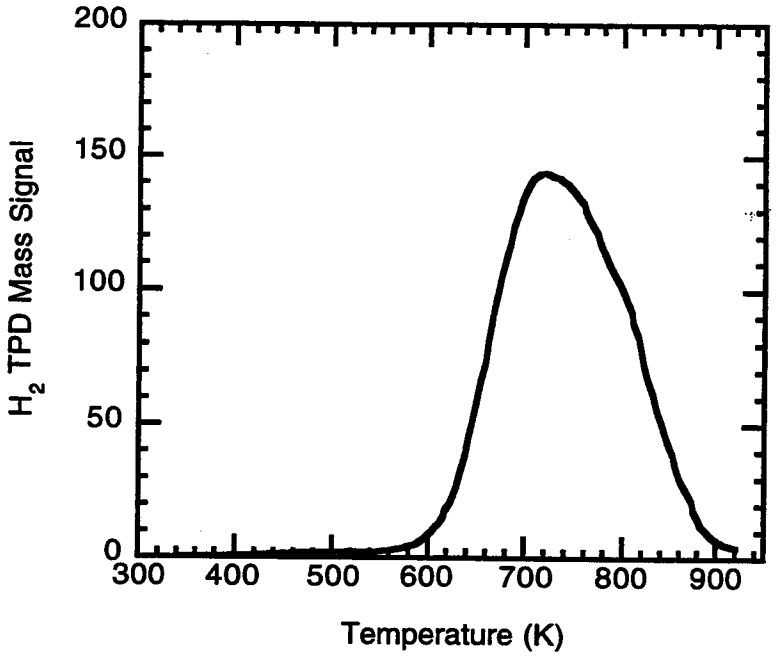

Figure 10: Hydrogen TPD Spectrum following reduction of laser-generated material in 650 psi H_2 at 775 K.

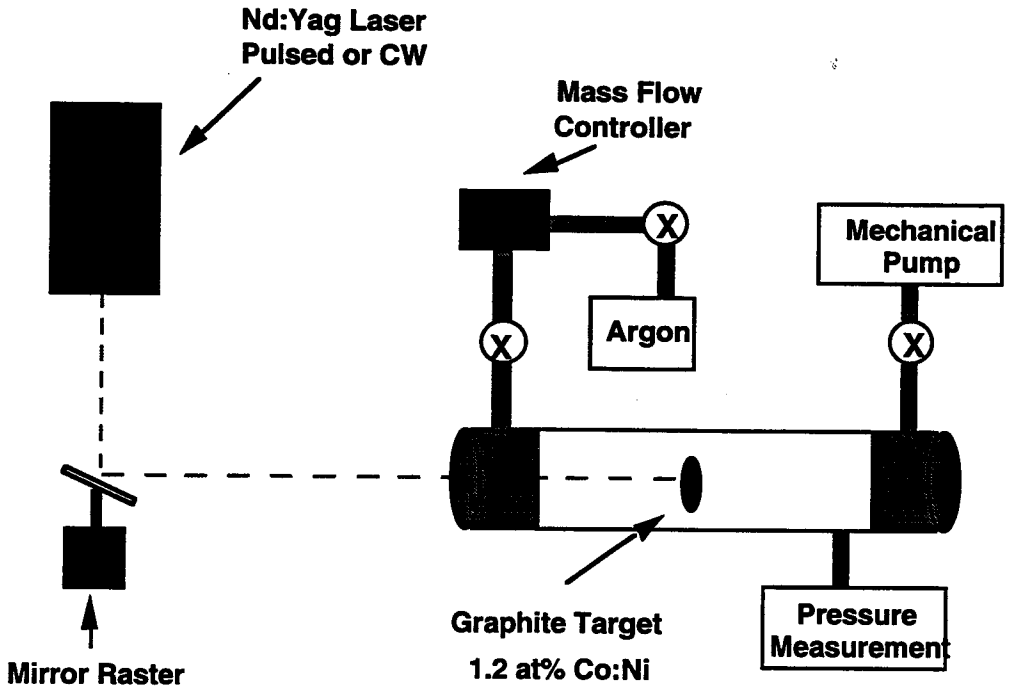

Figure 11: Schematic of set-up for laser-based synthesis of SWNTs

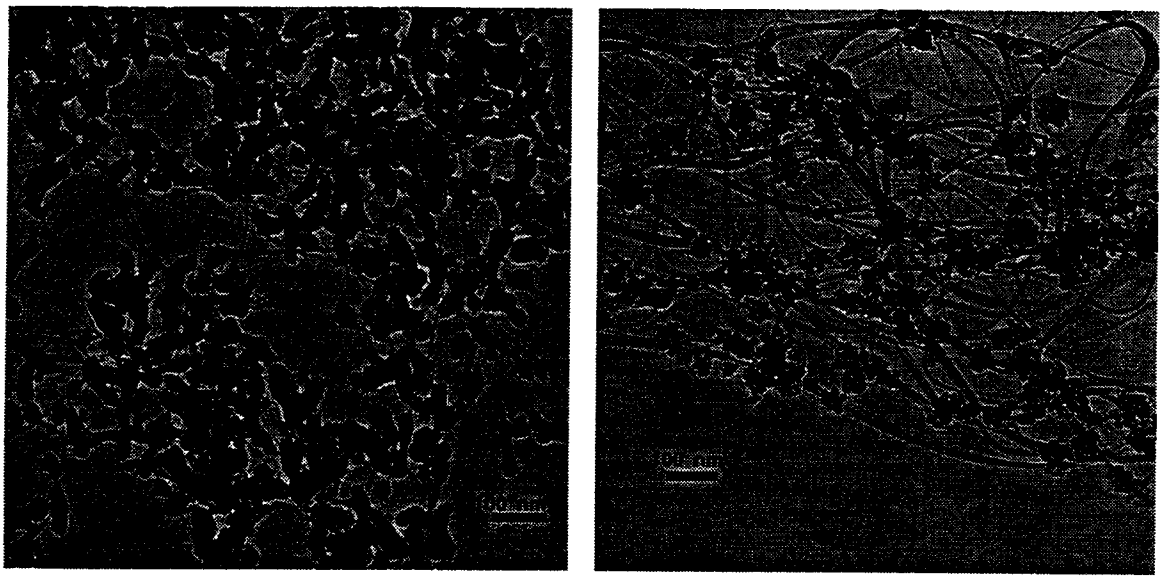

a) b)

Figure 12: Comparison of SWNTs made by (a) arc-discharge and (b) laser-vaporization.

DEVELOP IMPROVED METAL HYDRIDE TECHNOLOGY FOR THE STORAGE OF HYDROGEN

Krishna Sapru, Ned Stetson
Lu Ming and Jim Evans
1675 West Maple Road
Troy, Michigan 48084
Energy Conversion Devices, Inc.
Troy, MI 48084

Abstract

While metal hydrides are a very attractive means for hydrogen storage, in order to fabricate practical metal hydride-based energy storage systems, there is a need for new improved hydriding alloys and novel system engineering designs. Conventional high capacity hydrides need high temperatures to liberate the hydrogen whereas low temperature metal hydrides suffer from low gravimetric energy density. This work was done under a cost-shared USDOE contract #DE-FC36-96GO10145, during 1996-1997. The overall objective of this work is to develop commercially viable metal hydrides capable of storing between 3-5 wt.% hydrogen for use with PEM fuel cells and for other applications including hydrogen fueled internal combustion engine (HICE). During this contract period ECD has prepared and tested, proprietary Mg-based multi-component alloys made by a mechanical alloying process. These high capacity alloys have excellent kinetics at 300° C. The PCT characteristics of these alloys show indication of some modification of the Mg near-neighbor atomic configuration. While promising, additional work needs to be performed to achieve the goals of this work. We have also succeeded in substantially increasing the yield of the mechanical alloying process.

Introduction

Concerns about global warming, urban air quality, acid rain, and energy supply security are motivating increased interest in low-polluting alternative transportation fuels. The need to develop a sustainable energy system becomes even more urgent when we consider that in 1991 the United States spent $51 billion for imported oil, which accounted for more than 50% of the trade deficit.

Hydrogen is a high quality, exceptionally clean fuel that has been demonstrated in experimental cars, buses, trucks and airplanes. With hydrogen internal combustion engine (H-ICE) vehicles, the only pollutants are low levels of nitrogen oxides and with hydrogen fuel cell vehicles, even NO_x emissions would be eliminated. If hydrogen is produced from renewable resources, via water electrolysis using solar, wind, or hydroelectric power, it would be in principle possible to produce and use hydrogen as a transportation fuel on a large scale, resulting in zero emission vehicles.

In a typical hydrogen powered fuel cell, hydrogen fuel combines with oxygen from air to form water, heat and electricity. The primary fueling option for most applications will be direct hydrogen stored on-board the vehicle. Hydrogen fuel cell vehicles combine the best features of electric-battery vehicles (zero emissions, high efficiency, quiet, long life) with the convenience and flexibility of gasoline vehicles (fast refueling time, long range). The hydrogen powered proton exchange membrane (PEM) fuel cells appear the most likely type of fuel cells for passenger vehicles and light-duty applications. One of the most serious barriers to the utilization of fuel cell technology is the lack of a practical hydrogen storage system and the related infrastructure requirement.

Background

Large-scale introduction of hydrogen requires the development of compact, lightweight, cost-effective and safe means of storing the hydrogen for use in mobile and stationary applications. The desired hydrogen storage system must have high gravimetric and volumetric energy density, packaging flexibility, ease of recharging, ease of manufacturing, long life, environmental acceptability, and low to zero energy loss during storage. Hydrogen stored as compressed gas will neither result in high energy density nor the degree of safety and cost required. Liquid hydrogen requires special handling, and boil-off losses are a problem. The safest and most practical method for storing hydrogen is in the form of metal hydrides.

Metal hydrides consist of solid alloys that are capable of reversibly storing large amounts of hydrogen at ambient temperatures and at much lower pressures than gaseous or liquid hydrogen. There is much already known about the thermodynamic and kinetic properties of metal hydrides, and compared to all the carbon-based materials, metal hydrides have the advantage of low cost and ease of manufacture. They can provide a safe, energy efficient, environmentally sound means of storing hydrogen fuel for use with fuel cells and for H-ICE vehicles. An additional advantage of metal hydrides is their ability to deliver very pure hydrogen. This is an advantage for use in fuel cells which use catalysts that can be easily poisoned if any impurities (such as CO) are present in the hydrogen. Metal hydrides have negligible, if any, loss during storage, giving them extremely long shelf-life. A significant advantage of metal hydrides is their safety, since they are low pressure systems. Another important advantage is that their chemistry is well understood. This is a result of many years of research efforts by a large number of scientists worldwide.

Hydride storage has been demonstrated in vehicles in the US and overseas by Mercedes-Benz, Mazda and Toyota. However, vehicle range has been limited because low temperature alloys have

low gravimetric energy density and high capacity alloys are too stable for some applications. Significant opportunities exist to advance the state-of-the-art by developing high capacity alloys that can release hydrogen at low-medium temperatures. With rapid progress occurring in the development of renewable energy (such as PV and wind), water electrolysis, and PEM fuel cell technology, the market for new improved metal hydrides can be enormous.

Applications of metal hydrides include:

- Hydrogen storage/energy transportation medium
- Rechargeable batteries
- Non-CFC Heat pumps/air conditioners
- Hydrogen storage for fuel cells and hydrogen fueled vehicles
- Fuel storage for portable power fuel cells
- Catalysts
- Compressors
- H-gas separation medium

For practical applications, metal hydrides must have the following properties:

- Good reversibility
- High storage capacity
- Desired pressure/temperature characteristics
- Easy activation
- Low cost
- Stable in ambient environment
- Ease of scale-up
- No environmental consequences

According to DOE sponsored studies (DTI data), it is estimated that 3.58 kg of hydrogen is needed onboard a standard PEM fuel cell vehicle which will provide a range of 300 miles. This calculation takes into account fuel cell inefficiencies. Table1 shows the relationship between the hydrogen storage capacity of a metal hydride and the amount of alloy needed to store 3.58 kg of hydrogen.

Wt. % Storage Capacity	Wt. of alloy (kg)
1	358
2	179
3	119
4	89.5
5	71.6
7	51.1

At 4 wt.% storage capacity, metal hydride onboard storage of hydrogen becomes feasible. Addition of 20-30 % for the container/heat exchanger, etc. could bring the total weight to less than 120 kg. These rough estimates are for the average US passenger car giving in excess of 300 miles. For many transportation applications these numbers can be much lower, requiring a smaller amount of hydrogen to be stored onboard.

For all the other applications of metal hydrides requiring small amounts of hydrogen, such as

portable power and hydride air conditioners, even 2 wt.% alloys will be attractive. The overall market potential for metal hydrides can thus be enormous.

Due to the rapidly growing market for nickel/metal hydride batteries, large scale metal hydride alloy manufacturing facilities already exist for low temperature hydrides. ECD has pioneered the development of metal hydrides and metal hydride batteries and holds 45 patents in the US and 202 related patents worldwide, in this field. ECD currently has large-scale metal hydride manufacturing facilities at its subsidiary, the Ovonic Battery Company (OBC).

Overall Objectives

The overall objective of this work is to develop commercially viable metal hydrides capable of storing between 3-4 wt.% hydrogen for use with PEM fuel cells and for other applications such as the hydrogen fueled internal combustion engine (HICE). This includes the development of low cost bulk methods for commercial manufacturing of the alloys, and improved hydride bed/container designs.

The specific technical objectives are as follows:

1. To reduce the desorption temperature of Mg-based alloys while maintaining acceptable storage capacity.

2. To achieve the desired equilibrium hydrogen pressures for practical applications.

3. To ensure long cycle life, low cost, ease of manufacturing.

4. Explore novel methods of alloy preparation, in addition to mechanical alloying. This should allow for greater degree of alloying, in addition to making homogeneous materials of small particle size (nano-size).

Technical Discussion

Overall Approach and Background

The greatest challenge in the development of low temperature Mg-based hydrides is to affect the thermodynamic properties of these alloys in order to reduce their H-desorption temperature without drastically lowering their hydrogen storage capacity. This problem is even more challenging due to Mg's low miscibility with most transition metals, it's low melting temperature and high vapor pressure. The use of novel alloy preparation techniques needs to be explored to obtain near-neighbor interactions between Mg and modifier elements since traditional high temperature melting techniques have not been successful. In addition to alloy composition, processing conditions become very important.

In order to obtain high hydrogen storage capacity, a low weight hydride former such as Mg is required. However Mg suffers from slow H-sorption kinetics and high desorption temperatures (>300° C).
These problems can be diminished by surface and bulk modification to: 1) increase the number of catalytically active sites and 2) to modify the local sites for metal-hydrogen bonding. Thus, judiciously designed Mg-based small grain/particle-sized alloys have the potential of overcoming the problems of slow kinetics and high H-desorption temperatures. While Mg readily alloys with Ni, hydrides of Mg-Ni alloys are also too stable. Thus our approach is to use non-conventional

processes that will allow the alloying of Mg with selected transition metal (TM) and rare earth (RE) elements coupled with surface modifications. Such novel processes include:

1. Mechanical alloying
2. Gas Phase Condensation
3. Melt Spinning
4. Gas Atomization

Past Results and Summary of Recent Achievements

Past Results

In the early 1980's, ECD developed and patented several families of Mg-based alloys having superior hydrogen storage properties. These alloys were prepared using thin film techniques such as sputtering. Under the DOE cost-shared program we have successfully scaled up these materials from thin film to bulk, using a mechanical alloying process. Mg- based multi-component alloys have been prepared and characterized. Results to date have been very encouraging. Alloys having above 5 wt.% hydrogen storage capacity and good cycle life have been prepared.

Summary of recent achievements

A. Process Optimization
B. Alloy Optimization
C. Product and Market Research

Process Optimization

We have demonstrated that the grinding speed during mechanical alloying can have a significant effect on the degree and nature of the alloying. We demonstrated that in order for the Mg and the TM elements to be in close proximity and enhance the probability of alloying, high grinding speeds are desirable. Alloying was done at speeds varying from 150 to 1000 rpm.

In addition to higher grinding speeds, we experimented with the addition of grinding aids. Two types of grinding aids have been used. Graphitic carbon was used as a solid grinding aid and heptane as a liquid grinding aid. Addition of heptane improves the alloy yield substantially. Carbon addition has two effects, it acts as a lubricant and also has a significant effect on the enhancement of sorption kinetics. Figures 1 - 9 show the experimental results of process optimization.

Alloy Optimization

Research on alloy optimization includes the following approaches:

1. Effect of processing conditions on alloy properties.
2. Modification of Mg with pre-alloyed, low temperature hydride formers such as FeTi.
3. Modification of Mg with individual elements of low temperature hydride, i.e. Mg+Fe+Ti.
4. Modification of Mg with pre-formed alloy of a number of TM elements.
5. Modification of Mg with individual elements of the TM alloy.

6. Mechanical alloying of MgH_2 using the above modifiers.

Figure 10 shows the desorption kinetics of the modification of Mg by the addition of FeTi in three different ways:

a) Simultaneous grinding of Mg, Fe, and Ti
b) Grinding of Mg with an inductively melted alloy of FeTi and
c) Pre-alloying of FeTi by mechanical alloying before the addition of Mg.

Figure 11 shows the X-ray diffraction patterns of the alloys made using the three different means of alloy preparation.

The effect of the addition of multiple transition elements in the form and a pre-alloy and as individual elements is shown in figure 12 which shows somewhat improved kinetics by the addition of individual elements. Figure 13 shows the corresponding XRD data.

The most important aspect of the above modification is affect on the PCT characteristics as shown in figure 14. We see the presence of additional small plateau regions in the PCT profile which are not attributable to MgH_2 or MgNi alloy. There is indication that we may have actually begun to affect the near neighbor atomic and electronic configuration of the Mg atoms. This result while preliminary, is the first of its kind and very encouraging.

As mentioned above, one approach that may prove promising is to use MgH_2 as a starting material instead of Mg. The XRD pattern of a preliminary experiment in this direction is shown in figure 15.

The results of the process and alloy optimization to date can be summarized as follows:

1. Alloy yield has been substantially increased.
2. Increasing the grinding speed improves the diffusion of TM elements into the Mg particles, enhancing break-up into smaller particles, resulting in improved kinetics.
3. Addition of graphitic carbon and heptane drastically improves the alloy yield and also it's kinetics.
4. For a fixed alloy composition, processing parameters have an effect on the alloy properties.
5. Addition of C improves the alloy kinetics.
6. We have shown that several TM elements can be added to Mg without substantially reducing the alloys H-storage capacity. The resulting alloy has excellent kinetics at 300°C and its PCT profile shows the presence of some species other than Mg, having small regions of plateau pressure which is higher than that of Mg or Mg-Ni.

Recent Publications and Presentations

"An investigation of the Partial Substitution of Nickel in Mechanically Alloyed Mg-based Hydrides," N.T. Stetson; L. Ming; J. Evans; K. Sapru, Proc. International Sump. Metal Hydrogen Systems, (J. Alloys Compds.) Les Diablerets, Switzerland, Aug. 25-30, 1996, in press.

"Overview of The USDOE Hydrogen Program," K. Sapru, Paper presented at the UNDP workshop on hydrogen held at Banaras Hindu University, India in December 1996.

"Development of Improved Metal Hydride Technology," K. Sapru, Paper presented at the UNDP workshop on hydrogen held at Banaras Hindu University, India in December 1996.

"Development of a Small Scale Hydrogen Production-Storage System for Hydrogen Applications," K. Sapru; N.T. Stetson; S.R. Ovshinsky; J. Yang; G. Fritz; M. Fairlie; A.T.B. Stuart, Proc. Intersociety Energy Conversion Engineering Conference, invited to paper, Honolulu, Hawaii, July 27-August 1, 1997, in press.

28th ACS Central Regional Meeting: Metal Hydrogen Systems Symposium, 9-12 June, 1996, Dayton, OH, "investigation of the effect on the equilibrium plateau pressure by the partial substitution of Ni by various metals in Mg-based hydrides."

11th World Hydrogen Energy Conference, 23-28 June, 1996, Stuttgart, Germany, "The kinetics of some specially tailored Mg-based alloys."

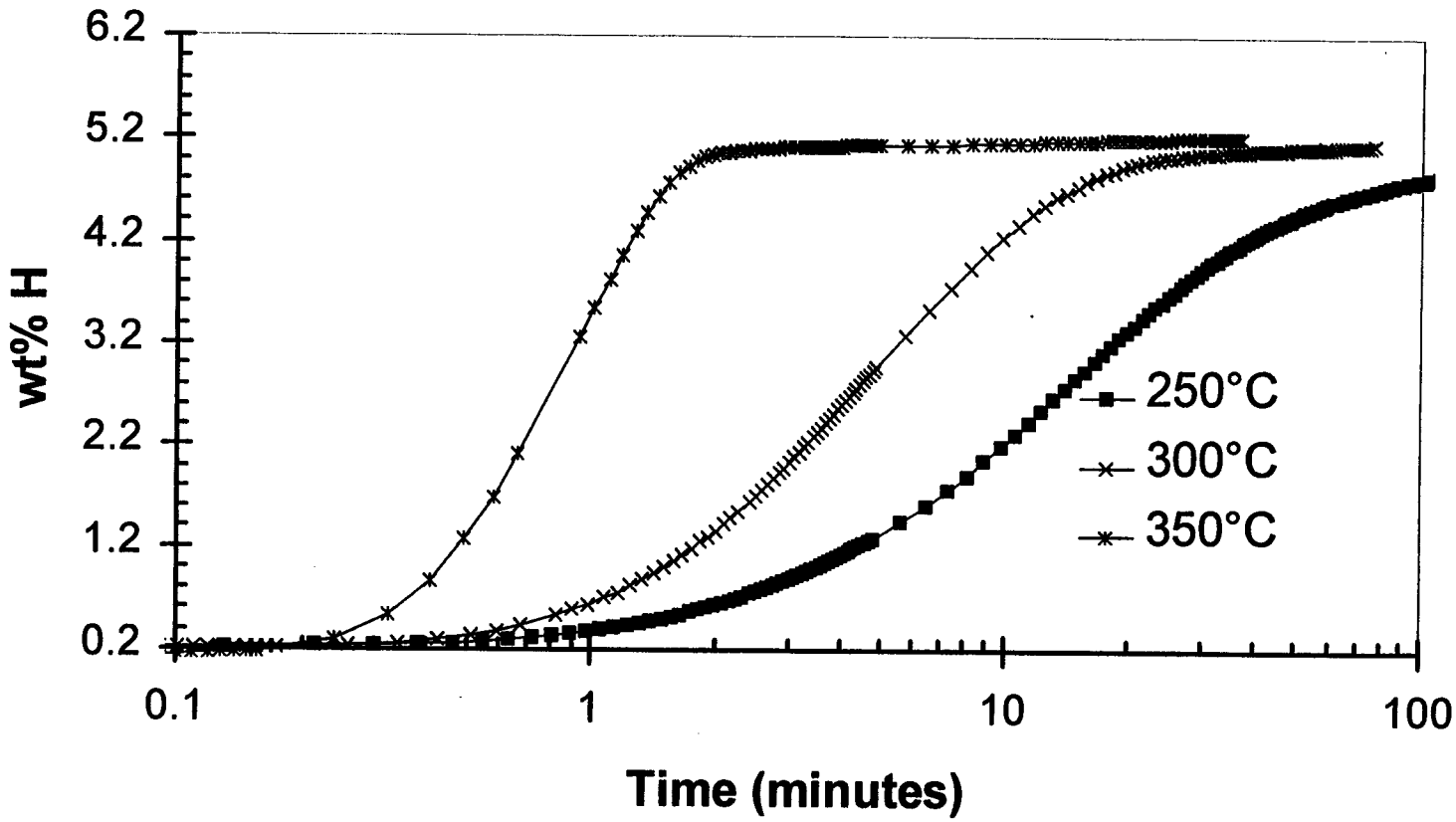

Hydrogen Desorption Kinetics

Figure 1

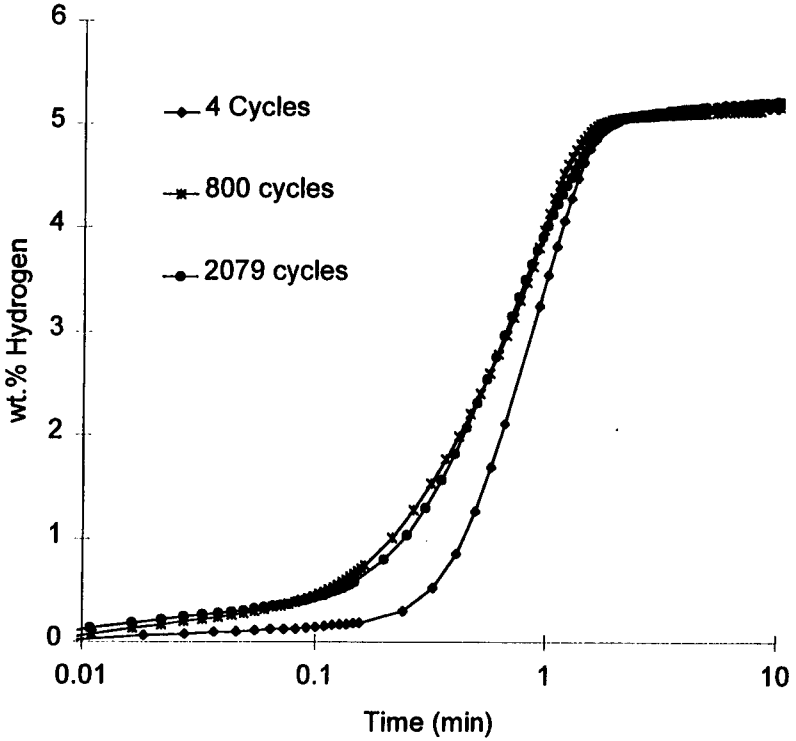
6
5
4
3
2
1
0
wt.% Hydrogen
4 Cycles
800 cycles
2079 cycles
0.01
0.1
1
10
Time (min)

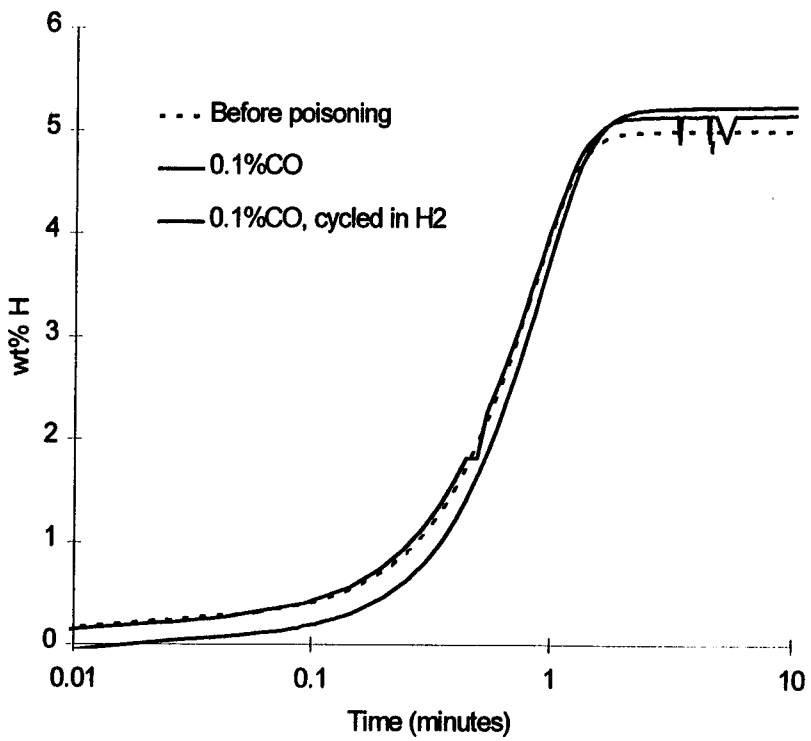
6
5
4
3
2
1
0
wt% H
Before poisoning
0.1%CO
0.1%CO, cycled in H2
0.01
0.1
1
10
Time (minutes)

Figure 2

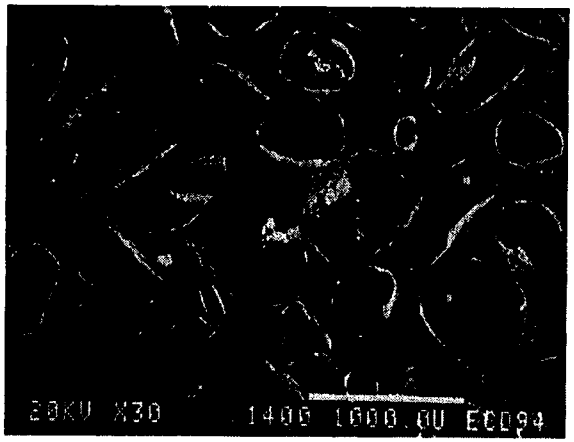

150 rpm/3 hours

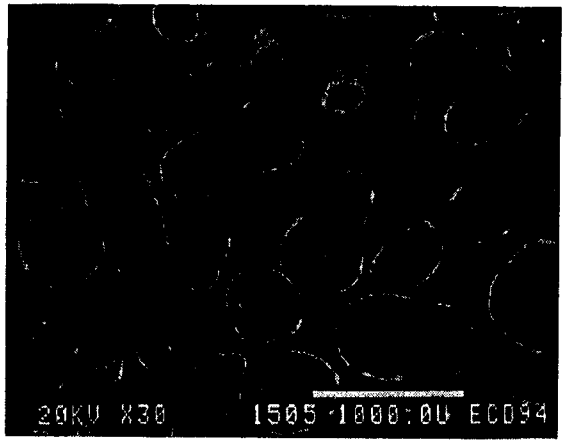

300 rpm/3 hours

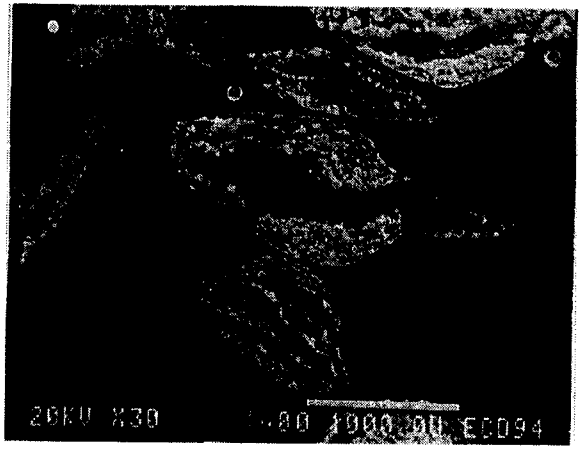

600 rpm/3 hours

Example: Effect of grinding/processing speed

Figure 3

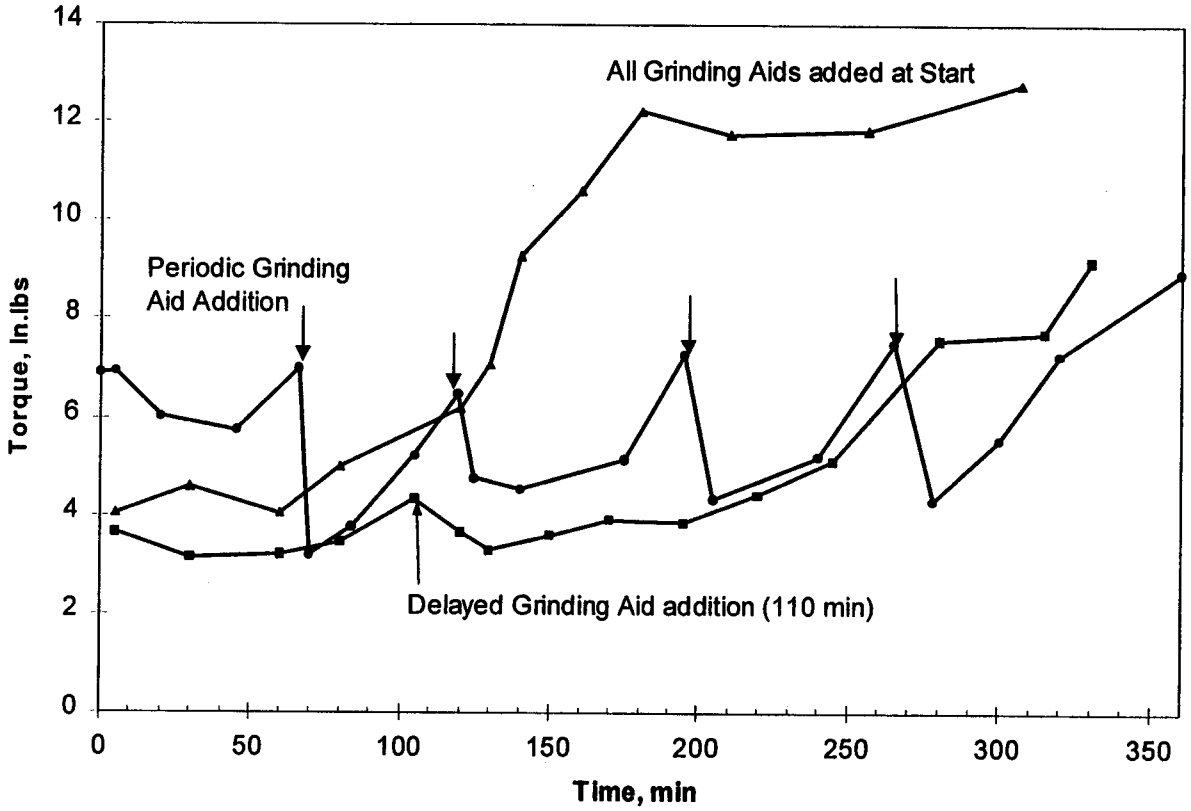

Effect of Grinding Aid Addition on Torque
(liquid and solid grinding aids, 600 rpm, Ar environment)

Figure 4

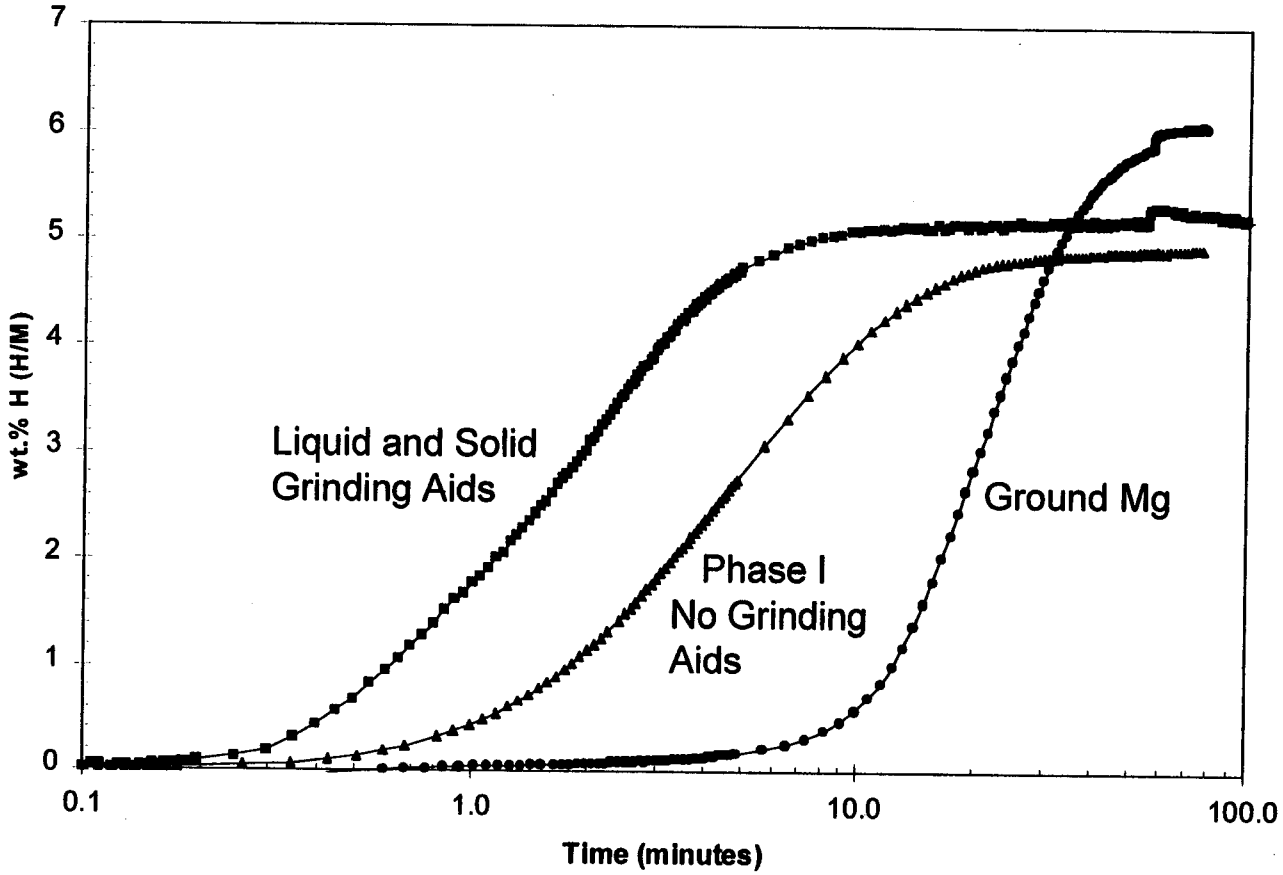

Effect of Grinding Aid Addition on 300°C Desorption Kinetics

Figure 5

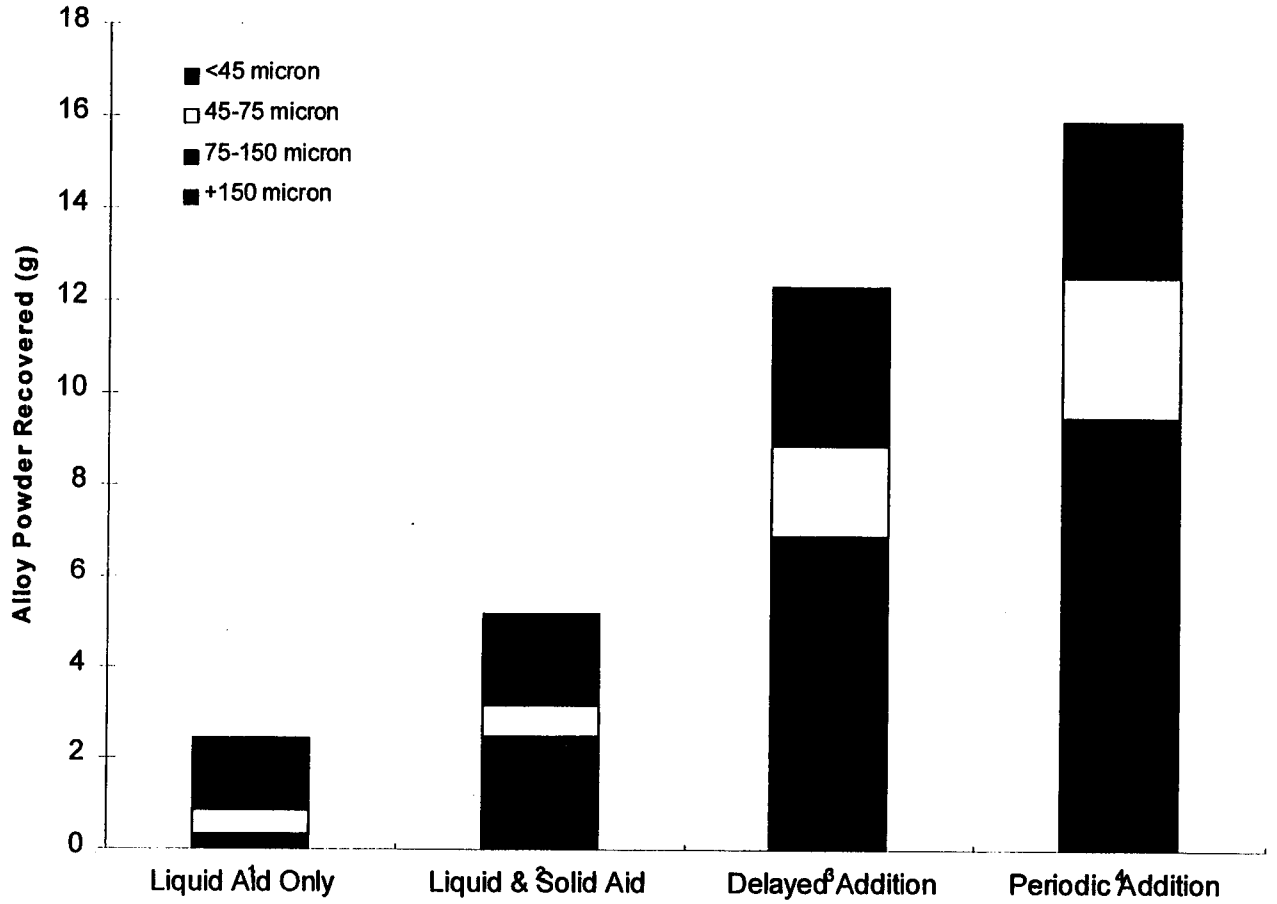

Effect of Grinding Aid Addition on Yield and Particle Size

Figure 6

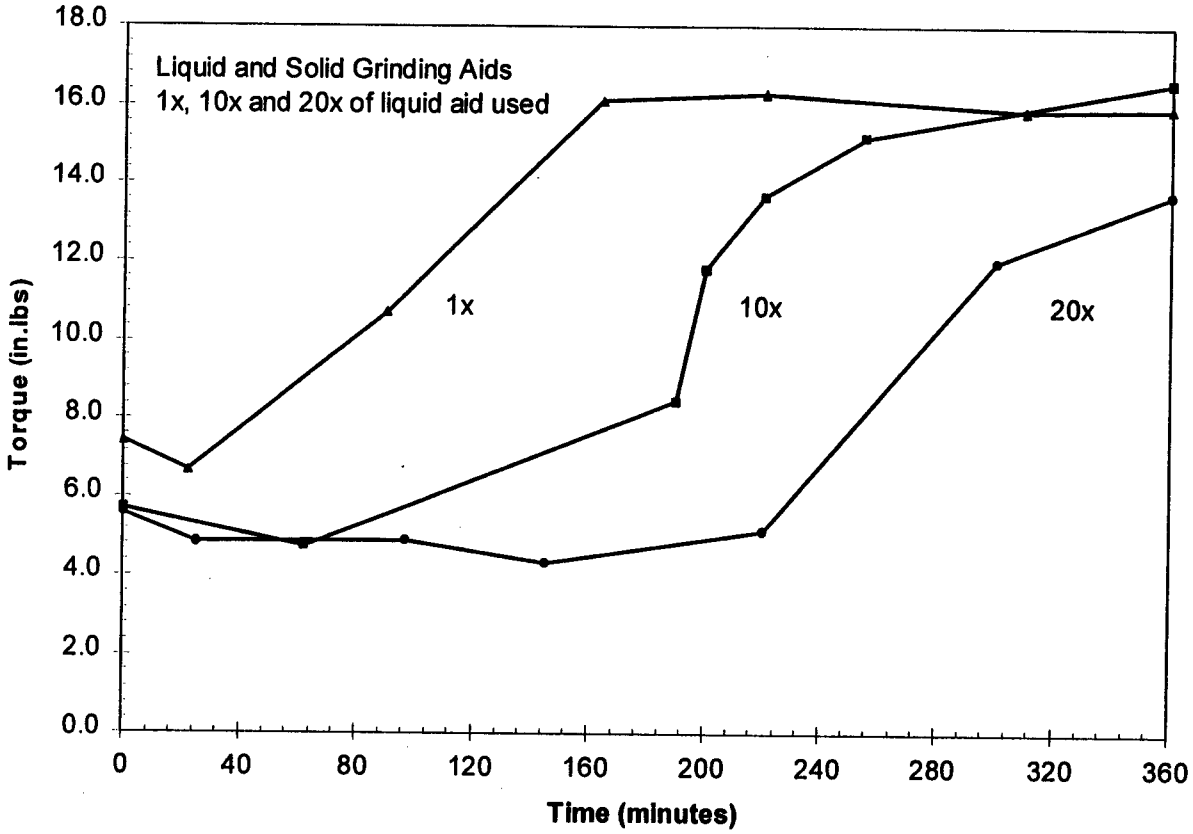

Effect of Liquid Aid Quantity on Torque

Figure 7

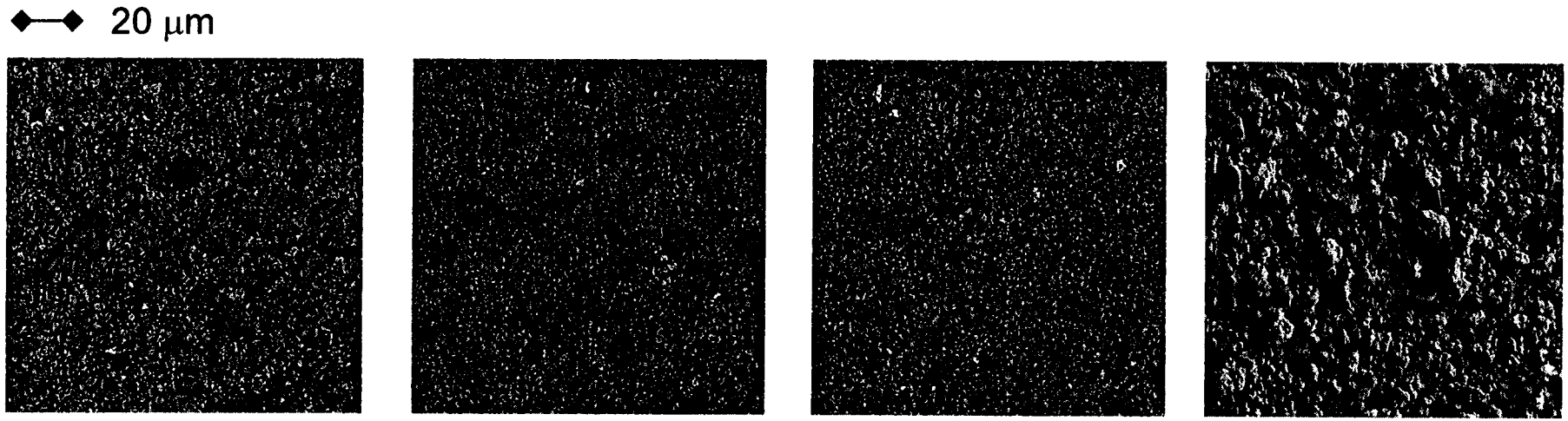

SEMs showing Effect of Liquid Aid Quantity (600x)

Figure 8

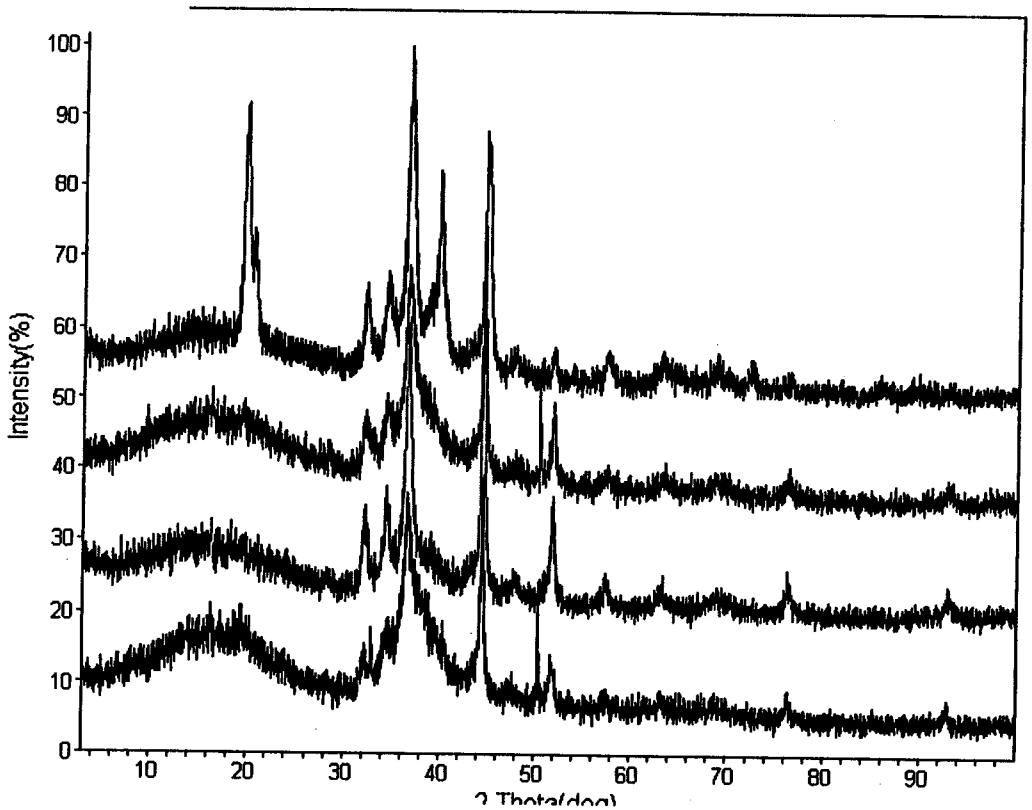

Effect of Liquid Aid Quantity on X-ray Diffraction

Figure 9

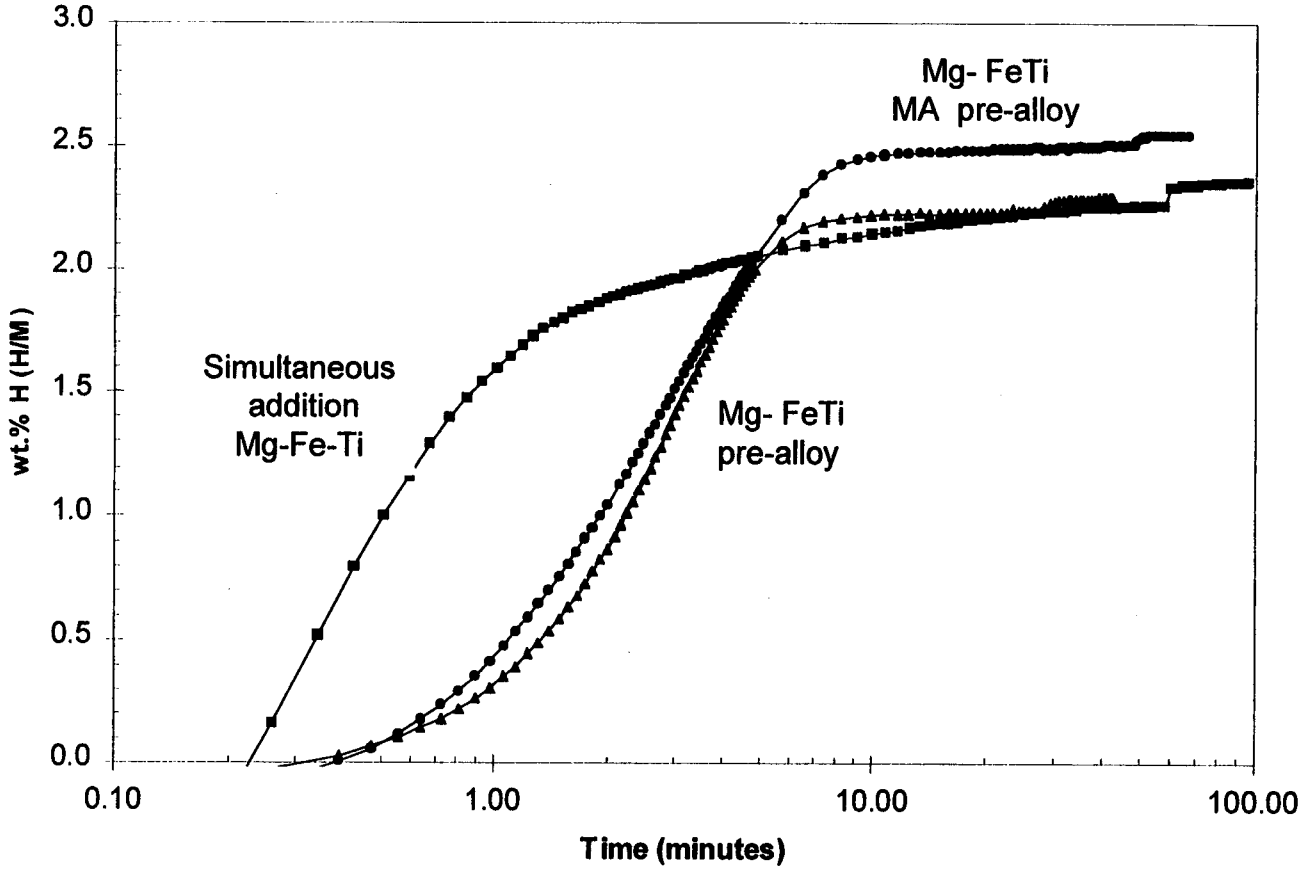

300°C Desorption Kinetics for Mg-Fe-Ti Alloys

Figure 10

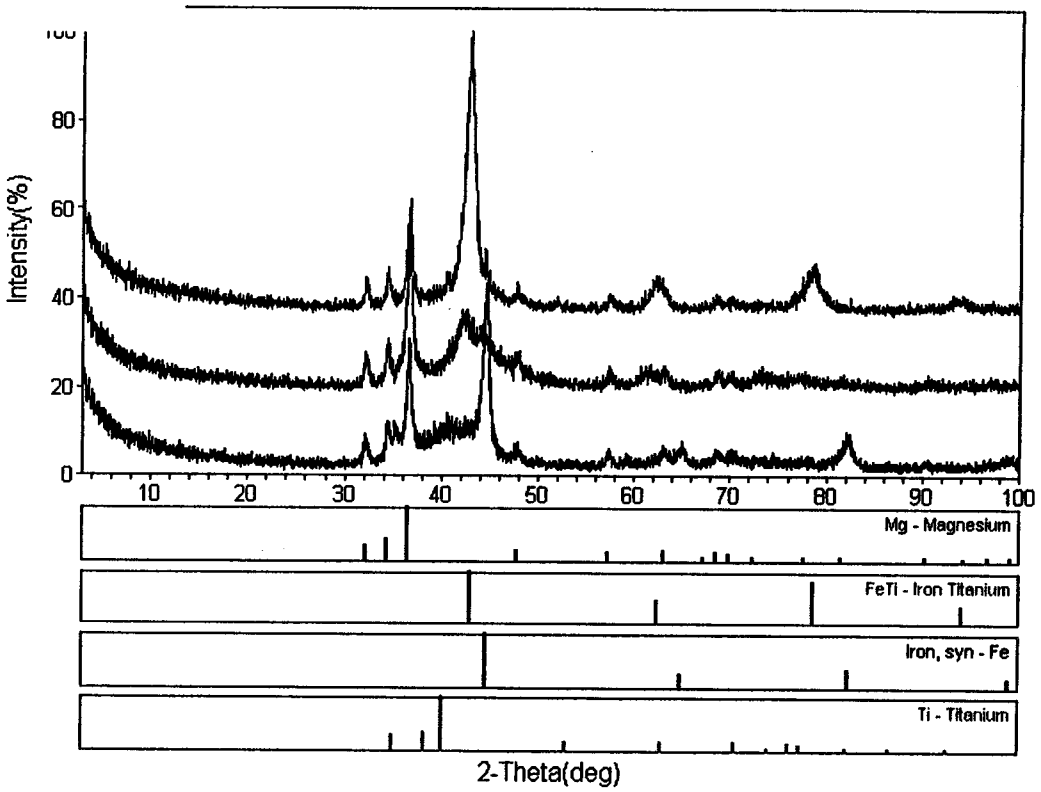

X-ray Diffraction Patterns for Mg-FeTi based Alloys

Figure 11

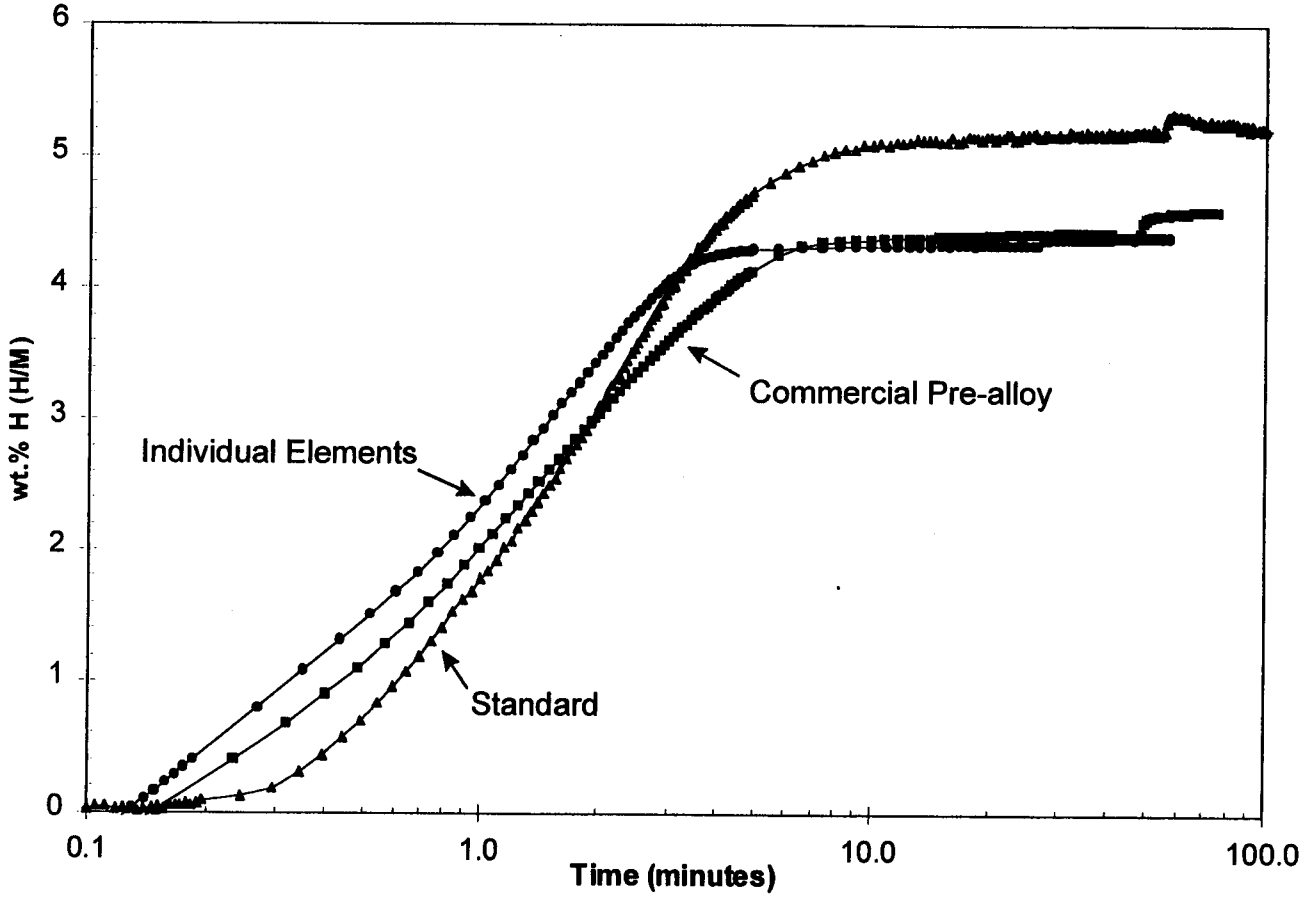

300°C Desorption Kinetics for Mg-Ni based Alloys

Figure 12

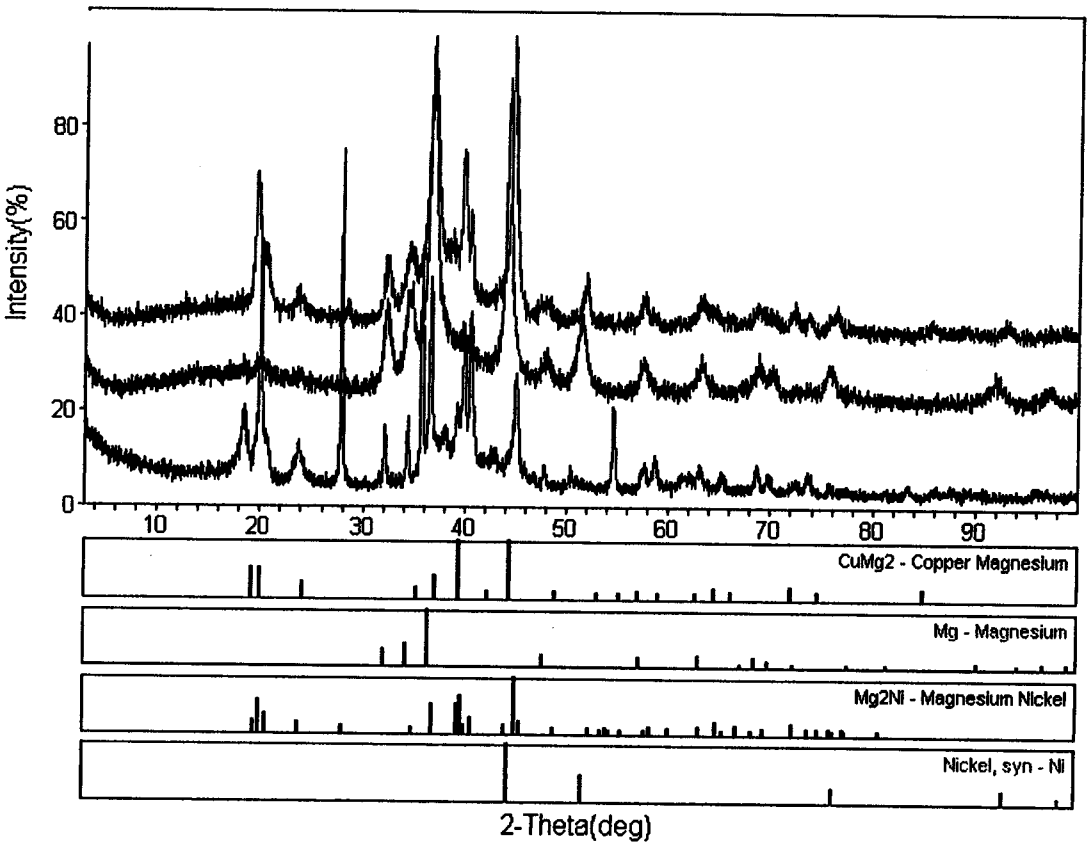

X-ray Diffraction Patterns for Mg-Ni based Alloys

Figure 13

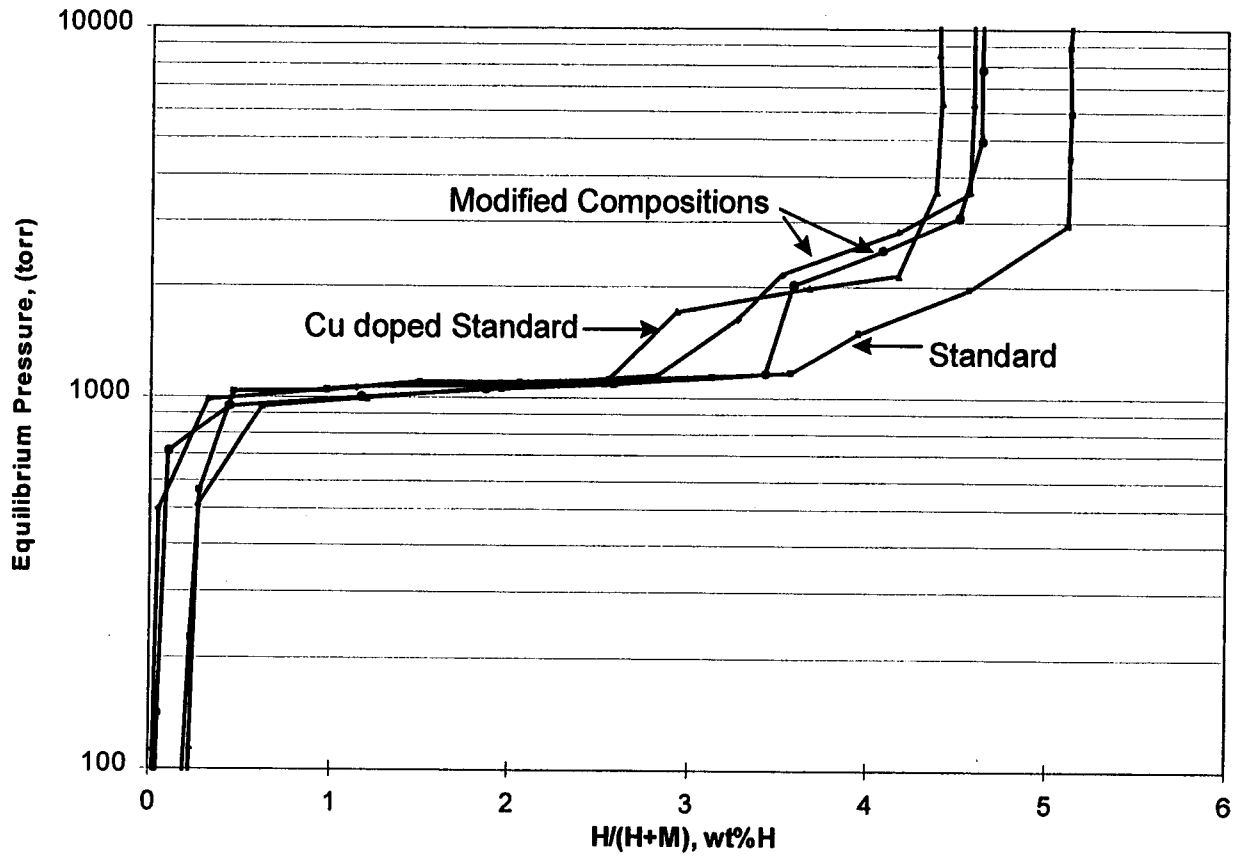

300°C Desorption P-C-T Curves for several Mg-Ni based Alloys

Figure 14

SIMULTANEOUS PURIFICATION AND STORAGE OF HYDROGEN

Scott Hynek, Gus Block, Eric Carlson, Robert Weber and Ware Fuller
Arthur D. Little, Inc.
Cambridge, MA

Abstract

Specially coated magnesium particles have been shown to selectively absorb hydrogen from a hydrogen-rich gas stream. These coated magnesium particles can store the absorbed hydrogen as required and subsequently deliver pure hydrogen, just as uncoated magnesium particles can. These coated magnesium particles could be used in a device that accepts a steady stream of reformate, as from a methane reformer, stores the selectively absorbed hydrogen indefinitely,and delivers purified hydrogen on demand.

Introduction

Magnesium is a superior metal for hydriding from the standpoints of capacity and cost. Magnesium hydride holds 7.6% hydrogen by weight, considerably more than any other practical metal hydride. Also, magnesium is much less expensive than the more commonly used hydridable alloys.

There are three reasons why magnesium is not more commonly used in hydrogen storage applications:

1. *Its reaction kinetics are poor.* This can be remedied by catalyzing the dissociation of molecular hydrogen at or near the surface of the magnesium particles. Bogdanovic[1] has demonstrated the effectiveness of co-macerating the magnesium powder with powdered nickel to accomplish this. The authors[2] have demonstrated the effectiveness of coating the magnesium powder with a thin layer of nickel to accomplish the same thing.

2. *The considerable energy to dehydride magnesium hydride must be provided at inconveniently high temperatures.* The energy required to dehydride magnesium hydride is 27% of the higher heating value (HHV) of the hydrogen released. Most metal hydrides require roughly 10% of the HHV of hydrogen to dehydride. In some applications, this energy can be provided by waste heat such as the sensible heat in engine exhaust or in fuel cell tailgas. However, magnesium hydride must be dehydrided at temperatures well above vehicular fuel cell operating temperatures. This limitation can be remedied by storing the energy from the hydriding reaction at high temperature by using it to melt a phase change material, and by subsequently

[1]Borislav Bogdanovic, "Method of Preparing Active Magnesium-Hydride or Magnesium Hydrogen-Storer Systems," US Patent No. 5,199,972, April 6, 1993.
[2] S. J. Hynek and W. D. Fuller, "Stationary Hydrogen Storage Using a Phase Change Material," *Proceedings of the 11th World Hydrogen Energy Conference,* Stuttgart, Germany, June, 1996.

recovering that heat of fusion to supply the dehydriding energy. This concept was patented by Sandrock and Snape[3] for hydridable materials in general and demonstrated specifically for magnesium by the authors[4].

3. *Magnesium will react with some of the non-hydrogen species found in reformate.* This limitation does not apply to using magnesium to store pure hydrogen, but it does apply to using magnesium to selectively absorb hydrogen from reformate. It also applies to using nickel-coated magnesium to selectively absorb hydrogen from reformate. It was this limitation that prompted the development of the special coating to be discussed below.

Hydrogen is typically produced by reforming methane, purified by a pressure swing adsorber (PSA), and stored as a compressed gas (unless the production rate is large enough to justify liquefaction and cryogenic storage). Magnesium particles coated with a hydrogen-permselective material would permit the construction of a device that could simultaneously purify and store the hydrogen. This device could replace both the PSA and much, if not all of the compressed gas storage.

Such a device is represented schematically by Figure 1. This device could accept a steady flow of reformate from a methane reformer, and it could satisfy an intermittent demand for hydrogen by a small industrial user of hydrogen or by a hydrogen fueling station. The mismatch between reformate supply and hydrogen demand is accommodated by the hydrogen storage capacity of the coated magnesium particles. The thermal mismatch between heat rejected by the hydriding bed and the heat accepted by the dehydriding bed is accommodated by the thermal storage capacity of the phase change material.

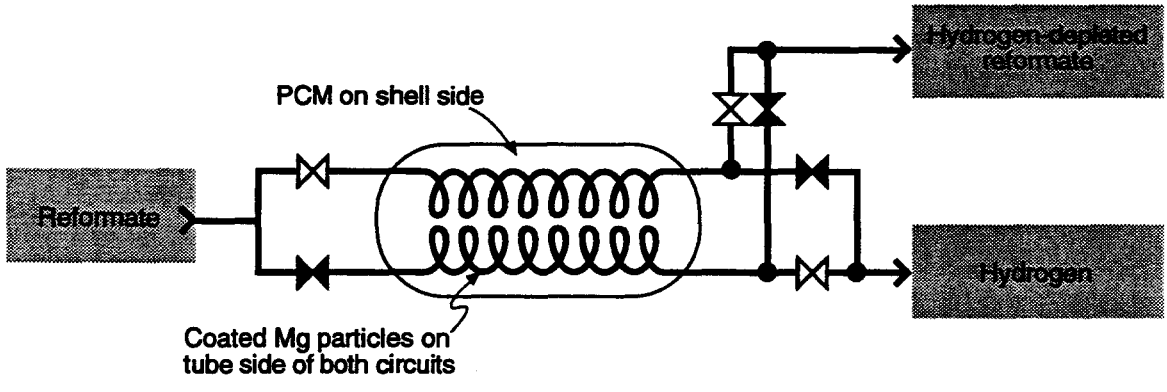

Figure 1 - Schematic Flow Diagram of Device to Accept Steady Flow of Reformate and Deliver Intermittent Flow of Hydrogen

[3] Gary D. Sandrock and Edwin Snape, "Reaction Heat Storage Method for Hydride Tanks," US Patent No. 4,566,281, January 28, 1986.

[4] "High Efficiency Stationary Hydrogen Storage," final technical report to NREL, Arthur D. Little Reference No. 45781, February, 1995.

Discussion

Hydrogen can be separated from the other species in a hydrogen-rich gas mixture by pressurizing that mixture and exposing it to a hydrogen-permselective membrane. Usually these membranes are supported by some sort of substrate, and the thickness of that membrane is determined by a compromise: both performance and cost favor thin membranes, while the ability to withstand high pressure drops and the ability to use substrates with practical pore sizes both favor thick membranes.

Alternatively, if the membrane is deployed as a coating on an essentially spherical, non-porous particle, then the membrane can be very thin indeed. It can be so thin that the natural gaps that attend very thin layers, such as lattice discontinuities, exist. If these natural gaps exist, and if they are small enough to permit the passage of hydrogen but not other species, then this coating constitutes a hydrogen-permselective membrane. And if that spherical particle is made of a hydridable material such as magnesium, then the coated particle should be able to absorb hydrogen selectively from a hydrogen-rich gas mixture.

A suitable coating material for magnesium particles should possess the following four characteristics:

1. *Hydrogen Permselectivity* - It must pass hydrogen, but it must not pass any other species with which the magnesium might react.

2. *Chemical Inertia* - It must not itself react with the other species, lest it lose its hydrogen-permselectivity.

3. *Compound of Magnesium* - If this coating is formed from the surface of the magnesium particle itself, then its adherence to that particle should be greatly enhanced. This is important given the swelling and contracting that attend, respectively, hydriding and dehydriding of magnesium particles.

4. *Inexpensive* - Magnesium is attractive as a hydridable material partly because it is inexpensive. Were its coating to be expensive, this advantage would diminish.

These coated particles would have to be used in conjunction with a suitable catalyst for dissociating molecular hydrogen. This catalyst should also be inexpensive and inert to the other species, but it need not be hydrogen-permselective, and it need not be a compound of magnesium. This catalyst could be co-macerated with the coated magnesium particles, or it could be applied as a secondary, discontinuous coating.

Results

Our preliminary results indicate that a coating that possesses the above characteristics may be achievable.

1. We have established that magnesium particles can easily be coated with magnesium nitride by means of chemical vapor deposition (CVD) in a fluidized bed reactor.

2. We have established that these magnesium nitride coatings do not degrade the ability of the magnesium particles to hydride and dehydride in the presence of pure hydrogen.

3. We have established that these coated magnesium particles can repeatedly hydride and dehydride in the presence of a mixture of hydrogen, steam, and carbon dioxide.

We measured the ability of magnesium particles to hydride and dehydride using a closed, heated volume in which is contained the magnesium particles (with or without coatings) and a gas (either pure hydrogen or a mixture of hydrogen and other species). Our technique consists of the following steps:

1. Allow the particles and the hydrogen in the gas to reach equilibrium at 300°C ,

2. Vent some of the gas until the hydrogen partial pressure equals the hydrogen/magnesium hydride equilibrium pressure at 300°C (1.45 atm),

3. Allow the particles and the hydrogen in the gas to reach equilibrium at 400°C,

4. Allow the particles and the hydrogen in the gas to reach equilibrium at 300°C ,

Steps 3 and 4 are repeated as long as desired.

Figure 2 shows the result of Step 3 (above) using uncoated magnesium particles in pure hydrogen. The hydrogen pressure is seen to rise when the temperature is increased to 400°C, indicating that the magnesium particles are dehydriding.

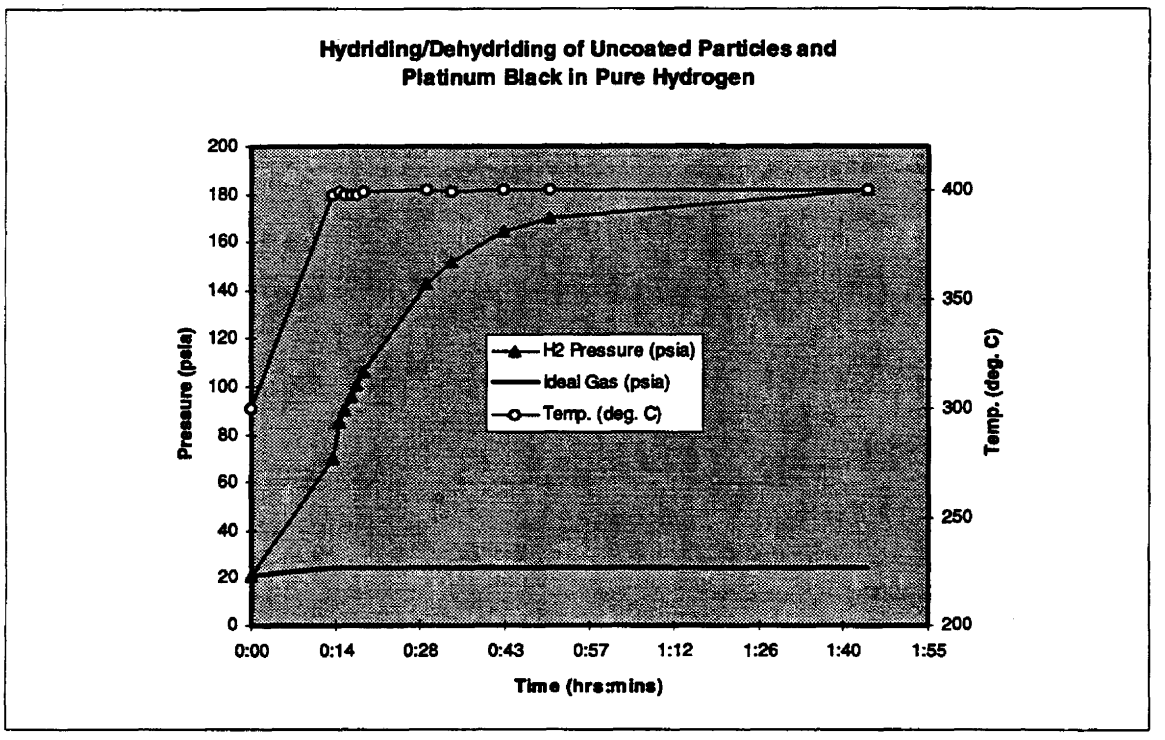

Figure 2 - Uncoated Magnesium Particles Dehydriding in Pure Hydrogen

Even if the particles did not dehydride at all, the pressure within the closed volume would rise somewhat. Even if the particles were made of an inert substance such as sand instead of magnesium, the gas pressure would rise with temperature in accordance with the perfect gas laws. The pressure rise in that case would be much less than the one observed, and would match the solid line on Figure 2.

Figure 3 shows the results of Steps 3 and 4 (above) using coated magnesium particles in pure hydrogen. Again, the hydrogen pressure is seen to rise when the temperature is increased to 400°C and to fall when the temperature is decreased to 300°C, indicating that the magnesium particles are dehydriding and hydriding again. If the magnesium nitride coating were not permeable to hydrogen, then there could be no such hydriding and dehydriding. If the magnesium nitride coating were not permeable to hydrogen, then the magnesium particles would "behave like sand" and the pressure of the closed volume would rise and fall only in accordance with the solid line on Figure 3.

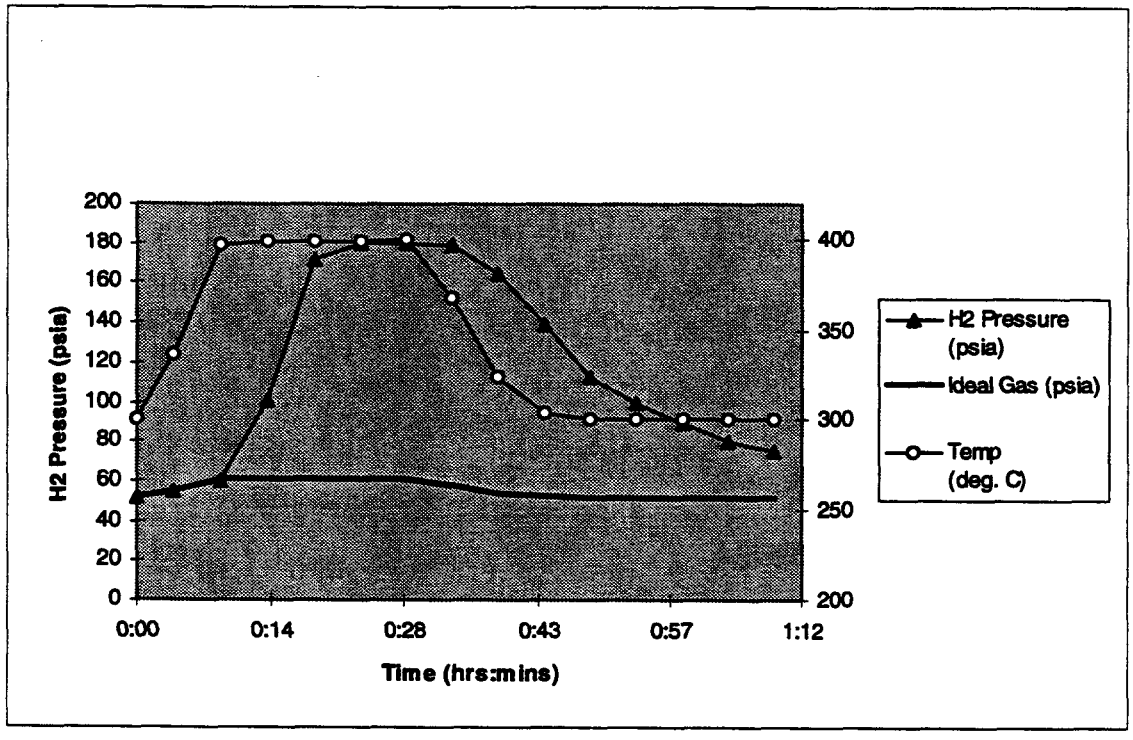

Figure 3 - Coated Magnesium Particles Dehydriding and Hydriding in Pure Hydrogen

Figure 4 shows the results of repeated cycling using coated magnesium particles in a gas mixture that is roughly one part steam, one part carbon dioxide and two parts hydrogen ("quasi-reformate"). In this gas mixture, suggestive of reformate, the uncoated particles were observed to "behave like sand" as the non-hydrogen species reacted with the magnesium to prevent its hydriding/dehydriding; the pressure rose and fell with the temperature only in accord with the perfect gas laws. However, the coated particles in the simulated reformate stream were observed to hydride and dehydride over eleven cycles.

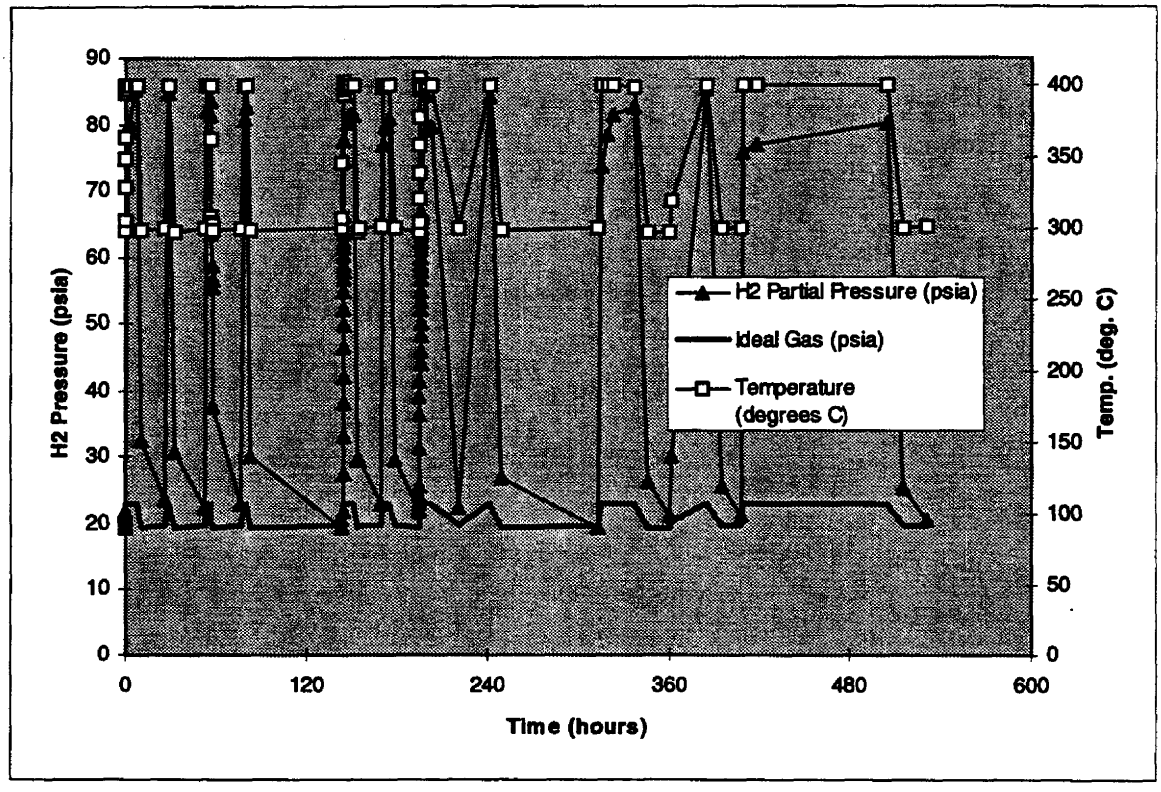

Figure 4 - Coated Magnesium Particles Dehydriding and Hydriding in Quasi-Reformate

Conclusions

1. It is apparent that a magnesium nitride coating does indeed permit magnesium particles to selectively absorb hydrogen from a hydrogen-rich mixture.

2. It is also apparent that there is room for improvement in this coating. Magnesium particles with an "ideal" coating would exhibit the same hydrogen partial pressure swing in quasi-reformate as would uncoated magnesium particles in pure hydrogen.

3. These magnesium nitride coatings offer the potential to construct devices that could reduce both the cost and the size of small hydrogen supply systems for industrial or vehicular refueling applications.

4. Additional testing is needed to optimize the coated particles with respect to reaction kinetics and completion of reaction.

DESIGN AND INITIAL TESTING OF HYDRIDE BED MODULES FOR MOBILE, FUEL CELL APPLICATIONS

M. E. Malinowski and K. D. Stewart
Sandia National Laboratories
Livermore, CA 94550

Abstract

A prototype hydride bed for supplying hydrogen to a fuel cell on a mobile vehicle has been designed and tested in the laboratory. The original bed design consists of 8 modules and is intended for use with the fuel cell on the Palm Desert Vehicle (PDV) under development at the Schatz Energy Center, Humbolt State University. Each module contains approximately 2 kg of a commercially available, low temperature, hydride-forming alloy. Waste heat from the fuel cell in the form of heated water is used to desorb hydrogen from the alloy for supplying feed hydrogen to the fuel cell. In order to help determine the performance of such a modular bed system, six modules were constructed and tested. The design and construction of the modules is described in detail. In laboratory testing, the modules meet or exceed all design criteria: Initial testing of the modules both individually and as a group showed that each module can store ~30 g of hydrogen (at 165 PSIA fill pressure, 17 °C), could be filled with hydrogen in 6 minutes at 75 standard liters/min (slm) fueling rate, and could supply hydrogen during desorption at rates of 25 slm, the maximum anticipated hydrogen fuel cell input requirement. Tests made of 5 modules as a group indicated that the behavior of the group run in parallel both in fueling and gas delivery could be directly predicted from the corresponding, single module characteristics by using an appropriate scaling factor.

Introduction

Fuel cells are emerging as attractive sources of power for electric vehicles because of their low emissions and quiet operation. Air (or oxygen) and hydrogen are the feed gases for these cells, and various types of hydrogen supplies such as high pressure hydrogen tanks, liquid hydrogen, hydrogen reformers, and metal hydrides have either been used or planned for use with fuel cells. Examples of vehicular systems include a 250 W phosphoric acid fuel cell supplied by a hydride bed and powering a golf cart (Shindo, 1993), 15 kW fuel cells used in different "green" vehicles and fueled with hydrogen from high pressure tanks (Nadal, 1996), and small scale, conceptual systems for railroad locomotives powered by fuel cell - hydride bed combinations (Hasegawa, 1995). Fuel cells for submarine use (Brighton, 1994) have been proposed . It is clear that fuel cell applications abound, and that the best choice for the hydrogen supply will depend critically on the exact configuration and requirements of the fuel cell system.

This current work describes the design, construction, and initial laboratory testing of a metal hydride bed system which was designed to supply hydrogen to a nominal 5 kW fuel cell made by the Schatz Energy Research Center (SERC), Humboldt State University, Arcata, CA and used in SERC's Palm Desert Vehicle (PDV). Although the design and construction of the bed system was dictated by the performance and constructional requirements of the SERC fuel cell PDV, it is likely that the general design features used to make the present hydride bed could be incorporated in future bed systems serving other fuel cells. Primary goals in this work were to make a practical hydride system which satisfied all hydrogen supply requirements of the PDV fuel cell system, and could be built with existing hydride bed fabrication techniques and commercially available, metal hydride-forming alloys. It was the intent of this work to make a hydride bed system which would be prototype, working device, for use in the PDV. It is expected that working experience with this bed system both in the laboratory and, eventually, in a working vehicle, will lead to the development and manufacture of less expensive bed system with improved performance characteristics.

Design and Construction

The primary, SERC PDV requirements for a hydride bed used as a hydrogen supply are given in Table 1. These requirements were determined by combining the performance statistics of compressed hydrogen tanks currently used on the PDV with anticipated operational conditions using a hydride bed. Note that some of the requirements are rather arbitrary: For instance, the refueling time of $\leq$ 10 minutes is long compared to a typical "tanking up" at a gasoline station ($\leq$ 2 minutes), but was considered an acceptable time to refill the hydride bed. (Bed refueling times are only relevant to the refueling scenario where gas is put back into the beds at a drive-up refueling station. It may be that a complete bed changeout/exchange in the end is the best means for "refueling."). The environmental requirement, operating temperatures of ~5 ^{0}C to ~ 65 ^{0}C, is

one which has not been actually measured but, rather, is an estimate of the temperatures which the hydride bed might experience.

Table 1. Hydride Bed Requirements for the SERC PDV

Requirement	Amount
Hydrogen Supply	
Total hydrogen stored	~160 grams
Maximum delivery rate	~25 slm
Refueling time	≤ 10 minutes
Environmental Temperature Range	~5 °C to ~ 65 °C
Overall Size	Fit in space ~ 3" x 20" x 21"
Bed Heating	
"normal," steady state operation	water, fuel cell waste heat (≤2.5 kW max.)
startup	batteries,12 - 36 V, ~ 600- 1000 kJ max

Modular Bed Details

A "modular" hydride bed is one made up of several, smaller beds configured so that the overall hydrogen capacity is the sum of the smaller (modular) individual bed capacities. Hydrogen Components, Inc. (HCI), Littleton, CO, has experience in construction of similar beds (HCI/Frank Lynch, 1993), and it has developed effective techniques to control unwanted hydride swelling. Therefore, we decided to design a modular bed based on HCI's proven bed construction techniques and to have HCI build the modular beds based on our design requirements.

A modular, prototype system was chosen primarily because it should best utilize the small amounts of waste heat available from the fuel cell (discussed below), would fit in the space available, could be mounted in the PDV so that the bed modules would be readily accessible, and, if necessary, could be reconfigured to be used in different hydrogen-delivery gas manifolds. However, a modular design is most likely not optimized from a capacity standpoint, and would also involve more gas and water connections than a single, larger bed with the same amount of hydride alloy.

A drawing of one of the proposed modular beds is shown in Figure 1. The entire bed assembly would consist of 8 such beds, and one possible, planar arrangement of these beds in the PDV space is shown in Figure 2 (The gas plumbing for the beds is not shown in this Figure). The space available for the entire bed assembly is located underneath the fuel cell and above the belly pan of the PDV, and is basically a volume ~ 20" x 21" x 3" in size. Other components necessary for interfacing the metal hydride bed system to the fuel cell water cooling/heating system, such as heat exchanger, water pump, etc., would fit in other available space in the PDV.

Even though each of the eight modules looks the same as the others, there are actually two types of modules with different hydride-forming alloys:

• "Main Module." This is the primary bed module and there would be 7 such modules in the bed. Each main module contains approximately 1900 g of C15 (Aits, 1995), a hydride-forming alloy made by GfE in Nuremberg, FRG. C15 was chosen because, when hydrided, it had hydrogen overpressures which were in the proper range, ~ 1 - 15 bar. The module consists of 9, hydride-containing tubes approximately 11/16" in diameter. The C15 is loaded in the tubes to a packing density of ~3 g/cc; the loading of the material is done such that the 15" length of each tube is physically partitioned into separate zones, each of which is approximately 3/4" long (this technique is called the "bar stool" arrangement by HCI). In addition, an eccentrically mounted, fritted gas tube runs the entire length of each of the hydride tubes. The hydrogen outputs of the tubes are connected in parallel internally in the bed in a plenum (see Figure 1, "Side View"). Connections to the plenum consist of a single, manual valve, for external gas delivery, and a pressure relief valve, set at a nominal 250 PSIG. All the hydride tubes are encased in a water-cooled, stainless steel jacket. Lexan rods, with either square or triangular cross sections and running the length of the module, are inserted between the hydride tubes in order to reduce the cross-sectional water flow area , a strategy employed to increase the water flow velocity in the module and to promote turbulent flow for improved heat transfer inside the module. On the ends of the jacket are welded brackets which will be used to attach each module to the angle-iron frame of the PDV.

• "Cold Start Module." There is one such module, and it will contain an alloy which is less stable (higher hydrogen pressure at the same temperature) than C15. The main purpose of this module was to provide higher output pressure than the C15 during "cold start" (temperatures below ~20 °C) starting conditions. The alloy used in the system which was made is Ergenics Hy-Stor 208 (Huston, 1980).

Six modules were built by HCI and their specifications are given in Table 2. Note that the first five modules (1.1-1 through 1.1-4 and 3.1-1) contain C15, while the sixth module has Hy-Stor 208. As shown in Table 2, each module weighs about 4 kilograms, of which ~45-50% is hydride alloy weight. Also given in the last column are the predicted weights of hydrogen stored in the alloys for 1.5 weight per cent (w/o) loading and the overall, effective w/o of hydrogen storage in the module. This last number underscores the necessity of considering an often-neglected component in hydride systems - the container. The w/o figures quoted for many alloy systems must always be put into practical perspectives by including container weights. As indicate above, it was not the intent of the current study to achieve optimum w/o figures with the modular system.

Table 2. Module Specifications

Module	Alloy	Weights (g)							Overall H w/o
		Entire Module	Alloy	S.S. parts	Lexan rods	w/o alloy	water	H , 1.5 w/o	(1.5 w/o in alloy)
1.1-1	C15	4178	1940	2238	192	46.42	92.00	29.09	0.70
1.1-2	C15	4058	1822	2236	192	44.89	92.00	27.33	0.67
1.1-3	C15	4060	1821	2239	192	44.86	92.00	27.32	0.67
1.1-4	C15	4068	1825	2243	192	44.87	92.00	27.37	0.67
3.1-1	C15	4114	1823	2292	192	44.30	92.00	27.34	0.66
2.1-1	Hystor208	4417	2190	2228	192	49.57	92.00	32.85	0.74
Totals (g)		24896	11420	13476				171.3	
average		4149	1903	2246	192.00	45.82	92.00	28.55	0.69

Available Energy and System Design

A simplified, block diagram of the assumed functional relationship of the modular bed with the fuel cell is shown in Figure 3. There are two water loops in this system: one water loop cools the fuel cell; the second loop heats the modular hydride bed. Energy is transferred from the first water circuit to a second by a heat exchanger. An onboard battery/ regulator system provides power to run such items as the water pumps, valves, and electrical heater. This heater is located in the bed water circuit and is used to heat the water when reject heat from the fuel cell is insufficient to heat the hydride bed, a situation which would occur most often during "cold start" conditions, those times when the fuel cell is first used and the ambient bed temperature is not high enough to satisfy energy demands for hydrogen desorption.

There are two basic modes of operation for the fuel cell/hydride bed system: "steady state," and "startup," or transient operation . During steady state operation, all system components are at the nominal operating temperature, and the only energy required for hydride bed operation is the amount necessary to supply the heat of desorption of hydrogen from the metal hydride alloy: Since the maximum anticipated use of hydrogen by the fuel cell is about 25 slm (~0.0186 moles hydrogen/s), and the heat of desorption of hydrogen in C15 is about 34 kJ/mole hydrogen (Pechoff, 1996), during steady state desorption of hydrogen from the hydride, a heat input of ~0.0186•34 ≈0.6 kW, is required.

In principle, the reject heat from the fuel cell should be more than this 0.6 kW, since the fuel cell used in the PDV has a maximum power rating of ~ 5 kW and is ~ 50% efficient. Thus, ≤ 2.5 kW could be reject heat and available for transfer to the hydride bed heating loop. Although the exact amount of available heat depends on the load on the fuel cell and can vary, there should be enough waste heat generated by the fuel cell for maintaining desorption of hydrogen from the hydride. It is also important to recognize that high hydrogen demand is coupled with high load on the fuel cell. The high load produces more available heat, but the availability of this heat will lag the demand by times determined by the thermal transfer characteristics of the water heating/cooling system.

These steady state estimates, however, do not take into consideration the amount of energy necessary to heat the hydride bed to operating temperatures, a situation which would occur during "cold start" conditions. In this case, when insufficient reject ("useful") heat is available from the operating fuel cell, an electric immersion heater powered by onboard batteries would be used to heat the water in the bed water loop. Estimates of the maximum amount of energy available from the 3 x 12V = 36 V onboard batteries range from about 36 V x 5-8 amp-hours (P. Berger and R. Chamberlain, 1996).

In order to maximize the effectiveness of these small amounts of energy available in the PDV, energy should not be used to heat components which do not directly contribute to the production of necessary hydrogen fuel. This suggests that the bed system heat capacity should be lowered, if possible. One way of doing this is to divide the bed into smaller beds, or modules, and to heat one bed module at a time, as needed, for hydrogen supply. Heating one bed module at a time also decreases the time required to reach operating temperatures, an important consideration in cold start situations. Even though a modular system has more complex plumbing and control than a single, monolithic bed, the potential improvement in response times and energy economy would seem to more than justify the added system complexity . In this current work, it was therefore decided to design and build a bed system based on this modular concept.

In order to provide an estimate of the bed heating required in transient or start up conditions, it is necessary to know the heat capacities of the bed module system. Estimates of heat capacities for a module are given in Table 3 below. The approximate, total heat capacity per module is thus about 3 kJ/K. To estimate the amount of energy to heat up a bed to temperature, however, the total amount of water and other equipment in the module water loop also must be considered: For instance, this must include at least the heat capacity of the water, water pump, and heater . If there were ~ 2 liters of water in this loop (not an exceptionally large amount), the heat capacity of the water would be about 4 kJ/K, slightly larger than that of a single module. The water pump, heater and other plumbing connections could easily add to this value to increase the heat capacity of the loop system external to a single module to ~6 kJ / K, about twice that of a single module. Using these estimates, therefore, the total heat capacity of a single module system would be ~ 10 kJ / K, while that for an 8 module system would be ~30 kJ / K.

Table 3. Heat Capacities of A Typical Bed Module with 1.5 w/o Hydrogen

MODULE PART	SPECIFIC HEAT (J/g-K)	HEAT CAPACITY(J/K)	% OF TOTAL
hydrogen	14.226	406.15	13.9
stainless steel	0.460	945.29	32.4
C15*	0.470	894.64	30.6
water	4.184	384.93	13.2
Lexan rods	1.5	288.00	9.9
TOTALS		2919.01	100.00

Thus, based on these estimates, a single module system would require no more than 1/3 the power than a full module system to have a given time-temperature heating cycle, and that ~ 200 kJ would be required to raise the temperature of a single module system 20 °C. If a 1 kW heater in the fuel cell loop were present, it would take ~ 3.5 minutes to heat up the system. If, on the other hand, all eight modules were heated, the corresponding energy amounts would be ~ 600 kJ and ~ 10 minutes. These considerations demonstrate the necessity of minimizing the heat capacity of the bed system, and form the rational basis for adopting a modular bed design for the PDV. These estimates also underscore the fact that the actual performance of the bed heating system will depend on the exact system details and amount of heat capacity in the fuel cell-hydride bed water loops.

Module Testing

The performance characteristics of the six modules were determined using the Hydride Bed Testing Laboratory (HBTL). Initially one module alone (Module 1.1-1, Table 2) was tested. That module was then sent to SERC for collaborative testing on one of their test stands. In parallel with that activity, the remaining 5 modules were put on the HBTL and tested both individually and as a group. The results discussed in this section were taken from this group of 5 modules; the first module (1.1-1) had characteristics essentially identical to the other C15-containing modules except that it container more C15 alloy (~ 1940 g vs. 1820 g), the result of having smaller diameter gas delivery tubes in the hydride tubes.

The Test System

A simplified schematic of the module test system is shown in Figure 4. This figure shows the arrangement for one module; when 5 modules were tested the hydrogen outputs from the modules were connected in parallel and the input and output water lines could likewise be connected to in parallel. A water bath heater circulator, with approximately 11 liters water

inventory, was used to heat or cool the bed module by circulating water through the module water jacket; water flows up to approximately 1.2 gallons per minute (gpm) could be achieved in one module when using the circulator. The input and output water temperatures were measured with sheathed chromel-alumel thermocouples directly in the water flow. Water temperatures from 11 °C to 70 °C could be routinely achieved using the current bath/circulator configuration.

When testing a module, the main module valve, labeled V1 in Figure 4, was opened. To hydride, or fuel, a bed, 99.995% pure hydrogen from external tanks was supplied to a pressure regulator. In most tests discussed in the current work, the output pressure of the regulator was set to ~165 PSIA. The fueling of the module was performed by opening valve V2 and controlling the hydrogen flow, F_{in} , into the module by manually adjusting valve V2 . The hydrogen mass flowmeter (MFM) had a range of 0 - 400 standard liters/ minute (400 slm). During this process, the hydrogen mass flow controller (MFC) shown in the figure was kept closed. The bed pressure was measured by a strain gage pressure transducer, P_{out} , while the supply pressure to valve V2 was measured by a similar transducer, P_{in} . All data from the pressure gauges, thermocouples, flowmeter and hydrogen mass flow controller were recorded and display using a computer-based acquisition system.

During gas delivery from the bed, valve V2 would be closed and the bed be heated and the hydrogen vented through a mass flow controller, which has a range of 0 - 50 slm. In many desorption/ hydrogen delivery data runs, the mass flow controller would be set to a constant value; when the bed started running out of hydrogen, the bed temperature would be increased to a maximum of 70 °C to desorb all hydrogen.

Since the bed fueling was determined with the 400 slm MFM, while the gas delivery measured with the MFC, there was typically a discrepancy of ~ 2% in integrated amounts between absorption and desorption of a module. This is much less than the manufacturer's quoted ± 1% of full scale accuracy (± 4.4 slm total) of the MFM/MFC combination.

Results: Single Module

PCT Data

Figure 5a shows the predicted mid-plateau hydrogen pressures for both the C15 and Hy-Stor 208 alloys. These data, which were derived from PCT taken on C15 and from literature parameters for a material similar in composition to Hy-Stor 208 (Huston, 1980), show that Hy-Stor does have a higher overpressure than the C15, the primary basis for choosing Hy-Stor 208 as the "cold start" bed material. As a check on the actual behavior of each different alloys, 15 °C isotherms were measured in two different modules (1.1-4 for the C15, 2.1-1 for the Hy-Stor 208). The data are shown in Figure 5b as a function of the total amounts of hydrogen stored in the two different modules; absorption and desorption isotherms are indicated by the different arrows on the graph.

The experimental results shown in Figure 5b indicate the following:

1. The Hy-Stor 208 has a higher overpressure than the C15 at any given amount of stored hydrogen. In addition, the Hy-Stor has less hysteresis and flatter plateau pressures than the C15.

2. In a given module, the C15 has a higher capacity. The ~34 g stored hydrogen in the C15 module corresponds to ~ 1.8 w/o storage, while the ~27 g stored in the Hy-Stor 208 module corresponds to ~1.1 w/o storage. Note that these total amounts stored in the modules are higher than the amounts reversibly available: in the case of C15, the amount reversibly available in the current experimental setup is ~ 30 g, which corresponds to ~ 1.64 w/o, while in the Hy-Stor, the reversibly available amount is ~ 25 g. The "reversibly available amounts" are defined as those amounts of hydrogen which can be desorbed from the alloys by heating the alloys to ~70 °C and venting the hydrogen at ~1 bar, conditions which are relevant to PDV operation and used in the HBTL testing of the modules.

These data indicate that the Hy-Stor module will have a higher overpressure, but lower capacity than the C15 modules. These characteristics will be important when discussing hydrogen delivery characteristics below.

Module Fueling

Figure 6a gives the fueling results for a C15 module, Figure 6b, for the Hy-Stor 208 module. In each graph, the mass of hydrogen absorbed by the module is shown as a function of time for different, nominal fueling rates. All the data presented were acquired with water flows of 0.6 gallons/minute (gpm) through the modules. Data were also acquired with module cooling of 1.2 gpm and were essentially identical to the data shown in the figures for the lower water flow of 0.6 gpm.

The fueling rates indicated on the graphs were maintained as long as possible: beyond a certain time in fueling a module, the difference between the supply pressure, which was ~165 PSIA, and the module overpressure became too low to support the original flow. At this point, the fueling rate decreases and results in the deviation from linearity observed in all curves. This deviation is probably directly related to the heating of the modules (and, hence, increase in the effective equilibrium overpressure) caused by the absorption of hydrogen by the alloys. The amounts of hydrogen fueled and shown in these figures are reversibly available from the modules by heating the modules to temperatures ≥ 60 °C.

Note that in both types of modules, (1) the fueling characteristics of both modules are very similar; (2) the times required to fuel the module to 95% of capacity decreased with increased fueling rates; (3) the modules could be fueled to 95% in less than 10 minutes, one of the design requirements (a minimum fueling time of ~ 5-6 minutes is observed for the C15 module); (4) the storage capacity of a C15 module is ~30 g at 17 °C; and (5) fueling at rates in excess of ~ 50-75 slm did not result in significantly reduced times to achieve 95% fueling.

Module Gas Delivery

Figures 7a and 7b show the results of a series of gas delivery experiments with a C15 module and a Hy-Stor 208 module. Figure 7a shows gas delivery from fully loaded modules (~ 34 g in the C15, 27 g in the Hy-Stor 208), while Figure 7b shows delivery from modules that were intentionally filled to approximately 50 % capacity. In both figures, the initial temperature of the modules was approximately 11 °C, the lowest temperature achievable in the existing experimental test stand. This starting temperature approximates a "cold start" condition for the modules. In all the results graphed, at the time corresponding to t= 0 minutes, the modules were heated at nominally the same rate. Simultaneously with the start of heating, gas was withdrawn from the modules at rates determined by the mass flow controller (MFC - see Figure 4). In each separate figure, the delivery rate -time profile for the C15 and Hy-Stor modules were the same: For instance, in Figure 7a, for the first 3 minutes 10 slm were delivered, after which, 25 slm, the maximum required delivery rate, was delivered as long as each module could supply the gas. A similar delivery-time schedule was followed in the data of Figure 7b. In both figures, the module pressures and inlet water temperatures are also plotted.

As both Figures show, the modules are capable of supplying hydrogen at 25 slm, one of the design requirements. Figure 7a shows that this rate can be sustained for about 12 minutes with a C15 module, and for about 9 minutes with a Hy-Stor 208 module and directly demonstrates the higher capacity of the C15 module. When, however, the modules are half loaded, the Hy-Stor can supply hydrogen at the maximum rate for about twice the length of time than that with the C15 module. This is because of the higher overpressure in the Hy-Stor 208.

Thus, the initial module hydrogen gas content and temporal variations of both the module temperature and the gas delivery demand all influence the observed performance of the modules. The data present in Figures 7a and 7b suggest that, for fully loaded modules, there may be no advantage to a "cold start" bed, while in partially loaded modules, the cold start bed would be able to supply gas at higher rates for longer lengths of time than with the C15 modules. Heating the modules more quickly, which could occur in systems with water heating loops with lower volumes than the 10 liters of the current work, could also improve the performance of both modules. These results further demonstrate that there is more to employing a cold start bed than might be expected on plateau overpressure considerations (Figures 5a, 5b) alone, and they suggest that minimizing water loop inventories to improve module thermal response will be an important ingredient in vehicular applications of this modular system.

Results: Multiple Modules

Fueling and delivery tests were run with two, different module groupings: 3 of the C15 modules as a group and all five modules - 4 C15 and 1 Hy-Stor 208- as a second group. In both cases, the two different groupings were fueled in parallel and the gas delivered from the groups in parallel. This corresponds physically to running the modules as one bed, and one would expect that the

fueling and delivery of such an arrangement would be directly predicted from the corresponding characteristics of a single module.

Figure 8a shows the fueling characteristics of the first group (3 - C15 modules). The fueling rate for this group was 150 slm. For comparison, the fueling - time behavior of a single C15 bed fueled at 50 slm (see Figure 6a, 50 slm curve) is scaled by a factor of 3 and plotted on the same graph. As the data indicate, parallel fueling behavior of a group can be directly scale from the characteristics of a single module. A similar result was obtained when fueling the five module group.

The delivery from the second group (4 - C15 modules, 1 - Hy-Stor 208 module) is shown in Figure 8b. As indicated, the maximum delivery rate of 25 slm can be sustained for about an hour, which is about a factor of 5 greater than the maximum rate, delivery time observed in a single module (Figure 7a). Note, in addition, that a steady state temperature of only about 40 °C is necessary to maintain this rate and that the total amount of gas available from this six module system is about 145 g, which is the sum of the total amounts available from four C15 (4 x 30 =120 g) and one Hy-Stor 208 (25 g) modules. These results show that when a 6 module bed system is used and fueled at 17 °C, a total of 175 g would be available from the complete system. This exceeds the capacity requirement of 160 g., even though only 6, and not 8 beds as originally planned, are used.

Summary

In the current work, a modular, hydride beds for supplying hydrogen to a fuel cell have been designed, constructed, and subjected to initial testing. Based on experimental data, this bed system consisting of 8 modules would have a usable hydrogen capacity of about 235 grams when fueled at 17 °C and 165 PSIA, a capacity which exceeds the original design goal of 160 grams of hydrogen. Fueling at higher temperatures would lower the stored amount of hydrogen, while fueling at higher pressures would raise it. The exact amount of hydrogen which would be stored onboard a vehicle will depend on the particular operating temperatures expected and the fueling scenario chosen. In spite of these variables, the current work shows that the modular system built should meet or exceed capacity requirements.

The results directly demonstrate that module refueling times of less than 10 minutes are readily achievable at fueling rates of 50 - 75 slm / module and cooling water flows of 0.6 gpm / module. 95% refueling times of ~ 5 - 6 minutes with the current module design were demonstrated. Ongoing thermal modeling of the modular system indicates that the basic limitation on fueling times is related to neither hydrogen fueling rate nor water flow, but rather to the low thermal conductance of the hydride within the hydride tubes.

Gas delivery rates of 25 slm were readily achievable at bed temperatures of ~35-40 °C. The data comparing the C15 module with the Hy-Stor 208 module indicate that, in order to make the modular concept work and provide a thermal response advantage over a larger single bed, the

water inventory in the heating cooling loop must be reduced from the amount used in these tests. The arguments presented in the section on "Available Energy and System Design" indicate that amounts as low as possible should be used and suggest an inventory of ~2 liters would make a desirable goal for use with an 8 module system.

The modules as made should be excellent candidates for deployment in a prototypical hydride bed - fuel cell test vehicle, and should be so used in order to evaluate the true utility of such beds in actual, working environments. When so used, the next step in this bed work is the design and testing of the bed system, that is, the interconnection, control and end use of the separate modules operating as a group.

Acknowledgments

We acknowledge the support of G. J. Thomas, and the help of both Steve Guthrie in collaborative, first module testing, and Abby Sieber in initial technical assistance. The continuing collaboration of the SERC team with us in applying the modular bed system to use on their PDV platform has been essential to the progress of this work. Advice from Frank Lynch of Hydrogen Components, Incorporated formed a critical ingredient of our modular bed design. Informative discussions with both Dr. Meinhard Aits, GfE, and Dr. G. Sandrock, are also acknowledged.

List of References

Meinhard Aits, GfE Metalle und Materialien, private communication (March 28, 1995)

P. Berger and C. Chamberlain, Schatz Energy Research Center, private communication (August 20, 1996).

D. R. Brighton, P. L. Mart, G. A. Clark and M. J. M. Rowan, Journal of Power Sources **51**, 375 (1994).

HCI/Frank Lynch, "Metal Hydride Heat Pump Engineering Demonstration and Evaluation Model," NASA Report NAS9-17819 (October, 1993)

H. Hasegawa and Y. Ohki, "Development of a Model of On-Board PEMFC Powered Locomotive with a Metal Hydride Cylinder," in *Materials for Electrochemical Energy Storage and Conversion - Batteries, Capacitors and Fuel Cells,* D. H. Doughty, Brijesh Vyas, T. Takamura, and J. R. Huff (eds.), Materials Research Society, Pittsburgh, PA (1995).

E. L. Huston and G. D. Sandrock, "Engineering Properties of Metal Hydrides," J. Less-Common Metals **74**, 435 (1980).

M. Nadal and F. Barbir, "Development of a Hybrid Fuel Cell/ Battery Powered Electric Vehicle," Int. J. Hydrogen Energy **21**, 497 (1996).

R. Pechloff, GfE Metalle und Materialien, private communication (November 22, 1996)

K. Shindo, A. Watanabe, M. Nishioka, M. Tsutsumi, M. Fujiwara and T. Itoh, "The Phosphoric Acid Fuel Cell/Battery for Golf Cart Applications," in *Proceedings of the Batteries and Fuel Cells for Stationary and Electric Vehicle Applications*, 183rd Meeting of the Electrochemical Society (1993).

Figure Captions

Figure 1. Drawings of a single, hydride bed module. The module cross-section in the upper left hand side of the drawing shows the internal module construction.

Figure 2. A sketch of the volume on the PDV where an 8 bed, module-based hydride system could fit.

Figure 3. Simplified schematic of a fuel cell- hydride bed system.

Figure 4. Simplified schematic of the experimental system used to test the modules.

Figure 5. Selected static properties of C15 and Hy-Stor 208, the alloys used in the hydride modules.

Figure 5a (upper). Mid-plateau overpressures of the two alloys.

Figure 5b (lower). 15 °C isotherms for the two alloys; isotherms measured using actual modules.

Figure 6. Dynamic, fueling properties of single, C15 and Hy-Stor 208 modules.

Figure 6a(upper). Fueling of C15 module.

Figure 6b(lower). Fueling of Hy-Stor 208 module.

Figure 7. Hydrogen delivery from single, C15 and Hy-Stor 208 modules.

Figure 7a (upper). Delivery from fully fueled modules.

Figure 7b (lower). Delivery from half-fueled modules.

Figure 8. Hydrogen fueling and delivery from groups of modules.

Figure 8a (upper). Fueling behavior of a group of 3, C15 modules fueled and water-cooled in parallel.

Figure 8b (lower). Delivery from a group of 4, C15 + 1, Hy-Stor 208 modules heated in parallel and delivering gas in parallel.

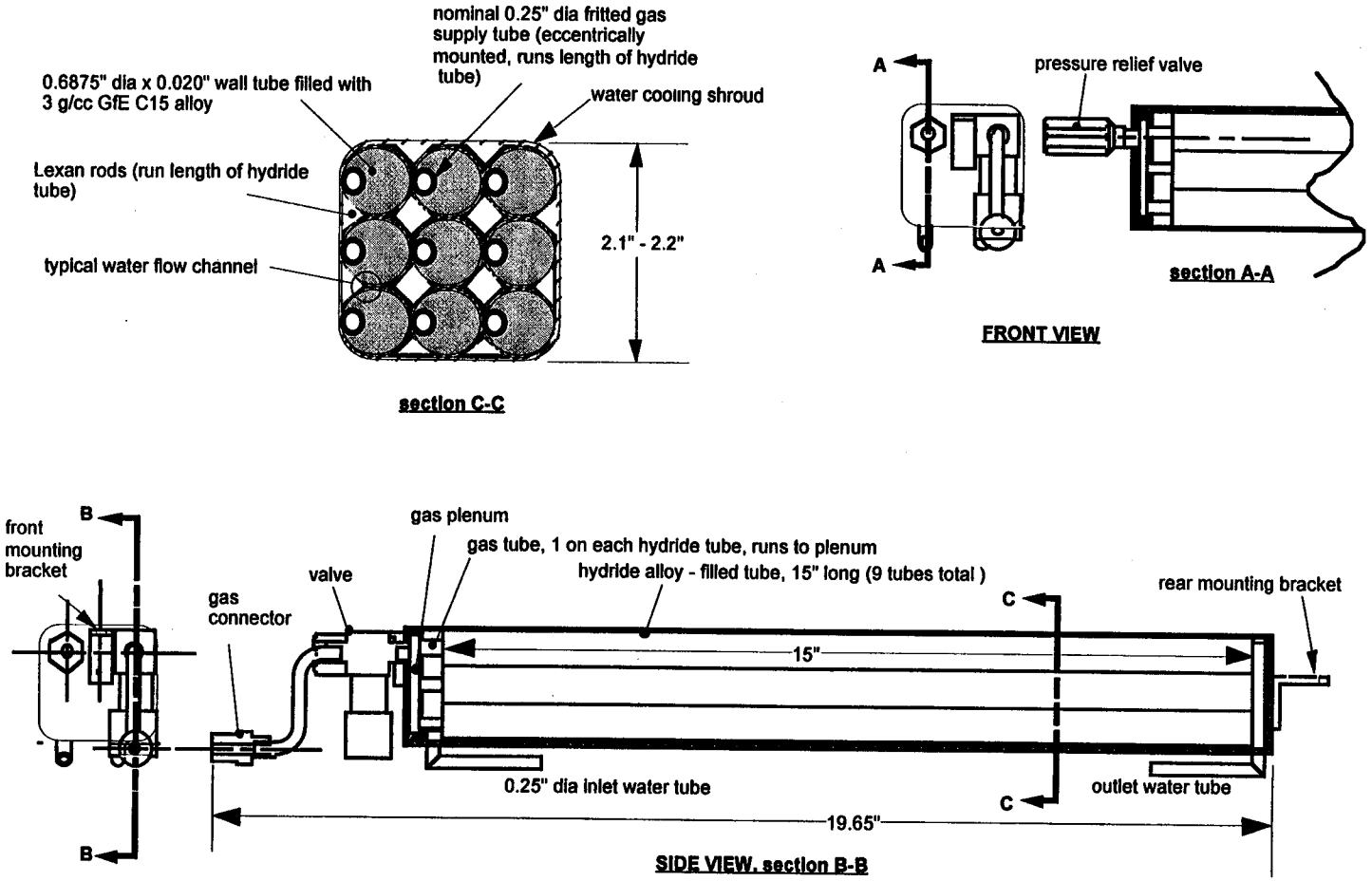
nominal 0.25" dia fritted gas supply tube (eccentrically mounted, runs length of hydride tube)
0.6875" dia x 0.020" wall tube filled with 3 g/cc GfE C15 alloy
water cooling shroud
Lexan rods (run length of hydride tube)
typical water flow channel
2.1" - 2.2"
section C-C
A
A
pressure relief valve
section A-A
FRONT VIEW
front mounting bracket
B
B
gas connector
valve
gas plenum
gas tube, 1 on each hydride tube, runs to plenum
hydride alloy - filled tube, 15" long (9 tubes total)
C
C
15"
rear mounting bracket
0.25" dia inlet water tube
outlet water tube
19.65"
SIDE VIEW, section B-B

Figure 1

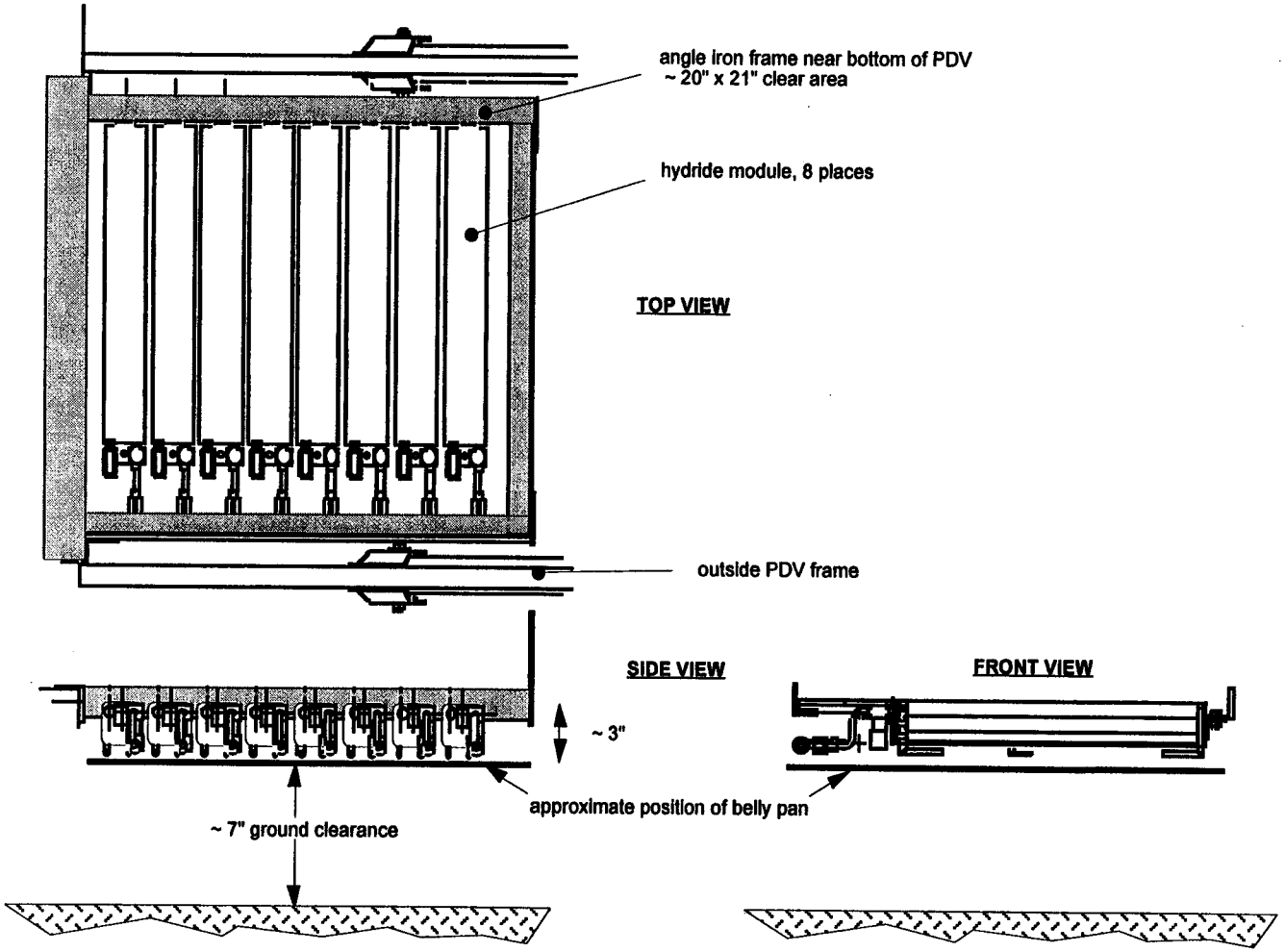
angle iron frame near bottom of PDV
~ 20" x 21" clear area
hydride module, 8 places
TOP VIEW
outside PDV frame
SIDE VIEW
FRONT VIEW
~ 3"
approximate position of belly pan
~ 7" ground clearance

Figure 2

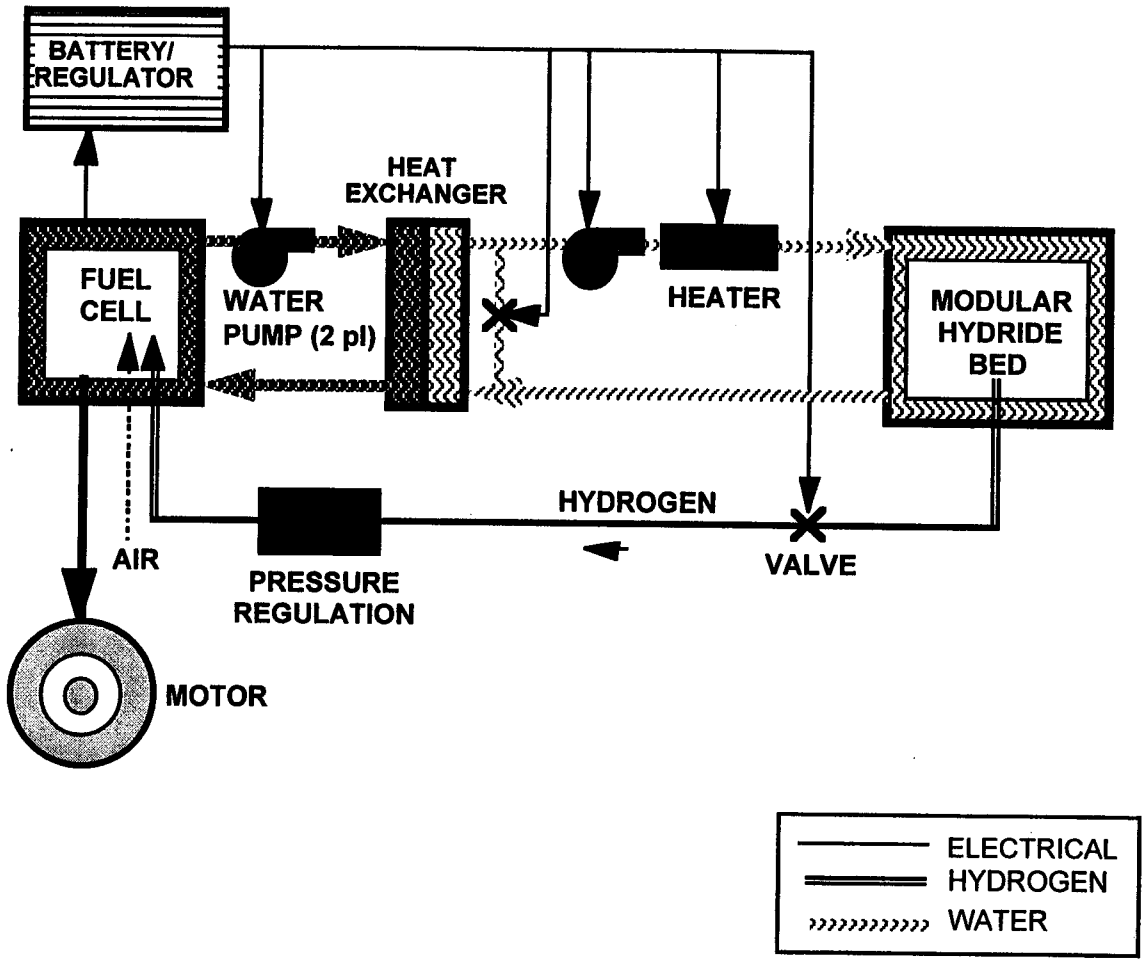
BATTERY/
REGULATOR
HEAT
EXCHANGER
FUEL
CELL
WATER
PUMP (2 pl)
HEATER
MODULAR
HYDRIDE
BED
HYDROGEN
AIR
PRESSURE
REGULATION
VALVE
MOTOR
ELECTRICAL
HYDROGEN
WATER

301

Figure 3

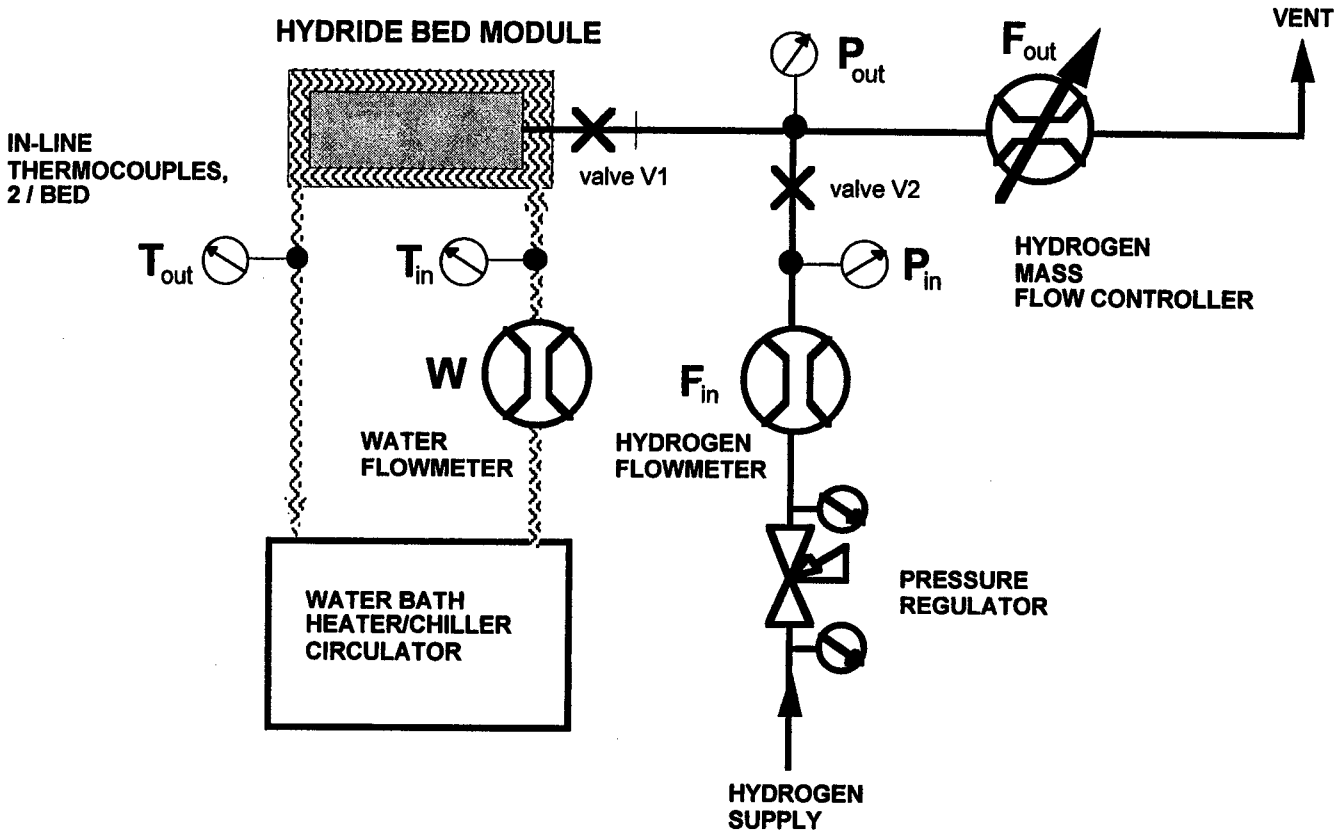
HYDRIDE BED MODULE
IN-LINE
THERMOCOUPLES,
2 / BED
T_{out}
T_{in}
W
WATER
FLOWMETER
WATER BATH
HEATER/CHILLER
CIRCULATOR
valve V1
P_{out}
valve V2
P_{in}
F_{in}
HYDROGEN
FLOWMETER
PRESSURE
REGULATOR
HYDROGEN
SUPPLY
F_{out}
VENT
HYDROGEN
MASS
FLOW CONTROLLER

Figure 4

302

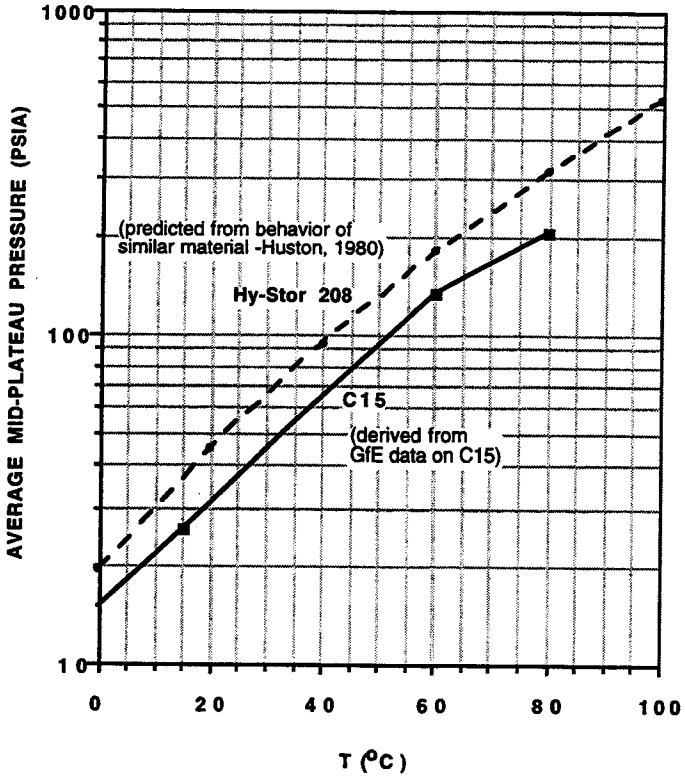

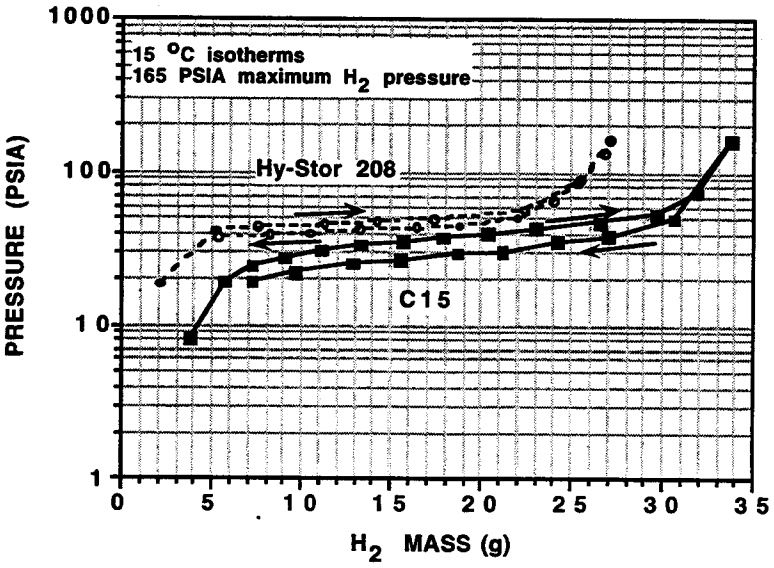

Figure 5a (upper) and Figure 5b (lower)

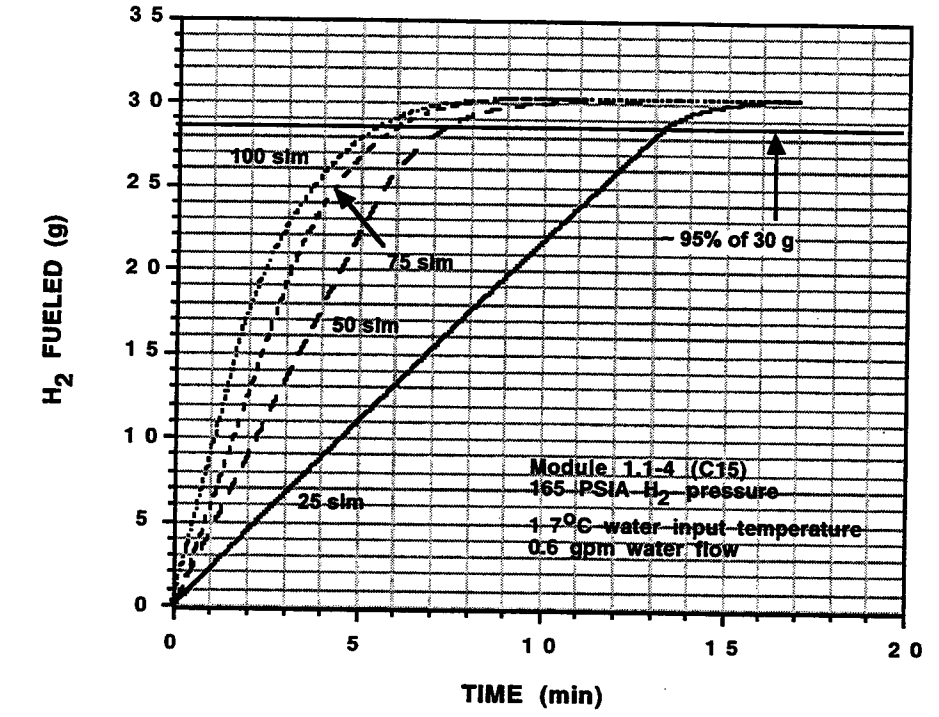

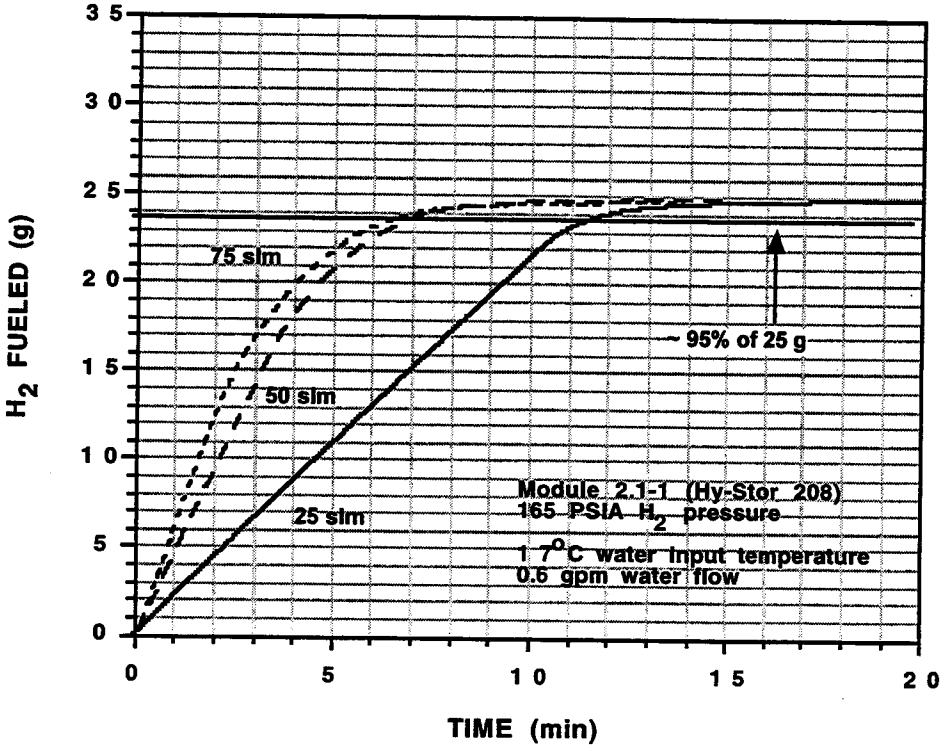

Figure 6a (upper) and Figure 6b (lower)

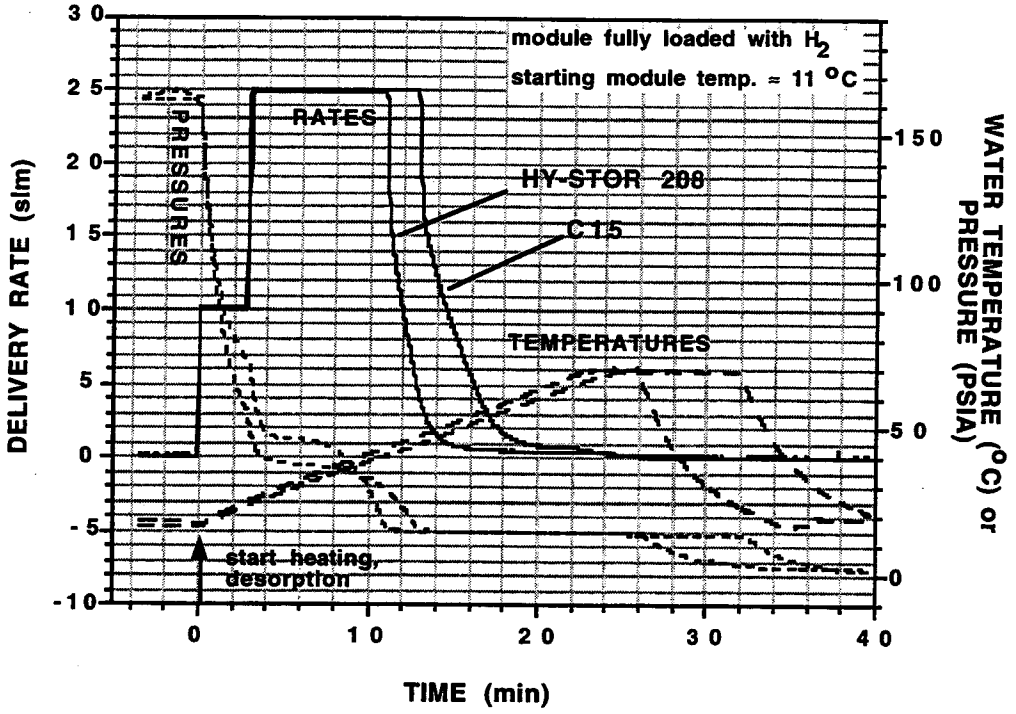

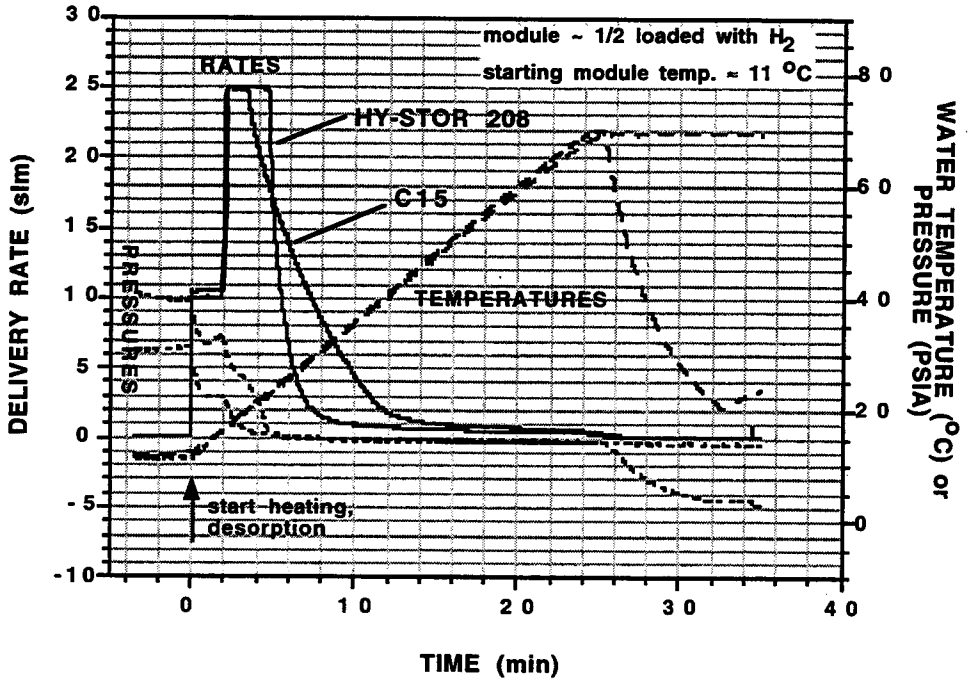

Figure 7a (upper) and Figure 7b (lower)

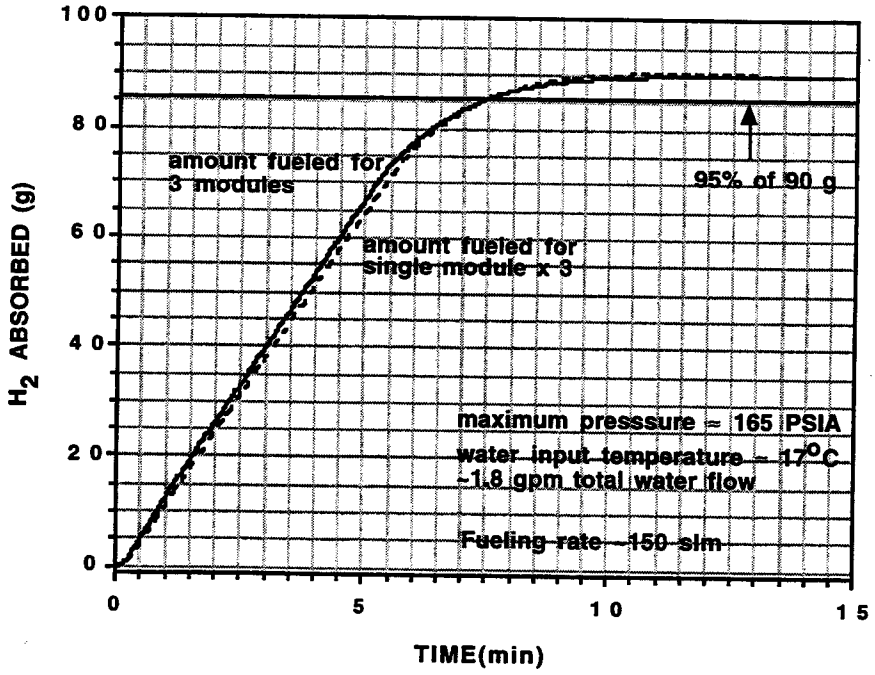

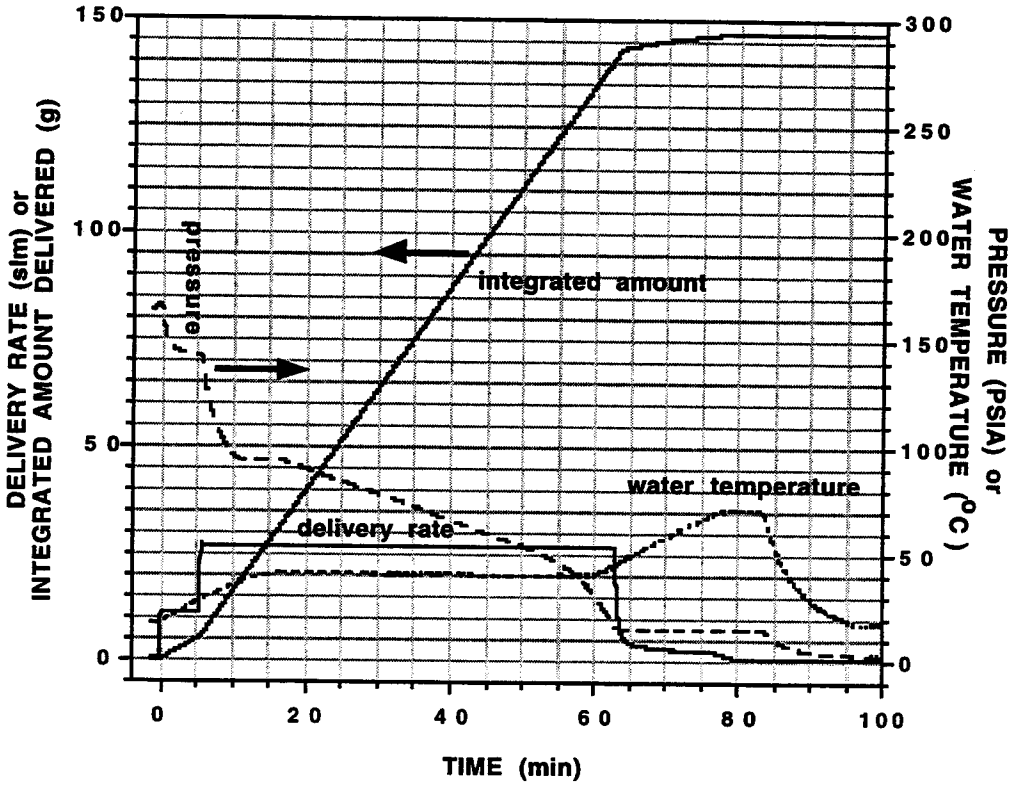

Figure 8a (upper) and Figure 8b (lower)

HYDROGEN STORAGE VIA POLYHYDRIDE COMPLEXES

Craig M. Jensen
Department of Chemistry
University of Hawaii
Honolulu, HI 96822

Abstract

A hydrogen storage system which capitalizes on the favorable energetics of reversible hydrogen binding and C-H bond activation by polyhydride complexes is under development. The iridium P-C-P pincer complex, $IrH_4\{C_6H_3\text{-}2,6\text{-}(CH_2PBu^t_2)_2\}$ (**1**) was found to be an unusually robust and active catalysts for the transfer dehydrogenation of cycloalkanes (cyclohexane, methylcyclohexane, decalin, and dicycolhexyl) to aromatic hydrocarbons (benzene, toluene, naphthalene, and biphenyl) in the presence of the hydrogen acceptor, t-butylethylene at temperatures as low as 100 °C. Hydrogen can also be directly evolved from the system through a PdAg membrane at 200 °C rather than transferred from the cycloalkane to an acceptor. The system can be efficiently recharged by the hydrogenation of arenes to cycloalkanes at 150 °C and 50 atm H_2. A maximized system will efficiently release greater than 7 weight percent hydrogen from the dehydrogenation of cycloalkanes to arenes at temperatures less than 200 °C.

Introduction

A major concern in the development of hydrogen as a fuel is the problem of hydrogen storage. High pressure and cryogenic hydrogen storage systems are impractical for vehicular applications due to safety concerns and volumetric constraints. This has prompted an extensive effort to develop solid hydrogen storage systems. Unfortunately, despite decades of extensive effort, especially in the area of metallic hydrides, (Sandrock, 1992; Sandrock, 1995) no material has been found which as has the combination of a high gravimeteric hydrogen density, adequate hydrogen dissociation energetics, and low cost required for commercial vehicular application (Sandrock, 1995; Suda and Sandrock, 1995). The dehydrogenation of cycloalkanes to arenes releases approximately 7 weight percent hydrogen. Thus cycloalkanes meet high hydrogen density as well as the low cost criteria. Their use as onboard hydrogen carriers is, however, generally considered to be impractical due to the high loadings of heterogeneous precious

catalysts and temperatures in excess of 300 °C required for their dehydrogenation (Linstead, 1938).

We have sought to develop a hydrogen storage system which capitalizes on the favorable energetic of reversible hydrogen binding and C-H bond activation by polyhydride complexes (Mediati et al., 1990; Le-Husebo et al, 1993; Eckert et al. 1995). Our studies of the reversible dehydrogenation of cycloalkanes to arenes were initiated by our finding that $IrH_5(PPr^i_3)_3$ and $RhCl(PPh_3)_3$ catalyzed this reaction at 150 °C. We subsequently found that the complex, $IrH_2\{C_6H_3\text{-}2,6\text{-}(Bu^t_2PC_2H_4)_2\}$ (**1**) is a catalyst for the dehydrogenation of alkanes to alkenes of

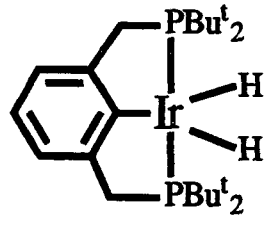

1

unprecedented thermal stability (Gupta et al., 1996). The unique reactivity can be ascribed to the P-C-P ligand which renders the metal center reactive with saturated hydrocarbons but restricts its access to the ligand P-C bonds. We initially studied a transfer dehydrogenation process at temperatures as low as 100 °C (Gupta et al., 1996) but soon found that catalytic dehydrogenation also occurs without a sacrificial hydrogen acceptor at 200 °C (Xu et al., 1997). These results have prompted us to explore the feasibility of a hydrogen storage system based on the reversible dehydrogenation of cycloalkanes to arenes catalyzed by **1**. Towards this goal, we have examined **1** as a catalyst for the dehydrogenation of methylcyclohexane to toluene in the absence of a hydrogen acceptor as well as the reverse reaction, the hydrogenation of toluene to methylcyclohexane (Gupta et al., 1997).

Results

P-C-P Pincer Complex Catalyzed Dehydrogenation of Cycloalkanes to Arenes.

The activity of **1** as a catalyst for transfer-dehydrogenation of cycloalkanes to arenes was investigated using solutions of cycloalkanes (4.0 mL), tbe (0.20 mL, 1.55 mmol), and **1** (3 mg, 0.005 mmol). The results of the catalytic dehydrogenation experiments are summarized in Table 1. The solutions were sealed in tubes under argon, and fully immersed in an oil bath for the prescribed reaction times. The orange solutions became red upon heating but did not further darken or discolor during the reaction period. The reaction was unaffected by the addition of metallic mercury to the solution, indicating that metallic iridium is not involved in the hydrogen transfer (Anton and Crabtree, 1982). The products were identified by GC-MS analysis and quantified by gas chromatography. As seen in Table 1, our quantification balances the number of dehydrogenated C-C bonds within 4% to the amount of tbe hydrogenated to t-butylethane (tba) in all experiments. The rates of the dehydrogenation of cyclohexane and methylcyclohexane are comparable to those previously found for the dehydrogenation of cyclooctane to cyclooctene by **1** (Gupta et al., 1996). The dehydrogenation of decalin required longer reaction times to yield products in adequate amounts for accurate quantification. This

Table 1. Catalytic dehydrogenation with 1.

Substrate	time (h)	T (°C)	Products (mol / mol of 1)	dehydrogenated/ hydrogenated C-C bonds
Cyclohexane	1	150	cyclohexene (44) benzene (54), tba (211)	0.98
Cyclohexane	0.5	200	cyclohexene (86) benzene (77), tba (310)	1.02
Methylcyclohexane	1	150	methylcyclohexenes: 1 (8), 3 (20), 4 (41) toluene (11), tba (105)	0.97
Methylcyclohexane	1	200	methylcyclohexenes: 1 (27), 3 (39), 4 (70) toluene (54), tba (310)	0.96
Methylcyclohexane	120	200	methylcyclohexenes: 1 (67), 3 (13), 4 (25) toluene (65), tba (310)	0.97
Decalin	72	150	octahydronaphthalenes (24) tetrahydronaphthalene (8) naphthalene (4), tba (71)	0.96
Decalin	1	200	octahydronaphthalenes (69) tetrahydronaphthalene (16) naphthalene (7), tba (159)	0.96

reduced reactivity reflects the stringent steric constraints at the metal center. The solutions containing **1** remained active to the limit of complete hydrogenation of the hydrogen acceptor. The 5 day experiment with methylcyclohexane shows that while the total number of unsaturated C-C bonds does not change after the tbe acceptor has been consumed. However, the distribution of dehydrogenated products continues to shift towards the tri-substituted, 1-cyclohexene and toluene as a result of the 3- and 4-cyclcohexenes acting hydrogen acceptors. As previously found for the dehydrogenation of cyclooctane by **1**, the system is inhibited at tbe to catalyst ratios greater than 350:1. Thus, high turnover numbers can be achieved only in solutions containing a limited amount of tbe which must be added periodically. The dehydrogenation activity resumes following incremental additions of tbe (0.20 mL, 1.55 mmol). However, the products apparently compete with tbe for coordination to the iridium center. After 1000 total turnovers there is no increase in the total amount of dehydrogenated products.

To our knowledge, our system if the first for the conversion of cycloalkanes to arenes which is completely catalytic in precious metal. Our moderate temperature, homogeneous catalysts may represent a breakthrough in the development of a feasible hydrogen storage system based on the dehydrogenation of cycloalkanes to arenes. Towards this goal, we have developed methods whereby hydrogen is directly evolved from the system rather than transferred from the cycloalkane to an acceptor. We initially found that significant amounts of hydrogen are produced in reactions carried out under reduced pressure (Xu et al., 1997). In a typical experiment, a solution of cycloalkane (4.0 mL) and **1** (3 mg, 0.005 mmol) was sealed in a tube under an 0.007 mbar of argon and fully immersed in a 200 °C oil bath for 0.5 h. Gas chromatographic analysis of the reaction mixture indicated that 10 turnovers of cyclooctene had been produced. The production of molecular hydrogen was confirmed by gas chromatographic

analysis of the vapor above the reaction mixture. Increased levels of cyclooctane dehydrogenation were not observed in solutions which were heated for longer reaction times. However, additional dehydrogenation activity was achieved in solutions which had been heated to 200 °C for 0.5 by removing the resulting molecular hydrogen by freeze-pump-thaw degassing. A total of 36 turnovers of cyclooctene were obtained in an experiment in which molecular hydrogen was removed 4 times through this procedure. These results demonstrate that the catalytic dehydrogenation of cyclooctane by **1** is limited by equilibrium constraints rather than catalyst stability.

We recently have found that hydrogen can be evolved more efficiently from an autoclave containing solution of methylcyclohexane (8.0 mL) and **1** (6 mg, 0.010 mmol) through a PdAg filter tube. In contrast to transfer dehydrogenation of methylcyclohexane, only toluene is the only observed product of the catalytic dehydrogenation. The absence of methylcyclohexenes in the reaction mixture suggests that the dehydrogenation reaction, like the hydrogenation reaction, occurs by a roll over mechanism. The observed rate of methylcyclohexane dehydrogenation is about 3 times slower than those observed in transfer dehydrogenation experiments. However, no attempt was made to maximize the configuration of the filter tube in the reactor. Thus the difference in the rates of direct and transfer dehydrogenation is most likely due to mass transfer limitations rather than the relative rates of the two catalytic reactions. The major limitation of the catalytic reaction is that pronounced product inhibition was observed after about 5% conversion of methylcyclohexane to toluene. A similar effect was previously observed to occur in transfer dehydrogenation of cycloalkanes to arenes catalyzed by **1**.

P-C-P Pincer Complex Catalyzed Hydrogenation of Arenes to Cycloalkanes.

The polyhydride complex, **1** has also been found to catalyze the reverse reaction, the hydrogenation of arenes. The activity of **1** as a catalyst for arene hydrogenation was investigated using solutions of cycloalkanes (8.0 mL) containing **1** (6 mg, 0.010 mmol). The solutions were loaded in an autoclave under 1 atm of argon which was pressurized with 10 atm of hydrogen and heated for the prescribed reaction times. The results of these experiments are summarized in Table 2. The products were quantified by gas chromatography and their identities verifiedby

Table 2. Catalytic hydrogenation with 1.

Substrate	time	*T* (°C)	Products (mol / mol of **2**)
benzene	12	150	cyclohexane (210)
benzene	72	150	cyclohexane (524)
benzene	12	25	no products observed
toluene	12	150	methylcyclohexane (144)
naphthalene	12	150	decalin (51)

GC-MS. Cyclohexenes were not observed along with the cyclohexane products. We therefore conclude that the hydrogenation occurs through a roll over mechanism whereby the hydrocarbon remains coordinated to the metal center until it is fully dehydrogenated to the arene. The rate of toluene hydrogenation is linear in both temperature and hydrogen pressure. Although the rate is significantly reduced at longer reaction times, up to 85% conversion to methylcyclohexane can be achieved. Several transition metal complexes have been found to catalyze the homogeneous hydrogenation of arene to cycloalkanes (Russell et al., 1977; Bennett et al., 1978; Muetterties

and Bleeke, 1979; Bennett, 1980). The hydrogenation activity of **1** is comparable to that $\{(\eta^6\text{-}C_6Me_6)Ru(\mu\text{-}H)\}_2(\mu\text{-}Cl)$ which is the most active and stable that has been reported (Bennett, 1980). However, unlike any of the previously reported catalysts, **1** also catalyzes the reverse, dehydrogenation reaction.

The dehydrogenation/hydrogenation of metylcyclohexane in a single reactor has been carried out. The reactivity observed for the pincer complex thus represents the basis for a hydrogen storage system which operates under mild conditions as seen in Scheme 1. A maximized system

Scheme 1

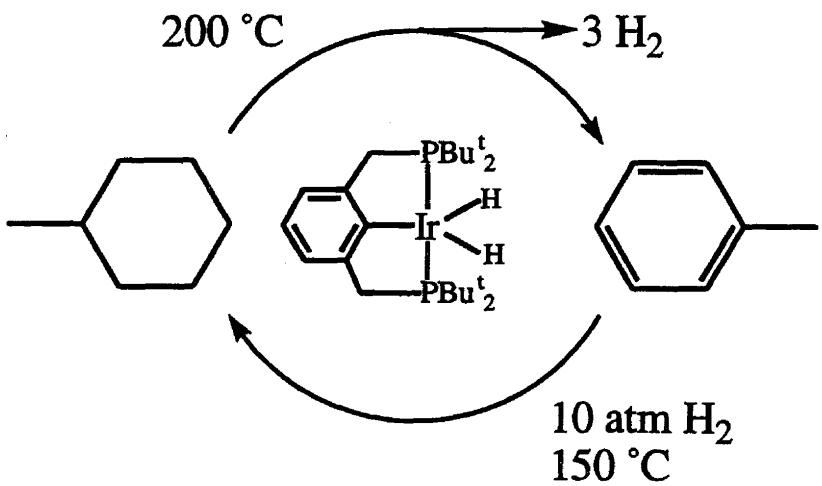

will efficiently release greater than 7 weight percent hydrogen from the dehydrogenation of cycloalkanes to arenes at temperatures less than 200 °C and rechargeable at 150 °C under 50 atm of hydrogen pressure. This technology is especially attractive since it is compatible with existing gasoline infrastructure.

Future Directions

Anthryl P-C-P Pincer Complexes

The major obstacle to the application of our catalytic system to hydrogen storage is that pronounced product inhibition occurs at high conversion of cycloalkanes. The dissociation of the arene products from the catalyst is apparently reversible and, at high concentrations, arenes effectively compete with cycloalkanes for coordination to **1**. In order eliminate the problem of product inhibition, the electronic environment at the metal center must be altered to improve the arene/cycloalkane binding selectivity. This can be accomplished by replacement of the alkyl substituents on the phosphorous by more electronegative groups which will render the phosphorous a weaker σ-donor and a stronger π-acceptor (Lukehart,1985). As a result, the modified pincer catalysts will have markedly reduced alkene affinities than **1**. These same electronic factors should confer a greater cycloalkane affinity on the modified pincer catalysts and thus further alleviate the product inhibition problem. Our studies have indicated that the elimination of the arene product from the metal center is the rate limiting step in the catalytic

reaction. Thus the reduced alkene affinity of the modified pincer complexes should also improve the kinetics of the dehydrogenation reactions.

We have synthesized an iridium 1,8-bis(phosphino)anthryl pincer complex. We originally prepared this complex expecting it to have much greater stability than the xylenyl complex, 1 since it has no C-H bonds proximal to the metal center. The phosphorous is directly attached to the aromatic anthryl backbone in this complex. Therefore, the the desired substitution of the phosphorous with a more electronegative group has also been accomplished. The anthryl complex will be characterized by multinuclear NMR spectroscopy and X-ray crystallography. The activity of this complex as catalysts for the dehydrogenation of cycloalkanes to aromatic hydrocarbons in the 200-300 °C temperature range will examined.

System Development.

The number dehydrogenation/hydrogenation cycles which can be carried out with a single loading of cycloalkane and catalyst is presently under investigation. We also plan to explore where bulkier cycloalkanes such as decalin and bicyclohexyl can be dehydrogenationed beyond the 5% limit found for methylcyclohexane. Finally, we plan to explore whether improved rates of dehydrogenation can be achieved by different configurations of the PdAg filter tube.

Testing of Low Molecular Weight Iron Complexes as Catalysts for Cycloalkane Dehydrogenation.

Economic considerations dictate that low catalyst loadings would be required for a precious metal catalyzed hydrogen storage system. In order for such a system to be economically viable, an iridium complex with catalytic activities approximately 2 orders of magnitude greater than those of the xylenyl P-C-P complex would be required in order to achieve an acceptable rate of dehydrogenation. Alternatively, a systems which employ iron complexes for dehydrogenation could economically tolerate higher catalyst loadings in order to achieve satisfactory rates of dehydrogenation. Towards this end, we plan to explore iron complexes as catalysts for the reversible dehydrogenation of cycloalkanes to arenes. Our catalyst screening will begin with the cyclopentadienyl iron complexes which were synthesized as part of our Hydrogen Program studies during the period 1989-1992. Due to their low molecular weights, these complexes have low melting points and in cases are liquids at room temperatures. This unusual property of these complexes my provide an advantage in the engineering of hydrogen storage systems.

References

Anton, D.R. and R.H. Crabtree. 1982. *Organometallics* 2:855.

Bennett, M.A.; T.N. Huang, A.K. Smith, and T.W. Turney. 1978. *Chem. Commun.*, 582.

Bennett, M.A. 1980. *Chem. Tech.*, 10:444.

Eckert, J., C.M. Jensen, T.F. Koetzle, T.L. Husebo, J. Nicol, and P. Wu. 1995. *J. Am. Chem. Soc.*, 117:7271.

Gupta, M.; C. Hagen, W.C. Kaska, R. Flesher, and C.M. Jensen. 1996. *Chem. Commun.*, 2083.

Gupta, M., C. Hagen, C.; W.C. Kaska, W.C.; R.E. Cramer, and C.M. Jensen. 1997. *J. Am. Chem. Soc.*, 119:840.

Le-Husebo, T., and C.M. Jensen. 1993. *Inorg. Chem.*, 31:3.

Linstead, R.P.; A.F. Millidge, S.L.S. Thomas, and A.L. Walpole. 1938. *J. Chem. Soc.*, 1146.

Lukehart, C.M. 1985. *Fundemental Transition Metal Organometallic Chemistry.* Monterey, CA: Brooks/Cole.

Mediati, M., G.N. Tachibana, and C.M. Jensen. 1992. *Inorg. Chem.*, 31:1827.

Muetterties, E.L. and J.R. Bleeke. 1979. *Acc. Chem. Res.*, 12:324

Russell, M. J., C. White, and P.M. Maitlis. 1977. *Chem. Commun.*, 427.

Sandrock, G., S. Suda, and L. Schlapbach. 1992. *Topics in Appl. Phys.*, 67:197.

Sandrock, G. 1992. *Application of Hydrides* in *Hydrogen Energy Systems* (ed Yurum). Netherlands: Kluwer Academic Publishers. p 253-280.

Suda, S. and G. Sandrock. 1994. *Z. Phys. Chem.*, 183:149.

Xu, W., G.P. Rosini, M. Gupta, C.M. Jensen, W.C. Kaska, K. Krough-Jespersen, and A. Goldman. 1997. *J. Am. Chem. Soc.*, in press.

THERMAL MANAGEMENT FOR FULLERENE-BASED HYDROGEN STORAGE

R. W. Murphy, J. C. Wang, and F. C. Chen
Oak Ridge National Laboratory
Oak Ridge, TN 37831

R. O. Loutfy and X. Lu
Materials and Electrochemical Research (MER) Corporation
Tucson, AZ 85706

Abstract

Although fullerenes have the potential for high gravimetric and volumetric hydrogen storage densities, the large heats of hydrogenation attributed to most members of the alkene family and the high activation energies associated with relevant absorption and desorption processes indicate potential difficulties in the realization of such attractive storage performance in practical designs. Past efforts on this project using limited experimental data indicated that simple physical models could provide reasonable characterizations of both the absorption and desorption processes in fullerenes. Recent commercialization efforts by one of the organizations cooperating in this project have pointed toward substantial price reductions for this unique class of materials. Initial combustion calorimetry measurements accomplished during the past year have provided preliminary substantiation of earlier estimates for fullerene heat of hydrogenation from absorption/desorption data. New data and calculations have been incorporated into an integrated model considering fullerene hydrogenation and dehydrogenation as thermally-activated processes. The model has been used to predict the impact of reductions in activation energy on effective desorption operating temperature. Tests employing two different solid catalyst systems were conducted, but they showed no significant decreases in desorption activation energy. Investigations of improved materials and preparation methods were initiated along three avenues: solid catalyst mechanically alloyed with fullerene; solid catalyst in solvent with fullerene; and liquid catalyst with fullerene. The latter two of these showed positive results in early tests. Thermal management simulations employing a commercial code based on finite control volume methods were validated for simplified situations by comparison to analytical solutions. Simulations were extended to transient hydrogen desorption in a more practical storage device design. A plan for future work was developed.

Introduction

Fullerenes are giant cyclic alkene molecules as illustrated for C_{60} and C_{70} in Fig. 1. They may represent attractive hydrogen storage media because, in these structures, each constituent carbon atom has an associated double bond—offering the possibility of achieving the relatively high gravimetric and volumetric storage densities characteristic of hydrogenation up to one hydrogen atom per carbon atom. Furthermore, Materials & Electrochemical Research Corporation has developed and published (Withers, Loutfy, and Rowe 1997) a vision for fullerene commercialization which projects continuing improvements in production processes and substantial reductions in prices for this unique class of materials. However, the large heats of hydrogenation attributed to most members of the alkene family and the high activation energies associated with the relevant absorption and desorption processes indicated potential difficulties in the realization of such attractive storage performance in practical designs.

Background

Earlier experimental results have shown that:

- as expected, adsorption processes did not show significant promise (Wang, Chen, Lu, Loutfy, and Veksler 1996; Lu, Loutfy, Veksler, and Wang 1996),
- absorption methods with C_{60} could achieve substantial storage levels—up to about 6 wt% of hydrogen (corresponding to $C_{60}H_{48}$),
- the absorbed hydrogen can be released by heating (Wang, Chen, Lu, and Loutfy 1995b), and
- the rates of the absorption-desorption processes can be tailored by the use of various catalysts (Wang, Chen, Lu, and Loutfy 1995a).

Preliminary heat generation/transfer simulation results indicated that the characteristics of a hydrogen storage device can be significantly controlled by the heating and cooling rates in the device.

Approach

The approach adopted in the present project is to utilize the expertise at Oak Ridge National Laboratory and Materials & Electrochemical Research (MER) Corporation in the areas of materials science, electrochemistry, solid state physics, and thermal management to:

- Understand the mechanism of hydrogen storage in fullerenes.
- Optimize the hydrogen absorption/desorption properties of fullerene-based media.

- Develop the thermal management technology needed for hydrogen storage in such media.

- Construct and demonstrate an experimental hydrogen storage device based on the lessons learned.

The near-term strategy is to acquire experimental data, develop physical and heat transfer models to describe hydrogen absorption/desorption in fullerenes and their derivatives, to characterize the behavior of the dynamic storage process, and to design practical configurations to accommodate thermal management in hydrogen storage devices.

Past Results

The initial effort on this project emphasized the use of simple physical models to interpret limited experimental data related to the hydrogenation and dehydrogenation of fullerene samples. It was found that crude representations based on thermal activation mechanisms provided reasonable characterizations of both the absorption and desorption measurements. The results were employed to estimate the temperature profiles and hydrogen release associated with heating of an idealized fullerene storage medium using selected values for heat of dehydrogenation and thermal diffusivity (Wang, Chen, and Murphy 1996).

Current Year Accomplishments

During the current year progress was made in several areas. Preliminary combustion calorimetry experiments were conducted to determine heat of dehydrogenation for a fullerene hydride sample. Comparisons of dehydrogenation heat estimates from absorption and desorption tests were made to values deduced from the combustion calorimetry experiments. Based on estimates of dehydrogenation heat, desorption activation energy, and absorption energy an integrated model for the absorption and desorption processes was constructed. Thermal management simulations of a sample storage device were created. Investigations of improved materials and preparation methods were initiated along three avenues: solid catalyst mechanically alloyed with fullerene; solid catalyst in solvent with fullerene; and liquid catalyst with fullerene.

Heat of Hydrogenation

A C_{60} sample produced by MER was hydrogenated to $C_{60}H_{31.1}$ as characterized by mass spectrum measurements. Preliminary combustion calorimetry measurements on this sample were conducted at the National Institute of Standards and Technology to estimate the heat of formation for this hydride. Fullerene heat of formation was estimated from two foreign combustion calorimetry measurements in the literature. From these data a preliminary estimate for the average heat of hydrogenation for

$$C_{60}H_x + H_2 \rightarrow C_{60}H_{x+2}$$

was determined to be 59.3 kJ/g-mole H_2. This value was found to be in good agreement with the 60 kJ/g-mole H_2 estimated previously from our absorption/desorption data.

Catalysts/Activation Energies

In this work, fullerene heat of hydrogenation has been interpreted as the difference between the activation energy required for hydrogen absorption and that for hydrogen desorption. That is, this quantity represents the net amount of energy that must be removed to accomplish isothermal hydrogenation or that must be added to accomplish isothermal dehydrogenation of the fullerene. However, the size of the respective activation energies can be substantially greater than the heat of hydrogenation. For example, in one case from our earlier work with fullerenes, effective dehydrogenation of fullerenes required heating to the 400°C temperature range, with an associated desorption activation energy estimated to be 160 kJ/g-mole H_2 (approximately 1.6 eV/H_2).

This elevated temperature requirement is not likely to lead to a viable hydrogen storage design. If, however, as shown in Fig. 2, the desorption activation energy can be reduced from 1.6 eV/H_2 to, for example, 1.2 eV/H_2 by catalytic or other means, the effective dehydrogenation temperature would drop to about 230°C. A further decrease to 1.0 eV/H_2 would cut the effective operating temperature to about 150°C.

In an effort to reduce the activation energies and associated operating temperatures, dehydrogenation tests were conducted using mixed fullerenes with two solid catalyst systems. As illustrated by the representative data presented in Fig. 3, neither system showed a consistent ability to reduce activation temperature by a significant amount. As a result, efforts involving improved materials and preparation methods were initiated along three avenues—two of which have already shown significant potential.

Preliminary results from the first avenue, solid catalyst in solvent with fullerene, indicate substantial reductions in activation energy—enabling the absorption process to take place under much milder conditions. From the Arrhenius plot data presented in Fig. 4, it appears that two different mechanisms (one for low hydrogen concentrations and one for high hydrogen concentrations) may be responsible for the observed improvement. In this interpretation, two distinct activation energies, 22 kJ/g-mole H_2 and 4.3 kJ/g-mole H_2, are evident, but both are much smaller than the 100 kJ/mole estimated earlier for the solid-phase hydrogenation experiments (in which no such indications of a second mechanism were observed).

Initial trials from the second avenue, liquid catalyst with fullerene, conducted in cooperation with the University of Hawaii, using polyhydride metal complex catalysts with mixed fullerenes showed effective reduction of dehydrogenation temperatures into the 200°C range. Plans were developed for a third avenue, involving the mechanical alloying of fullerenes with solid catalyst, to be pursued in cooperation with Sandia National Laboratories.

Thermal Management Simulation

The data acquired were used to develop estimates for heat of hydrogenation, desorption activation energy, and absorption energy. Based on these values, an integrated model considering fullerene hydrogenation and dehydrogenation as thermally-activated processes was constructed. A commercial computational fluid dynamics code employing finite control volume methods was applied to a metal tube/fullerene rod geometry (Fig. 5). The code was used to calculate temperature profiles (Fig. 6) for representative transient heating situations. Comparisons of these results to analytical solutions available for these simplified situations were used to validate the accuracy of this method.

The code was then used to extend the simulations to a device of a more practical geometry (Fig. 7) which incorporated metal fins and fullerene disks in a metal cylinder, with hydrogen distribution accomplished by means of a central porous metal tube and heating (or cooling) provided at the periphery. The scenario described is one in which the initial condition is a system at a uniform temperature of 301 K (28°C) with the fullerene hydrogenated to 400 std l/kg. From this point the outer periphery is specified to increase in temperature at a constant rate for 10 min, at which time the periphery has reached 673 K (400°C). Subsequently, the temperature of the periphery is maintained constant at this elevated level.

The first set of calculated isotherms presented in Fig. 8 shows that, at the end of the 10-min periphery temperature increase period, temperature gradients within the fullerene disk are relatively small—with a peak temperature of about 608 K (335°C, still substantially below the effective dehydrogenation activation temperature of about 400°C for this example). The corresponding hydrogen concentration distribution given in Fig. 9 shows that hydrogen evolution at the 10-min mark is very limited and has essentially been confined the portions of the disk that are immediately adjacent to the metal surfaces. However, at the 20-min mark, Fig. 9 shows that significant dehydrogenation has occurred (more than 80% of the initial charge has been removed), with meaningful concentrations remaining only in the central regions of the disk. The corresponding temperature distribution in Fig. 8 shows relatively large temperature gradients at the 20-min mark. Because dehydrogenation is an endothermic process, heat is removed from the fullerene in the regions undergoing hydrogen removal. At the 20-min mark the portions of the fullerene disk near the metal surfaces have undergone essentially complete dehydrogenation and have had time to receive heat by conduction and, thereby, to experience significant temperature recovery. The interior sections are still undergoing hydrogen desorption, and the sensible heat taken from the fullerene to this process has not yet been replenished by conduction through the intervening material. This combination leads to the more than 150 K temperature difference between the extremes of these respective regions indicated in Fig. 8.

Plans for Future Work

The following plans primarily address the fullerene options; however the methodology developed and the experience gained for hydrogen storage in fullerenes and their derivatives can be applied to other options:

- Extend heat of hydrogenation measurements for fullerenes in cooperation with the National Institute of Standards and Technology.
- Expand data base for solvent/catalyst absorption and solid-phase absorption/desorption of hydrogen in fullerenes.
- Evaluate mechanical alloying of fullerenes with selected catalysts to determine the potential advantages of improved solid/solid contact in cooperation with Sandia National Laboratories.
- Investigate potential improvements using metal-complex liquid catalysts with fullerenes in cooperation with the University of Hawaii.
- Interpret all new information to determine the most attractive fullerene-based options.
- Employ characteristics of the most attractive options to create relevant models and simulations of practical hydrogen storage units.
- Examine thermal management issues of carbon nanotube storage systems in cooperation with the National Renewable Energy Laboratory.
- Explore the potential of other novel options for hydrogen storage.

Acknowledgments

This work was sponsored by the U.S. Department of Energy under contract No. DE-AC05-96OR22464 with Lockheed Martin Energy Research Corporation. The authors wish to thank D. T. Chen of the University of Tennessee for providing computational fluid dynamic modeling support, D. R. Kirklin of the Physical and Chemical Properties Division at the National Institute of Standards and Technology for performing preliminary combustion calorimetry tests on our fullerene hydride samples, and C. M. Jensen of the Department of Chemistry at the University of Hawaii for conducting initial experiments using dihydrido iridium bisphosphine complexes as dehydrogenation catalysts for our mixed fullerene hydride samples.

References

Lu, X., R. O. Loutfy, E. Veksler, and J. C. Wang. 1996. "Hydrogen Gas Adsorption on C_{60}/C_{70} Fullerenes." In *Proceedings of the Symposium of Recent Advances in the Chemistry and Physics of Fullerenes and Related Materials*, Volume 3, edited by K. M. Kadish, and R. S. Ruoff, the Electrochemical Society, Inc.

Wang, J. C., F. C. Chen, X. Lu, and R. O. Loutfy. 1995a. "Model for Hydrogenation and De-Hydrogenation of C_{60}/C_{70} Fullerene." Presented at *Symposium FF: Fullerenes, Buckytubes, and Related Materials—Science and Applications*, Materials Research Society 1995 Fall Meeting, Boston, MA.

Wang, J. C., F. C. Chen, X. Lu, and R. O. Loutfy. 1995b. "Analysis of Hydrogen Storage in Fullerenes," CRADA Final Report ORNL-94-0277. Oak Ridge National Laboratory, Oak Ridge, TN.

Wang, J. C., F. C. Chen, and R. W. Murphy. 1996. "Thermal Management Technology for Hydrogen Storage: The Fullerene Option." In *Proceedings of the 1996 U.S. DOE Hydrogen Program Review*, 2:819–829.

Wang, J. C., F. C. Chen, X. Lu, R. O. Loutfy, and E. Veksler. 1996. "Intercalation of Hydrogen into C_{60} Fullerene." Presented at *Symposium D: Properties and Applications of Electronic Organic Materials and Fullerenes*, Materials Research Society 1996 Fall Meeting, Boston, MA.

Withers, J. C., R. O. Loutfy, and T. P. Lowe. 1997. "Fullerene Commercial Vision." *Fullerene Science and Technology*, 5:1–31.

Figure Captions

Fig. 1. C_{60}/C_{70} fullerene structures.

Fig. 2. Effects of reduced desorption activation energies on operating temperature.

Fig. 3. Representative mixed fullerene dehydrogenation performance with solid catalyst system.

Fig. 4. Arrhenius plot for fullerene hydrogenation using solid catalyst in solvent.

Fig. 5. Simple metal tube/fullerene rod geometry for validation of computational simulation.

Fig. 6. Computed radial temperature profiles for simple geometry during heating process.

Fig. 7. Metal fin/fullerene disk geometry for hydrogen storage.

Fig. 8. Temperature (K) distributions in hydrogenated fullerene disk after 10 and 20 min of heating.

Fig. 9. Hydrogen concentration distributions (std l/kg) in hydrogenated fullerene disk after 10 and 20 min of heating.

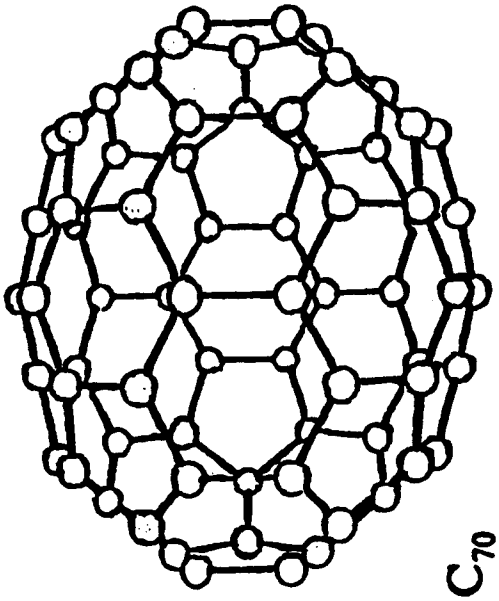

C_{70}

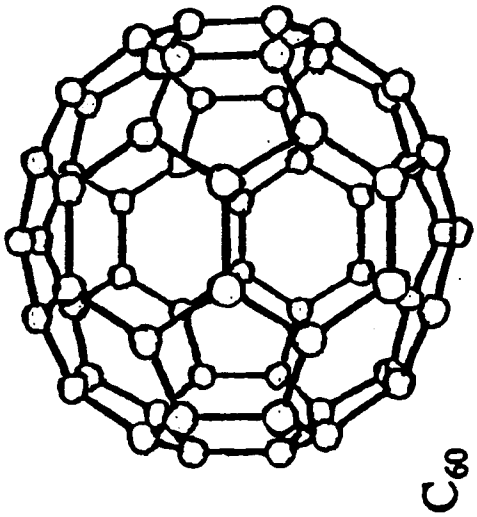

C_{60}

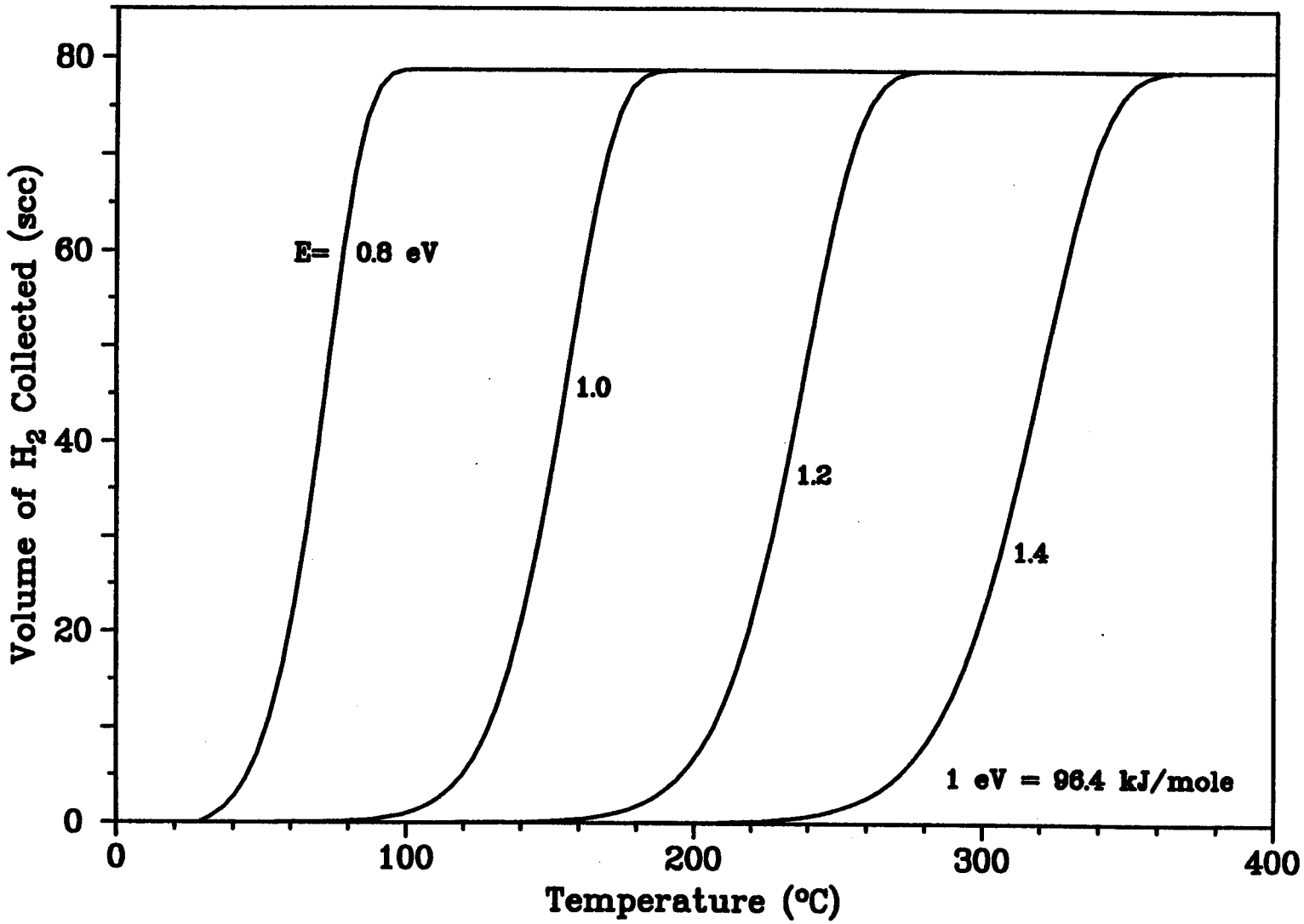
Volume of H_2 Collected (scc)
80
60
40
20
0
0
100
200
300
400
Temperature (°C)
E= 0.8 eV
1.0
1.2
1.4
1 eV = 96.4 kJ/mole

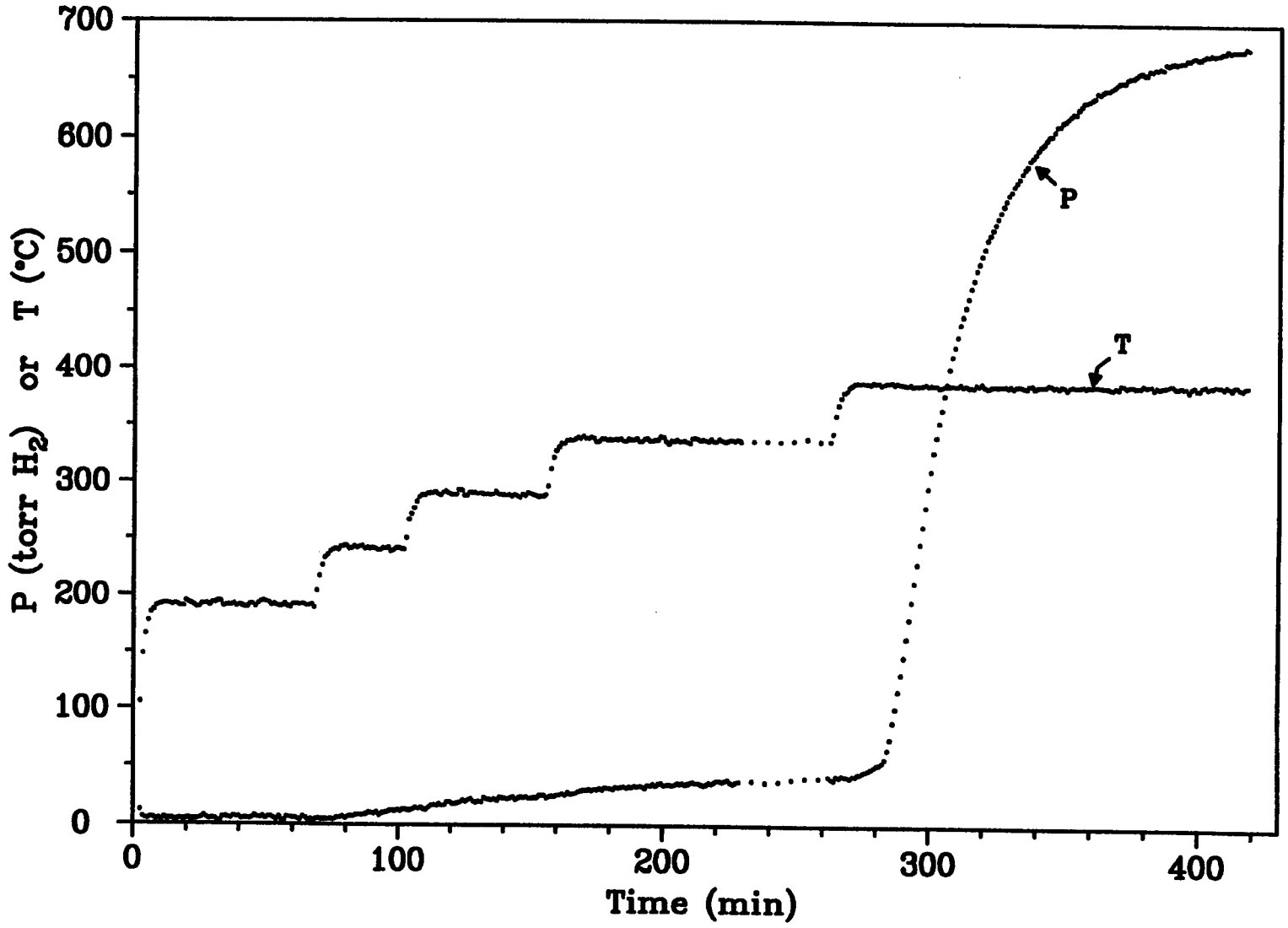
700
600
500
400
300
200
100
0
P (torr H_2) or T (°C)
0
100
200
300
400
Time (min)
P
T

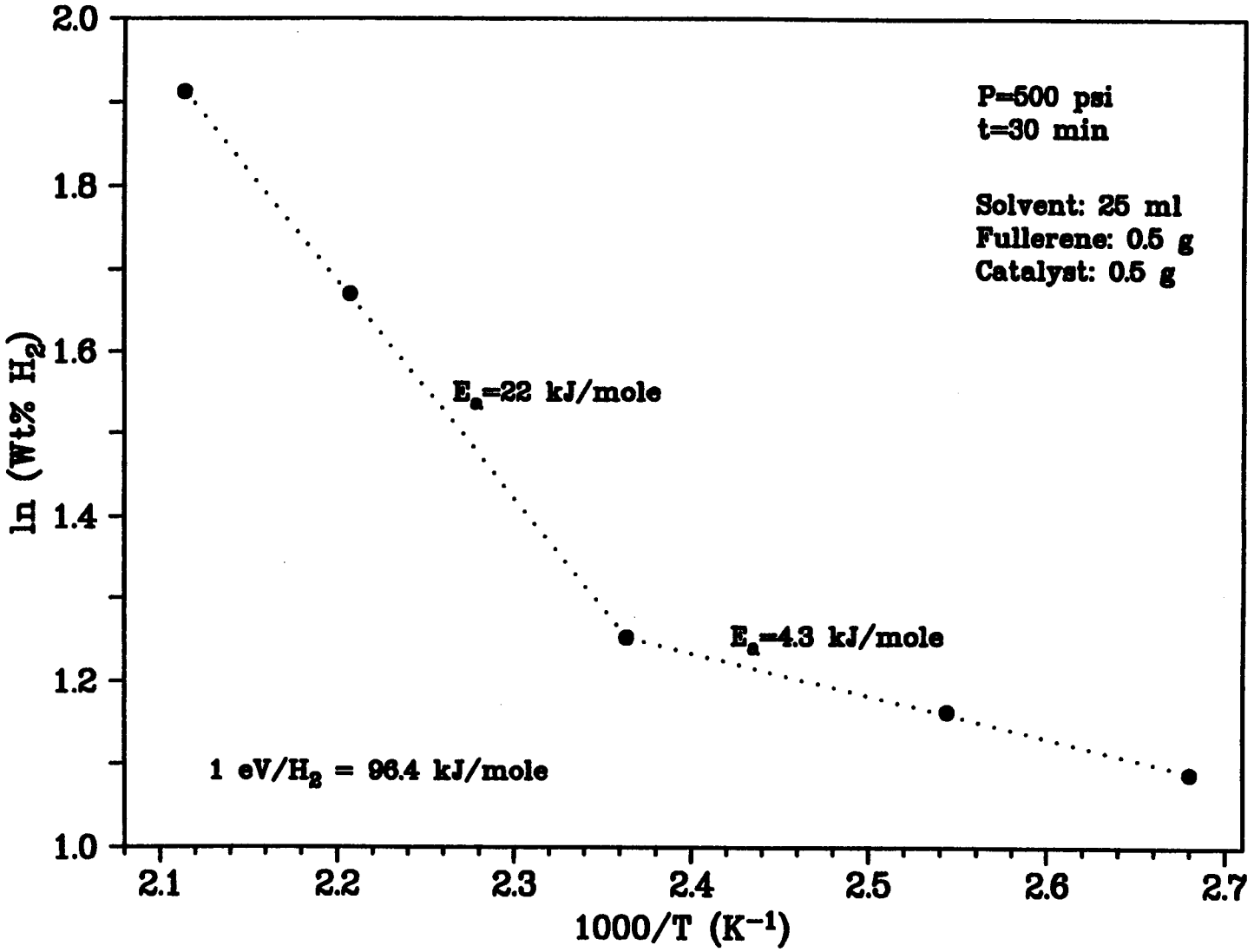
2.0
1.8
1.6
1.4
1.2
1.0
ln (Wt% H_2)
2.1
2.2
2.3
2.4
2.5
2.6
2.7
1000/T (K^{-1})
P=500 psi
t=30 min
Solvent: 25 ml
Fullerene: 0.5 g
Catalyst: 0.5 g
E_a=22 kJ/mole
E_a=4.3 kJ/mole
1 eV/H_2 = 96.4 kJ/mole

Dimension: 1.005 m x 0.0125 m x (2x3.14159)
Grid Points: 404 x 12 x 3

Fullerene Powder:
Density = 1720 kg/m^3
Specific Heat = 739 J/kg.K
Thermal Conductivity = 0.07749 W/m.K

Carbon Steel Tube
Thickness = 0.0025 m

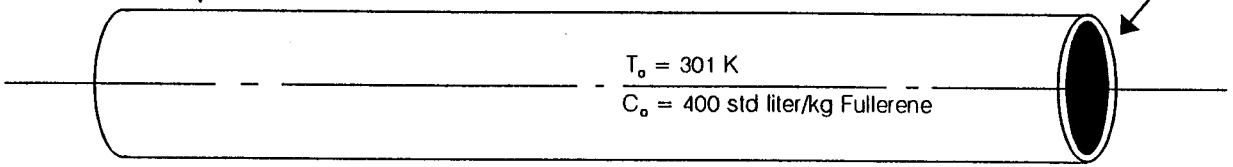

Boundary Conditions:

T(K) = 301 + 0.62 t	t = 0 - 600 sec
T(K) = 673 K	t > 600 sec

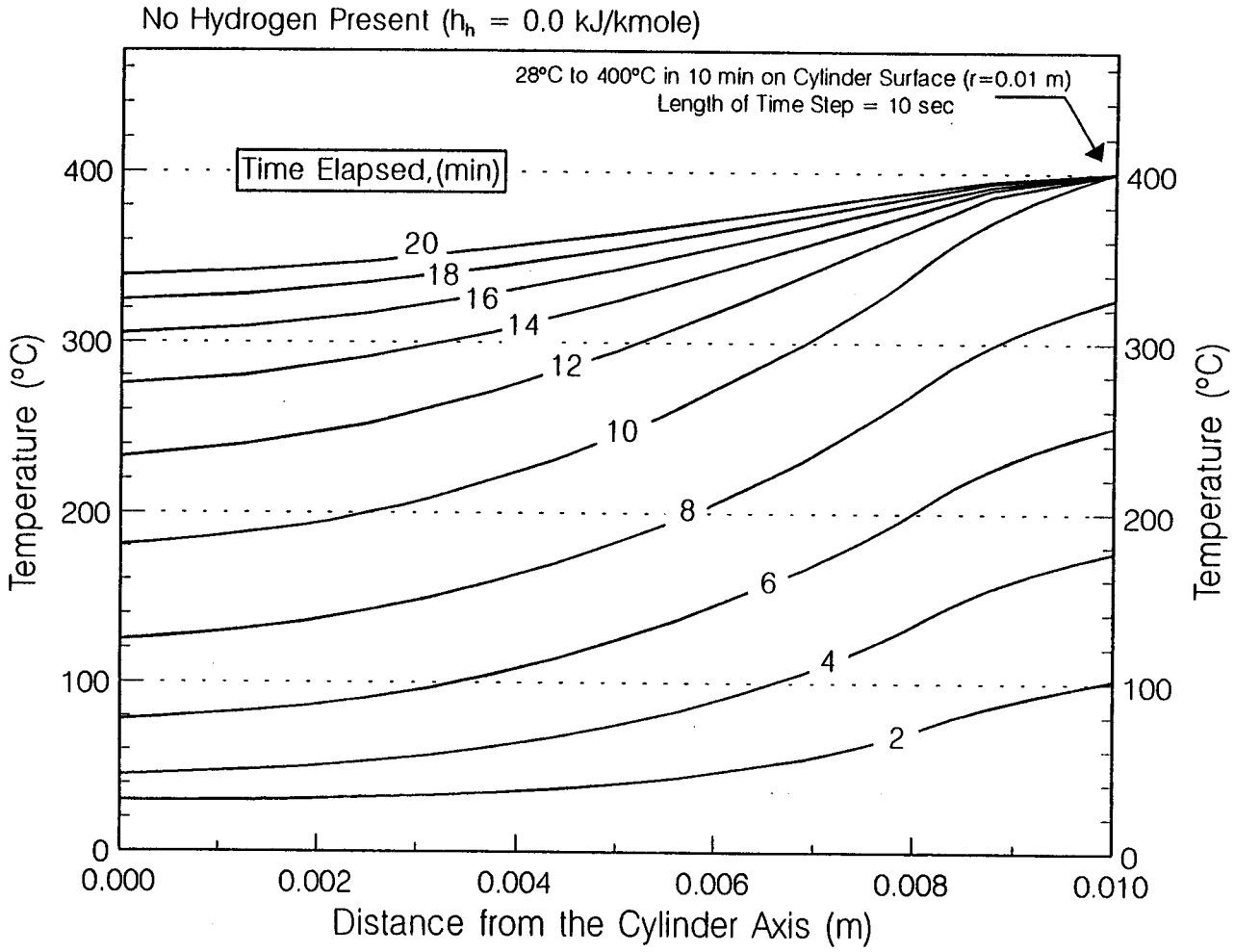
No Hydrogen Present (h_h = 0.0 kJ/kmole)
28°C to 400°C in 10 min on Cylinder Surface (r=0.01 m)
Length of Time Step = 10 sec
Time Elapsed,(min)
20
18
16
14
12
10
8
6
4
2
400
300
200
100
0
Temperature (°C)
0.000
0.002
0.004
0.006
0.008
0.010
Distance from the Cylinder Axis (m)

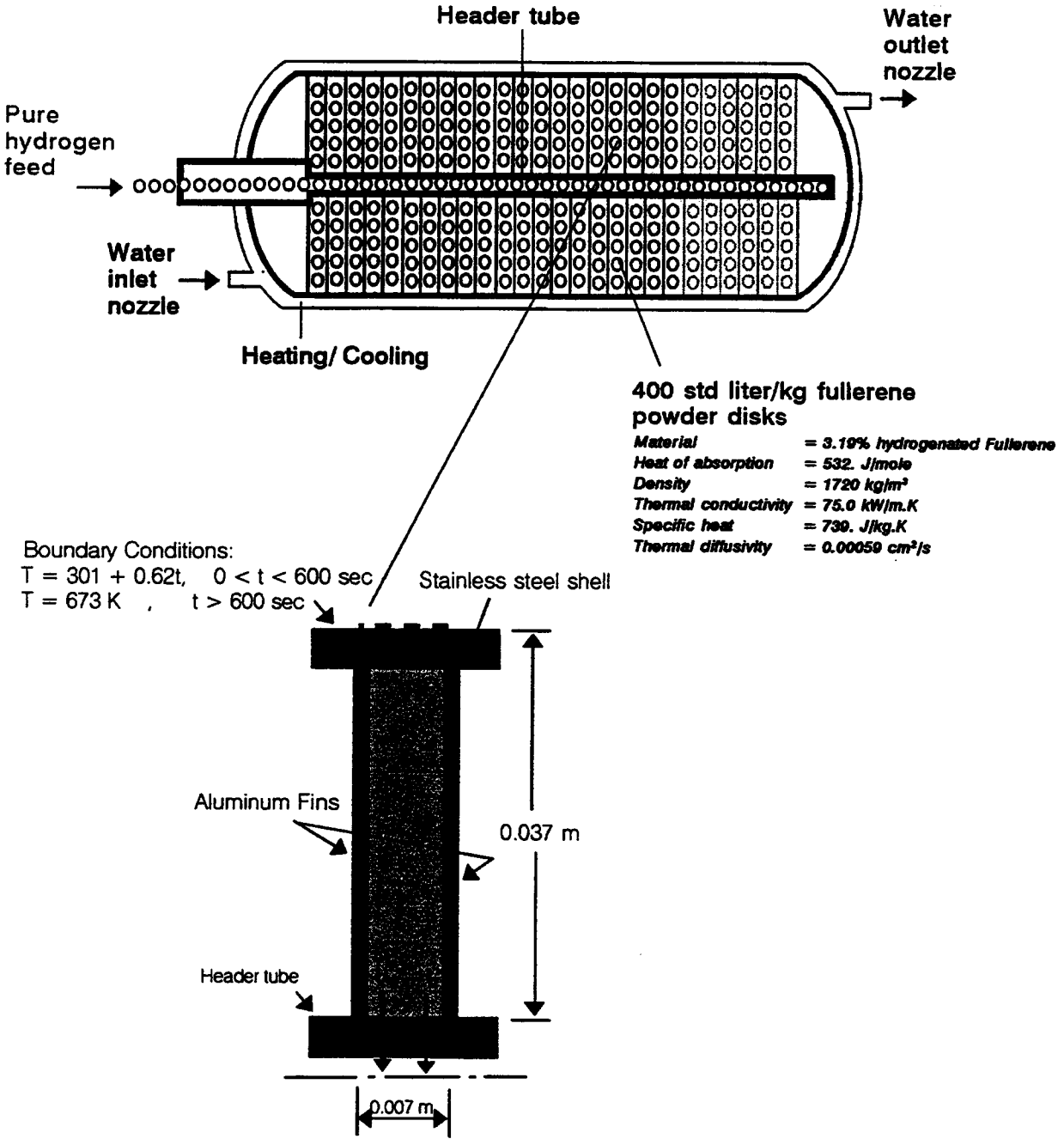
Header tube
Water outlet nozzle
Pure hydrogen feed
Water inlet nozzle
Heating/ Cooling
400 std liter/kg fullerene powder disks
Material = 3.19% hydrogenated Fullerene
Heat of absorption = 532. J/mole
Density = 1720 kg/m³
Thermal conductivity = 75.0 kW/m.K
Specific heat = 739. J/kg.K
Thermal diffusivity = 0.00059 cm²/s
Boundary Conditions:
T = 301 + 0.62t, 0 < t < 600 sec
T = 673 K , t > 600 sec
Stainless steel shell
Aluminum Fins
0.037 m
Header tube
0.007 m

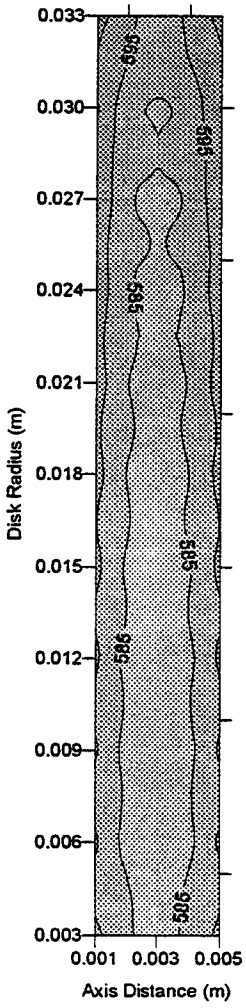

t = 10 min

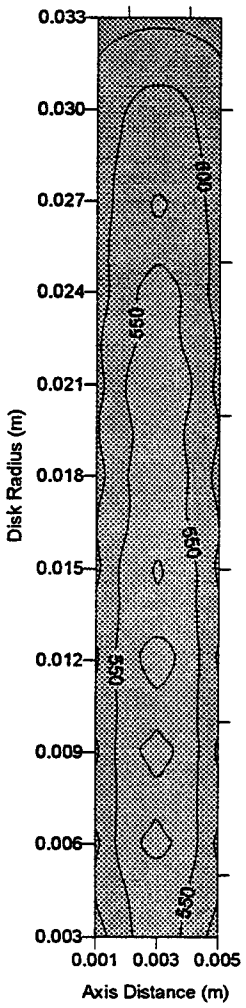

t = 20 min

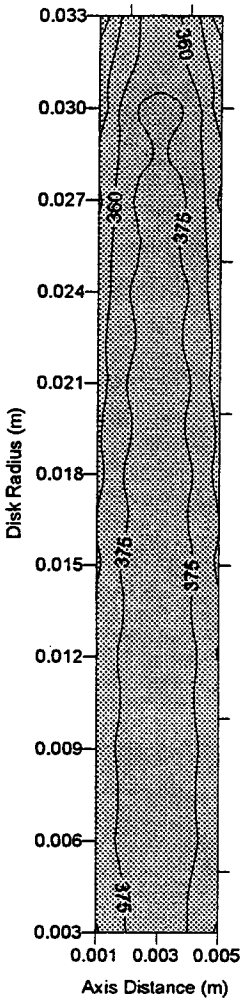

t = 10 min

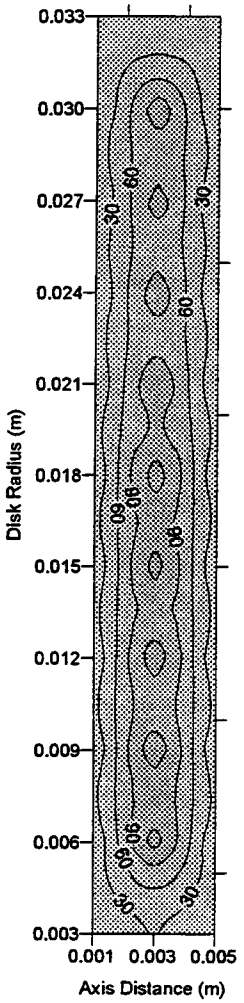

t = 20 min

Advanced Hydrogen Fueled Internal Combustion Engines

Peter Van Blarigan

Sandia National Laboratory

7011 East Avenue

Livermore, CA 94550

Abstract

The Hydrogen Program at Sandia National Laboratories is developing internal combustion engine generators for application in series hybrid vehicles and stationary power units. The program consists of two approaches: investigating the utilization of hydrogen in a conventional crankshaft driven engine and in an advanced free piston configuration.

The conventional engine program has taken the direction of utilizing the unique ability to spark ignite homogeneous fuel/air mixtures of hydrogen at low equivalence ratios ($\phi \approx 0.4$) to achieve low NO_x emissions and high thermal efficiency.

The goal is to translate the indicated thermal efficiency of single cylinder engines into multi-cylinder configurations achieving at least 40% brake thermal efficiency. When coupled to an electrical generator the fuel to electricity conversion efficiency would be approximately 37%.

A modified Perkins 3.152 Diesel engine (850 cubic centimeters) is currently being tested, and has achieved an indicated thermal efficiency of 45% in preliminary operations.

The advanced free piston design utilizes a new approach to IC engine combustion. A double-ended free piston is used to compression ignite homogeneous fuel/air mixtures as it oscillates inside a closed cylinder. Through this oscillation, electrical energy is generated in a linear alternator which acts also to control the piston motion by dynamically adjusting the electromagnetic forces felt by the piston. Electricity is the output of this engine, and electronic

This paper will appear in a special hydrogen edition of Energy & Fuels.

NUMERICAL MODELING OF HYDROGEN-FUELED INTERNAL COMBUSTION ENGINES

Norman L. Johnson and Anthony A. Amsden
Los Alamos National Laboratory
Theoretical Division, Group T-3
Los Alamos, NM 87545
(NLJ@LANL.GOV)

ABSTRACT

The planned use of hydrogen as the energy carrier of the future introduces new challenges and opportunities, especially to the engine design community. Hydrogen is a bio-friendly fuel that can be produced from renewable resources and has no carbon dioxide combustion products; and in a properly designed ICE, almost zero NO_X and hydrocarbon emissions can be achieved. Because of the unique properties of hydrogen combustion — in particular the highly wrinkled nature of the laminar flame front due to the preferential diffusion instability — modeling approaches for hydrocarbon gaseous fuels are not generally applicable to hydrogen combustion. This paper reports on the current progress to develop a engine design capability based on the KIVA family of codes for hydrogen-fueled, spark-ignited engines in support of the National Hydrogen Program. A turbulent combustion model, based on a modified eddy-turnover model in conjunction with an intake flow valve model, is found to describe well the efficiency and NO_X emissions for an experimental engine over a wide range of ignition timings. The NO_X emissions of this engine satisfy the Equivalent Zero Emission Vehicle (EZEV) standard established by the California Air Resource Board.

Key-words: hydrogen, zero-emissions, high-efficiency, internal combustion engine

Introduction

Hydrogen has long been considered the ideal energy carrier of the future — displacing hydrocarbon fuels — because of its production from renewable resources and as a "greenhouse-friendly" fuel. One challenge of the proposed increased use of hydrogen is the development of an inexpensive, emission-free and reliable powerplant for stationary power generation and transportation [1-4]. Fuels cells have been the promised solution for decades. But for the near to medium term, the high cost, the sensitivity to impurities and the lack of fuel flexibility will limit the use of fuel cells. And in developing countries, which may be the largest polluters in the future, low-technology solutions must be found. The likely solution, then, will be a hydrogen-fueled, high efficiency, low emission ICE — a "mechanical fuel cell." Because hybrid vehicles and stationary powerplants require fixed power output with constant fueling and engine speed, a unique opportunity exists to optimize the engine for a single operating speed, in contract to the compromised performance in all prior ICE that operate at a variety of RPM and fueling conditions. Because a limited experience-base exists for hydrogen-fueled ICEs, simulation codes will be an even more essential component to the design process.
A challenge to modeling arises because pure hydrogen or hydrogen mixtures have atypical combustion characteristics, exemplified by extremely high flame speeds, unstable flame fronts under typical equivalence ratios, and ignitability at extremely low equivalence ratios, in comparison to hydrocarbon gases. While these characteristics can be advantageous in engines, they require re-evaluation of traditional approaches and possibly alternative approaches to modeling hydrogen-fueled engines.

This paper reports on the progress towards developing a simulation capability for designing hydrogen-fueled ICE, based on the recently released KIVA-3V code from Los Alamos National Laboratory [5]. The capability has been benchmarked to the experimental results in a companion program at Sandia National Laboratories [6] for a modified Onan engine. The experimental program has demonstrated that an ICE without exhaust clean-up can satisfy the Equivalent Zero Emission Vehicle (EZEV) standard established by the California Air Resource Board (CARB) [7] with high indicated thermodynamic efficiency (45-50%) for both pure hydrogen and hydrogen-hydrocarbon gas mixtures, with zero carbon dioxide emissions for pure hydrogen.

The first part of the paper summarizes the progress in understanding the unique combustion characteristics of hydrogen as applied to multidimensional simulations. The latter part of the paper presents the success in modeling the experimental engine.

Hydrogen Combustion

The main questions to be answered in this section are: How does turbulent combustion of hydrogen differ from hydrocarbon gases? And can the models for hydrocarbon turbulent combustion be used accurately for hydrogen combustion? For a predictive simulation capability, the combustion model must accurately describe the dependencies of turbulence, fuel-oxygen ratio, fuel mixtures, temperature and pressure *and* also not be so computationally intensive as to prohibit full engine simulations.

Unique Laminar Combustion

Most researchers are familiar with the low flammability limit of hydrogen and high flame speeds or burning velocities of hydrogen — about 3.5 m/s in air at standard temperature and pressure (STP) [8,9] or about ten times the flame speed as found in low molecular weight hydrocarbon gases [10,11]. What is not broadly understood is the origins of these differences.

The extremely high molecular diffusivity of hydrogen relative to oxygen produces many of the unique properties of hydrogen, such as the desirable traits of flammability and robust combustion at lean mixtures for both hydrogen-air and hydrogen-hydrocarbon gas-air mixtures. The high mobility of the hydrogen also contributes to an instability in a laminar flame front, the fuel equivalence ratio (here, an unstable flame front means that a protuberance in the flame front will speed up and a trough will slow down — making a wrinkle grow in size). The instability occurs because the hydrogen is depleted in the troughs and collects in the tips, coupled with the increase in the flame speed with increasing hydrogen concentration in this regime.

Although an instability in a planar flame front occurs for all combustion gases at some concentration due to the difference in molecular weight of oxygen and the gaseous fuel, what is unusual for hydrogen is that this instability in air occurs at values of φ in the normal operating conditions of engines: at a φ less than 1.5 at standard temperatures and pressures (STP). This is in contrast to the region that is unstable for methane ($\varphi < 0.74$), propane ($\varphi > 1.44$), ethane ($\varphi > 1.68$) and ethylene ($\varphi > 1.95$) [11-13]. The existence of the laminar flame instability has been neglected in theories of laminar flame propagation for hydrogen and generally brings into question the validity of kinetic calculations that assume the flame front is one dimensional and the assumption of a thin, resolved flame front in most treatments of turbulent combustion. This will be discussed in the later section on turbulent combustion.

Another unique aspect of hydrogen combustion, which is not well understood, is the separation in the value of φ at the maximum temperature (1.0) and at the maximum flame speed (1.8) [13, 14]; for all hydrocarbon fuels, φ for these maximums coincide and occur in the range of values for φ between 1.0–1.2. This observation is a good illustration that even laminar hydrogen combustion is uniquely different than hydrocarbon combustion.

The kinetics of hydrogen combustion have been extensively studied, although comparisons between theory and experiments have been complicated by the diffusive instabilities described above. A successful effort by Warnatz [14] in producing a limited reaction set of 18 equations concluded the following. 1) The existence of two competing mechanisms for hydrogen oxidation significantly complicates the laminar kinetics and is the source of unexpected sensitivity to initial temperature, pressure and equivalence ratio. As a consequence, the laminar flame speed has a strong dependence on initial temperature, rising from 3.5 m/s for stoichiometric conditions ($\varphi = 1$) in air at STP to about 23 m/s at 1000K, typical of temperatures at ignition in a high compression engine. The higher pressure at the time of combustion also increases the laminar flame speed, but to a weaker power ($p^{0.2}$). 2) The Zeldovich model for NO_x production is better suited to hydrogen combustion than hydrocarbon combustion due to the absence of HC radicals which encourage the formation of "prompt" NO_x.

Turbulent Combustion Data

Little experimental information is available on the turbulent combustion of hydrogen, and what is available is at conditions different than typical engine regimes. The most complete set of data was developed to support nuclear reactor safety studies [9], with other data in [8,12,15-19]. Some relevant data on lean methane turbulent combustion can also be found in [20].

In Fig. 1 the data from [9] was analyzed to evaluate the dependence of the flame speed on turbulence. The error bars are inversely proportional to the goodness of the least-squares fit of the data. A major conclusion, as observed in Fig. 1, is that the effect of turbulence is large for slow burning mixtures, and small for fast burning mixtures. At fuel concentrations around $\varphi = 0.4$, the turbulent flame velocity in air is found to be proportional to u' or $k^{0.5}$.

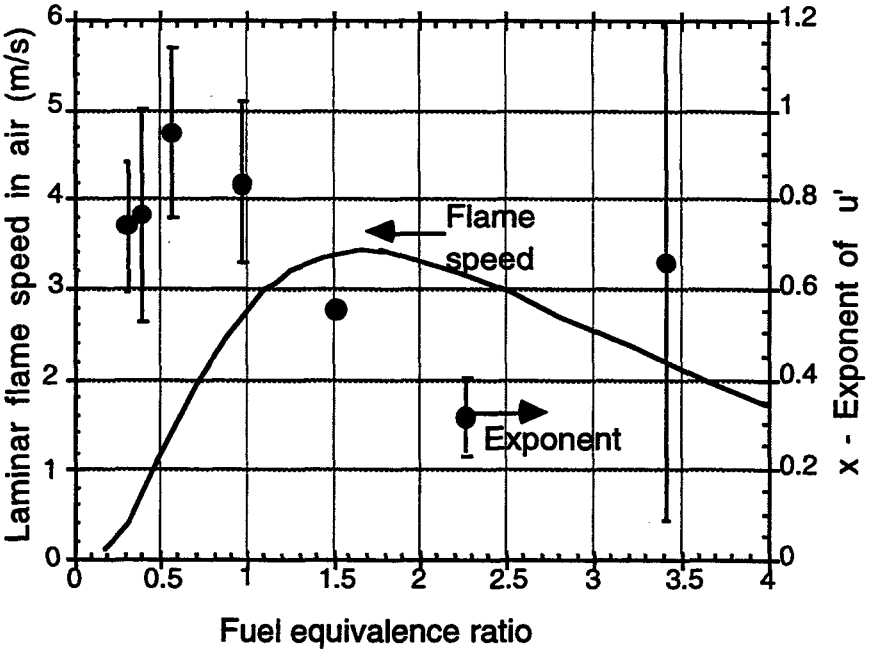

Figure 1. The dependence of the turbulent flame speed, S_t, on the turbulence intensity, u', from fitting $S_t = a\,u'^x$ on the experimental data [9].

For hybrid ICE engines, the planned operating conditions (φ around 0.4) are in the unstable regime ($\varphi < 1.5$) in order to reduce the flame temperature and hence the NO_x formation, which increases rapidly above φ of 0.5. In this region, the flame speed increases 10 times the laminar flame speed at a turbulence intensity of 2.4 m/s. At the maximum laminar flame speed, the increase is 7 times at 2.4 m/s. Note that the typical turbulence intensities for the Onan engine during combustion are found from the KIVA simulations to be in the range of 1–3 m/s.

Turbulent Combustion Modeling

Because all spark-ignited engines have flame fronts that propagate in the presence of turbulence, an accurate combustion model for engine simulations must include the effects of turbulence. For hydrocarbon fuels, a typical approach in large scale SI engine simulations is to neglect the laminar kinetics and to use models that include only the effect of turbulence on the combustion rate. In recent years, significant progress has been made in understanding the details of the turbulent combustion by the introduction of a flamelet or coherent flame models, e.g., [21]. These models solve for the generation and destruction of flame surface based on the turbulent model. Tables of laminar flame speed, as a function of pressure, temperature and composition, are then used to determine the reaction rate at any time. The key assumption of the flamelet approach is that the flame thickness is thin compared to the dimensions of the turbulent eddies and the problem dimensions.

Given this background in the current state of modeling turbulent combustion, the occurrence of the unstable laminar flame front in the regime of interest would seem to question the validity of applying traditional models developed for hydrocarbon turbulent combustion to hydrogen.

Standard KIVA Turbulent Combustion Model

In rest of the paper the simulations using a turbulent combustion model use the standard model available in KIVA-3V [5]. The model is a generalization of the eddy-turnover model proposed by Magnussen [22] and is applicable to both premixed and heterogeneous

combustion. The model contains one free parameter, A, that must be adjusted for the engine operating conditions.

1-D Combustion study

To better understand and verify the standard turbulence combustion model on initial turbulence intensity, pressure, temperature, and fuel equivalence ratio, a series of one-dimensional KIVA-3 runs were made at parametric values of pressures ($1–5x10^7$ dynes/cm^2), turbulence intensity ($10^2–10^6$ cm^2/s^2), and fuel equivalence ratios (0.4–0.8) and the following were examined: the flame speed, time to steady ignition, final combustion temperature, peak temperature, temperature at ignition and NO_x production. The initial gas temperature was taken to be 900K, the typical gas temperature at the time of ignition in the Onan engine.

The one-dimensional configuration was chosen to have approximately constant pressure combustion conditions (unlike an actual engine that has a significant increase in pressure), and the simulation was forced to have a constant turbulence intensity (k) and dissipation rate (ε). The enforcement of constant turbulence levels prohibits the occurrence of flame generated turbulence, which can increase the flame speed [9]. This is expected to be small for lean fuel mixtures of current interest due to the smaller expansion of the flame front. The parameter A is taken to be 18, typical of diesel fuels.

A least-squares fit to the steady-state turbulent flame speed, S_t, gave a good fit and provides a compact summary of the simulations results:

$$s_t = 1.70\ k^{0.487}\ \phi^{0.366}\ p^{-0.027}$$

with S_t in cm/s, k is the turbulent kinetic energy (cm^2/s^2), ϕ is the fuel equivalence ratio, and p is the pressure (dynes/cm^2). The adjusted correlation coefficient, r^2, for the multiple regression is 0.9997, indicating an excellent fit of the data.

The expected exponent of k is 0.5, based on an analysis of the model, is recovered in the implementation and, more importantly, approximately duplicates the observed coefficient for hydrogen combustion for $\phi = 0.4$, as seen in Fig. 1 (note that u' is proportional to the square root of k). The pressure dependence is observed to be almost zero ($p^{-0.027}$), as expected from an analysis of the model. No experimental information on the pressure dependence of the turbulent flame speed could be found, but one might expect that the dominant effect of pressure is on the laminar flame speed in the turbulent eddies, and, consequently, the pressure dependence would be the same as the laminar flame speed, or approximately proportional to $p^{0.2}$ [14]. The steady-state temperature was observed to depend only on the fuel equivalence ratio, as expected, since this determines the net heat released. Finally, no dependency was observed on the eddy dissipation rate, ε, as expected from the formulation of the model.

The above correlation gives a flame speed of 160.0 cm/s for (k,ϕ,p) = ($5.0x10^4$ cm^2/s^2,0.4, $1.0x10^6$ dyne/cm^2), in comparison to the experimentally observed value for hydrogen in air of 230 cm/s [9] (the experimental laminar flame speed is 60 cm/s). This difference is expected, because the flame speeds for hydrogen are larger than for diesel fuels. This suggests that the parameter A in the eddy-turnover model should be increased to 25 from 18 for constant pressure ignition at 900K. In an actual engine simulation where temperatures continue to increase during combustion, the flame speed would increase, and A would be correspondingly larger. This was observed in the full engine KIVA simulations, as noted below.

The dependence of the NO_x formation in the parametric study was examined using the standard Zeldovich model. NO_x was produced in the flame front. Behind the flame front, the NO_x production was constant with time under these constant pressure and temperature conditions. Because of the time for significant NOx to be produced was much longer than

the simulation time in these 1-D problems, no useful conclusions could be made about the NO_x formation of in the presence of turbulence.

An Approach to Turbulence Combustion Modeling

We have argued that more sophisticated turbulent combustion models that assume a thin flame front are not applicable to hydrogen combustion in the operating conditions of interest (ϕ around 0.4). The above review of the literature and of the one-dimensional KIVA simulations suggest that eddy-turnover model used for hydrocarbon-based fuels may be appropriate for turbulent combustion in the regime of operation of the Onan engine where the turbulent flame speed is proportional to k. The use of such a model will capture the primary effect of the proper heat release as the turbulence intensity changes during combustion.

In the following section with three-dimensional engine simulations, the eddy-turnover model is applied to the hydrogen turbulent combustion in KIVA-3V, with understanding that the parameter A must be adjusted to account for the increased flame speed. Because A is taken to be a constant and is not dependent on the changing conditions during ignition, we expect there to be some deficiencies in the details of the model. Comparable difficulties arise in the application of the same model for hydrocarbon fuels.

Description of the Onan Engine and Mesh

Details of the modified Onan engine can be found in Table 1 and in references [6,23,24]. The intake ports and head of the original Onan engine were replaced with a design that was intended to produce a quiescent combustion to minimize heat exchange and maximize efficiency. To compensate for the longer burn time, two spark plugs are used.
The mesh, shown in Fig. 2, was generated with 41 pseudo-blocks, resulting in 5 logically hexahedral blocks of mesh with about 75,000 cells in the full 360° mesh. The full mesh includes a slight azimuthal twist of 27° in the intake port as occurs in the Onan engine. Without this twist in the intake port, the flow and combustion are symmetric through a plane passing through the two valves. Run times were about two hours on a Cray YMP from intake

Table 1. Onan engine specifications and simulation parameters

Bore	82.55 mm
Stroke	92.08 mm
Displacement	0.4928 L
Geometric compression ratio	14.04:1
Combustion chamber geometry	pancake
Premixed combustion ignited with two spark plugs	
Ignition timing (BTDC)	5-40°
Ignition duration	10°
Engine speed (RPM)	1800
Time-dependent intake manifold pressure from experiment	
Time-dependent exhaust manifold pressure from experiment	
Piston temperature	430 K
Exhaust valve temperature	585 K
Wall, intake valve, head temperature	373 K
Fuel equivalence ratio	0.41

. valve opening to exhaust valve opening.

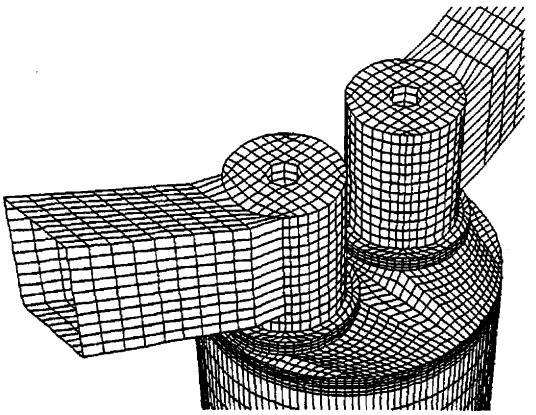

Figure 2a. A detail of the exterior of the mesh for the Onan engine.

The only major simplification made in the computational mesh was the square cross-section of the intake and exhaust ports — a limitation of the KIVA-3V mesh generator at the time. To reduce the effect of the simplification, the flow area of the simulated and actual manifolds are identical. The valve shapes and seating were modeled accurately to within the resolution of the mesh (Fig. 2b). Two types of boundary conditions were used to model the intake flow of the Onan engine: a constant pressure boundary condition and a time-varying boundary condition as taken from the experimental pressure measurements in the intake port. For studies of the comparison between different simulation runs, the former was used. The latter boundary condition was used for comparison to the Onan experiments. Other boundary conditions for the engine simulation are given in Table 1.

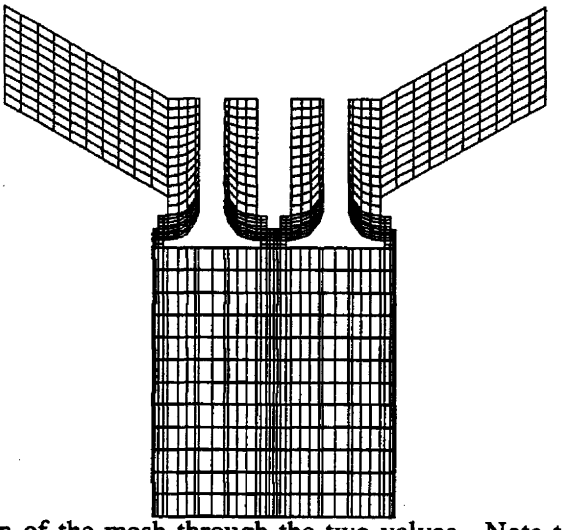

Figure 2b. Cross-section of the mesh through the two valves. Note the detailed rendering of the valves.

Modeling of the Intake Ports and Valve shrouds

Intake Port Modifications

One of the challenges of any engine simulation is the approach used to duplicate the experimental conditions for the air delivery. The complication is that the computational mesh for the simulation must be terminated at some point and an appropriate boundary condition applied. Many simulations were done in an attempt to duplicate the complex

pressure behavior during the intake process: the cylinder pressure during the early intake flow (0–100 CA) typically oscillates with a frequency of 180–260 Hz and a large amplitude of 1–3 psi. Both longer intake ports and different experimental pressure histories in the highly diagnosed intake port were examined. Because either the amplitude or the frequency of the pressure oscillations in the cylinder could be matched, a compromise was to use a short intake port as shown in Fig. 1 with an experimental intake port pressure history that reproduced the observed volumetric efficiency.

Shrouded-Valve Model

Based on KIVA simulations of the engine, the dominant flow in the cylinder was observed to be a tumble flow, not the quiescent flow that was the intent in the design. Because tumble generates more turbulence at TDC than a swirl-dominated flow [25], it was thought that converting the tumble to swirl during intake might improve the efficiency. The experimental technique of inducing the swirl was the addition of a shroud on the intake valve. Various shroud heights and extents on the edge of the valve were tried experimentally, and it was found that the apparent introduction of a moderate amount of swirl increased the efficiency of the engine [24]. It was observed that the engine had its peak efficiency with the 1.5 mm shroud and had lower efficiency for either higher shroud heights or no shroud. Because excessive turbulence can increase heat transfer to the wall, it was thought that the efficiency increased with the shroud because of the more favorable turbulence intensity history.

In KIVA-3V the shroud was modeled by adding a zero-thickness wall at an element boundary at the perimeter of the valve to duplicate the blocking of the flow by the shroud. For a full-height shroud, this wall extended up into the valve pocket, thereby preventing all flow through the valve gap at that azimuthal angle. For a lower-height shroud that allows flow past the shroud at large valve openings, a constant number of element sides above the edge of the valve where similarly blocked. The number of element sides that were blocked where chosen such that the average height of the numerical shroud was similar to the experimental height of the shroud. This approach allowed for full blockage of the flow for small valve openings and allowed the flow over the shroud at large valve openings.

To resolve the question as to the cause of the increased efficiency, four simulations were compared: with and without the 1.5 mm shroud and for two ignition timings of 20° and 12.5° BTDC, using the standard turbulent combustion model in KIVA-3V with A equal to 50. Fig. 3 illustrates that the addition of the shroud does indeed increase the swirl, although these values are low for engines designed to have swirl [6,26]. The indicated thermal efficiencies were calculated for the simulations by integrating over the compression, combustion and expansion cycle the work done by the cylinder pressure due to the change of cylinder volume and then dividing by the total energy produced by the hydrogen fuel. The resulting efficiencies are plotted in Fig. 4. Although experimental data does not exist for the same operating conditions, preliminary Onan data with and without the 1.5 mm shroud tended to exhibit a 3% increase in the thermal efficiency, when it was observed to have an effect.

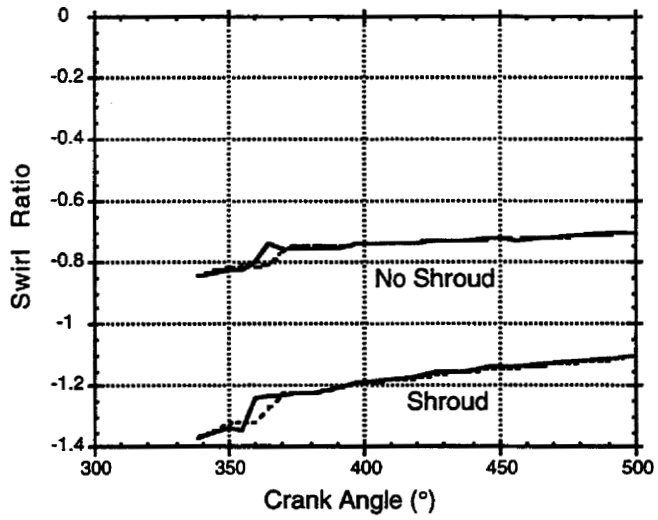

Figure 3. The swirl ratio for KIVA-3 simulations with and without a 1.5 mm shroud and for two ignitions timings (20° and 12.5° BTDC). The swirl ratio is the angular momentum in the cylinder divided by the product of the total mass in the cylinder and the angular velocity of the piston.

In Fig. 5 the turbulence intensity is plotted for all of the simulations during the time of combustion and expansion. It is immediately apparent that the turbulence intensity, and hence the turbulent flame speed, would be similar for these four simulations. In fact, a more careful examination of the turbulence intensity shows that the different timing of ignition has a larger effect on the turbulence intensity than the presence or absence of the shroud. An examination of the heat transfer to the wall in Fig. 6 yields a similar conclusion that the dominant effect is the ignition timing. Note that even though the simulations with the shroud have a higher heat loss to the wall, the more optimal pressure histories of the runs with the shroud compensate of the additional heat losses, thereby either improving the efficiency at 12.5° case or keeping the efficiency constant in 20° case.

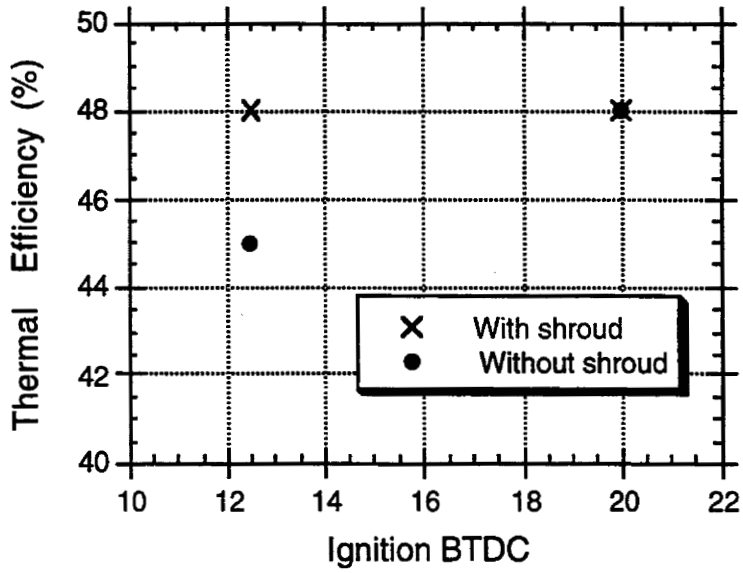

Figure 4. The indicated efficiencies for the KIVA simulations.

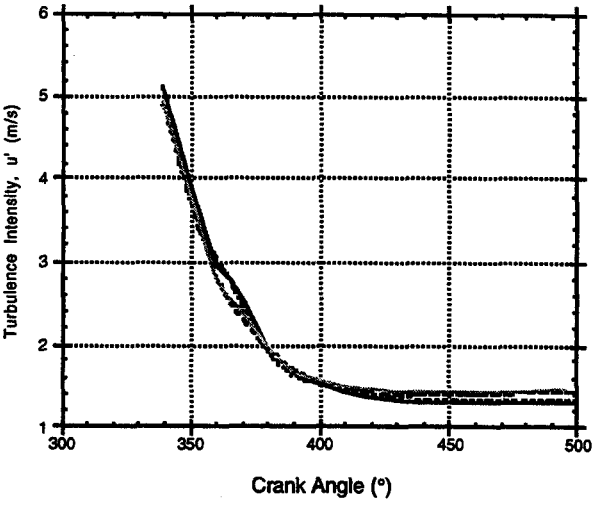

Figure 5. The turbulence intensity for four simulations are shown, illustrating that the turbulent intensities are almost the same for all the simulations.

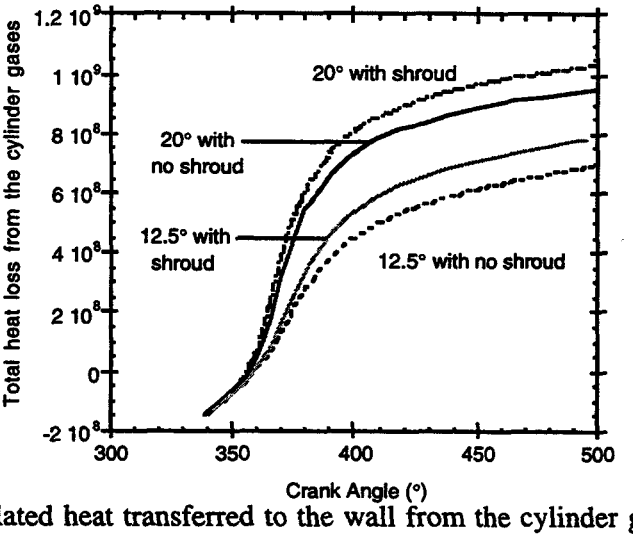

Figure 6. The accumulated heat transferred to the wall from the cylinder gases.

The plot of the hydrogen mass in Fig. 7 as a function of crank angle illustrates that even though all the simulations have similar turbulence intensity histories, the consumption of hydrogen is faster for the simulations with the shroud than without, even though the turbulence levels and hence the local combustion rates are comparable. By examining the shapes of the combustion fronts, the source of the different combustion rates was found to be different stretching of the flame front by the slow swirling flow. The increased efficiency with the shrouded valve is due to the faster combustion rate from the bulk flow from the gentle swirl, thereby producing more work near TDC, but no so much swirl that would cause a loss of efficiency due to increased heat loss.

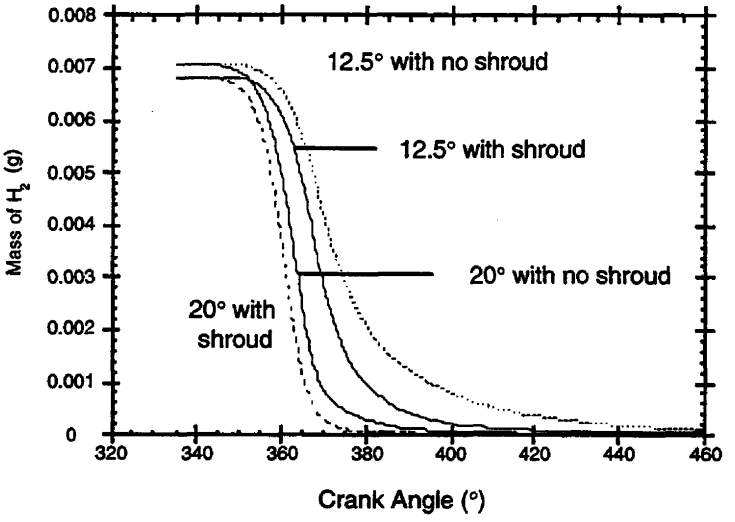

Figure 7. The mass of hydrogen in the cylinder for the four KIVA simulations.

Comparison to the NO_x and Efficiency

The ability to compare the KIVA simulations with the Onan engine data is the fundamental test of the turbulent combustion model and the intake and turbulent modeling. The KIVA simulations were done at both 1200 and 1800 RPM and at a variety of ignition timings (from 20° to 7.5° BTDC) at an equivalence ratio of 0.4. The results presented here are for the 1800 RPM simulations.

As discussed in the section on modeling turbulence combustion, the eddy-turnover model has one free parameter that must be determined from a comparison to the experiments and is comparable to determining the laminar flame speed for a specific hydrogen-air mixture at a certain temperature and pressure. This was accomplished by picking a value for A (50) that best matched the pressure history of one Onan simulation. The parameter A was then held constant for all other simulations with different ignition times and engine speed, but with the same equivalence ratio and volumetric efficiency. By then applying the model to a variety of ignition times, a fairly severe test of the model is achieved because by changing the ignition times, the conditions during combustion — the turbulence, pressure and temperature history — also change significantly.

The resulting NO_X values from the simulations compare excellently with the experimental values, without any adjustment of the NO_X model for hydrogen (Fig. 8). Because NO_X is very sensitive to the burn rate and flame temperature, this is a sensitive test for the accuracy of the turbulent combustion model. This comparison is better than is generally found for hydrocarbon simulations and supports the conclusion in the literature [14] that the slow NO_X kinetics are more accurate for hydrogen combustion. The difference in the slope of between the simulations and experiments is likely due to keeping A constant when it should be varying with the changing conditions at ignition and during combustion. Inclusion of these effects would increase the flame speed and the combustion temperature at later spark timing, and hence the NO_X levels, resulting in even better agreement at other spark timings.

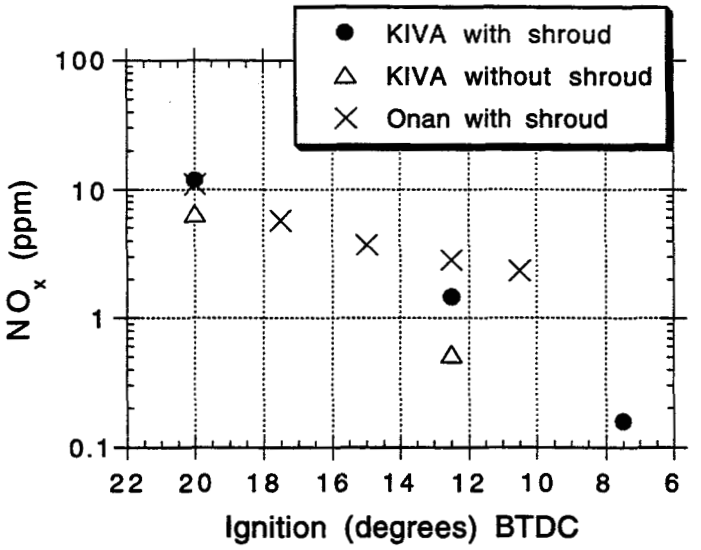

Figure 8. Comparison of the NO_x for the KIVA simulations and Onan experiments.

Comparisons of the efficiencies and pressure histories between experiments were also made (Fig. 9). The trend in the indicated thermal efficiencies duplicates the Onan data, but the values in the KIVA simulations are about 4% higher than in the experimental data. Because of the uncertainty in the wall temperatures in the engine and the difficulty in experimental determination of efficiencies, the offset is not unexpected. The duplication of the trend is an important validation of the turbulence and combustion model in KIVA. The rapid drop in the efficiency of the data at small ignition advance is generally seen to occur in other experimental data and is an expected trend in the simulation results.

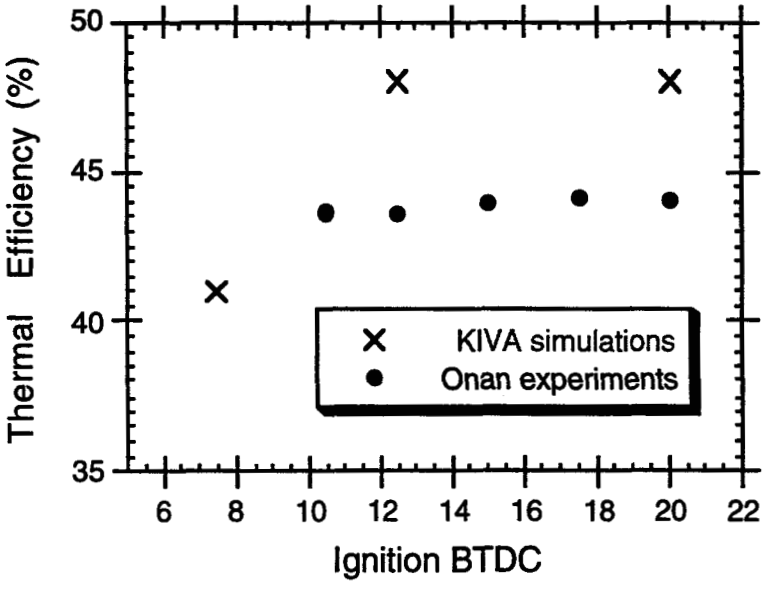

Figure 10. Comparison of the indicated thermal efficiency for the KIVA simulations and Onan experiments.

Conclusion

In summary, KIVA-3V simulations of the Onan engine agreed well with the experimental results and largely validates the chosen approach for the intake flow modeling and the turbulence combustion modeling. Indeed, fewer "adjustments" of the models in KIVA were required than is typically necessary for modeling hydrocarbon-fuel engines. The simulations also clarified the source of the improved efficiency with the slight shroud on the intake valve: the increased combustion rate due to the stretching of the flame front from the increased swirl. A current limitation of the turbulent combustion model is the applicability of the combustion rate being proportional turbulent intensity, u' or to fuel equivalent ratios below one. This is not a significant shortcoming because most engine designs using hydrogen fuel will operate in this regime in order to take advantage of the reduced NO_x production.

Future work will include the addition of the dependence on the fuel equivalence ratio, pressure and temperature on the parameter A, through the known dependence of the laminar flame speed on these variables. This should significantly improve the predictability of the model. Because hydrogen-hydrocarbon mixtures are expected to be the transition fuel to an all-hydrogen-based usage, a similar development of a turbulent combustion model for these mixtures is also planned. These developments are significantly complicated by the potential for a double flame front in hydrogen-hydrocarbon mixers [18].

Because of the high efficiency possible at almost zero emissions in hydrogen-fueled ICE, an exciting opportunity arises for engine designers to provide the ideal powerplants of the future. The current work is the beginning of providing the computational tools for these future designs.

Acknowledgments

This work was funded by the U. S. Department of Energy, Office of Solar Thermal, Biomass Power and Hydrogen Technologies, with special thanks to Program Manager Neil P. Rossmeissl for his continued support. The authors wish to acknowledge the invaluable assistance of many colleagues at Los Alamos, Sandia and Livermore National Laboratories.

References

[1] M.R. Cuddy and K.B. Wipke, "Analysis of the Fuel Economy Benefit of Drivetrain Hybridization," SAE Technical Paper Series, 970289, 1997.

[2] M. Hayashida, K. Narusawa, M. Odaka, and A. Noda, "Study on Series Hybrid Electric Commuter-Car Concept," SAE Technical Paper Series, 970197, 1997.

[3] A. Nikopoulos, H. Hong, and T. Krepec, "Energy Consumption Study for a Hybrid Electric Vehicle," SAE Technical Paper Series, 970198, 1997.

[4] S.M. Aceves and J.R. Smith, "Hybrid and Conventional Hydrogen Engine Vehicles that Meet EZEV Emissions," SAE Technical Paper Series, 970290, 1997.

[5] A.A. Amsden, "KIVA-3V: A Block-Structured KIVA Program for Engines with Vertical or Canted Valves," Los Alamos National Laboratory Report LA-133313-MS, 1997.

[6] P. Van Blarigan, "Development of a hydrogen fueled internal combustion engine designed for single speed/power operation," SAE Technical Paper Series, 961690, 1996.

[7] C.A.R.B. (CARB), "Proposed equivalent zero emission vehicle standards," IEEE Spectrum p. 72,1995,.

[8] K.J. Al-Khishali and D. Bradley, "Turbulent Combustion of Near-Limit Hydrogen-Air Mixtures," Comb. and Flame, **54**, 61-70, 1983.

[9] G.W. Koroll, R.K. Kumar, and E.M. Bowles, "Burning Velocities of Hydrogen-Air Mixtures," Comb. and Flames, **94**, 330-340, 1993.

[10] D.D.S. Liu and R. MacFarlane, "Laminar Burning Velocities of Hydrogen-Air and Hydrogen-Air-Steam Flames," Comb. and Flame, **49**, 59-71, 1983.

[11] L.K. Tseng, M.A. Ismail, and G.M. Faeth, "Laminar Burning Velocities and Markstein Numbers of Hydrocarbon/Air Flames," Comb. and Flame, **95**, 410-426, 1993.

[12] M.S. Wu, S. Kwon, J.F. Driscoll, and G.M. Faeth, "Preferential Diffusion Effects on the Surface Structure of Turbulent Premixed Hydrogen/Air Flames," Comb. Sci. Tech., **78**, 69-96, 1991.

[13] S. Kwon, L.K. Tseng, and G.M. Faeth, "Laminar Burning Velocities and Transition to Unstable Flames in H2/O2/N2 and C3H8/O2/N2 Mixtures," Comb. and Flame, **90**, 230-246, 1992.

[14] J. Warnatz, "Concentration-, Pressure-, and Temperature-Dependence of the Flame Velocity in Hydrogen-Oxygen-Nitrogen Mixtures," Comb. Sci. Tech., **26**, 203-213, 1981.

[15] M.S. Kwon, J.F. Driscoll, and G.M. Faeth, "Turbulent Premixed Hydrogen/Air Flames at High Reynolds Numbers," Comb. Sci. and Tech., **73**, 327-350, 1990.

[16] S. Kwon, M.S. Wu, J.F. Driscoll, and G.M. Faeth, "Flame Surface Properties of Premixed Flames in Isotropic Turbulence: Measurements and Numerical Simulations," Comb. and Flame, **88**, 221-238, 1992.

[17] F. Meier, J. Köhler, W. Stolz, W.H. Bloss, and M. Al-Garni, "Cycle-Resolved Hydrogen Flame Speed Measurements with High Speed Schlieren Technique in a Hydrogen Direct Injection SI Engine," SAE Technical Paper Series, 942036, 1994.

[18] N. Apostolescu and R. Chiriac, "A Study of Combustion of Hydrogen-Enriched Gasoline in a Spark Ignition Engine," SAE Technical Paper Series, 960603, 1996.

[19] K. Collier, R.L. Hoekstra, N. Mulligan, C. Jones, and D. Hahn, "Untreated Exhaust Emissions of a Hydrogen-Enriched CNG Production Engine Conversion," SAE Technical Paper Series, 960858, 1996.

[20] D.S.-K. Ting, M.D. Checkel, and B. Johansson, "The Importance of High-Frequency, Small-Eddy Turbulence in Spark Ignited, Premixed Engine Combustion," SAE Technical Paper Series, 952409, 1995.

[21] B. Dillies, K. Marx, J. Dec, and C. Espey, "Diesel Engine Combustion Modeling Using the Coherent Flame Model in Kiva-II," SAE Technical Paper Series, 930074, 1993.

[22] B.F. Magnussen and B.H. Hjertager, "On Mathematical Modeling of Turbulent Combustion with Special Emphasis on Soot Formation and Combustion," in 16th Symposium on Combustion (The Combustion Institute, 1978.

[23] P. Van Blarigan, "Experimental Program for the Development of the Hybrid Engine," in The 1995 DOE/NREL Hydrogen Program Review, Vol. II (Coral Gables, Florida: National Renewable Energy Laboratory, 1995.

[24] R.L. Hoekstra, P.V. Blarigan, and N. Mulligan, "NO_X Emissions and Efficiency of Hydrogen, Natural Gas and Hydrogen/Natural Gas Blended Fuels," SAE Technical Paper Series, 961103, 1996.

[25] B. Khalighi, S.H.E. Tahry, D.C. Haworth, and M.S. Huebler, "Computation and Measurement of Flow and Combustion in a Four-Valve Engine with Intake Variations," SAE Technical Paper Series, 950287, 1995.

[26] A. Floch, J.V. Frank, and A. Ahmed, "Comparison of the Effects of Intake-Generated Swirl and Tumble on Turbulence Characteristics in a 4-Valve Engine," SAE Technical Paper Series, 952457, 1995.

Appendix

The main body of this report will be published as an invited paper in the *Proceedings of the 3rd International Conference ICE97, Internal Combustion Engines: Experiments and Modeling*, with the title "Hydrogen as a Zero-Emission, High-Efficiency Fuel: Uniqueness, Experiments and Simulations." The following supplements the main text, in order to include material of interest to the Hydrogen Program.

Appendix A: Status on Perkins Engine Simulations

Preliminary simulations of the Perkins engine were performed using a mesh based on a cast of the Perkins intake port supplied to LANL by SNL. Because of the advances in the mesh generation of ports and valves, the resulting mesh is significantly more realistic than the mesh used for the Onan engine (compare figures below).

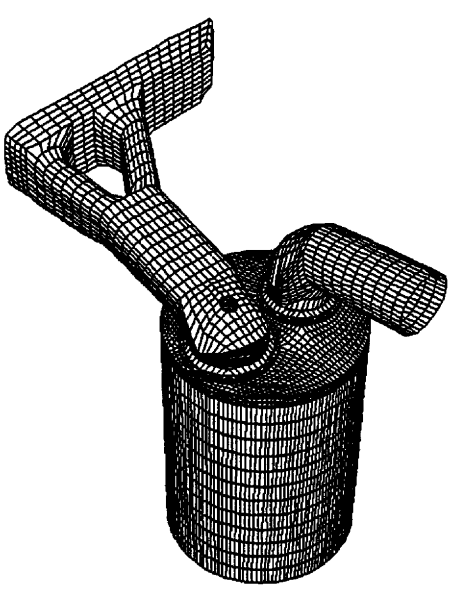

Perkins Engine

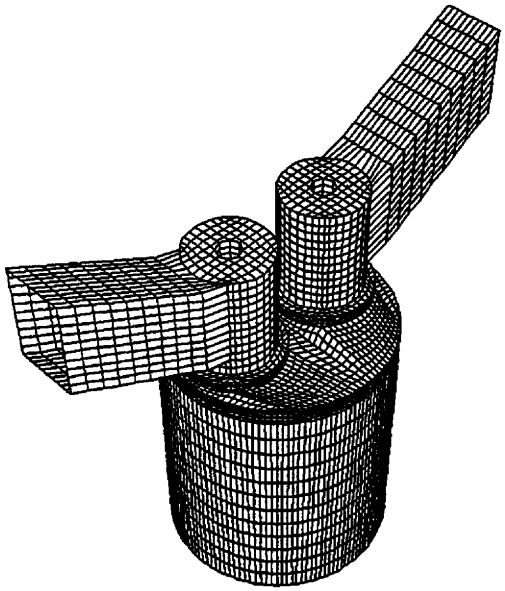

Onan Engine

The Perkins engine has an almost identical compression ratio and combustion chamber geometry ("pancake") as the Onan engine, but about double the volume, as illustrated in the figure below.

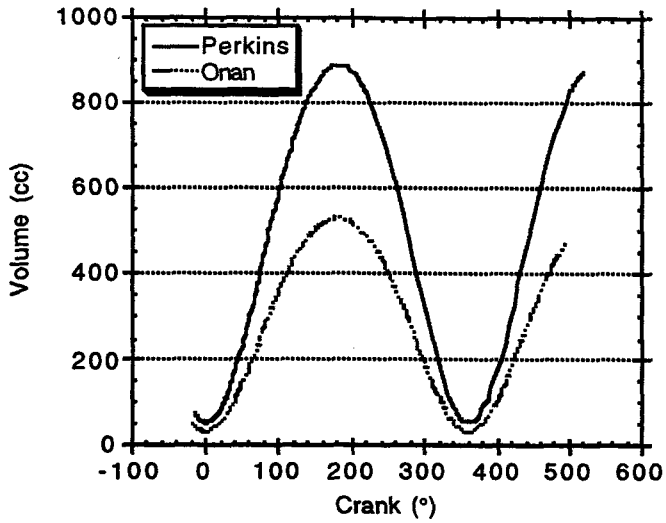

The Perkins engine simulations show a swirl ratio double that of the Onan engine with the optimal height of the valve shroud and identical driving pressures (figure at left below). The significantly different bulk flow behavior is due primarily to the orientation of the intake ports (Compare the meshes in the figures above). The preliminary simulations also indicated a higher efficiency is observed, as also observed in the SNL experiments, validating the expected observation that efficiency increases with engine size. These simulations indicate that even a higher efficiency could be obtained in the larger Perkins by reducing the swirl - as has been done computationally by rotating the intake port by 90 degrees (compare the mesh below with the mesh for the unrotated engine above). The ease by which alternative engine geometries can be examined illustrates the utility of simulations.

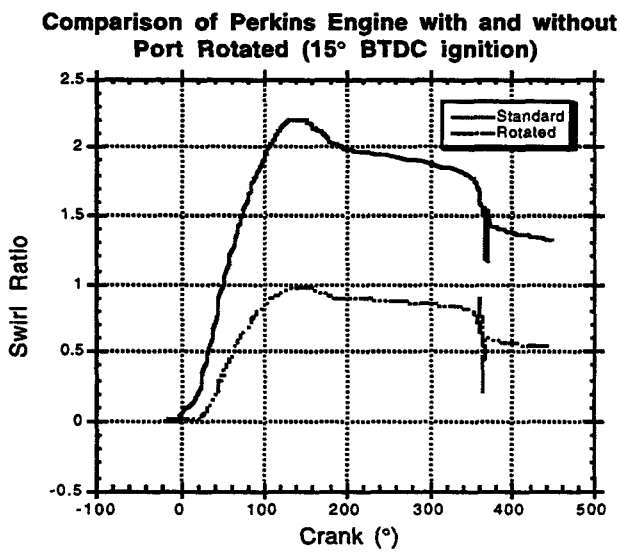

Swirl ratio comparisons

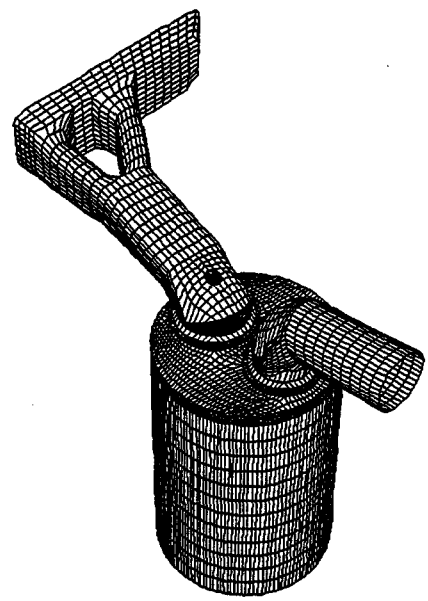

Rotated Perkins Geometry

The figure below comparing the mass of hydrogen and NOx production illustrates how the Perkins engine exhibits more swirl than is optimal. By reducing the swirl, the combustion rate actually *increases,* indicating that the stretching of the flame front by the swirl is reducing the reaction rate. Note that this is just the opposite conclusion as in the Onan

engine, where increasing the swirl improved the efficiency. The explanation is that two little or too much swirl can limit efficiency. The simulation of the Perkins engine is a major milestone in our progress this year. Detailed comparisons with experimental data will be done as the Perkins data comes available.

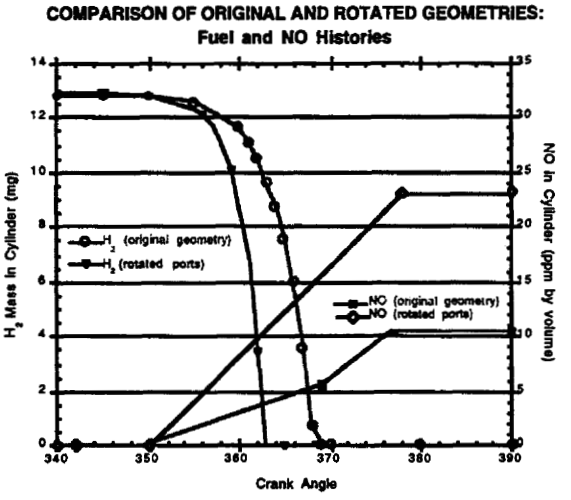

Hydrogen fuel and NO_x history comparison

Appendix B: Technology Transfer and Outreach

In preparation for the *Annual Hydrogen Peer Review* in May, we surveyed the use of KIVA within the combustion modeling community using publications by SAE as a measure. We found forty-five papers were published in calendar 1996 by SAE, and forty papers in 1997 to date, a significant increase. Fifteen papers have or will be published using the new version of KIVA-3V, illustrating the rapid acceptance of the new version. These numbers, limited to just one publisher, strongly indicate the successful outreach, and more importantly, illustrates the significant seeding of the hydrogen modeling capability into industry and academia. This capability will be in place when interest in hydrogen combustion matures. No other mechanism for distribution of the modeling technology would be as effective.

The *7th International KIVA Users Meeting* and the *2nd KIVA Workshop* were held prior to the *1997 SAE International Congress and Exposition* in Detroit, hosted by Cray Research and organized by LANL and University of Wisconsin-Madison. Presentations on the new version of the KIVA-3 (see next appendix) covered the developments supported under the Hydrogen Program and were well received. Just prior to the SAE meeting, Professor Rutland from the Engine Research Center (ERC) at UW-Madison visited LANL to discuss turbulence modeling, future versions of KIVA and hydrogen turbulent combustion. This was the first extended visit from a UW professor from the ERC and laid the basis for a mutually beneficial collaboration in the future.

Salvador Aceves (LLNL) and Norman Johnson presented a paper at the *11th Annual National Educators' Workshop* at Los Alamos on the use of simulation codes in hybrid vehicle design. The talk was attended by about 80 educators from colleges and high schools. The Hybrid Vehicle Evaluation Code (HVEC) was distributed to about 40 interested attendees, to be used in classrooms and research programs around the country.

A summary of the DOE Hydrogen Program and the development of tools for the design of hydrogen-fueled engines was presented during an invited lecture by Norman Johnson at the 1996 Canadian CFD Conference in Ottawa and at a seminar at the Chalk River Laboratory. About 280 attendees were present at the talks.

Appendix C: Release of New Version of KIVA-3

The spring release of the updated version of KIVA-3, called KIVA-3V (V for valves), satisfies a major milestone; the version has been distributed to about 100 researchers or laboratories. The non-commercial nature of KIVA-3 and its wide use in universities and industry makes it possible to disseminate the new capability quickly throughout the CFD community, as illustrated by large number of publications that used KIVA-3, described in the last appendix.

A significant capability in KIVA-3V is the option to model intake ports with moving valves, as needed to accurately model the bulk flow and turbulence levels at the time of combustion. The release includes all capabilities described in last year's annual report, plus two new capabilities: the ability to model non-vertical valves and to model overlapping valves, as shown in the figure below. During the operation of the engine, the intake and exhaust valves occupy the same location in the cylinder at different times. This capability was thought to be an essential, but difficult, feature, but by careful use of the remapping option in KIVA-3, the capability was implemented without significant development. Future hydrogen engines will likely use this design because of the better control of the gas flow at the time of combustion and its ability to use larger valves.

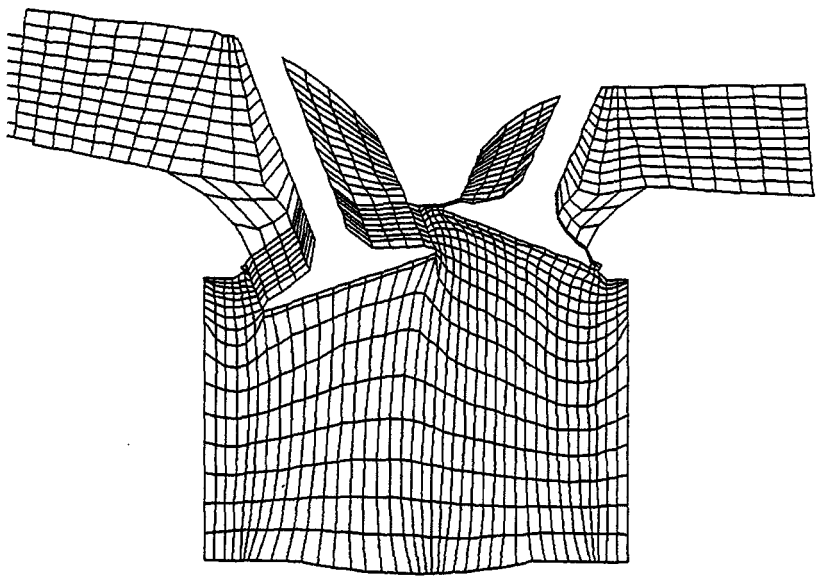

A cross-section of the mesh in a 4-valve engine, showing an intake valve fully open and an exhaust valve fully closed.

In summary, all the predominant valve/combustion geometries can now be modeled: the vertical valve design typical of diesel engines, the 2-valve wedge design typical of older automotive engines and the 4-valve pentroof engine typical of modern auto engines.

Appendix D: Enhancement of Turbulence Modeling in KIVA-3V

We used the opportunity of Dr. Zhiyu Han's visit from UW Madison to address the suggestion of the review panel to assess and improve the turbulence models in KIVA. During his stay at LANL, the RNG turbulence model (a compressible variation of the k-epsilon model) was implemented into the standard version of KIVA-3V. This implementation of the RNG model has been tested extensively at the UW Engine Research Center and either performs as well or better than the standard k-epsilon model in KIVA-3. It is now the basis of all simulations using KIVA at UW Madison. This model was also the most requested new feature for KIVA-3 at the 1996 KIVA User Meeting. Research at UW and during the past month at LANL indicates that the improved accuracy of the RNG model is due to the tendency of the model to have a lower turbulence viscosity, thereby enabling larger eddies in a simulation to be

treated more accurately by the resolved flow equations, rather than the less accurate, time-average turbulence equations. A standard engine simulation was used to validate that the RNG model in the LANL version reproduced the RNG model in the UW version.

To further test the RNG model beyond the idealized flow and the full engine simulations done at UW, we examined the Dyer experiments performed at Purdue (Wahiduzzaman thesis, 1985). These experiments are of a hot gas injection into a fixed volume which creates a strong swirling flow and simulates a possible swirling engine flow. Turbulence intensity, velocities, and temperatures were measured in the experiment. Numerical simulations of this flow have had limited success in duplicating the temperature and velocity measurements. The best agreement between the simulations and experiments has been obtained with a large eddy simulation that restricts the turbulence model to small length scales. Simulations using the RNG model were found to do no better than the moderate agreement found with the standard k-epsilon model in a two-dimensional simulation; this supported similar conclusions by other researchers. We believe that better performance would have been obtained if a three-dimensional simulation had been used. Also, in discussion with spectral turbulence modelers in our group, they have identified the missing terms in the turbulence model for flows with large density variations that explain the limited agreement. As time permits, these additional terms will be included in the RNG model, but because the Dyer experiments have much greater density gradients than in a typical 4-stroke engine, the need for these terms for the current hydrogen applications is minimal.

The validated RNG model was applied to the KIVA-3 simulations of the Onan engine. The intake flow, which determines the turbulence levels at time of ignition, was in most aspects similar to the comparable simulation using the k-epsilon model. The mass charge and the average dissipation rate in the cylinder were almost identical in the two simulations. Other quantities differed moderately: the swirl ratio and turbulence intensity were about 10% higher for the RNG model. In conclusion, we feel the addition of the RNG extension of the k-epsilon model is a significant improvement to KIVA based on the experience of other researchers. For the current hydrogen simulations, the effect of the model is minimal and indicates that the current good agreement with experiments need not be questioned in this regard.

DEVELOPMENT OF COMBUSTION TECHNOLOGIES FOR HYDROGEN UTILIZATION

J. O. Keller
Sandia National Laboratories
Livermore, CA 94551-0969

The long-term mandate of the hydrogen program is to develop the technologies needed to establish a hydrogen economy. This project addresses at least four end use sectors that are recognized by the H_2 program and addressed by this project. These end uses are: 1) power generation from stationary turbines, 2) generation heat or steam for use in industrial processes or for power production, 3) commercial and residential direct use applications and 4) combustion support in fuel pre-processors for fuel cells (steam reforming and partial oxidation).

Robert Williams makes a very compelling argument for CO_2 sequestration, if one reforms a hydrocarbon or carbon fuel into CO_2 and H_2 at the well head (see "Fuel Decarbonization for Fuel Cell Applications and Sequestration of the Separated CO_2", Robert Williams, PU/CEES Report No. 295, January 1996). The by-product of the hydrocarbon reformation process is CO_2, and thus, the additional cost for sequestration can be an insignificant increase in the overall cost of producing the fuel. This is even true for coal, using the water gas shift reaction the energy stored as carbon (coal) is moved to hydrogen with CO_2 as the by-product. In both of these examples the CO_2 by-product exists in an easily sequestered form , leaving hydrogen as a non-polluting energy carrier. This provides us with the ability to make use of our vast coal and natural gas reserves as a transition strategy without emitting all of the hazardous compounds associated with hydrocarbon and/or coal combustion, including CO_2. With modest modifications coal or natural gas fired power plants they can be made to operate on hydrogen, making use of our existing coal or natural gas (now hydrogen) equipment (and capital) and easing the transition to renewable sources without harm to the environment.

The principal emission from hydrogen combustion is NO_x, which results from thermal NO production. Thermal NO is minimized by reducing the peak combustion temperature and the residence time at the peak temperature. NO can be reduced to extremely low levels (a few ppm) by operating under sufficiently lean conditions and reducing the peak combustion temperatures to below 1700 to 1800 K. The objectives for this project to:

- develop environmentally benign and safe hydrogen combustion technologies;
- provide a facility in which fundamental investigations can be performed in support of other hydrogen programs.

The fundamental driving principle is to understand and develop hydrogen combustion technologies that control the combustion fluid dynamics in such a way to force the reaction to occur in a safe premixed manner. This will allow combustion fluid dynamic strategies to be developed through a careful first principles approach both in the laboratory and in the accompanying modeling effort. Combustion control strategies will be developed in parallel with the development of the combustion fluid dynamics. The specific project elements Sandia will pursue in this program are the construction of a basic burner configuration. The best burner concept that emerges as a result of the experimental, modeling and controls effort will be scaled up and tested either in the existing laboratory or in BERL depending on laboratory availability and burner size. As a result of this activity a unique facility exists that provides a service to the hydrogen community at large. It can readily be called a on to perform reacting flow studies in support of other projects. For example; there is value added to the development of this core capability and to the community at large in providing experimental support to those interested in combustion characteristics of methane hydrogen blends, hydrocarbon reformation process, steam reformation, partial oxidation, or making hydrogen from coal. All such activities add to increasing the fundamental knowledge of hydrogen combustion systems and to our ability to control these combustion processes. In addition, because this facility is in place one can execute these individual investigations for little or no addition cost.

In this work we will capitalize on the fluid dynamic features necessary to: 1) suppress the reaction (through controlling the fluid dynamic strain rates), 2) provide a controlled mixing environment to rapidly mix reactants on a macroscopic scale (through controlling large scale coherent vortical structures), and 3) provide a controlled mixing environment to rapidly and thoroughly mix reactants on a microscopic scale (through controlling the three-dimensional breakdown of the large structures, and enhanced fine scale velocity fluctuations to promote thorough microscopic mixing). Static and periodic methods of controlling vorticity deposition rate and subsequent behavior of the resulting large scale coherent structure will be investigated. Control over the rate and quality of the three-dimensional breakdown of these coherent structures will be achieved through careful deposition of additional components of vorticity and/or by promoting the natural breakdown of these large scale structures by introducing flow features that promote the natural breakdown phenomenon.

This work will be performed by careful systematic investigations into the detailed fluid dynamics, thermodynamics, and the subsequent combustion characteristics of the flow field. The diagnostics that will be used during this investigation include, but are not limited to, two component LDV for velocity, Rayleigh scattering for temperature, laser sheet mie scattering, schlieren phase resolved images and exhaust emission measurements of pollutant species (NO_x). Selective laser sheet mie scattering and planar laser induced fluorescence (PLIF) will be used to measure the degree to which the reactants have mixed.

Detailed analytical programs are designed to be synergistic with the experimental program. This is to include the development of detailed chemical kinetic mechanisms and modeling of hydrogen and hydrogen/methane mixtures combined with detailed combustion fluid dynamic modeling of the

hydrogen hydrogen/methane combustion processes. Detailed combustion fluid dynamic control strategies will also be developed in parallel with the experimental and modeling efforts. Information from the experimental portions of this work will be used to improve the fundamental understanding of the controlling physics necessary to guide the development of this technology, and will provide valuable support to the further development of the models. In return, the models will provide valuable insight into the fundamental fluid dynamic mixing mechanism controlling the combustion process of hydrogen and hydrogen/methane mixtures.

Chemical Kinetic Modeling of Hydrogen under Conditions Found in Internal Combustion Engines

N. M. Marinov, H. J. Curran, W.J. Pitz* and C.K. Westbrook
Lawrence Livermore National Laboratory
P. O. Box 808; L-14
Livermore, CA 94551
email: pitz@llnl.gov
fax: (510) 422-2644

ABSTRACT

A chemical kinetic model is used to study the combustion characteristics of hydrogen under conditions found in internal combustion engines. Laminar flame speeds are predicted under the high pressure and high temperature conditions found in an spark ignition engine. The variation of laminar flame speed with temperature, pressure and equivalence ratio is examined. The autoignition of hydrogen and hydrogen/natural gas mixtures is also studied under conditions found in a free-piston compression-ignition engine. This engine is expected to exhibit high efficiencies operating on hydrogen. The results suggest that adding small amounts of natural gas to hydrogen will reduce NOx emissions from a free-piston compression-ignition engine.

This paper will appear in a special hydrogen edition of Energy & Fuels.

A Comparison of Hydrogen, Natural Gas, LPG, and Gasoline Leakage in A Residential Garage

Dr. Michael R. Swain
Jeremy Shriber
Department of Mechanical Engineering
University of Miami
P.O. box 248294
Coral Gables, FL 33124

Dr. Matthew N. Swain
Analytical Technologies, Inc.
14-57 SW 140th St.
Miami, FL 33186

Abstract

This paper compares the relative safety risks of four types of vehicle fuels. The fuels considered are hydrogen, natural gas, LPG, and gasoline. The accident scenario considered is a vehicle parked in a single car garage for 2 hours with a fuel line leak. The comparison is made on the basis of the volume of combustible gas produced by each fuel. Only LPG and gasoline produced appreciable volumes of combustible gas.

This paper will appear in a special hydrogen edition of Energy & Fuels.

FRICTIONAL ANALYSIS FOR HYDROGEN FUELED ENGINES

Michael R Swain
University of Miami
Coral Gables, FL 33124

Matthew N. Swain
Analytical Technologies, Inc.
Miami, FL 33186

Abstract

The following is the beginning of a study on the effect of friction on brake thermal efficiency in a rapid combustion, lean mixture, hydrogen fueled internal combustion engine. The work was not completed due to reduction in funds. Friction plays a larger role in hydrogen fueled internal combustion engine operation, than in gasoline fueled internal combustion engine operation, for two reasons. First, hydrogen fueled engines operate at lower indicated mean effective pressure than do gasoline fueled engines. Therefore, the same amount of friction causes a larger percentage drop in brake thermal efficiency in hydrogen fueled engines than in gasoline fueled engines. Secondly, oil control is more critical in hydrogen fueled engines and piston designs with increased oil control generally produce more friction. This work effort was the design, construction, and testing of five low friction, rapid combustion, lean mixture, hydrogen fueled engines.

Introduction

Friction work is defined as the work done to the pistons by the gases minus the work at the flywheel. Friction work is lost as heat in various manners, notably when two moving parts come into contact. This survey deals with friction lost in the piston and piston rings. Research on piston assembly friction has been ongoing since the beginning of the century. Work before the mid-century concluded that mixed lubrication of the piston ring and cylinder liner did occur. It had been generally accepted that friction increases linearly with piston velocity. In the 60's and 70's, it was shown that the oil film (the layer which protects the cylinder liner from the piston) generally breaks down at top and bottom dead center.

Engine Internal Friction

The amount of work dissipated in the piston assembly is a substantial amount of the total engine friction. McGeehan (McGeehan, 78) suggests that the piston/ring assembly may be responsible for 60-75% of the mechanical engine friction (McGeehan, 78) and Feng concludes 60% of mechanical engine friction is due to the piston/ring assembly (Feng and Stodolsky, 95). Uras agrees that the piston/ring assembly may be responsible for 60-75% of the mechanical engine friction (Uras and Patterson, 83). Furuhama concludes that 75% of the total piston/ring assembly friction is due to the rings (Furuhama et.al., 81). And more specifically, ring friction attributes approximately 25 to 50 percent of total engine mechanical engine friction (Sui and Ariga, 93). The piston/ring assembly plays a significant role in determining the proportion of indicated work done to the piston that is available as brake work at the flywheel.

In a traditional three-ring package, ring functions are divided as follows (Figure 1):

- Top ring function is gas sealing, but helps in oil control
- 2nd ring function is gas sealing and oil control
- Oil ring function is oil control

The distribution of frictional losses among the rings is generally accepted to be approximately 60% to the oil rings (Sui and Ariga, 93; Kovach et.al., 82). 22% to the second compression ring, and 18% to the top compression ring (Sui and Ariga, 93).

Types of Lubrication

There are three types of lubrication that occur between oiled surfaces (boundary, mixed, and hydrodynamic). Because of the various conditions at which the piston assembly operates, all three types of lubrication may occur. However, the lubrication of the piston assembly is principally mixed or hydrodynamic.

Originally designed for friction in bearings, the Stribeck diagram gives a good description of the behavior of lubrication at different conditions (see figure 2). The Stribeck diagram is applicable to lubrication in the piston and piston rings (Dearlove and Cheng, 95). The Stribeck diagram shows the relationship between the coefficient of friction and a dimensionless parameter dependent on lubricant

dynamic viscosity, relative surface speed, and loading force per unit area. The three regimes where lubrication may exist are boundary, mixed (or partial) or hydrodynamic. For a piston assembly, the coefficient of friction at boundary conditions is around 0.15. This occurs at very low speed or very high unit load. Metal-to-metal contact is almost certain to occur because the viscosity is insufficient to prevent that contact. At mixed lubrication, load is not very high and/or speed is higher than in boundary lubrication. At hydrodynamic lubrication, the speed of moving parts is high enough to allow the oil to form a liquid film between the moving surfaces.

There is generally good agreement in the literature that the piston and piston rings undergo both mixed and hydrodynamic lubrication during normal operation. The following trends are exhibited during operation. Top rings tend toward hydrodynamic lubrication while the second compression rings and oil rings operate under mostly mixed lubrication (Sui and Ariga, 93; Grice and Sherrington, 93). Mixed lubrication is most likely to occur where piston velocity is low near top dead center and bottom dead center (Yun et.al, 95; McGeehan, 78). The work lost to friction is large where the piston velocities are high (midstroke). This is also where the lubrication tends to be hydrodynamic (Yun et.al, 95; Ting, 93; Ting, 93). Though frictional forces are high at top and bottom dead center the work lost to friction is low because piston speed is low. The total piston friction (piston and rings) is greatest during the first half of the expansion stroke due to the thrust force of the piston skirt against the cylinder wall (Furuhama et.al., 81).

The Strieck diagram shows the trends in frictional coefficient. In the hydrodynamic region, Reynolds equation can be used to calculate friction losses. In the mixed region, load is distributed in the oil film and asperity contact. It is necessary to use Reynolds equation and elastic contact equations. In the boundary region, coefficient of friction is constant, so friction can be found by balancing forces occurring in the piston assembly.

Topics for this Research

Forces acting on the piston assembly are: ring drag, gas pressure forces, and inertia forces. The major design factors that affect friction are: ring width, ring face profile, ring tension, ring gap, liner temperature, ring land width and clearances, skirt geometry, and piston to cylinder bore clearance. The variables that were studied in this research were:

1. Ring geometry
2. Piston to cylinder bore clearance.

In addition, special attention was given to minimizing friction in the engine in three areas.

1. Minimizing pumping mean effective pressure (PMEP) by redesign of the intake port/valve geometry.
2. Minimizing piston/connecting rod friction by weight, skirt length and bearing length reduction.
3. Minimizing valve train friction with the use of roller lifter and rockers.

Friction Measurement

Before discussing the results found in the literature, it is important to compare the different types of experiments done by the authors mentioned in this survey. The most realistic way of measuring friction is to perform the experiment on a firing engine. But this is a difficult and expensive way to gather the data. Motoring experiments are the most common method of acquiring information on friction. Experimental setup is relatively easy, and a large amount of information can be acquired in a short period of time.

There are inherent problems in analyzing the data gathered from a motored experiment. For example, oil temperature strongly affects frictional losses. If the oil temperature is lower than what it would be in a running engine, then the viscosity will be higher and friction will be higher in the motored engine. The results from a lower temperature test will be unclear, according to Heywood (Heywood, 88). Since there is no combustion and no combustion pressures in a motored test, less force will be applied to the rings, and this tends to make the friction lower in the motored test than in a running engine. Additionally, at TDC in a firing engine, piston speed is very low (at one point it has to become zero) and the combustion pressures can cause the ring to break through the oil film. In a motoring test, this is thought not to occur, and this tends to make friction lower in the motoring tests.

Models use mathematical equations to describe the behavior of systems. In a piston ring assembly, Reynolds equation is widely used in predicting friction. Reynolds equation estimates the thickness of the lubricant film so friction, and power loss, can be derived from the calculation of viscous drag.

FLARE, a computer model developed by GM Research labs, was used to analyze friction in piston skirt, piston rings, bearings, and valve train (Goenka et.al., 92). Since piston skirt and piston rings function in mixed and hydrodynamic regimes, the authors found it necessary to calculate rigid body contact between skirt and cylinder wall. FLARE combines individual components together with the kinematics and dynamics of the engine in order to give outputs. Three running engines, two V6 and one V8, were used for the experiment. The authors compared the friction parameters for the three engines under different RPM's.

Ricardo Consulting Co. (Ball et.al., 86) conducted an experiment in which frictional mean effective pressure (FMEP) was calculated. Using a piezoelectric cylinder transducer, measurements of indicated mean effective pressure in each cylinder of an engine were made. The average indicated mean effective pressure (IMEP) was compared with the brake mean effective pressure (BMEP) and auxiliary loss data, and a partial friction breakdown of the engine was done. It was found that the piston/crank assembly accounts for majority of losses at all speeds in both gasoline and diesel fueled engines. Ricardo reports that results obtained could have been greatly influenced by how accurately crank angle position was known. They state that a 0.1° change in angle can cause a 4% change in FMEP, so great care should be taken when using this method to find FMEP. This was the method used in this research effort to measure FMEP. Measurement of pumping losses as pumping mean effective pressure (PMEP) was done by analysis of the pressure versus volume diagrams generated with an in-cylinder piezoelectric pressure transducer.

As stated before, one of the advantages of running a motored test rather than a firing one is the relatively ease in setting up the experiment. As shown in a paper by Kovach, the ranking of friction from each part of an engine can be set up for a more detailed analysis using a motored engine (Kovach et.al., 82). The order, given by importance, is: piston/rings, valve train, crankshaft, oil pump. Kovach suggests that the ranking of each component of friction does not change from motored to firing experiment. It is generally agreed that the ranking of friction from each part of an engine does not change from the motored test to a running engine. Since the largest component of mechanical friction was piston/ring assembly friction, the principal subject of this research effort was piston/ring assembly friction.

Component Friction

The reported effects of component design on engine friction are presented below.

Ring Friction

Ring friction is strongly affected by the contact force applied on the cylinder wall by the ring. The contact force must be large enough to maintain sealing. Sealing prevents blow-by (leakage of combustion gases past the piston) and oil consumption (leakage of oil past the piston). For compression rings (particularly the top compression ring), the contact force has two components - ring tension and gas pressure force. Ring tension is created when the ring, which is machined larger than the bore, is compressed to a smaller diameter to fit in the cylinder bore. Gas pressure force is created when positive gas pressure in the combustion chamber acts behind the ring, in the ring groove, and adds to the contact force. As cylinder pressure rises the ring is forced to the bottom of the groove in the piston that supports the ring. The ring seals against the bottom of the ring groove and gas pressure, at the back of the ring groove, forces the ring into the cylinder wall.

The two main components of contact force are affected by ring geometry: free gap, radial width, and ring thickness affect ring tension, and ring thickness affects the gas pressure force.

Goto recorded a reduction in friction at 1600 RPM when the thickness of the top compression ring was reduced from 2.0 mm to 1.2 mm (Goto, et.al., 85). The ring tension was the same for both rings. However, the contact force due to gas pressure was reduced due to the reduced area at back of the ring groove.

Kovach found that by reducing ring thickness (top from 1.6mm to 1.5; 2nd from 2.0mm to 1.5mm; and oil ring segment from 0.6mm to 0.4mm), and tension (top from 24N to 12N; 2nd from 20N to 14; oil from 49N to 33N), a friction reduction of 1 psi (6.9kPa) was possible (Kovach, et.al., 82).

Hill was able to improve FMEP by 5.6 psi by reducing ring tension and expander force (oil ring tension) without increasing oil consumption (Hill and Newman, 84).

Furuhama deduced that, in theory, a reduction in ring thickness will not produce a reduction in friction without a concomitant reduction in ring tension (Furuhama, et.al., 81).

Jeng concluded, with the use of computer modeling, that an increase in ring tension produces a reduction in power output, due to a reduction in friction (Jeng, 92). It was also concluded that an increase in ring thickness caused an increase in power at below 3000 RPM and a decrease in power above 3000 RPM. This indicated that a reduction in thickness may not always cause a reduction in friction.

From the literature survey, changes in friction due to changes in ring thickness are dependent on cylinder pressure history and piston speed. The effects in hydrogen fueled engines were to be measured in this work effort.

Piston Friction

Piston design affects mechanical friction in several ways. Piston weight influences the inertial forces that the piston exerts on the cylinder walls and connecting rod bearings. It has been generally accepted that FMEP due to the piston skirt is linearly proportional to piston skirt length (Bishop, 64; Rosenberg, 82). There is no general agreement in the literature as to the effect of piston to cylinder wall clearance on friction. Piston weight reduction is generally accepted as a means to reduce mechanical friction. (Feng and Stodolsky, 95) calculated the effect of weight reduction on mechanical friction. The values at 2000 RPM and 3000 RPM are given in Table 1.

Table 1

	Friction reduction	
Reduction in mass	2000 RPM	3000 RPM
20%	2.7%	4.8%
30%	4.1%	7.2%
40%	5.4%	9.6%

Kovach measured a 0.1 psi drop in FMEP at 1500 RPM due to a 25% reduction in piston weight (Kovach, et.al., 82). This would indicate a negligible effect.

Fujii concluded that the effect of piston weight was too large to be neglected in their empirically derived equation of engine friction (Fujii, et.al., 88).

Changes in piston to cylinder wall clearance and piston surface finish have produced a variety of effects on friction.

Kovach found a 50% reduction in skirt area and an increase in piston to cylinder wall clearance from 0.4 mm to 0.6 mm produced no change in friction at 1500 RPM (Kovach, et.al., 82). It was conjectured that the reduction in skirt area made the oil film thinner which offset any advantage that may have occurred.

Takigochi varied piston to cylinder wall clearance from 60 μm to 0 μm (Takigochi, et.al., 88). Little difference in friction was noted until the clearance was reduced below 10 μm where friction increased

dramatically. It was postulated that the friction increase was due to a transition from hydrodynamic to mixed lubrication. It should be noted that these clearances are all less than the standard clearances for the test engine used and no data was taken at larger clearances.

Furuhama found that variations in piston clearance, in the range from 0.013 inches (0.33 mm) to 0.007 inches (0.17 mm), and skirt finish had a negligible affect on engine friction (Furuhama, et.al., 81).

Sui concluded that the top compression ring is dominated by hydrodynamic lubrication and therefore not strongly affected by surface finish. However, cylinder wall surface finish can affect ring friction by ±5% (Sui and Ariga, 93).

Wakuri recorded a 7.25 psi reduction in FMEP with a worn piston/cylinder wall combination. This indicates the potential for significant changes in friction with changes in surface finish (Wakuri, et.al., 95).

Goenka and Paranjpe concluded that piston to cylinder wall clearance affects friction (Goenka et.al., 92; Paranjpe and Gusenza, 92; Goenka and Meernik, 92).

From the literature survey it was concluded that the piston weight should be reduced if possible. The literature survey indicated that the effect of piston to cylinder wall clearance was not predictable so the effect of piston to cylinder wall clearance was to be measured in this work effort.

Connecting Rod Friction

Connecting rod design affects friction in two ways. The weight of the connecting rod affects the magnitude of inertial forces applied to the connecting rod bearings. The size of the connecting rod bearings affects the bearing friction.

Martin concluded, through the use of computer modeling, that increasing connecting rod mass increases engine friction (Martin and Xu, 93).

It is generally accepted that connecting rod bearing friction increases linearly with bearing width (Conway-Jones and Tarver, 93; Bishop, 64; Thring, 92; Fujii, 88).

The literature survey showed good agreement that connecting rod weight and connecting rod bearing size should be reduced if possible.

Pumping Losses

Pumping losses are not a part of mechanical engine friction. Pumping losses are a measure of the work done to pump burned exhaust gases out of the engine and fresh unburned mixture into the engine. The amount of work necessary to accomplish this can be appreciable. Patton estimates pumping work to be 16.5% of the total frictional losses (mechanical and pumping losses) at 2000 RPM and wide open throttle (WOT) and 25.3% of the total frictional losses at 3000 RPM WOT (Patton; 89). Gomi calculated pumping losses to be 34.2% of the total frictional losses at 3000 RPM WOT (Gomi, et.al.

96). The magnitude of the pumping losses is a function of valve sizes, port flow coefficients and valve timing parameters.

From the literature survey it was concluded that increasing intake port flow coefficients, particularly at low valve lifts, was important in preventing pumping loses and reducing PMEP.

Oil Control

Oil control in a hydrogen fueled engine is more critical than in a gasoline fueled engine. Fortunately, it is inherently easier to accomplish good oil control in a hydrogen fueled engine because a hydrogen fueled engine can operate over a wide range of power outputs in an unthrottled mode. A hydrogen fueled engine does operate more efficiently, and with lower emissions, with some throttling at light loads. However, efficient hydrogen fueled operation does not require the high intake manifold vacuums that gasoline fueled operation requires. The lack of high intake manifold vacuum eases the oil control problem.

As with gasoline fueled engines, oil control becomes more difficult as RPM increases (Furuhama et.al., 79). A larger ring contact force reduces the oil control problem. As ring contact force increases the oil film thickness, between the ring and the cylinder wall, decreases reducing the flow of oil past the ring. Unfortunately, a higher ring contact force also causes higher engine friction.

Improved oil control is accomplished in two ways at a given ring tension (McGeehan, 79; Mattsson, 95).

1. Minimize axial and lateral oil pumping action in the ring grooves.
2. Maintain cylinder roundness during engine operation.

Minimizing the axial and lateral motion of the ring in the ring groove improves oil control because motion tends to pump oil past the ring/piston interface.

The ring is initially circular and the more cylindrical the bore is the more likely the ring will remain in contact with the cylinder bore. After boring and honing the cylinder bore is generally cylindrical to within ±0.00005 inches, on the diameter. Cylinder head bolt clamping force, uneven thermal expansion during operation, and piston thrust loading can distort the cylinder from its original cylindrical condition.

Reductions in FMEP of up to 39 KPa can be affected with concomitant improvements in oil control at part load (Hill and Newman, 84; Ting, 85).

A low radial width oil ring and/or high ring tension produces good oil control due to good flexibility (ability to conform to non-circular cylinder bore) and improvements in axial movement. Oil rings move from the bottom of the ring groove on the upstroke to the top of the ring groove on the downstroke. If ring mass is high, inertial moves the ring from the bottom to the top of the ring groove before reaching top dead center (TDC). If ring mass is low the ring does not move from the bottom to the top of the

ring groove until the piston starts downward after TDC. The latter is the preferred case. The same can be said at bottom dead center (BDC) though the directions are reversed (McGeehan, 79).

Oil that passes the rings, toward the combustion chamber, is primarily thrown off the piston at TDC during the exhaust stroke (McGeehan, 79). If oil enters the combustion chamber, in this manner, in sufficient quantities at light loads (piston temperature below 350 °F) it will accumulate. As the transition is made to high load the oil will flash off in the combustion chamber and cause flash back in a hydrogen fueled engine.

A measure of the comparative importance of oil control in hydrogen fueled engines over that in gasoline fueled engines can be found in the difference in allowable bore distortion for the two fuels. Normal bore distortions for gasoline fueled engines is typically 0.0002 to 0.0004 inches (Hill and Newman, 84). Experience dictates that bore distortions of less than or equal to 0.0002 inches are necessary for hydrogen fueled operation. These measurements were for conventional rings and are a function of radial width. Bore distortion is a measure of out-of-roundness in the cylinder bore. An initially round ring must conform to the out-of-round cylinder bore in order to maintain good oil control. McGeehan determined that a 0.0004 inch bore distortion increases oil consumption by a factor of 10 over that of a 0.00008 inch bore distortion. Bore distortions of less than 0.00008 produced negligible oil consumption (McGeehan, 79).

Jeng concluded, through his modeling, that there is a trade-off between friction and oil consumption. Lower ring tension decreases friction, but it increases oil consumption. Larger oil ring width tends to lead to larger oil consumption (Jeng, 92).

The literature survey agreed with previous findings. The cylinder bores must be a round as possible and ring tension must be adequate to prevent oil leakage into the combustion chamber but reduced as much as possible to reduce friction.

Component Design

The design of the engine components for this research effort is described below.

Cylinder Block Selection

The original design of the engine was done using dimensions and specifications from the Pontiac 10093306 cylinder block (Table 2). It was discovered early in the project that this cylinder block was no longer available and a survey of available cylinder blocks was conducted. The Pontiac 1984 R type block, which utilized a standard hydraulic cam, was selected for the initial testing because the original project plan included running baseline tests with a standard hydraulic cam. Testing versions of the engine constructed in subsequent years, that utilized a roller cam, would have allowed the difference in friction between the standard cam and roller cam to be determined.

Table 2 - Engine specs for the original design:

Displacement	184 cubic inch displacement (CID) (3.0 liter)
Bore	4.02 inches (10.2 cm)
Stroke	3.625 inches (9.208 cm)
Con Rod	5.875 inches (14.92 cm)
Intake valve dia.	2.055 inches (5.220 cm)
Exhaust valve dia.	1.562 inches (3.967 cm)
Intake valve lift	0.452 inches (1.15 cm)
Exhaust valve lift	0.478 inches (1.21 cm)
Intake valve duration	190° @ 0.050 inch lift
Exhaust valve duration	202° @ 0.050 inch lift
Intake valve duration	261° @ 0.006 inch lift
Exhaust valve duration	273° @ 0.006 inch lift
Lobe centerline	111°
Valve overlap	46°

The first 1984 R type block had a loose number 3 main cap. Since it was necessary to acquire a second cylinder block, further investigation into interior block dimensions was conducted. It was noted that the lifter bores in the 1985, 1986 and 1987 (S-10 only) blocks were extended 0.20 inches such that either a standard or roller camshaft could be utilized in the same block. It was decided, at that point, to use those blocks for the remainder of the program.

Subsequent discussions with Sandia National Labs led to the conclusion that all testing should be conducted with roller camshafts. During the course of the project it was noted that the 1985 through 1987 S-10 blocks had thinner cylinder walls than the 1985 through 1986 front wheel drive vehicle blocks. Therefore the 1985 and 1986 cylinder blocks from front wheel drive vehicles were chosen as the preferred cylinder block.

It should also be noted that one aluminum and one magnesium cylinder block were acquired during the project. Though additional difficulties would surround the use of these cylinder blocks it would appear an engine of approximately 200 pounds and 100 horsepower could be constructed.

Cylinder Block Preparation

Cylinder block preparation is more critical for a hydrogen fueled engine than for a gasoline fueled engine. This is due to the more critical oil control needed in a hydrogen fueled engine. Adequate oil control requires the cylinder bores to be circular to within 0.0002 inches on the diameter. A cylinder bored and honed to within this tolerance changes shape due to the applied clamping force when the cylinder head bolts are installed. The cylinder head bolts must maintain adequate clamping force to seal the head gasket but not enough force to distort the cylinder bore substantially.

A review of the approaches used, by Pontiac, to tighten cylinder head bolts reveals the difficulty in reaching a compromise between sealing the head gasket and distorting the cylinder bore. The

following techniques have been used by Pontiac to tighten the cylinder head bolts on the 2.5 liter Pontiac engine.

1. Tighten all the cylinder head bolts to 95 ftlb in at least three steps.
2. Tighten all the cylinder head bolts to 85 ftlb in at least three steps.
3. Tighten all the cylinder head bolts to 92 ftlb in at least three steps.
4. Tighten all the cylinder head bolts to 18 ftlb. Tighten all the head bolts, except number 9, to 22 ftlb. Tighten number 9 to 29 ftlb. Tighten all the head bolts, except number 9, an additional 120°. Tighten number 9 an additional 90°.
5. Tighten all the cylinder head bolts to 18 ftlb. Tighten all the head bolts, except number 9, to 22 ftlb. Tighten number 9 to 30 ftlb. Tighten all the cylinder head bolts, except number 9, an additional 120°. Tighten number 9 an additional 90°.
6. Tighten all the cylinder head bolts to 40 ftlb. Tighten all the cylinder head bolts to 70 ftlb. Tighten all the cylinder head bolts to 90 ftlb
7. Tighten all the cylinder head bolts to 40 ftlb. Tighten all the cylinder head bolts to 70 ftlb. Tighten all the cylinder head bolts to 92 ftlb

Cylinder bore measurements made at the top of the cylinder bore showed that the Pontiac cylinder bore could change by as much as 0.0007 inches on the diameter due to cylinder head bolt clamping force. To assess the repeatability of the bore distortion, when using the standard head bolts, tests were conducted with four types of cylinder head gaskets. The gaskets used were: McCord 7084, Felpro 1015, Victor 5701, and Pro-Torque HG32770. The Felpro 1015 was chosen as the preferred gasket but the standard head bolts would not produce adequately repeatable bore distortion with any of the gaskets. Previous work has shown that changes of more than 0.0002 inches in bore diameter are unacceptable for hydrogen fueled operation (Swain et.al, 96). Two changes were made to the cylinder head bolts, and two modifications were made to the cylinder bore machining process, to control cylinder bore out-of-roundness.

In the standard Pontiac configuration cylinder head bolt number 9 was 2.9 inches long while the remaining bolts were 3.9 inches long. Equal length studs, with spacers, were substituted for the cylinder head bolts. Studs prevent torque from being placed on the threads in the block. They also allowed a constant thread depth, in the block, to be maintained. The threads on the top of the studs (for the nuts) were of a finer pitch than those on the head bolts and increased the clamping force at a given torque by 14%.

The cylinder bore machining process was modified by using an aluminum plate bolted in place of the cylinder head during the boring and honing process. The final selected plate thickness was 1.75 inches. A 1.00 inch thick plate was found to be insufficiently rigid. The plate allowed the cylinder head studs to distort the cylinder block in the same manner as when the cylinder head was installed. The cylinder block was then out-of round when the plate was removed but returned to the proper tolerance when the cylinder head was installed. Dimensions of the cylinder block are given in Table 3. These are the final dimensions after the block had been prepared for hydrogen use. The studs were torqued to 80 ftlb for cylinder head installation.

TABLE 3	Location	After machining before torque plate was removed	Without torque plate installed	With cylinder head installed
Bore diameter error measurements in inches difference from standard				
Cylinder 1	A	+0.00050	+0.00055	+0.00060
	B	+0.00055	+0.00090	+0.00050
	C	+0.00050	+0.00110	+0.00055
	D	+0.00055	+0.00110	+0.00070
Cylinder 2	A	+0.00025	+0.00070	+0.00020
	B	+0.00030	+0.00080	+0.00020
	C	+0.00030	+0.00040	+0.00015
	D	+0.00020	+0.00065	+0.00030
Cylinder 3	A	+0.00020	+0.00055	+0.00020
	B	+0.00025	+0.00065	+0.00025
	C	+0.00030	+0.00045	+0.00010
	D	+0.00030	+0.00080	+0.00035
Cylinder 4	A	+0.00030	+0.00050	+0.00025
	B	+0.00040	+0.00055	+0.00030
	C	+0.00030	+0.00060	+0.00025
	D	+0.00035	+0.00090	+0.00020

The cylinder bore machining process was also modified by installing the main caps in place and torquing them to 70 ftlb during the machining process. The final installed torque was also 70 ftlb.

The prototype pistons provided by Federal Mogul were provided with a compression height that is too high to clear the cylinder head. This was done to allow the squish distance to be specified in the final machining process, prior to final assembly. This also produces a high top compression ring location. A high top compression ring location reduces the quantity of unburned gases trapped between the piston and cylinder wall. However, a high top compression ring location also allows the top compression ring to reach further into the region of the cylinder bore most likely to be distorted by cylinder head bolt clamping force. This increases the importance of maintaining the 0.0002 inch cylinder bore out-of-round tolerance.

The cylinder block machining was accomplished with the main caps installed and torqued to 70 ftlb and the cylinder head studs installed, with the 1.75 inch aluminum plate, and torqued to 80 ftlb. The cylinders were rough cut to 0.003 inches undersize with 70 grit stones. They were then honed to 0.0005 inches undersize with 220 grit stones and finished to size with 400 grit stones.

Cylinder head studs were all installed to the same depth in the cylinder block. A cylinder head gasket of the same type and size used for testing was installed between the plate and the cylinder block during the machining operations. 10W30 motor oil was used on the cylinder head studs whenever they were torqued.

Piston Design

There are principally three types of pistons available for automotive type internal combustion engines. They are cast eutectic, forged, and cast hypereutectic. The aluminum alloys used to manufacture the pistons vary in silicon content. Typical cast eutectic and forged pistons have a silicon content in the

11% to 13% range. Hypereutectic pistons have silicon content typically in the 16% to 18% range. Hypereutectic pistons with as much as 24% silicon content do exist (Mahle 244 alloy). The advantage that high silicon content pistons provide is their low coefficient of thermal expansion and favorable wear resistance. The disadvantage to high silicon content pistons is their lower strength and greater difficulty in manufacturing. Silicon content in excess of 12.5% typically causes cracking during the forging process. Though forged prototype pistons with as high as 14% silicon content have been made in Japan they are not in production at this time.

A low coefficient of thermal expansion is very desirable for hydrogen fueled internal combustion engines. A low coefficient of thermal expansion produces less piston growth during engine warm up. This means the original piston to cylinder bore clearance can be made smaller for hypereutectic pistons than for cast eutectic or forged eutectic pistons (Forged pistons generally require the largest initial piston to cylinder bore clearance). The smaller piston to cylinder bore clearance reduces oil control problems. The reduction in strength with hypereutectic pistons does not produce a problem in lean burn hydrogen fueled engines.

The low coefficient of thermal expansion of the hypereutectic pistons make them an ideal choice for a hydrogen fueled engine. In previous work a hypereutectic piston was manufactured from a production piston. Starting with a dished Nissan piston a low compression height, flat top piston was manufactured for the Toyota engine that was used in that research. A thorough search of existing production pistons was conducted for this research effort. No available production pistons could be obtained with a variety of ring package configurations, a 4.02 inch bore, and with a flat top (no valve reliefs). Nor was it possible to machine a production piston into a useable configuration.

Without the availability of modifiable production pistons, custom piston manufacturers were contacted to manufacture pistons for the project. The following custom piston manufacturers were contacted: JE Pistons, Huntington Beach CA, Arias, Gardenia CA, Bill Miller Engineering, Carson City NV, Manley, Lakewood NJ, Ross Racing Pistons, Hawthorne CA, Venolia, Long Beach CA, and Wiseco Pistons, Mentor OH. However, none of the custom piston manufacturers make hypereutectic pistons. They make cast eutectic or forged pistons. Unfortunately; the manufacturers of custom cast pistons, which require less piston to cylinder bore clearance than forged pistons, tend to produce pistons with lower production tolerances. One of the highest precision custom piston manufacturers is Wiseco Pistons in Mentor, Ohio. At the beginning of the project it was planned to have Wiseco make the pistons for the project even though this would have mandated the use of Alcoa 4032 aluminum alloy with a 21.4×10-6 1/°K coefficient of thermal expansion. This was the alloy (11.3% to 12.5% Silicon) used by Weisco to forge custom pistons.

It is possible to modify a forged piston to reduce the necessary piston to cylinder bore clearance. Forged pistons typically require 0.0025 inches more piston to cylinder bore clearance than comparable cast eutectic pistons. This is necessary even though the forged pistons have a similar coefficient of thermal expansion. The main reason for the difference is that forged pistons generally have a higher piston skirt temperature than cast eutectic pistons. The reason the forged piston skirt runs at a higher temperature is that the forged piston skirt is generally in better thermal communication with the head of the piston than the skirt of the cast piston. The oil return passages in cast pistons are typically slots that thermally insulate the skirt from the head of the piston. The oil return passages in forged pistons are

typically drilled through holes which leave more metal between the skirt and head than does the slot. To reduce the skirt temperature of a forged piston the oil return holes are machined into slots. This would have had to be done if it had been necessary to use the Weisco forged pistons. This modification would have allowed 0.0025 inch piston to cylinder bore clearances for the forged piston. If oil control problems had occurred they would have been solved by lowering the pressure in the crankcase.

It was learned in September that Federal Mogul would be willing to manufacture prototype hypereutectic pistons for the project. The pistons were FM244 aluminum alloy with 16.5% silicon content. The pistons were a modification of an existing production piston (H113P-20). The pistons were made with four different ring package configurations and by deleting the valve reliefs. The compression height was in excess of what was needed, which allowed squish distance (the distance between the cylinder head and piston at top dead center) to be adjusted during the final machining process in Miami. The piston skirt diameter was to be defined during the final machining process in Miami. The prototype pistons weighed 449 grams as opposed to the standard production pistons for the engine which weighed 621 grams.

Ring Design

Four ring packages were selected for testing. Two top compression ring sizes were utilized; 1.5 mm thickness and 1.0 mm thickness. Both sizes were barrel-faced inlaid molybdenum rectangular rings. All the ring packages utilized the same second compression ring. It was a 1.5 mm thickness cast iron taper faced reverse twist ring. Two sizes of oil scraper rings were utilized; 4.0 mm thickness and 3.0 mm thickness. Both sizes are constructed with two independent chromium-faced steel rails and a ring expander assembly.

The four ring packages were as follows (Table 4):

TABLE 4	Top compression	Second compression	Oil ring
Package 1	1.5 mm	1.5 mm	4.0 mm
Package 2	1.0 mm	1.5 mm	4.0 mm
Package 3	1.5 mm	1.5 mm	3.0 mm
Package 4	1.0 mm	1.5 mm	3.0 mm

Ring package 1 was used on the piston set that was modified to increase piston to cylinder wall clearance by 0.001 inch. The same ring package was used on both the standard, and the increased piston to cylinder wall clearance pistons. This was done so any change in friction due to a change in ring friction could be eliminated from the assessment of change in friction due to piston to cylinder wall clearance.

Final Engine Design

The use of the Federal Mogul pistons and 1985/1986 front wheel drive 2.5L cylinder block required redesign of the crankshaft/connecting rod combination for the engine (Table 5).

Table 5 - Engine specs for the final design:

Displacement	171 CID (3.0 liter)
Bore	4.02 inches (10.2 cm)
Stroke	3.375 inches (9.208 cm)
Con Rod	6.25 inches (14.92 cm)
Intake valve dia.	2.055 inches (5.220 cm)
Exhaust valve dia.	1.562 inches (3.967 cm)
Intake and Exhaust valve lift	0.398 inches (1.01 cm)
Intake and Exhaust valve duration	192° @ 0.050 inch lift
Intake and Exhaust valve duration	256° @ 0.006 inch lift
Lobe centerline	109°

Cylinder Head Design Goals

In order to determine the effect that a given ring package or cylinder wall clearance will have on engine friction the cylinder pressure versus volume, and therefore the piston loading, in the test engine should duplicate that of the hydrogen fueled engine to be designed. For this research, the hydrogen fueled engine to be designed is a high compression, rapid burn, lean mixture hydrogen fueled engine.

To provide a cylinder head capable of this type operation, two cylinder heads were designed. The first cylinder head was designed with the aid of Pontiac Motor Division of General Motors. Pontiac provided the raw cylinder head casting. They were cast at Brodix Cylinder Heads in Mena, Arkansas. The Brodix foundry is used by Pontiac to cast their high performance cylinder heads, among other related hardware. The second cylinder head was designed in cooperation with Joe Fontana of Fontana Automobile, Inc. He was contacted in December, 1996, in Columbus, Ohio. He was enthusiastic about supporting the project and felt he would be able to supply cylinder heads with in excess of 20% squish area for the project.

Brodix Cylinder Head Design

The aluminum Brodix cylinder head was chosen for modification because it provided a relatively open combustion chamber with a low swirl intake port/valve pocket which could accommodate intake valve from 1.94 to 2.08 inches in diameter. Pontiac was willing to provide cylinder head castings without water jackets (cast solid). This allowed for the installation of two spark plugs (Figure 3) on opposite sides of the combustion chamber without the added complication of avoiding the existing water jackets. The use of two spark plugs, rather than swirl, to promote rapid combustion reduces the heat transfer losses induced by the swirl gas velocities. It should be noted that a cast iron, single plug, high swirl, 14.0:1 compression ratio cylinder head was prepared for comparison.

The Brodix cylinder heads provided by Pontiac are capable of a 14:1 compression ratio with flat top pistons due to the lack of conventional water jackets. The cylinder head water jackets that were designed for this project included an open channel around the outside of the combustion chamber, on the cylinder head surface. That channel gathered heat that transferred out of the combustion chamber in the radial direction. The design of the channel allowed the compression ratio to increased from 10:1 to

14:1 by removing metal from the cylinder head surface and shortening the pushrods, without modifying the water jackets.

The Brodix cylinder head provided an excellent base for development of a low restriction intake port. The 1987 Pontiac engine tested, to date, had an estimated PMEP of 2 psi at 1800 RPM. This was due to operating at a Mach Index Number of 0.21 at 1800 RPM. That produced a PMEP of approximately 1.3 psi with an additional 0.7 psi PMEP due to the 1.4 inches of mercury manifold vacuum needed to match the volumetric efficiency of the 1972 Toyota hydrogen fueled engine. The target PMEP for the finished hydrogen fueled engine is 1 psi at 1800 RPM. This value of PMEP is needed to reach the target of 13 psi total FMEP at 1800 RPM. This would not have been possible with the standard cylinder head. A thorough flow bench test of the Brodix cylinder head with valve sizes ranging from 1.94 inches to 2.06 inches was conducted to determine which port/valve pocket/seat geometry provided the best low lift coefficients. The pumping loop which creates PMEP at low Mach Index Numbers is most affected by low lift valve coefficients. Poor low lift flow coefficients produce the drop in cylinder pressure, when the intake valve is opening, that is characteristic of low Mach Index Number pressure versus volume diagrams.

To assist in the design of the Brodix cylinder head a survey of existing production intake ports was conducted using a flow bench to determine which intake port geometry produced the best low lift flow coefficients. The following cylinder heads were assessed: 305 CID Chevrolet modified and unmodified, 350 CID Chevrolet modified and unmodified, 302 CID Ford modified and unmodified, 460 CID Ford unmodified, and Ford 351 CID Cleveland modified and unmodified. Unexpectedly, the Ford 351 CID Cleveland modified with a 2.06 inch diameter intake valve was superior to any of the other port geometries. The final Pontiac intake port was patterned after the Ford port.

Figure 4 shows the modified Brodix cylinder head including valve seats, head bolts and all spark plugs.

Fontana Cylinder Head Design

The cylinder head serves two main functions: to serve as an inlet and outlet to gases, and to control the combustion process. This analysis deals with improving the combustion process. The goal of this analysis was to find a suitable location for a second spark plug to be installed in a cylinder head, and analyze the effect on thermal efficiency. The cylinder head chosen for redesign was a racing head provided by Fontana Automobile, Inc. The head had a single spark plug. A computer aided design (CAD) drawing was created in order to view, and chose from, all possible sites available around the combustion chamber. Only one cylinder was drawn due to the symmetry of all four cylinders. After deciding on a position; calculations were performed, with a computer model that incorporated piston motion and combustion chamber geometry, to estimate squish velocity versus crank angle.

The standard Fontana cylinder head and engine used as a basis for the redesigned cylinder head had the specifications given in Table 6. In order to make a valid comparison between the existing design and the redesigned cylinder head, the compression ratio was kept the same, which in this case was 11.4:1.

TABLE 6

BORE	4.02	in
STROKE	3.375	in
CONNECTING ROD	6.25	in
PIN OFFSET	0.06	in
EFFECTIVE HEIGHT OF COMBUSTION CHAMBER	0.325	in
HEAD GASKET CLEARANCE	0.038	in
PERIMETER COMBUSTION CHAMBER	11.42	in
AREA OF COMBUSTION CHAMBER	9.61	in^2
DISPLACEMENT	42.84	in^3
COMPRESSION SPACE/CLEARANCE VOLUME	4.12	in^3
COMPRESSION RATIO	11.4:1	

The first step in creating the CAD drawing was to find the angles of the valves in relation to the cylinder head surface. This was done using a digital level. The next step was to find the locations of the holes for the head bolts and pushrods. Knowing these locations, it was possible to find the location for the exhaust and intake valve. Then the location of the guides, valve seats and the openings of the ports were measured from the actual head and inserted in the drawing.

The next step was to find the shape of the intake and exhaust ports, and of the combustion chamber. Based on previous work, it was decided to make a mold of each port or chamber. The material used to make the mold is BLAK-STRETCHY® CMC, a plasticized polysulfide base synthetic rubber with reinforcing pigments and curing time controls. The compound is produced by Perma-Flex Mold Co., Inc. The rubber was poured (right after mixing with a curative) into the cylinder head and allowed to set up for over 24 hours. The rubber hardened in the shape of the port or chamber. In order to quantify the three dimensional shape of the rubber it was necessary to cut the molds into multiple slices and obtain the outline of each slice. By entering the outline and thickness of each slice a close copy of the cylinder ports and combustion chamber were produced in the CAD drawing.

The region where the second spark plug should be inserted was determined from inspection of the cylinder head and CAD drawing. Figure 5 shows the location chosen for the second spark plug (original spark plug not shown). Space constraints determined the actual angles and position of the second plug. The intake port was at an angle of 45° from the vertical and the spark plug was placed parallel to it. This angle allowed the plug to enter the combustion chamber at the same height as the original spark plug, while clearing both ports.

With the addition of the second spark plug, metal had to be taken out of the combustion chamber. In Figure 6, the outline of the new combustion chamber can be seen (Configuration 2). The new shape was found by using a mold of the actual combustion chamber and using clay to form the new region. The shape was designed to give good propagation of the flame as it moves away from the second spark plug. The volume of the clay used to form the new combustion chamber was used in the 'Calculation of squish velocity' section.

Calculation of squish velocity

As stated before, metal had to be taken out of the cylinder head in order for the second spark plug to enter. The removal of metal from the combustion chamber affects the squish velocities. Squish velocity is the average speed at which gases move from the peripheral volume of the combustion chamber, formed between the cylinder head and piston top around the periphery of the chamber, into the main combustion chamber volume. It was calculated by performing a gas motion analysis.

Squish velocities were estimated by calculating the change in peripheral volume with respect to time at a given crankshaft position and dividing by the area available for the squish gases to escape from the peripheral volume. To estimate the maximum squish velocities, the investigation was performed in the range 12° BTDC to 2° ATDC at an interval of 1°. Maximum squish velocities are usually found at 8° BTDC for this engine.

The three modified combustion chambers, configurations 2 through 4, (Figure 6) were investigated to assess the change in squish velocities with respect to the standard Fontana combustion chamber (configuration 1). The maximum squish velocities for configuration 1 were 18.1 ft/sec.

As stated before, the location of the second spark plug was found utilizing the CAD drawing. Installing the second spark plug required removal of metal, increasing the combustion chamber volume. Removal of metal from the combustion chamber, in general, reduced squish velocities. Table 7 shows the steps taken to achieve the smallest reduction in squish velocities. The compression ratio must stay the same in order for the comparison between designs to be valid. Hence, the configuration 2 would require the cylinder head to be planed 0.036 inches. Maximum squish velocity in configuration 2 was 8.5 ft/sec.

TABLE 7

Cylinder head	Quench area	Squish height	Compression Ratio	Maximum squish velocity
Standard Fontana chamber (configuration 1)	24.3 %	0.038 inches	11.4	18.1 ft/sec
Configuration 2	15.0 %	0.038 inches	11.4	8.5 ft/sec
Configuration 3	15.0 %	0.030 inches	11.4	12.7 ft/sec
Configuration 4	16.0 %	0.030 inches	11.4	13.4 ft/sec

In order to regain some of the lost squish velocity head gasket thickness was reduced in configuration 3. The original head gasket thickness was 0.038 in, while previous work had shown, a thickness of 0.030 inches was feasible. Configuration 3 required planing the cylinder head only 0.026 inches instead of 0.036 inches to achieve a 11.4:1 compression ratio. Maximum squish velocity for configuration 3 was 12.7 ft/s.

An attempt to increase maximum squish velocity, by adding more metal near the location of the second spark plug (Figure 6), was made with configuration 4. Maximum squish velocity increased to

13.4 ft/sec in configuration 4. However, configuration 4 was not chosen for the final design because of shrouding of the number two spark plug.

Configuration 3 was chosen for the final design for the Fontana cylinder head. Fontana Automobile, Inc. has offered to cast the cylinder head in configuration number 3 but has not been requested to do so.

Connecting Rod Design

The final design required a 6.25 inch long connecting rod rather than the 6.05 inch connecting rod that was used in the gasoline fueled factory production version of the engine. Reductions in connecting rod weight translate into friction reduction in the engine. The inertial forces on the connecting rod are substantial and increase the bearing loads during operation. The factory production version of the connecting rod weighed 607 grams. A 6.25 inch long connecting rod with a 2.1 inch journal diameter that weighed 588 grams was available from Manley Lakewood in New Jersey. The connecting rod was narrowed during the final machining so it could be used in the Pontiac based hydrogen fueled engine for this project. The Manley connecting rod was designed for a 0.842 inch wide bearing which is the standard width for a 400 CID Chevrolet V-8. The connecting rod was narrowed to allow the use of a 0.713 inch wide bearing for the hydrogen fueled engine. We have used these bearings under much more severe operating conditions without failure.

Crankshaft Design

Seven rebuildable crankshafts were acquired for this project. Four were of the standard stroke length (3.00 inches). One was a marine crankshaft with a stroke length of 3.25 inches. The completed crankshaft had a 3.375 inch stroke and was finished with offset journals for the Manley connecting rods. The remaining crankshaft was of 3.625 inch stroke length and together with the 5.875 inch 1972 360 CID American Motors connecting rods could be used, with either the aluminum or magnesium cylinder block, to produce an engine of up to 188 CID.

Data and Analysis

The only data recorded during this research was with a slightly modified 1987 2.5L Pontiac engine. This was an example of the engine that was to be further modified and used to construct the final hydrogen fueled engine for this project. The engine was installed on a new dynamometer stand and operated to facilitate testing of instrumentation during the delay in delivery of the prototype Federal-Mogul pistons. The engine was stock with the exception of high mileage oil ring expanders and a water pump installation that ran at a 10% lower RPM than the standard application.

The 1987 Pontiac engine was run on hydrogen duplicating the equivalence ratio (Φ) = 0.50, volumetric efficiency (VE) = 80%, and 1800 RPM, of data taken previously with a 1972 Toyota 2TC 1600 cc hydrogen fueled engine (Table 8). Both engines operated with a 9.0:1 compression ratio. The 1987 Pontiac produced a measured 9.4% increase in brake thermal efficiency (BTE), over that of the Toyota engine data. This was produced in spite of the 1.4 inches of mercury manifold vacuum required by the

Pontiac engine to duplicate the 80% volumetric efficiency produced at wide open throttle by the 1972 Toyota engine. No pressure versus volume data was gathered with the Pontiac 2.5L engine.

A crude analysis of the gain in brake thermal efficiency is presented below. The 1972 Toyota data shown in Table 8 is from previous research, and was gathered with an engine that had inherently high internal friction. The data shown for the 1987 Pontiac was gathered at the same equivalence ratio, volumetric efficiency, and RPM. Comparison of the required spark advance (24° BTDC for the 1987 Pontiac versus 26 ° BTDC for the 1972 Toyota) gives an indication that the required best efficiency spark advances (BESA) were similar so combustion duration could be assumed to be similar. Since the combustion durations were similar, and the equivalence ratio and volumetric efficiency were equal, the indicated thermal efficiencies could be assumed equal. Since the two engines were run at the same volumetric efficiency and equivalence ratio, and the indicated thermal efficiencies could be assumed equal, it followed that the IMEP was the same for the two motors (79.0 psi). The Total Frictional Mean Effective Pressure (TFMEP) for the 1987 Pontiac engine was then calculated as 17.4 psi (TFMEP = IMEP-BMEP). Since the 1972 Toyota engine had a TFMEP of 22.8 psi the 9.4% increase in brake thermal efficiency measured for the 1987 Pontiac engine was probably due to the 4.4 psi change in TFMEP between the two engines.

Performance predictions for a hydrogen fueled engine, as yet untested, are presented n Table 8. Sandia National Labs recorded an ITE of 45% and an IMEP of 92.8 psi for a 14:1 compression ratio, rapid combustion, 100% volumetric efficiency hydrogen fueled engine, operated at an equivalence ratio of 0.39. Using the IMEP of 92.8 psi and assuming a TFMEP of 13.0 psi yielded a 79.8 psi BMEP. The brake thermal efficiency was then:

$$45\% \times \frac{79.8\,psi}{92.8\,psi} = 38.7\%\,BTE$$

Some discussion of the assumed TFMEP (TFMEP=FMEP+PMEP) is in order. 13 psi TFMEP at 1800 RPM and 79.8 psi BMEP should be attainable. Existing low friction engines have attained values of 12.6 psi mechanical FMEP (Ball et.al., 86). Ball achieved that with a 1.6L engine operating at 1800 RPM and 88.2 psi BMEP. A PMEP of 0.4 psi would then yield a TFMEP of 13.0 psi. A PMEP of 0.4 psi is extremely low but additional improvements in mechanical FMEP over those observed by Ball should be possible, increasing the required PMEP to 1.0 psi.

TABLE 8

	1972 Toyota	1987 Pontiac	Predicted
RPM	1800	1800	–
Compression Ratio CR	9.0:1	9.0:1	14.0:1
Volumetric Efficiency VE	80%	80% (required 1.4 inHg manifold vacuum)	100%
Equivalence Ratio ϕ	0.5	0.5	0.39
Best Efficiency Spark Advance BESA	26° BTDC	24° BTDC	–
Brake Mean Effective Pressure BMEP	56.2 psi	61.2 psi	79.8 psi
Total Frictional Mean Effective Pressure TFMEP	22.8 psi	17.4 psi	13.0 psi
Indicated Mean Effective Pressure IMEP	79.0 psi	79.0 psi	92.8 psi
Brake Thermal Efficiency BTE	28.7%	31.4%	38.7%
Indicated Thermal Efficiency ITE	40.3%	40.3%	45.0%

References

Ball, W.F., N.S. Jackson, A.D. Pilley, and B.C. Porter. 1986. "The Friction of a 1.6 Litre Automotive Engine - Gasoline and Diesel" SAE paper No. 860418.

Bishop, I.N., 1964. "Effect of Design Variables on Friction and Economy", SAE Paper 812A.

Conway-Jones, J.M. and N. Tarver. 1993. "Refinement of Engine Bearing Design Techniques", SAE Paper 932901.

Dearlove, J., and W.K. Cheng. 1995. "Simultaneous Piston Ring Friction and Oil Film Thickness Measurements in a Reciprocating Test Rig" SAE paper No. 952470.

Feng, A., and F. Stodolsky. 1995. "Modeling the Effect of Engine Assembly Mass on Engine Friction and Vehicle Fuel Economy", SAE Paper 950988.

Fujii, I., S. Yagi, H. Sono, and H. Kamiya. 1988. "Total Engine Friction in Four Stroke S.I. Motorcycle Engine" SAE paper No. 880268.

Furuhama, S., M. Hiruma, and M. Tsuzita. 1979. "Piston Ring Motion and Its Influence on Engine Tribology" SAE paper No. 790860.

Furuhama, S., M. Takiguchi. 1979. "Measurement of Piston Frictional Force in Actual Operating Diesel Engine" SAE paper No. 790855.

Furuhama, S., M. Takiguchi, K. Tomizawa. 1981. "Effect of Piston and Piston Ring Designs on the Piston Friction Forces in Diesel Engines" SAE paper No. 810977.

Goenka, P.K., and P.R. Meernik. 1992. "Lubrication Analysis of Piston Skirts", SAE Paper 920490.

Goenka, P.K., R.S. Paranjpe, and Y. Jeng. 1992. "Flare: An Integrated Software Package for Friction and Lubrication Analysis of Automotive Engines - Part I: Overview and Applications" SAE paper No. 920487.

Gomi, T., T. Suzaki and M. Yoshida. 1996. "A Method of Estimating Gasoline Engine Performance" SAE paper No. 960011.

Goto, T., S. Aoyama, S. Nagumo, Y. Nakajima, M. Onoda. 1985. "Measurement of Piston and Piston ring Assembly Friction Force" SAE paper No. 851671.

Grice, N., and I. Sherrington. 1993. "An Experimental Investigation into the Lubrication of Piston Rings in an Internal Combustion Engine- Oil Film Thickness Trends, Film Stability and Cavitation" SAE paper No. 930688.

Heywood, J.B. 1988. Internal Combustion Engine Fundamentals. McGraw-Hill: New York.

Hill, S.H., and B.A. Newman. 1984. "Piston Ring Designs for Reduced Friction" SAE paper No. 841222.

Hoult, D.P., J.P. Lux, V.W. Wong, and S.A. Billian. 1988. "Calibration of Laser Fluorescence Measurements of Lubricant Film Thickness in Engines" SAE paper No. 881587.

Jeng, Y. 1992. "Friction and Lubrication Analysis of a Piston-Ring Pack" SAE paper No. 920492.

Kovach, J.T., E.A. Tsakiris, and L.T. Wond. 1982. "Engine Friction Reduction for Improved Fuel Economy" SAE paper No. 820085.

Martin, F.A., and H. Xu. 1993. "Improved Oil Flow Prediction Method for Connecting-Rod Bearings Fed by a Single Hole in the Crankpin", SAE Paper 930791.

Mattsson, C. 1995. "Measurement of the Oil Film Thickness Between the Cylinder Liner and the Piston Rings in a Heavy Duty Directly Injected Diesel Engine" SAE paper No. 952469.

McGeehan, J.A. 1978. "A Literature Review of the Effects of Piston and Ring Friction and Lubricating Oil Viscosity on Fuel Economy" SAE paper No.780673.

Paranjpe, R.S., and A. Cusenza. 1992. "Flare: An Integrated Software Package for Friction and Lubrication Analysis of Automotive Engines - Part II: Experimental Validation" ,SAE Paper 920488.

Patton, K.J., R.G. Nitschke and J.B. Heywood. 1989. "Development and Evaluation of a Friction Model for Spark-ignition Engines" SAE paper No. 890836.

Rosenberg, R.C. 1982. "General Friction Considerations for Engine Design" SAE paper No. 821576.

Shaw B.T., T. Byron, D.P. Hoult, and V.W. Wong. 1992. "Development of Engine Lubricant Film Thickness Diagnostics Using Fiber Optics and Laser Fluorescence" SAE paper No. 920651.

Sui, P.C., and S. Ariga. 1993. "Piston Ring Pack Friction and Lubrication Analysis of an Automotive Engine Using a Mixed Lubrication Model" SAE paper No. 931937.

Swain, M.R., G.J. Schade, and M.N. Swain. 1996. "Design and Testing of a Dedicated Hydrogen Fueled Engine", SAE Paper 961077.

Takiguchi, M., H. Kikuchi, and S. Furuhama. 1988. "Influence of Clearance Between Piston and Cylinder on Piston Friction" SAE paper No. 881621.

Thring, R.H. 1992. "Engine Friction Modeling" SAE Paper 920482

Ting, L.L. 1993. "Development of a Reciprocating Test Rig for Tribological Studies of Piston Engine Moving Components - Part I: Rig Design and Piston Ring Friction Coefficients Measuring Method" SAE paper No. 930685.

Ting, L.L. 1993. "Development of a Reciprocating Test Rig for Tribological Studies of Piston Engine Moving Components - Part II: Measurements of Piston Ring Friction Coefficients and Rig Test Confirmation" SAE paper No. 930686.

Ting, L.L. 1985. "A Review of Present Information on Piston Ring Tribology", SAE Paper 852355.

Uras, H.M., and D.J. Patterson. 1983. "Measurement of Piston and Ring Assembly Friction Instantaneous IMEP Method" SAE paper No. 830416.

VanBlarigan, P. 1996. "Development of a Hydrogen Fueled Internal Combustion Engine Designed for Single Speed/Power Operation", SAE Paper 961690.

Wakuri, Y., M. Soejima, Y. Ejima, T. Hamatake, and T. Kitahara. 1995. "Studies on Friction Characteristics of Reciprocating Engines", SAE Paper 952471.

Yagi, S., K. Fujiwara, N. Kuroki, Y. Maeda. 1991. "Estimate of Total Engine Loss and Engine Output in Four Stroke S.I. Engines", SAE Paper 910347.

Yagi, S., Y. Ishibasi and H. Sono. 1990. "Experimental Analysis of Total Engine Friction in Four stroke S.I. Engines" SAE paper No. 900223.

Yun, J.E., Y. Chung, S.M. Chun, and K.Y. Lee. 1995. "An Application of Simplified Average Reynolds Equation for Mixed Lubrication Analysis of Piston Ring Assembly in an Internal Combustion Engine", SAE Paper 952562.

Top Compression Ring

2nd Compression Ring

Oil Ring

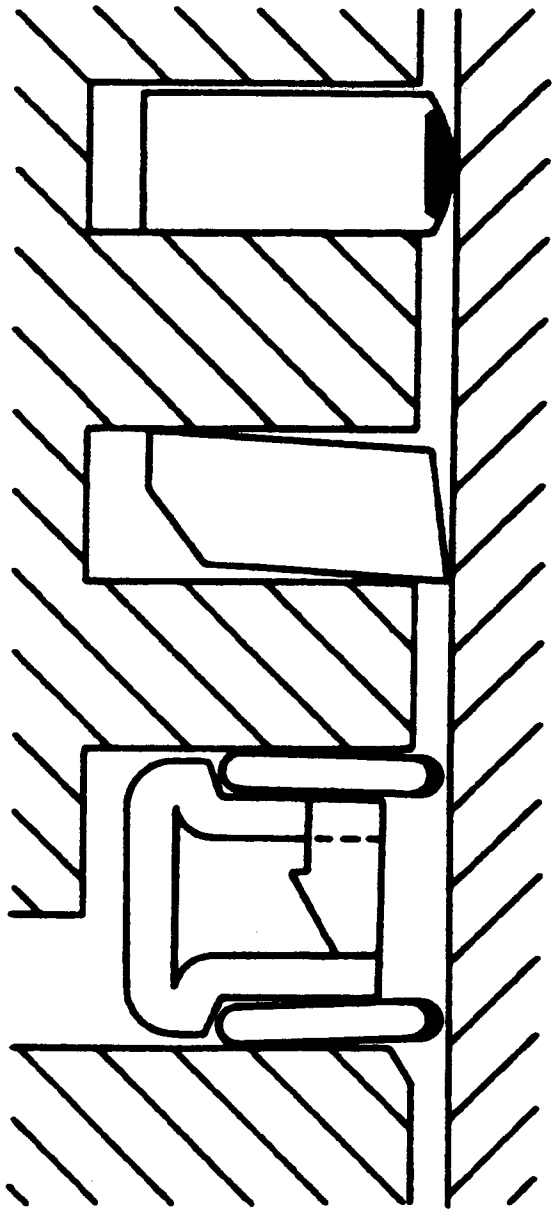

Figure 1

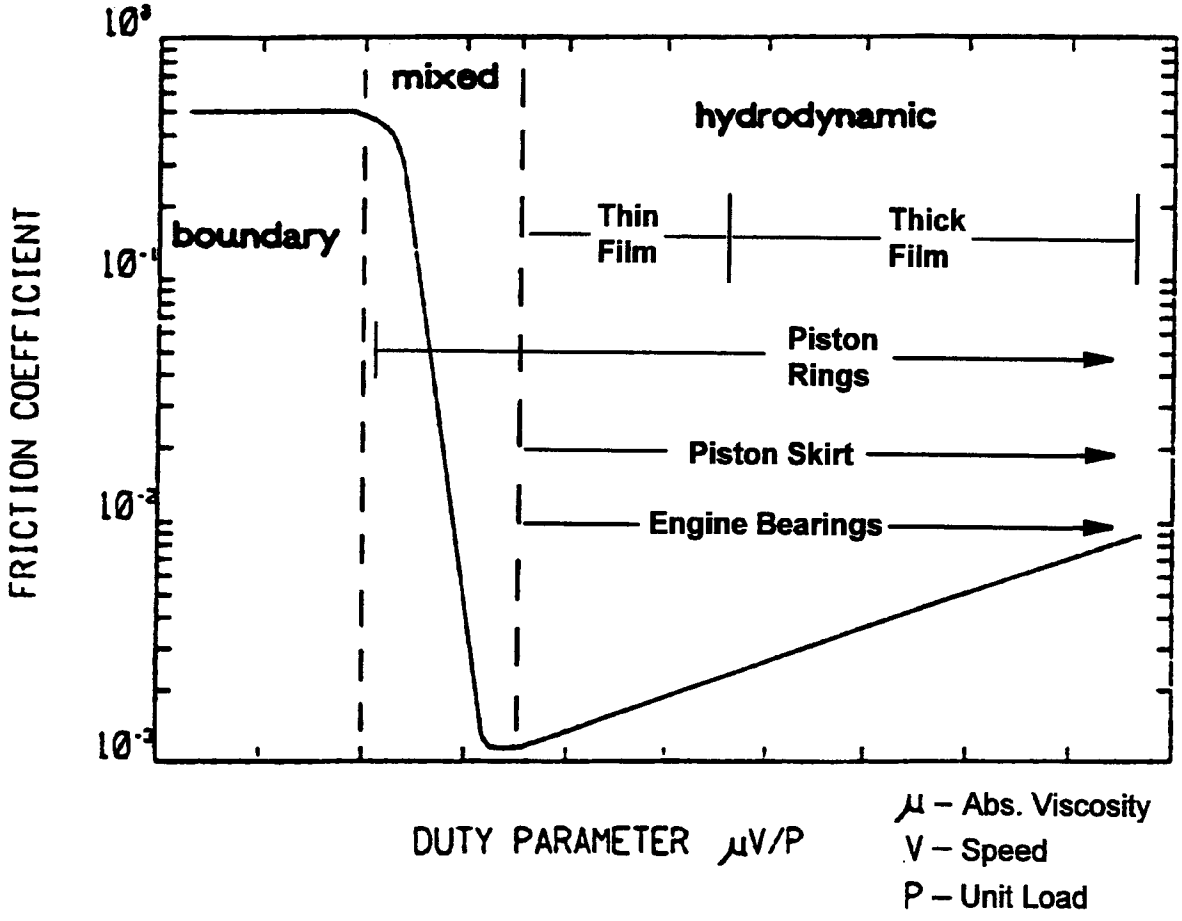
FRICTION COEFFICIENT
mixed
hydrodynamic
boundary
Thin Film
Thick Film
Piston Rings
Piston Skirt
Engine Bearings
DUTY PARAMETER μV/P
μ – Abs. Viscosity
V – Speed
P – Unit Load

Figure 2

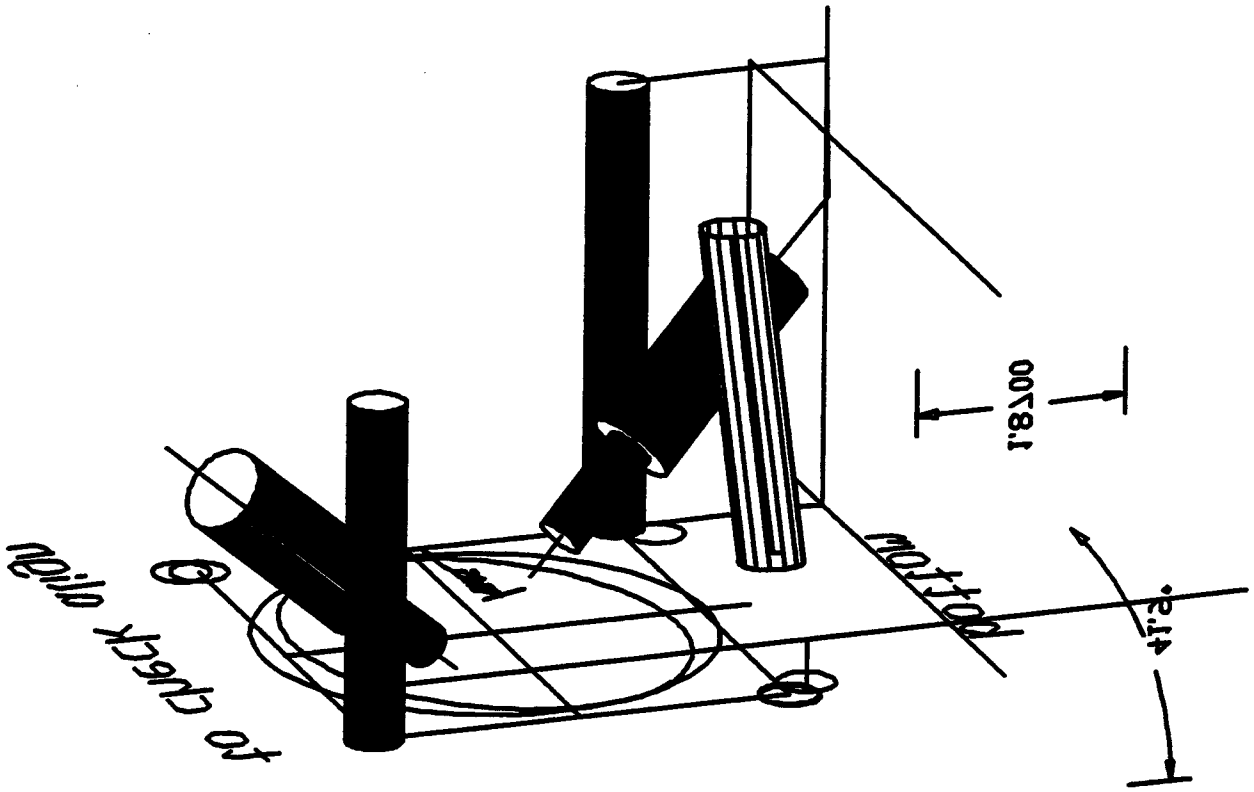

Figure 3

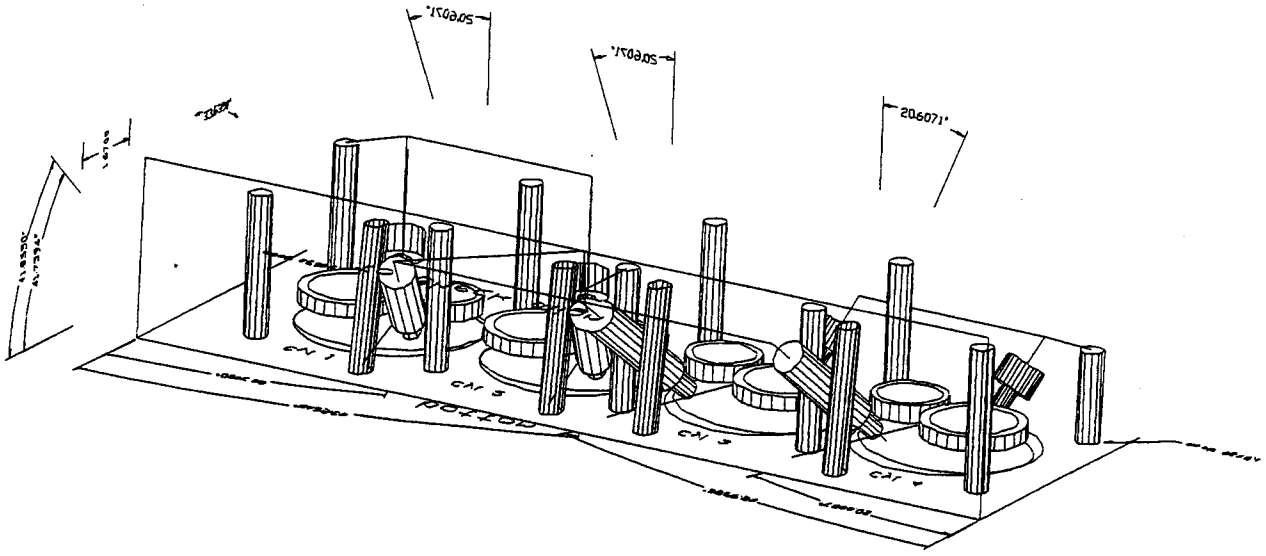

Figure 4

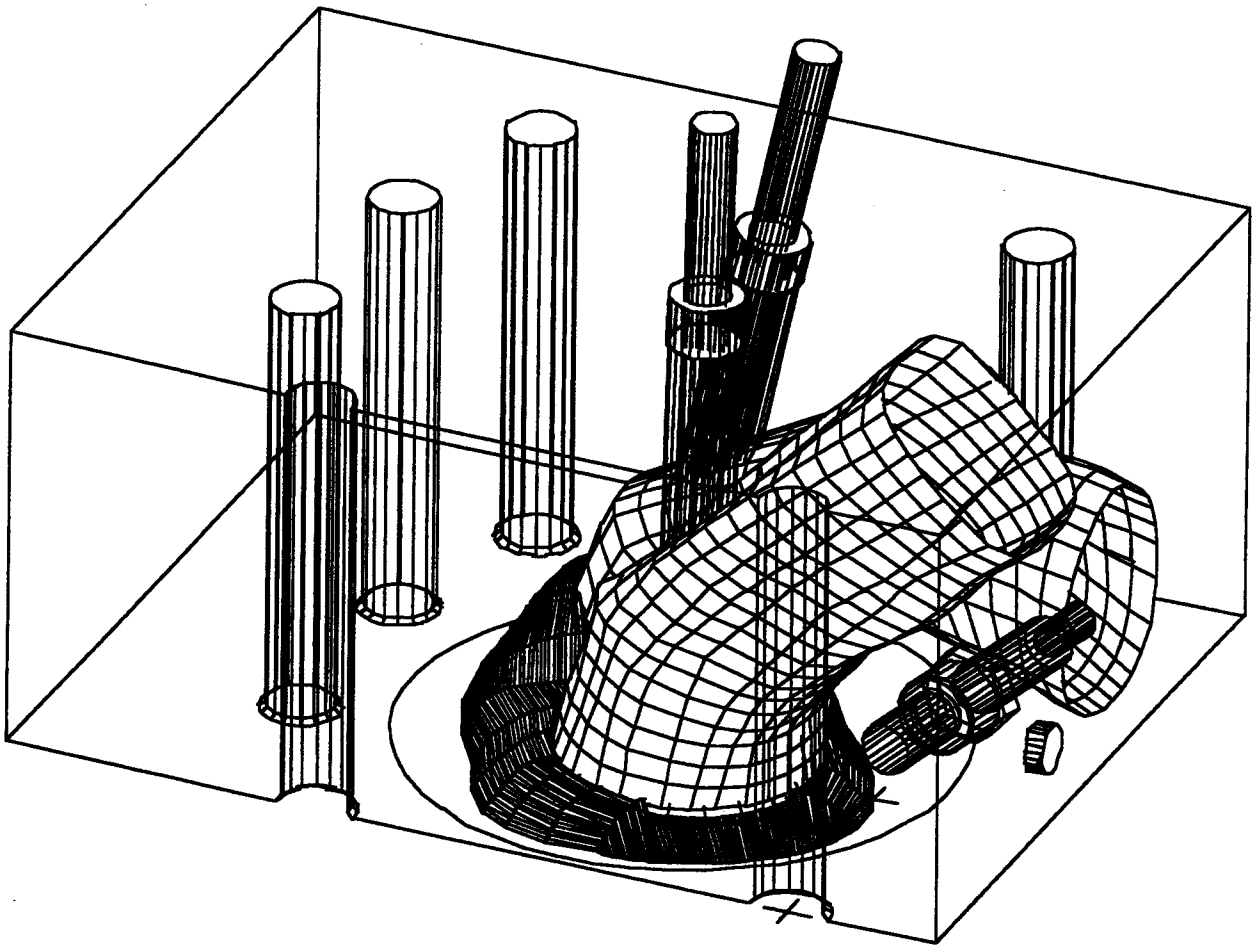

Figure 5

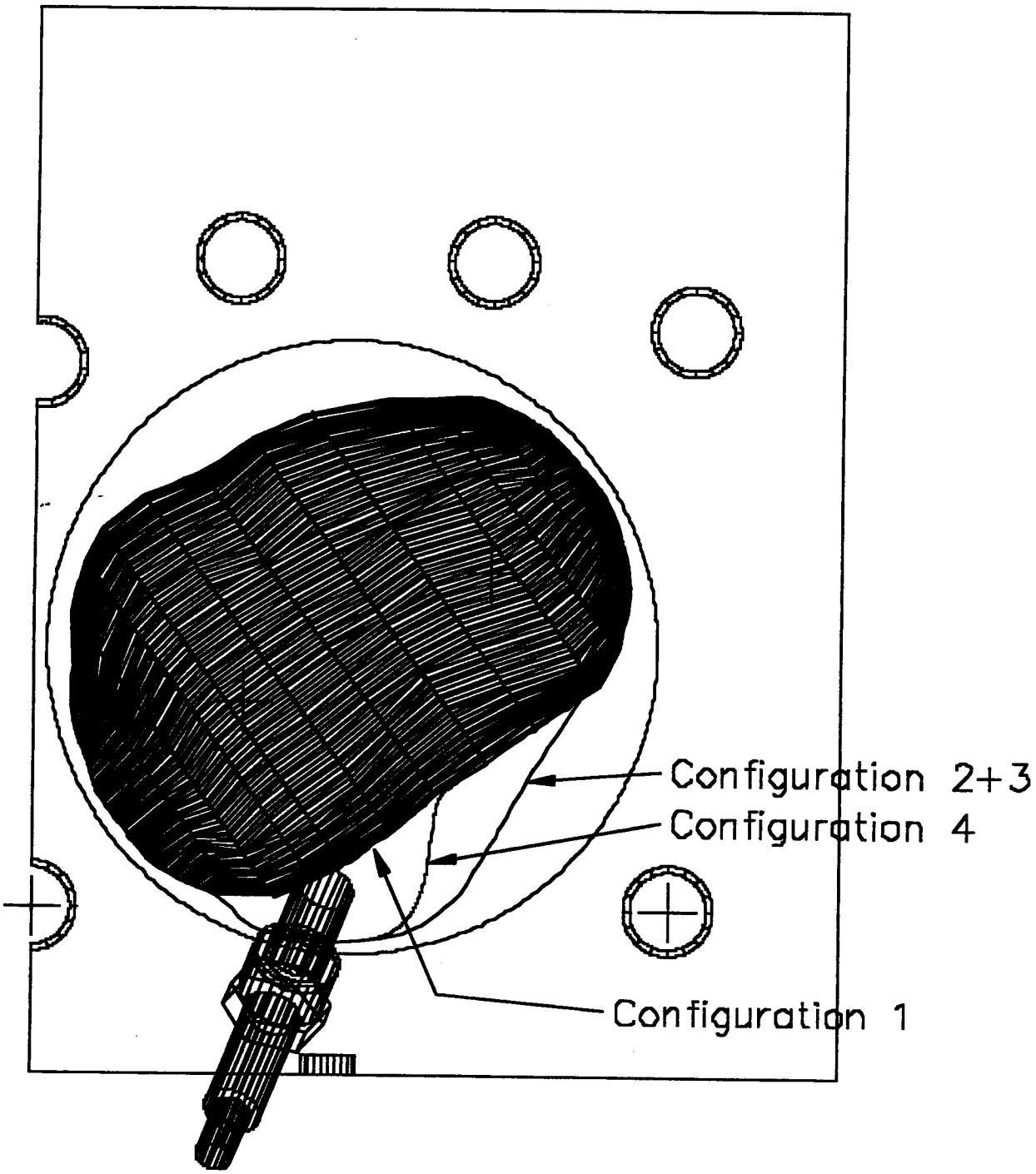

Figure 6

PRODUCTION OF HBR FROM BROMINE-STEAM AND BROMINE-STEAM-METHANE REACTIONS FOR ELECTROLYTIC HYDROGEN PRODUCTION

R. E. Schlief, M. A. Stoy, H. L. Heaton, and R. J. Hanrahan
SRT Group, Inc.
Miami, FL 33133
and
Department of Chemistry, University of Florida
Gainesville, FL 32611

Abstract

Efficient, low cost production of hydrogen will become important as clean air standards become more stringent and the demand for hydrogen powered vehicles increases. Hydrogen finds many industrial uses as well. SRT has undertaken research and development of a new process for hydrogen generation that utilizes bromine and steam to generate an intermediate hydrogen carrier, hydrobromic acid (HBr). The acid is subsequently electrolyzed with low cost off-peak electricity to recover the bromine and produce hydrogen. If the electrolyzer is replaced with a reversible fuel cell, stored hydrogen and bromine can be used for energy storage and electrical load leveling as well as for hydrogen production.

Since HBr electrolysis is a well-developed technology, the principal objective of the project was to identify a process that economically produced HBr. The use of concentrated sunlight to drive the reaction between bromine and steam at high temperatures seemed promising. The use of a renewable energy source for hydrogen generation was particularly attractive. To this end, a nominal 10 kW_s solar reactor was tested at the National Renewable Energy Laboratory's (NREL) High Flux Solar Furnace. The principal goal was to demonstrate high conversion rates of bromine to

hydrogen bromide. A secondary goal was to demonstrate the utility of using a halogen gas as an efficient absorber and heat transfer medium for solar energy. A bromine conversion of up to 23% at 1075 °K was measured, and gas temperature increases of 400 °C were measured when bromine was introduced into the reactor as an absorber.

An economic analysis of the process based upon the NREL results and thermodynamic calculations was performed by Energetics, Inc. The relatively low HBr yields, cost of the solar array, cost of heat exchangers and other capital equipment resulted in too high a hydrogen production cost. In an effort to reduce the cost of the process, a variant on the hydrogen production scheme was proposed and investigated. It involved adding methane, which is a source of both carbon and hydrogen, to bromine and steam. It has several important advantages over the solar bromine-steam process: (1) operation at lower temperatures, (2) higher bromine to hydrogen bromide conversion rates, (3) simpler overall process, and (4) safer operation. A preliminary economic analysis performed in-house indicates that the cost to produce hydrogen is about $10/Mbtu even at small scales of operation (2200 m^3/day). This is a scale significantly smaller than that at which most steam methane reforming plants operate.

An apparatus for preliminary studies of the reaction was assembled. The increase in bromine conversion to hydrogen bromide upon addition of methane was very dramatic, with values of up to 92% attained at 650 - 800 °C. It was found that some of the methane was converted into an array of organic products, indicating that the reaction was not optimized. The organic products were extracted with methylene chloride and analyzed with a GC-MS.

Introduction

Solar Reactor Technologies, Inc. (SRT) had a long-term goal of commercializing its process for generating solar hydrogen combined with utility load-leveling (Parker, 1993). Hydrogen is produced in a two-step hybrid process. The first step is the high temperature reaction between bromine and steam:

$$Br_2 + H_2O \rightarrow 2\,HBr + 1/2\,O_2. \quad (1)$$

The second step is the electrolysis of HBr in a reversible fuel cell/electrolyzer:

$$2\,HBr \rightarrow Br_2 + H_2. \quad (2)$$

The hydrogen is stored for future use or sale, while bromine is recycled through reaction (1). The fuel cell/electrolyzer is also used in utility load-leveling. It provides electric power for peak demand periods during the day by combining hydrogen and bromine:

$$Br_2 + H_2 \rightarrow 2\,HBr. \quad (3)$$

During a portion of the off-peak period, bromine and hydrogen for the load-leveling operation are regenerated via electrolysis. During the remainder, HBr produced by the solar reactor is electrolyzed. The net effect of the SRT process is to split water into hydrogen and oxygen using solar and electrical energy. Since HBr electrolysis is a better-established technology (Balko, 1981), the emphasis in the present research was demonstration of efficient solar HBr production. A complementary goal was to better understand reaction kinetics and the dependence of HBr yield on reactor operating conditions.

The research effort for studying reaction (1) described here is a continuation of work performed previously, involving a small-scale reactor at a 500 - 1000 W power level. The HBr yield was measured in purely thermal experiments (electrical furnace heating) and solar experiments (furnace plus solar concentrator). Within experimental uncertainties, there was no discernible difference in HBr production between the those two sets of experiments.

The goal of the present endeavor was to scale up the laboratory reactor and measure the conversion of bromine to HBr with all the reaction energy supplied by solar photons. A larger reactor, designed for 10 kW illumination, was designed and fabricated along with a suitable bromine and steam delivery system. Experimental bromine conversions were compared to those predicted by a kinetic model and thermodynamics. Real-time FTIR was employed to measure the reactor steam temperature and HBr mole fraction.

Solar Reactor Testing

Figure 1a shows a general schematic of the experimental setup. More detail on the fluid delivery system and reactor are shown in Figures 1b and 2, respectively.

Testing was undertaken at the National Renewable Energy Laboratory's High Flux Solar Furnace. Data on reactor performance and HBr yield were taken using a variety of diagnostic methods, which will be discussed later.

Apparatus

The steam delivery system consisted of an electrically heated steam generator, needle valve V4, differential pressure transmitter, control valve V5, and controller. Steam could be switched between a calibration leg, consisting of a water-cooled condenser, and the reactor (See Figure 1b).

The bromine day tank was a Tefzel-lined steel tank. The mass of bromine in the tank was measured by a load cell. The change in mass reading over time was calibrated to give a bromine delivery rate in g/min., allowing the flow rate to be monitored in real time. The day tank was filled from an external tank in which the bromine was originally shipped. After filling, the day tank was pressurized to 75 psig for delivery. Bromine exited the day tank via a Monel dip tube, passed through a needle valve (V1), and was heated in a heat exchanger to 100 - 115 °C. The 75 psig was sufficient to keep bromine liquid at those temperatures. It was subsequently flashed to a

vapor by dropping the pressure across valve V3. Pressure transmitters for metering bromine were coupled with PID controllers for V2 and V3 (See Figure 2). The hot bromine vapor could be switched between a calibration leg or the reactor. The calibration leg consisted of a water-cooled condenser and a laboratory balance. Tubing carrying hot bromine was steam traced.

Bromine vapor and steam were mixed in a perfluoralkoxy (PFA) tee. Two steam traced PFA lines delivered the feed mixture to the reactor and returned the product mixture, which was condensed in a third condenser. Liquid samples were collected and stored in Erlenmeyer flasks with ground glass joints.

It was found that the steam delivery system behaved satisfactorily at flow rates above about 5 g/min., the basis for the original design. Manually setting the flash valve (V2) for flow rates above about 10 - 15 g/min. resulted in satisfactorily constant delivery. This was especially true for prolonged operation, i.e., longer than 30 min. at one setting. At lower flow rates, delivery was perturbed by reactor upsets and showed long term drift.

Standard experimental procedure consisted of warming up the reactor to operating temperature with solar energy. During warm up nitrogen was passed through the reactor to prevent overheating. Steam and bromine flow rates were established and calibrated in the calibration legs. Next, the N_2 flow to the reactor was stopped and replaced by steam. Bromine was then added to the steam. FTIR measurements were taken before and after bromine was added to the reactor. Bromine and steam flow rates were kept constant during each experiment, only the solar power, and hence the reaction temperature, was varied during any particular experiment. Solar power was varied by the position of a mechanical shutter which could partially or completely block the beam.

The reactor consisted of a 4" quartz tube with a curved front window (See Fig. 2). The exit tube was about 2.5" behind the front window. FTIR windows were mounted transversely about 3" behind the front window. Inlet and outlet tubes were concentric at the back of the reactor. The reactant gas mixture was preheated by a porous frit, which was mounted in the back half of the reactor. Its front surface was illuminated by the solar flux, and the sides by radiation from the Inconel housing. A shallow thermocouple well 3" behind the window (labeled "Fr Reactor" in Fig. 2) facilitated wall temperature measurements. Another thermocouple was mounted at the back of the reactor (Bk Reactor), behind the frit, for measuring gas inlet temperatures.

The reactor was housed in an Inconel 800 alloy tube with a back plate. It prevented losses by reflection and radiation out the sides. Energy absorbed by the housing was re-radiated in the infrared, heating the quartz walls and steam. The Inconel tube was insulated with a ceramic fiber blanket (Cotronics Inc.), surrounded by an outer stainless steel jacket. Three thermocouples measured the housing temperature: Fr Tube, Bk Tube, and Bk Wall (See Figure 2).

The reactor was attached to a quartz tube and shell heat exchanger. The tube side preheated the incoming reactant gases. Hot product gases were cooled in the shell side (See Figure 1a).

Thermodynamic and Kinetic Modeling

A useful quantity in describing the best-possible performance of the SRT process is the Br_2 conversion calculated by thermodynamics. In the following discussion, the conversion of bromine to HBr (or yield Y) is defined as:

$$Y = n_{HBr}/(2\, n_{Br2}), \tag{4}$$

where n_{HBr} are the moles of HBr exiting the reactor, and n_{Br2} the moles Br_2 entering it. According to thermodynamic predictions for equation (1), HBr yield increases with temperature but decreases with bromine mole fraction (See Figure 3a). At temperatures approaching 2000 K, the yield increases only slightly for $\chi_{Br2} > 0.3$. It declines for $\chi_{Br2} < 0.3$. This is attributed to increasing thermal dissociation of Br_2:

$$Br_2 \rightarrow 2\,Br, \tag{5}$$

and HBr. The dissociation reactions offer an alternate reaction channel for bromine molecules, shifting the equilibrium of Reaction (1) back toward the left. For $\chi_{Br2} = 0.25$ and a 1300 K mean reactor temperature, typical operating conditions, a 19% yield is predicted.

Alternately, one can plot the HBr mole fraction in the equilibrium gas mixture (χ_{HBr}) as a function of feed stream bromine mole fraction (χ_{Br2}). This is shown in Figure 3b. The Br radicals formed by thermal dissociation are included in these mole fractions. As in Figure 3a, χ_{HBr} increases with temperature. A curve with maximum values is reached around 1800 K. The maximum χ_{HBr} for a given temperature occurs at the stoichiometric ratio, i.e. $\chi_{Br2} = 0.5$.

A reactor flow model was developed by Sandia, California (Steve R. Vosen) The emissivity of the reacting gas mixture was the only adjustable parameter. A set of 32 reactions were used and an AM 1.0 solar spectrum assumed. The effect of photon absorption by bromine was treated solely as thermal gas heating. Experimental gas temperatures and HBr mole fractions were reproduced to within 22%.

A plot of predicted gas temperature vs. distance from the porous frit is depicted in Figure 4a. The gas emissivity in the model was varied until a satisfactory fit was obtained at the FTIR measurement location, x = 0.12 m. The steam temperature was assumed to be the same as that of the total gas mixture. The model assumed molar flow rates identical to those for Sample 1 in Table 2. Note the very sharp rise in temperature near the window at x = 0.15 m. A complementary plot of HBr mole fraction vs. distance is shown in Figure 4b. It is based on the same reactor conditions. Here, the increase in HBr mole fraction for x > 0.10 m is more sensitive to window proximity than the gas temperature.

Near the front of the reactor, according to the model, the largest fraction of solar energy is absorbed by bromine molecules. Upon their dissociation and recombination, they impart much of this energy to the surrounding molecules. This creates a high local gas temperature and hence a high χ_{HBr} is predicted at the front of the reactor.

Experimental Measurement Techniques

Several complementary measurement techniques were employed in studying Reaction (1). Reactor (wall) temperatures were measured with thermocouples. Solar power was determined from a normalized incident periheliometer and the percentage of furnace shutter attenuation. Fourier Transform Infrared (FTIR) spectroscopy was used to measure gas temperatures and HBr mole fraction. A Molecular Beam Mass Spectrometer (MBMS) was used to monitor real-time species concentration in the effluent stream. Liquid samples were collected and the acid concentration determined via titration.

At the start of each experiment, N_2 was flowed through the reactor and the solar power level increased in steps to avoid reactor damage. When operating temperature was attained, the N_2 flow was switched over to steam. After bromine flow was established, reactor power was decreased stepwise to achieve a series of temperatures with bromine flowing, during which FTIR data and liquid samples were collected.

The greatest signal variability (or rms change) was registered by the front reactor thermocouple. It was located nearest the window and was most sensitive to perturbations in beam position. The other readings showed the same general features as the front thermocouple.

FTIR Data

The steam temperature and HBr mole fraction during reactor operation were measured with an FTIR instrument. Details of the method can be found in a soon to be published paper (Cosgrove, 1997). Infrared wavelengths at which there was minimal solar background were chosen. Absorption at wavelengths in the region where the water spectrum was weakest facilitated HBr measurements. The absorption and emission by steam at other wavelengths was employed in the gas temperature measurements. The infrared beam was directed through a pair of windows which were centered about three inches (7.5 cm) behind the front surface of the reactor window.

When bromine flow to the reactor was initiated under full illumination, the steam temperature increased by up to 400 °C upon (See Figure 5a). This was due to a fluid absorber effect: bromine absorbs 25 - 35% of the incident flux, photodissociates, and imparts this energy to surrounding gas molecules, thereby heating them. There was a fairly constant 200 K gradient between the cooler outside wall and the gas in the reactor. It is also interesting to note that steam temperatures were not markedly influenced by large fluctuations in the solar power. This can be explained by a significant amount of thermal inertia.

In Figure 5b, the steam temperature and χ_{HBr} (mole fraction) for the same run as in Figure 5a are superimposed. As predicted by thermodynamic calculations, χ_{HBr} is very sensitive to decreases in temperature.

MBMS Data

Another diagnostic tool used was molecular beam mass spectroscopy (MBMS). A fixed percentage of the gas stream leaving the reactor was diverted through the MBMS via an eductor, where it was cooled to about 150 °C in a N_2 quenching stream. The time of flight between the eductor and the detector was 20 - 30 ms, as estimated by the NREL operators.

The MBMS was used as a system diagnostic by measuring the Br_2, H_2O, HBr and O_2 exiting the reactor in real time. Their concentrations underwent period variation, which were thought to be due to variations in flow rates or heliostat tracking. A detailed mass spectrum revealed no additional species in the reactor effluent (See Figure 6).

Liquid Sample Analysis

Liquid samples were titrated with a standardized sodium hydroxide solution and a pH electrode. The endpoint was chosen as the inflection point of the titration curve, which corresponded to pH values less than 7. The Br_2 conversion was interpolated from a plot of Br_2 conversion vs. [HBr] appropriate for the experimental reactant mole fractions. The uncertainty in this method has been estimated as 5-10 %, and is due primarily to uncertainty in χ_{Br2}.

Comparison with Predictions

A comparison of thermodynamic with experimental χ_{HBr} values based on FTIR measurements is shown in Table 1. Incident solar power is denoted by P, FTIR steam temperature by T_{FTIR}, and reactor front thermocouple temperature by T_{wall}. The uncertainty in the input bromine mole fraction χ_{Br2} was estimated as 5 - 10%. χ_{HBr} is the experimentally measured FTIR HBr mole fraction, while $\chi_{HBr,TD}$ and $\chi_{HBr,mod}$ are those predicted by thermodynamics and the Sandia, California reactor model, respectively, at T_{FTIR}.

The P, T_{FTIR}, T_{wall}, χ_{Br2}, and χ_{HBr} values in Table 1 were averaged over the period in which liquid samples were collected. χ_{HBr} for sample 6 was assumed to be the same as Sample 5, since T_{wall} values were identical. χ_{HBr} values are 60 - 80% of those predicted by thermodynamics ($\chi_{HBr,TD}$). On the other hand, they are greater than, or roughly equal to, those predicted by the reactor model ($\chi_{HBr,mod}$). Note also the consistent 180 - 200 K difference between T_{FTIR} and T_{wall}.

Table 1. Experimental and Predicted HBr Mole Fractions

Sample	P (kW)	T_{FTIR} (K)	T_{wall} (K)	χ_{Br2}	χ_{HBr}	$\chi_{HBr,TD}$	$\chi_{HBr,Mod}$
1	2.3	1350	1150	0.257	0.085	0.103	0.071
2	2.3	1330	1150	0.257	0.060	0.097	0.062
3	2.0	1300	1110	0.257	0.046	0.089	0.048
4	1.6	1200	1020	0.257	0.037	0.062	0.017
5	1.3	1150	970	0.257	0.024	0.050	
6	1.3	(1150)	970	0.257	(0.0234)	0.050	
7	2.3	1370	1150	0.210	0.059	0.101	
8	2.0	1300	1110	0.210	0.071	0.083	

Bromine conversion determined from liquid samples are tabulated in Table 2. Aqueous phase HBr concentration ($[HBr]_{liq}$) was determined by titration, as described previously. Y_{liquid} is the yield interpolated from $[HBr]_{liq}$. $\chi_{HBr,liq}$ and $wt\%_{HBr,liq}$ are the HBr mole fraction and corresponding weight % calculated from $[HBr]_{liq}$ and based on the total reactor product stream: HBr, O_2, H_2O, and Br_2.

$\chi_{HBr,liq}$ was greater than $\chi_{HBr,TD}$ for $T_{FTIR} > 1150$ K (Samples 1 - 4, 7, and 8); at lower temperatures, it was less than $\chi_{HBr,TD}$ (Samples 5 and 6). χ_{HBr}, which was measured by the FTIR method, was always less than $\chi_{HBr,liq}$. According to the reactor model, HBr mole fraction increases greatly near the reactor the window (See Figure 4b). The FTIR windows were about 3" behind the front of the reactor. It is surmised that additional HBr was produced as the reactor gases moved toward the window and thence the exit tube. Much of this "enriched" composition remained after quenching in the reactor outlet, resulting in the higher HBr mole fraction observed in the liquid samples. The value in parenthesis in Table 2 for run 7 is the conversion estimated for $\chi_{Br2} = 0.17$, rather than 0.21. From this difference, a 5 - 10% uncertainty has been assigned to all Y_{liquid} values. Reactor residence times were estimated as 1 - 2 seconds for Samples 1 - 6 and 3 - 4 seconds for Samples 7 and 8.

Table 2. Summary of Liquid Samples

Sample	T_{FTIR} (K)	χ_{Br2}	$[HBr]_{liq}$ (M)	Y_{liquid}	$\chi_{HBr,liq}$	$wt\%_{HBr,liq}$
1	1350	0.257	4.5	0.228	0.128	18.1
2	1330	0.257	4.2	0.216	0.120	17.1
3	1300	0.257	3.7	0.191	0.105	15.1
4	1200	0.257	2.7	0.144	0.078	11.3
5	1150	0.257	2.0	0.077	0.041	6.0
6	1150	0.257	1.9	0069	0.036	5.3
7	1370	0.210	2.7	0.141 (0.186)	0.063	10.3
8	1300	0.210	4.4	0.250	0.119	18.8

The 0.13 and 0.12 HBr mole fractions measured in Samples 1 and 2 are very encouraging. They are comparable to the thermodynamic limit for a representative FTIR reactor temperature near the window.

Economic Analysis Of The Solar Driven Process

Energetics, Inc. performed an economic analysis of the solar process based upon results of the NREL testing. The analysis was an attempt to predict the cost of hydrogen produced by the process. The analysis included cost items such as cost of materials, labor, capital, land, etc. The price of hydrogen generated by the solar process was predicted to be too high for near-term

market success, e.g. $43/MBtu. The major cost factor identified was the high capital cost of an envisioned plant. In particular the solar heliostat field, central power tower, heat exchangers, and fuel cell were identified as the costliest items. Once the cost impact of these items was determined an effort was made to modify the process to reduce the cost of, or eliminate them.

Several alternative processes were evaluated: (1) a reaction between chlorine and steam to produce HCl, (2) a dedicated energy storage/load leveling with a H_2-Br_2 fuel cell, (3) a reaction between bromine, steam and a form of sulfur and (4) a reaction between bromine, steam and a carbon source. The best alternative, from an economic standpoint, was a variant of option (4), in which methane acts as both a carbon and hydrogen source. Due to the exothermic nature of the reaction, a significant amount of the water should react at temperatures around 500 °C. This is much lower than those required in the solar reaction, typically in excess of 1000 °C.

Experimental work was undertaken to confirm thermodynamic predictions. It was found that the steam-bromine-methane reaction was indeed highly effective in producing HBr. When coupled with an HBr electrolysis cell (not a reversible fuel cell), an economic analysis showed that the process could produce hydrogen at $9.57/MMBTU, even at small (76 kSCFD) scales. It reduces the capital cost and siting limitations inherent in using solar energy. This makes the approach more attractive to merchant hydrogen producers and utilities. The remainder of this document addresses this new process.

Bromine-Steam-Methane Process

Several alternative reactions to produce HBr efficiently were investigated. Many involved the reaction of water and bromine with a carbonaceous material, such as charcoal, coal, or biomass. Others involved the use of sulfur containing compounds. Previous work in this area indicated that bromine conversions of 95-100% could be attained at temperatures below 500 °C (773 K). The process is also exothermic, producing rather than requiring heat. A disadvantage of the prior work was that the carbonaceous material used was a solid, tending to complicate the processes to the point of being uneconomic.

Researchers at SRT had the idea that the use of methane (natural gas) to drive the reaction might be a useful way to simplify the process and make it economically feasible. Thermodynamic calculations confirmed that this would a useful avenue of investigation. The reaction between bromine, steam, and methane is postulated as:

$$2\,H_2O_{(l)} + 4\,Br_{2(l)} + CH_{4(g)} \rightarrow 8\,HBr_{(aq)} + CO_{2(g)}. \qquad \Delta H^\circ_{298} = -719.4.2\ kJ \quad (6)$$

The corresponding reaction leading to CO is also possible:

$$H_2O_{(l)} + 3\,Br_{2(l)} + CH_{4(g)} \rightarrow 6\,HBr_{(aq)} + CO_{(g)}. \quad \Delta H^\circ_{298} = -479.1\ kJ \quad (7)$$

SRT personnel built a laboratory sized bromine-steam-methane reactor and tested it. First results showed that the conversion was effective. The reactor product stream was sampled and analyzed for HBr content. Concentrations up to 13 M in HBr were generated at conversion rates approaching 95% at a temperature of 750 °C. No catalyst was used.

Based on these early results, SRT has designed a new hydrogen production process utilizing the bromine/steam/methane reaction and presently available commercial electrolysis cells. This is described next.

Concept Description

The new system is designed for small to medium sized installations. It is small, compact, and produces hydrogen as a pure gas, without the requirement for production of syngas intermediates or product separation and purification. Product separation and purification makes conventional steam/methane reforming uneconomical on a small scale. The process is illustrated in Figure 7.

Methane is mixed with steam and bromine in the reactor, where conversion to HBr and CO_2 takes place. The hot gasses exit the reactor and go through heat exchangers, which capture some of the heat, to pre-heat the incoming reactants. Since the reaction is exothermic, excess heat is produced. The product gasses then pass into an absorber, where the HBr is absorbed into water, raising the incoming HBr concentration from 20 wt% to 40 wt% upon exiting. The CO_2 is not absorbed to any appreciable extent and passes into the scrubber. The scrubber passes the CO_2 through the incoming water, removing any residual HBr. The CO_2 exiting the process will be essentially pure and will have value as an inert gas or for other chemical use. The 40 wt% HBr stream exiting the absorber will be pressurized by a pump and fed to the electrolyzer, producing H_2 and Br_2. In advanced electrolyzers, H_2 can exit the electrolyzer at high pressure, thus not requiring compression for storage. The liquid mixture exiting the electrolyzer will be depleted in HBr to 20 wt% and will have bromine dissolved into it. This liquid will be passed through a pressure reducing valve into a flash drum where the bromine will boil off, due its low boiling point. The bromine vapor will be conveyed back to the reactor, after being reheated, while the remaining liquid will return to the absorber, completing the cycle. A mass balance for the process is presented in Appendix 1. For purposes of size visualization, at 76,000 scfd, the pump for the 40 wt% HBr stream has a capacity of 10 GPM.

A noteworthy feature of the process is that all of the components shown, even those that are required to be bromine compatible, are commercially available. The only exception is the reactor, which is expected to be constructed of glass-lined steel. Another noteworthy feature is that elemental bromine (Br_2) is only present in the flash drum and piping leading to the reactor. At all other times in the process cycle, bromine is present as HBr, a safer chemical to handle. The amount of elemental bromine present at any one time is small, and when the bromine is formed, it is immediately consumed in the reactor to make more HBr. Shutting down the electrolyzer (for example in the event of a power failure) would stop bromine production. This results in a safe system, with minimal potential for damage in the event of a failure in a piece of equipment.

Reaction Thermodynamics

The free energy of the two methane reactions (6) and (7) is compared to that for the bromine-steam reaction, reaction (1) in Figure 8. The reaction between methane and bromine yielding HBr and carbon is shown for reference purposes as well:

$$2\,Br_{2\,(l)} + CH_{4\,(g)} \rightarrow 4\,HBr_{(aq)} + C_{(s)}. \qquad \Delta H^{\circ}_{298} = -70.7\ kJ \qquad (8)$$

It is very obvious how much more thermodynamically favorable reactions (6), (7), and (8) are compared to (1). Of the three exothermic reactions, the one producing CO_2 is more favorable than the one producing CO, which in turn is more favorable than the one yielding C.

In Figure 9, the standard enthalpies involved in a hypothetical three step process involving reactions (6) followed by electrolysis, reaction (2), followed by fuel combustion of H_2 is shown. Note the very large negative enthalpy of the first step. This is due to the exothermic nature of the reaction in addition to the large heat of solvation for HBr vapor.

Experimental Apparatus and Technique

Figure 10 shows SRT's initial apparatus for preliminary studies of the reaction between bromine, steam, and methane. Bromine was stored in a Tefzel-lined steel tank, whose change in mass was monitored by a load cell. Nitrogen (about 20 psig) was used to push bromine through the tank's dip tube, through a metering valve, and into a steam-jacketed heat exchanger, where it was vaporized. The reactor was run at atmospheric pressure. Steam was supplied by a commercial steam generator and metered by a metering valve. Methane (99.3%) was metered with a rotameter and pressure gauge.

In a second set of experiments, the configuration was slightly modified. The bromine metering valve was placed before the heat exchanger. It was thought that this would simplify operation and improve the uniformity of bromine delivery. A calibration leg for the bromine delivery was added after the heat exchanger.

All three vapor streams were mixed in a heated manifold made of Kynar fittings and tubing. A medium porosity frit supplied about a 5 psi back pressure, sufficient to seat the three check valves in the input streams. The intent was to reduce upstream corrosion in both the bromine and steam lines.

The reactor was a quartz tube of 11 mm i.d. bent 4 times in a double-S configuration. Its empty volume was 200 ml. For a total molar flow rate of 0.25 mol/min and an 800 °C mean reactor temperature, this corresponds to a 0.54 second residence time. It was heated by an 18" long, 3" i.d. Omega tube furnace, controlled by a PID controller. The product gas stream was condensed in a water cooled condenser and sampled with a Pyrex adapter having a two-way valve. Samples

were collected in Erlenmeyer flasks with ground glass joints. They were weighed before and after the run, then stored in a refrigerator until analyzed. For the second set of experiments, a water scrubber solution (typically 225 ml) was added to an empty flask connected in series after the sample flask. The mass of the scrubber solution before and after a run was determined by mass difference and was stored in a tared Erlenmeyer flask.

A concentrated HBr solution was used to scrub any Br_2 passing through the water scrubber. In a second modification of the sampling system, the product stream was bubbled through two water solutions before passing through the HBr solution in a cold trap and a second empty cold trap. Both cold traps were cooled to about -25 °C by a dry ice/ethylene glycol slush. A significant amount of gas not scrubbed by this last HBr solution was generated in the reactor. It was sampled with a gas syringe and injected into a gas chromatograph for analysis.

Analysis and Results

Samples in the first experimental run were analyzed in the following manner: each sample was weighed, aqueous phase density determined, and then an aliquot (2 or 0.2 ml) titrated for H^+ with standardized NaOH. The pH was plotted as a function of base added. The inflection point was chosen as the endpoint. In the second set of experimental runs, the water scrubber solutions were titrated as well, since a large portion of the HBr generated did not condense in the first sample bottle. This was critical for more accurately determining the total amount of HBr produced.

It was found that the concentration of HBr in samples was much higher when methane was flowed through the reactor than without, all other conditions constant (See Tables 3 and 4). In fact, the samples collected fumed in the presence of moist air. The 11 - 13 M concentrations determined by titration were well above that of the commercially available HBr azeotrope, which is only 48-49 wt% or 8.9 M.

Table 3. Effect of Methane on the Bromine-Steam Reaction
(650 °C Exit Temperature)

Sample	XBr_2	XH_2O	XCH_4	[HBr] (M)
2	0.479	0.521	0.000	0.46
3	0.467	0.533	0.000	0.50
4	0.433	0.493	0.074	11.3
5	0.433	0.493	0.074	11.3

Table 4. Bromine-Steam-Methane Reaction
(800 °C Exit temperature)

Sample	XBr_2	XH_2O	XCH_4	[HBr] Sample	[HBr] Scrub	n_{scrub}/n_{sample}	% Conversion
1	0.433	0.567	0.000	1.82	0.000	0.00	2.3
2	0.433	0.567	0.000	1.82	0.000	0.00	2.2
3	0.352	0.559	0.089	12.7	0.668	2.47	6.2
5	0.352	0.559	0.089	13.1	0.678	3.15	59
6	0.368	0.585	0.047	8.1	0.159	0.548	30
7	0.368	0.585	0.047	8.9	0.154	0.495	30

It is apparent from Table 4 that an appreciable amount of HBr was collected in the scrubber solutions. The column n_{scrub}/n_{sample} refers to ratio of moles HBr in scrubber solution to those in the concentrated sample. This was reflected in an increase in their mass during the course of the experiment. In fact, the amount of HBr scrubbed was 2 - 3 times that collected in the samples for the highest methane flow rates. Reactant mole fractions were about 0.35 Br_2, 0.55 H_2O, and 0.1 CH_4. Bromine conversion efficiencies of 60% were attained. Higher values should be realized in future experiments through changes in the input mole fraction, temperature, and residence time.

In a third series of experiments, bromine flow rates were reduced by a factor of 2 - 4 and methane by a factor of 5. In Table 5, these results are compared to those previously discussed. Experiments A and B refer to the data in Tables 3 and 4, respectively, while C, D, and E refer to the lower rates. By running the reactor methane rich, the product mixture contained very little free bromine. This made the analysis much simpler. In particular, the organic impurities could readily be extracted without the need for distilling off large amounts of bromine. The conversion of bromine to HBr was comparable to that in A and B, i.e. between 30 and 70%. The 92% conversion for Experiment E, Sample 1 is an upper limit, based on reasonable values for the bromine delivery rate, which was not constant.

Since it is difficult to accurately measure gas temperatures in a tube furnace, the two temperatures listed in Table 5 are upper and lower bounds to an effective temperature. T_{set} and T_{exit} refer to the furnace and exit gas temperatures, respectively. The furnace temperature was measured by the furnace controller thermocouple. The exit temperature was measured by a thermocouple in a well bathed by the exit gas stream just inside the furnace. Based on the data in Table 5, there was no increase in conversion due to the longer residence times.

Table 5. Comparison of Bromine-Steam-Methane Experiments.

Exp	Run	T_{set} (C)	T_{exit} (C)	XBr_2	XCH_4	XH_2O	XBr_2/ XCH_4	% Br_2 Conv
A	4	750	650	0.43	0.07	0.49	5.8	24
	5	750	650	0.43	0.07	0.49	5.8	25
B	3	900	790	0.35	0.09	0.56	4.0	62
	4	900	790	0.35	0.09	0.56	4.0	
	5	900	790	0.35	0.09	0.56	4.0	59
	6	900	790	0.37	0.05	0.59	8.0	30
	7	900	790	0.37	0.05	0.59	8.0	30
C	1	650	500	0.28	0.09	0.64	3.3	33
D	1	950	815	0.51	0.09	0.43	5.5	67
E	1	750	650	0.16	0.08	0.76	1.8	92
	2	750	650	0.21	0.08	0.71	2.5	54

A problem associated with Reaction (6) were side reactions leading to the production of brominated and non-brominated hydrocarbon compounds. This was manifested by the appearance of a black residue in the sampling system and a characteristic odor. This organic residue may be eliminated via two approaches: (1) operate the reactor at higher gas temperatures, or (2) employ a catalyst to destroy the organic species. A possible candidate is iron oxide, Fe_3O_4.

The organic portion of aqueous samples were extracted with methylene chloride. The same was done for the black filtrate. The samples were refrigerated and shielded from light, to prevent possible photoreactions. A GC-MS instrument that was set up to quickly elute methylene chloride was used. It had high resolution and very good separation characteristics. Many of the compounds positively identified were aromatic compounds, such as biphenyl, naphthalene, anthracene, etc. A significant number were brominated. In one of the aqueous extracts, most of the compounds identified were aromatic, while those from a run on a different day were mainly aliphatic. This suggests that the composition of by-products is quite sensitive to operating conditions, e.g. temperature and mole fractions. Optimization of the reactor operating parameters will minimize or eliminate these materials from the product stream. These compounds occur at trace levels, and much of the black filtrate collected could just be carbon in the form of soot or graphite. More careful analytical work will be required to quantify their total amount.

The gas stream exiting the second cold trap in Experiments C, D, and E was analyzed by gas chromatography. A Tracor 550 GC with TCD detector was employed. Using a silica gel column, He carrier gas (20 ml/min), and a 50 °C column temperature, CO, air, and CH_4 were eluted first. With a temperature program of 25 °C/min, CO_2 then eluted off the column at later time. HBr was shown not to interfere, since it eluted at much longer times. A peak identified as CO_2 was measured in most gas samples collected after the second cold trap. In one sample, there was a hint of a very small CO peak. The fact that these two gasses were detected indicate that water is indeed taking part in the reaction.

Economic Evaluation Of The Steam/Bromine/Methane Reaction

The process of Figure 7 has been evaluated by SRT for its economic potential. The analysis involves a spreadsheet model of the process containing input costs and output prices. It is patterned after a similar analysis performed by Energetics Inc. for reversible electrochemical cells. The base scenario assumes:

- 76,000 SCFD production (18 hours/ day production time)
- Electrolyzer cost of $400/kW
- Off-Peak electricity cost of $ 0.01/kWh
- Natural gas cost of $2.70/MMBTU
- After tax Internal Rate of Return (IRR) of 15% or more

Given these constraints, the process of Figure 7 can produce hydrogen at $9.57/MMBTU. Figures 11a, 11b, and 11c show how the IRR varies as a function of plant size, electricity costs, and natural gas cost, respectively.

Analysis of current hydrogen markets reveal that in many cases companies are paying up to $25.00/MMBTU for merchant hydrogen. These customers consume from 50 to 100kSCFD, making them good candidates for this technology. Hydrogen plants could be situated on-site for maximum economic return.

Future Work

System Improvements

SRT has planned a series of experiments in which reactor operating conditions are to be varied to determine the effect on the product mixture. Bromine conversion to HBr will be optimized, while the amount of reaction by-products will be minimized. Parameters include: (1) reactor temperature, (2) residence time, (3) input mole fraction, and (4) use of a catalyst or substrate.

The system used in the work reported here will be upgraded for continued testing. Bromine will be heated in a Monel tube with electric heater tapes, rather than steam, allowing greater operating flexibility. Bromine and water will be metered as liquids. Methane will be metered as a gas. An

inert gas, such as Ar or He, may be used for additional flexibility in controlling the residence time and or relative mole fractions. Reactants will be brought up to temperature in a preheater. The reactor will consist of a quartz tube.

Analytical Improvements

The liquid and gas sampling system will require some improvements as well. The gas exiting the water solutions will be passed through a drying column and sampled in a bag for GC-MS analysis. The volume of gas evolved will be measured with a wet test meter.

Free bromine needs to be determined in the sample solutions. A spectroscopic technique or $KI/Na_2S_2O_3$ titration will be used. The amount of water collected will be determined by careful density measurements and mass difference. GC gas sampling methods for CO, CO_2, O_2, and CH_4 are being improved. Analysis for other gases in the mixture will be by GC-MS.

Conclusion

An alternative to SRT's former hydrogen generating concept, in which Br_2 and H_2O react at high temperatures to yield HBr, involves the addition of a carbon source. This makes the reaction quite exothermic. SRT has chosen methane as a gaseous source of carbon as well as hydrogen.

Preliminary research has shown that the reaction proceeds at favorable rates at 700 - 900 °C. Lower temperature operation should be possible with the selection of a proper catalyst, increase in heat transfer area, or longer residence time. HBr concentrations of 11 - 13 M, well above those of the commercially available HBr azeotrope (9M), were produced. The beauty of the reaction with methane is the production of only a minimal amount of reaction by-product waste when the system is fully optimized. Other sources of carbon, such coal or biomass, would produce more ash residues, translating in a greater waste disposal problem.

In order to better characterize the reaction, an improved flow delivery system, reactor, sampling system, and sample analytical scheme are being developed. The goal will be to demonstrate comparable bromine conversions at lower temperatures, e.g. 500 °C, and a decrease in organic by-products. The effect of temperature, reactant mix, residence time, and catalysts need to be studied in a systematic manner.

The SRT concept represents an integrated approach toward developing a viable near-term hydrogen production process. It holds promise for being competitive with small-scale steam methane reforming (~$9/MMBTU). This effort is an important step forward in the U.S. realization of energy self-sufficiency and clean fuel technology, with implications for America's balance of trade.

Acknowledgments

The U.S. DOE is gratefully acknowledged for its support of this research effort. The authors wish to express their thanks to several individuals. S. R. Vosen, (Sandia National Laboratory, California) performed thermochemical and kinetic analyses. G. C. Glatzmaier, C. Bingham, and A. Lewandowski (all of NREL) provided assistance in the design of the 10 kW reactor and experimental support. J. E. Cosgrove and J. R. Markham (Advanced Fuel Research, Inc) performed *in-situ* gas temperature and HBr mole fraction measurements using their FTIR instrument. R. French and M. Ratcliff (NREL) set up the MBMS mass spectrometer and collected data. Jim McElroy (Hamilton Standard, Inc.) provided valuable input on the design and operation of reversible H_2-Br_2 fuel cells. Alejandro Posada (SRT) generated the plots of [HBr] vs. % Br_2 conversion and assisted in assembly of the Pathfinder fluid delivery system. Martin Megregian (SRT) was instrumental in construction, testing, and data collection for the bromine-steam-methane apparatus. Larry Land (SRT) developed and implemented the GC analytical method for CO, CO_2, and CH_4. The staff of the mass spectra facility at the University of Florida are to be acknowledged for their helpful feedback. The authors also would like to extend their thanks to Phil DePietro of Energetics, Inc. for his economic analysis of the envisioned SRT solar hydrogen process. Clovis Linkous of the Florida Solar Energy Center provided insight on product separation for the solar process and HBr electrolysis as well as sample titration.

References

Parker, R. Z. Hanrahan, R. J. and Gupta, A. K. 1993. "Hydrogen Generation and Utility Load Leveling System and the Method Therefore." Washington, D.C.: U.S. Patent Office, Patent 5,219,671.

Balko, E. N. McElroy, J. F. and LaConti, A. B. 1981. "Halogen Acid Electrolysis in Solid Polymer Electrolyte Cells." *Int. J. Hydrogen Energy* **6**: 577-587.

Markham, J. R. Cosgrove, J. E. Nelson, C. M. Bonanno, A. S. Schlief, R. E. Stoy, M. A. Glatzmaier, G. C. Bingham, C. E. and Lewandowski, A. A. 1997. "In-Situ FT-IR Monitoring of a Solar Flux Induced Chemical Process," *J. Solar Energy Eng.*, in press.

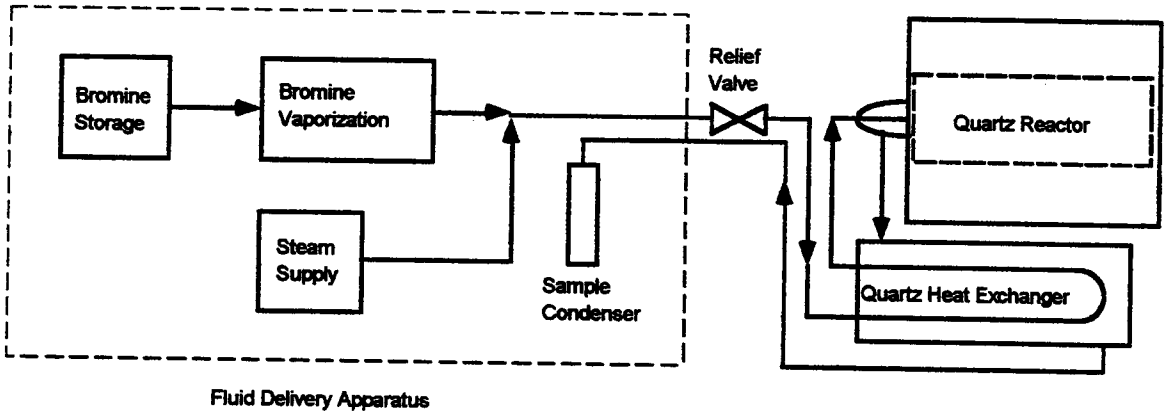

Figure 1a. Fluid Delivery System and 10 kW Reactor.

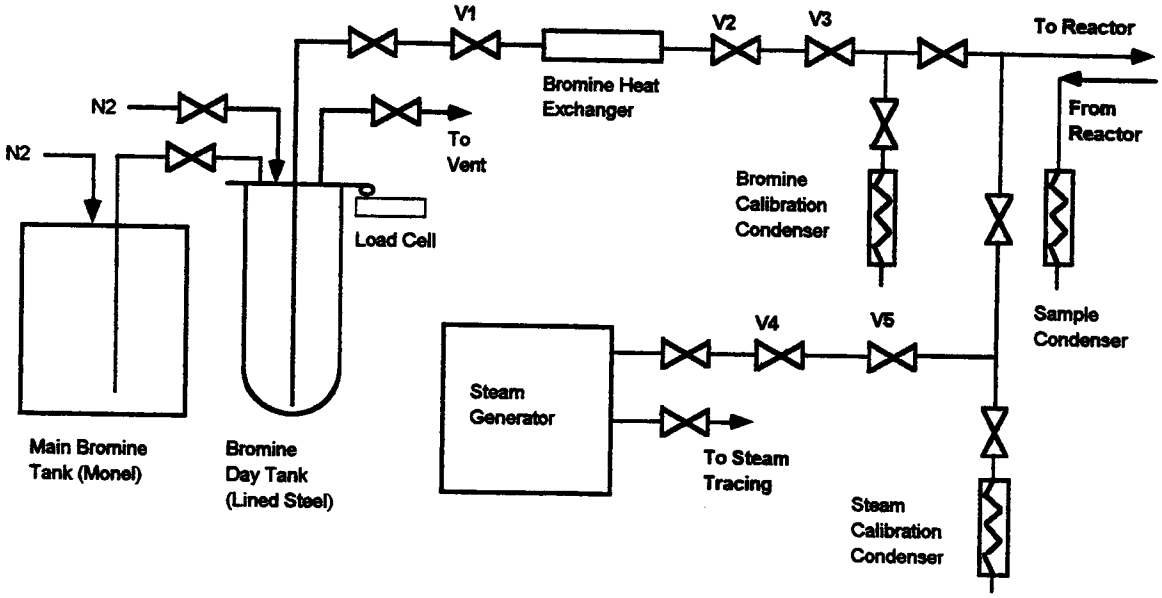

Figure 1b. Schematic of Fluid Delivery System.

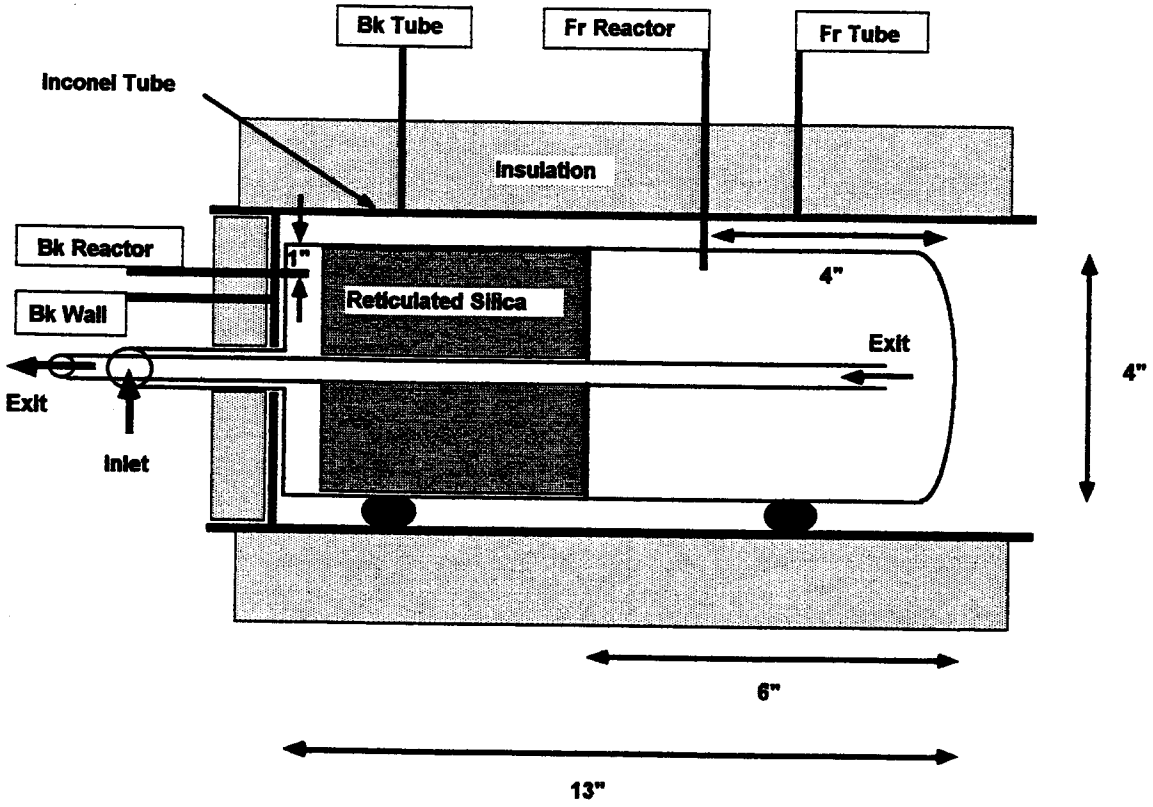

Figure 2. 10 kW Quartz Reactor and Absorber Cavity.

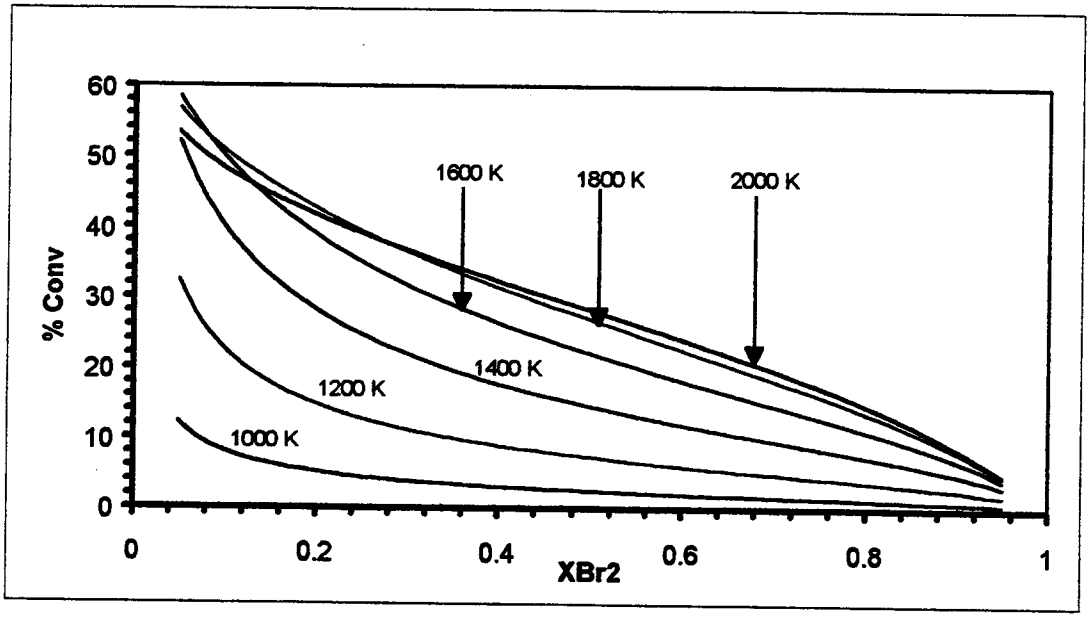

Figure 3a. Thermodynamic Bromine Conversion.

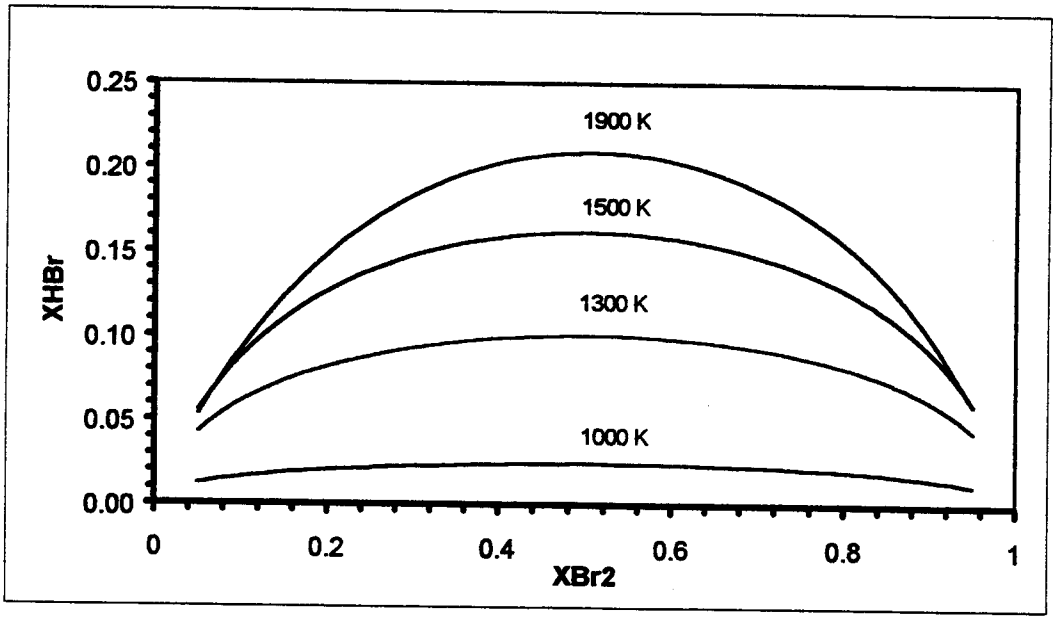

Figure 3b. Thermodynamic HBr Mole Fraction.

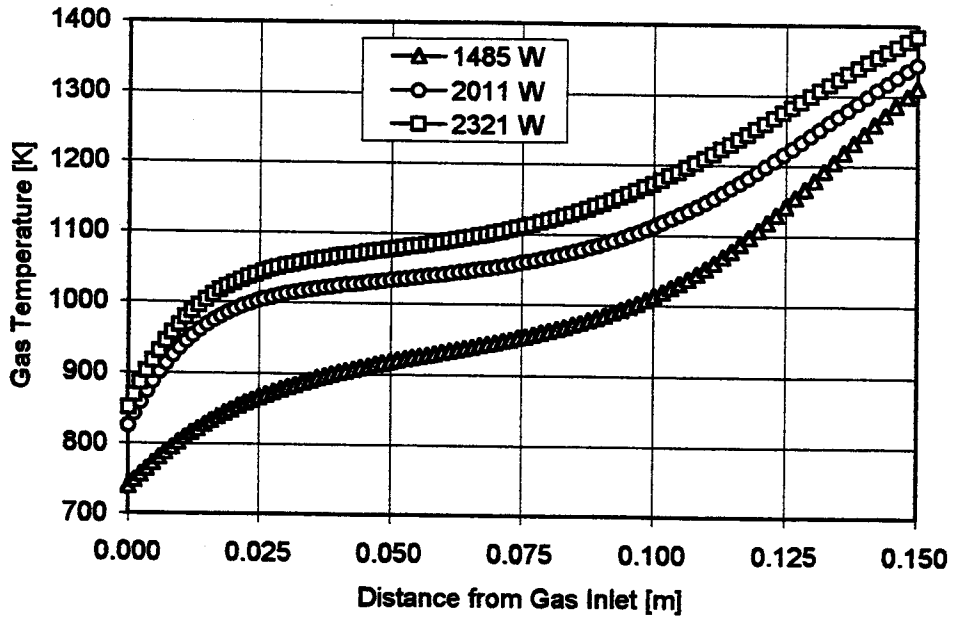

Figure 4a. Rector Model Gas Temperature.

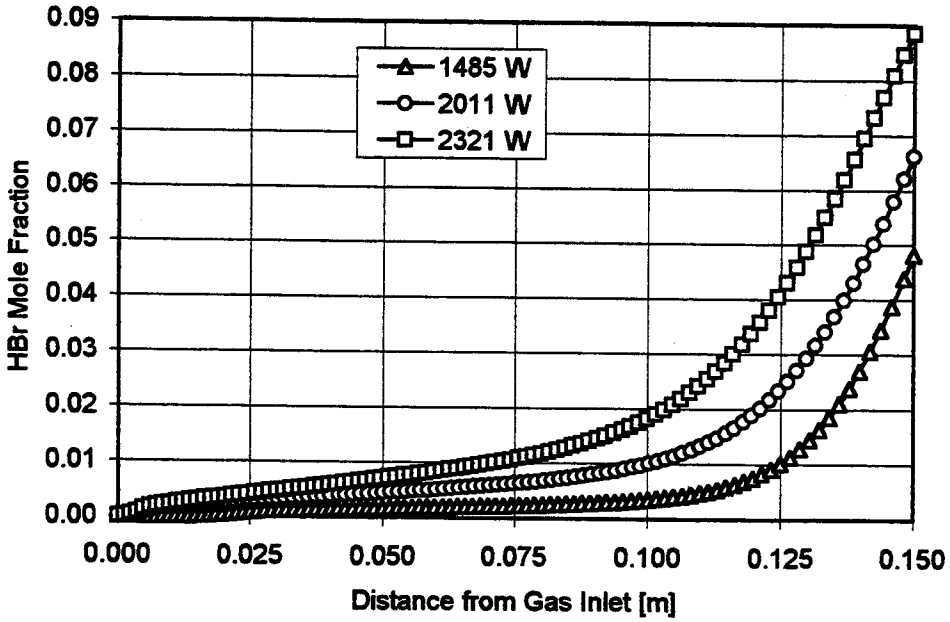

Figure 4b. Reactor Model HBr Mole Fraction.

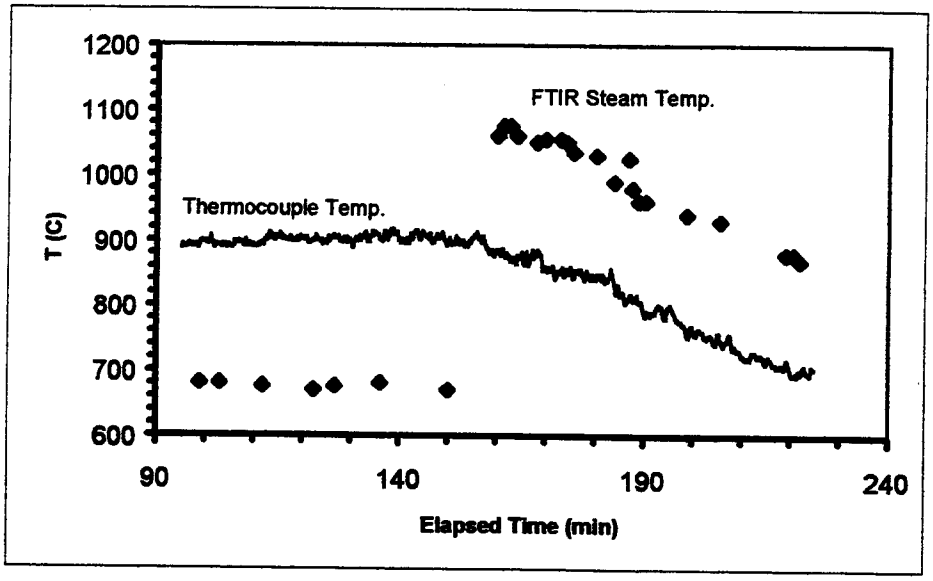

Figure 5a. Jump in FTIR Steam Temperature With Bromine.

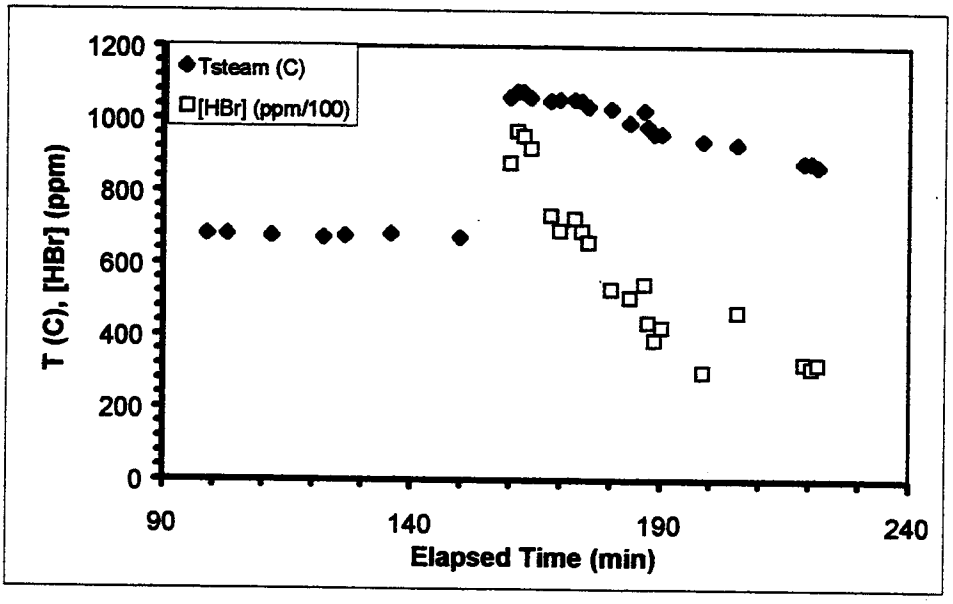

Figure 5b. FTIR HBr Mole Fraction.

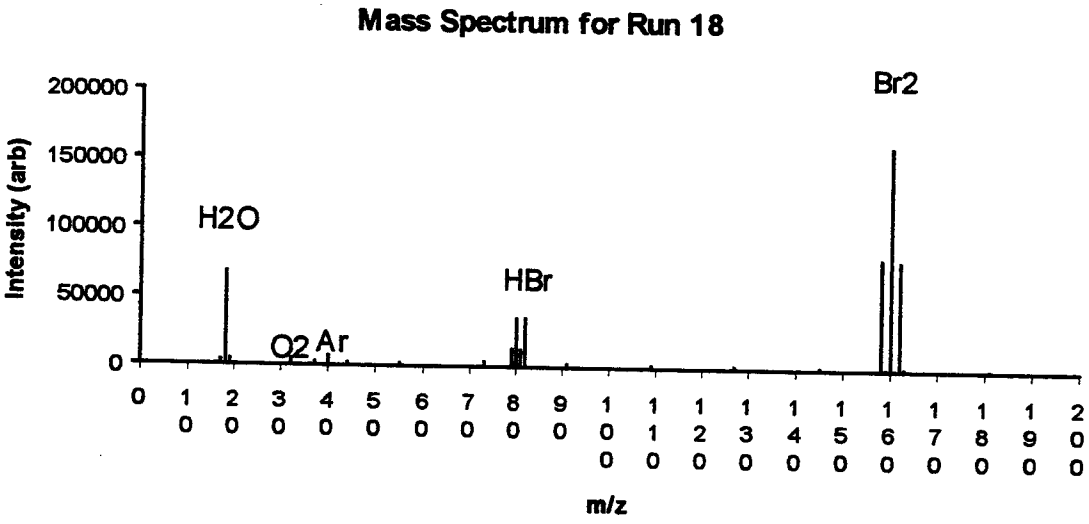

Figure 6. Mass Spectrum of Reactor Product Mixture.

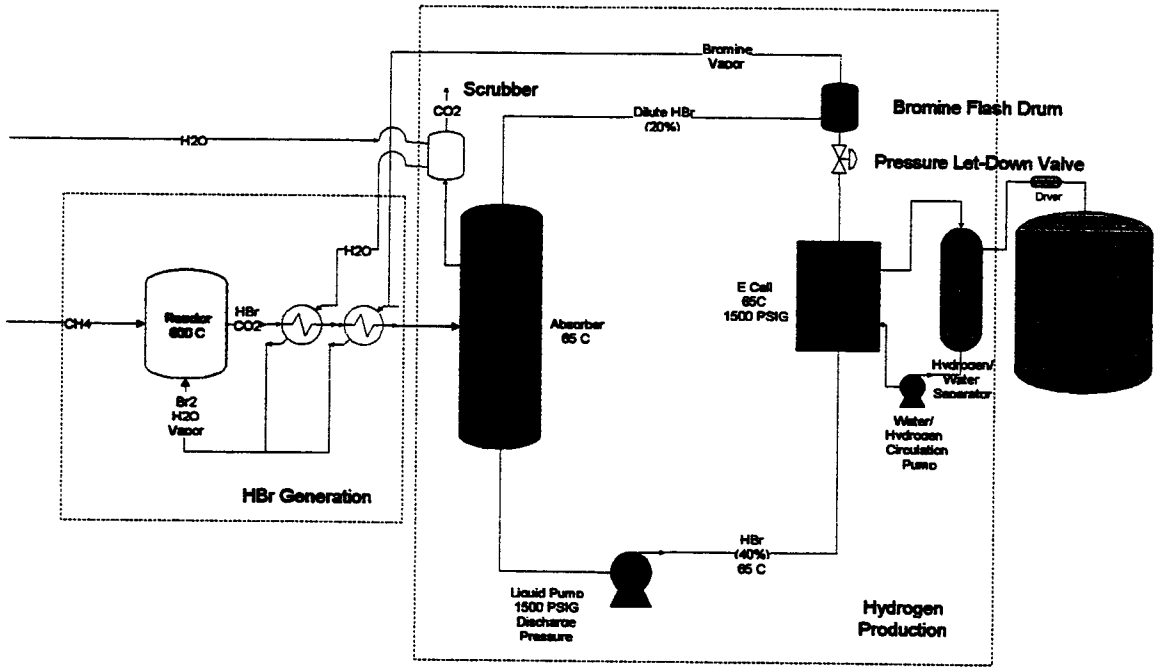

Figure 7. Hybrid Bromine-Steam-Methane Process Flow Diagram.

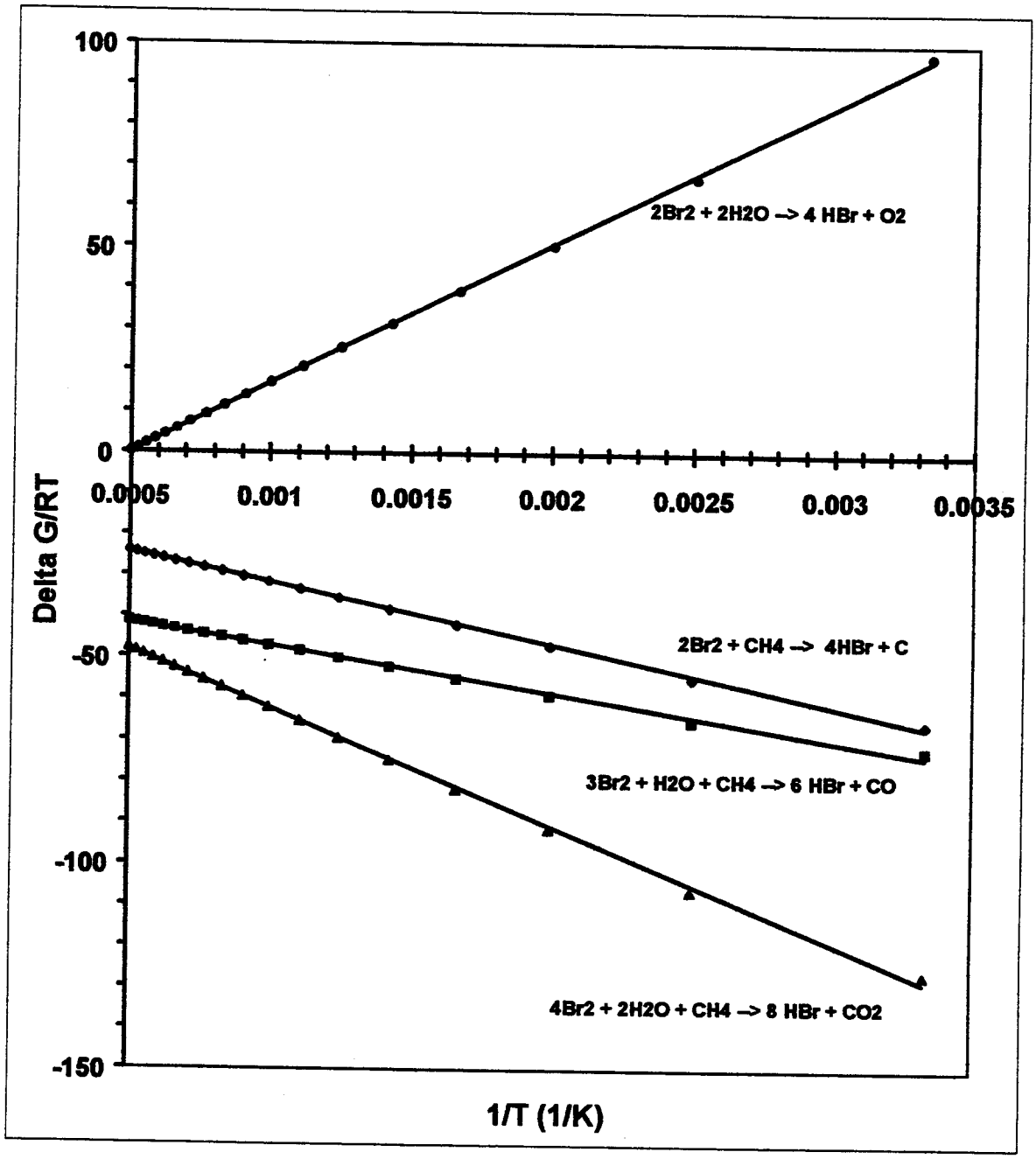

Figure 8. Free Energy of Bromine Reactions.

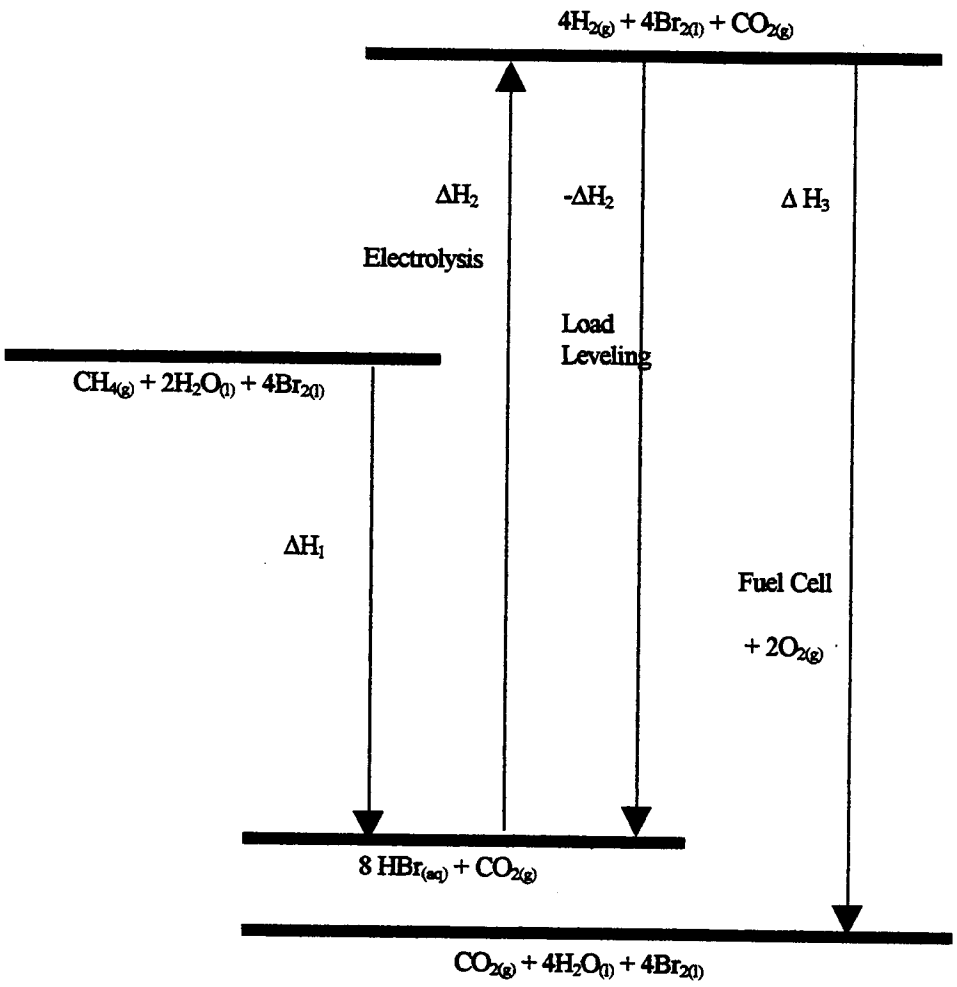

Standard Heats of Reaction, 298 K:

$\Delta H_1 = -719.4$ kJ
$\Delta H_2 = +972.4$ kJ
$\Delta H_3 = -1143.2$ kJ

Figure 9. Enthalpy Changes in Bromine-Steam-Methane Process.

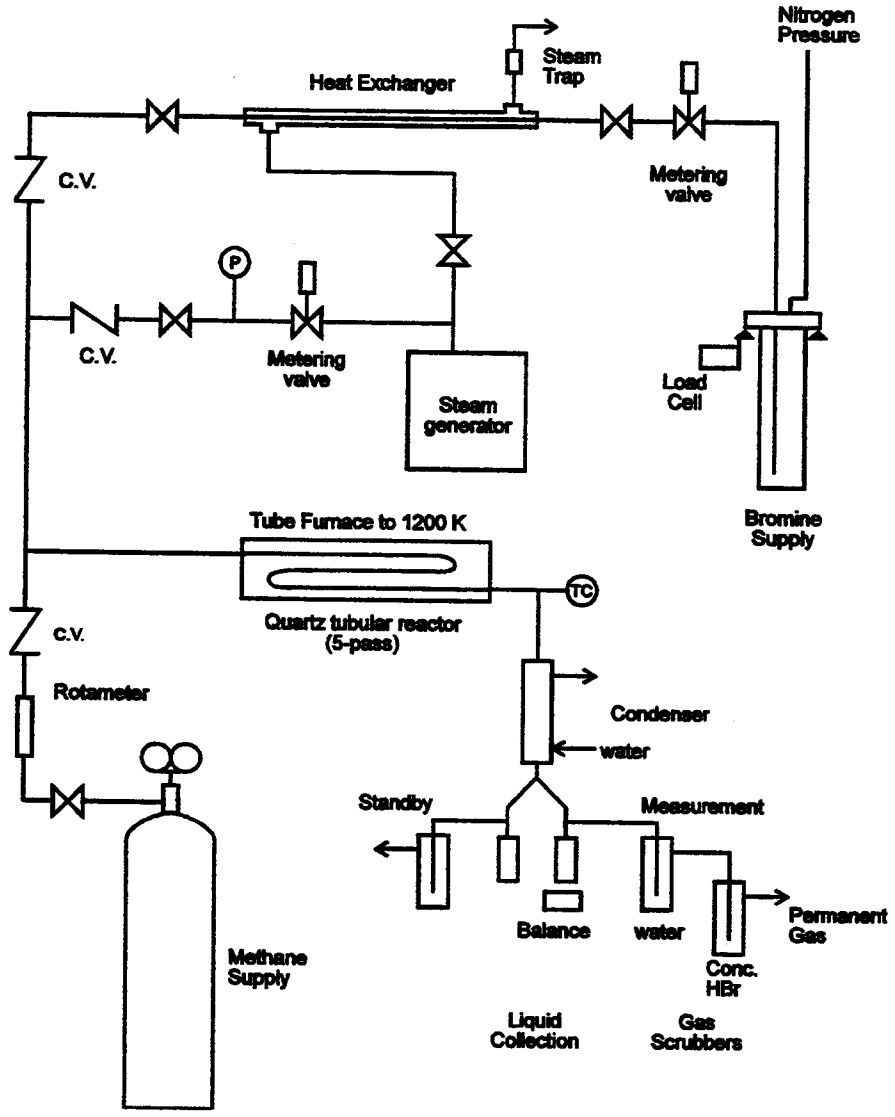

Figure 10. Experimental Bromine-Steam-Methane Apparatus.

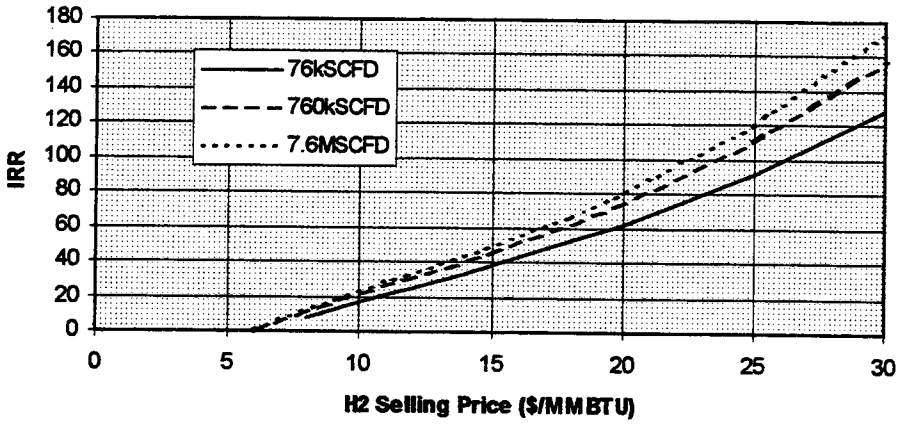

Figure 11a. Economic Model: Effect of plant size on IRR.

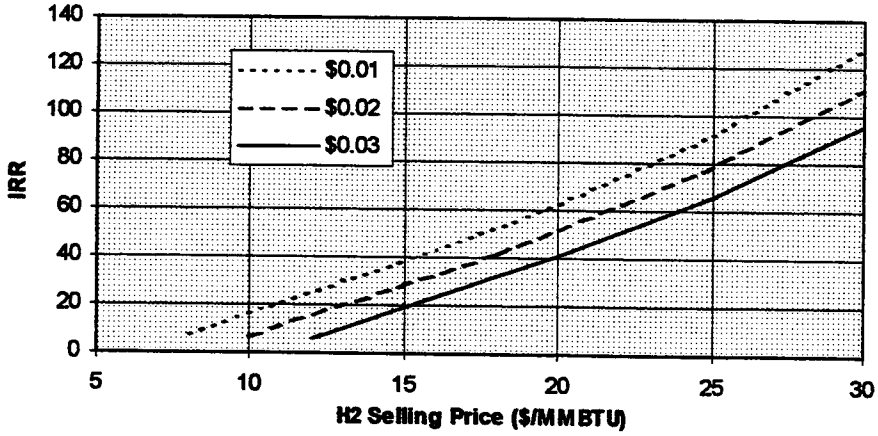

Figure 11b. Effect of Off-Peak Electricity Cost ($/kWh) on IRR.

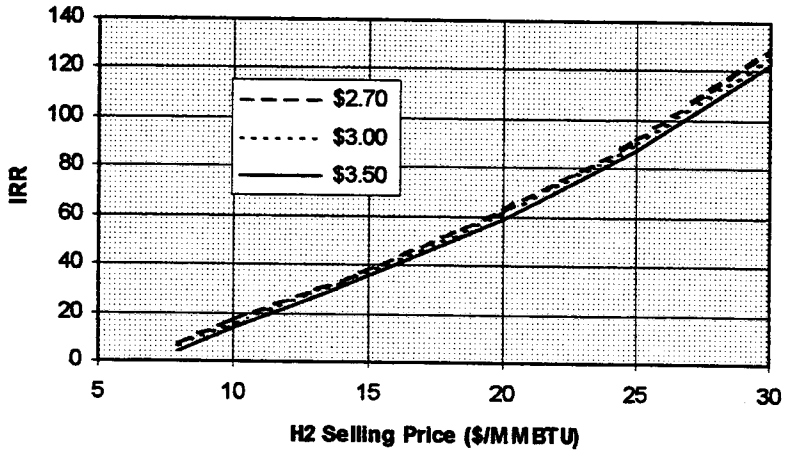

Figure 11c. Effect of Natural Gas Price ($/MMBTU) on IRR.

HYDROGEN-ENRICHED FUELS

Kirk Collier
NRG Technologies, Inc.
681 Edison Way
Reno, NV 89502

Abstract

NRG Technologies, Inc. is attempting to develop hardware and infrastructure that will allow mixtures of hydrogen and conventional fuels to become viable alternatives to conventional fuels alone. This commercialization can be successful if we are able to achieve exhaust emission levels of less than 0.03 g/kw-hr NO_x and CO; and 0.15 g/kw-hr NMHC at full engine power without the use of exhaust catalysts. The major barriers to achieving these goals are that the lean burn regimes required to meet exhaust emissions goals reduce engine output substantially and tend to exhibit higher-than-normal THC emissions. Also, hydrogen addition to conventional fuels increases fuel cost, and reduces both vehicle range and engine output power. Maintaining low emissions during transient driving cycles has not been demonstrated.

Our approach to overcoming these problems will be to investigate the applicability of known concepts and technologies that can overcome the barriers to success. To recuperate lost engine power, super/turbocharging, and increasing volumetric efficiency, compression ratio, engine speed and displacement are options. Combustion chamber design, valve timing and the "optimization" of tradeoffs between engine power and efficiency with spark timing are also important parameters.

During this initial year of funding, a test plan has been formulated to investigate questions regarding the nature of hydrocarbon emissions. Two fundamental questions to be answered are: (1) What is the ratio of reactive hydrocarbons in the exhaust stream to that of the fuel? and (2) Are any new hydrocarbon chemical species created in the exhaust? A test facility has been completed at the University of Nevada, Reno that will automate experimentation significantly. Tests can be made on both single-cylinder research engines as well as full-sized automotive and truck engines.

Background

The purpose of adding hydrogen to conventional fuels is to extend the lean limit of combustion to the point where harmful exhaust emissions become acceptable. Figure 1 shows a graphical representation of this principle. When excess oxygen is supplied to the combustable mixture, oxides of nitrogen, carbon monoxide and hydrocarbons all decrease. As excess oxygen increases, a point is reached where hydrocarbon emissions increase at a rapid rate. This point is called the lean limit. For conventional fuels operating in conventional engines, the emissions of oxides of nitrogen are not low enough to out perform catalyst technology. The addition of hydrogen allows greater amounts of excess oxygen without experiencing the rapidly increasing hydrocarbon emissions associated with the lean limit of combustion. Increasing the excess oxygen content allows for continuted reduction in oxides of nitogen emissions. The number one question is "How much hydrogen must be added to achieve desired exhaust emissions?"

Previous work in this area was performed by the NRG Technologies staff while at the Florida Solar Energy Center[1]. The results of that work are summarized in figures 2 through 4. Figure 2 shows the total hydrocarbon emissions as a function of equivalence ratio and percent of the volume of fuel mixture that is hydrogen. The base fuel is natural gas, consisting of 96% methane, and the engine was a Ford 4.6L V8. Notice that as hydrogen is added to the base fuel, the rapid rise in hydrocarbon emissions occurs at greater amounts of excess air (lower equivalence ratio). The anomalies here being that 10 and 20 percent hydrogen act similarly, as does 30 and 40 percent. The major extensions of the lean limit occur between 0 and 10, 20 and 30, and 40 to 50 percent hydrogen. Figure 3 shows the same relationships for oxides of nitrogen emissions. In this case the progression of lean limit extension as a function of hydrogen percentage does not exist. The reason for this discrepancy has to do with ignition timing. This set of tests were all performed with ignition timing set at a condition known as "MBT". This means the minimum ignition advance that results in the maximum brake torque of the engine. To understand the problems associated with the data in figure 3 an examination of the data shown in figure 4 is required. In figure 4, hydrogen percentage and equivalence ratio is fixed at 30% and 0.65 respectively. Oxides of nitrogen and hydrocarbon emissions are shown along with thermal efficiency plotted against ignition timing. Notice that NO_x emissions change over a factor of two while thermal efficiency changes only 10% for 12 degrees of ignition timing variation. The bottom line here is that for the test conditions, NO_x emissions are very sensitive to ignition timing while thermal efficiency (maximum brake torque) is not. Figure 5 demonstrates that this phenomenon is not inconsistent with the physics of internal combustion engines. This figure shows that emissions vary dramatically with ignition timing, but at a given air-fuel ratio, the thermal efficiency (specific fuel consumption) does not. These data were taken for gasoline in a standardized test engine.

Other research dealing with hydrogen-natural gas mixtures and lean burn has been conducted. The Bartlesville Energy Research Center[2] (BERC) and a joint project between Hydrogen Consultants, Inc. and Colorado State University[3] have published results. The BERC project investigated up to 20%, by volume, of hydrogen supplementation of natural gas. They concluded that:

1. The lean limit of combustion is extended by the addition of hydrogen.
2. The lean limit is not extended sufficiently to obtain exhaust emissions lower than that

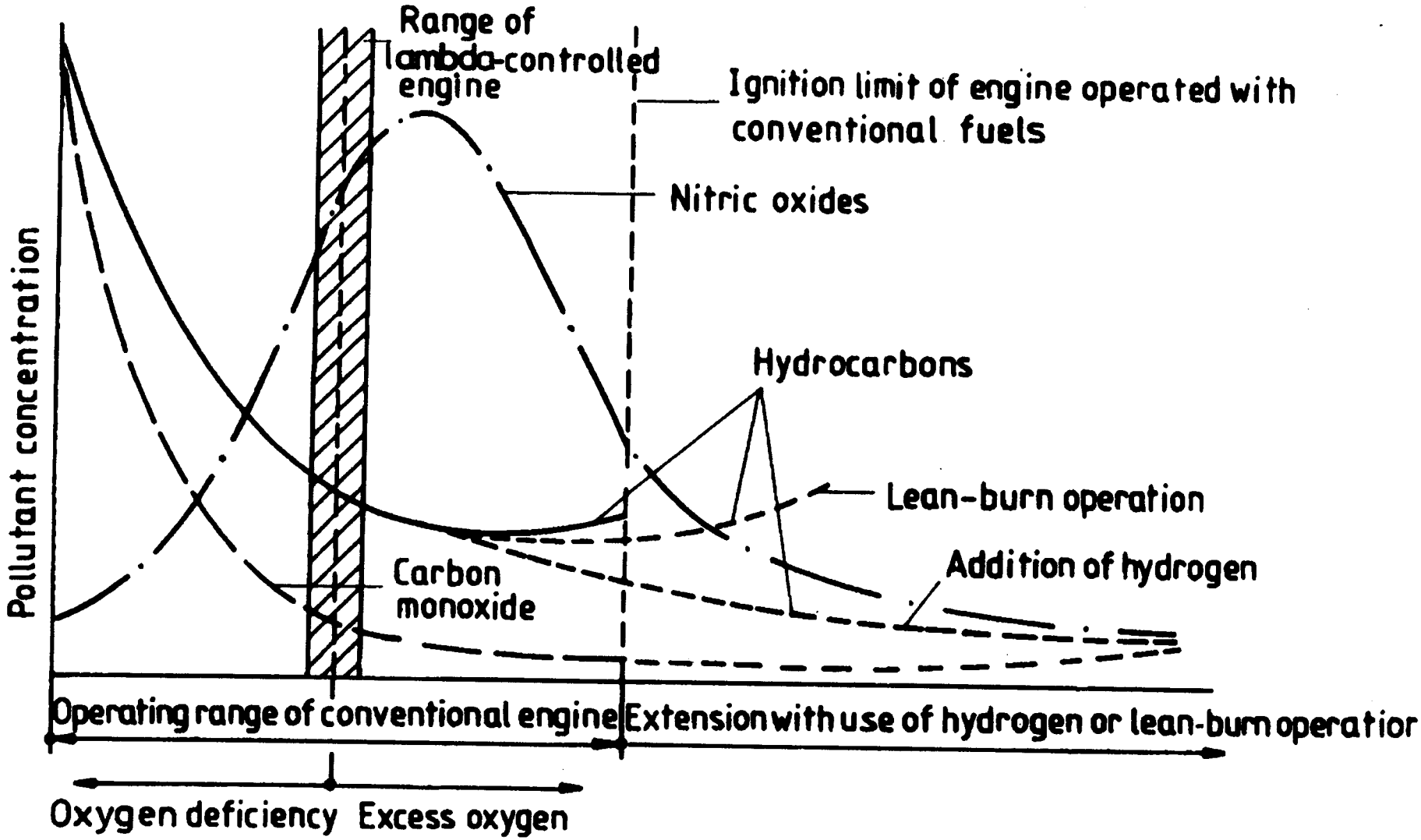

Figure 1. Exhaust emissions vs. air fuel ratio.

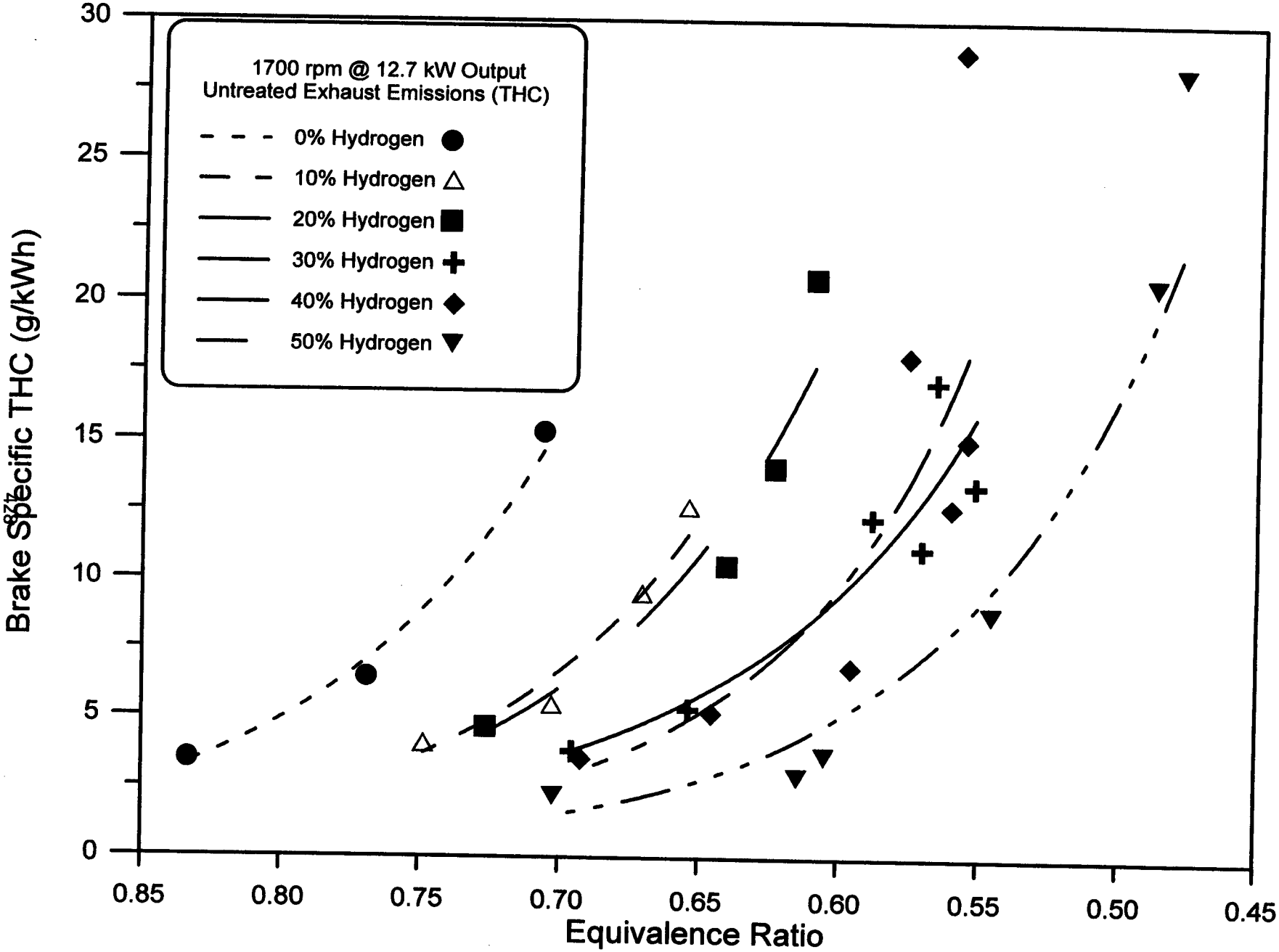

Figure 2. Hydrocarbon emissions vs. equivalence ratio for variable hydrogen content.

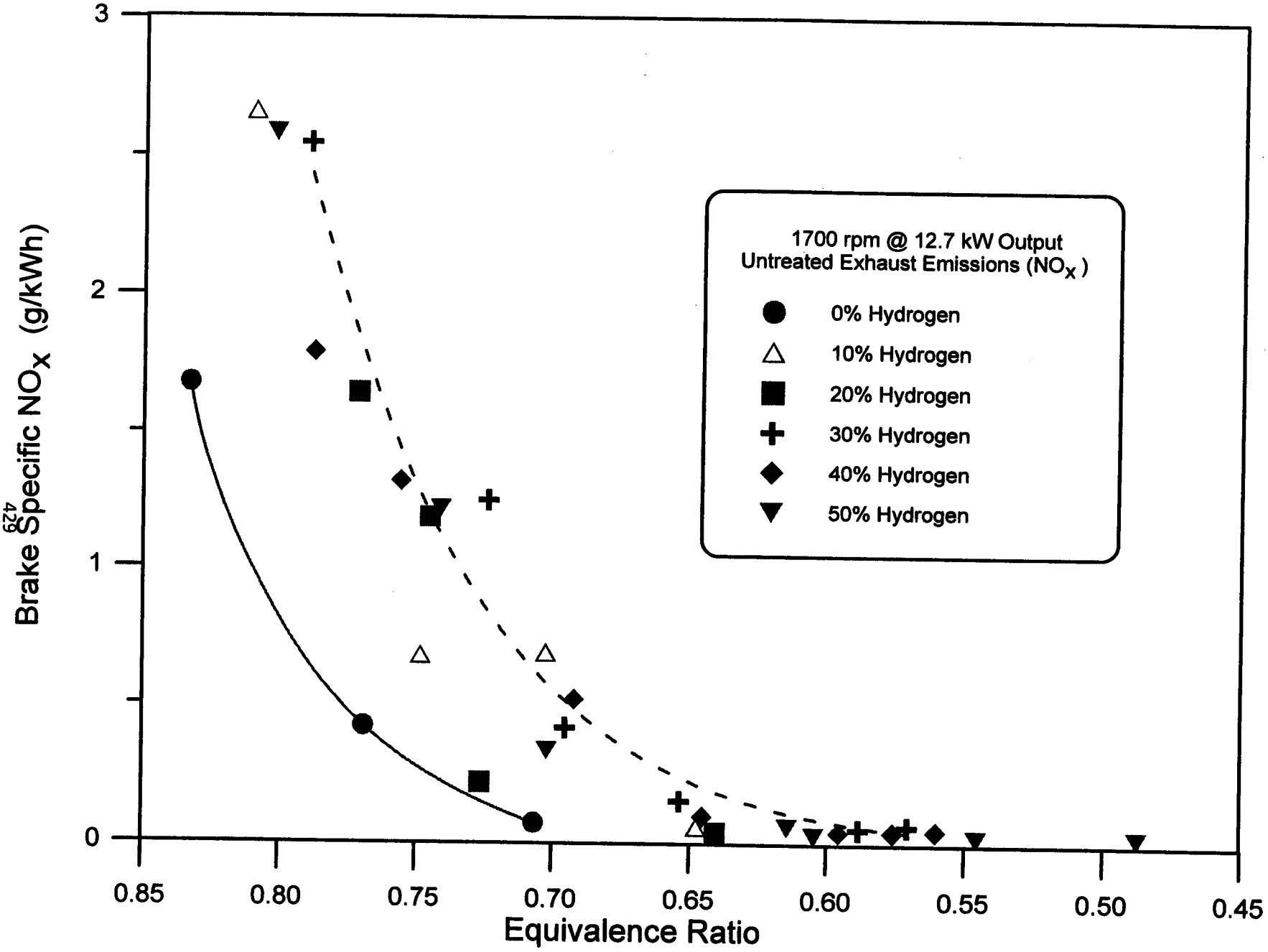

Figure 3. NO_x emissions vs. equivalence ratio for variable hydrogen content.

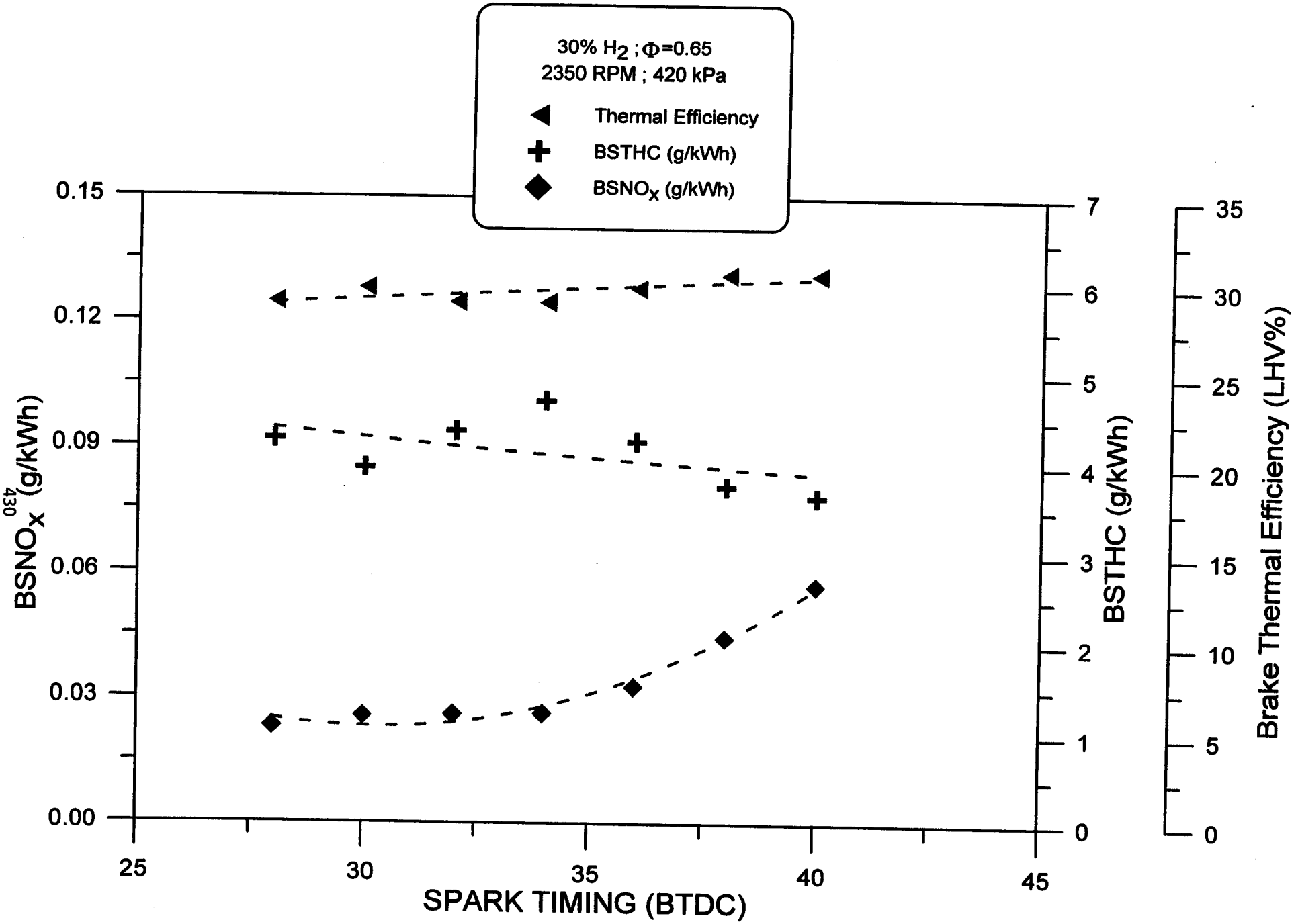

Figure 4. Exhaust emissions and thermal efficiency as a function of spark timing.

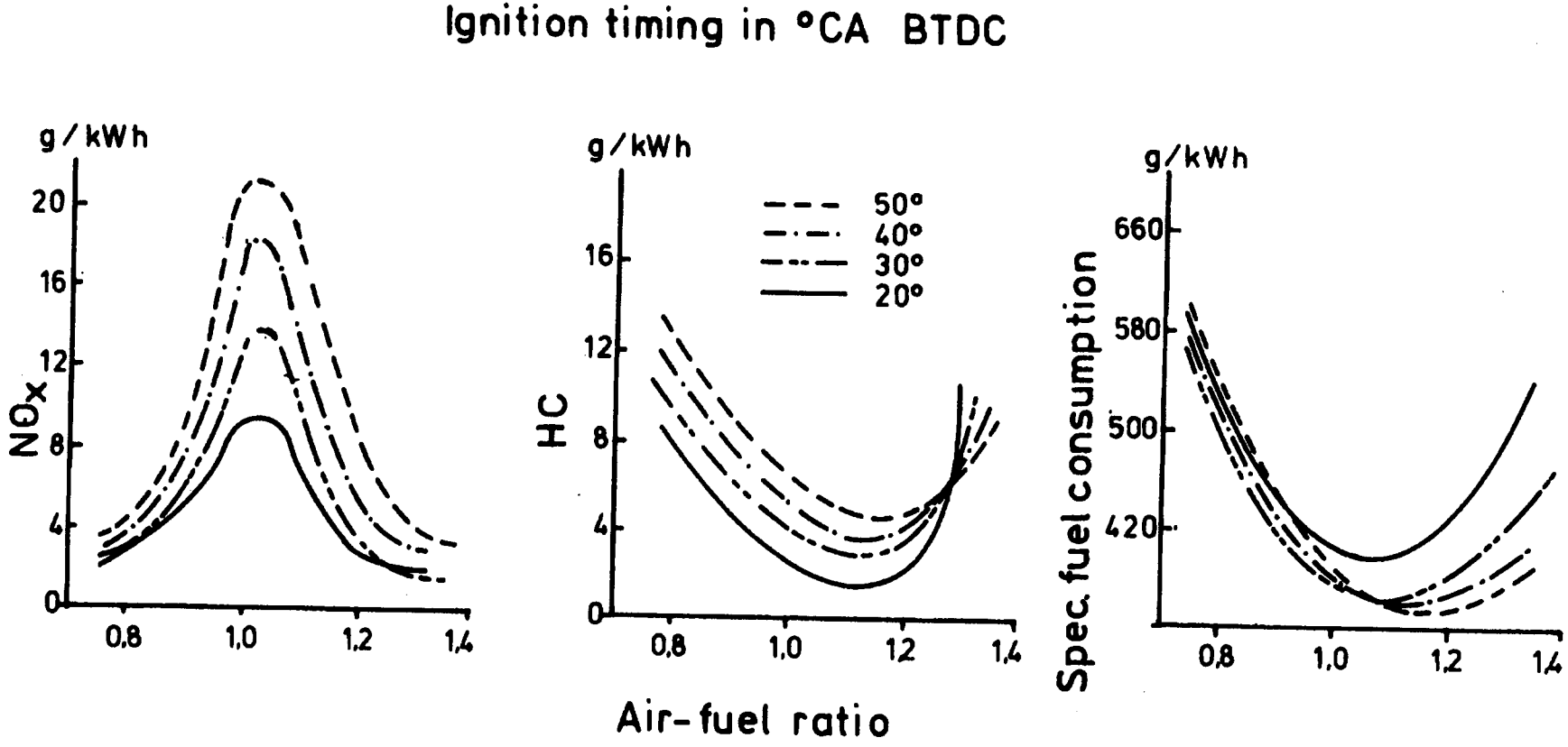

Figure 5. Exhaust emissions and efficency vs. air-fuel ratio for various ignition timings.

achieved by catalyst systems.

3. Exhaust gases are generally less reactive with hydrogen addition.

The HCI/CSU work looked at 15 to 30% hydrogen addition. Although that work looked at many other aspects to hydrogen natural gas mixtures, one lean-burn result is shown in figure 6. With retarded spark timing, they were able to produce extremely low NOx emissions with 30% hydrogen mixtures and equivalence ratios below 0.65. These data essentially verify the FSEC work.

Critical Areas of Interest

Relationship Between Hydrogen Content, Spark Timing and Emissions

To be a commercial success, the cost of the fuel must be kept to a minimum. This means that the hydrogen content of the fuel should be minimized. Although the work at FSEC was an important first step, the same degree of thoroughness must be applied to percentages of hydrogen other than 30%.

Photoreactive Hydrocarbon Emissions

Total hydrocarbon emissions are not sufficient to judge the efficacy of the concept. The portion of those emissions that are photoreactive in the atmosphere is the determining factor. At this time, that data is not available, but is critical to the technology.

Carbon Monoxide Emissions

None of the emissions data from FSEC included carbon monoxide. The HCI/CSU work indicated that CO emissions could be made near zero with an oxidizing catalyst. CO emissions are a critical pollutant whose effects must be quantified.

Recuperating Power Loss

A critical component of any transportation system is driveability. For approximately equal efficiency, the amount of power output will be proportional to the amount of fuel burned. Since the air fuel ratio is predetermined to achieve low emissions, the critical factor in determining power output will be the amount of air that can be passed through the engine. For the same amount of air, lean burn engines will produce less power. To maintain driveability, this power loss must be compensated for somehow.

Emissions Under Transient Conditions

Here-to-fore all of the emissions data available for lean burn mixtures of hydrogen and natural gas have been steady state data. Real world driving conditions as well as vehicle emissions testing involve transient driving conditions. It is mandatary that low exhaust emissions under transient conditions be demonstrated for the technology.

Relationship Between BMEP and Exhaust Emissions

The recuperation of power loss may include a scenario to increase the BMEP of the engine above that attainable by an unaltered induction system. Although the FSEC data would indicate that exhaust emissions are not a function of the engine BMEP, the maximum values of

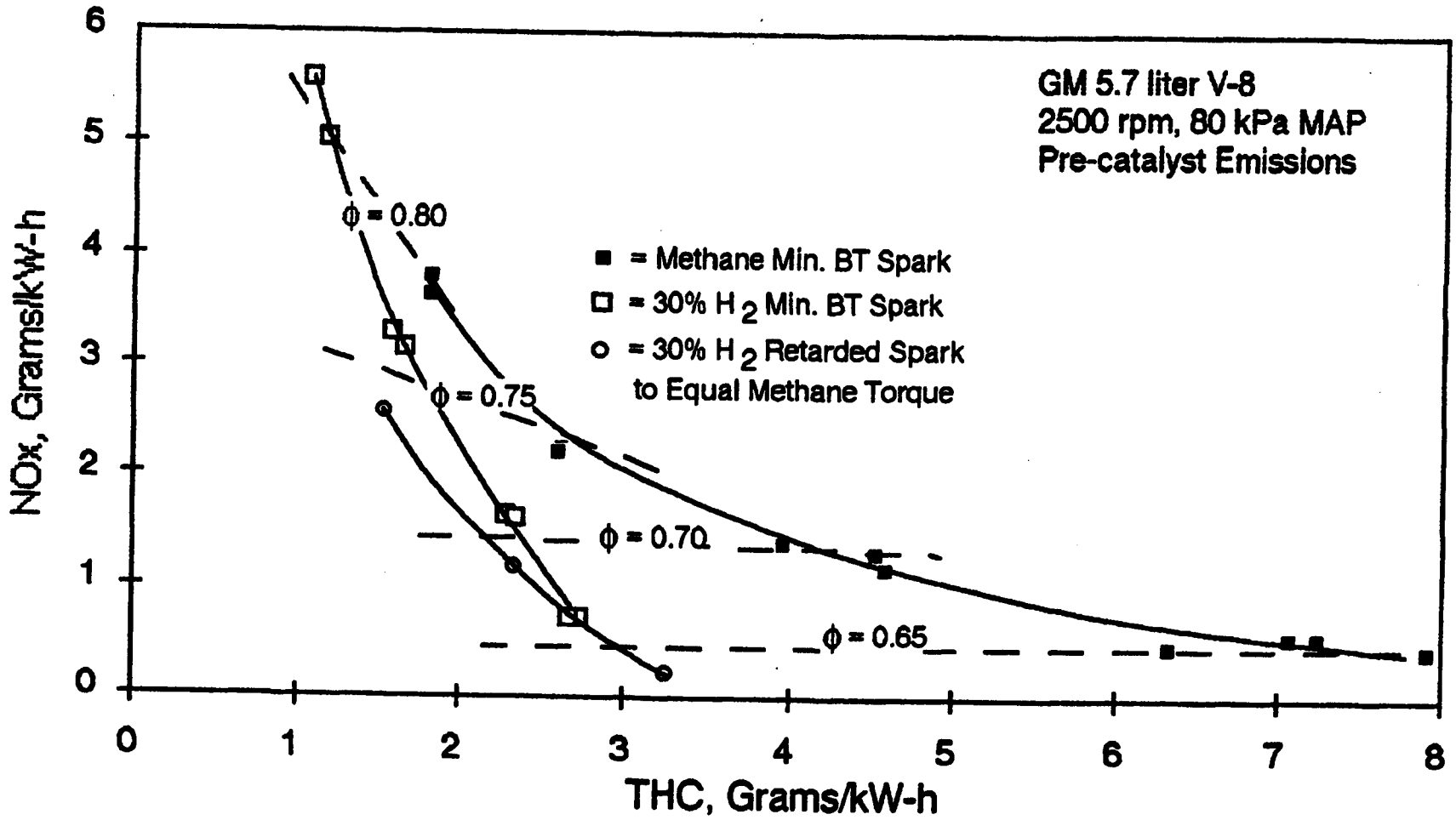

Figure 6. Exhaust emissions of various fuel blends and spark timings. (From Fulton et. al.)[3]

BMEP were low relative to that achieved with gasoline. The upper limit of BMEP to obtain 0.02 g/kWh of NO_x emissions is desirable. Also, it is important to know the trade-offs between high BMEP and NO_x emissions.

Engine Design Parameters

Compression Ratio:

Generally speaking, increasing compression ratio extends the lean limit of combustion, improves thermal efficiency and increases NO_x emissions. Therefore, the determination of optimum engine compression ratio will be a tradeoff between all of the above considerations.

Variable Valve Timing:

Figure 7 shows the tradeoffs between valve overlap and exhaust emissions. Basically, increasing valve overlap decreases NO_x emissions, but increase hydrocarbon emissions. Determining optimum valve overlap or implementing variable valve overlap as a function of engine load will be influential in engine configuration.

Bore-to-Stroke Ratio:

Figure 8 shows the relationships between bore-to-stroke ratio (s/D), cylinder volume, and air-fuel ratio. The indication is that hydrocarbon emissions will be influenced by both of these geometric parameters for all values of air-fuel ratio. In particular, this variation increases dramatically as lean burn conditions are reached. This phenomenon will influence the optimum cylinder geometry as well as the engine applications most suited to this technology.

Exhaust Gas Recirculation (EGR):

EGR is one of the most important techniques now used to control NO_x emissions. As shown in figure 9, EGR produces much lower hydrocarbon emissions for a given level of NO_x emissions than does lean burn. The major advantage to lean burn, is higher thermal efficiency. What is not shown is the combination of lean burn and EGR. Anecdotal evidence from this research team has indicated that EGR in combination with lean burn using hydrogen gas fuel mixtures did not improve NO_x emissions. In fact, that data showed increased NO_x emissions with any degree of external EGR. Philosophically, EGR creates an oxygen deficient mixture by introducing a semi-inert gas (nitrogen). Lean burn is just the opposite, it creates a surplus of oxygen in the mixture. The relationship between these two operational modes should be more scientifically investigated for hydrogen gas fuel mixtures.

Work Plan (Year One)

The Work Plan for the first year of the contract focuses on answering some of the questions posed in the previous section. One of the most important questions to be answered is the determination untreated exhaust emissions as a function of hydrogen content in the fuel. Although a great deal of work in this general area has already been done, a systematic study where all of the important engine operational parameters are optimized is still missing. The work at FSEC was very thorough at characterizing 30% hydrogen mixtures; however, the same degree of thoroughness for other fuel compositions is missing. As stated earlier, the intended purpose of introducing hydrogen to the fuel mix is to extend the lean limit of combustion. BERC concluded,

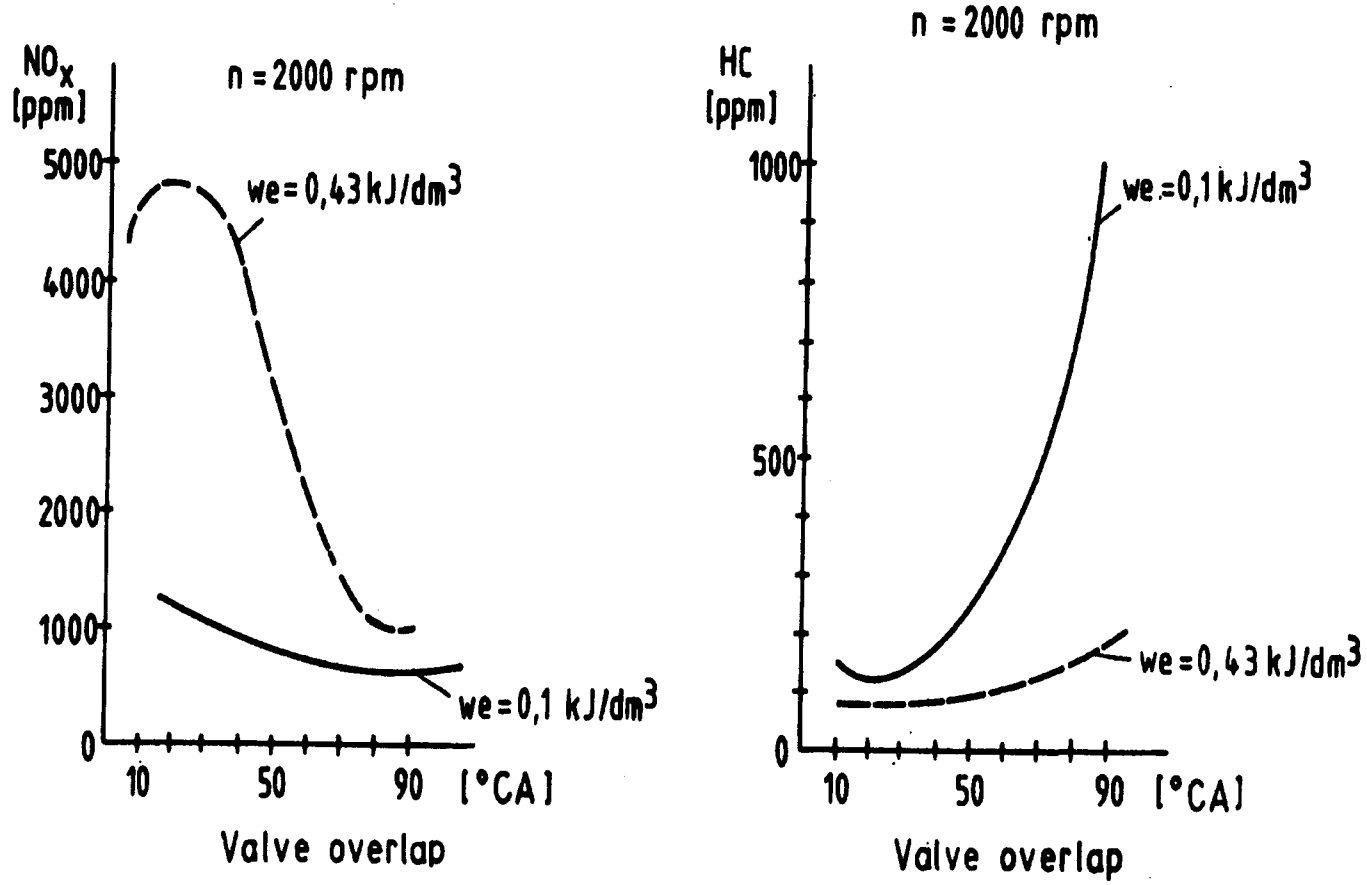

Figure 7. Exhaust emissions vs. valve overlap for variable engine loads.

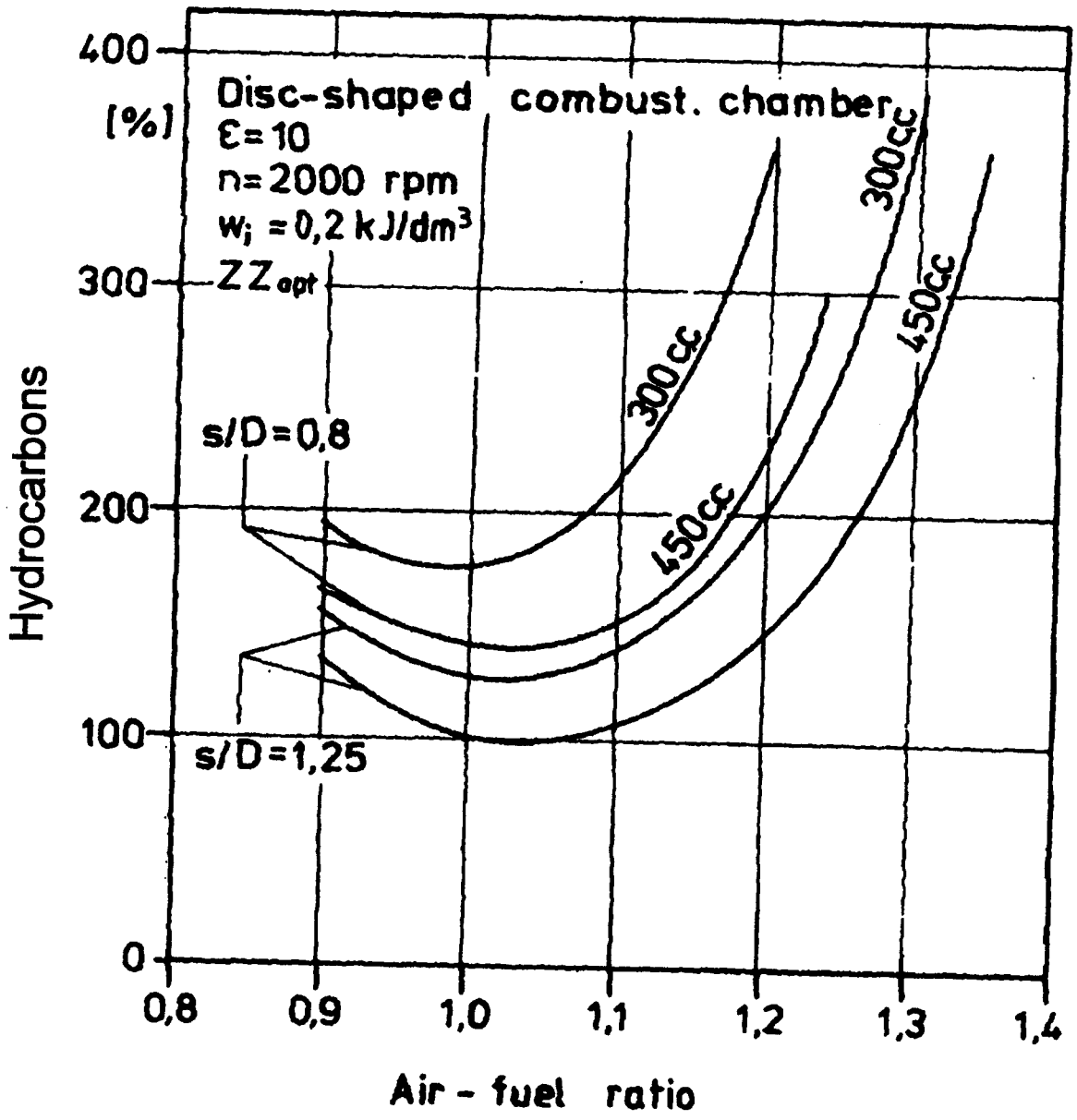

Figure 8. Hydrocarbon emissions vs. air-fuel ratio for various cylinder geometries.

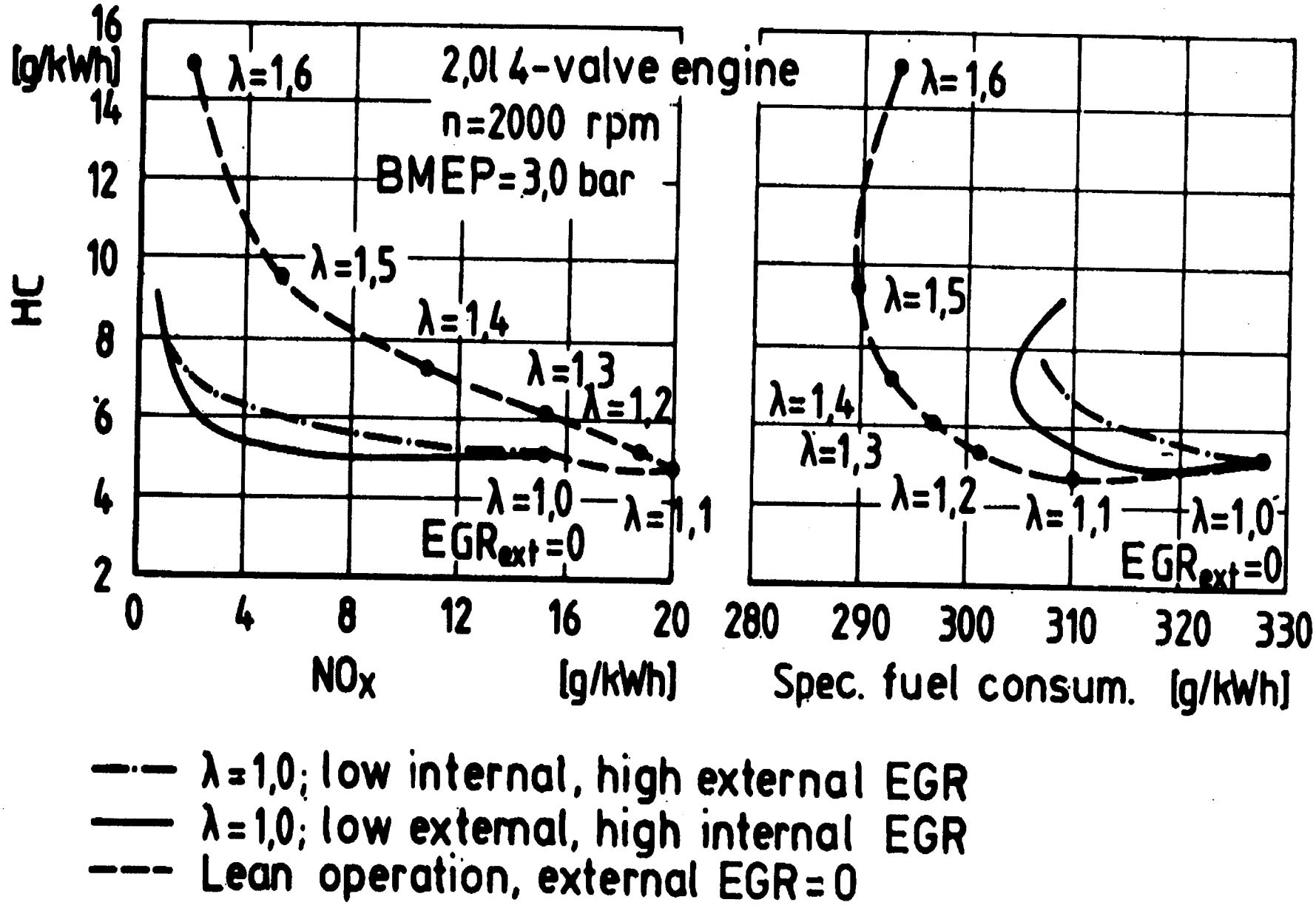

Figure 9. Exhaust emissions and engine efficiency vs. EGR and lean burn.

as did this research team while at FSEC, that 20% hydrogen addition does not produce lean burn exhaust emissions low enough to warrant the use of the fuel. What is needed is an analysis, similar to that done by FSEC, that characterizes emission levels for the primary engine parameters as a function of hydrogen content of the fuel. A complete map of these data is required to judge the commercialization potential of the technology.

Another important question regarding the performance of hydrogen gas fuel mixtures is the portion of hydrocarbon emissions that are photoreactive. An extensive test plan has been prepared to quantify this parameter. Gas mixtures have been prepared with known quantities of methane, hydrogen, propane and ethane. Testing will be performed to determine the ratio of propane and ethane exhaust emissions to that of the composition of the fuel. In addition, we want to determine if the chemical nature of the hydrocarbon exhaust emissions has changed from that of the fuel. Are we creating new photoreactive hydrocarbon emissions that were not present in the fuel? The speciation of these hydrocarbon emissions will be accomplished with a gas chromatograph and mass spectroscopy.

The commercial success of this technology will not be achieved without the demonstration of a driveable, clean vehicle. The last aspect of the first year's statement of work is to demonstrate that driveable vehicle. A 1997 Ford F-150 truck has been chosen as the platform of choice. There are two major reasons for this choice of vehicles. One is that the engine, a 4.6L V8 is the same engine that was used for the emissions studies performed previously by the current research team. The other is that a truck will allow for more fuel storage tank than a passenger car, thereby extending the driveable range of the vehicle to be more commensurate with that of a gasoline-powered vehicle.

Progress-to-Date

An engine test facility has been built at the Mechanical Engineering Department of the University of Nevada, Reno. The facility contains two dynamometer systems. One is a 1000 horsepower water brake used for developing fuel and spark maps on full-sized engines. The other is a 60 horsepower eddy-current used for research. A single-cylinder research engine has been developed that will serve as the platform to perform the research tasks detailed earlier.

Other features of this facility include: electronic throttle control, constant load/constant speed feedback control, computer-controlled spark timing and fuel delivery, fuel mass flow (coriolis device), air mass flow (exhaust lambda sensor in conjunction with laminar flow element), in-cylinder pressure transducer (optical), computer-based data acquisition system, in-cylinder data analysis package, and exhaust gas analysis equipment to measure CO, NO_x, and total hydrocarbon emissions with 0.1 ppm sensitivity.

The Ford F-150 vehicle has been converted operate on gaseous fuels. A composite compressed gas fuel storage tank is located within a tool box in the bed of the truck. The system is designed such that loads 8 feet long will still fit in the bed with the tail gate closed, up to a vertical height of 8 inches. This feature allows almost 100% utilization of the bed while still incorporating almost 1500 standard cubic feet of fuel. The gasoline fuel injection system has been

replaced by a gaseous system of our own design. An aftermarket engine computer system has been incorporated into the present wiring harness such that both the Ford engine computer and the added computer can jointly read sensors and perform dual functions. The vehicle has been successfully operated on both 25% and 30% hydrogen-natural gas mixtures. At this time, the fuel and spark maps developed are rudimentary (similar to those developed by this research team previously in Florida). They have been developed through on-the-road testing and have not been optimized for minimizing exhaust emissions. Finalized fuel and spark maps will be developed at the dynamometer facility.

References

1. Collier, K., et. al., "Untreated Exhaust Emissions of a Hydrogen-Enriched CNG Production Engine Conversion", SAE Technical Paper Series 960858, International Congress and Exposition, Detroit, Michigan, February 26-29, 1996.

2. Eccleston, D.B., and R.D. Fleming, "Engine Emissions Using Natural Gas, Hydrogen-Enriched Natural Gas, and Gas Manufactured from Coal (Synthane)", Bureau of Mines Automotive Exhaust Emissions Program, U.S. Department of Interior, Technical Progress Report-48, 1972.

3. Fulton, J., et. al., "Hydrogen for Reducing Emissions from Alternative Fuel Vehicles", SAE Technical Paper Series 931813, Future Transportation and Technology Conference, San Antonio, Texas, August 9-12, 1993.

INCORPORATING CARBON DIOXIDE SEQUESTRATION INTO HYDROGEN ENERGY SYSTEMS

Phil DiPietro
Energetics, Inc.
501 School Street SW
Washington, DC 20024

ABSTRACT

Adding carbon dioxide (CO_2) recovery to a grass-roots natural gas reforming plant with a hydrogen production capacity of 25 MMSCFD or more increases the cost of hydrogen by roughly 0.5 $/MMBtu. For a system of distributed gas-station-size hydrogen production units, the incremental cost of CO_2 capture and transport to a sequestration area is 3 $/MMBtu. Adding CO_2 recovery to a conventional natural-gas-based hydrogen energy system reduces the full life-cycle CO_2 emissions by 35%. For biomass systems, the impact of CO_2 sequestration is much higher. Advanced natural gas and biomass-based hydrogen production technologies, funded by the Hydrogen Program, increase the percent of total CO_2 emissions that are captured compared to conventional options.

INTRODUCTION

Dr. Robert Williams of Princeton University has proposed that capturing and sequestering CO_2 from hydrogen-based energy systems is a good, low-cost means of reducing CO_2 emissions in the transportation sector. The essence of his idea is that in a reformer/pressure swing adsorber (PSA) system, CO_2 is in a concentrated form relative to the flue gas from other energy systems. Previous studies have shown that capturing CO_2 represents most of the total cost of sequestration (Williams, 1996). Thus, if capturing CO_2 from a hydrogen system is inexpensive, the incremental cost of sequestration should be small. The Hydrogen Program systems analysis team was asked to assess Dr. Williams' concept, verify the cost estimates for capturing carbon dioxide, and assess the degree to which currently funded activities are complimentary to the concept of CO_2 sequestration.

The approach of this analysis is to estimate the cost and full life-cycle carbon dioxide emissions of several conceptual systems designed to provide hydrogen gas at 5,000 psi pressure to fuel cell-powered passenger vehicles, both with and without carbon dioxide sequestration systems. Using fuel efficiency projections for fuel cell-powered passenger vehicles, the results are normalized per mile of transportation provided. The cost and emissions from the natural gas- and biomass-based hydrogen systems are compared to both a gasoline internal combustion engine (ICE) system and a hydrogen system based on electrolytic hydrogen production.

Table 1. Hydrogen Production and Delivery Systems
Large-scale steam reforming of natural gas A steam reformer/shift reactor/PSA unit is built near a large natural gas supply. Carbon dioxide is recovered from the PSA and transported via pipeline to a depleted natural gas well where it is sequestered. A pipeline transports the hydrogen from the reformer to an urban area where it supplies a network of vehicle fueling stations. Each station consists of a connection to the pipeline, a high-pressure hydrogen compressor, a cascade hydrogen storage system, and a dispensing bay. The reformer operates at a level production rate, and the pipeline and the high-pressure storage tanks are used to buffer hydrogen supply and demand.
Distributed steam reforming of natural gas A small-scale steam reformer/shift reactor/PSA unit is located at a dispensing station and uses natural gas from the existing pipeline infrastructure. Carbon dioxide is captured from each dispensing station. The CO_2 from a geographic cluster of stations is aggregated into a large pipeline and transported to a depleted gas well or other suitable geological structure where it is sequestered. Hydrogen from the reformer unit is compressed and stored on-site. The reformer operates at a level production rate, and high-pressure storage tanks are used to buffer hydrogen supply and demand.
Biomass pyrolysis; reforming of biocrude A large-scale biomass pyrolysis unit is located in a rural area with good dedicated biomass resources. Biomass feedstock is pyrolyzed forming a liquid product which is then separated into two fractions. One fraction is sold as a feedstock for adhesive manufacture; the other is reformed to produce hydrogen gas. The reforming feedstock is a liquid at ambient conditions and is transported by truck or rail to a network of gas-station-size reformers, eliminating the need for a hydrogen pipeline. The pyrolysis oil reformer is similar to the small-scale natural gas reformer, and the hydrogen compression and storage systems and the CO_2 recovery and sequestration system are the same.
Large-scale biomass gasification A large-scale biomass gasifier is located in a rural area with good dedicated biomass resources. The gasifier feeds syngas to a reformer/shift reactor/PSA system. Carbon dioxide is recovered from the PSA and transported via pipeline to a depleted natural gas well where it is injected. A pipeline transports the hydrogen from the gasification unit to an urban area where it supplies a network of vehicle fueling stations. Each station consists of a connection to the pipeline, a hydrogen compressor, a cascade hydrogen storage system, and a dispensing bay. The gasifier operates at a level production rate, and the pipeline and the high-pressure storage tanks are used to buffer hydrogen supply and demand.
Wind turbine / distributed PEM electrolyzer Electricity is produced by a group of wind turbines located in a remote area with high-quality wind resources (e.g., North Dakota). During off-peak hours, electricity from the wind turbines is used to produce hydrogen via electrolysis. Electricity is wheeled through several utility districts to a network of small scale PEM electrolyzers/ dispensing stations. Hydrogen from the electrolyzers is compressed and stored on-site. This is a non-CO_2-producing control case.

The carbon dioxide sequestration scenarios developed by Dr. Williams assume large-scale hydrogen production systems near a CO_2 injection site with the hydrogen product pipelined to the users. Analyses performed previously by the Hydrogen Program indicate that small-scale distributed hydrogen production sites are needed to serve the initially small and geographically dispersed hydrogen-fueled vehicle market. We have assessed the economics of adding CO_2 sequestration to the centralized hydrogen production systems envisioned by Dr. Williams, and of adding a CO_2 capture and sequestration system to an existing network of dispersed, small-scale hydrogen production sites. The hydrogen energy systems considered are described in Table 1.

The Hydrogen Program is funding research into several natural gas- and biomass-based technologies. Notable among these are the Air Products & Chemicals' Sorbent Enhanced

Reforming Process (SERP), the Ion Transport Membrane (ITM) gasification process being developed by the Hydrogen Program in cooperation with the Office of Fossil Energy, and the biomass pyrolysis process being developed at NREL. We have assessed how amenable each of these technologies is to carbon dioxide sequestration as compared to conventional systems.

ASSUMPTIONS

The systems are set 20-30 years in the future. Each system is designed to produce 25 MMSCFD of hydrogen, which is enough fuel to supply roughly 170,000 fuel-cell passenger vehicles, all of which are to be operated within a single metropolitan area. In some instances, significant cost reductions have been assumed based on technology development and/or large volume manufacturing.

The full implications of sequestering large amounts of CO_2 in oil fields and saline aquifers is not known. Without studying the issue in detail, we assume there are no significant detrimental effects.

It is assumed that on-board hydrogen storage and hydrogen-fueled power systems will advance to the point that if hydrogen vehicle fuel costs are compatible with gasoline, hydrogen cars will be competitive with gasoline ICE vehicles.

In normalizing the fuel costs and CO_2 emissions for the gasoline and hydrogen systems to a "per mile" basis, it is assumed that the gasoline car (most likely not a conventional ICE power system) gets 80 mpg and the fuel-cell vehicle (FCV) travels 180 miles per kg of hydrogen. The fuel-cell vehicle efficiencies are taken from work done by DTI for the Ford Motor Company.

The analysis includes an electrolysis-based hydrogen production system in which off-peak electricity from a remote high-quality resource is wheeled to a city and distributed to a network of PEM electrolyzers. This system assumes advanced electricity transmission and distribution technology and a more open contractual access to transmission lines. These assumptions are both possible outcomes of utility industry deregulation.

Maintaining the capability to dispense hydrogen during O&M-related down-time is an issue for all of the systems evaluated, but especially for the small-scale distributed hydrogen production systems. Backup liquid hydrogen storage or other measures are assumed to be unnecessary.

RESULTS

Figure 1 shows the cost of hydrogen production for the various hydrogen energy systems considered. The distributed reformer system has hydrogen production cost comparable to the centralized hydrogen production options, but it is not as amenable to CO_2 sequestration. The renewable electricity / electrolysis system, even under aggressive assumptions regarding component costs, is more expensive than the large-scale natural gas-based hydrogen production system with carbon dioxide sequestration, although the natural gas has higher full life cycle CO_2 emissions.

Figure 2 shows the hydrogen costs normalized per mile of transport. The costs are presented as a ratio to the cost per mile for an 80 mpg gasoline vehicle. Figure 2 shows that the potential future fuel costs for hydrogen systems are comparable to gasoline (even at 80 mpg). Also, the cost impact of CO_2 sequestration is small for large-volume hydrogen production.

Figure 3 shows the full life-cycle CO_2 emissions from the 80 mpg gasoline vehicle and the various hydrogen energy systems considered. A significant improvement in CO_2 emissions is achieved just by changing from gasoline to SMR-based hydrogen. The addition of CO_2 sequestration reduces the emissions by another 40-50%. The overall CO_2 performance of biomass-based systems is better than natural gas based systems, and the introduction of CO_2 sequestration produces more significant effects.

In a conventional steam reformer, roughly 35% of the feedstock is burned to provide heat. The CO_2 from the burned feedstock is non-capturable. Two advanced hydrogen production technologies supported by the Hydrogen Program can potentially reduce the amount of non-capturable CO_2 for carbon-based processes, and improve the CO_2 emissions performance of hydrogen-based energy systems overall. The SERP process reduces the temperature of the reforming reactor and thus lowers the heat requirement. Also, recovering CO_2 from the SERP process may be easier than the separation required in a conventional reformer. In a partial oxidation unit (POX) unit, all the carbon is contained in the process stream, and the percent of the total CO_2 that can be recovered is limited by the efficiency of the separation process. The ITM technology has the potential to enhance the economics of POX by eliminating the need for an oxygen source. Figure 4 shows CO_2 emitted and captured in hydrogen energy systems with conventional and advanced natural gas-based hydrogen production technologies. Figure 4 also shows that emissions due the consumption of grid electricity are a significant contributor to full life-cycle emissions.

SENSITIVITY OF RESULTS

Because the key process components of the sequestration systems (a steam reformer or gasifier, a PSA with a CO_2 recovery system, gas pipelines, and compressors) are mature technologies, the feasibility and cost of capturing CO_2 does not rely on technology development.

Site-specific factors cause significant variation in the cost of hydrogen pipelines, especially at the distribution level. For the hydrogen pipeline systems, increasing the distribution pipeline cost from 300,000 to 600,000 $/mile would raise the cost of hydrogen by 10-15%.

Although small-scale reformers are currently being built through a joint venture with IFC and Praxair, the capital and O&M costs achievable under mass production are unknown. For the small-scale natural gas reformer system, increasing the capital cost and O&M of the reformer by 50% raises the cost of delivered hydrogen by 7%.

Including a liquid hydrogen backup system to keep the stations operable during maintenance activities would increase the cost of delivered hydrogen by 5-10%.

ACKNOWLEDGMENTS

This analysis draws heavily on work previously performed by Sandy Thomas, Joan Ogden, and Maggie Mann. Their input and technical review of the draft substantially improved the analysis product.

REFERENCES

Fuel Decarbonization for Fuel Cell Applications and Sequestration of the Separated CO_2, Robert H. Williams, PU/SEES Report No. 295, January 1996

"Hydrogen Production from Natural Gas, Sequestration of Recovered CO_2 in Depleted Gas Wells, and Enhanced Natural Gas Recovery," K. Block et al. *Energy*, Vol 22 No. 2/3, pp. 161-168, 1997

Technical and Economic Assessment of Producing Hydrogen by Reforming Syngas from the Battelle Indirectly Heated Biomass Gasifier, Margaret K. Mann, NREL/TP-431-8143, August, 1995

SRI International Economics Program, Report No. 212, Options for Refinery Hydrogen, Susan M. Leiby, February, 1994

"Hydrogen and Carbon Dioxide Coproduction from SMR Offgas by Pressure Swing Adsorption," W.C. Kratz et.al., AIChESymposium Series, 1988

Ford Hydrogen Infrastructure Report, Bob Moore, March, 1996

Hydrogen Production and Fueling System Infrastructure for PEM Fuel Cell-Powered Vehicles, T.G. Halvorson, C.E. Terbot, and W. Wisz, Praxiar, Inc., April, 1996

Annual Energy Outlook 1997, DOE/EIA-0383(97), December, 1996

"U.S. pipelines report mixed results for 1993," *Oil & Gas Journal*, Nov. 21, 1994, pp. 41- 63

The Economics of Biomass Production in the United States, R.L. Grahm et. al., 1995

"Summary of Wind Resource Assessment Activities in Minnesota," Rory Artig, American Wind Energy Association 1995 Annual Report, pp. 419-426

DOE Office of Utility Technologies Technology Characterization, Joe Cohen, Jack Cadogan, 12/96

"Catching a Steady Breeze: Putting Wind Power to Work on Electric Utility Systems," *The Electricity Journal*, March, 1995, M. Brower and M. Tennis

Transmission Line Capital Costs, K.R. Hughes, D.R. Brown of PNNL, prepared for US DOE under contract DE-AC06-76RLO 1830, May 1995

Figure 1. Hydrogen Production Cost from Various Options

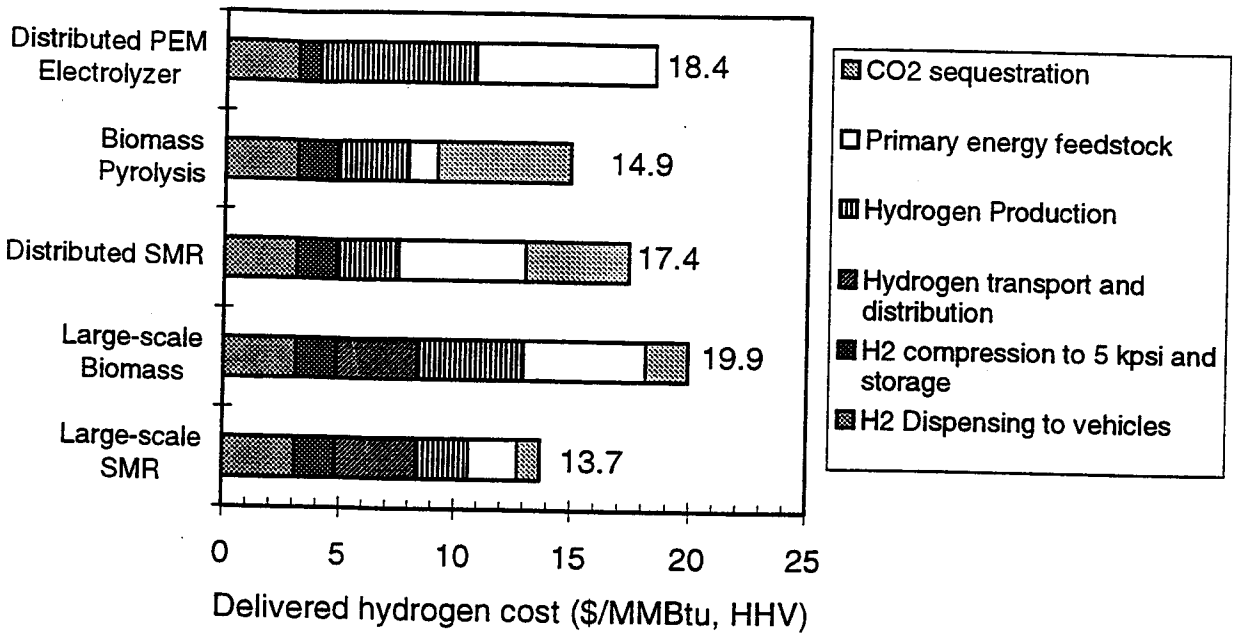

Figure 2. Cost of Hydrogen Delivered to a Vehicle at 5 kpsi Compared to Gasoline

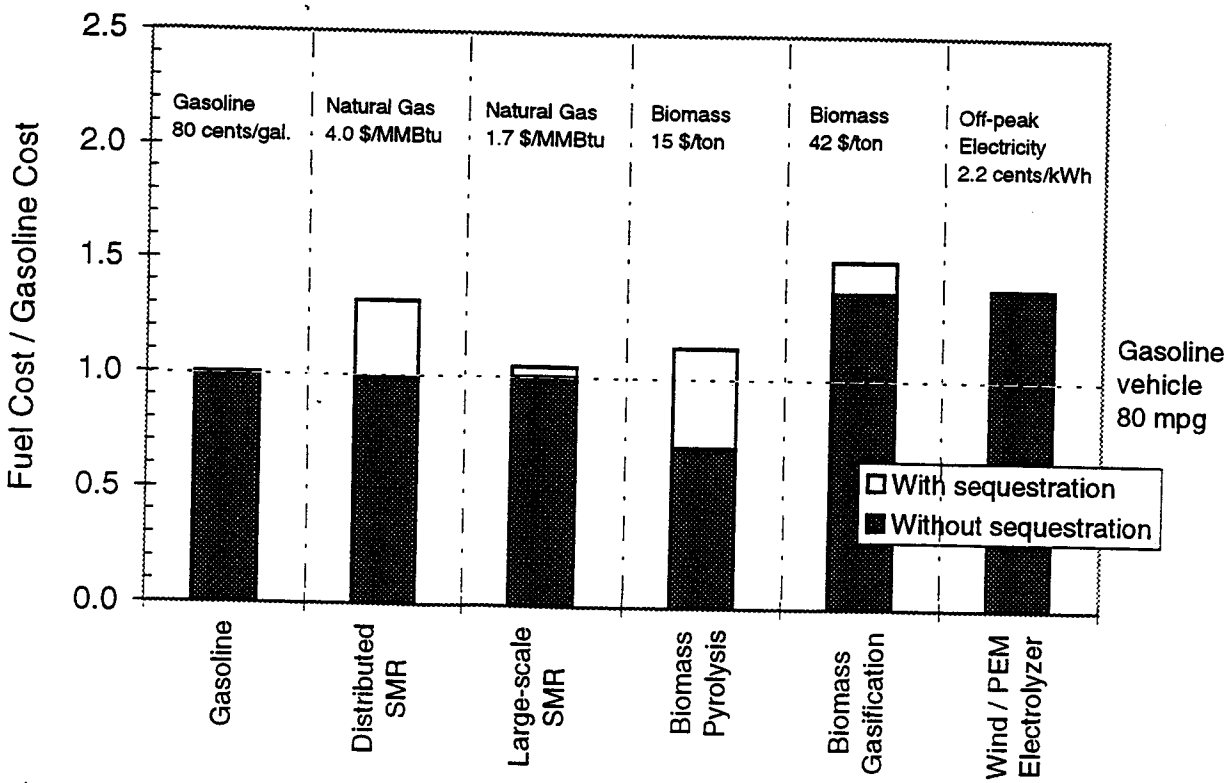

Cost based on systems serving 170,000 vehicles in a single metropolitan area.
FCV efficiency 180 miles per kg.

Figure 3. Full Life-Cycle Carbon Dioxide Emissions for Hydrogen Options Compared to a Gasoline ICE

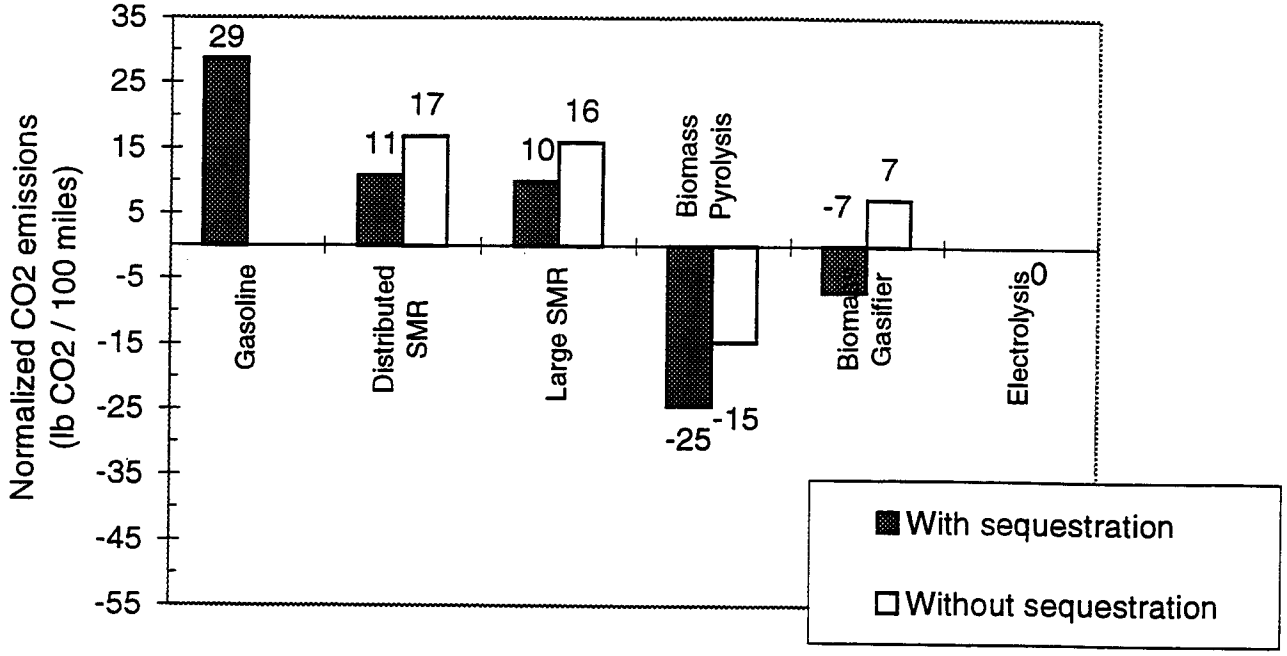

Gasoline ICE efficiency 80 mpg, FCV efficiency 180 miles per kg H2

Figure 4. Capturable and Non-capturable Emissions from Hydrogen Production Systems

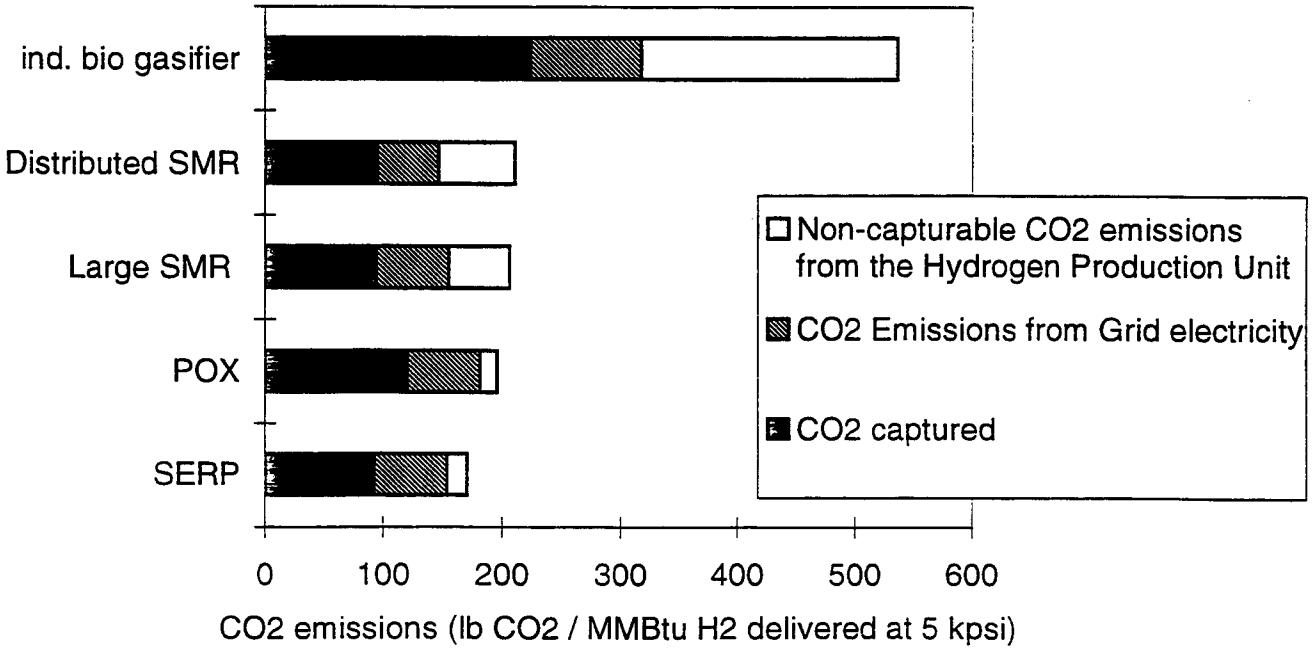

Grid electricity emissions based on 1.76 lbs CO2 / kWh
SERP emissions based on 25% feedstock use reduction compared to large scale reformer

Figure 1. Hydrogen Production Cost from Various Options

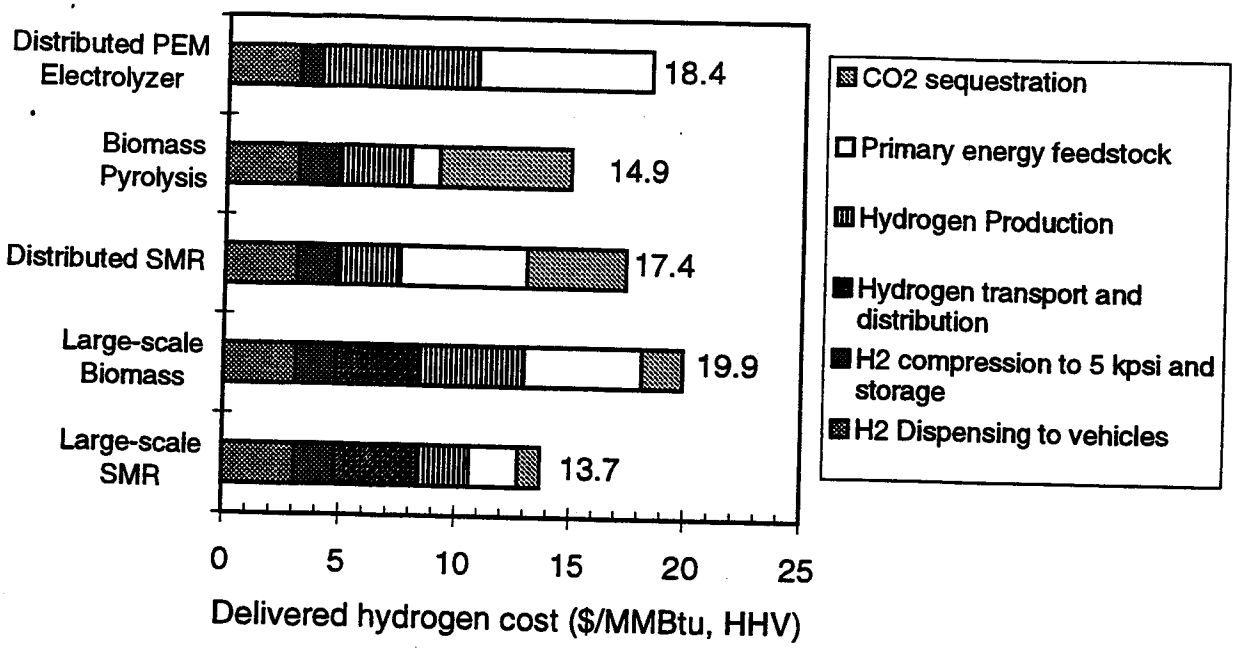

Figure 2. Cost of Hydrogen Delivered to a Vehicle at 5 kpsi Compared to Gasoline

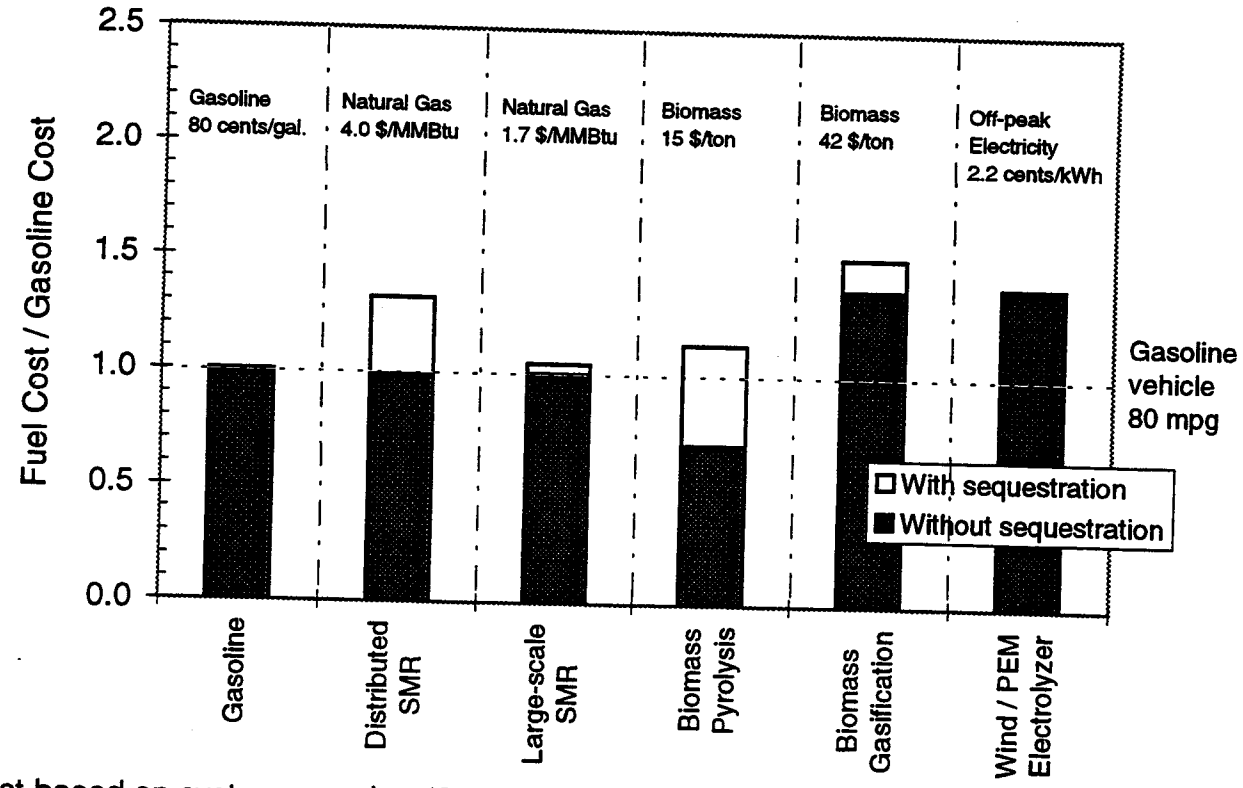

Cost based on systems serving 170,000 vehicles in a single metropolitan area.
FCV efficiency 180 miles per kg.

Figure 3. Full Life-Cycle Carbon Dioxide Emissions for Hydrogen Options Compared to a Gasoline ICE

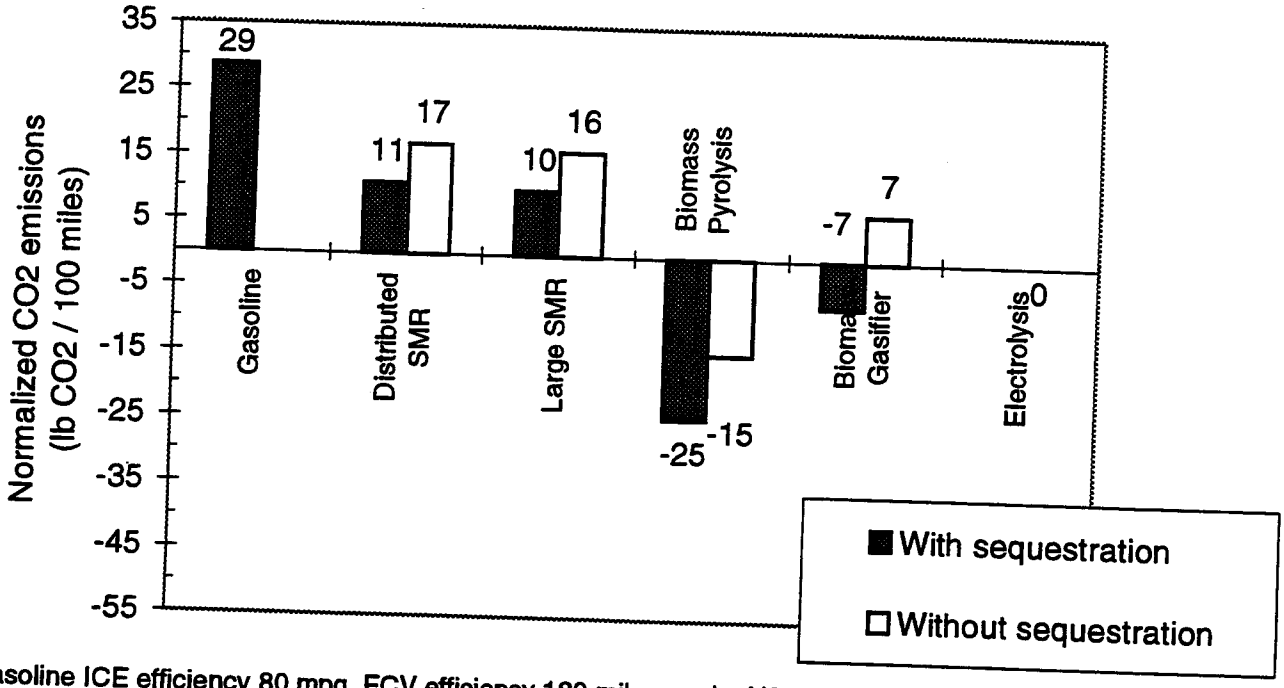

Gasoline ICE efficiency 80 mpg, FCV efficiency 180 miles per kg H2

Figure 4. Capturable and Non-capturable Emissions from Hydrogen Production Systems

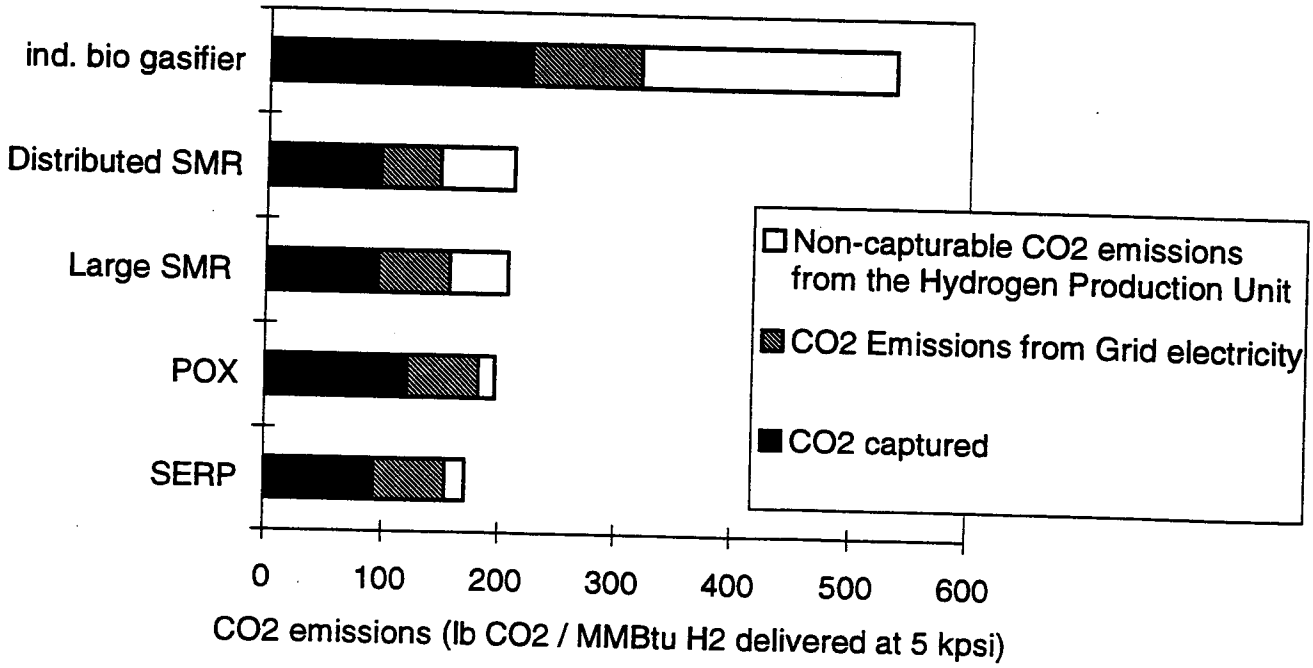

Grid electricity emissions based on 1.76 lbs CO2 / kWh
SERP emissions based on 25% feedstock use reduction compared to large scale reformer

MARKET PENETRATION SCENARIOS FOR FUEL CELL VEHICLES

by C. E. (Sandy) Thomas
Brian D. James and
Franklin D. Lomax, Jr.
Directed Technologies, Inc.
Arlington, Virginia 22203

Abstract

Fuel cell vehicles may create the first mass market for hydrogen as an energy carrier. Directed Technologies, Inc., working with the U.S. Department of Energy hydrogen systems analysis team, has developed a time-dependent computer market penetration model. This model estimates the number of fuel cell vehicles that would be purchased over time as a function of their cost and the cost of hydrogen relative to the costs of competing vehicles and fuels. The model then calculates the return on investment for fuel cell vehicle manufacturers and hydrogen fuel suppliers. The model also projects the benefit/cost ratio for government -- the ratio of societal benefits such as reduced oil consumption, reduced urban air pollution and reduced greenhouse gas emissions to the government cost for assisting the development of hydrogen energy and fuel cell vehicle technologies.

The purpose of this model is to assist industry and government in choosing the best investment strategies to achieve significant return on investment and to maximize benefit/cost ratios. The model can illustrate trends and highlight the sensitivity of market penetration to various parameters such as fuel cell efficiency, cost, weight, and hydrogen cost. It can also illustrate the potential benefits of successful R&D and early demonstration projects.

Results are given comparing the market penetration and return on investment estimates for direct hydrogen fuel cell vehicles compared to fuel cell vehicles with onboard fuel processors including methanol steam reformers and gasoline partial oxidation systems. The market penetration of these fuel cell vehicles are also compared with natural gas vehicles and vehicles fueled with natural gas/hydrogen mixtures.

Introduction

Fuel cell vehicle market penetration will require significant investments by both industry and government. Government support will be required to fund R&D and technology validation demonstrations, before industry is convinced of fuel cell vehicle market profitability. Much larger industry investments will eventually be needed to develop and mass produce fuel cell vehicles and to build a hydrogen fueling infrastructure. Neither can succeed alone. Government cannot afford the large investments required for commercialization, and industry will not make the necessary high risk investments with payoffs many years or even decades in the future. And government alone has the charter to develop those technologies that will benefit society, including reduced environmental impact and reduced dependence on imported fossil fuels.

Key decision makers in both industry and government must choose between many options to achieve their respective goals of profitability and improved social conditions. Within the transportation sector, fuel cell vehicles must compete with other alternative vehicles including natural gas vehicles and a range of various hybrid electric vehicles that could achieve similar reductions in pollution and oil imports. And the fuel cell vehicle itself could utilize onboard hydrogen storage or it could include an onboard liquid fuel processing system. The intent of the computer simulation model described here is to assist those decision makers as they weigh the costs and benefits of various clean car transportation options.

General Model Description

The basic model combines four key aspects of the fuel cell vehicle domain: vehicle technology, fuel, vehicle markets, and government actions (for more details, see Thomas 1997a).

The key input variables to the model include vehicle market scenarios and government actions, as illustrated in Figure 1. The major outputs include the return on investment for the automobile industry and for the hydrogen gas supply industry, along with estimates of benefit/cost ratios for government. Government benefit/cost ratios are calculated for the environment and for oil import reductions.

While this model produces a quantitative estimate of future profitability and future environmental improvements, it is not meant to predict the future. Rather, the model outputs should be taken as a very broad, qualitative indication of what is possible over the long run. Its greatest value will be in comparing alternative transportation options, and in assessing the impacts of various government and industry actions. This model should be seen as just one of many tools that can assist officials as they choose between alternative transportation options.

The model currently calculates eight major time functions as shown in Figure 1, including the number and cost of the fuel cell vehicles on the road each year, the quantity and cost of hydrogen, and the investments and profits for the auto and hydrogen gas industries. These functions are all linked to

the number of fuel cell vehicles sold each year. The quantity of hydrogen is determined directly by the number of vehicles on the road and their fuel economy. The annual investment is determined by the increase in vehicle sales "N" years in the future, where "N" is the construction time of the production plant or equipment (taking advantage of perfect predictive capability inherent in such a computer model.)

Market Penetration Model

The number of fuel cell vehicles sold each year is determined by two price elasticity curves --one for vehicles and one for hydrogen -- and two vehicle markets -- the zero emission vehicle (ZEV) market and the conventional (non-ZEV) light duty vehicle market.

The ZEV market currently includes California and the five northeastern "opt-in" states, beginning with 10% of the new car sales in 2003. The model assumes that 50% of this ZEV market is available to FCVs. The actual number of FCV's sold out of this 50% potential market depends on the FCV price each year, and on the price of hydrogen relative to gasoline.

The vehicle price elasticity curve shown in Figure 2 has two parameters: the price of the competitive vehicle and the market share for FCVs at twice the price of the competition. For the ZEV market, the baseline model assumes that the battery electric vehicle is the competition, with a default price of $25,000. The model assumes that the FCV will capture 50% of the available ZEV market (or 25% of all ZEVs sold) if it also costs $25,000, which may be conservative since most drivers would probably opt for the FCV over a battery EV, given the FCV's superior range. But the sales of FCVs will also be impeded initially by the lack of hydrogen refueling facilities. The price elasticity curve drops very sharply as the FCV price rises, falling to only 0.1 percent of the ZEV available market if the FCV costs twice the battery EV or $50,000. This long tail on the elasticity curve reflects the "early adopters" -- those special few who will spend $50,000 to be the first on their block to own a new, ultra-clean technology.

This price elasticity curve is compared with a market survey of car owners taken by the Ford Motor Company in California (Buist 1993). Ford asked their customers if they would be willing to pay $600, $2,000 or $3,000 more for a vehicle if the vehicle reduced emissions. Unfortunately, they only asked about zero emissions for the highest price. In this case, 9% of the drivers said that they would be willing to pay $3,000 extra for a ZEV. The price elasticity curve used here projects a 4.4% market share for this price premium, or less than half the survey results. However, surveys of this type are notorious for over estimating actual consumer behavior -- not all who *say* they will purchase an item will actually buy that item.

The market share is also dependent on the price of hydrogen. The hydrogen market share multiplier (Figure 3) is less steep than the vehicle curve, on the assumption that fuel price will be less of an inhibitor than initial vehicle price. The default hydrogen price curve would cut market sales by one half, for example, if hydrogen cost twice as much (high range) or 1.5 times as much (low range) as

Table 1. Comparison of Fuel Cell Vehicle Price Market Multiplier with Market Survey Results

Alternative Fueled Vehicle Price Increase:	Percentage of Car Owners Who Would Purchase Alternative Fueled Vehicles		
	Results from Ford Market Study	Model Market Share Function	
		Market Share Multiplier at 2X ICEV Price:	
		0.01	0.001 (Base Case)
$600	9% for 20% emissions reduction 14% for 40% emissions reduction	10.9%	10.2%
$2,000	3% for 40% reduction 4% for 60% reduction	8.1%	6.2%
$3,000	**9% for ZEV**	**6.5%**	**4.4%**

gasoline per mile driven. As shown, this curve gives a slight boost to FCV sales if hydrogen costs less than gasoline, which we predict will occur at large sales volumes. The model also includes sales to 25% (default value) of the conventional (non-ZEV) car market, with a competitive price of $18,000 for conventional gasoline internal combustion engine vehicles (ICEVs).

Cost Models

The model calculates the cost of hydrogen and compressed natural gas and the cost of fuel cell vehicles and natural gas vehicles each year, based on cumulative sales through the previous year. In general prices fall with increased production volume. For example, Figure 4 shows the constant dollar price of the Model T Ford over its lifetime (Flavin and Lenssen 1994). The Model T price fell an average of 13.4% for every doubling of production, or a "progress ratio" of 86.6%. Figure 5 shows an analysis of the progress ratios for a wide variety of products, which tend to range between 70% to 90% (Dutton and Thomas 1984). These progress ratios include all forms of cost reduction, including labor productivity gains (called "learning curves"), other improvements in the product, the process, management, etc. within a given company. In addition, costs can be driven down by competing companies within an industry, sometimes called "experience curves." We do not assume industry-wide experience curves in this model, but assume that each company follows its own progress ratio curve. For example, the total number of FCVs sold is divided by the number of automobile companies (default value is three) before applying the progress ratio cost reduction calculation.

Fuel Cell Vehicle Component Costing

The preferred costing methodology does not, however, rely on estimation of arbitrary progress ratios

for each component. Rather, we use the progress ratios to bridge current component prices with estimated future prices in mass production. For example, Directed Technologies, Inc. has worked with the Ford costing department to estimate the manufacturing cost of fuel cell stacks in large volume production (Lomax 1997), using the Design for Manufacturing and Assembly (DFMA) methodology used by industry both to select the lowest cost technique for manufacturing a given component, and to accurately estimate the large volume cost of each component (Boothroyd 1994). This detailed costing process scrutinizes every part, analyzing not only bulk material costs but also the least costly method of fabrication in large, automotive production volumes. As a result of this process, we estimate that the cost of PEM fuel cells could be reduced from about $1,500/kW today down to the neighborhood of $40/kW at the 300,000 unit production level (or 900,000 total vehicles assuming three major auto manufacturers.).

Given these initial and 300,000 production quantity prices, the model then calculates the progress ratio to tie these two values together -- in this case requiring a progress ratio of 82.1%.[1] Similar estimates were made for the other major components unique to the fuel cell vehicle, as summarized in Table 2. The third column of this table indicates the calculated price after the production of 110 transit buses, which is the main government/industry cost-shared project assumed in this model to drive down the initial cost of FCVs. The battery and motor/controller cost estimates were based on values in the literature, and the hydrogen storage tank estimates were estimated by DTI (James 1996).

Table 2. Baseline Fuel Cell Vehicle Pricing Parameters

	Price at Start Program (Input Data)	Price after 110 Buses (start of FCV Production) (calculated)	Progress ratio (calculated)	Price at 300,000 Production Level (Input Data)
Fuel Cell System ($/kW)	1,500	413	0.821	40
Peak Power Battery ($/kW)	80	34.9	0.881	7.8
Motor & Controller ($/kW)	490	133.6	0.819	12.7
Hydrogen Tank ($/kg of stored H_2)	510	316	0.929	133

[1]For production above 300,000 per manufacturer, the model switches the progress ratio to a default value of 0.98, which yields only two percent price reduction for each doubling after one million items are produced.

Natural Gas Vehicle Costing

The model assumes that natural gas vehicles will initially cost about $4,000 more than conventional vehicles, including the cost of 24.8 MPa (3,600 psia) compressed natural gas tanks and the necessary fuel injection system and other modifications to the ICE. This differential falls to $604 at the 300,000 production level, as summarized in Table 3.

Table 3. Estimated Differential Costs for a Natural Gas Vehicle vs. a Conventional Vehicle

	Current Cost	High Volume (300,000) Production Cost
Storage Tanks	2,000	500
Fuel Injection and Balance of System	2,000	104
Total:	4,000	604

The projected high volume NGV cost differential ($604) is consistent with other estimates. For example, EA Engineering, in a study for the Oak Ridge National Laboratory, estimated that natural gas vehicles would cost about $460 more than a conventional vehicle in mass production.

Hythane[2] Vehicle Costing

We assume that all vehicles in this analysis can achieve the same performance as the standard Ford Taurus, including 380 miles range. Since hythane is less compressible than natural gas and has a lower energy density, the storage tank for hythane must increase in size by about 42% to provide the same range as the natural gas vehicle, which adds $840 to the cost initially and $189 at the 300,000 vehicle level.

Hydrogen Costing

The cost of hydrogen was based on a detailed, industry-led costing project funded by the Ford Motor Company under a cost-shared contract with the Department of Energy's direct hydrogen fuel cell vehicle program (Thomas et al., 1997b). One major conclusion from this study is that hydrogen in a FCV could be competitive with gasoline even if the hydrogen were made in small scale, factory-built steam methane reformers or small scale electrolyzers. These small scale hydrogen fueling appliances

[2]Hythane is a registered trademark of Hydrogen Components, Inc. of Littleton, Colorado, and is taken here to mean the mixture of 30% by volume hydrogen with 70% natural gas.

are a key feature of this market penetration scenario. These inexpensive fueling systems can be installed at local bus garages and local fleet operators, avoiding the "chicken and egg" dilemma inherent with building large scale steam methane reformers and hydrogen pipelines or liquid hydrogen tanker trucks before fuel cell vehicles are plentiful.

The model estimates the number of FCVs within range of fueling stations each year in the California and opt-in ZEV states, assuming three miles between each station in the mature market. Four types of hydrogen fueling stations are assumed: those supporting less than 50 FCVs, 50 to 100, 100 to 300 and greater than 300 FCVs[3]. Electrolyzers are the only cost effective option for the smaller fueling stations. Steam methane reformers become more cost effective for the larger units. The initial cost estimates are summarized in Table 3. The electrolyzer costs were derived from a detailed DFMA

Table 3. Cost Parameters for Small Scale Electrolyzers and Steam Methane Reformers

	Electrolyzers	Steam Methane Reformer Systems		
Nominal Hydrogen Production Rate (kg/day)	2.72	44.2	88.5	272
No. of FCVs Supported	2.7	50	100	375
Initial Capital Cost[4] ($)	15,500	221,900	256,000	447,000
Manufacturing Progress Ratio Factor[5]	0.819	.85	0.85	0.85
Capital Cost at 10,000 Quantity ($)	4,380	33,400	39,950	76,000
Cost/per Vehicle ($/FCV)	1,622	667	400	203

type costing exercise with Electrolyser Corporation and Ford. We have not yet evaluated the large volume costs of factory-built steam methane reformers, but use an 85% progress ratio instead. The initial cost for the 272 kg/day steam methane reformer is based on the reformer that is part of the 200-kW stationary phosphoric acid fuel cell system manufactured by the ONSI Division of International Fuel Cells of South Windsor, Connecticut. We have assumed scaling factors for each of the major system components to extrapolate from the 272 kg/day unit down to the two smaller units. All costs include hydrogen compression to 41.4 MPa (6,000 psia), storage and dispensing into

[3]The number of vehicles supported by a station is approximately eight times the number of vehicles actually refueling each day. Thus a fueling station supporting 300 FCVs would refuel about 38 vehicles on an average day.

[4]Initial capital cost for electrolyzers assumes production of 100 units minimum.

[5]Progress ratios varied for different components; values shown are approximate for the total system.

the vehicle tanks.

Natural Gas Costing

Based on recent case studies of natural gas refueling station costs, we estimate that natural gas can be compressed to 24.8 MPa and dispensed into vehicle tanks for about $3.12/GJ initially, assuming low pressure natural gas costs $2.18/GJ. When 20,000 such natural gas dispensing stations are built (enough to supply 300,000 vehicles), the price of compressed natural gas is projected to fall to $2.62/GJ.

The cost of hythane is calculated from the 30% hydrogen and 70% natural gas ratio. The model takes into account the cumulative production of hydrogen, so three times more hythane vehicles must be sold to achieve a given hydrogen cost reduction than a pure hydrogen vehicle.

Investments

The model assumes that both government and industry make investments to bring the fuel cell vehicle to market. Initial cost-shared projects to supply 110 fuel cell buses and 232 fleet FCVs serve to bring costs down via the progress ratios described above. For example, the first FCVs cost $178,000. By the end of the bus project, costs have fallen to $55,300 per FCV. These lower costs then provide a small market for "early adopters," which in turn gradually increase market share in subsequent years, slowly driving down prices.

Government Investments

The model assumes that the federal government continues funding R&D in fuel cells for transportation, and also initiates cost-shared projects to develop and demonstrate small scale electrolyzers and steam methane reformers for hydrogen fueling applications. The government is also assumed to 50% cost-share two vehicle demonstration projects: a 110-bus project ($113 million of government funds) extending the three fuel cell buses slated for Chicago, and also a smaller fleet vehicle program ($7.7 million government) that supports 232 FCVs. Total government investments are $432 million over the 1995-2008 time period, as summarized in Table 4. No government investment is assumed for the natural gas vehicles.

Industry Investments

The automobile industry is assumed to invest $3,125 per FCV annual production capacity, plus two percent of annual sales for capital replacement. Plant construction time is three years, so the model looks ahead and calculates increased capacity needed three years in the future. The model adds this investment incrementally, although the actual investments would be made in discrete steps as new production volume was added. This incremental as-needed investment optimizes capital utilization and overestimates return on investment compared to the real world, but this approximation will apply

to all the vehicle options. Again, the relative comparisons between vehicle options should still be valid. Total industry investment over the 1997-2030 time period is projected at $22.6 billion, split between three companies.

Table 4. Government Investments (in 1996 U.S. Million Dollars) in Fuel Cell and Hydrogen Infrastructure Projects

Year	R&D			Technology Validation Demonstrations (Cost Shared with Industry)				Annual Totals
	Fuel Cell	Electrolyzer	Steam Methane Reformer	FC Buses	FC Vehicles	Electrolyzer Fueling Station	SMR Fueling Station	
1995	22			1.6				23.6
1996	25			0				25.0
1997	30	0.4	0.2	4.2	0.09			34.9
1998	35	0.5	0.4	7.2	0.08	5.33		48.5
1999	30	0.2	1.4	10	0.28	5.33		47.2
2000	25		2.5	40	1.64	0.33		69.5
2001	20			50	0.40			70.4
2002	20				2.43			22.4
2003	20				2.77			22.8
2004	15							15.0
2005	15							15.0
2006	10						7.5	17.5
2007	5						7.5	12.5
2008							7.5	7.5
Totals	272	1.1	4.5	113	7.69	10.99	22.5	431.8

The model assumes that one electrolyzer company invests $20 million, plus four percent of electrolyzer sales. The steam methane reformer companies (three assumed) invest $15 million each and four percent of sales, or a total of $328 million over the full period. In addition, the fueling stations invest $10.8 billion to purchase the fueling appliances over this period.

Government Benefit/Cost Ratios[6]

The model also calculates the societal benefits of replacing gasoline ICE vehicles with FCVs, including the reduced costs of importing oil, and the reduced costs of environmental degradation. Estimating environmental damage is highly speculative. Instead of damage costs, the model uses the lowest of several estimated avoided costs of alternative methods of reducing pollution, as summarized Table 5.

Table 5. Air Pollution Avoided Costs ($/ton)

	U.S.					Southern California		
	(Tellus 1990)	Mass. (EEI 1994)	Nev. (EEI 1994)	N.Y. (Mark 1996)	Used Here:	(Tellus 1990)	(Mark 1996)	Used Here:
VOC	5,300	6,140	6,190	17,300	**5,300**	29,000	18,000	**18,000**
CO	870	1,010	1,040	2,100	**870**	870	350	**350**
NOx	6,500	7,540	7,650	14,400	**6,500**	262,500	17,000	**17,000**
CO_2	22	26	25		**22**			

The environmental benefit/cost ratio is then the net present worth of avoided environmental costs over the 1997-2030 time period, divided by the present worth of the government investments, using a three percent societal discount rate. Similarly, the oil import benefit/cost ratio is the present worth of avoided oil purchases divided by the present worth of government investments, again using three percent discount rate for social effects.

Baseline Direct Hydrogen Fuel Cell Vehicle Results

The various time-lines for the direct hydrogen fuel cell vehicle industry are shown in Figure 6a, and for the hydrogen gas industry in Figure 6b, illustrating how increasing sales drive down costs over time. The investment curves show how relatively small government investments initially help to drive down prices, leading to dramatically larger industry investment once profitability has been demonstrated.

The basic results of the analysis for the direct hydrogen fuel cell vehicle are summarized in Table 6

[6]The benefit/cost ratios have no meaning for the natural gas vehicles, since their cost is low enough to achieve significant market penetration without any government intervention with the price elasticity curves assumed here. Hence benefit/cost ratios are given only for the FCVs.

for industry return on investment, and in Table 7 for the government benefit/cost ratios. The automobile, gas and hydrogen retail suppliers all make over 17% returns on their investments. The electrolyzer business, however, never takes off in the baseline model. Although electrolyzers are essential to get the market started by providing low cost hydrogen fueling systems for just a few vehicles, the steam methane reformers produce lower cost hydrogen, and soon dominate the market.

The oil import benefit/cost ratio is between 28 and 61 to 1 -- oil imports savings exceed government investments by a factor of 28 to 62. The environmental avoided costs are 14 to 33 times greater than the government total investment of $432 million ($371 million net present worth at 3% discount rate) over the 1996-2008 time period.

Table 6. Industry Return on Investments (30-year Baseline Totals - High / Low Ranges)

	Investment ($U. S. Millions)	Return on Investment
Fuel Cell Vehicle Industry (36 / 21 Million FCVs)	20,570 / 16,050	21.8% / 17.2%
Hydrogen Production Industry:		
Electrolyzer Fueling Appliances	20.1 / 17.7	2.9% / 1.2%
Natural Gas Reformer Fueling Appliances	318 / 234	27.2% / 26.9%
Hydrogen Retail Suppliers	14,470 / 7,500	24.7% / 21.4%

Table 7. Government Benefit/Cost Ratios (30-year Totals)

	($ U. S. Millions)		Benefit/Cost Ratios @3% Discount
	Current $M	Present Worth @ 3%	
Total Government Investment	432	371	
Oil Import Savings (11.5 / 5.2 Quads)	54,750 / 26,380	22,650 / 10,400	61 / 28
Environmental Savings	29,200 / 13,400	12,200 / 5,300	33 / 14

Onboard Fuel Processors

The current model also includes fuel cell vehicles powered by methanol and by gasoline. The onboard chemical processors required to convert these liquid fuels into hydrogen change vehicle performance and cost. These fuel processors add weight to the vehicle, and also reduce the fuel cell peak power, which in turn requires larger fuel cells and slightly larger motors to maintain equal vehicle

performance in terms of drive train power to vehicle weight ratio. The resulting extra weight in turn requires larger drivetrain components -- the weight compounding phenomenon.

Methanol Fuel Processor

The model assumes an onboard steam methanol reformer with water gas shift reactors to convert most of the carbon monoxide to hydrogen and water. Since CO poisons the anode catalyst of a PEM fuel cell, a gas cleanup device such as a preferential oxidizer is also required to reduce CO down to less than 10 ppm. The gas stream from this system will include approximately 25% CO_2 and 75% hydrogen (excluding water vapor). To avoid buildup of this CO_2 in the anode chamber, the fuel cell cannot be operated "dead-ended," which is possible with pure hydrogen. Rather, the anode must have a significant exhaust component, which also means that a significant fraction (10% to 20%) of the hydrogen will pass through the fuel cell unreacted. Some of this unreacted hydrogen can be returned to a boiler to preheat the methanol or to raise steam for the reaction, but only with a loss of efficiency in the burner and heat exchangers. Hence the fuel cell operating on reformate must necessarily have lower efficiency than the same fuel cell operating on pure hydrogen.

Furthermore, existing PEM fuel cell systems have lower performance operating on a dilute mixture of hydrogen. Figure 7 compares the polarization curves measured by the Los Alamos National Laboratory for an older Ballard fuel cell operating on pure and dilute hydrogen, with hydrogen content varying from 40% to 75% (Inbody 1996). The anode gas stream also included 2% air to reduce the deleterious effects of CO_2, which also reduces performance -- without this air bleed performance would have been worse. The measured drop in peak power was about 12% for the 75% hydrogen case characteristic of a methanol reformer output. The model assumes that the fuel cell size is therefore increased by 12% to maintain vehicle power to weight ratio.

Even after increasing fuel cell size, however, the system efficiency on 75% hydrogen is still slightly lower than that for pure hydrogen, as shown in Figure 8. The solid upper curve shows the fuel cell system efficiency as a function of net output power operating on pure hydrogen with variable air compressor power from 1.2 atmospheres at low power up to 3 atmospheres at full power. The three lower curves in Figure 8 show theoretical and experimental data from Los Alamos for 75% hydrogen mixtures. The two theoretical curves were generated from computer models of the anode performance (Gottesfeld 1996).

Given these efficiency data, the model estimates the weight of the vehicle after weight compounding, and a separate driving cycle simulation code estimates the fuel economy of the vehicle over the EPA combined urban/highway driving cycle with each velocity segment multiplied by 1.25 (a more realistic "real world" driving schedule). Two estimates are made for each methanol FCV parameter: a high range with optimistic assumptions, and a low range assuming fuel processor developments do not meet expectations. The parameters for the methanol processor are summarized in Table 8. The methanol FCV would have about 28% to 38% lower fuel economy than a direct hydrogen fuel cell vehicle. Since methanol production is also slightly less efficient than hydrogen production from

natural gas (eg., 64% to 72%), greenhouse gas emissions will also be greater for methanol by at least 30% per vehicle.

Gasoline Fuel Processor

The model assumes that gasoline is processed with an onboard partial oxidation (POX) system combined with water gas shift reactors and gas cleanup. This system would be similar to the methanol processor, but with even lower performance. The hydrogen content would be only 40% instead of 75%, causing a measured drop of 36% in peak power with the old Ballard fuel cell stack, or a 21% drop using the optimistic LANL theoretical data. In addition, the POX processor will not need the excess thermal energy contained in the hydrogen in the anode exhaust. It may be more difficult to recover this wasted hydrogen energy. The overall gasoline processor parameters are summarized in Table 9. The estimated gasoline FCV fuel economy would be 38% to 57% less than that of a hydrogen FCV, although still 20% to 72% better than that of a gasoline-fueled ICEV.

Table 8. Characteristics of Low and High Range Methanol-Powered Fuel Cell Vehicles

	High Range	Low Range
Fuel Cell Size Increase w/r to H_2 FCV	-10%	-12%
Fuel Cell Efficiency Curve	LANL Theory (R_{CL}=0.025)	LANL Experimental
Hydrogen Utilization	90%	83.3%
CO_2 Degradation	None	(Included in exp. data)
Methanol Reformer Efficiency (H_2/MeOH -LHV)	84.5%	77%
Methanol Reformer Weight (kg)	46	60
Vehicle Weight Increase (kg)	110	135
Fuel Economy (1.25 X Combined Cycle) in km/l (mpg-equivalent)	20.7 (48.7)	17.8 (41.9)
Fuel Economy w/r to ICEV	1.98	1.70
Fuel Economy Decrease w/r to H_2 FCV	-28.6%	-38.5%

Table 9. Characteristics of Low and High Range Gasoline-Powered Fuel Cell Vehicles

	High Range	Low Range
Fuel Cell Size Increase(w/r to H_2 FCV)	1.21	1.36
Fuel Cell Efficiency Curve	LANL Theory (R_{CL}=0.025)	LANL Experimental
Hydrogen Utilization	90%	83.3%
CO_2 Degradation	None	(Included in exp. data)
Gasoline POX Efficiency (H_2/Gasoline - LHV)	75%	70%
Anode Gas Heat Recovery	70%	0
Gasoline POX Reformer Weight (kg)	55	87
Vehicle Weight Increase (kg)	109	186
Fuel Economy (1.25 X Combined Cycle) in km/l (mpg-equivalent)	17.9 (42.3)	12.5 (29.4)
Fuel Economy w/r to ICEV	1.72	1.20
Fuel Economy Decrease w/r to H_2 FCV	-38.3%	-56.9%

Comparison of Direct Hydrogen with Methanol and Gasoline Fuel Cell Vehicles

Vehicle Cost Comparison

The lower fuel cell performance and the added weight of the liquid-fueled FCVs also translates into added cost. Part of the additional cost is due to the requirement for larger fuel cell stacks, larger peak power batteries and larger motor controllers to maintain vehicle power to weight ratio, as summarized in Table 10 for methanol-powered FCVs and Table 11 for gasoline-powered FCVs. To a first approximation, the extra power train costs cancel the savings derived from eliminating the compressed hydrogen tank, leaving the cost of the onboard processor as a net addition to the hydrogen FCV cost. The estimated vehicle prices are shown in Figure 9, assuming that the base gasoline AIV Sable costs $18,000.

Table 10. Incremental Cost Estimates (1996 U.S. Dollars) for Methanol-Powered Fuel Cell Vehicle (High Volume Mass Production Costs)

	Direct Hydrogen FCV		Methanol FCV Cost		Cost Differential (MeOH FCV - H_2 FCV)	
	Size	Cost	High	Low	High	Low
Fuel Cell System ($40/kW)	50 kW	2000	2400	2440	400	440
Peak Power Battery ($7.8/kW)	40 kW	312	337	343	25	31
Motor/Controller ($12.7/kW)	79 kW	1000	1080	1100	80	100
Hydrogen Tank ($133/kg)	5.78 kg	768	0	0	-768	-768
Methanol Processor ($10/kW -High & $20/kW-Low)	-	0	540	1100	540	1100
Totals		4080	4357	4983	277	903

Table 11. Incremental Cost Estimates (1996 U.S. Dollars) for Gasoline-Powered Fuel Cell Vehicle (High Volume Mass Production Costs)

/11T	Direct Hydrogen FCV		Gasoline-POX FCV Cost		Cost Differential (Gasoline FCV - H_2 FCV)	
	Size	Cost	High	Low	High	Low
Fuel Cell System ($40/kW)	50 kW	2000	2630	3120	630	1120
Peak Power Battery ($7.8/kW)	40 kW	312	337	355	25	43
Motor/Controller ($12.7/kW)	79 kW	1000	1080	1140	80	140
Hydrogen Tank ($133/kg)	5.78 kg	768	0	0	-768	-768
Gasoline-POX Processor ($10/kW -High & $20/kW-Low)	-	0	540	1140	540	1140
Totals		4080	4587	5755	507	1675

Fuel Economy Comparison

The fuel economies of the three vehicles are compared in Figure 10, in miles per gallon of gasoline equivalent (LHV) on the 1.25 times accelerated EPA combined driving schedule. The natural gas and hythane vehicles are assumed to have the same fuel economy as the gasoline ICEV. Higher efficiency may be possible with natural gas, but improved efficiency often must be traded off for low emissions.

Vehicle Emissions Comparison

The estimated local air pollution and global greenhouse gas emissions per vehicle for these three FCVs are compared with battery EVs and with a FCV storing liquid hydrogen onboard in Figure 11, all normalized to one for the gasoline ICE vehicle in the 2000^+ time period. The most striking result is that the greenhouse gases associated with electrolytic hydrogen would be 65% greater than those from a gasoline ICEV. This results from the projected composition of the average U.S. marginal grid mix in the 2000^+ time period -- 70% coal and 25% natural gas. Since the clean generators (nuclear and hydro-electric) are operated near capacity, any new power demand requires primarily additional coal consumption. As discussed earlier, however, the steam methane reformers rapidly take over most of the hydrogen market, providing greater greenhouse gas reductions than any other option.

Any of the FCVs nearly eliminate CO and NOx emissions. However, both methanol and gasoline will have significant evaporative emissions unless fueling systems and refueling procedures are modified for liquid fuels. Methanol is both less volatile and less photoreactive than gasoline vapors, so its impact on ozone smog is less than that of gasoline.

The per vehicle greenhouse gas emissions are compared in Figure 12 for six vehicles in grams of CO_2 equivalent. This full fuel cycle analysis shows that natural gas vehicles offer only a 10 to 15% improvement over gasoline ICEVs. Hythane will always produce more greenhouse gas emissions than a natural gas vehicle, unless the hythane engine is tuned for higher efficiency at the sacrifice of higher NOx emissions (or hydrogen is made from renewable sources). Hythane increases greenhouse gas emissions since hydrogen is either made from natural gas at less than 100% efficiency, or it is made from electrolysis of water which produces considerably more greenhouse gases as shown in Figure 12 with projected utility grid marginal generator mix. The direct hydrogen FCV provides the greatest reduction in greenhouse gases if hydrogen is made by steam methane reforming, but also produces the worst increase with electrolytic hydrogen.

Market Penetration Comparisons

As shown in Figure 13, the market penetration of methanol- and gasoline-powered FCVs lags behind that of the direct hydrogen FCV, due to higher initial vehicle cost, even though hydrogen initially costs more per mile than methanol or gasoline. Only the high ranges for the liquid fueled FCVs show up on Figure 13. The low range cases never penetrate the market with the baseline parameters -- they remain too expensive to gain significant market share. Market penetration for the lower range hydrogen FCV case[7] is very similar to the methanol high range case -- the market share penalty as a result of the high initial cost of hydrogen nearly equals the market loss due to the higher initial purchase price of the methanol-powered FCV.

The natural gas vehicles obtain a large market share early, even though they cannon compete in the ZEV market. The model assumes that 25% of the non-ZEV market is available for alternatively fueled vehicles competing with $18,000 ICEVs (vs. $25,000 battery EVs for the ZEV competition.) After 2025 the direct hydrogen FCVs exceed the NGVs, since the model assumes that 50% of all vehicles sold in California and the five opt-in states in the Northeast must be ZEVs. Thus the direct hydrogen FCV has a larger market base.

The hythane vehicle sales lag the NGV sales due to the slightly higher cost of the hythane tanks and, more importantly, due to the higher cost of hythane due to the hydrogen component.

As a result of reduced market penetration, the return on investment is generally less for the methanol-

[7]The low range hydrogen case assumes that the hydrogen cost market share multiplier falls to 50% when the cost of hydrogen is 1.5 times the cost of gasoline, compared to 2 times the cost of gasoline for the hydrogen high range case (See Figure 3.)

and gasoline-powered FCVs (Figure 14), although the high range methanol case yields slightly higher returns than the low range hydrogen case. Again, only the high range estimates are shown on Figure 14 for the methanol- and gasoline-FCVs -- there is no return for the low range assumptions for either liquid fueled FCV.

The government environmental benefit/cost ratios also decline for the FCVs with onboard reformers (Figure 15), due both to lower market penetration and also due to lower per vehicle environmental benefits. In this case the high range methanol-FCV environmental benefit / cost ratio is only slightly less than the low range direct hydrogen FCV case.

Finally, Figure 16 shows the corresponding oil import benefit/cost ratios for these three FCV types.

Cumulative Environmental Savings

The cumulative environmental savings over the 1997-2030 time period are summarized in Figure 17 for the three FCVs and for natural gas and hythane vehicles. The natural gas and hythane vehicles provide the greatest overall savings due to their early market penetration. In terms of cumulative greenhouse gas emissions, however, the direct hydrogen fuel cell vehicle provides the largest reduction, even though fewer FCVs are sold (Figure 18). This large climate change advantage of the direct hydrogen fuel cell is due to the large fraction of hydrogen being produced by steam methane reforming, which produces less than half the per vehicle greenhouse gases as a natural gas or hythane vehicle.

Conclusions

This market penetration model shows a plausible scenario whereby small scale electrolyzers and small scale natural gas steam reformers could provide economic hydrogen to support a growing fuel cell vehicle market. Based on detailed assessment of fuel cell vehicle and hydrogen costs in mass production, the model illustrates that both the automotive industry and the hydrogen gas industry could make over 20% return on investment, provided that the federal government invested over $400 million between now and 2008 in the further development and demonstration of fuel cell vehicles and in hydrogen infrastructure development.

Electrolyzers, on the other hand, have mixed review: they are essential in the startup phases to provide very small fueling appliances to support early fleets of 2 to 50 vehicles. But the model indicates that electrolyzer manufacturers could not make adequate return on investment on the FCV market alone, since steam methane reformers would take over the market as fuel cell vehicle sales increased. In any case, electrolytic hydrogen would dramatically increase greenhouse gases with the projected marginal utility mix in the U. S. in the early 21st century. Thus both economic and environmental concerns impede mid term use of electrolytic hydrogen. Only substantial utility grid penetration of renewable electricity would make electrolytic hydrogen environmentally acceptable. Renewable electricity would have to saturate the grid during peak use, for example, in which case producing hydrogen from excess renewable electricity would reduce overall greenhouse gases.

Otherwise, displacing fossil fuel electricity at any time of the day or night with renewable electricity would reduce greenhouse gases more than making hydrogen for use in a FCV.[8]

This model also indicates that methanol- or gasoline-powered FCVs would be less attractive in the marketplace, due primarily to an expected increase in vehicle costs. Although the onboard processor itself might be cost competitive with the compressed hydrogen tank it would replace, the lower peak power and lower efficiency of the fuel cell operating on dilute mixtures of hydrogen would require larger fuel cells and slightly larger drivetrain components, driving up the vehicle cost.

Natural gas vehicles would have much greater market penetration than the fuel cell vehicles due both to lower initial vehicle cost and lower fuel cost. As a result of this higher market penetration, natural gas vehicles would provide greater overall environmental savings (local urban pollution plus greenhouse gases) than fuel cell vehicles. However, in terms of greenhouse gases alone, the direct hydrogen fuel cell vehicle could provide over twice the climate change benefits over the 1997-2030 time period as the natural gas vehicle, despite fewer vehicle sales.

Hythane (30% hydrogen with 70% natural gas) would have marginal or negative benefits. The hythane vehicle would cost more due to larger tanks to maintain vehicle range, and fuel costs would be higher, reducing market penetration slightly with respect to a pure natural gas vehicle. Nonetheless, total environmental savings with hythane could be larger (lean burn) or they could be less (stoichiometric) than pure natural gas. From a climate change perspective, however, hythane would cut greenhouse gas benefits in half compared to the pure natural gas vehicle.

If reducing greenhouse gases is a major societal goal, then direct hydrogen fuel cell vehicles are the best choice, with methanol fuel cell vehicles second, natural gas vehicles third, hythane vehicles fourth, and gasoline fuel cell vehicles last, as summarized in Figure 18.

Acknowledgements

The authors wish to thank the Department of Energy for their support of this work under Modification No. 3 to Subcontract No. ACF-4-14266-01, and also Dr. Jim Ohi of the National Renewable Energy Laboratory, the technical contract monitor for this work. We also thank the Ford Motor Company for providing support under the DOE direct hydrogen fuel cell vehicle program, which provided cost data for both fuel cell vehicles and for components of the hydrogen infrastructure. We also appreciate many useful discussions with our colleagues at Directed Technologies, Inc. (Ira Kuhn and George Baum), Los Alamos National Laboratory (Shimshon Gottesfeld, Mike Inbody and Nick Vanderborgh), Praxair (Tom Halvorson), Princeton (Joan Ogden and Margaret Steinbugler), Air Products and Chemicals (Venki Raman and Bob Moore), at BOC

[8]For example, wind or solar electricity that displaces the marginal U. S. utility generation mix would reduce greenhouse gas emissions by a factor of 1.8 times more than making hydrogen and displacing gasoline ICEVs with hydrogen FCVs.

Gases (Anne Kotar), Electrolyser Corporation (Matthew Fairlie), International Fuel Cells (Al Meyer and Paul Farris), Livermore National Laboratory (Bob Schock, Ray Smith and Gene Berry), Union of Concerned Scientists (Jason Mark) and Oak Ridge National Laboratory (Geoff Wood).

References

Boothroyd, G., P. Dewhurst, and W. Knight 1994. *Product Design for Manufacture and Assembly*. New York: Marcel Dekker, Inc.

Buist, Donald R. 1993. "An Automotive Manufacturer's Alternative Fuels Perspective," *Proceedings of the First Annual World Car 2001 Conference*, p. 54. Riverside, California: University of California at Riverside.

Dutton, J. M. and Thomas, A. 1984 "Treating Progress Functions as a Managerial Opportunity," *The Academy of Management Review*, Vol. 9, No. 1, pp 235-246.

EA Engineering 1993. "AFV Differential Costs and Performance Attributes," prepared for the Oak Ridge National Laboratory

Flavin, C. and Lenssen, N. 1994. *Power Surge: Guide to the Coming Revolution*, Washington, D. C.: The Worldwatch Institute, p. 305.

Gottesfeld, S. 1996. "Hydrogen Dilution Effect on Anode at Constant Utilization."

Inbody, M., Tafoya, J., Hedstrom, J., Vanderborgh, N., "Fuel Cell Stack Testing at Los Alamos National Laboratory," *DOE Fuel Cells for Transportation Exploratory R&D Program*, Washington, D. C.: Los Alamos National Laboratory

James, B. D., Baum, G. N., Lomax, F. D., Thomas, C. E., Kuhn, I. F. 1996. *Comparison of Onboard Hydrogen Storage for Fuel Cell Vehicles*, Task 4.2 Final Report under Ford Subcontract 47-2-R31148. Arlington, Virginia: Directed Technologies, Inc.

Lomax, F. D., James, B. D., and Mooradian, R. P. 1997. "PEM Fuel Cell Cost Minimization Using 'Design for Manufacture and Assembly' Techniques," *Proceedings of the National Hydrogen Association's 8th Annual U. S. Hydrogen Meeting*

Thomas, C.E. 1997a. *Integrated Analysis of Transportation Demand Pathway Options for Hydrogen Production, Storage and Distribution*, NREL Subcontract No. ACF-4-14266-01. Arlington, Virginia: Directed Technologies, Inc.

Figure 1. Major Functional Relationships for Programmatic Pathway Analysis

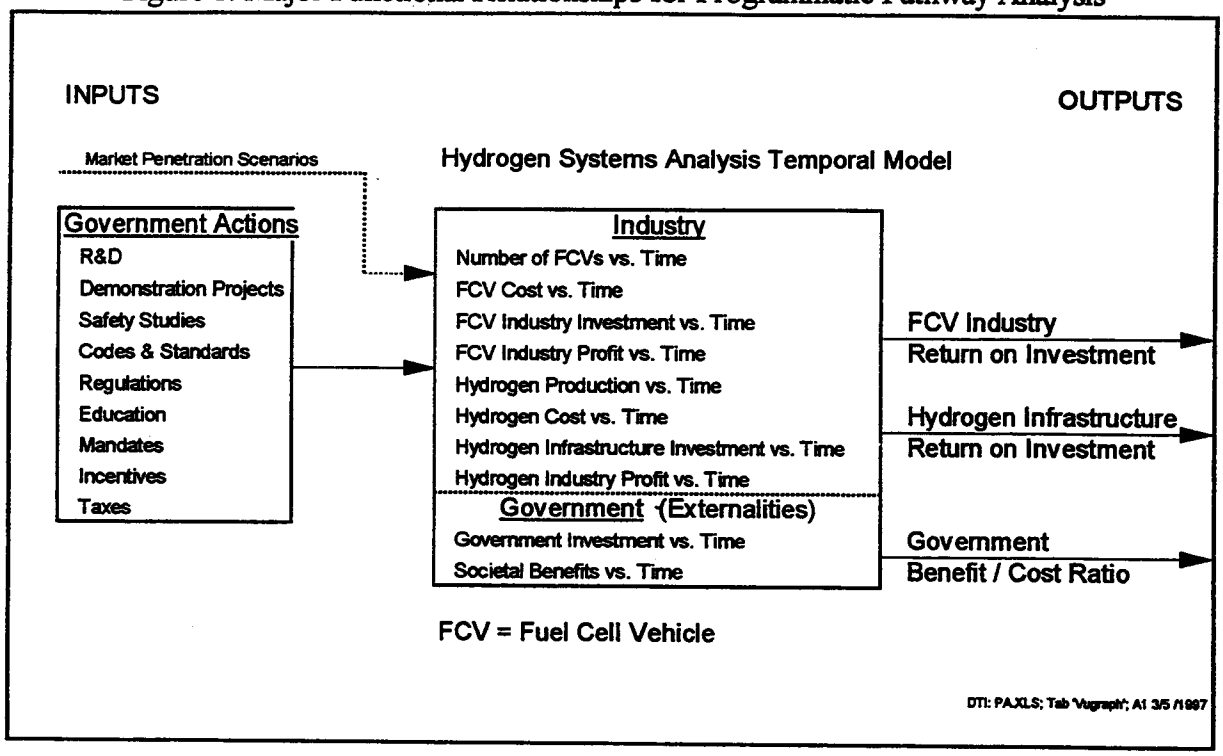

Figure 2. Fuel Cell Vehicle Market Share vs. Vehicle Price

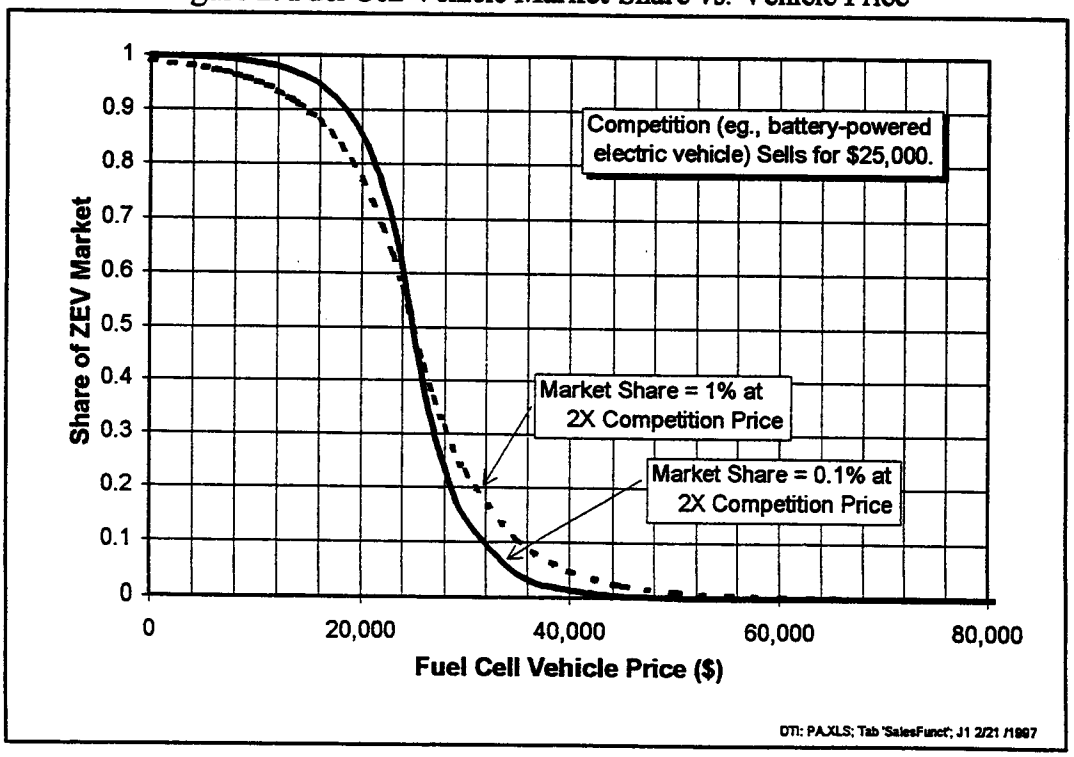

Figure 3. Hydrogen Price Market Share Multiplier

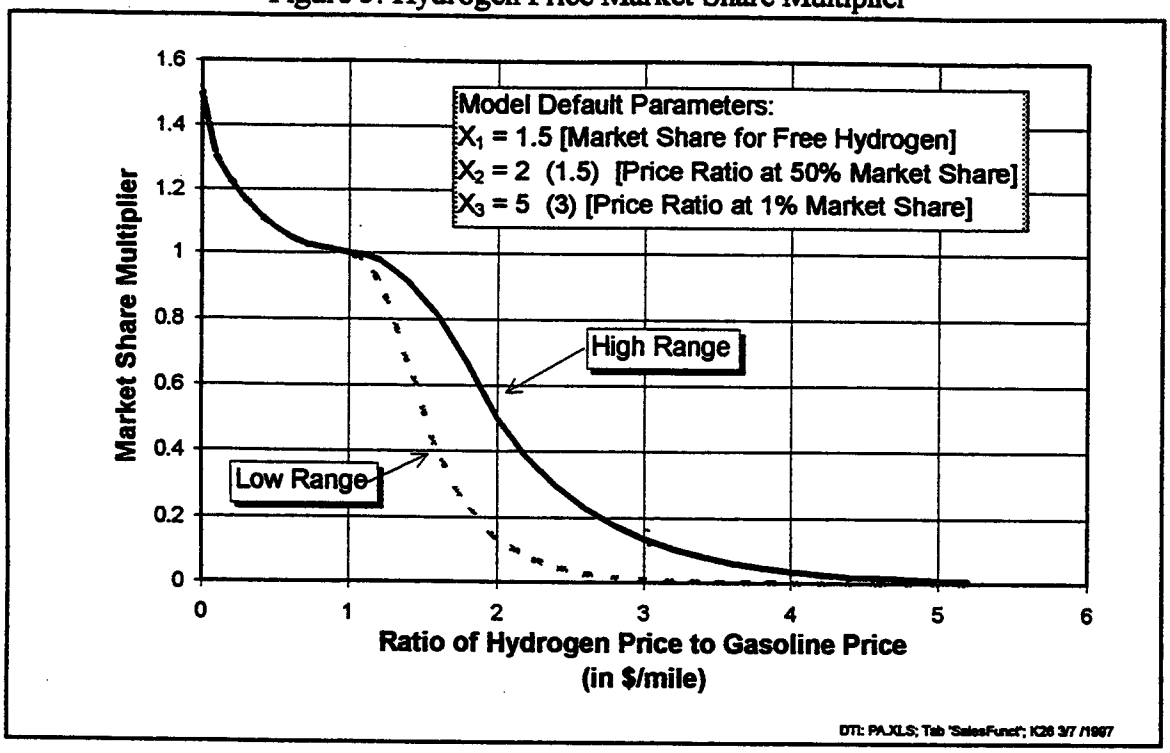

Figure 4. Ford Model T Price (Constant 1978 $) vs. Cumulative Production

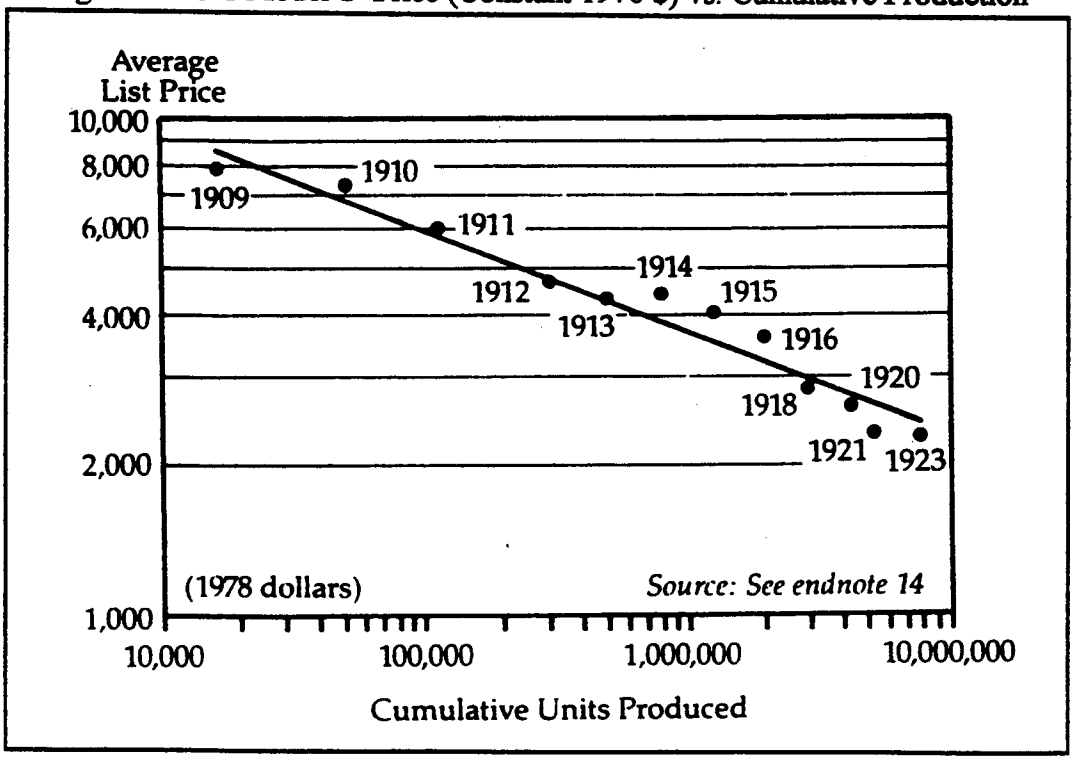

Figure 5. Distribution of Progress Ratios Observed in 22 Field Studies

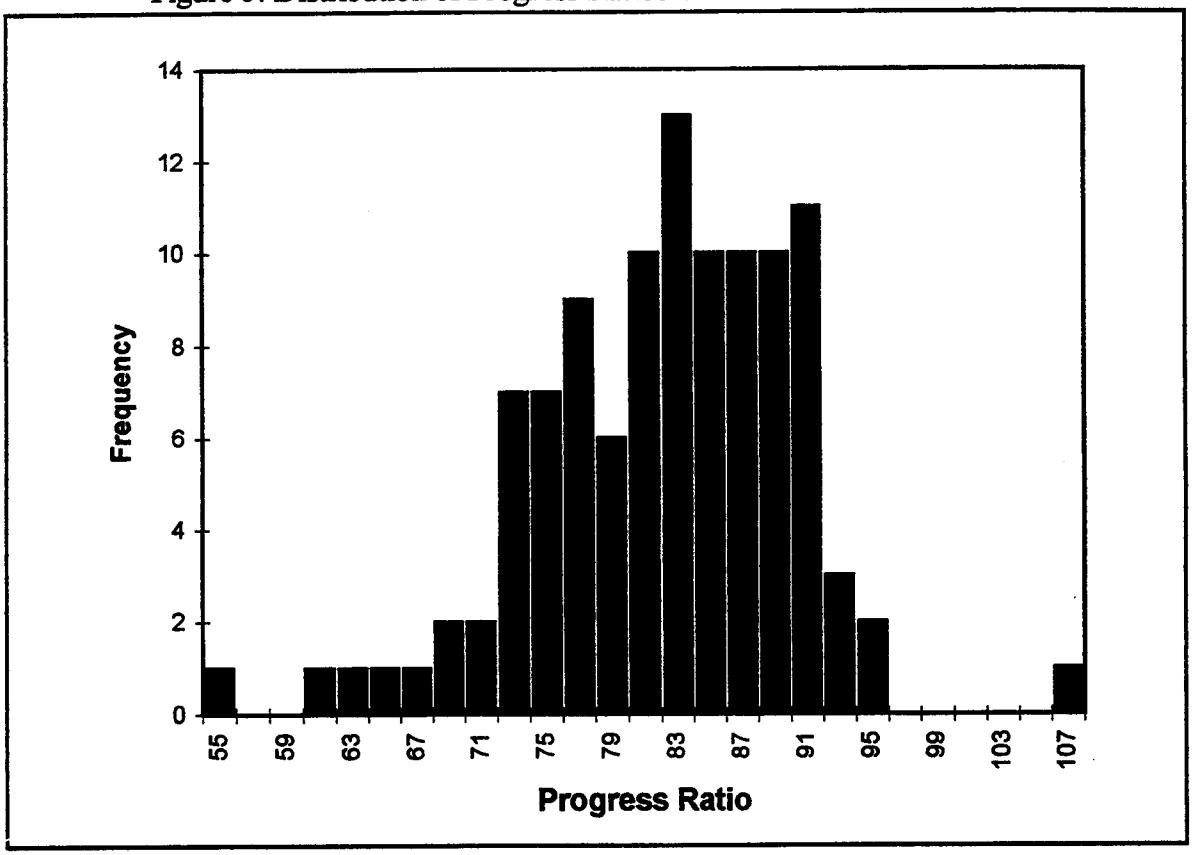

Figure 6a. Example of Fuel Cell Vehicle Industry Programmatic Pathway Projections (All Costs in 1996 U. S. Dollars)

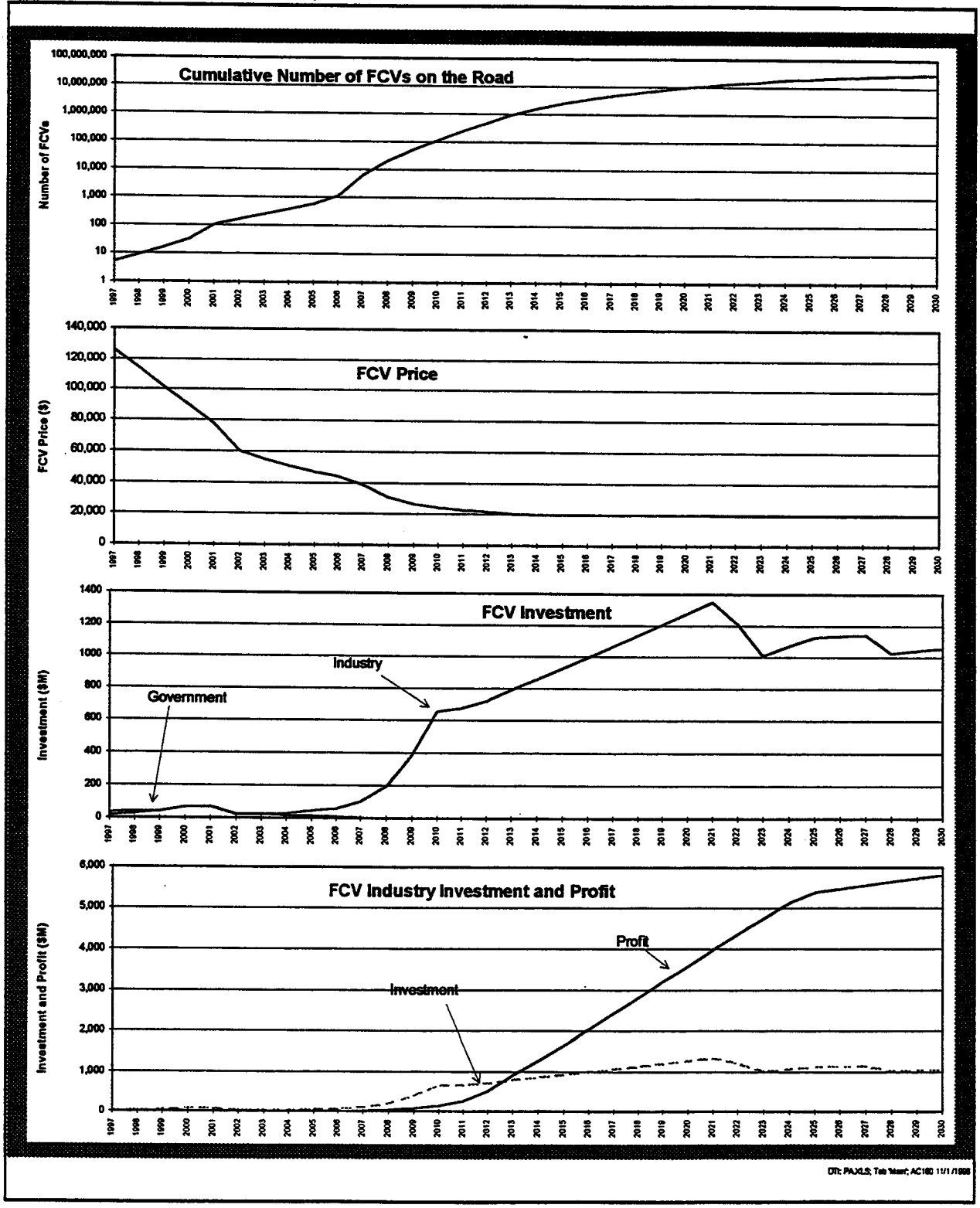

Figure 6b. Example of Hydrogen Industry Programmatic Pathway Projections (All Costs in 1996 U. S. Dollars)

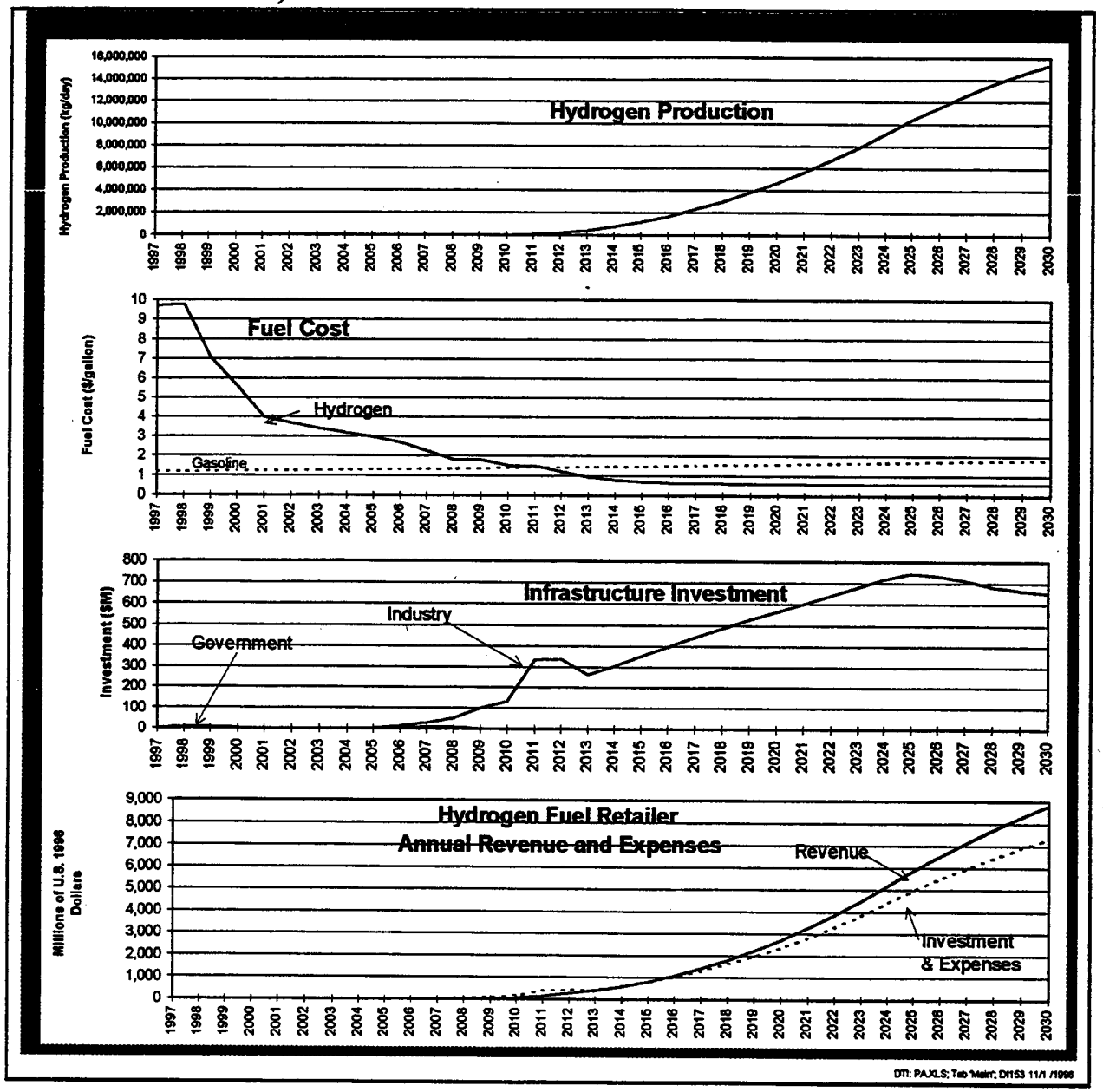

Figure 7. Measured Fuel Cell Polarization Curves with Dilute Mixtures of Hydrogen

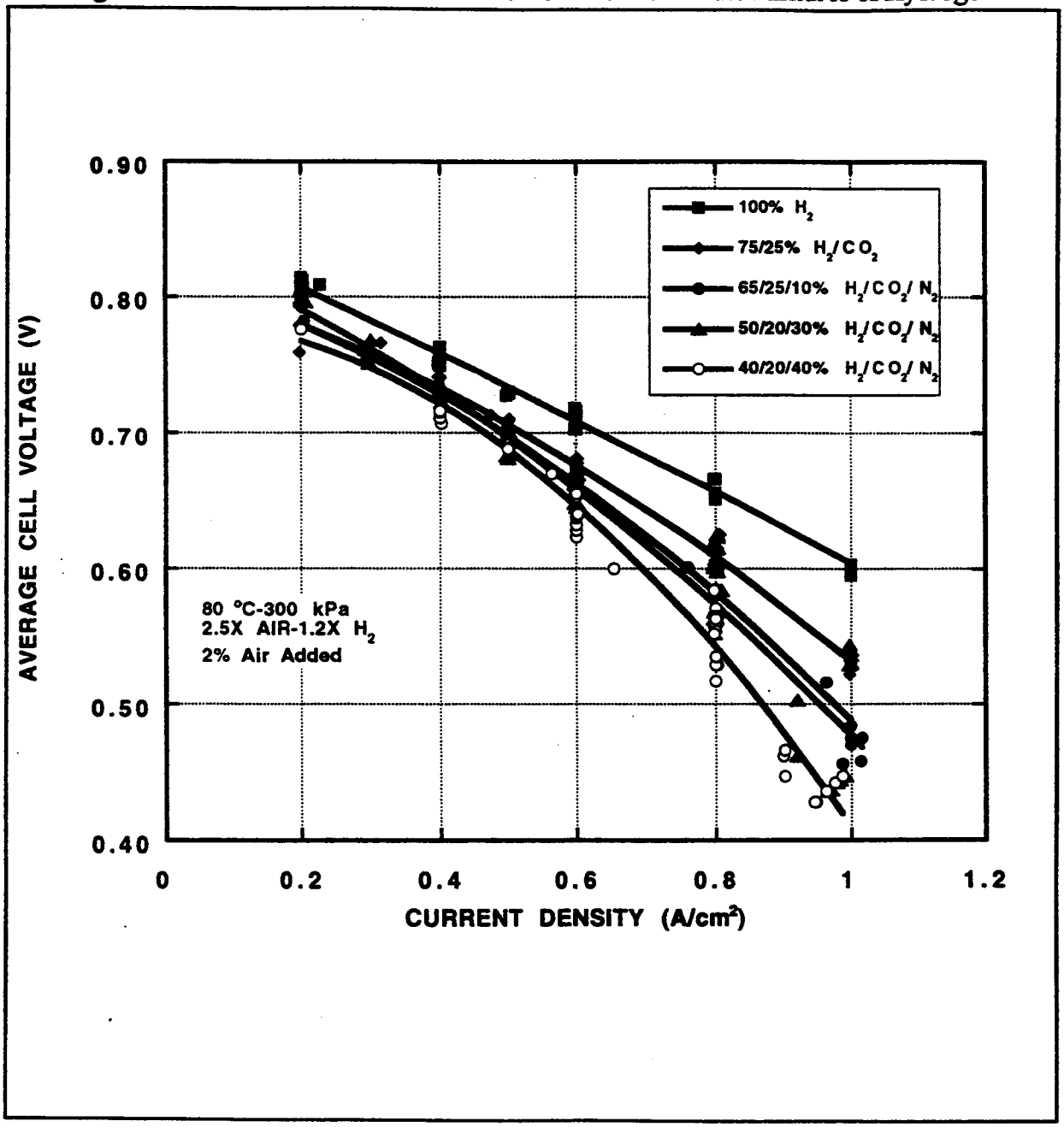

Figure 8. Fuel Cell System Net Efficiency vs. Output Power for Pure Hydrogen and Simulated Methanol Reformate

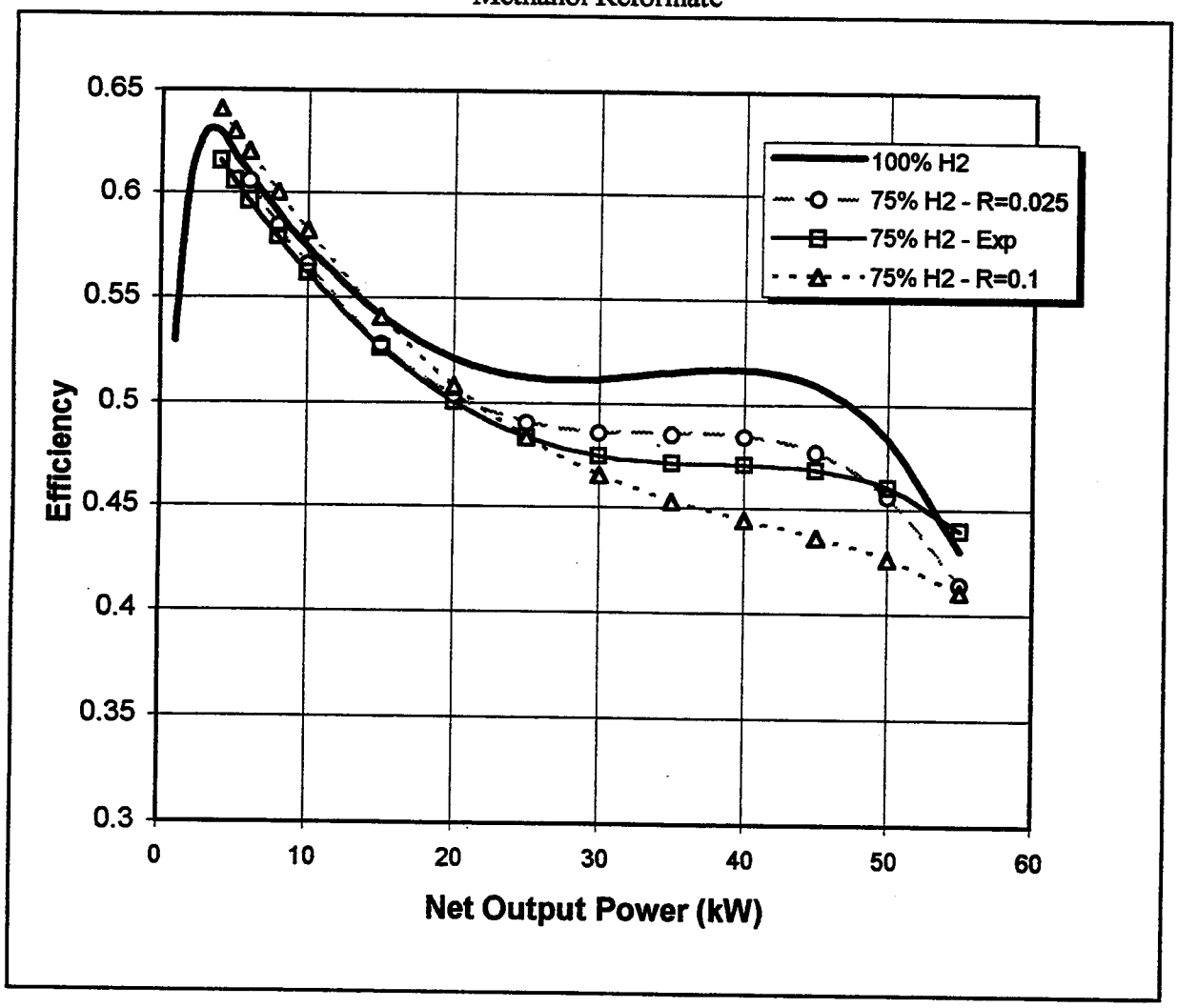

Figure 9. Estimated Purchase Price of Vehicles in 2003

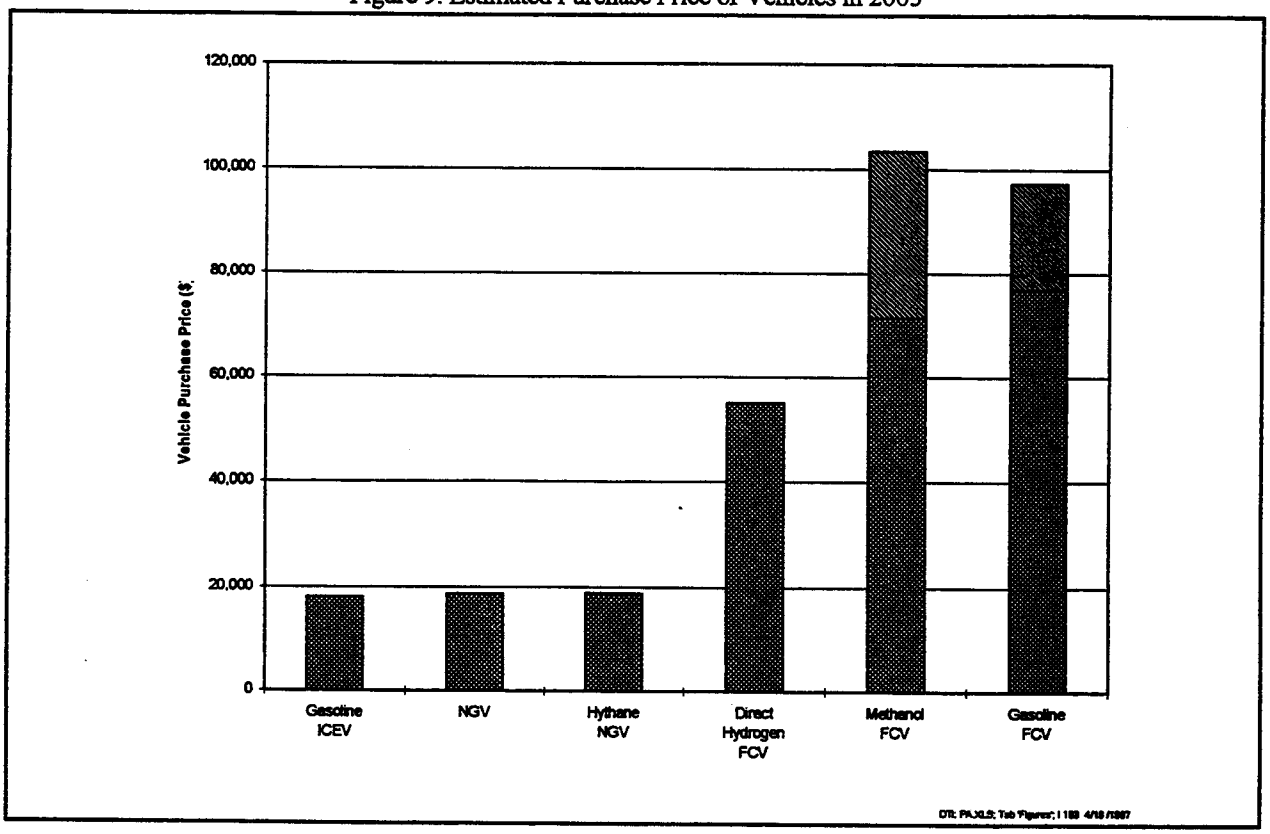

Figure 10. Onboard Fuel Economy for Fuel Cell Vehicles Compared to a Conventional Vehicle

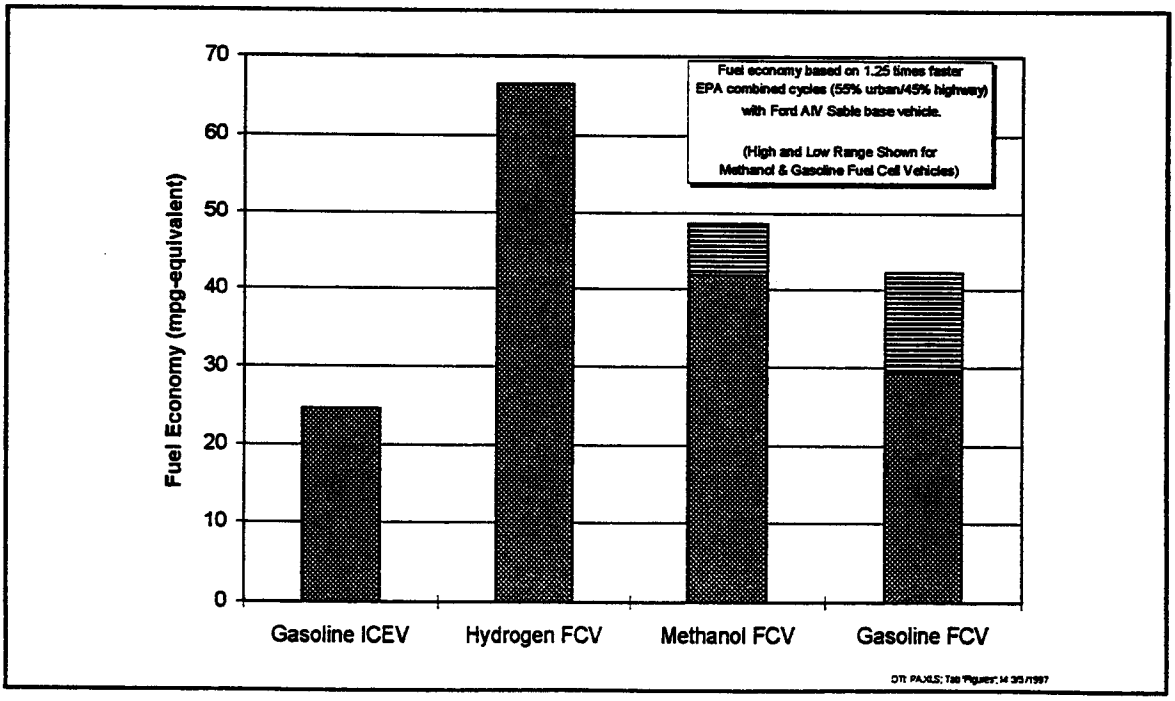

Figure 11. Fuel Cell Vehicle Emissions
Normalized to One for the Gasoline Internal Combustion Engine Vehicle

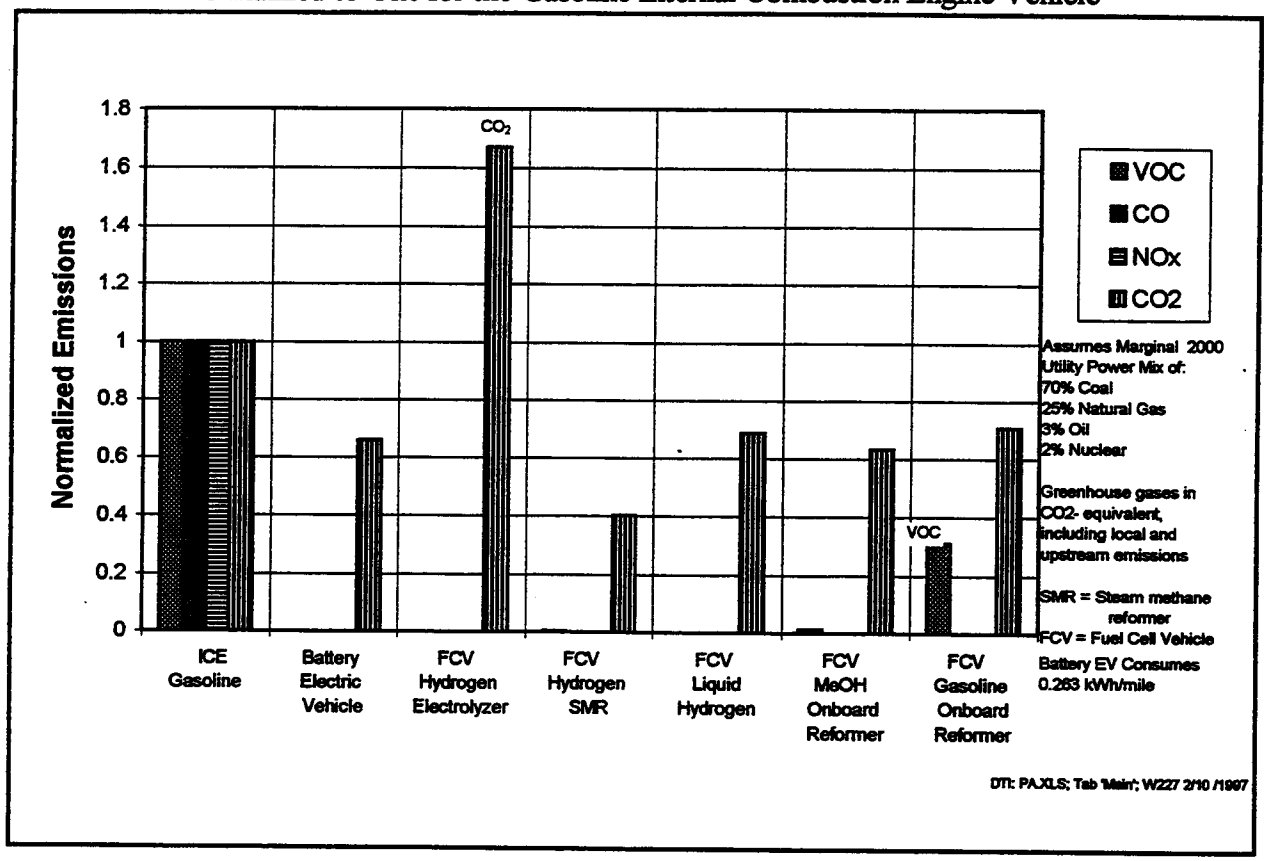

Figure 12. Per Vehicle Greenhouse Gas Emissions in CO_2-Equivalent Grams/Mile

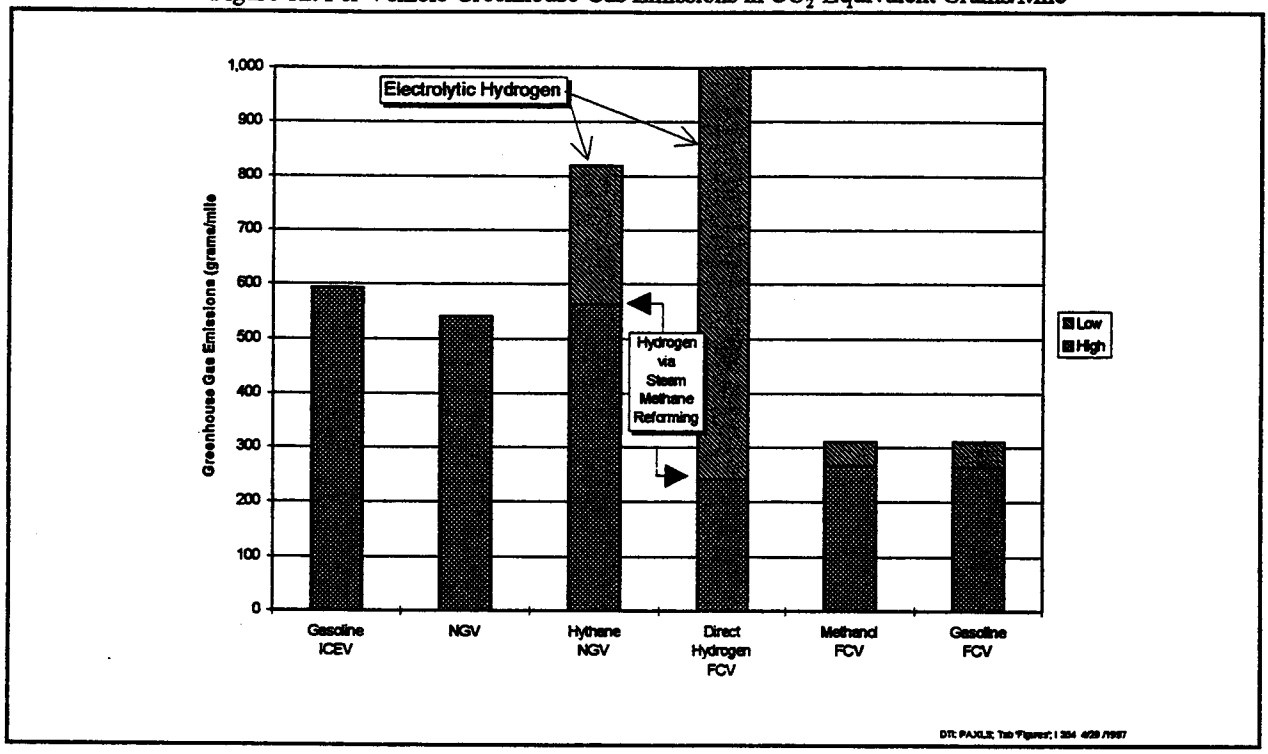

Figure 13. Number of Alternatively-Fueled Vehicles vs. Time

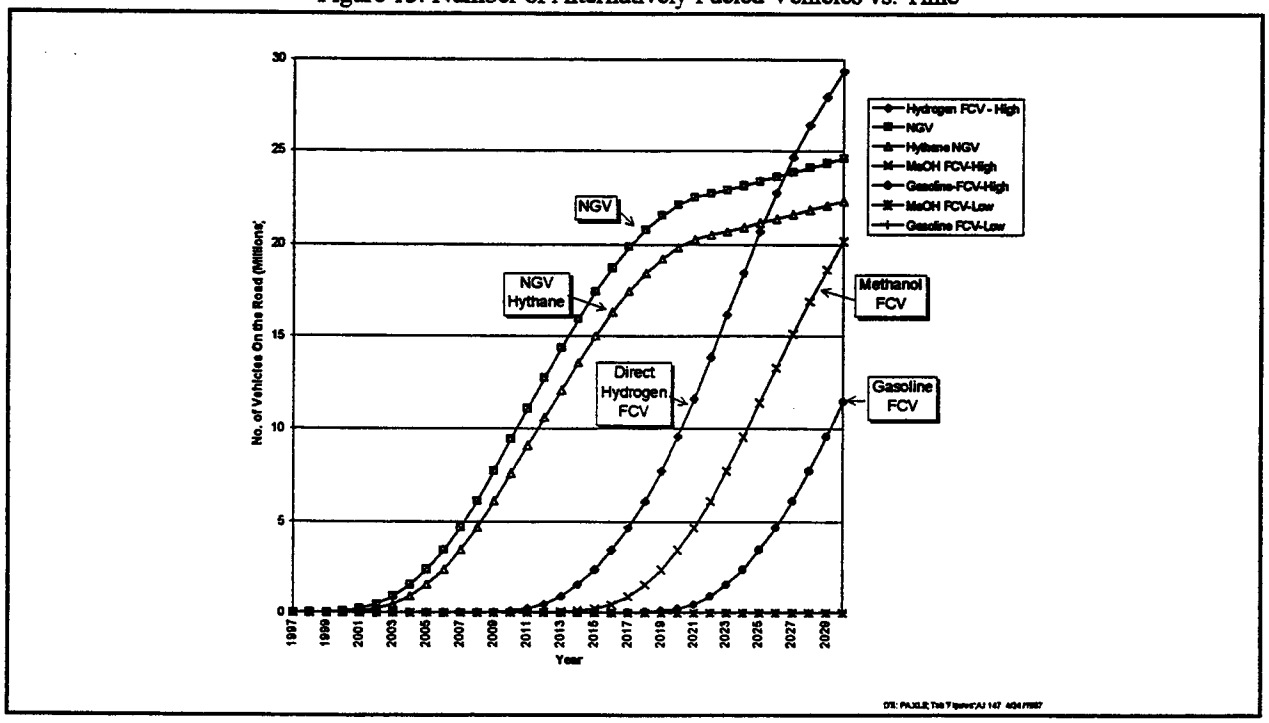

Figure 14. Estimated Pretax Return on Investment for Fuel Cell Vehicle Manufacturers

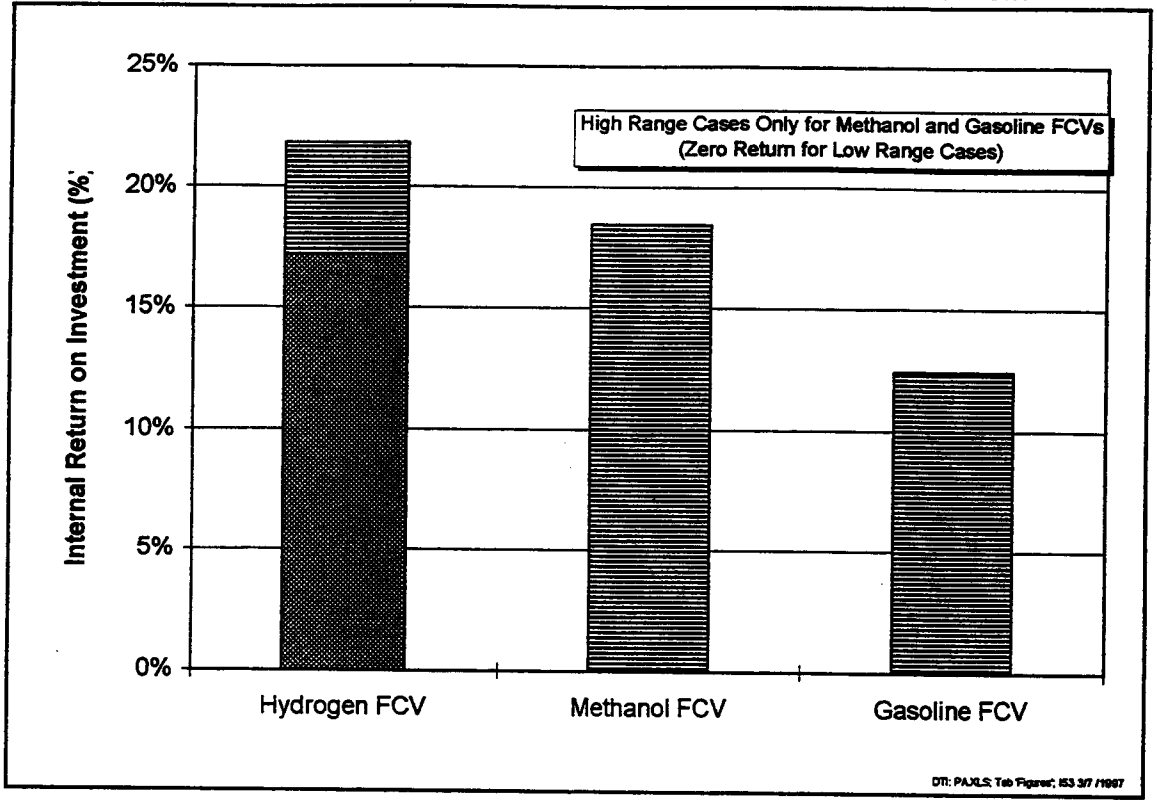

Figure 15. Environmental Benefit / Cost Ratios for Fuel Cell Vehicles

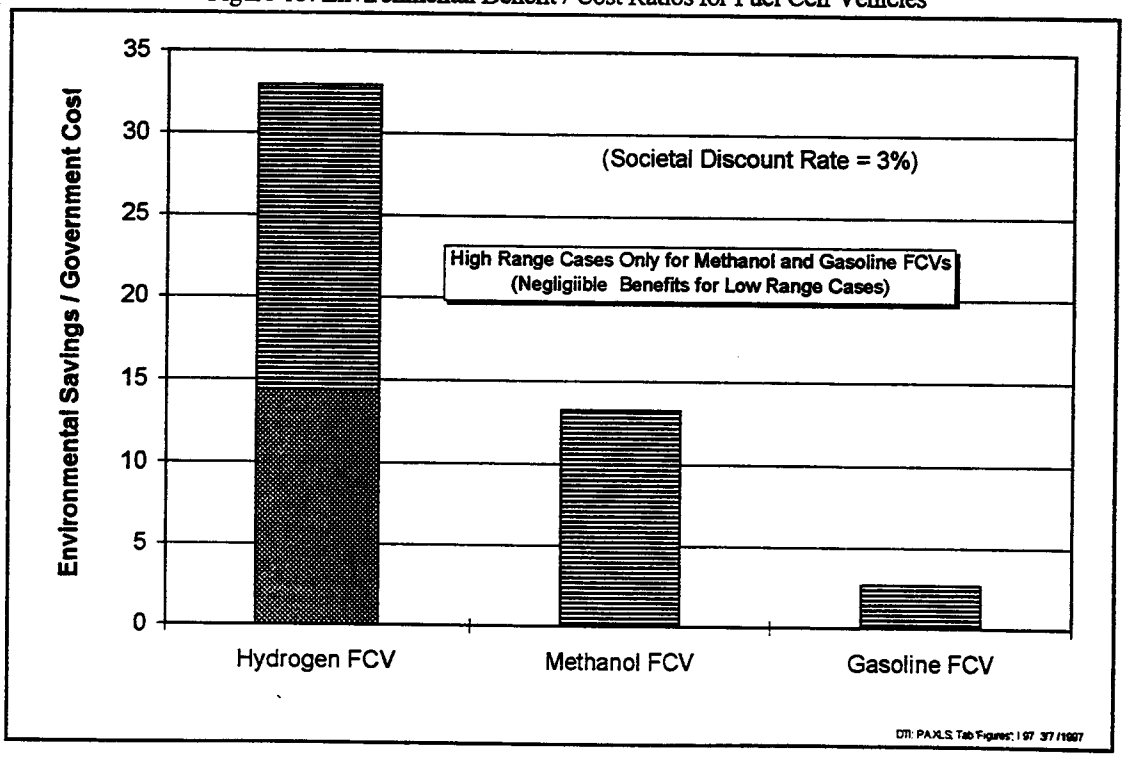

Figure 16. Oil Import Benefit / Cost Ratios for Fuel Cell Vehicles

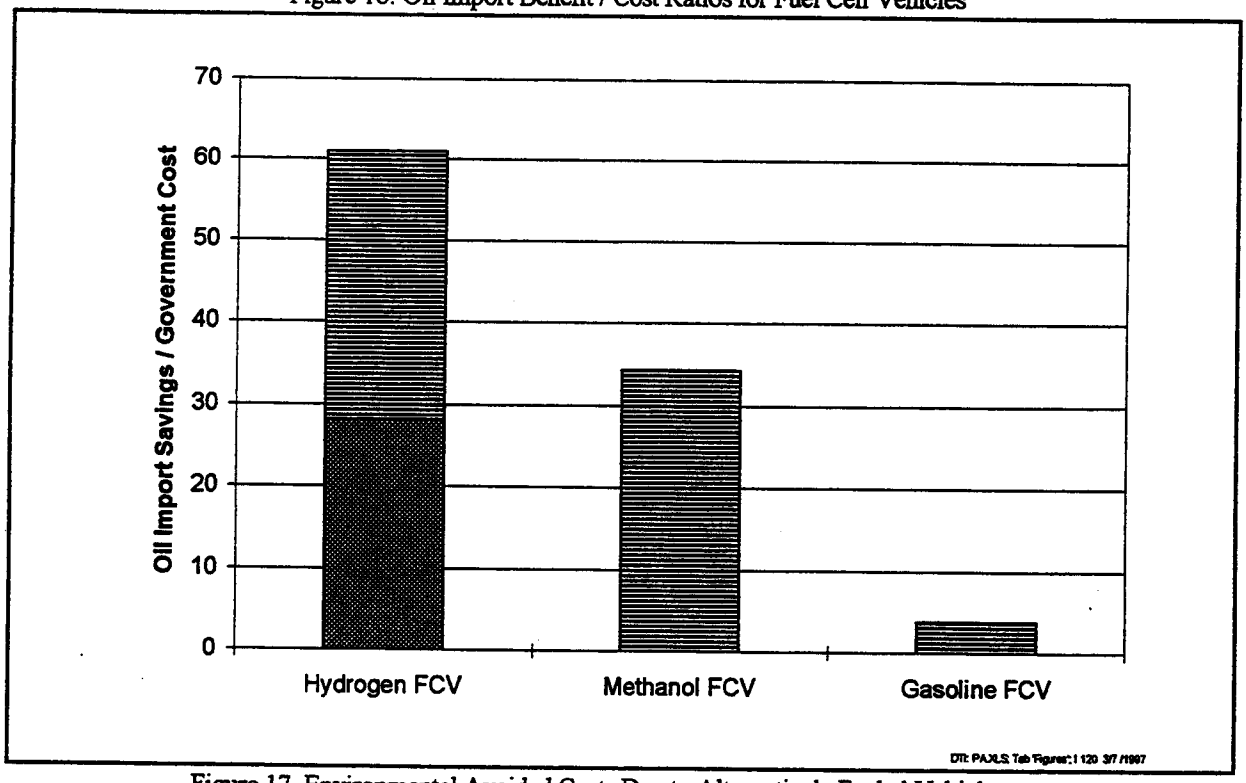

Figure 17. Environmental Avoided Costs Due to Alternatively Fueled Vehicles

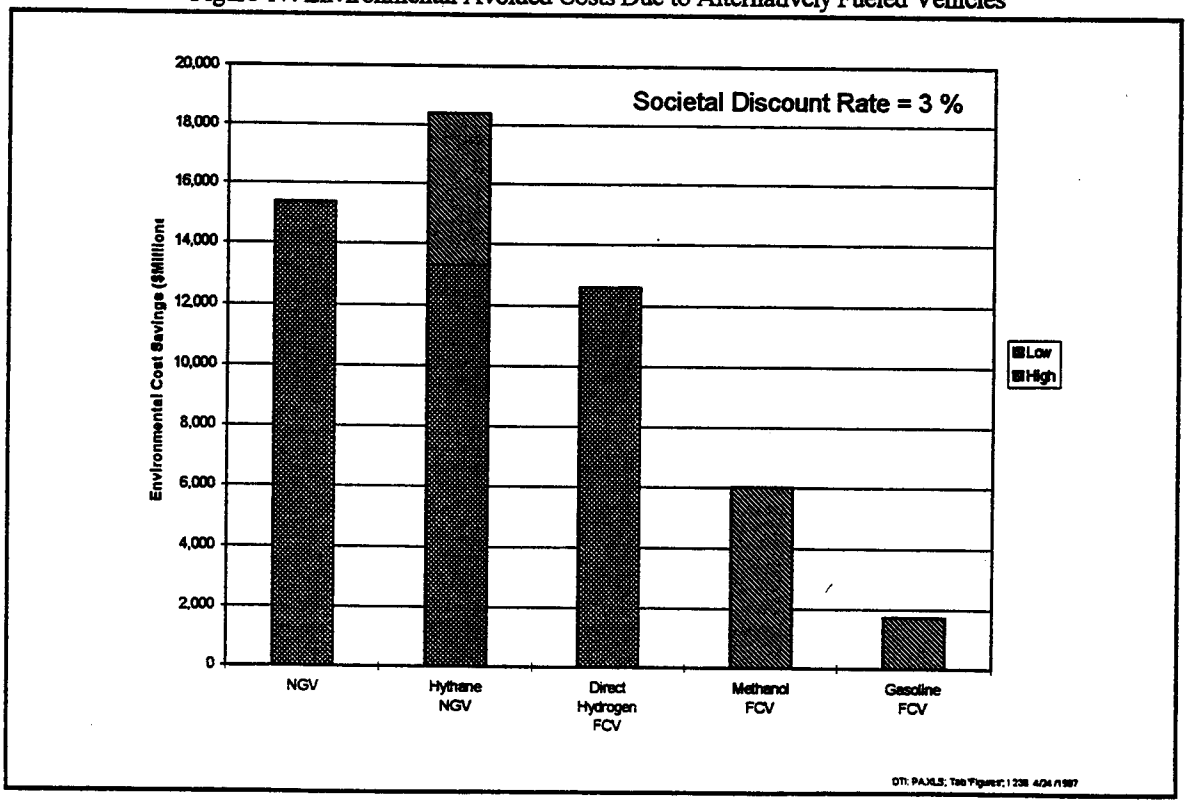

Figure 18. Cumulative Greenhouse Gas Reductions Due to Alternatively Fueled Vehicles, 1997-2030

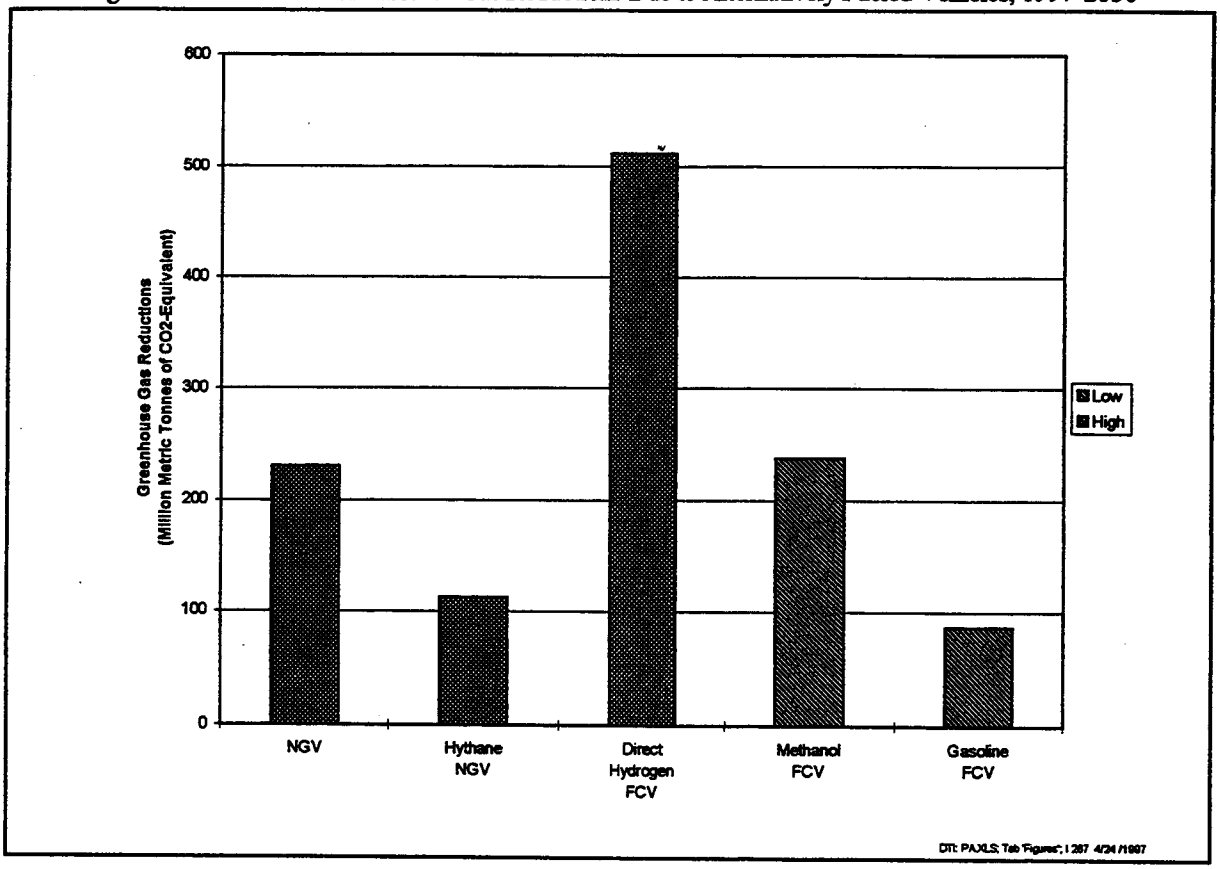

A TECHNICAL AND ECONOMIC ASSESSMENT OF HYDROGEN AS A FUEL FOR FUEL CELL VEHICLES

Joan Ogden, Margaret Steinbugler and Thomas Kreutz

Center for Energy and Environmental Studies
Princeton University
Princeton, NJ 08544 USA

Abstract

In this progress report, we summarize our results to date from an ongoing technical and economic assessment of hydrogen as a fuel for fuel cell vehicles. This work is being carried out as part of the systems analysis activity of the US Department of Energy Hydrogen R&D Program.

Five tasks are currently underway:

Task 1: Evaluate the projected performance and cost characteristics of alternative fuel cell vehicles with:

* compressed gas hydrogen storage
* onboard steam reforming of methanol
* onboard partial oxidation (POX) of hydrocarbon fuels derived from crude oil

Task 2: Evalute refueling infrastructure requirements for each alternative for Southern California conditions.

Task 3: Determine the delivered fuel cost for Southern California conditions for various fuel cell vehicle fuels including: hydrogen from natural gas, coal, biomass, off-peak power, solar; methanol from natural gas, coal, biomass; hydrocarbon fuels such as gasoline from crude oil.

Task 4: Calculate the lifecycle cost of transportation for Southern California conditions for each alternative fuel cell vehicle type and fuel.

Task 5: Compare the design and economics of hydrogen refueling station options, including small scale onsite steam reforming of natural gas, partial oxidation processing (POX) of hydrocarbon fuels and electrolysis.

Introduction

Summary of Approach/Rationale

Since 1986, researchers at Princeton University's Center for Energy and Environmental Studies have carried out technical and economic assessments of hydrogen energy systems. The goal of our work is to illuminate possible pathways leading from present hydrogen markets and technologies toward wide scale use of hydrogen as an energy carrier, highlighting important technologies for RD&D. Our approach has been to assess the entire hydrogen energy system from production through end-use from several perspectives (fuel producer, consumer, society) considering technical performance, economics (e.g. capital cost, delivered hydrogen cost, cost of energy services), infrastructure, environmental and resource issues. This work has been part of the systems analysis activity of the DOE Hydrogen Program since 1991.

Past Results

Initially, we focussed on the long term potential of hydrogen derived from renewables (solar, wind, biomass). These studies suggested that renewable hydrogen used in energy efficient end-use devices (e.g. fuel cells) could become economically competitive, beginning in the next century. More recently we have explored how a transition to large scale use of hydrogen energy might begin. The goal of this work is to identify promising strategies leading from near term hydrogen markets and technologies toward eventual large scale use of hydrogen as an energy carrier.

Over the past few years our focus has been on strategies for producing, distributing and using hydrogen as a fuel for zero emission vehicles. We have looked in detail at the various near term options available for providing hydrogen transportation fuel to vehicles (production of hydrogen from natural gas or off-peak power). We have also considered longer term options such as gasification of biomass or municipal solid waste (MSW) and hydrogen from wind or solar. In FY '95 and FY '96 we assessed the potential impact of advances in small scale hydrogen production technologies (steam reforming of natural gas, electrolysis using off-peak power) on the cost of hydrogen transportation fuel. In particular, we assessed the possibilities for low cost, small scale hydrogen production from natural gas. During FY'96, we completed a case study of developing a hydrogen refueling infrastructure in Southern California.

Current Year Results

Cost And Performance Benchmarks For Hydrogen As A Fuel For Fuel Cell Vehicles

All fuel cells currently being developed for near term use in vehicles require hydrogen as a fuel. Hydrogen can be stored directly or produced onboard the vehicle by reforming methanol or hydrocarbon fuels derived from crude oil (e.g. Diesel, gasoline or middle distillates). The vehicle design is simpler with direct hydrogen storage, but requires developing a more complex refueling infrastructure.

While most in the fuel cell vehicle community would agree that widespread public use of hydrogen fuel cell cars is the ultimate aim, there is an ongoing debate about the most direct path to this goal. Much of this debate centers around which fuel to use and when to use it.

This year we have concentrated on a set of related tasks aimed at assessing the potential for using hydrogen directly as a fuel for fuel cell vehicles. This work builds on our earlier studies of hydrogen infrastructure, and extends it to consider alternative fuel cell vehicle designs as well as the refueling system.

We compare three leading options for fuel storage onboard fuel cell vehicles (see Figure 1):

* compressed gas hydrogen storage
* onboard steam reforming of methanol
* onboard partial oxidation (POX) of hydrocarbon fuels derived from crude oil

with respect to vehicle performance, fuel economy and cost, and infrastructure requirements.

The following specific tasks are being addressed.

* Task 1. Evaluate the projected performance and cost characteristics of alternative fuel cell vehicles with:

  (a) compressed gas hydrogen storage
  (b) onboard reforming of methanol
  (c) onboard partial oxidation of hydrocarbon fuels derived from crude oil

  To estimate the performance of fuel cell vehicles, we employ fuel cell vehicle models developed at Princeton. We also draw on existing vehicle modelling work ongoing as part of the DOE/OTT (DOE/Office of Transportation Technologies) and PNGV (Partnership for a New Generation of Vehicles) programs on fuel cell vehicles, and related studies by other academic groups (UC Davis, U of Michigan, Georgetown U.). Although a considerable amount of modelling work has been done on hydrogen and methanol fuel cell vehicles, there is little published data on vehicles where hydrogen is produced onboard via partial oxidation of hydrocarbon fuels derived from crude oil. We have concentrated on understanding the issues for this alternative. Equilibrium, kinetic and heat integrated (ASPEN) models have been developed to estimate the performance of onboard fuel processors.

* Task 2. Evaluate the refueling infrastructure requirements for each alternative, for the case of Southern California. Capital costs for hydrogen refueling infrastructure development are estimated for various near term hydrogen supply options, and the cost of delivered hydrogen to the consumer is calculated. The overall infrastructure costs per car are also compared for gaseous hydrogen, methanol and hydrocarbon fuels from crude oil, including the added costs of fuel production, storage, distribution and refueling stations.(This task extends our earlier studies of hydrogen infrastructure in Southern California.) As part of this study we consider strategies for building a hydrogen infrastructure, e.g. examine how hydrogen might be introduced for centrally refueled buses and automotive fleets first, eventually moving to public use.

* Task 3. Determine the delivered fuel cost for Southern California conditions of the various fuels including hydrogen from natural gas, coal, solar, wind, biomass or nuclear; methanol from natural gas, biomass or coal; and hydrocarbon fuels such as gasoline or Diesel from crude oil.

* Task 4. Calculate the lifecycle cost of transportation for Southern California conditions for each alternative.

* Task 5. Compare the design and economics of hydrogen refueling station options including using small scale onsite steam reforming of natural gas and methanol, POX processing of hydrocarbon fuels and electrolysis. The results of this task will be a comparison of designs for hydrogen refueling stations, which might be appropriate for vehicle demonstrations. This builds on previous work at Princeton, as well as work published as part of the PNGV and DOE/OTT programs.

In this report, detailed results from Tasks 1 and 2 are given. Results from Tasks 3, 4, and 5, which are scheduled for completion by November 1997, will be given in subsequent reports.

Goals of Current Year's Work

The goals of our current study of hydrogen as a fuel for fuel cell vehicles are:

* To provide valuable data and suggest possible implementation strategies as the Hydrogen Program plans demonstrations of hydrogen vehicles and refueling infrastructure.

* To work with researchers at Directed Technologies, Inc. (DTI), Lawrence Livermore National Laboratories, and DOE to assist the DOE Hydrogen Program managers define performance and cost benchmarks that hydrogen vehicle and fuel supply technologies must meet to compete in transportation markets.

Data Sources

To estimate the infrastructure requirements for various fuels, we have used data developed as part of earlier studies of hydrogen refueling systems as well as data published as part of the PNGV and DOE/OTT programs. The emphasis is on studying infrastructure issues in Southern California, a likely site for hydrogen vehicle and refueling infrastructure demonstrations.

The work also involves estimating the cost and performance of alternative fuel cell vehicles. These estimates draw in part on existing published studies of fuel cell vehicle designs by Ford, GM, Chrysler and other PNGV participants. We also use the results of fuel cell vehicle component models developed at Princeton and at DTI. A large number of industry, government and academic sources have provided the data needed for our fuel cell vehicle calculations.

Carrying out conceptual designs of hydrogen energy systems requires a large data base on the performance and cost of hydrogen production, distribution and end-use equipment. A

Table 0. Conversion Factors And Economic Assumptions

1 GJ (Gigajoule) = 10^9 Joules = 0.95 Million BTU
1 EJ (Exajoule) = 10^{18} Joules = 0.95 Quadrillion (10^{15}) BTUs

1 million standard cubic feet (scf) = 28,300 Normal cubic meters (m_N^3) = 362 GJ (HHV)
1 million scf/day = 2.80 tons/day = 4.19 MW H_2 (based on the HHV of hydrogen)

1 scf H_2 = 362 kJ (HHV) = 344 BTU (HHV); 1 lb H_2 = 64.4 MJ (HHV) = 61.4 kBTU (HHV) = 178.5 scf
1 m_N^3 = 12.8 MJ (HHV); 1 kg H_2 =141.9 MJ (HHV) = 393 scf

1 gallon gasoline = 130.8 MJ (HHV); $1/gallon gasoline = $7.67/GJ (HHV)

All costs are given in constant $1993.

Capital recovery factor for hydrogen production systems, distribution systems and refueling stations = 15%

Table 1. Industrial, Government and Academic Data Sources

INDUSTRY

Industrial Gas Suppliers
- Air Products and Chemicals, Inc.
- Praxair
- BOC

Reformer Manufacturers
- Howe-Baker Engineering
- Hydrochem
- Haldor-Topsoe
- KTI
- Hydrogen Burner Technology

Electric and Gas Utilities
- Southern California Gas
- Southern California Edison

Fuel Cell Developers
- Ballard Power Systems
- International Fuel Cells
- Energy Partners
- H-Power

Manufacturers of Hydrogen Compressors and Cylinders
- Christy Park Industries
- RIX Compressors

Electrolysis Manufacturers
- Electrolyser, Inc.
- Teledyne

Automotive Companies
- Ford
- GM
- Chrysler
- Daimler-Benz
- Toyota
- Mazda

Oil Companies
- Exxon
- Mobil

Engineering/Research Companies
- Directed Technologies, Inc.
- Arthur D. Little
- Xerox/Clean Air Now Project
- Gas Research Institute
- Glyn Short (consultant)

GOVERNMENT

National Laboratories
- National Renewable Energy Laboratory
- Lawrence Livermore National Laboratories
- Los Alamos National Laboratories
- Argonne National Laboratories
- Sandia National Laboratories
- Oak Ridge National Laboratories

US Department of Energy

South Coast Air Quality Management District

California Air Resources Board

Los Angeles Metropolitan Transit Authority

ACADEMIC INSTITUTIONS
- University of California at Davis
- University of California at Riverside
- University of Michigan
- TexasA&M
- Humboldt State University
- Georgetown University

partial list of industrial, government, and academic sources used in the work is contained in Table 1.

Methods Of Analysis

As discussed below, where necessary, engineering models of fuel cell vehicles, fuel processors, and refueling station equipment have been developed.

The levelized cost of hydrogen production, delivered hydrogen cost and lifecycle costs of transportation are estimated using standard microeconomic techniques.

Interaction With Other Groups/Technology Transfer

In this research Princeton has coordinated with Directed Technologies, Inc. (DTI), Lawrence Livermore National Laboratory (LLNL) and other members of the Hydrogen Program Analysis Team (under the direction of Jim Ohi of NREL) to discuss cost and performance issues for hydrogen as a fuel for fuel cell vehicles. It has been particularly useful to compare our results with those from a recent infrastructure study undertaken by DTI for Ford and the Office of Transportation Technology.

This work has also involved interaction with fuel cell manufacturers and with automotive companies (including Ford, Chrysler and GM and their subcontractors) which are considering or planning fuel cell vehicle demonstrations as part of the DOE/OTT and PNGV programs. We have also interacted with groups at Los Alamos National Laboratory, and Argonne National Laboratory who are studying fuel cell vehicle systems, as well as other academic groups (UC Davis, U of Michigan, Georgetown U), fuel providers (Exxon, Mobil, ARCO), and other companies such as Arthur D. Little (ADL). A partial list of groups who have assisted us with useful data and discussions is given in Table 1.

Results to Date

Task 1: Comparison Of Alternative Designs For Fuel Cell Vehicles

Model Of Fuel Cell Vehicles

A computer model for proton exchange membrane fuel cell vehicles has been developed (Steinbugler 1996, Steinbugler and Ogden 1996, Steinbugler 1997). This program allows us to estimate the performance, fuel economy and cost of alternative fuel cell vehicle designs.

Input parameters to the model include:

* the driving schedule [the Federal Urban Driving Schedule (FUDS), Federal Highway Driving Schedule (FHDS) or others may be used]
* vehicle parameters (the base vehicle weight without the power train, the aerodynamic drag, the rolling resistance, vehicle frontal area, accessory loads),
* fuel cell system parameters (fuel cell current-voltage characteristic, fuel cell system weight),

* peak power battery characteristics (behavior on charging and discharging, weight), and

* fuel processor parameters (conversion efficiency, response time, weight, hydrogen utilization in the fuel cell).

First, the fuel cell system and peak power device are sized according to the following criteria:

* The fuel cell system alone must provide enough power to sustain a speed of 55 mph on a 6.5% grade.

* The output of the fuel cell system plus the peak power device must allow acceleration for high speed passing of 3 mph/sec at 65 mph.

These criteria are consistent with the goals set by the Partnership for a New Generation of Vehicles (PNGV).

Once the components are sized, the vehicle weight is calculated, (accounting for any extra structural weight needed on the vehicle to support the power system). Then the fuel economy is calculated for a desired driving schedule. At each time step of the driving schedule the road load equation [1] is solved to find the total power P_D needed from the vehicle's electrical power system (fuel cell plus peak power device).

$$P_D = P_{aux} + (mav + mgC_R v + 0.5\,\rho\,C_D\,A_F\,v^3)/\eta \qquad [1]$$

where:

P_D = total electrical power demanded of vehicle's power system (Watts)
P_{aux} = power needed for accessories such as lights and wipers (Watts)
m = vehicle mass (kg)
a = vehicle acceleration (m/s^2)
v = vehicle velocity (m/s)
g = acceleration of gravity = 9.8 m/s^2
C_R = rolling resistance
ρ = density of air (kg/m^3)
C_D = aerodynamic drag coefficient
A_F = vehicle frontal area (m^2)
η = efficiency of electric motor, controller and gearing

If the fuel cell alone cannot supply the power needed, the peak power battery is called upon. Power demanded is allocated between the fuel cell and battery in a way that both accounts for fuel processor response time and aims to maintain the battery at a target state of charge. (The program is set up to keep the battery near its ideal state of charge, by recharging from the fuel cell during driving.) Knowing the fuel processor efficiency, the fuel consumed in each time step can be estimated. Fuel consumption is summed over the drive cycle and divided into the distance travelled to give a fuel economy, expressed in miles per equivalent gallon of gasoline.

Fuel Storage Capacity and Range

The vehicle range is allowed to vary, but all fuel storage systems are assumed to weigh 50 kg. We assume that 7.5% hydrogen by weight can be stored in a compressed gas tank at 5000 psia. For gasoline and methanol, 13 gallons of fuel are stored in a 12 kg tank.

Model of Fuel Cell System

The fuel cell is modelled based on current-voltage curves for existing PEM fuel cells (Steinbugler and Ogden 1996). For hydrogen-air fuel cells operated at 3 atm, with cathode stoichiometry of 2, the voltage current relation is given by [Steinbugler 1997]:

$$V = 0.787 - 0.0533 \log i - 0.148\, i + V_{comp/exp} - V_{reformate} \qquad [2]$$

where:

V = voltage output in volts
i = current density is amps/cm^2

$V_{comp/exp}$ = voltage correction for power consumed/generated by net air compression/expansion.
= -0.08 for hydrogen
= +0.067 for methanol steam reforming
= 0 for gasoline POX

$V_{reformate}$ = voltage penalty due to H_2 dilution when operating on reformate
= 0 (hydrogen)
= 0.06 i for methanol reformate
= 0.128 i for gasoline/POX

This expression is valid for $0 < i < 1.5$ amps/cm^2.

Both the power produced by the fuel cell and the power required for cathode air compression are proportional to the flow of hydrogen through the fuel cell (or the current drawn from it.) Thus in order to properly account for the net auxiliary power (compression-expansion) we apply a constant voltage drop of $V_{comp/exp}$ to the polarization curve, as shown in Eq. 1.

The output of PEM fuel cells varies with the concentration of hydrogen in the anode feed gas. For compressed gas hydrogen storage, the feed gas to the fuel cell anode is pure hydrogen. For the case of methanol steam reforming, the hydrogen content is about 75% by volume and for gasoline partial oxidation about 35%. The voltage and power output of the fuel cell on different anode feed gases is shown in Figure 2. The peak power output is highest on pure hydrogen. The higher the hydrogen content, the better the fuel cell performance, and the greater its power density.

Model of Peak Power Battery

We have modelled our peak power battery as a thin film, spiral wound, lead-acid technology, based on data from the Bolder Battery company (Juergens 1995, Keating 1996, Plichta 1995). The battery system specific weight is assumed to be 1.0 kg/kW. To ensure a long lifetime, the battery is kept near its initial state of charge of 50% by recharging from the fuel cell during driving. The battery charge and discharge rates depend

on the battery power demand, the state of charge and on the battery resistance. The charging current is limited to 30 amps.

It is assumed that energy is recaptured via regenerative braking, up to the battery's maximum charge rate. When the battery state of charge exceeds its nominal value of 50%, the program demands more power from the battery and less from the fuel cell, in order to bring the battery state of charge back down to the nominal 50% level.

Models Of Onboard Fuel Processors

Onboard fuel processors convert a liquid fuel (methanol or gasoline) to a hydrogen rich gas for use in the fuel cell.

Heat integrated methanol steam reformer and gasoline partial oxidation systems have been modelled using ASPEN-plus software (Kreutz, Steinbugler and Ogden 1996, Kartha, Fischer and Kreutz 1996). Configurations for a methanol steam reformer /fuel cell system and a gasoline partial oxidation/fuel cell system are shown in Figures 3 and 4.

For the methanol steam reformer, the fuel cell anode exhaust gas is used as fuel in the reformer burner. The energy is recovered as heat input to the steam reforming reaction. The critical feedback loop, in which the anode exhaust is burned to partially satisfy the heat requirements for the steam reforming reaction, complicates a clear definition of the steam reformer efficiency independent of the fuel cell. As a gauge of system efficiency we employ the product of the steam reformer efficiency (HHV of hydrogen produced/HHV of methanol feed) times the hydrogen utilization in the fuel cell. This yields a system fuel reformer efficiency corresponding to the (HHV of the hydrogen consumed in the fuel cell)/(HHV of the methanol feed) = 62%. However, the expander work significantly exceeds that required for air compression, accounted for by a $V_{comp/exp}$=0.067 or on average an 8% increase in the DC output of the system.

In contrast to methanol steam reforming, which requires heat input, partial oxidation is an exothermic reaction. A well heat integrated POX reformer has no need for the energy contained in the anode exhaust. Some of the energy in the anode exhaust gas can be recovered for uses other than the POX reaction. For example, anode exhaust can be burned to vaporize the incoming gasoline and also to provide expander work to offset the required air compressor work. The expander work exceeds power demands for compression, but the excess power produced (<1 kWe) is not sufficient to warrant a separate generator. The conversion efficiency for the POX reactor is well defined (HHV H2 out/HHV gasoline in) and has been measured as the near-equilibrium value of 86.7% (Mitchell 1996).

For comparison with the steam reformer efficiency note that the product of the POX efficiency times the 80% hydrogen utilization in the fuel cell gives a POX system efficiency = (HHV H2 consumed/HHV gasoline in) of 69.4%.

Plotting the power demand P_D from Eq. 1, we see that the demands on the power system change rapidly over a typical drving cycle. This is shown in Figure 5, where the power required by the Federal Urban Driving Schedule is plotted vs. time. (When P_D is negative, the vehicle is braking.)

In a hydrogen fuel cell vehicle, the fuel cell should be able to follow the rapidly changing demands of the driving schedule. However, onboard fuel processors can have a longer response time, as it can take many seconds or even minutes to change the gas output of the

reformer. It may be difficult for the fuel processor/fuel cell system to follow the rapidly changing demands.

For POX reactors this may not be much of an issue, as the response time is expected to be quite fast. For steam reformers, it may be longer, on the order of several seconds or more. To model the effect of response time, we assumed that the fuel processor tries to follow the demands of the driving cycle, reaching the desired level in a characteristic response time. Meanwhile, the peak power battery supplies the power needed by the drive cycle, until the fuel processor can "catch up". The peak power battery is recharged while driving from the fuel cell, when the power is lower, or from regenerative braking.

The drive cycle power demand and the output of the fuel cell system are plotted in Figure 6 for fuel processor cases with 1 and 5 second response times. The fuel cell output matches the power demand well for the 1 second case, but lags the power demand significantly for the 5 second case. The battery state of charge is also shown for each case. For the 5 second response time, the battery is used more often and the battery state of charge has larger excursions away from its target value. The amount of energy routed through the battery is shown in Figure 7 as a function of fuel processor response time for the FUDS and FHDS cycles. The longer the response time, the more the battery must be used. For a 5 second response time 40-50% of the energy reaching the wheels on the FUDS cycle has been routed through the battery.

Model Results: Vehicle Performance, Fuel Economy and Cost for Alternative Fuel Cell Vehicle Designs

We now apply the model to compare alternative designs for fuel cell vehicles. Table 2 summarizes the assumptions used in our calculations. Table 3 shows the results for vehicle mass,the required size for the fuel cell and peaking battery, the fuel economy and range for alternative fuel cell vehicle designs.

Vehicle Weight

The vehicle mass varies with the vehicle type. The various components' contributions to the total vehicle mass are shown for hydrogen, methanol and gasoline fuel cells cars in Figure 8. Vehicles with onboard fuel processors are heavier for several reasons. First, the fuel processor adds weight. Second, the fuel cell/fuel processor system is less energy efficient than a pure hydrogen system, so a larger fuel cell is needed to provide the same power output, if the fuel cell is run on reformate. Third, the mass of the vehicle support structure is increased by 15% of the additional weight it carries. The methanol fuel cell vehicle weighs about 10% more than the hydrogen vehicle, the gasoline POX vehicle about 19% more.

Power Requirements for the Fuel Cell and Peak Power Device

The peak power required is shown in Table 3 for various fuel cell vehicle designs. Roughly, the fuel cell and battery each provide about half the peak power. For hydrogen, a lower peak power output is needed because the vehicle is lighter. In Figure 9, we have plotted a histogram showing the power demands of the FUDS and FHDS cycles (fraction of the time a certain power is demanded vs. power). The power required by the FUDS and FHDS cycles is considerably less than the fuel cell power, when the fuel cell is sized for sustained hill climbing. However, the long fuel processor response time means that the battery is used even during the FUDS cycle.

Table 2. Parameters Used in Fuel Cell Vehicle Modelling

Vehicle Parameters	
Glider Weight (= vehicle - power train)[a]	800 kg
Drag Coefficient[a]	0.20
Rolling Resistance[b]	0.007
Frontal Area[a]	2.0 m^2
Accessory Load[c]	0.4 kW
Structural Weight Compounding Factor[d]	15%
Fuel Cell System	
Operating pressure	3 atm
Cathode Stoichiometry	2
System weight (including air handling, thermal and water management)[e]	4.0 kg/kW
Fuel Processor Systems	
Methanol Steam Reformer	
Gross efficiency (HHV H2 consumed in fuel cell/HHV MeOH in)	62%
$V_{comp/exp}$	0.067 Volts
Hydrogen utilization[g]	80%
Voltage Penalty for reformate operation[h]	0.06 x current (amp/cm^2)
Weight of system[i]	32 kg+1.1 kg/kW
Response time	5 sec
Reformate Composition	70% H_2, 24% CO_2, 6% N_2
Gasoline POX	
Efficiency (HHV H2 consumed/HHV gasoline in)[j]	69.4%
Hydrogen utilization[g]	80%
Voltage Penalty for reformate operation[h]	0.128 x current (amp/cm^2)
Weight of system[i]	32 kg+1.1 kg/kW
Response time	1 sec
Reformate Composition	42% N_2, 38% H_2, 18% CO_2, 2% CH_4
Peak Power Battery	
Battery type	Spiral wound, thin film, lead-acid
System weight[k]	1.0 kg/kW
Maximum charge rate	30 amps
Nominal state of charge[k]	50%
Energy stored[k]	15 Wh/kg
Motor and Controller	
Overall efficiency[b]	77%
Overall weight[l]	2.0 kg/kW
Fuel Storage	
Hydrogen[d]	5000 psi compressed gas tank total weight 50 kg, 7.5% H2 by weight
Methanol, Gasoline	12 kg tank, 13 gallon capacity total weight 50 kg
Driving schedules	FUDS, FHDS
Regenerative braking recovered up to battery capabilities	

Notes for Table 2

a. Based on PNGV targets. (Source: CALSTART website. http://www.calstart.org/about/pngv/pngv_ta.html)

b. Energy and Environmental Analysis, "Analysis of Fuel Economy Boundary for 2010 and Comparison to Prototypes," p. 4-11, prepared for Martin Marietta Energy Systems, Contract No. 11X-SB0824, November 1990.

c. Ross, M. and W. Wu, "Fuel Economy Analysis for a Hybrid Concept Car Based on a Buffered Fuel-Engine Operating at a Single Point," SAE Paper No. 950958, presented at the SAE Interantional Exposition, Detroit, MI, Feb 27-March 2, 1995.

d. C.E. Thomas and R. Sims, "Overview of Onboard Liquid Fuel Storage and Reforming Systems," "Fueling Aspects of Hydrogen Fuel Cell Powered Vehicles," Society of Automotive Engineers, Proceedings, Fuel Cells for Transportation TOPTEC, April 1-2, 1996, Arlington, VA.

e. Based on a Ballard-type PEM fuel cell system with a stack power density of 1 kg/kW. Other weight is due to auxiliaries for heat and water management equipment and air compression.

f.Arthur D. Little 1994. "Multi-Fuel Reformers for Fuel Cells Used in Transportation, Multi-Fuel Reformers, Phase I Final Report," USDOE Office of Transportation Technologies, Contract No. DE-AC02-92-CE50343-2.

g. This estimate was verified with fuel cell developers.

h. The voltage penalty for operation on reformate is based on models by Shimson Gottesfeld at Los Alamos National Laboratory.

i. William Mitchell, Arthur D. Little, private communications, 1997.

j. Mitchell, W. April 2, 1996. "Development of a Partial Oxidation Reformer for Liquid Fuels," Society of Automotive Engineers, Proceedings, Fuel Cells for Transportation TOPTEC, Arlington, VA.

k. Keating, J., B. Schroeder and R. Nelson 1996. "Development of a Valve-Regulated, Lead/Acid Battery for Power-Assist Hybrid Electric Vehicle Use," Bolder Technologies Corporation, Wheat Ridge, CO.

l. Chang, L. "Recent Developments of Electric Vehicles and Their Propulsion Systems," Proceedings of the 28th Intersociety Engineering Conference, vol. 2, pp. 2.205-2.210, American Chemical Society, 1993.

Table 3.
Model Results: Comparison of Alternative Fuel Cell Vehicle Designs

Fuel Storage/ H2 Generation System	Vehicle mass (kg)	Peak Power (kW) (FC/Battery)	FUDS mpeg	FHDS mpeg	Combined 55% FUDS 45% FHDS mpeg	range (mi)
Direct H2	1170	77.5 (34.4/43.1)	100	115	106	425
Methanol Steam Reformer	1287	83.7 (37.0/46.7)	62	79	69	460
Gasoline POX	1395	89.4 (39.4/50.0)	65	80	71	940

For the assumptions in Table 2.

Fuel Economy

The fuel economy is shown for the FUDS, FHDS, and combined driving cycles. The combined driving cycle fuel economy is defined as:

mpg (combined) = 1/(.55/mpg FUDS + .45/mpg FHDS)

For mid-sized automobiles, with PNGV type characteristics, the fuel economy of a hydrogen fuel cell vehicle is estimated to be more than 100 miles per gallon on an energy equivalent basis. The energy efficiencies of the methanol and gasoline fuel cell vehicles are about 2/3 that of the hydrogen fuel cell vehicle. The loss of efficiency is due to several effects, as shown in Figure 10. First is the 15-25% energy loss in converting methanol or gasoline to hydrogen. Second, operation on reformate means that the fuel cell has a lower efficiency. Third, the vehicle weighs 10-20% more with an onboard fuel processor. Finally, for the methanol steam reformer, the 5 second response time means that a significant fraction (40-50%) of the energy must be routed through the battery, with attendant losses in charging and discharging.

Range

The vehicle range exceeds the PNGV goal of 380 miles, for all the fuel cell vehicle cases considered in Table 3.

Vehicle Cost

The cost of alternative fuel cell vehicles is shown in Figure 11. Table 4 summarizes our cost assumptions for fuel cell vehicle components in high volume mass production. Two sets of cases are shown, one corresponding to a low range of values for fuel cell, fuel processor, battery and hydrogen storage mass produced costs, the other to a high range of values. We see that the first cost of fuel cell vehicles with onboard methanol steam reformers would be higher than that for hydrogen fuel cell vehicles by about $400-430/car. We estimate gasoline POX fuel cell cars would cost $660-870/car than hydrogen vehicles.

For comparison the manufacturing cost of corresponding parts for a gasoline internal combustion engine vehicle (e.g. the engine, transmission, electrical system, fuel and tank, and emission control systems) might be about $39/kW (Steinbugler 1997). For a gasoline IC engine car with an 94 kW engine (the estimated power for an aluminum intensive Ford Sable), this would be about $3666/car. To achieve a first cost similar to that of today's gasoline ICEVs, fuel cell vehicle components must meet stringent cost goals.

Summary

In summary, for the same performance, hydrogen fuel cell vehicles are likely to be simpler in design, lighter, more energy efficient, and less expensive than methanol or gasoline fuel cell vehicles. And the tailpipe emissions will be strictly zero.

Table 4. Cost Estimates for Mass Produced Fuel Cell Vehicle Components

Component	High estimate	Low estimate
Fuel cell system[a]	$100/kW	$50/kW
Fuel processor system [b]	$25/kW	$15/kW
Hydrogen storage cylinder rated at 5000 psia[c]	$1000	$500
Motor and controller[d]	$26/kW	$13/kW
Peak power battery[e]	$20/kW	$10/kW
Extra structural support	$1/kg	$1/kg
Cost of 12 kg gasoline or methanol tank	$100	$100

a. Based on a range of estimates found in the literature. For example, GM/Allison projects a fuel cell "electrochemical engine" cost of $3899 for a 60 kW system including the fuel cell, fuel processor (methanol reformer), heat and water management. This is about $65/kW (at the rated power of 60 kW) or $46/kWpeak. About 45% of the cost per peak kW ($21/kW) is for the fuel cell stack, 28% ($13/kW) for the methanol reformer and the rest for auxiliaries. This cost assumes large scale mass production. (Allison Gas Turbine Division of General Motors December 16, 1992).

Mark Delucchi of Institute of Transportation Studies at UC Davis estimates a retail cost of $2954 for a mass produced 25 kW hydrogen/air PEM fuel cell system or about $120/kW. (The manufacturing cost is $59/kW, with a materials costs for the fuel cell stack plus auxiliaries estimated to be $41/kW, and the labor cost $18/kW.) (J. M. Ogden, E.D. Larson and M.A. Delucchi May 1994).

A study by Directed Technologies for the USDOE estimated a cost in mass production of $2712 for a hydrogen/air fuel cell plus auxiliaries with net output of 85 kW power (about $32/kW). Directed Technologies is now working with Ford Motor Company on fuel cell vehicles as part of the PNGV program. (Ref: B.D. James, G.N. Baum and I.F. Kuhn, Directed Technologies, Inc. "Technology Development Goals for Automotive Fuel Cell Power Systems," prepared for the Electrochemical Technology Division, Argonne National Laboratory, Contract No. W-31-109-Eng-28, February 1994.)

Chrysler estimates that even with current fuel cell manufacturing technology, mass produced costs would be $200/kW (Chris Boroni-Bird, private communications 1997).

b. W. Mitchell, J. Thijssen, J.M. Bentley, "Development of a Catalytic Partial Oxiidation Ethanol Reformer for Fuel Cell Applications," Society of Automotive Engineers, Paper No. 9527611, 1995.

c. C.E. Thomas and R. Sims, "Overview of Onboard Liquid Fuel Storage and Reforming Systems," "Fueling Aspects of Hydrogen Fuel Cell Powered Vehicles," Society of Automotive Engineers, Proceedings, Fuel Cells for Transportation TOPTEC, April 1-2, 1996, Arlington, VA.

d. Derived from estimates in B. James, G. Baum, I. Kuhn, "Development Goals for Automotive Fuel Cell Power Systems," ANL-94/44, August 1994.

e. Based on PNGV goals

Task 2: Refueling Infrastructure Requirements for Fuel Cell Vehicles

Developing a Refueling Infrastructure for Hydrogen Vehicles

The relative simplicity of vehicle design for the hydrogen fuel cell vehicle must be weighed against the added complexity and cost of developing a hydrogen refueling infrastructure. Indeed, hydrogen infrastructure is often seen as a "show-stopper" for hydrogen fuel cell vehicles.

We have assessed the technical feasibility and economics of developing a hydrogen vehicle refueling infrastructure (Ogden, Dennis, Steinbugler and Strohbehn 1995, Ogden, Cox and White 1996, Ogden 1997). A number of near term possibilities for producing and delivering gaseous hydrogen transportation fuel were considered (using commercial or near commercial technologies for hydrogen production, storage and distribution). These include (see Figure 12):

* hydrogen produced from natural gas in a large, centralized steam reforming plant, and truck delivered as a liquid to refueling stations,

* hydrogen produced at the refueling station via small scale steam reforming of natural gas, (in either a conventional steam reformer or an advanced steam reformer of the type developed as part of fuel cell cogeneration systems)

* hydrogen produced in a large, centralized steam reforming plant, and delivered via small scale hydrogen gas pipeline to refueling stations,

* hydrogen produced via small scale electrolysis at the refueling station,

* hydrogen from chemical industry sources (e.g. excess capacity in ammonia plants, refineries which have recently upgraded their hydrogen production capacity, etc.), with pipeline delivery to a refuelingstation.

Economics Of Hydrogen Production And Delivery

Delivered cost of hydrogen transportation fuel

The delivered (levelized) cost of hydrogen transportation fuel (to the vehicle) from these sources is estimated in Figure 13. Delivered fuel costs are given in $/GJ. (On a higher heating value basis, the energy cost of $1/gallon gasoline is equivalent to $7.7/GJ -- see Table 0.) In this example, we have used energy prices in the Los Angeles area, where the natural gas cost is low ($2.8/GJ), and the cost of off-peak power is relatively high (3 cents/kWh). A capital recovery factor of 15% is assumed. (For other assumptions, the delivered costs will vary.) The cost contributions of various factors are shown for each technology over a range of refueling station sizes from 0.1 to 2.0 million scf/day (e.g. stations capable of refueling about 80-1600 fuel cell cars/day or 8-160 fuel cell buses/day). Although all the supply options are roughly competitive, several points are readily apparent.

* Onsite production of hydrogen via small scale steam reforming of natural gas is economically attractive and has the advantage that no hydrogen distribution system is required. Delivered hydrogen costs are

shown for onsite reforming of natural gas based on: 1) conventional small steam reformer systems and 2) advanced low cost reformers, which have just been introduced for stationary hydrogen production (Farris 1996, Halvorson et.al 1997). With conventional reformer technology, hydrogen is expensive at small station sizes, but is economically attractive at larger station sizes. As discussed in a recent report (Ogden et.al. 1996), adopting lower cost, advanced steam methane reformer designs based on fuel cell reformers could substantially reduce the delivered cost of hydrogen especially at small station size. With advanced reformers, onsite reforming is competitive with liquid hydrogen truck delivery and pipeline delivery over the whole range of station sizes considered.

* Truck delivered liquid hydrogen gives a delivered hydrogen cost of $20-30/GJ, depending on the station size. This alternative would be also attractive for early demonstration projects, as the capital requirements for the refueling station would be relatively small (Ogden et.al. 1995, Ogden et.al. 1996), and no pipeline infrastructure development would be required.

* Under certain conditions, a local pipeline bringing centrally produced hydrogen to users could offer low delivered costs. Centrally produced hydrogen ranges in cost from $3/GJ (for refinery excess) to $5-9/GJ for large scale steam reforming to $8-10/GJ for hydrogen from biomass, coal or MSW). If the cost of hydrogen production is low, higher pipeline costs could be tolerated. Still, for pipeline hydrogen to be competitive with truck delivery or onsite reforming, pipeline costs can be no more than a few $/GJ. For a small scale hydrogen pipeline system to be economically competitive a large, fairly localized demand would be required. Alternatively, a small demand might be served by a nearby, low cost supply of hydrogen.

* It appears that onsite electrolysis would be somewhat more expensive than other options, largely because of the relatively high cost of off-peak power (3 cents/kWh) assumed in the study. If the cost of off-peak power were reduced from 3 cents/kWh to 1-1.5 cents/kWh, hydrogen costs would become much more competitive.

Capital cost of building a hydrogen refueling infrastructure

The capital cost of building a hydrogen refueling infrastructure is often cited as a serious impediment to use of hydrogen in vehicles. In Figure 14 and Tables 5a and 5b, we show the capital cost of building a hydrogen refueling infrastructure for the various options discussed in the previous section. We consider two levels of infrastructure development.

* Early development of distribution system and refueling stations to bring excess hydrogen from existing hydrogen capacity to users. We assume that no new centralized hydrogen production capacity is needed. Two refueling stations serve a total fleet of 13,000 cars, each station dispensing 1 million scf H2/day to 800 cars/day. The options for providing hydrogen include: 1) Liquid hydrogen delivery via truck from existing capacity, 2) pipeline hydrogen delivery from a nearby large

Table 5a. Capital Cost for Developing New Hydrogen Delivery and Refueling Station Infrastructure Serving a Total Fleet of 13,000 FCV Cars, Delivering 2 million scf H_2/day (assuming that existing production capacity is used)

	Centralized Production via Steam Reforming of Natural Gas w/LH2 Delivery	Centralized Production via Steam Reforming of Natural Gas w/Pipeline Delivery	Onsite Steam Reforming of Natural Gas: Conventional Steam Methane Reformer	Onsite Steam Reforming of Natural Gas: Fuel Cell Steam Methane Reformer	Onsite Advanced Electrolysis Using Off-Peak Power
Centralized Hydrogen Production	0 (assumed that existing capacity is used)	0 (assumed that existing capacity is used)			
Hydrogen Distribution	0 (assumed that existing trucks are used)	10 km pipeline = $6.2 million (at $1 million per mile)			
2 Refueling Stations each serving 800 cars/day	$1.4 million ($0.7 per station)	$3.4 million ($1.7 million per station)	$10.8 million ($5.4 million per station)	$6.8 million ($3.4 million per station)	$11.4 million ($5.7 million per station)
TOTAL	$1.4 million	$9.6 million	$10.8 million	$6.8 million	$11.4 million
infrastructure cost per car	$105	$740	$830	$520	$880

Adapted from Ogden, Kreutz, Iwan and Kartha 1996.

Table 5b. Capital Cost for Developing New Hydrogen Production, Delivery and Refueling Station Infrastructure Serving a Total Fleet of 1 million Fuel Cell Cars, Delivering 153 million scf H_2/day

	Centralized Production via Steam Reforming of Natural Gas w/LH2 Delivery	Centralized Production via Steam Reforming of Natural Gas w/Pipeline Delivery	Onsite Steam Reforming of Natural Gas: Conventional Steam Methane Reformer	Onsite Steam Reforming of Natural Gas: Fuel Cell Steam Methane Reformer	Onsite Advanced Electrolysis Using Off-Peak Power
Centralized Hydrogen Production	$100 million for reformer + $ 200 million for liquefier + LH2 storage	$170 million for reformer + H_2 compressor			
Hydrogen Distribution	80 LH2 trucks each with a 3 tonne capacity, each making 2 local deliveries/day = $40 million	600 km pipeline = $380 million (at $1 million per mile)			
153 1 million scf H2/day Refueling Stations each serving 800 cars/day	$104 million ($0.7 million per station)	$260 million ($1.7 million per station)	$830 million ($5.4 million per station)	$516 million ($3.4 million per station)	$870 million $5.7 million per station)
TOTAL	$440 million	$810 million	$830 million	$516 million	$870 million
Infrastructure Cost per Car	$440	$810	$830	$516	$870

Adapted from Ogden, Kreutz, Iwan and Kartha 1996.

hydrogen plant or refinery, 3) onsite production from steam reforming of natural gas and 4) onsite production from electrolysis

* Development of new hydrogen production, delivery and refueling capacity to meet growing demands for hydrogen transportation fuel. The system serves a total fleet of 1 million cars, each station dispensing 1 million scf H2/day to 800 cars/day. Options for providing hydrogen are: 1) liquid hydrogen delivery via truck from new centralized steam reformer capacity, 2) pipeline hydrogen delivery from a new centralized hydrogen plant, 3) onsite production from steam reforming of natural gas and 4) onsite production from electrolysis.

The range of infrastructure capital costs for a system serving 13,000 fuel cell cars, is about $1.4-11.4 million or $100-900/car. The range of infrastructure capital costs for a system serving 1 million fuel cell cars, is about $400-900 million or $400-900/car.

It is important to keep in mind the results of Figure 13 for the total delivered cost of hydrogen transportation fuel, as well as the capital cost of infrastructure. Some of the lower capital cost options such as liquid hydrogen delivery, can give a higher delivered fuel cost than pipeline delivery or onsite reforming. Onsite small scale steam reforming is attractive as having both a relatively low capital cost (for fuel cell type reformers), and a low delivered fuel cost.

Developing a Refueling Infrastructure for Methanol Fuel Cell Vehicles

A modest distribution system for chemical methanol exists at present. To service a significant number of fuel cell cars, this network would have to be expanded in some places. To bring methanol to millions of fuel cell cars might involve increases in methanol production capacity as well.

The cost of truck delivery is estimated to be about the same for methanol and gasoline on a volumetric basis. Given the lower energy density of methanol, truck delivery would cost about $1.9/GJ, as compared to $1.0/GJ for gasoline (Ogden, Larson and Delucchi 1994).

The capital cost of retrofitting a refueling station from gasoline to methanol use has been estimated at about $20,000 per station. If a new methanol refueling station were built, the cost should be comparable to that for a new gasoline station, so no incremental cost as compared to gasoline is would be expected.

The costs to develop methanol refueling infrastructure should be relatively small compared to hydrogen infrastructure costs. As a first approximation, we assume additional infrastructure costs for methanol are zero.

Cost of Infrastructure for Gasoline Fuel Cell Vehicles

For this study, we have assumed that there is no extra capital cost for developing gasoline infrastructure for fuel cell vehicles. This may be an oversimplification. For example, if a new type of gasoline (e.g. very low sulfur) is needed for gasoline/POX fuel cell vehicles, this would entail extra costs at the refinery. Environmental effects of gasoline refueling stations are not considered (e.g. remediation of pollution from leaking underground storage tanks). The costs of maintaining the existing gasoline infrastructure are not considered.

Total Infrastructure Costs (On And Off The Vehicle) For Fuel Cell Vehicles: Hydrogen Compared To Methanol And Gasoline

It is often stated that use of methanol or gasoline with onboard reformers would greatly reduce (for methanol) or eliminate (for gasoline) the problem of developing a new fuel infrastructure. How does the capital cost of building a hydrogen refueling infrastructure compare to the capital cost of infrastructure development for methanol or gasoline fuel cell vehicles?

Defining "infrastructure" to mean all the equipment (both on and off the vehicle) required to bring hydrogen to the fuel cell, it is clear that gasoline and methanol fuel cell vehicles also entail extra costs -- largely for onboard fuel processing. In the case of hydrogen, the infrastructure development capital cost is paid by the fuel producer (and passed along to the consumer as a higher fuel cost). In the case of methanol or gasoline fuel cell vehicles, the capital cost is paid by the consumer buying the car.

In Figure 15 we combine our estimates of the cost of alternative fuel cell vehicles (Figure 11) and off-board refueling infrastructure (Figure 14). Our estimates show that gasoline POX fuel cell vehicles are likely to cost $660-870 more than comparable hydrogen fuel cell vehicles. The added cost of off-board refueling infrastructure for hydrogen is in the range $500-900/vehicle. The total cost for infrastructure on and off the vehicle would be comparable for hydrogen and gasoline fuel cell vehicles.

A recent study by Directed Technologies, Inc. also concluded that when the total infrastructure cost (on and off the vehicle) is considered, hydrogen infrastructure capital costs are comparable to those for methanol and gasoline (Thomas 1996).

Discussion: Is Hydrogen Refueling Infrastructure A "Show-Stopper" For Hydrogen Fuel Cell Vehicles

Our study suggests several reasons why hydrogen infrastructure development may not be an insurmountable obstacle to introducing hydrogen fuel cell vehicles.

* The technologies to produce, deliver and dispense hydrogen are well known. There appear to be no major technical hurdles to providing hydrogen transportation fuel.

* The capital cost of building a hydrogen refueling infrastructure off the vehicle appears to be comparable to the added cost of putting individual small hydrogen production systems (fuel processors) onboard each vehicle.

* There are ample resources for making hydrogen. For the next few decades, hydrogen from natural gas appears to be the least expensive option in many locations. In the longer term, gasification of biomass, municipal solid waste or coal (with sequestration of the CO_2) may offer relatively low hydrogen costs. Onsite electrolysis in areas with low cost off-peak power may be attractive as well. (Ogden, Cox and White 1996).

* In a recent case study of potential hydrogen supply and demand in the Los Angeles area (Ogden, Cox and White 1996, Ogden 1997), we found that it would be possible to introduce significant numbers of fuel

cell vehicles, even without building any new hydrogen production capacity. The excess hydrogen capacity available from industrial suppliers and refineries in LA today might fuel 700-2000 PEM fuel cell buses or 30,000-100,000 PEM fuel cell cars.

Of course, hydrogen faces the same "chicken and egg" problem as any non-gasoline alternative automotive fuel, in moving beyond centrally refueled niche markets into general public refueling. More than the cost of hydrogen instructure (which appears to be comparable to the added vehicle cost of using onboard fuel processors), the issue may be getting enough hydrogen fuel cell vehicles on the road to reduce the cost of fuel cells via mass production, thereby opening the way to general automotive markets.

Strategies For Developing Fuel Cell Vehicles: The Potential Role Of Hydrogen

Hydrogen in Early Fuel Cell Fleet Demonstrations

Hydrogen is likely to play an important role in early fuel cell vehicle demonstrations. The first fuel cell vehicle fleets may be hydrogen fueled PEM fuel cell buses, for several reasons:

* Ballard will be demonstrating hydrogen fueled PEMFC buses in several cities starting in 1997, with commercialization planned for 1998.

* Refueling with hydrogen or any alternative fuel is easier at centralized fleet locations such as bus garages.

* The daily demand for hydrogen for a bus depot would be large enough to bring the delivered cost of hydrogen down somewhat because of economies of scale, especially for stations based on small scale reformers.

* Fuel cells might be economically competitive first in bus markets, where cost goals are not as stringent as for automobiles.

Early fuel cell fleet demonstrations offer an excellent opportunity to demonstrate hydrogen refueling systems as well. We recommend that hydrogen infrastructure demonstrations be an important part of hydrogen fuel cell bus projects. Demonstrations of small scale methane reformers may be of particular interest. (A fleet of about 8 PEMFC buses could be refueled daily using a small scale reformer producing 100,000 scf H2/day. Rapid developments in small scale reformer technology are making this an increasingly attractive supply option. (Halvorson, Victor and Farris 1997)

Introduction of Fuel Cell Automobiles

Several major automobile manufacturers are conducting R&D on PEM fuel cell cars (including Chrysler, GM, Ford, Daimler-Benz, Mazda, Toyota, and Honda). A PEMFC mini-van using compressed hydrogen gas storage was demonstrated in May 1996 by Daimler-Benz. Recently Daimler-Benz and Ballard Power Systems announced a $450 million venture to develop fuel cell vehicles (Ballard Press Release April 14, 1997). In October of 1996, Toyota demonstrated a hydrogen fuel cell car at an electric car show in Osaka (Toyota Press Release October 4, 1996). Chrysler has announced plans to demonstrate a gasoline POX fuel cell automobile, with commercialization possible around

2005 (Detroit Free Press, January 7, 1997). Ford has announced its intention to develop a prototype hydrogen fuel cell automobile, which could be ready for evaluation by the year 2000 (New York Times, April 22, 1997, p.). It is likely that the first mid-size PEMFC automobiles may be demonstrated before the year 2000. The first mass-produced commercial models might be available a few years later in the 2004-2010 time frame.

If onboard partial oxidation of gasoline is perfected, this might allow a rapid introduction of fuel cell cars to the general public, with attendant lowering of fuel cell costs in mass production. But onboard POX vehicles appear to have penalties in terms of vehicle cost, complexity, efficiency and emissions, which may make hydrogen vehicles an extremely attractive successor or alternative. Given the lower first costs for hydrogen fuel cell vehicles (see Figure 11), there may be a strong incentive to switch to hydrogen fuel, even if large numbers of gasoline/POX fuel cell cars are introduced first, bringing the cost of fuel cells down via mass production. [Recent studies by Directed Technologies, Inc. suggest that the most economically attractive route to fuel cell vehicle commercialization may be starting with hydrogen fuel cell vehicles rather than gasoline (Thomas 1997).]

We recommend that demonstrations of hydrogen refueling systems (especially small scale reformers) be conducted as part of hydrogen vehicle demonstrations (bus and automotive fleets) over the next few years. (In fleet applications hydrogen fuel cell vehicles may be preferred from the beginning for reasons of vehicle simplicity and cost.) As vehicle demonstrations progress, design issues for various types of fuel cell vehicles will be better understood and the path to commercialization should become clearer.

Conclusions

* Simulation programs of fuel cell vehicles and onboard fuel processors have been developed. For the same performance, we found that hydrogen fuel cell vehicles are simpler in design, lighter weight, more energy efficient and lower cost than those with onboard fuel processors.

* Vehicles with onboard steam reforming of methanol or partial oxidation of gasoline have about two thirds the fuel economy of direct hydrogen vehicles. The efficiency is lower because of the conversion losses in the fuel processor (losses in making hydrogen from another fuel), reduced fuel cell performance on reformate, added weight of fuel processor compents, and effects of fuel processor response time.

* For mid-size automobiles with PNGV type characteristics (base vehicle weight of 800 kg -- e.g. weight without the power train and fuel storage, aerodynamic drag of 0.20, and rolling resistance of 0.007), fuel economies (on the combined FUDS/FHDS drving cycle) are projected to be about 106 mpeg for hydrogen fuel cell vehicles, 69 mpeg for fuel cell vehicles with onboard methanol steam reforming, and 71 mpeg for onboard gasoline partial oxidation.

* Based on projections for mass produced fuel cell vehicles, methanol fuel cell automobiles are projected to cost about $400-430 more than comparable hydrogen fuel cell vehicles. Gasoline/POX fuel cell automobiles are projected to cost $660-870 more than hydrogen fuel cell vehicles.

* The cost of developing hydrogen refueling infrastructure based on near term technologies would be about $500-900/car depending on the type of hydrogen supply. No extra costs are assumed for developing gasoline or methanol infrastructure.

* Defining "infrastructure" to mean all the equipment (both on and off the vehicle) required to bring hydrogen to the fuel cell, we find that the cost is comparable for hydrogen, methanol and gasoline POX fuel cell vehicles.

* Hydrogen is the prefered fuel for fuel cell vehicles, for reasons of vehicle design, cost and efficiency, as well as potential energy supply and environmental benefits. The cost of developing hydrogen refueling infrastructure is comparable to the total cost (on and off the vehicle) for gasoline fuel cell vehicles. Like CNG or methanol, hydrogen faces the issue of reaching beyond centrally refueled fleet markets. Valuable experience can be gained in the near term by building the refueling systems for centrally refueled hydrogen fuel cell vehicle demonstrations, and investing now in technologies which could play a role in a future hydrogen infrastructure.

Proposed Future Work

Assessment Of Potential Supplies And Demands For Hydrogen Energy In The New York/New Jersey Area

The New York City metropolitan area is a possible candidate for demonstrations of hydrogen energy technologies. In the future we propose to do a preliminary study of potential hydrogen demands and supplies in the New York/New Jersey, similar to our earlier work in Southern California. Like California, New York and New Jersey have severe urban air quality problems and are considering the use of zero and low emission vehicles. Moreover, New Jersey is becoming a center of fuel cell development activity, as evidenced by the recent joint venture of GPU and Ballard to develop PEM fuel cell cogeneration systems. Unlike California, relatively little analysis has been done looking into the possibilities for hydrogen vehicles.

In particular, we would like to address the following:

* What are potential demands for hydrogen for transportation markets in the New York/New Jersey area. We would consider centrally refueled applications such as urban buses, vans and fleet autos, as well as public automobiles.

* What are potential supplies for hydrogen in the New York area, considering:

  a) truck delivered or pipeline delivered merchant hydrogen,
  b) hydrogen byproduct from chemical plants and refineries,
  c) onsite hydrogen production from steam reforming of natural gas at small scale,

d) electrolytic hydrogen from off-peak power,
e) hydrogen from gasification of municipal solid waste.

* What is the production cost and delivered cost of hydrogen transportation fuel from these various sources.

* How do the projected fuel cost per kilometer and lifecycle cost of transportation compare for hydrogen vehicles and other alternative vehicles.

Implications Of CO_2 Sequestration For Hydrogen Energy Systems

Recently, it has been proposed that hydrogen could be produced at large scale via steam reforming of natural gas, or gasification of coal or biomass, with low cost separation of CO2 and permanent sequestration underground. Fossil fuels could be used with significantly reduced greenhouse gas emissions.

CO2 sequestration raises a host of interesting systems questions, which we propose to address as part of our work for the Hydrogen R&D Program in FY'98. These include the following.

* When would it make sense to start sequestering CO2? In particular, at what scale of hydrogen production could you begin sequestering CO2? How large a demand must be in place before sequestering and long distance hydrogen transmission become attractive? Answering this question involves understanding the economies of scale of hydrogen production, CO2sequestering, and pipeline transmission.

* What is the cost of hydrogen production with sequestration compared to other hydrogen production methods? How does it compare to localized hydrogen production from natural gas and to fuel cycles with no net CO2 emissions (e.g. hydrogen from solar, wind or biomass)? How does the cost vary with demand? What are the potential impacts of new steam reformer technologies?

* What are plausible scenarios for a transition toward a large scale hydrogen energy system with sequestration? Under what conditions will pipeline hydrogen (produced via large scale steam reforming and transmitted via pipeline) compete with locally produced hydrogen (either at the city scale -- in a single city-sized refomer plant) or onsite (e.g. via small scale steam reforming at a hydrogen refueling station)?

Acknowledgments

The systems studies reported here were performed with support from U.S. Department of Energy Hydrogen R&D Program, under contract No. DE-FG36-95G010061.

For useful conversations, the author would like to thank Jeff Bentley (Arthur D. Little), Adam Cox (Princeton University), Paul Farris (IFC), Shimson Gottesfeld (Los Alamos National Laboratory), Brian James (Directed Technologies, Inc.), Sivan Kartha (Princeton University), Ryan Katofsky (Arthur D. Little), Michael Kerr (Praxair), Ira Kuhn (Directed Technologies, Inc.), Paul Kydd (BOC), Christian Lenci (Praxair), Frank Lomax (Directed Technologies, Inc.), Robert Miller (Air Products and Chemicals, Inc.), William Mitchell (Arthur D. Little), David Moard (Hydrogen Burner Technology), Robert Moore (Air Products and Chemicals, Inc.), David Nahmias (National Hydrogen Association), Venki Raman (Air Products and Chemicals, Inc.), Robert Socolow (Princeton University), Sandy Thomas (Directed Technologies, Inc.), Jason White (Princeton University) and Robert Williams (Princeton University).

References

Allison Gas Turbine Division of General Motors December 16, 1992. Final Report DOE/CH/10435-01, "Research and Development of Proton Exchange Membrane (PEM) Fuel Cell System for Transportation Applications," prepared for the US Department of Energy Office of Transportation Technologies.

Arthur D. Little 1994. "Multi-Fuel Reformers for Fuel Cells Used in Transportation, Assessment of Hydrogen Storage Technologies, Phase I Final Report," USDOE Office of Transportation Technologies, Contract No. DE-AC02-92-CE50343-1.

Arthur D. Little 1994. "Multi-Fuel Reformers for Fuel Cells Used in Transportation, Multi-Fuel Reformers, Phase I Final Report," USDOE Office of Transportation Technologies, Contract No. DE-AC02-92-CE50343-2.

Chang, L. 1993. "Recent Developments of Electric Vehicles and Their Propulsion Systems," Proceedings of the 28th Intersociety Engineering Conference, vol. 2, pp. 2.205-2.210, American Chemical Society.

Delucchi, M.A. 1992. "Hydrogen Fuel Cell Vehicles," UCD-ITS-RR-92-14, Institute of Transportation Studies, University of California, Davis.

Dennis, E.B. May 1994. "Design and Feasibility of a Gaseous Hydrogen Refueling Station Based on Small Scale Steam Reforming of Natural Gas," Princeton University senior thesis, Department of Chemical Engineering.

Farris, Paul 1996. International Fuel Cells, private communications.

Halvorson, T., R. Victor and P.J. Farris , January 19-22, 1997."Onsite Hydrogen Generator for Vehicle Refueling Application," to appear in Proceedings of the '97 World Car Conference, Riverside, CA.

James, B., G. Baum and I. Kuhn August 1994. "Technology Development Goals for Automotive Fuel Cell Power Systems," Argonne National Laboratory Report No. ANL-94/44.

Juergens, C. and R.F. Nelson 1995. "A New High-Rate, Fast-Charge, Lead/Acid Battery," Journal of Power Sources, Vol. 53, pp. 201-205.

Keating, J., B. Schroeder and R. Nelson 1996. "Development of a Valve-Regulated, Lead/Acid Battery for Power-Assist Hybrid Electric Vehicle Use," Bolder Technologies Corporation, Wheat Ridge, CO.

Kreutz, T., M. Steinbugler and J. Ogden Nov 17-20, 1996. "Onboard Fuel Reformers for Fuel Cell Vehicles: Equilibrium, Kinetic and System Modelling," Abstracts '96 Fuel Cell Seminar, Orlando, FL.

Kartha, S., S. Fischer and T. Kreutz Nov 17-20, 1996. "Analysis of Onboard Fuel Processing Designs for Fuel Cell Vehicles," 96 Fuel Cell Seminar, Orlando, FL.

Mitchell, W., J. Thijssen, J.M. Bentley 1995. "Development of a Catalytic Partial Oxiidation Ethanol Reformer for Fuel Cell Applications," Society of Automotive Engineers, Paper No. 9527611.

Mitchell, W. April 2, 1996. "Development of a Partial Oxidation Reformer for Liquid Fuels," Society of Automotive Engineers, Proceedings, Fuel Cells for Transportation TOPTEC, Arlington, VA.

Ogden, J.M., E.D. Larson and M.A. Delucchi May 27, 1994. "An Assessment of Renewable Transportation Fuels and Technologies," report to the US Congress Office of Technology Assessment.

Ogden, J.M., E. Dennis, M. Steinbugler and J. Strohbehn Jan. 18, 1995. "Hydrogen Energy Systems Studies," final report to USDOE for Contract No. XR-11265-2.

Ogden, J.M., E. Dennis and K. Montemayor March 1995. "Development of Refueling Infrastructure for Hydrogen Vehicles," Proceedings of the 6th National Hydrogen Association Meeting, p. 237.

Ogden, J., T. Kreutz, S. Kartha and L. Iwan November 26, 1996. " Assessment of Technologies for Producing Hydrogen from Natural Gas at Small Scale," Princeton University Center for Energy and Environmental Studies Draft Report.

Ogden, J.M. January 19-22, 1997. "Infrastructure for Hydrogen Fuel Cell Vehicles: A Southern California Case Study," to appear in Proceedings of the '97 World Car Conference, Riverside, CA.

Ogden, J.M., A Cox and J. White December 9, 1996." Case Study of Developing Hydrogen Refueling Infrastructure in Southern California," Princeton University Center for Energy and Environmental Studies Draft Report.

Plichta, E.J. and G. W. Au June 1995. "High Power Evaluation of Thin Metal Foil Lead-Acid Cells," Report No. ARL-TR-431, Army Research Laboratory.

Ross, M. and W. Wu Feb 27-March 2, 1995. "Fuel Economy Analysis for a Hybrid Concept Car Based on a Buffered Fuel-Engine Operating at a Single Point," SAE Paper No. 950958, presented at the SAE Interantional Exposition, Detroit, MI.

Steinbugler, M. September 17-19, 1996. "How Far, How Fast, How Much Fuel: Evaluating Fuel Cell Vehicle Configurations," presented at the Commercializing Fuel Cell Vehicles Conference, Intertech Conferences, Hyatt Regency O'Hare, Chicago.

Steinbugler , M. and J. Ogden Nov 17-20, 1996. "Fuel Economy and Range Estimates for Fuel Cell Vehicles," '96 Fuel Cell Seminar, Orlando, FL.

Steinbugler, M. 1997. "Modelling of PEM Fuel Cell Vehicles," Ph.D. Thesis (manuscript in preparation), Princeton University Center for Energy and Environmental Studies.

Thomas, C.E. and R. Sims April 1-2, 1996. "Overview of Onboard Liquid Fuel Storage and Reforming Systems," "Fueling Aspects of Hydrogen Fuel Cell Powered Vehicles," Society of Automotive Engineers, Proceedings, Fuel Cells for Transportation TOPTEC, Arlington, VA.

Thomas, C.E. January 19-22, 1997. "Affordable Hydrogen Supply Pathways for Fuel Cell Vehicles," presented at the '97 World Car Conference, Riverside, CA.

Figures

Figure 1: Possible Fuel Cell Vehicle Configurations

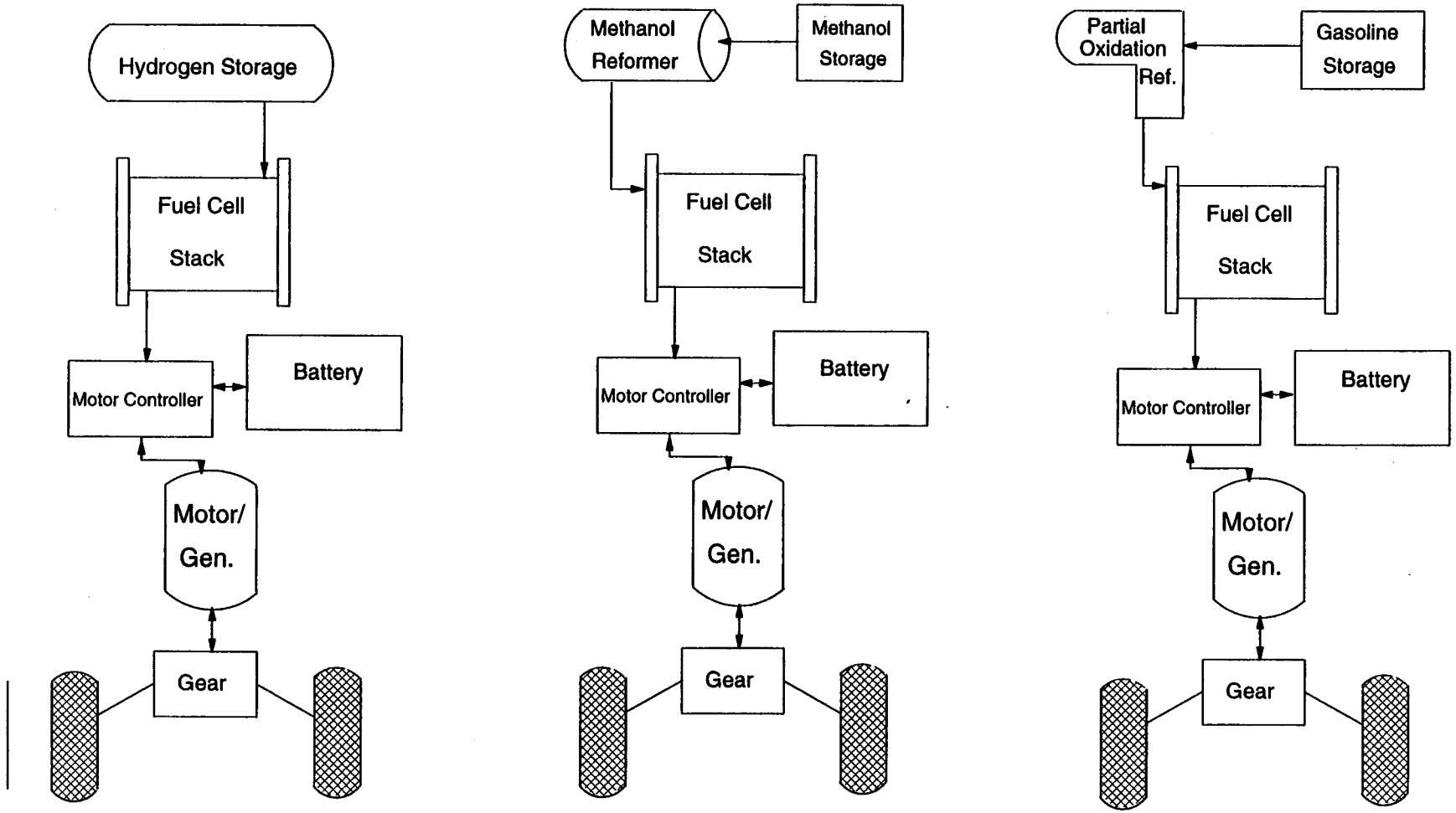

Fuel Cell Characteristics

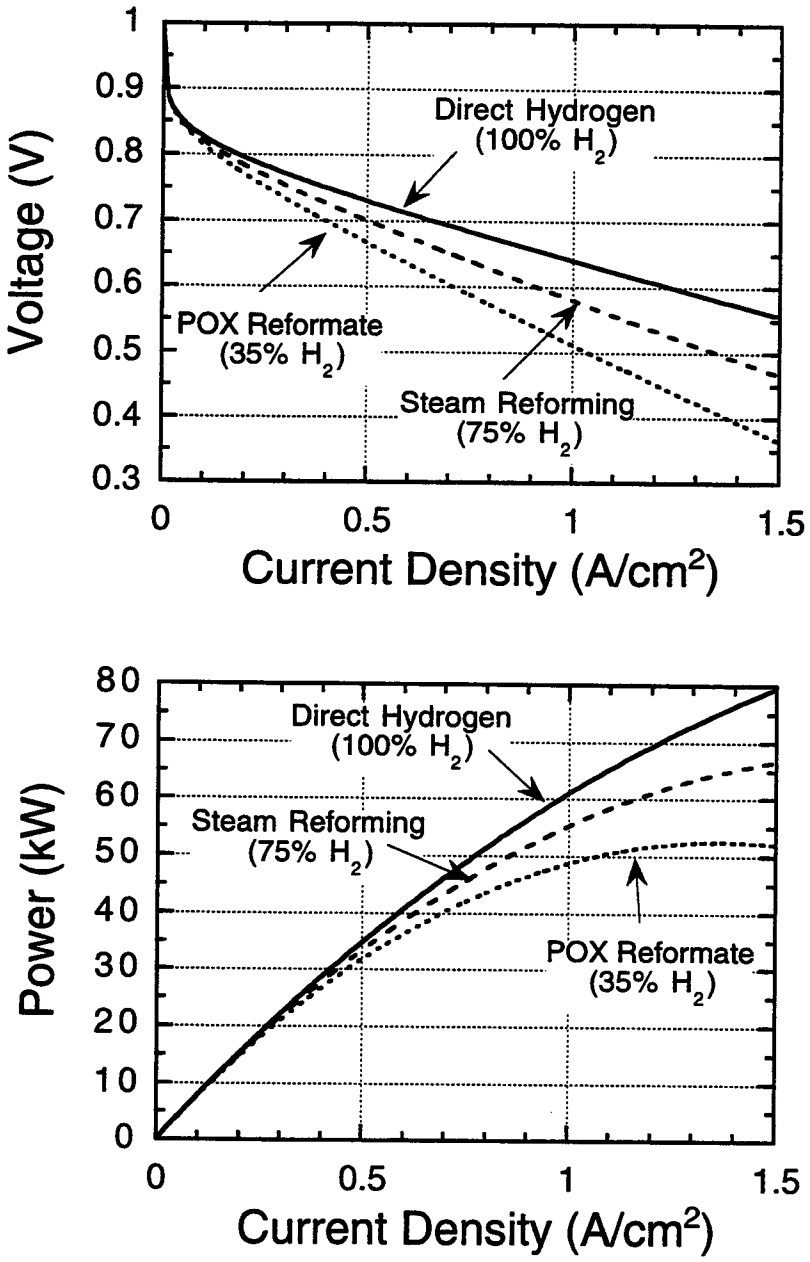

Figure 2. The fuel cell polarization curves and power output as a function of current density for pure hydrogen and two levels of dilution which roughly correspond to reformate from 1) gasoline POX, and 2) methanol steam reforming.

Methanol Steam Reformer System

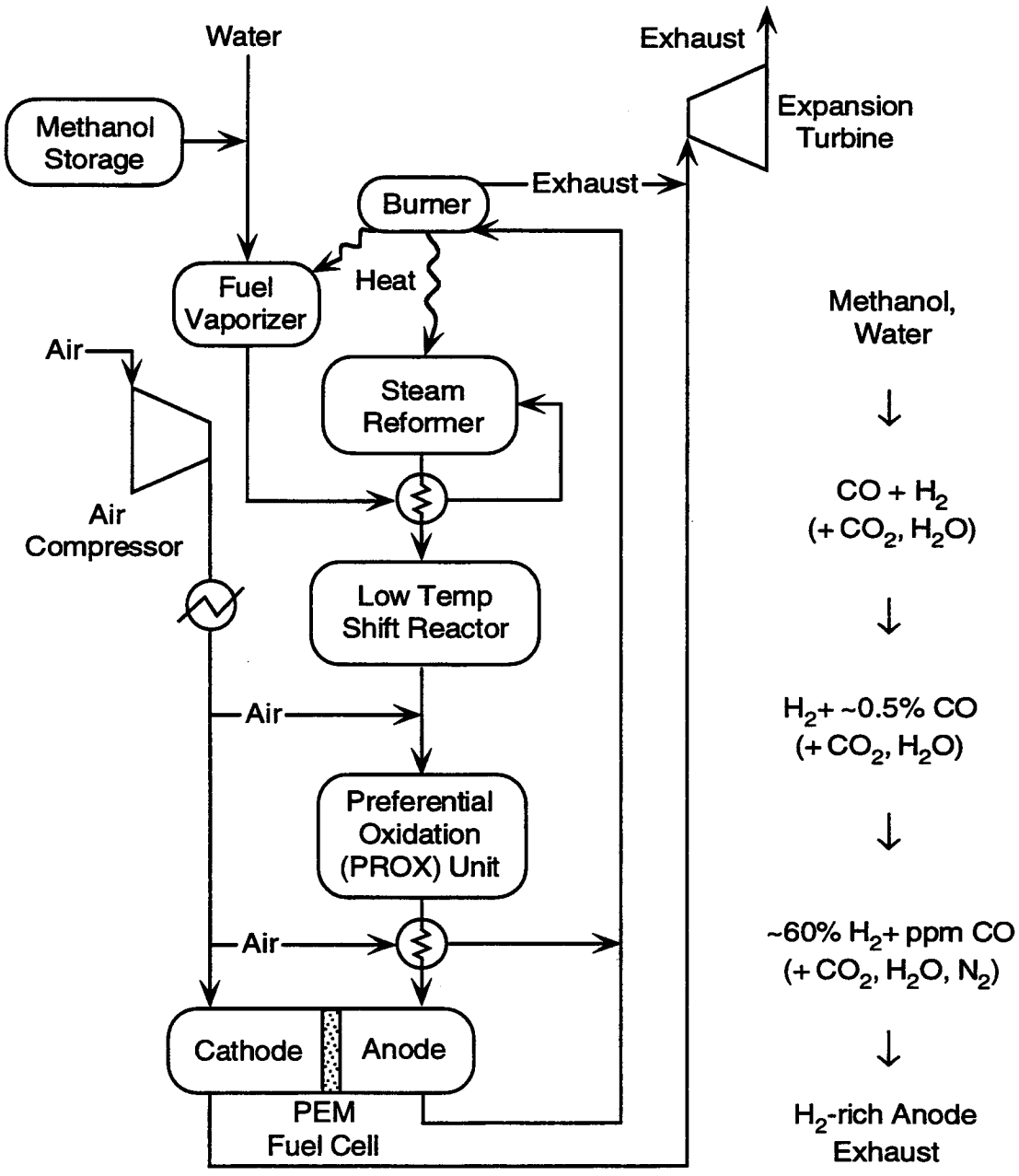

Figure 3. Schematic on-board methanol steam reforming system.

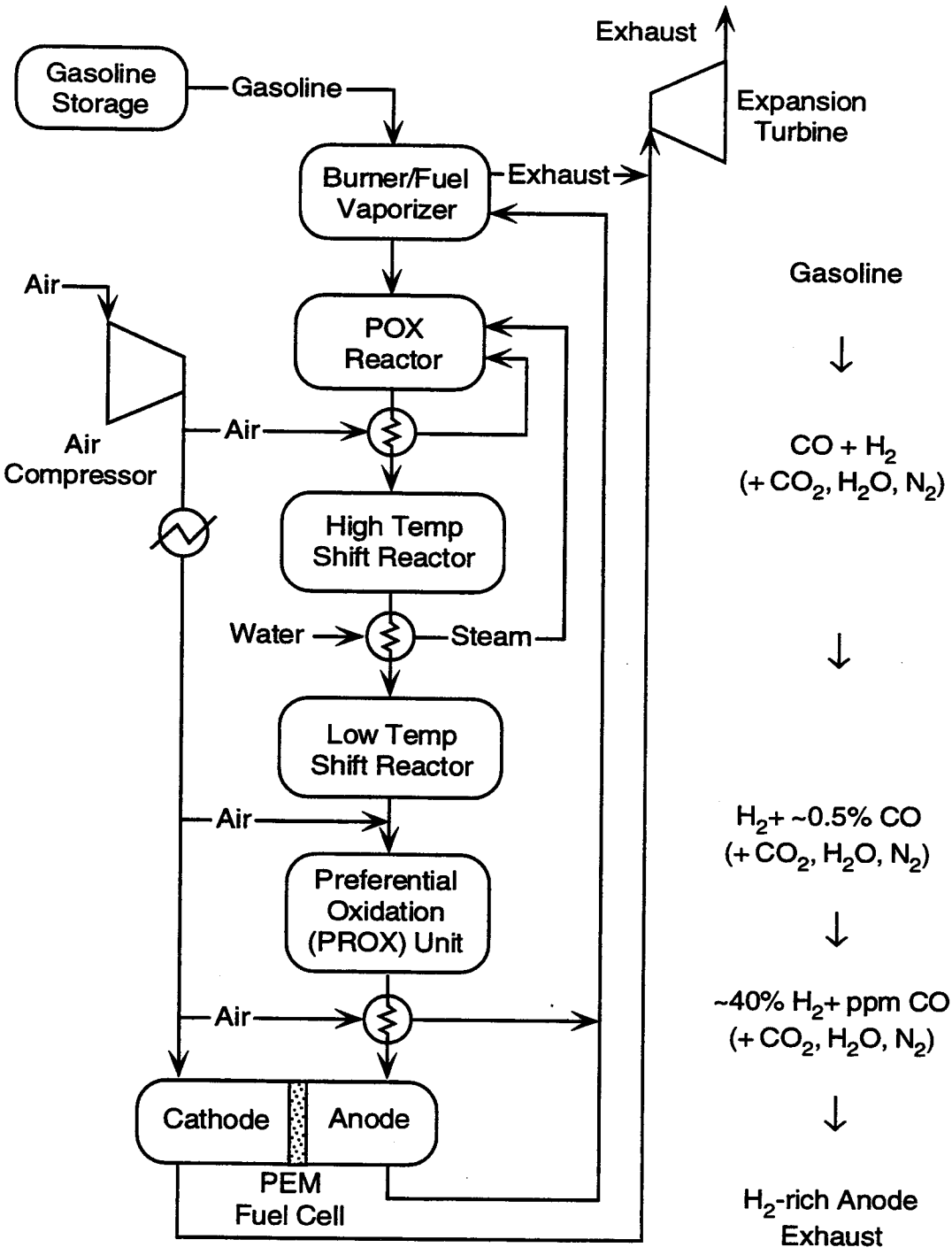

Figure 4. Schematic on-board gasoline partial oxidation (POX) reforming system.

Cycle Power Requirements and System Response

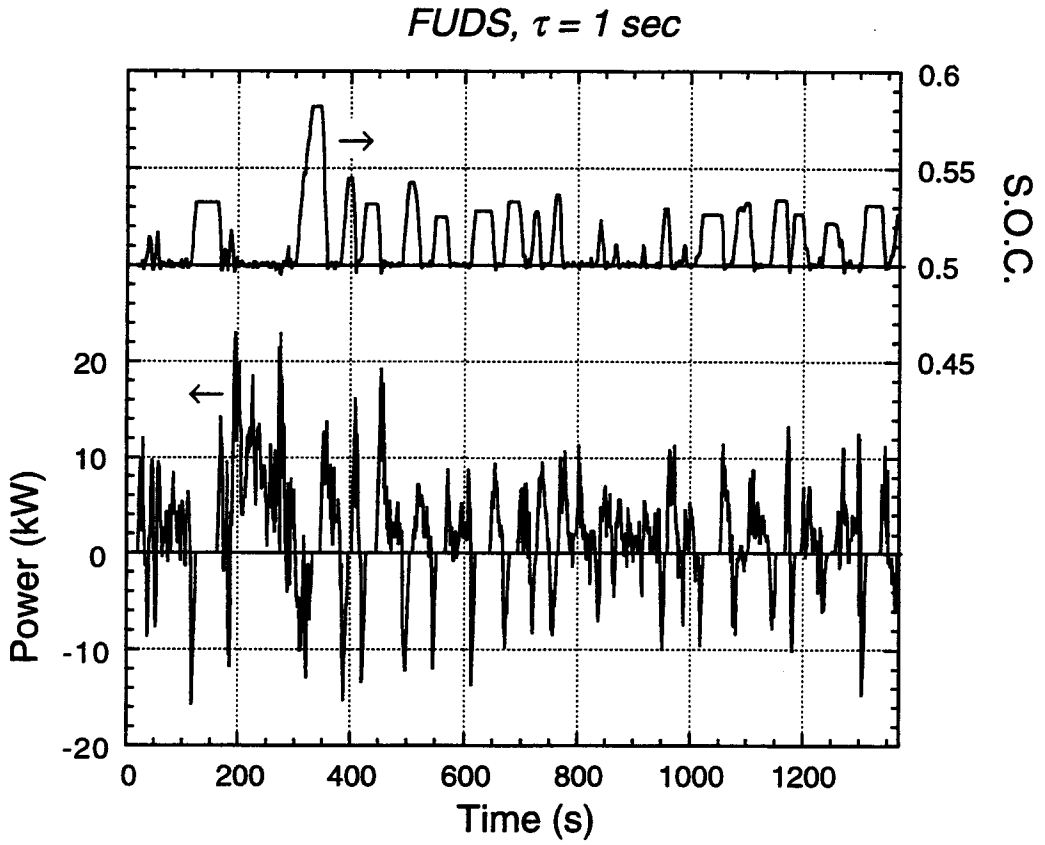

Figure 5. The power required of the fuel processor/fuel cell system during the FUDS cycle, and the resulting fractional battery state-of-charge (SOC). Conditions: 1000 kg vehicle mass, 1 sec fuel processor time constant, 0.36 kWh battery, 1 sec characteristic time for battery recharging, 28.9 kW baseload power, 0.77 motor/controller efficiency.

Time Constant Effects

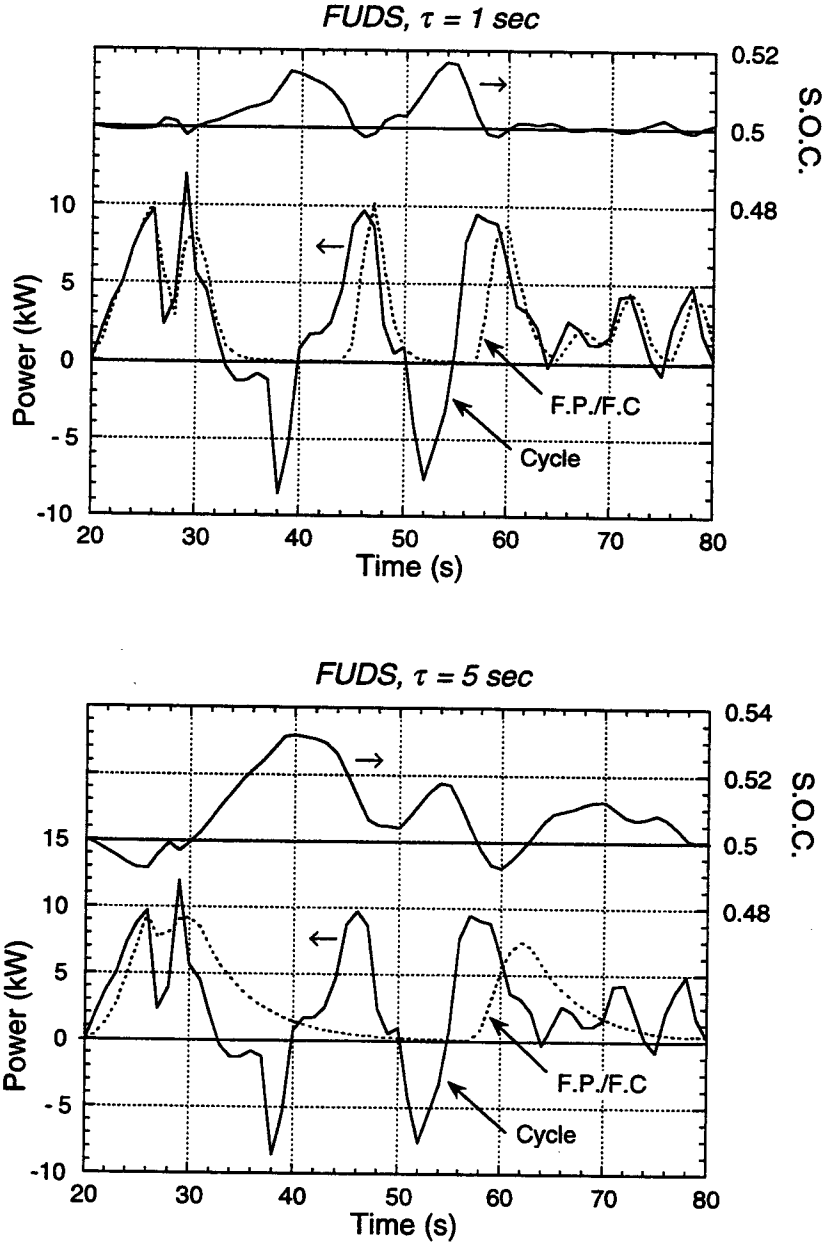

Figure 6. The power provided by the fuel processor/fuel cell - for both 1 and 5 second time constants - as a function of time in response to the power demanded by a portion of the FUDS cycle. The resulting battery fractional state of charge (SOC) is also shown, oscillating about its target value of 50%. Conditions: 1000 kg vehicle mass, 0.36 kWh battery, 1 sec characteristic time for battery recharging, 28.9 kW baseload power, 0.77 motor/controller efficiency.

Time Constant Effects:

Energy Routed Through Battery

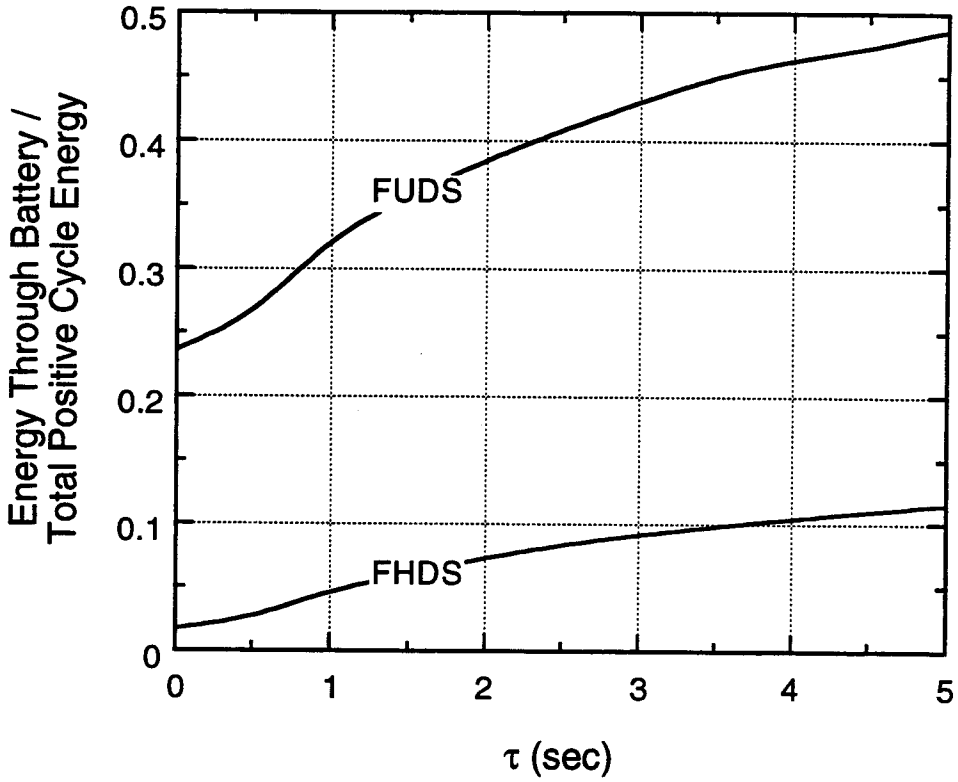

Figure 7. The fraction of the total positive cycle energy, for both the FUDS and FHDS driving cycles, that passes through the peaking device (e.g. battery), which acts as a buffer between the fuel processor/fuel cell system and the rapidly fluctuating demands of the driving cycle. Conditions: 1000 kg vehicle mass, 0.36 kWh battery, 1 sec characteristic time for battery recharging, 28.9 kW baseload power, 0.77 motor/controller efficiency.

Figure 8: Contributions to Vehicle Weight

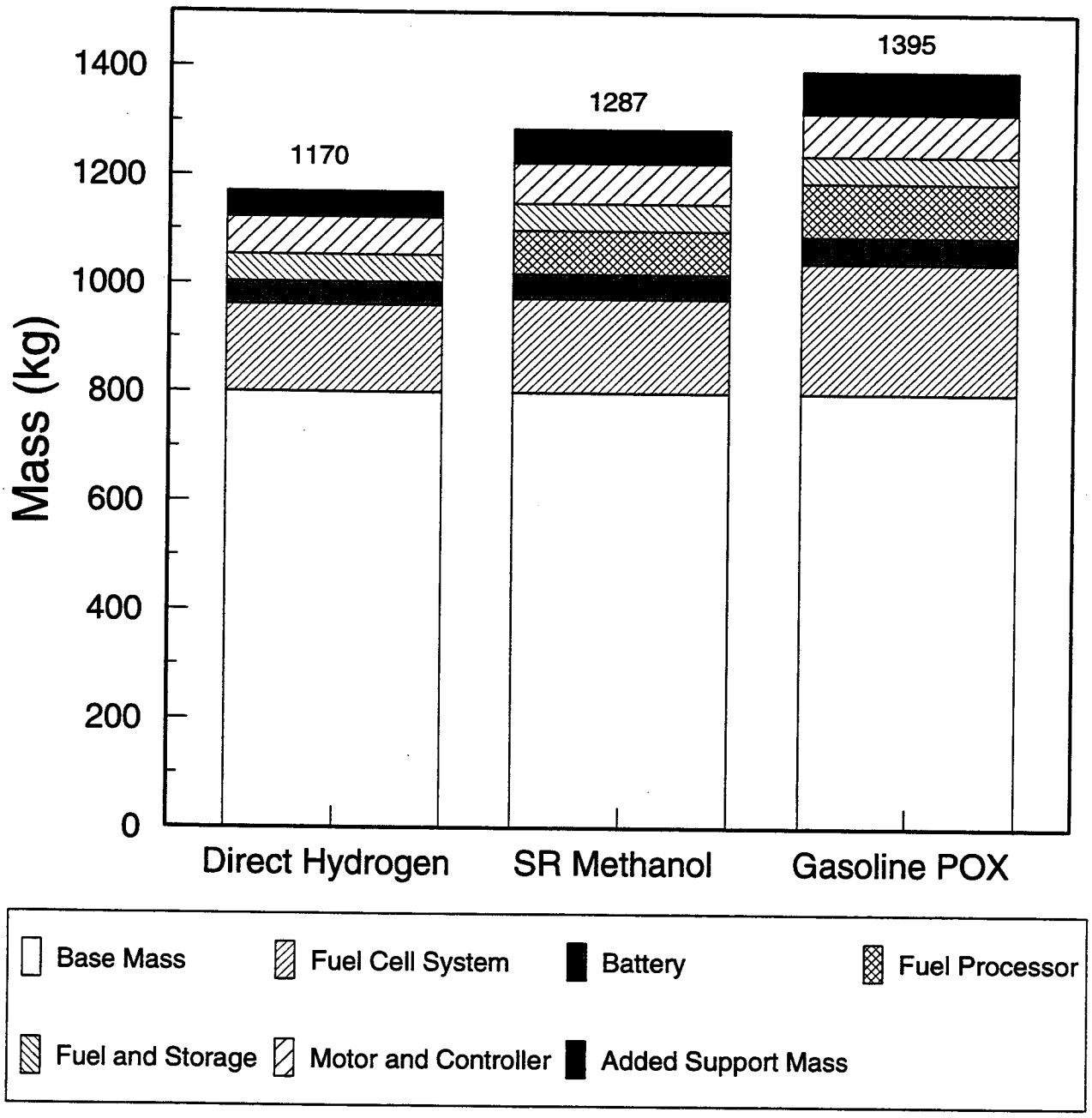

Required vs. Available Power

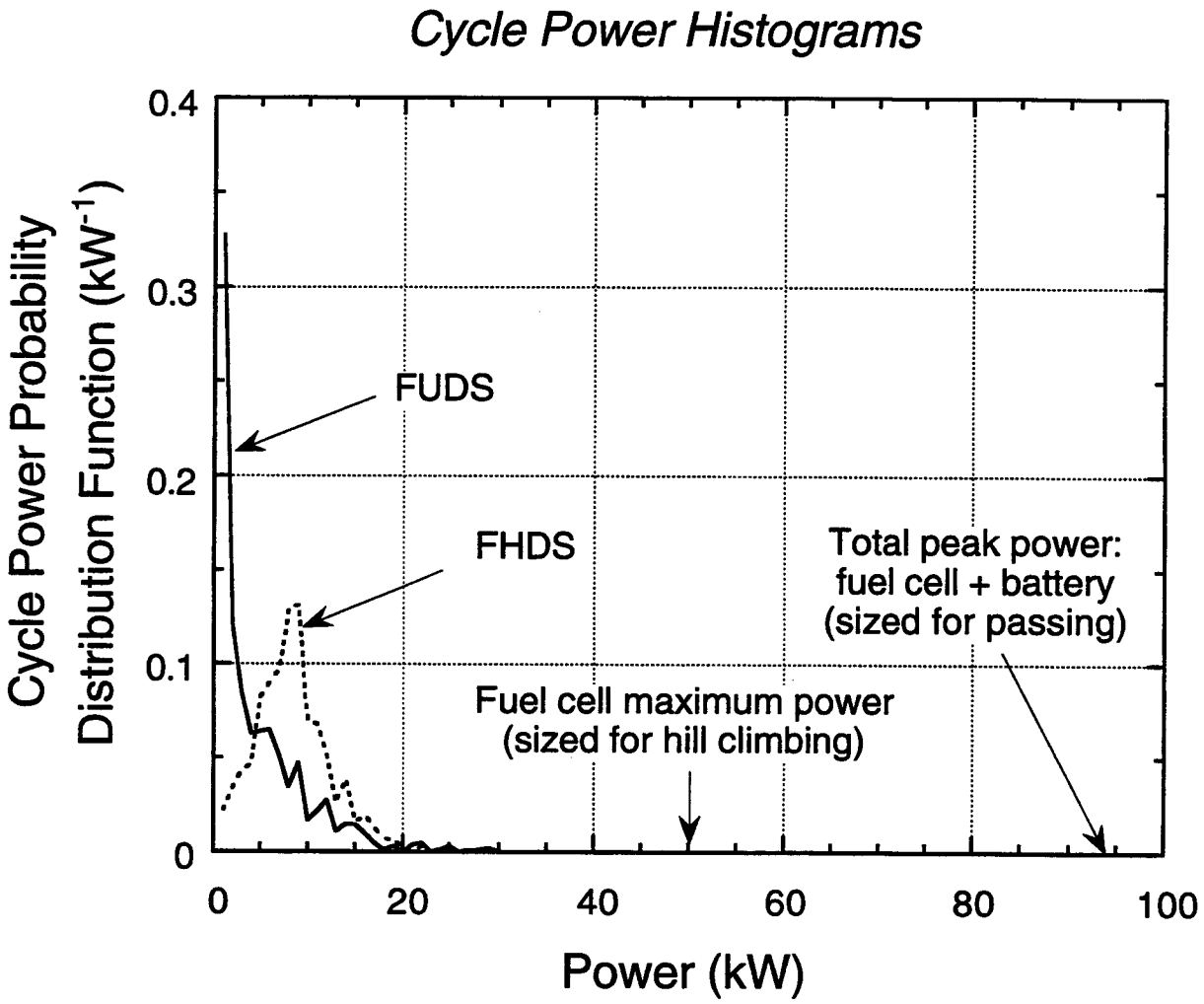

Figure 9. Histograms of the power required by the fuel processor/fuel cell system on the FUDS and FHDS driving cycles. As a result of the stiff performance requirements which govern the size of the fuel cell and the battery, much much more power is available than is usually called for under 'normal' driving conditions. Conditions: 1000 kg vehicle mass, 0.36 kWh battery, 1 sec characteristic time for battery recharging, 28.9 kW baseload power, 0.77 motor/controller efficiency.

Figure 10
Fuel Economy Penalties From On-Board Fuel Processing

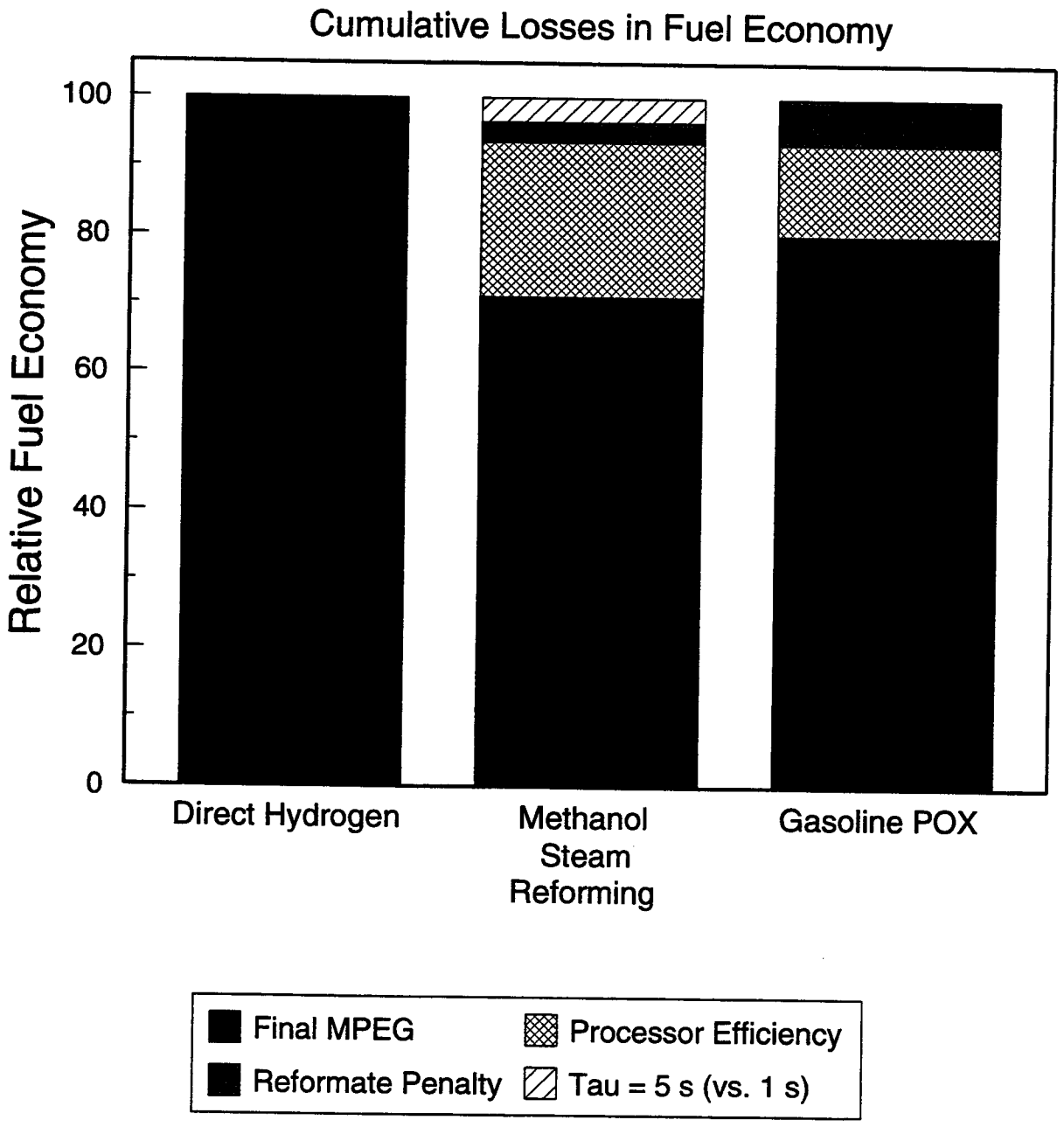

Fig. 11 Cost of Components in Alternative Fuel Cell Automobiles

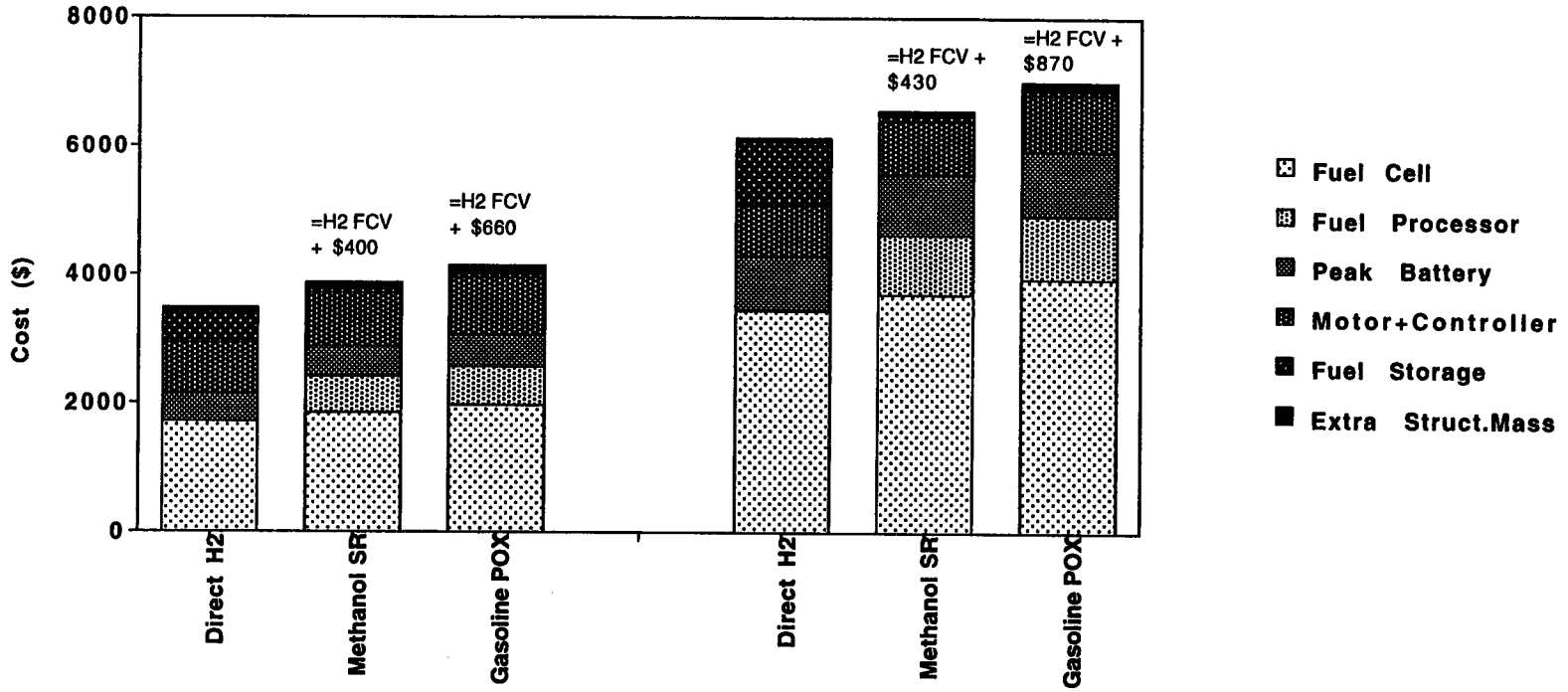

Fuel Cell = $50/kW
Fuel Processor = $15/kW
Peak Battery = $10/kW
H2 cylinder = $500
Motor+Controller=$13/kW
Gasoline or MeOH Tank =$100
Extra Struct. Mass = $1/kg

Fuel Cell = $100/kW
Fuel Processor = $25/kW
Peak Battery = $20/kW
H2 cylinder = $1000
Motor+Controller=$13/kW
Gasoline or MeOH Tank =$100
Extra Struct. Mass = $1/kg

FIG 12. NEAR TERM GASEOUS H2 SUPPLY OPTIONS

CENTRALIZED REFORMING

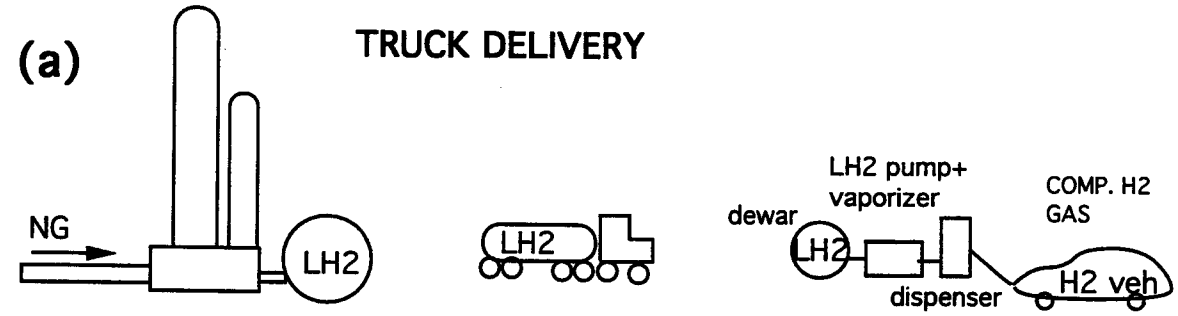

CHEMICAL BY-PRODUCT HYDROGEN

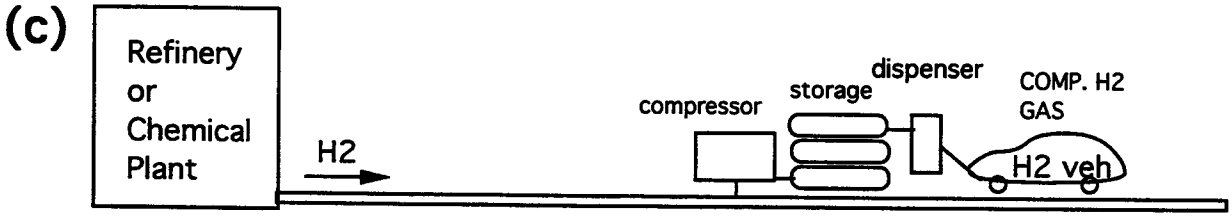

ONSITE REFORMING

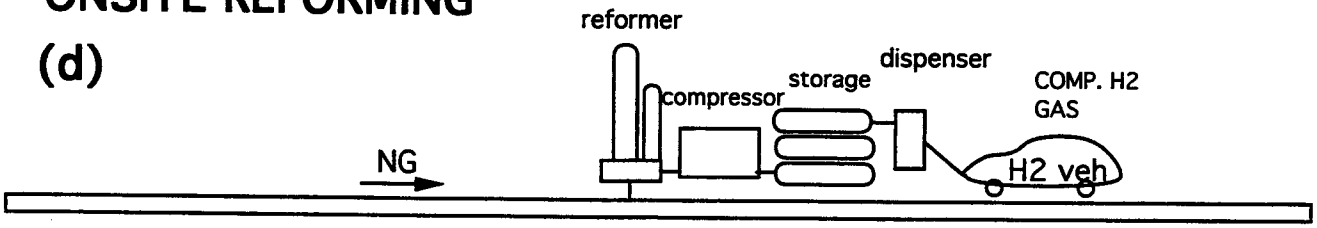

ONSITE ELECTROLYSIS

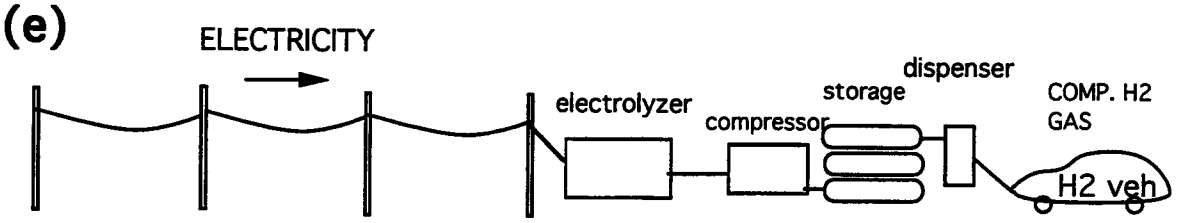

Figure 13. Delivered Cost of Hydrogen Transportation Fuel ($/GJ) vs. Station Size

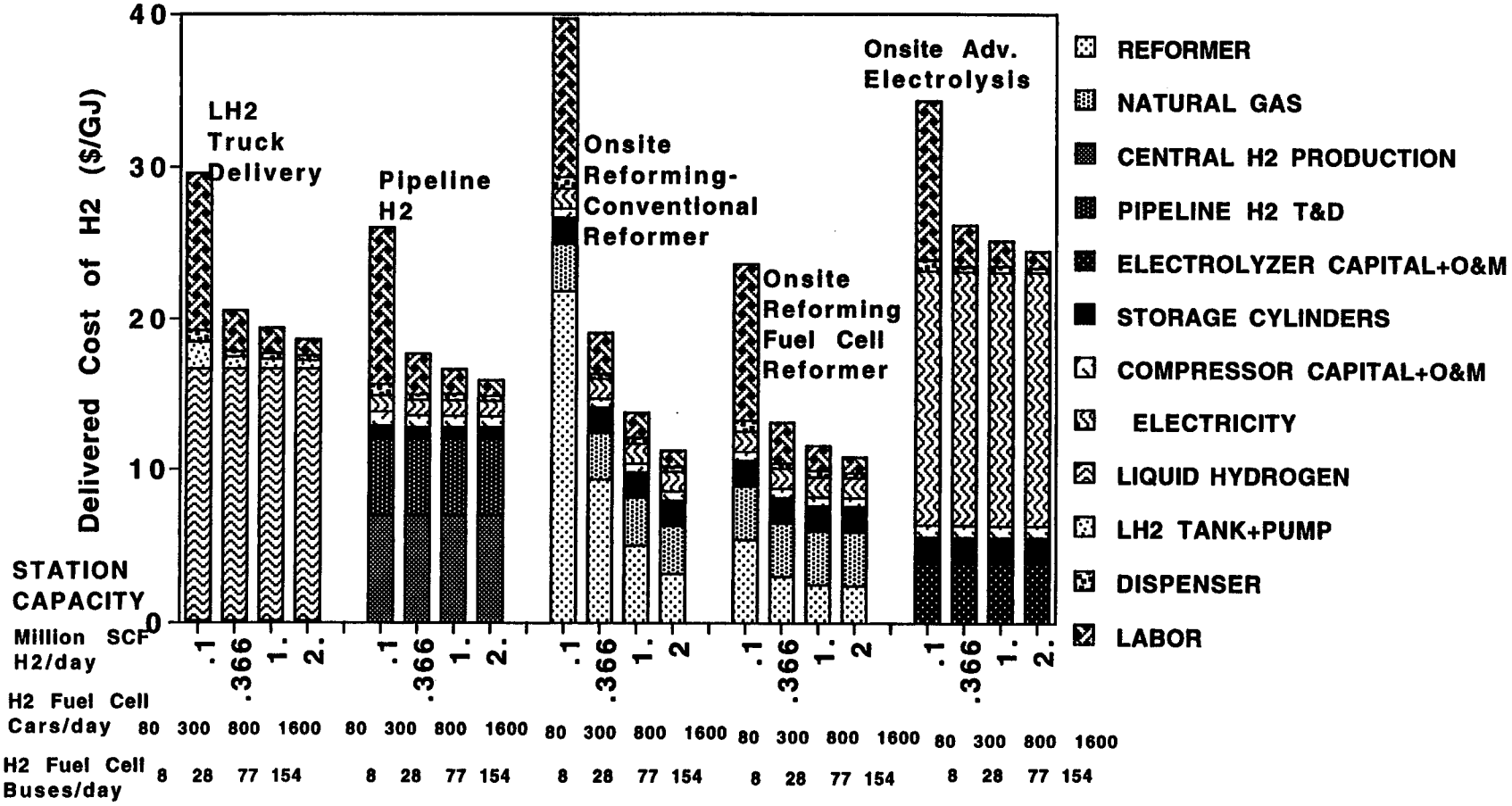

Figure 14. Capital Cost of Hydrogen Infrastructure

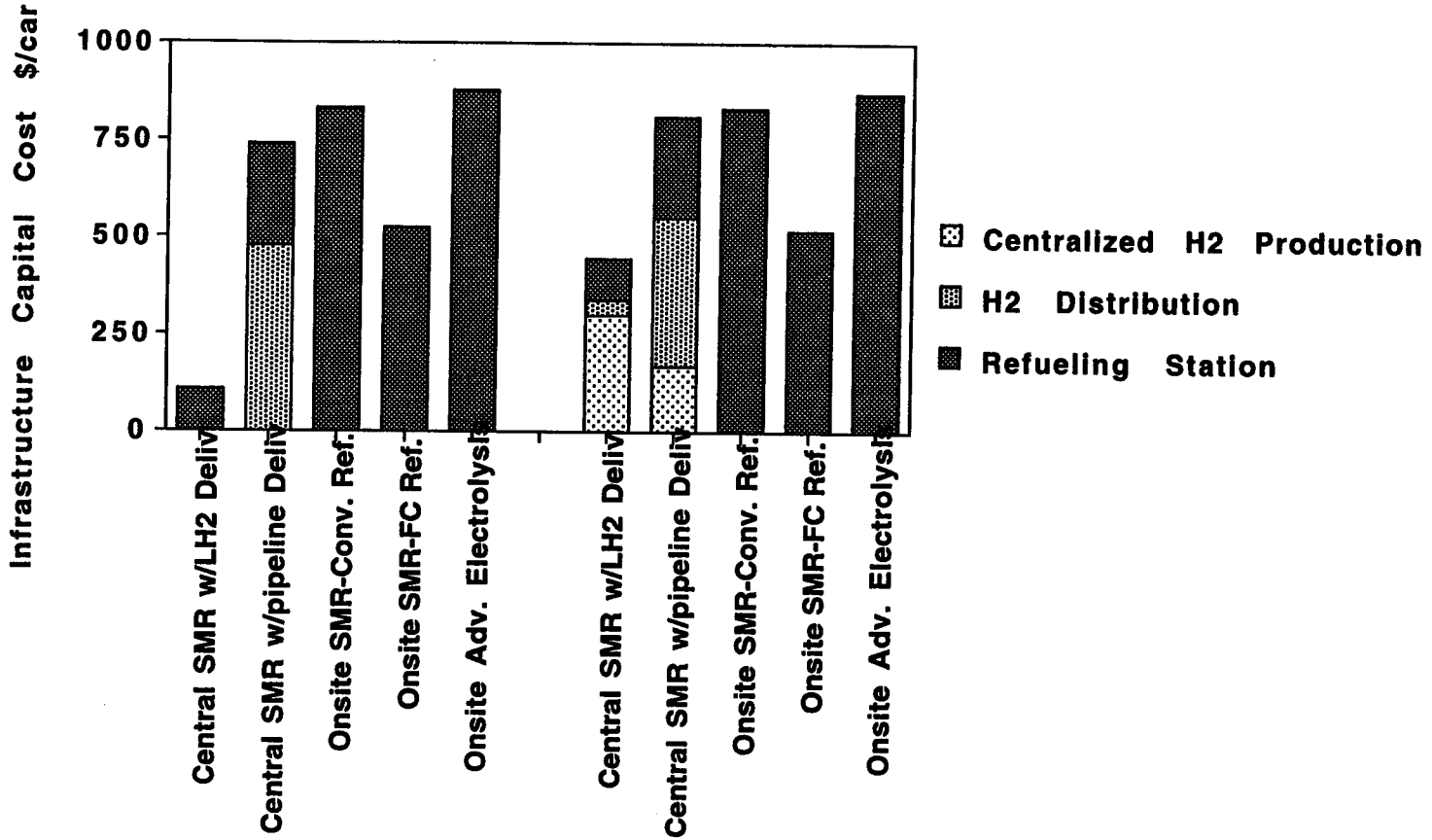

Early Development : Total fleet of 13,000 fuel cell cars. Centralized Options use Existing H2 Production Capacity

Extensive infrastructure development: Total fleet of 1 million fuel cell cars. Centralized options use new H2 Production Capacity

Fig. 15. Comparison of Incremental Costs for Vehicles (Compared to H2 Fuel Cell Vehicle) and Infrastructure (Compared to Gasoline)

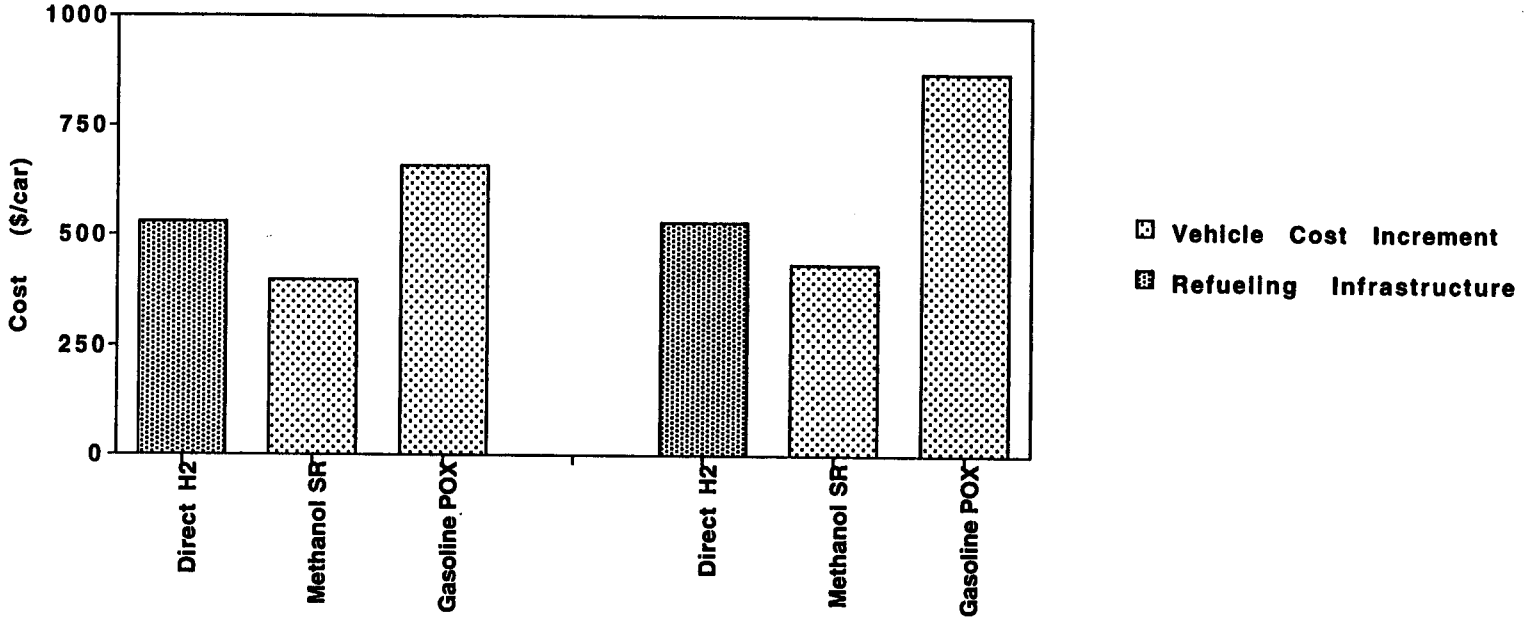

Fuel Cell = $50/kW
Fuel Processor = $15/kW
Peak Battery = $10/kW
H2 cylinder = $500
Motor+Controller=$13/kW
Gasoline or MeOH Tank =$100
Extra Struct. Mass = $1/kg

Fuel Cell = $100/kW
Fuel Processor = $25/kW
Peak Battery = $20/kW
H2 cylinder = $1000
Motor+Controller=$13/kW
Gasoline or MeOH Tank =$100
Extra Struct. Mass = $1/kg

H2 Refueling Infrastructure = $530/car (onsite reforming)
No extra infrastructure cost for gasoline

COUPLING RENEWABLES VIA HYDROGEN INTO UTILITIES: TEMPORAL AND SPATIAL ISSUES, AND TECHNOLOGY OPPORTUNITIES

Joseph J. Iannucci, Susan A. Horgan, James M. Eyer
Distributed Utility Associates
1062 Concannon Boulevard, Livermore CA 94550

Susan Schoenung
Longitude 122 West, Inc.
1010 Doyle Street, Suite 10
Menlo Park, CA 94025

Abstract

This paper discusses the technical potential for hydrogen used as an energy storage medium to couple time-dependent renewable energy into time-dependent electric utility loads. This analysis provides estimates of regional and national opportunities for hydrogen production, storage and conversion, based on current and near-term leading renewable energy and hydrogen production and storage technologies. Appropriate renewable technologies, wind, photovoltaics and solar thermal, are matched to their most viable regional resources. The renewables are assumed to produce electricity which will be instantaneously used by the local utility to meet its loads; any excess electricity was used to produce hydrogen electrolytically and stored for later use. Results are derived based on a range of assumptions of renewable power plant capacity and fraction of regional electric load to be met (e.g., the amount of hydrogen storage required to meet the Northwest region's top 10% of electric load).

For each renewable technology national and regional totals are developed for maximum hydrogen production per year and ranges of hydrogen storage capacity needed in each year (hydroelectric case excluded). The sensitivity of the answers to the fraction of peak load to be served and the land area dedicated for renewable resources are investigated. These analyses can serve as a starting point for projecting the market opportunity for hydrogen storage and distribution technologies. Sensitivities are performed for hydrogen production, conversion, and storage efficiencies representing current and near-term hydrogen technologies.

COUPLING RENEWABLES VIA HYDROGEN INTO UTILITIES: TEMPORAL AND SPATIAL ISSUES, AND TECHNOLOGY OPPORTUNITIES

The primary goal of this project has been to estimate the technical potential for systems comprised of renewable electricity generation and energy storage using hydrogen production, storage, and electricity conversion to meet some or all of a region's demand for electricity. Objectives were to evaluate regional capacity requirements for: renewable electricity generation and hydrogen storage reservoirs required to store renewable energy for use during low resource periods. As an extreme case the combinations of renewable capacity and hydrogen storage necessary to serve each region's entire load was calculated. Backing down from that maximum penetration, the same sizing algorithms were used to serve 80%, 60%, 40%, and 20% of the annual energy requirement.

The basic assumption in this approach is that renewables provide the "primary" energy and hydrogen storage is employed to compensate for time-related mismatches between renewables production and electric loads.

For intermittent renewables, hour-by-hour simulations were used to model the time dependence of three leading technologies–wind, photovoltaics, and solar thermal–in various regions of the U. S. Renewables' regional electricity production patterns were compared to local annual electric load demand shapes.

Figure S-1 shows the schematic model which simulates the flow of energy from the renewables plant to the regional load. The model determines how much renewable resource (e.g. peak megawatts and hence, the land area) is required to meet the specified load pattern, taking into account the temporal mismatch between the source and the load, placing the excess energy into storage as hydrogen.

Analysis for intermittent renewables yields:

- installed capacity of renewables generation
- hydrogen production capacity (via electrolysis)
- hydrogen storage capacity
- fuel cell generation capacity required in each region to meet the demand

For baseload renewables such as hydroelectric power, a simple annual energy production analysis was undertaken.

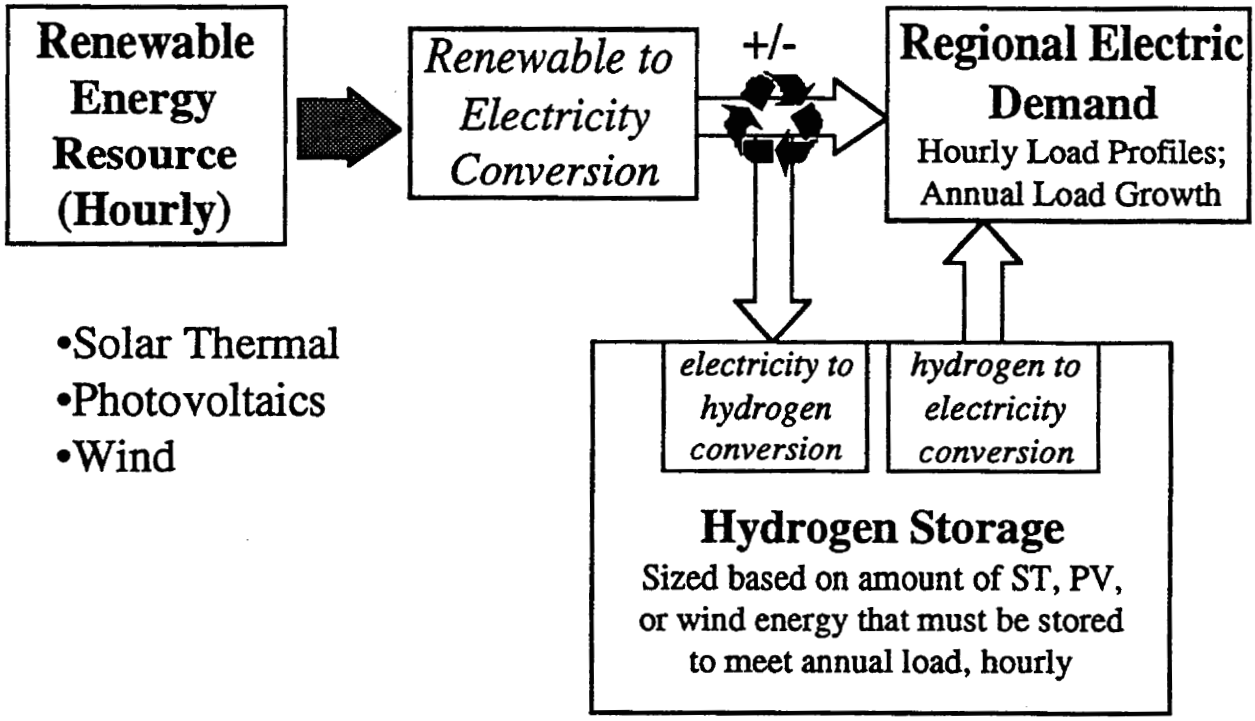

Figure S-1 Modeling Elements

The amount of renewable capacity required to meet the load depends on several variables:

1) the peak load requirements in the region and the annual energy consumed

2) the pattern of energy consumption as compared to the renewable supply pattern, in that poor temporal matching forces more energy to pass through the hydrogen storage unit and suffering its efficiency losses

The number of hours of hydrogen storage required depends primarily on the temporal match between the load and the renewable supply pattern.

The requirement to supply 100% of a region's load is fairly unrealistic, therefore a sensitivity was performed to supplying fractions of that load. To do so, hour-by-hour simulations are undertaken for regional peak loads whose magnitudes have been reduced such that the renewables/hydrogen storage system meets only a portion of annual energy needs (i.e., 20%, 40%, 60%, and 80% of full annual electric energy use).

For each renewable technology, regional estimates have been developed for maximum hydrogen production per year and alternative ranges of hydrogen storage

capacity needed in each year (for intermittent renewables). An energy flowchart for the model is shown in Figure S-2.

Electric peak load in each region is projected for the year 2010, and that year is used as a basis for all analysis. No economic analyses were performed in this study, since the scope of work only includes the technical feasibility and sizing of the components required to supply the loads with electricity.

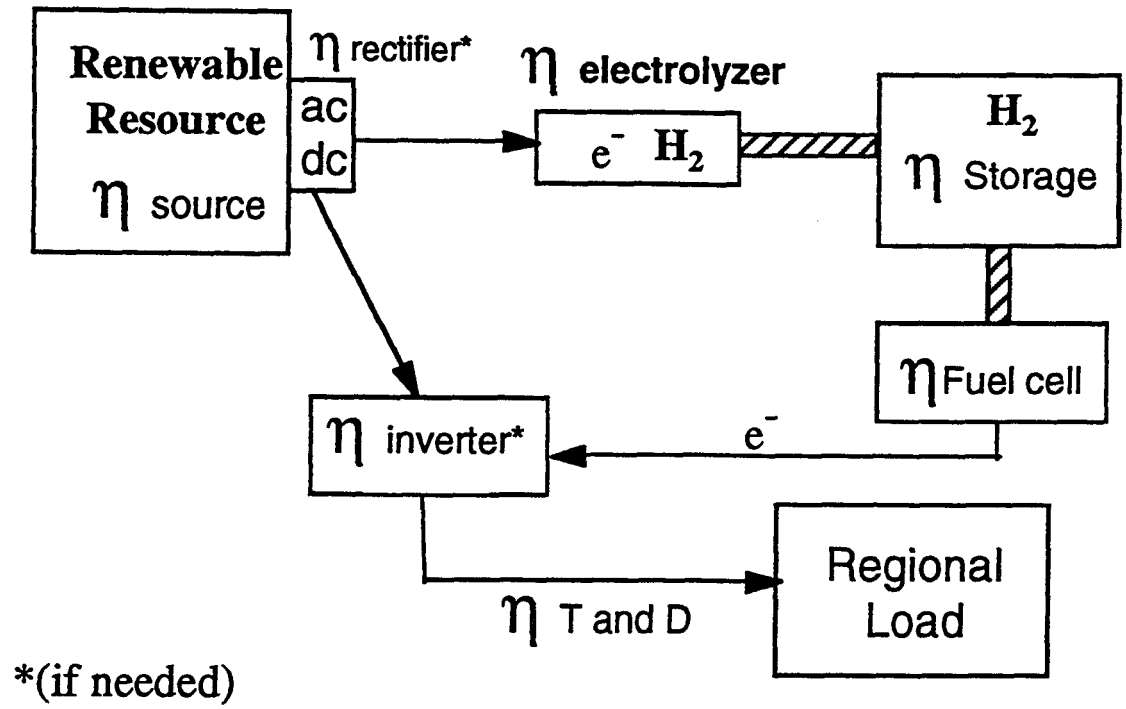

Figure S-2 Energy Flowchart

The analysis results indicate a potentially large market for hydrogen technologies in this application.

There is a very important family of storage and renewables combinations which are all perfectly feasible. It would take an economic analysis to select which of these pairs is optimal, but because the storage requirements decrease so quickly with small increments of renewables capacity beyond the critical size, the optimal economic solution is almost certainly not the critical renewables and critical hydrogen storage plant combination.

To allow the reader to appreciate the tradeoff between storage sizes and renewable plant over-sizing, in all cases the full set of storage and renewables combinations beyond the "critical" sizes is calculated and presented.

The results for the critical case (minimum renewable resource and maximum storage) are shown in Figure S-3.

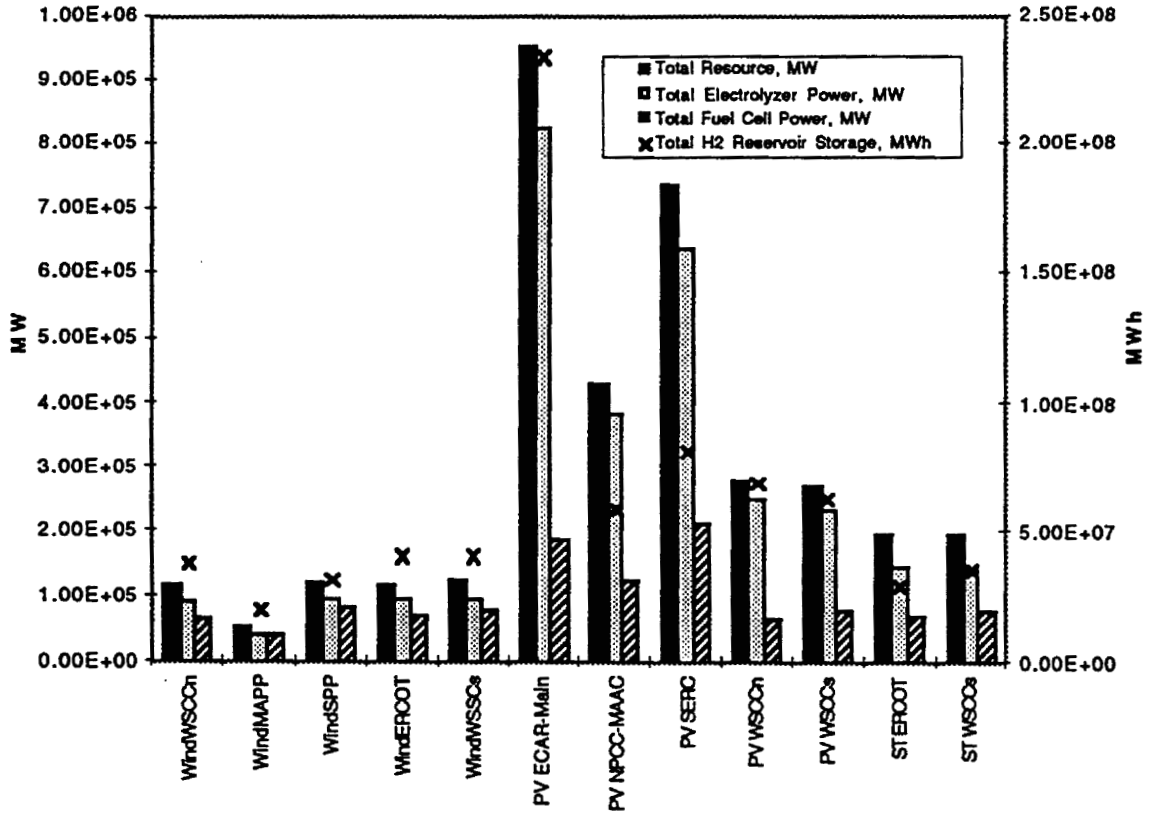

Figure S-3 Results

Each of the renewable/region combinations has its own requirements for hydrogen storage due to a unique matching between load and resource patterns. Wind requires the least storage capacity primarily due to its higher capacity factor.

There are three types of evaluations made by DUA's GenStorCalc model, the MS Excel spreadsheet used to perform the analysis.

First the spreadsheet undertakes a base case sizing for a given generation resource hourly production profile, electric hourly demand profile, and annual maximum demand for electricity (e.g. for the region under investigation).

During sizing GenStorCalc calculates, among other values, the size of the generation resource, the size of the storage reservoir needed, and the amount of hydrogen stored annually in order to satisfy demand for all electricity within the region being investigated. Figure S-4 below is a chart that for typical results that shows daily high and low charge states (amount of total energy stored) for the year, for the base case.

Note that at this scale, the shape is dominated by annual storage needs and that daily variations appear small. Note also that daily filling and emptying of storage determines the electrolyzer size and that most hydrogen is created and used daily.

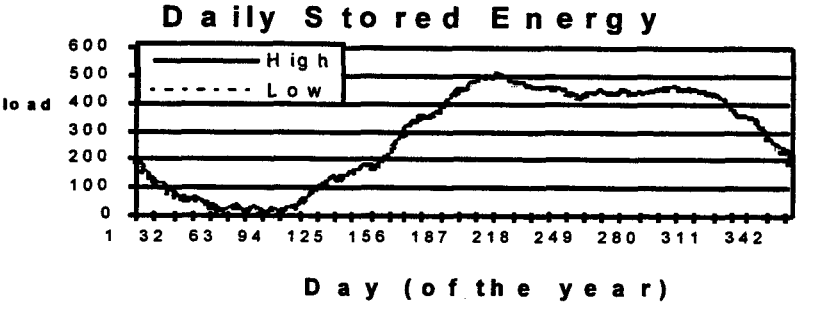

Figure S-4 Daily State-of-charge for the Energy Storage Reservoir

Second, as shown by the chart and numeric values in Figure S-5, the spreadsheet calculates storage reservoir size needed to satisfy all of a region's electricity demand given various degrees of "oversizing" of the generation resource (nameplate generating capacity). Oversizing is relative to the generation resource capacity calculated during the base case sizing, described just above.

The Resource Oversizing table in Figure S-5 shows: 1) generation resource oversizing *factor*, 2) the resulting resource nameplate generation *capacity* (base case capacity times oversizing factor), 3) the smallest energy storage *reservoir size*

needed to meet all energy demand given the oversized generation resource, and 4) the amount of *energy* that is stored throughout the year.

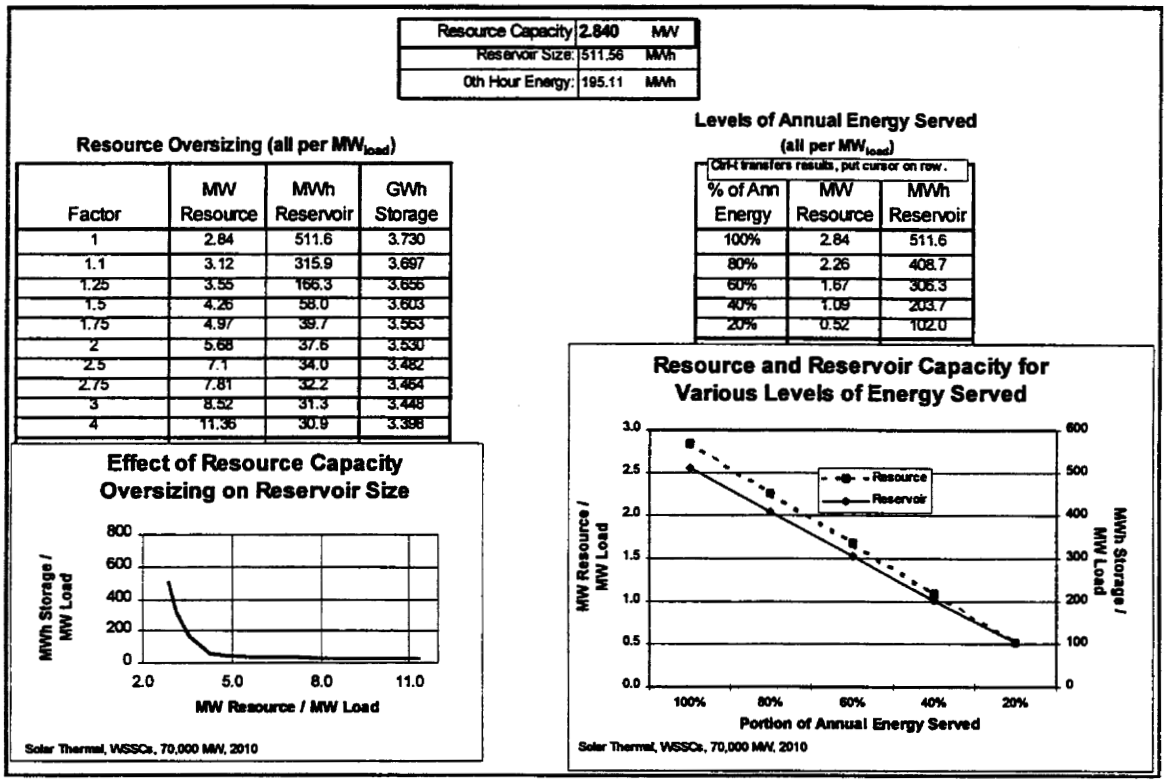

Figure S-5 Results for Resource Oversizing and Levels of Energy Demand Served

Third, GenStorCalc calculates the generation and storage capacity needed to meet only a *portion* of the total use of electric energy within a given region. For this study, sizing is undertaken for resource/reservoir capacity needed to supply 100% of energy used throughout the year, for 80%, for 60%, for 40% and for 20%. Typical results are shown in the Resource and Reservoir Capacity for Various Levels of Energy chart in Figure S-5.

The Levels of Annual Energy Served table in Figure S-5 shows: 1) portion (%) of all annual demand for electric energy met by the generation/storage plant, 2) the smallest generation resource nameplate generation capacity needed to meet the specified portion of annual energy use, and 3) the smallest energy storage reservoir size needed to meet the specified portion of annual energy use.

Table S-1 Selected Renewable Region Definitions (NERC region designations)

PV	Wind	Solar Thermal
SERC	SPP	ERCOT
ECAR / MAIN	MAPP	WSCC South
NPCC / MAAC	ERCOT	
WSCC South	WSCC South	
WSCC North	WSCC North	

The amount of renewable resource in each region was a prime determinate of its selection. Wind resource is the most limited of the three renewables in question, followed by solar thermal and photovoltaics. Thus wind resource size was used to choose its target regions , then solar thermal was selected, and finally photovoltaics was used in all remaining regions and in its most favored locations.

Wind is an enormous resource; several sources have estimated the high quality wind potential to be greater than the US electricity consumption nationally, but have shown regional variations; the Southeast is especially poor in wind resource. We have used regionally adjusted wind resource capacities to determine whether a region is resource or electric utility demand limited.

Flat plate photovoltaics can use any quality of insolation and thus are theoretically feasible throughout any of the regions, its penetration limited only by the annual energy consumption in every region for photovoltaics.

Solar thermal requires high levels of direct normal insolation, normally only available in the Southwest, California, and perhaps the South Central regions. We will assume that solar thermal could produce all of the load demand in those regions but none in the other regions.

Hydrogen storage analysis results

Each analysis case was a combination of an electrical region of the US and a reasonable renewable resource, the process for their selection was discussed in section ggg. When all twelve analysis cases were run, as might be expected, the amount of hydrogen storage, the rating of electrolyser and the quantity of renewable resource required varied dramatically from case to case.

The results should be expected to vary considerably from case to case due to variations in

1. hourly electric load patterns in each region
2. hourly renewables resource availability in each region
3. the interaction between these two patterns
4. the quality of the renewable resource in each region

Table S-2 Results Summary

Resource Type / Region		Resource Capacity MW*	Reservoir Size MWh*	Max. Hourly Charge MWh*	Annual Energy Stored GWh*	Annual Regional Load Factor --	Annual Renewable Capacity Factor --
FFP PV	ECAR - MAIN	5.60	1371.9	4.31	5.66	0.7	0.17
	NPCC - MAAC	3.85	516.8	3.06	3.72	0.5	0.18
	SERC	3.80	416.5	2.91	4.22	0.57	0.21
	WSCCn	4.76	1161.5	3.77	5.15	0.65	0.2
	WSCCs	3.84	894.7	2.98	4.41	0.58	0.23
Solar Thermal	ERCOT	3.14	454.7	2.32	3.70	0.55	0.23
	WSCCs	2.84	511.6	2.03	3.73	0.58	0.3
Wind	ERCOT	1.84	637.1	1.33	2.37	0.55	0.33
	MAPP	1.45	406.5	1.00	2.53	0.55	0.48
	SPP	1.58	516.0	1.13	2.05	0.47	0.33
	WSCCn	1.99	628.2	1.40	3.54	0.65	0.43
	WSCCs	1.78	571.5	1.24	3.16	0.58	0.43

* Per MW of Regional Peak Load

Wind plants required the least amount of MW capacity to meet the annual loads in any of the regions in which it was studied, due to its having the highest annual capacity factor of the three technologies. Solar thermal dishes require the next

most resource since they have the second highest capacity factor, and fixed flat plate photovoltaics needs the largest resource capacity in the regions studied due to its low capacity factor. No presumption should be made of the relative economic attractiveness of this result since no economic analysis is included in this study, only the technical sizing of the components was included.

In each analysis case, the minimum amount of MW to serve the annual load is determined simultaneously with the maximum amount of storage needed; this is called the "critical" renewables/storage combination. Further, we calculated the reduction in hydrogen storage capacity which is made possible by oversizing the renewables capacity beyond these critical sizes.

Cross-technology discussion of WSCCsouth Results

WSCCsouth has appreciable renewable resources for wind, fixed flat plate photovoltaics, and solar thermal dishes and therefore was studied for hydrogen storage applications for all three technologies.

Table S-3 WSCCsouth Results Summary, all renewable technologies (normalized to regional peak loads)

Resource Type / Region		Resource Capacity MW*	Reservoir Size MWh*	Max. Hourly Charge MWh*	Annual Energy Stored GWh*	Annual Load Factor --	Annual Capacity Factor --
PV	WSCCs	3.84	894.7	2.98	4.41	0.58	0.23
Solar Thermal	WSCCs	2.84	511.6	2.03	3.73	0.58	0.3
Wind	WSCCs	1.78	571.5	1.24	3.16	0.58	0.43

* Per MW of Regional Peak Load

Wind requires the second largest amount of hydrogen storage capacity (572 hours) but the lowest MW capacity (145 MW per 100 MW of regional peak load) of the three technologies considered in the WSCCsouth. The high wind capacity factor in WSCCsouth allows a low wind MW capacity to meet the annual energy needs of the region with wind, but the seasonal and daily mismatch of the wind resource with the regional load pattern requires a lot of storage capacity to meet the year's need for hydrogen storage.

Higher MW capacity plants are required for the solar options: 284 MW (per 100 MW of peak regional load) for solar thermal dishes, and 384 MW for fixed flat plate photovoltaics. The fixed flat plate photovoltaics system must have 895 hours of output stored to make it through the year.

The wind plant can be coupled to a 124 MW electrolyser in WSCCsouth but a 203 MW electrolyser is needed for the solar thermal dish plant and a 298 MW unit for the fixed flat plate photovoltaics. These results are driven primarily by the relative capacity factors of the technologies.

WSSCs		
Resource Tech:	FFP PV	
Year:	2010	
Region Peak Load:	70,000	MW
Block Size (MW):	100	MW
Resource to Load Eff.:	0.96	
Resource into Storage Eff.:	0.89	
Storage to Load Eff.:	0.64	
Resource Capacity	3.840	MW

Reservoir Size:	894.70	MWh	
0th Hour Energy:	311.53	MWh	
Annual Max:	894.7	MWh	
Annual Min:	0.00	MWh	
Present State, Last Hr:	311.12	MWh	
Reservoir "Ceiling Size":	894.7	MWh	
"Last Hour minus 0th Hour (Stored)":	-0.42	MWh	0.0
Max Hourly Charge:	2.978	MWh	
Annual Energy Stored:	4.41	GWh	
Annual Load Factor:	.58	(5,084 MWh / MW)	
Annual Capacity Factor:	.23	(2,055 MWh / MW)	

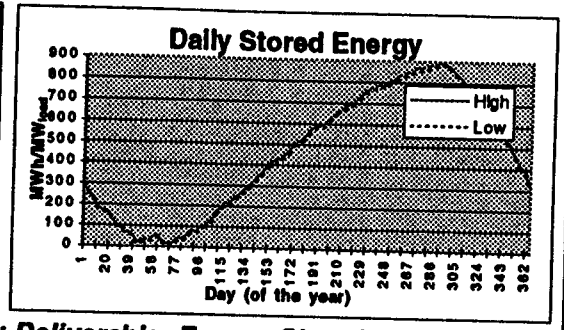

Totals		
Per MW Load		
Resource	3.84	MW
Reservoir	.8947	GWh
H_2 Stored	4.407	GWh
Gross		
Resource	266,817.5	MW
Reservoir	62,629	GWh
H_2 Stored	308,521	GWh
Blocks (100MW)		
Resource Blocks	2,666.2	
Reservoir/Blk	626.3	GWh
H_2 Stored	3,085.2	GWh

Reservoir Status--Hourly *Deliverable* Energy Stored (MWh)

Hour-> Day #	1	2	3	4	5	6	7	8	9	10	11	12	13	14	15	16	17	18	19	20	21	22	23	24
Min	9.89	9.06	2.48	1.89	1.29	0.68	0.00	0.32	1.48	9.90	8.82	8.51	11.11	11.39	11.95	10.99	10.18	9.29	8.35	7.44	6.58	5.77	5.02	4.39
Max	887.68	886.88	886.33	885.68	884.94	884.01	886.06	889.19	884.95	888.94	887.47	888.06	891.45	892.90	894.12	894.70	894.41	893.92	892.27	891.30	890.41	889.53	888.61	888.24
1	910.666	910.24	909.84	909.05	908.46	907.84	907.22	906.58	905.95	905.12	904.65	904.07	904.10	903.78	903.86	902.78	901.89	901.01	900.13	899.27	898.45	897.67	896.93	896.30
2	896.69	896.10	895.62	895.04	894.52	893.97	893.39	892.80	892.19	891.54	890.91	890.78	890.90	890.97	890.96	890.97	890.19	889.12	888.12	887.16	886.28	885.44	884.66	883.96
3	883.34	882.73	882.12	881.53	880.93	880.32	879.68	879.03	878.37	877.71	877.05	876.42	875.79	875.12	874.53	873.79	873.42	872.89	872.42	871.87	870.84	869.66	868.72	867.81
4	867.00	866.42	865.86	865.36	864.86	864.34	863.82	863.27	862.74	862.21	861.71	861.21	860.84	860.41	860.07	859.73	859.42	859.09	858.81	858.54	858.26	857.96	857.66	857.36
5	857.09	856.82	856.57	856.32	856.09	855.84	855.57	855.29	855.00	854.70	854.39	854.08	853.76	853.44	853.14	852.86	852.61	852.39	852.19	851.99	851.81	851.64	851.48	851.33
6	851.19	851.06	850.93	850.80	850.68	850.56	850.44	850.32	850.20	850.08	849.96	849.84	849.72	849.60	849.48	849.36	849.24	849.12	849.00	848.88	848.76	848.64	848.52	848.40
7	848.28	848.16	848.04	847.92	847.80	847.68	847.56	847.44	847.32	847.20	847.08	846.96	846.84	846.72	846.60	846.48	846.36	846.24	846.12	846.00	845.88	845.76	845.64	845.52
8	845.40	845.28	845.16	845.04	844.92	844.80	844.68	844.56	844.44	844.32	844.20	844.08	843.96	843.84	843.72	843.60	843.48	843.36	843.24	843.12	843.00	842.88	842.76	842.64
9	842.52	842.40	842.28	842.16	842.04	841.92	841.80	841.68	841.56	841.44	841.32	841.20	841.08	840.96	840.84	840.72	840.60	840.48	840.36	840.24	840.12	840.00	839.88	839.76
10	839.64	839.52	839.40	839.28	839.16	839.04	838.92	838.80	838.68	838.56	838.44	838.32	838.20	838.08	837.96	837.84	837.72	837.60	837.48	837.36	837.24	837.12	837.00	836.88
11	836.76	836.64	836.52	836.40	836.28	836.16	836.04	835.92	835.80	835.68	835.56	835.44	835.32	835.20	835.08	834.96	834.84	834.72	834.60	834.48	834.36	834.24	834.12	834.00
12	833.88	833.76	833.64	833.52	833.40	833.28	833.16	833.04	832.92	832.80	832.68	832.56	832.44	832.32	832.20	832.08	831.96	831.84	831.72	831.60	831.48	831.36	831.24	831.12
13	831.00	830.88	830.76	830.64	830.52	830.40	830.28	830.16	830.04	829.92	829.80	829.68	829.56	829.44	829.32	829.20	829.08	828.96	828.84	828.72	828.60	828.48	828.36	828.24
14	828.12	828.00	827.88	827.76	827.64	827.52	827.40	827.28	827.16	827.04	826.92	826.80	826.68	826.56	826.44	826.32	826.20	826.08	825.96	825.84	825.72	825.60	825.48	825.36
15	825.24	825.12	825.00	824.88	824.76	824.64	824.52	824.40	824.28	824.16	824.04	823.92	823.80	823.68	823.56	823.44	823.32	823.20	823.08	822.96	822.84	822.72	822.60	822.48
16	822.36	822.24	822.12	822.00	821.88	821.76	821.64	821.52	821.40	821.28	821.16	821.04	820.92	820.80	820.68	820.56	820.44	820.32	820.20	820.08	819.96	819.84	819.72	819.60
17	819.48	819.36	819.24	819.12	819.00	818.88	818.76	818.64	818.52	818.40	818.28	818.16	818.04	817.92	817.80	817.68	817.56	817.44	817.32	817.20	817.08	816.96	816.84	816.72
18	816.60	816.48	816.36	816.24	816.12	816.00	815.88	815.76	815.64	815.52	815.40	815.28	815.16	815.04	814.92	814.80	814.68	814.56	814.44	814.32	814.20	814.08	813.96	813.84
19	813.72	813.60	813.48	813.36	813.24	813.12	813.00	812.88	812.76	812.64	812.52	812.40	812.28	812.16	812.04	811.92	811.80	811.68	811.56	811.44	811.32	811.20	811.08	810.96
20	810.84	810.72	810.60	810.48	810.36	810.24	810.12	810.00	809.88	809.76	809.64	809.52	809.40	809.28	809.16	809.04	808.92	808.80	808.68	808.56	808.44	808.32	808.20	808.08
21	807.96	807.84	807.72	807.60	807.48	807.36	807.24	807.12	807.00	806.88	806.76	806.64	806.52	806.40	806.28	806.16	806.04	805.92	805.80	805.68	805.56	805.44	805.32	805.20
22	805.08	804.96	804.84	804.72	804.60	804.48	804.36	804.24	804.12	804.00	803.88	803.76	803.64	803.52	803.40	803.28	803.16	803.04	802.92	802.80	802.68	802.56	802.44	802.32
23	802.20	802.08	801.96	801.84	801.72	801.60	801.48	801.36	801.24	801.12	801.00	800.88	800.76	800.64	800.52	800.40	800.28	800.16	800.04	799.92	799.80	799.68	799.56	799.44
24	799.32	799.20	799.08	798.96	798.84	798.72	798.60	798.48	798.36	798.24	798.12	798.00	797.88	797.76	797.64	797.52	797.40	797.28	797.16	797.04	796.92	796.80	796.68	796.56
25	796.44	796.32	796.20	796.08	795.96	795.84	795.72	795.60	795.48	795.36	795.24	795.12	795.00	794.88	794.76	794.64	794.52	794.40	794.28	794.16	794.04	793.92	793.80	793.68
26	793.56	793.44	793.32	793.20	793.08	792.96	792.84	792.72	792.60	792.48	792.36	792.24	792.12	792.00	791.88	791.76	791.64	791.52	791.40	791.28	791.16	791.04	790.92	790.80

Reservoir Size:	894.70	MWh
0th Hour Energy:	311.53	MWh
Annual Max:	894.7	MWh
Annual Min:	0.00	MWh
Present State, Last Hr:	311.12	MWh
Reservoir 'Ceiling Size':	894.7	MWh
'Last Hour minus 0th Hour (Stored)':	-0.42	MWh 0.0
Max. Hourly Charge:	2.978	MWh
Annual Energy Stored:	4.41	GWh
Annual Load Factor:	.58	(5,084 MWh / MW)
Annual Capacity Factor:	.23	(2,055 MWh / MW)

Resource Oversizing (all per MW_{load})

Factor	MW Resource	MWh Reservoir	GWh Storage
1	3.84	894.7	4.407
1.1	4.22	755.0	4.375
1.25	4.8	563.0	4.335
1.5	5.76	324.3	4.293
1.75	6.72	232.9	4.266
2	7.68	143.3	4.248
2.5	9.6	94.3	4.220
2.75	10.56	87.3	4.210
3	11.52	80.4	4.200
4	15.36	59.4	4.169

Levels of Annual Energy Served
(all per MW_{load})

% of Ann Energy	MW Resource	MWh Reservoir
100%	3.84	894.7
80%	3.05	717.5
60%	2.27	539.9
40%	1.48	360.6
20%	0.71	184.2

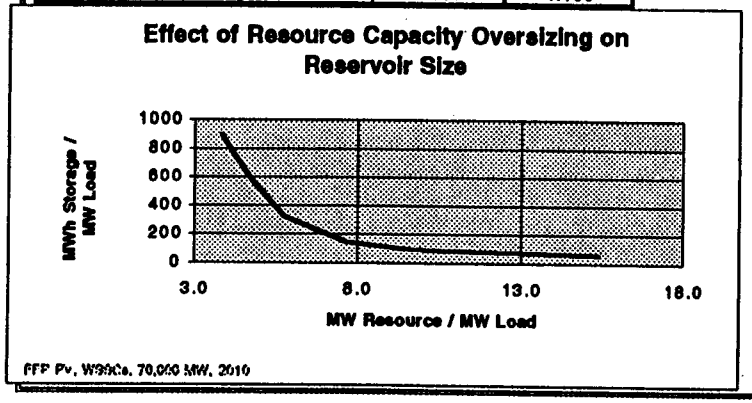

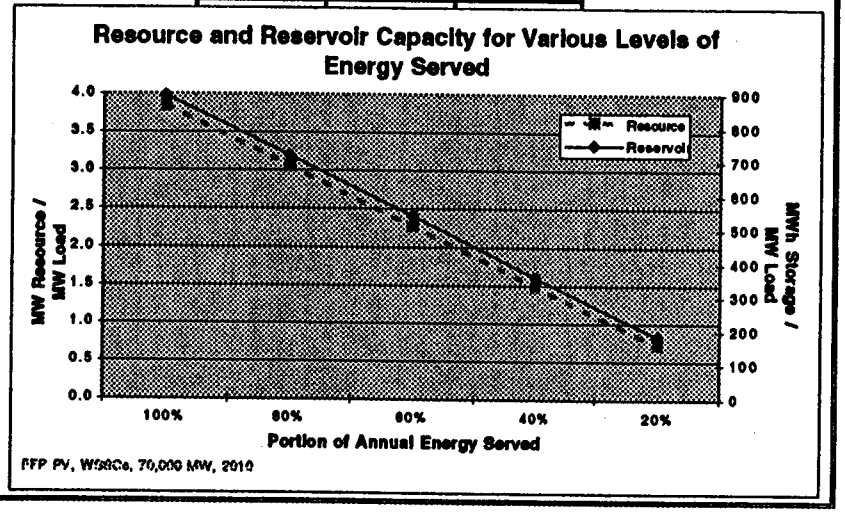

WSSCs		
Resource Tech:	Solar Thermal	
Year:	2010	
Region Peak Load:	70,000	MW
Block Size (MW):	100	MW
Resource to Load Eff.:	0.96	
Resource into Storage Eff.:	0.89	
Storage to Load Eff.:	0.64	
Resource Capacity (All values per MW of Load)	2,840	MW

Reservoir Size:	511.56	MWh
0th Hour Energy:	195.11	MWh
Annual Max:	511.6	MWh
Annual Min:	0.00	MWh
Present State, Last Hr:	195.13	MWh
Reservoir "Ceiling Size":	511.6	MWh
"Last Hour minus 0th Hour (Stored)":	0.02	MWh
Max. Hourly Charge:	2.029	MWh
Annual Energy Stored:	3.73	GWh
Annual Load Factor:	.58	(5,084 MWh / MW)
Annual Capacity Factor:	.3	(2,523 MWh / MW)

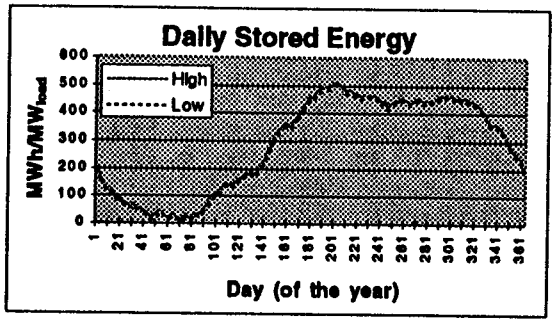

Totals		
Per MW Load		
Resource	2.84	MW
Reservoir	.5116	GWh
H_2 Stored	3.73	GWh
Gross		
Resource	198,790.8	MW
Reservoir	35,809	GWh
H_2 Stored	261,106	GWh
Blocks (100MW)		
Resource Blocks	1,987.9	
Reservoir/Blk	358.1	GWh
H_2 Stored	2,611.1	GWh

Reservoir Status–Hourly *Deliverable* Energy Stored (MWh)

Hour-> Day #	1	2	3	4	5	6	7	8	9	10	11	12	13	14	15	16	17	18	19	20	21	22	23	24
Min	3.06	3.91	2.07	2.09	1.36	0.00	0.00	0.76	2.16	2.74	5.13	5.51	5.02	5.36	5.56	10.35	10.76	9.59	8.59	7.90	6.95	6.06	5.92	4.62
Max	508.23	508.53	504.62	504.11	502.34	502.82	502.36	503.77	508.73	504.76	508.84	508.83	507.66	508.30	508.38	510.30	511.07	511.36	511.27	510.30	508.98	507.89	506.84	506.84
1	194.44	189.52	189.22	192.69	192.04	191.42	190.80	190.67	191.22	192.52	194.59	196.45	196.56	199.50	200.72	201.10	201.30	200.47	199.56	198.72	197.90	197.12	196.39	195.75
2	195.13	194.56	193.90	193.39	192.79	192.13	191.56	191.00	192.04	193.36	194.88	196.81	196.94	197.92	198.63	198.91	198.89	198.01	197.01	196.06	195.16	194.33	193.56	192.86
3	192.23	191.61	191.01	190.41	189.81	189.20	188.64	187.84	188.19	188.84	189.96	190.01	191.67	192.49	192.01	191.23	190.32	189.41	188.47	187.57	186.71	185.91	185.17	184.49
4	184.84	183.22	182.41	181.61	180.81	180.76	180.18	179.58	184.17	186.66	191.97	191.94	192.19	193.22	192.83	192.29	191.39	190.30	189.22	188.24	187.39	186.66	179.62	179.16
5	178.62	177.91	177.20	176.66	176.09	175.26	174.37	173.43	172.66	171.66	170.66	169.65	168.66	167.72	166.76	165.81	164.79	163.66	162.57	161.53	160.55	159.66	158.86	158.16
6	157.56	156.97	156.24	155.50	154.84	154.16	153.24	152.29	152.55	151.99	151.31	150.52	149.19	148.90	147.21	146.77	146.10	145.14	144.04	143.06	142.09	141.27	140.57	139.91
7	139.32	138.15	136.49	136.82	136.14	135.37	134.41	133.59	134.81	134.84	134.97	135.29	135.39	135.20	134.76	134.41	134.03	133.76	132.64	131.53	130.47	129.45	128.53	127.69
8	126.92	126.16	125.42	124.73	124.13	123.53	122.88	122.76	123.79	124.98	125.11	125.20	125.33	124.79	124.54	124.38	124.24	124.13	123.90	123.64	123.39	123.15	122.91	122.69
9	122.50	122.19	121.46	121.78	121.07	120.29	119.54	118.40	118.15	118.25	118.06	118.05	118.04	117.77	117.12	116.41	115.94	115.44	114.40	113.40	112.45	111.57	110.74	109.99
10	109.33	108.68	108.03	107.36	106.73	106.02	105.36	104.81	104.84	104.11	103.20	102.33	101.79	101.64	101.38	101.03	100.69	100.34	99.97	99.57	99.16	98.74	98.32	97.91
11	97.51	97.12	96.73	96.34	95.96	95.58	95.21	94.85	94.50	94.16	93.83	93.51	93.20	92.90	92.61	92.33	92.06	91.80	91.55	91.31	91.08	90.86	90.65	90.45
12	90.26	90.08	89.91	89.75	89.60	89.46	89.33	89.21	89.10	89.00	88.91	88.83	88.76	88.70	88.65	88.61	88.58	88.56	88.55	88.55	88.56	88.58	88.61	88.65
13	88.70	88.76	88.84	88.93	89.03	89.14	89.26	89.39	89.53	89.68	89.84	90.01	90.19	90.38	90.57	90.77	90.98	91.19	91.41	91.64	91.88	92.12	92.37	92.63
14	92.89	93.16	93.44	93.72	94.01	94.31	94.61	94.92	95.24	95.56	95.89	96.22	96.56	96.90	97.25	97.60	97.96	98.32	98.69	99.06	99.44	99.82	100.21	100.60
15	101.00	101.41	101.82	102.24	102.66	103.08	103.51	103.94	104.38	104.82	105.26	105.71	106.16	106.61	107.07	107.53	107.99	108.46	108.93	109.40	109.88	110.36	110.84	111.33
16	111.82	112.31	112.80	113.30	113.80	114.30	114.80	115.31	115.82	116.33	116.84	117.35	117.87	118.38	118.90	119.42	119.94	120.46	120.98	121.50	122.03	122.55	123.08	123.61
17	124.14	124.67	125.20	125.73	126.26	126.79	127.32	127.86	128.39	128.92	129.46	129.99	130.53	131.06	131.60	132.13	132.67	133.20	133.74	134.27	134.81	135.34	135.88	136.41
18	136.95	137.48	138.02	138.55	139.09	139.62	140.16	140.69	141.23	141.76	142.30	142.83	143.37	143.90	144.44	144.97	145.51	146.04	146.58	147.11	147.65	148.18	148.72	149.25
19	149.79	150.32	150.86	151.39	151.93	152.46	153.00	153.53	154.07	154.60	155.14	155.67	156.21	156.74	157.28	157.81	158.35	158.88	159.42	159.95	160.49	161.02	161.56	162.09
20	162.63	163.16	163.70	164.23	164.77	165.30	165.84	166.37	166.91	167.44	167.98	168.51	169.05	169.58	170.12	170.65	171.19	171.72	172.26	172.79	173.33	173.86	174.40	174.93
21	175.47	176.00	176.54	177.07	177.61	178.14	178.68	179.21	179.75	180.28	180.82	181.35	181.89	182.42	182.96	183.49	184.03	184.56	185.10	185.63	186.17	186.70	187.24	187.77
22	188.31	188.84	189.38	189.91	190.45	190.98	191.52	192.05	192.59	193.12	193.66	194.19	194.73	195.26	195.80	196.33	196.87	197.40	197.94	198.47	199.01	199.54	200.08	200.61
23	201.15	201.68	202.22	202.75	203.29	203.82	204.36	204.89	205.43	205.96	206.50	207.03	207.57	208.10	208.64	209.17	209.71	210.24	210.78	211.31	211.85	212.38	212.92	213.45
24	213.99	214.52	215.06	215.59	216.13	216.66	217.20	217.73	218.27	218.80	219.34	219.87	220.41	220.94	221.48	222.01	222.55	223.08	223.62	224.15	224.69	225.22	225.76	226.29
25	226.83	227.36	227.90	228.43	228.97	229.50	230.04	230.57	231.11	231.64	232.18	232.71	233.25	233.78	234.32	234.85	235.39	235.92	236.46	236.99	237.53	238.06	238.60	239.13
26	239.67	240.20	240.74	241.27	241.81	242.34	242.88	243.41	243.95	244.48	245.02	245.55	246.09	246.62	247.16	247.69	248.23	248.76	249.30	249.83	250.37	250.90	251.44	251.97

Solar Thermal WSCCs

Resource Capacity	2.840	MW
Reservoir Size:	511.56	MWh
0th Hour Energy:	195.11	MWh

Resource Oversizing (all per MW_{load})

Factor	MW Resource	MWh Reservoir	GWh Storage
1	2.84	511.6	3.730
1.1	3.12	315.9	3.697
1.25	3.55	166.3	3.656
1.5	4.26	58.0	3.603
1.75	4.97	39.7	3.563
2	5.68	37.6	3.530
2.5	7.1	34.0	3.482
2.75	7.81	32.2	3.464
3	8.52	31.3	3.448
4	11.36	30.9	3.398

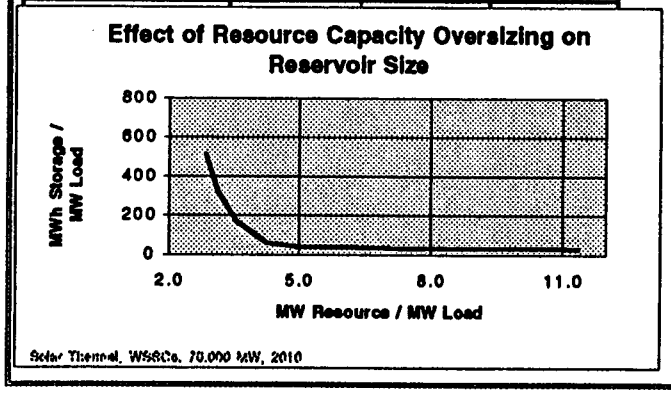

Levels of Annual Energy Served
(all per MW_{load})

% of Ann Energy	MW Resource	MWh Reservoir
100%	2.84	511.6
80%	2.26	406.7
60%	1.67	306.3
40%	1.09	203.7
20%	0.52	102.0

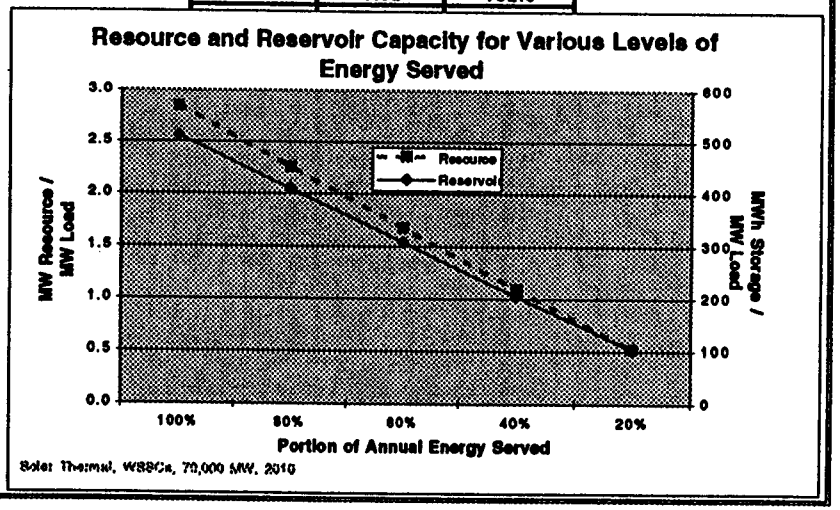

WSSCs		
Resource Tech:	Wind	
Year:	2010	
Region Peak Load:	70,000	MW
Block Size (MW):	100	MW
Resource to Load Eff.:	0.96	
Resource into Storage Eff.:	0.89	
Storage to Load Eff.:	0.64	
Resource Capacity (All values per MW of Load)	1.776	MW

Reservoir Size:	571.47	MWh
0th Hour Energy:	340.23	MWh
Annual Max:	571.5	MWh
Annual Min:	0.00	MWh
Present State, Last Hr:	336.76	MWh
Reservoir "Ceiling Size":	571.5	MWh
"Last Hour minus 0th Hour (Stored)":	-4.47	MWh
Max. Hourly Charge:	1.244	MWh
Annual Energy Stored:	3.16	GWh
Annual Load Factor:	.56	(5,084 MWh / MW)
Annual Capacity Factor:	.43	(3,788 MWh / MW)

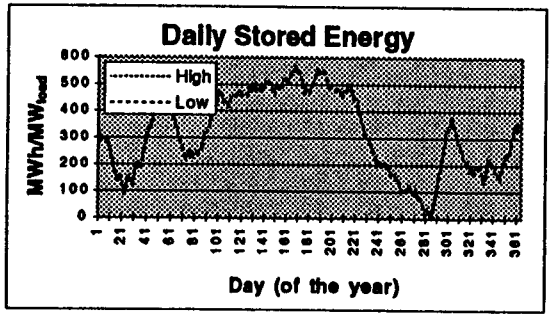

Totals		
Per MW Load		
Resource	1.776	MW
Reservoir	.5715	GWh
H_2 Stored	3.157	GWh
Gross		
Resource	124,310.1	MW
Reservoir	40,003	GWh
H_2 Stored	220,970	GWh
Blocks (100MW)		
Resource Blocks	1,243.1	
Reservoir/Blk	400.0	GWh
H_2 Stored	2,209.7	GWh

Reservoir Status–Hourly *Deliverable* Energy Stored (MWh)

Hour-> Day #	1	2	3	4	5	6	7	8	9	10	11	12	13	14	15	16	17	18	19	20	21	22	23	24
Min	0.36	0.60	1.74	2.90	3.70	4.26	4.81	4.96	5.23	5.76	6.45	7.29	8.23	9.06	8.26	7.21	6.20	5.14	4.10	3.12	2.22	1.43	0.71	0.00
Max	566.77	569.79	569.53	569.58	570.32	570.55	570.94	571.01	571.47	571.51	571.06	571.10	570.59	570.22	569.76	568.98	568.10	567.06	566.06	566.40	567.33	567.55	567.59	566.06
1	939.560	936.69	936.54	937.74	937.18	936.59	935.91	936.27	934.69	933.71	932.89	932.06	931.25	930.44	929.65	928.85	927.99	927.07	926.19	925.92	924.80	923.72	922.99	922.35
2	921.74	921.18	920.56	919.99	919.36	918.79	917.96	917.14	916.29	915.29	914.36	913.42	912.10	912.20	912.89	913.45	911.49	910.46	909.46	908.92	907.63	906.80	906.05	906.34
3	904.74	904.12	903.52	902.92	902.68	902.42	901.69	901.21	900.39	899.51	898.62	897.71	896.82	896.95	895.06	894.22	893.29	892.31	891.37	890.46	889.61	888.80	888.06	887.64
4	887.77	887.14	886.63	885.99	885.39	884.71	884.29	883.84	882.74	881.91	881.07	880.23	879.39	878.66	880.80	881.14	881.20	881.47	881.84	881.96	881.43	881.00	880.63	881.90
5	882.26	882.97	883.39	883.73	884.70	885.50	886.47	887.27	887.76	887.88	887.84	888.01	887.78	887.48	887.22	886.97	886.61	886.68	887.39	887.88	888.96	890.03	891.14	892.26
6	893.08	893.87	894.42	895.10	895.72	896.21	896.81	896.97	896.46	896.06	896.13	896.96	897.32	897.96	900.51	900.80	900.97	900.84	900.72	900.43	900.43	900.69	900.91	899.23
7	899.68	900.99	901.43	902.61	903.71	904.28	904.88	904.78	904.29	903.40	902.39	901.97	900.98	900.40	900.58	897.76	896.86	895.78	895.49	895.85	896.14	896.97	896.53	896.20
8	896.47	894.79	894.11	893.43	892.71	891.90	890.89	890.06	878.87	878.10	876.06	877.44	876.66	876.92	877.09	877.20	877.39	877.60	878.03	878.00	879.86	880.68	881.72	883.70
9	883.66	884.77	885.62	886.44	887.97	888.29	889.05	889.76	890.17	890.89	891.22	891.89	891.71	891.76	891.94	891.96	891.63	890.71	890.46	890.06	889.56	889.10	888.49	887.89
10	887.39	886.85	886.00	885.94	884.66	883.90	883.89	882.43	881.89	880.50	879.87	879.76	877.96	877.09	876.19	875.84	874.49	873.61	873.43	871.48	870.99	869.78	868.97	868.31
11	867.59	866.97	866.29	865.66	864.92	864.26	863.84	862.76	861.69	860.96	860.06	859.14	858.26	857.96	856.59	856.67	854.79	853.66	852.65	851.65	851.01	850.14	849.95	849.66
12	847.99	847.94	848.89	844.42	845.54	844.84	845.99	845.53	841.44	840.99	839.25	838.14	837.04	836.07	834.47	833.92	832.60	831.42	830.47	829.99	829.84	827.48	826.91	825.66
13	825.17	824.50	823.84	823.17	822.48	821.70	820.76	819.70	819.63	817.56	816.50	815.49	814.48	813.48	812.50	811.53	810.62	809.38	808.29	807.23	806.23	805.92	804.51	803.76
14	803.09	802.43	801.77	801.10	800.42	799.80	799.07	797.92	796.85	795.49	794.44	793.49	792.42	791.44	790.47	789.50	788.49	787.36	786.92	786.09	785.48	785.27	784.97	784.39
15	783.71	783.45	783.71	783.80	783.80	783.21	782.84	782.67	781.78	780.79	779.86	778.86	777.85	776.85	775.87	774.89	773.87	772.81	771.36	770.26	769.47	769.84	769.76	769.86
16	764.91	765.60	766.76	767.42	768.26	768.10	768.76	767.76	766.46	765.96	764.48	763.90	762.90	761.90	760.93	759.97	759.01	758.04	757.06	756.04	755.04	754.00	753.00	751.99
17	750.55	749.88	749.16	748.48	747.80	747.07	746.29	745.48	744.65	743.63	742.72	741.84	740.99	740.18	739.32	738.49	737.66	736.81	735.83	735.26	734.40	733.55	732.85	732.48
18	733.43	732.80	732.06	732.08	733.76	733.48	733.76	732.99	733.06	734.04	734.34	734.67	735.14	735.73	736.26	736.81	736.85	737.20	737.50	736.59	736.77	736.84	737.22	737.77
19	738.17	738.59	739.16	740.02	740.96	741.61	741.86	742.29	742.09	743.02	744.25	744.92	745.89	746.26	746.99	747.60	748.06	748.72	749.58	750.61	751.44	752.48	753.59	754.74
20	755.92	756.97	757.93	758.43	759.34	759.89	760.39	760.92	761.33	761.33	760.67	759.89	758.94	757.90	756.93	756.44	756.02	755.66	754.90	753.90	753.76	753.40	753.48	753.53
21	750.14	749.45	748.92	748.36	747.64	746.62	745.85	744.91	743.73	742.69	741.65	740.69	739.64	738.66	737.70	736.74	735.78	734.84	733.54	732.49	731.50	730.69	729.78	729.06
22	728.37	727.70	727.09	726.39	725.88	724.99	723.81	722.86	721.91	720.79	719.76	718.74	717.73	716.71	715.78	714.73	713.71	712.89	711.90	710.45	709.48	708.66	707.78	707.06
23	706.91	706.58	704.82	704.06	703.30	702.42	701.34	700.20	699.02	697.84	696.77	695.62	694.49	693.58	692.20	691.25	690.13	688.92	687.74	686.60	685.59	684.53	684.10	684.64
24	684.61	687.01	686.22	689.11	690.92	691.41	692.60	693.66	694.46	695.56	696.92	697.85	698.66	699.73	700.90	701.88	702.99	703.92	704.94	705.94	707.08	708.10	708.90	710.46
25	711.89	712.90	714.19	715.95	716.57	717.79	719.06	720.14	721.12	721.86	722.84	723.87	724.86	725.46	726.31	727.20	728.32	729.36	730.97	730.42	730.09	729.71	730.39	731.45
26	732.17	733.73	735.28	736.92	738.45	739.36	740.10	740.74	741.73	741.71	740.68	740.66	740.89	741.89	743.84	745.55	746.40	746.29	747.27	746.77	746.53	746.44	746.44	747.89

Reservoir Size:	571.47	MWh	
0th Hour Energy:	340.23	MWh	
Annual Max:	571.5	MWh	
Annual Min:	0.00	MWh	
Present State, Last Hr:	335.78	MWh	
Reservoir "Ceiling Size":	571.5	MWh	
"Last Hour minus 0th Hour (Stored)":	-4.47	MWh	0.0
Max. Hourly Charge:	1.244	MWh	
Annual Energy Stored:	3.18	GWh	
Annual Load Factor:	.58	(5,084 MWh / MW)	
Annual Capacity Factor:	.43	(3,798 MWh / MW)	

Resource Oversizing (all per MW_{load})

Factor	MW Resource	MWh Reservoir	GWh Storage
1	1.78	571.5	3.157
1.1	1.95	428.5	3.094
1.25	2.22	294.7	3.019
1.5	2.66	266.4	2.926
1.75	3.11	244.6	2.861
2	3.55	226.6	2.812
2.5	4.44	193.9	2.743
2.75	4.88	184.2	2.717
3	5.33	174.4	2.695
4	7.1	136.2	2.636

Levels of Annual Energy Served
(all per MW_{load})

% of Ann Energy	MW Resource	MWh Reservoir
100%	1.78	571.5
80%	1.42	455.9
60%	1.07	341.5
40%	0.71	226.2
20%	0.36	115.6

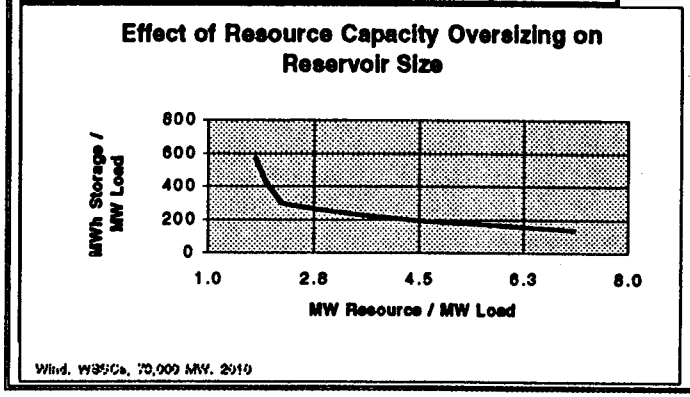

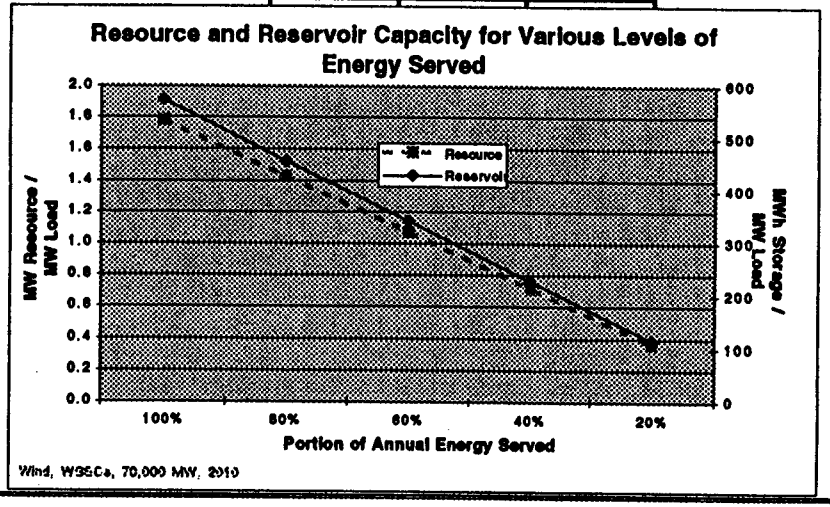

Onboard Storage Alternatives for Hydrogen Vehicles

by
Gene D. Berry
Salvador M. Aceves
Lawrence Livermore National Laboratory
7000 East Ave., L-640
Livermore, CA 94551
(510) 422 0864
fax (510) 423 0618
berry6@llnl.gov
saceves@llnl.gov

Abstract

Three viable technologies for storing hydrogen fuel on cars are currently available: compressed gas, metal hydride adsorption, and cryogenic liquid. However, each of these has significant disadvantages: volume, weight, boiling losses, or energy to compress or liquefy the hydrogen. Two alternative approaches are analyzed in this paper: pressure vessels with cryogenic capability and a combination of a metal hydride and liquid hydrogen storage. These alternatives are compared to baseline compressed hydrogen and liquid hydrogen storage in terms of volume, vehicle range, dormancy, energy required for fuel processing, and cost.

The results indicate that the alternative methods can result in a reduced volume, if packaging is a constraint; or in an extended range, if this is a desirable feature. Cryogenic pressure vessels have reduced boiling losses when compared to liquid hydrogen systems, even when insulation is reduced by a factor of 5. Energy requirements and cost estimates also look favorable for the alternative systems.

This paper will appear in a special hydrogen edition of Energy & Fuels.